Understanding the molecular, cellular, and circuit defects characterizing the early stages of Alzheimer's disease

Daniel Michael Virga

Submitted in partial fulfillment of the
requirements for the degree of
Doctor of Philosophy
under the Executive Committee
of the Graduate School of Arts and Sciences

COLUMBIA UNIVERSITY

2023

Abstract

Understanding the molecular, cellular, and circuit defects characterizing the early stages of Alzheimer's disease

Daniel Michael Virga

One of the most foundational and personal philosophical questions one can ask is what makes you, you? In large part, you are made up of your relationships, experiences, and memories. The hippocampus, a brain region which is critical for the formation of memories, has been the focus of neuroscience research for decades due partially to this function, which is foundational to our individuality. In Alzheimer's disease (AD), one of the most common and well-researched neurodegenerative diseases in the world, the hippocampus is one of the earliest targets. Despite extensive work on AD, we still lack a coherent understanding of what is causing the disease, the mechanisms by which it is causing neuronal dysfunction and death within the hippocampus and other brain regions, and how it ultimately causes deficits in cognition and behavior, leading to an erosion of our selves. In this thesis, I explore three independent but related questions: 1) what molecular mechanisms are causing early synaptic loss in AD, specifically within the hippocampus, 2) what molecular effectors are responsible for establishing and maintaining intracellular architecture in hippocampal neurons, which are exploited in early AD, and 3) how and when does the hippocampal circuit dysfunction in AD progression? Using a variety of experimental techniques, ranging from in utero and ex utero electroporation, primary murine and human neuronal cell culture, longitudinal confocal microscopy, immunohistochemistry, biochemistry, cell and molecular biology, *in vivo* two-photon calcium imaging, and behavioral assays, I have found that, within CA1 of the hippocampus, synapse loss requires degradation of the dendritic mitochondrial network, activity and input specificity are driving mitochondrial compartmentalization within CA1 neurons through the same pathway that is aberrantly overactivated in AD, and the hippocampal circuit is overly rigid in encoding the environment as the disease progresses.

Table of Contents

List of Figures

List of Abbreviations & Acronyms

2P	Two-photon microscopy
4SA	Quadruple alanine point mutations (S309, T441, S528, S547)
AA	Double alanine point mutations (S155A, S172A)
AD	Alzheimer's disease
ADP	Adenosine diphosphate
AICD	APP intracellular domain
AMP	Adenosine monophosphate
AMPA	α-amino-3-hydroxy-5-methyl-4-isoxazole propionate
AMPK	AMP-activated Kinase
APP	Amyloid precursor protein
APPInd	Amyloid precursor protein carrying the Indiana mutation (V717F)
APPSwe	Amyloid precursor protein carrying the Swedish mutation (K670N/M671L)
ATG1	Autophagy related 1
ATP	Adenosine triphosphate
AV	Autophagic vacuoles
Aβ	Amyloid-β
Aβ40	Amyloid-β, amino acids 1-40
Aβ42	Amyloid-β, amino acids 1-42
Aβ42o	Amyloid-β, amino acids 1-42 oligomers
BFP	Blue fluorescent protein
BIN1	Bridging integrator 1

BTSP	Behavioral timescale synaptic plasticity
ca-AMPK	Constitutively active AMPK
CA1	Cornu Ammonis 1
CA2	Cornu Ammonis 2
Ca^{2+}	Calcium
CA3	Cornu Ammonis 3
CAMKK2	Calcium/Calmodulin-dependent kinase kinase 2
Cas9	CRISPR associated protein 9
cDKO	Conditional double knock-out
CMV	Cytomegalovirus
CNS	Central nervous system
COMIC	Constriction of mitochondrial inner compartment
CRISPR	Clustered regularly interspaced short palindromic repeats
CTFα	Carboxyl terminal fragment α
CTFβ	Carboxyl terminal fragment β
DG	Dentate gyrus
DIV	Days *in vitro*
DMSO	Dimethyl sulfoxide
DNA	Deoxyribonucleic acid
Drp1	Dynamin-1-like protein
DsRed	Discosoma red fluorescent protein
E15	Embryonic development day 15

EC	Entorhinal cortex
EGFP	Enhanced green fluorescent protein
EM	Electron microscopy
ER	Endoplasmic reticulum
EUE	Ex utero electroporation
F/F	Double-floxed genetic allele
FAD	Familial Alzheimer's disease
FIJI	Fiji is Just Image J
FIS1	Fission 1
fMRI	Functional magnetic resonance imaging
GCaMP6f	GFP calmodulin protein 6 fast
GCaMP6s	GFP calmodulin protein 6 slow
GCaMP7f	GFP calmodulin protein 7 fast
GTPase	Guanosine triphosphatase
hAPP	Human APP
HEK	Human embryonic kidney
hESC	Human embryonic stem cell
Het	Heterozygous
hTau	Human tau
IMM	Inner mitochondrial membrane
iN	Induced neurons
Ind	Familial AD Indiana mutation (V717F)

INV42	Control, Inverted peptide of 42 amino acids
IP	Immunoprecipitation
IUE	In utero electroporation
J20	B6.Cg-Zbtb20Tg(PDGFB-APPSwInd)20Lms/2Mmjax AD Mouse model
JNK3	c-Jun N-terminal kinase 3
KCl	Potassium chloride
KI	Kinase inactive
KI	Knock-in
Kir2.1	Potassium inward rectifying channel 2.1
KM670/671NL	Lysine 670 to Asparagine, Methionine 671 to Leucine double-point mutation
KO	Knock-out
LAMP1	Lysosomal associated membrane protein 1
LC3	Microtubule-associated protein 1A/1B light chain 3, autophagosome associated protein
LEC	Lateral entorhinal cortex
LKB1	Liver kinase B1
Lphn3	Latrophilin 3
LTD	Long-term depression
LTP	Long-term potentiation
MCI	Mild cognitive impairment
MEC	Medial entorhinal cortex
mEPSC	Miniature excitatory potential synaptic currents
MFF	Mitochondrial fission factor

Mfn1	Mitofusin 1
Mfn2	Mitofusin 2
MiD49	Mitochondrial dynamics protein 49
MiD51	Mitochondrial dynamics protein 51
Mito	Mitochondria
Mt	mitochondria
mTagBFP2	Middle tumor antigen blue fluorescent protein 2
MTFR1L	Mitochondrial fission regulator 1-like protein
MTFR1LS2D	MTFR1L carrying two activating point mutations (Serine 103 to Aspartic Acid, Serine 238 to Aspartic Acid)
N	Number of replicates
N2A	Neuro2A neuroblastoma cells
ND	Neurodegenerative
NFT	Neurofibrillary tangles
Ngn2	Neurogenin 2
NMDA	N-methyl-D-aspartate
NUAK	AMPK-regulated kinase novel (nua) kinase family kinase
OMM	Outer mitochondrial membrane
OPA1	Optic atrophy protein 1
P165	Postnatal day 165
P21	Postnatal day 21
P2A	Porcine teschovirus-1 2A, self-cleavage genetic sequence
p3	Protein 3

P75	Postnatal day 75
P90	Postnatal day 90
pCAG	Plasmid containing a CMV enhancer element, the promoter region, the first exon, and the first intron of chicken β-actin gene, and the splice acceptor of the rabbit β-Globin gene
PDGFβ	Platelet derived growth factor β
PICALM	Phosphatidylinositol Binding Clathrin Assembly Protein
pLKO	Replication-incompetent lentiviral control vector
PN	Pyramidal neuron
PS1/2	Presenilin 44928
PSC	Pluripotent stem cell
PSEN1/2	Presenilin 44928
rAAV	Recombinant adeno-associated virus
RAB11	Ras-associated protein RabB11
RFP	Red fluorescent protein
ROI	Region of interest
S262A	Serine 262 to Alanine point mutation
sAPPα	Soluble amyloid precursor protein α
sAPPβ	Soluble amyloid precursor protein β
SCE	Single cell electroporation
SEM	Standard error of the mean
shNT	Non-targeting shRNA control
shRNA	Small hairpin ribonucleic acid

SL	Stratum lucidum
SLM	Stratum lacunosum moleculare
SM	Stratum moleculare
SO	Stratum oriens
SP	Stratum pyramidalis
SR	Stratum radiatum
STO-609	1,8-Naphthoylene benzimidazole-3-carboxylic acid
Swe	Familial AD Swedish mutation (K670N/M671L)
Tau	Tubulin associated unit
Tg	Transgenic
ULK1/2	Unc-51-like kinase 44928
V717F	Valine 717 to Phenylalanine point mutation
Veh	Vehicle control
VGCC	Voltage-gated calcium channel
VPS34	Phosphatidylinositol 3-kinase
WT	Wild-type
YFP	Yellow fluorescent protein

Acknowledgments

First, I'd like to thank all of my colleagues, past and present, in the Polleux lab. In particular, I'd like to thank Dr. Annie Lee, Dr. Heike Blockus, Dr. Justin O'Hare, Dr. Tommy Lewis, Dr. Yusuke Hirabayashi, Sergio Bernal-Garcia, Kevin Gonzalez, and Stevie Hamilton. Without Annie, I wouldn't have found the lab or this project, and I wouldn't have been set up to succeed in the ways that I was. Without Drs. Heike, Tommy, and Yusuke, I wouldn't have learned the vast majority of the baffling complex techniques that I learned throughout my time here. Specific thanks to Heike for her willingness to train me on all of the in *vivo* surgeries and imaging on which the majority of my thesis rested. Additional thanks to Justin, without whom I wouldn't have been able to analyze any of the two-photon data in this project. Without Sergio, Kevin, and Stevie, I wouldn't have remained sane throughout this journey. The three of them truly provided a foundation against which I could lean when I genuinely didn't think I could push through. In particular, Kevin's help navigating *in vivo* imaging while also keeping things funny made 2:00am imaging sessions and working in the height of a pandemic a little more bearable; Sergio's camaraderie as the only other Biology person made me feel much less isolated; and Stevie's truly incomparable friendship and support made every second a little bit better—I couldn't have asked for a better bench mate and wouldn't have lasted without her scientific collaboration, but more importantly her friendship. Thank you also to Qiaolian Liu, the true hero of any work coming out of the Polleux lab, who supplied me not only with never-ending kindness, but with a seemingly never-ending supply of mice—not a single experiment in this thesis would've been possible without her. Finally, I'd like to thank all of the other past and present members of the Polleux lab, including Natalie Park, Rhythm Sharma, Melba Colon, Dr. Miyako Hirabayashi, Dr. Daniel Iascone, Dr. Ewoud Schmidt, Dr. Martina Proietti Onori, Dr. Eugenie Peze-Heidsieck, Dr. Carlos Diaz Salazar Albeda, Dr. Emiliano Zamponi, and Dr. Victoria Hewitt.

I'd like to acknowledge my qualifying and thesis committees, all of whom supplied important input and suggestions for my project, including Dr. Wes Grueber, Dr. Marko Jovanovic, Dr. Attila Losonczy, and Dr. Erin Barnhart. An additional thank you to Dr. Martie Chalfie and Dr. Wes Grueber for their mentorship during my rotations, which genuinely shaped my initial time here at Columbia. I'd also like to acknowledge Dr. Franck Polleux, my thesis advisor, for providing me the space and funding to grow as an independent researcher.

I’d like to thank everyone who supported me from my cohort, as well as everyone in the Department of Biological Sciences.

I’d like to thank every teacher I have ever had throughout my education—in grade school for putting up with my insistence on being the best, in high school for being models of adulthood and success in my life and getting me into college when it didn’t look like that would happen, and in college for allowing me to fully realize who I was and what I wanted to achieve in life and did everything in their power to get me there.

I’d like to acknowledge the sacrifice of every single mouse at the hands of my research. With hundreds of *successful* surgeries during my time at Columbia, the countless number of mice whose lives were sacrificed for science made this entire thesis possible.

Finally, and most importantly, I wouldn’t have made it through this journey if it wasn’t for my friends and chosen family. Thank you for knowing the real me and supplying me endless, unconditional love, even when I might not have returned it. This is really for them.

Dedication

This thesis is dedicated in its entirety to my sister, Bea Alfia Virga, and the Queer community of New York City—past, present, and future.

Chapter 1: Introduction

Our memories make us who we are. They are these mysterious, intangible things that guide what choices we make and how we behave. Memories also act as building blocks for our personalities and sense of selves, stacking upon themselves over time to form a seldom complete representation of us. Oftentimes, these building blocks are replaced or re-examined, sometimes by traumatic force, other times with careful, deliberate effort and reflection. Nevertheless, you are continuously adding, removing, and reshaping these blocks to better fit your current self and experiences, the sum of which is you. Unfortunately, in diseases in which memories either cannot be formed or they are lost or damaged, such as in Alzheimer's disease, the fragility our selves is exposed—building blocks are gradually lost or damaged, the most vulnerable of which are those most recently added, the most vigilant of which are those at the foundations containing the most redundancy, until whole pillars of our selves are lost and we are neither recognizable to ourselves nor the people we care most about.

Neurodegenerative diseases that impact our selves and our ability to navigate the world are devastating and often have impossibly complex etiologies. Since being described in the early 1900's by Alois Alzheimer and Oskar Fischer, our understanding of Alzheimer's disease has expanded exponentially. Nevertheless, we still have no cure. Understanding how exactly a disease such as Alzheimer's disease impacts the brain—at molecular, cellular, circuit, and behavioral levels—is critical for therapeutic intervention. Though significant work has aimed to understand the molecular, and to some extent cellular, impacts of Alzheimer's, work that bridges from molecular to behavior, or focuses explicitly on circuit effects, is limited.

The aim of this thesis is to better understand how one of the most effected regions of the brain, the hippocampus, is changed throughout progression of Alzheimer's disease—mechanistically and functionally. The hippocampus is one of the very first areas of the brain impacted in Alzheimer's disease. Concurrently, spatial memory and navigation deficits are some of the earliest symptoms reported in most individuals with Alzheimer's disease. Importantly, one of the main functions of the hippocampus is to support spatial learning, memory, and navigation. Therefore, studying spatially tuned cells in the hippocampus in an Alzheimer's disease model is critical for understanding how the disease causes

cognitive and behavioral deficits. This thesis answers three fundamental questions: what are the molecular mechanisms driving synaptic loss in the hippocampus during Alzheimer's, what are the effectors responsible for maintaining hippocampal intracellular organization under physiological conditions, and how does Alzheimer's disease progression affect the hippocampal circuit?

First, I will introduce the necessary context and background information critical for understanding how Alzheimer's impacts the hippocampus. This introduction is divided into five sections, the first three of which will cover the hippocampus—its functions, anatomy, and connectivity, with specific focus on its populations of spatially tuned cells, while the final two sections focus on Alzheimer's disease—its clinical/pathological features, the role that Aβ plays in disease pathology, models used to study the disease, and the functional effects of AD, with specific focus on its impact on spatially tuned populations within the hippocampus. The thesis will then continue with three chapters directly addressing the three previously mentioned questions. I will end the thesis with a discussion summarizing the findings in Chapters 2-4, highlighting how they add to the broader context of the field, and what questions are left unanswered to be explored in future experiments.

1.1 Long-term Episodic Memory & Spatial Memory of the Hippocampus

The hippocampus is a relatively small, seahorse-shaped cortical structure hidden within the medial temporal lobes of each hemisphere of the brain. Found in all mammals (Insausti, 1993), the hippocampus was the focus of much of the pioneering research on learning and memory, and, to this day, remains a highly researched brain region in this sub-field of neuroscience. Though the hippocampus is not a recently discovered brain region, its broad functions have only recently been described, with much of what we know still remaining rather incomplete, complex, and highly debated. Below, I will discuss the functions of the hippocampus, specifically highlighting its role in declarative memory and spatial memory.

In 1953, a now famous individual named Henry Molaison, better known as Patient H.M., underwent a bilateral resection of large sections of his medial temporal lobes, including his hippocampi, in an attempt to prevent debilitating epileptic seizures. Though his seizures did stop as a result of his resection, Henry began showing severe anterograde amnesia, failing to form new memories (Scoville and Milner 1957). Through careful observations and experimentation, testing the limits of Henry's amnesia, and specifically probing the types of memories Henry could or could not form, researchers began teasing apart the different

categories of learning and memory. Through these discoveries in the broad categorizations of types of learning and memory, such as short-term versus long-term memory, researchers began hypothesizing the functions of the hippocampus (Scoville and Milner 1957; Squire 2009; Corkin 2002). Henry's retained ability to learn new visuomotor skills, but inability to remember the events of his day, allowed them to conclude that procedural long-term memory is hippocampal-independent, while declarative memory—that is, memory which involves facts, experiences, and is accessible via cognitive awareness—is hippocampal-dependent (Squire 1986).

In addition to anterograde amnesia, Henry Molaison, as well as others who have had bilateral hippocampal removal, often experience partial retrograde amnesia (Scoville and Milner 1957; Squire 1986). Interestingly, the retrograde amnesia often suffered by hippocampal lesion affects only memories that were formed relatively recently, while memories that were formed longer ago remain intact. Through these initial findings and subsequent work, it has now been shown that the hippocampus is necessary for the formation of declarative memories, but these memories are not ultimately stored within the hippocampus—rather, the information is consolidated over months to years to parts of the cortex through unknown mechanisms. If, therefore, the hippocampus is injured in any way during consolidation, you will not only lose the ability to develop new declarative memories, but any memories that were in the process of consolidation will be lost in part or in whole (Squire 1986).

Coincidental to research determining the function of the hippocampus as a brain region necessary for the formation of new explicit memories, as well as the region in which memories are consolidated and stored long-term in other brain regions, work also established the hippocampus as a brain region critical for spatial memory and navigation. First established in 1948, the concept that the hippocampus forms a cognitive map of the environment (Tolman 1948) was confirmed through discovery of cells within the hippocampus that increase their firing rate at specific locations within an animal's environment (O'Keefe and Dostrovsky 1971). With enough of these so called "place cells", a population of neurons that are individually spatially tuned can represent an entire environment, thus forming a cognitive map that might allow an animal to successfully navigate its spaces in behaviorally relevant ways. It was later through hippocampal lesion experiments that a more causal link was finally drawn between the hippocampus and spatial memory and navigation, but not the cortex, using the Morris Water Maze (Morris et al. 1982). More

recently, all-optical approaches using optogenetics and two-photon calcium imaging has shown that re-activation of ensembles of place cells can effectively bias the behavior of mice, such that the mice behave in the stimulation zone how they would in the natively encoded zone of their environment (Robinson et al. 2020). This provides an even more rigorous causal link between hippocampal place cell function and an animal's cognitive map, directly supporting spatial memory and navigation.

Though these two functions of the hippocampus, formation and consolidation of declarative memory and spatial memory/navigation seem disconnected from each other, more recent work has aimed to tie these two processes together in a more unifying hypothesis for how the hippocampus functions, and specifically what role the hippocampus provides in the broader context of the brain and behavior. One particularly attractive model is that both processes rely ultimately on an ability to tie behaviorally relevant aspects of an experience to sequences—either in space, time, or both (Eichenbaum 2017; Buzsáki & Tingley 2018; Benna & Fusi 2021; Stachenfeld et al. 2017). Returning to the concept of a cognitive map, whether that map represents individual locations within an environment or individual experiences in a one's life, both rely on foundationally similar mechanisms. None of these similar theories that abstract the role of the hippocampus beyond simply memory formation, consolidation, and spatial navigation have to be mutually exclusive—rather, their explanations of pattern separation and completion, sequence generation, associative learning, experiential compression, and experiential prediction could be facets of the same mechanisms. Ultimately, it seems the hippocampus is receiving sensory inputs, comparing those inputs to previous experiences, and updating existing representations of the world through each new experience—a process that is reflected perfectly in its anatomical and connective architecture.

1.2 Anatomy & Connectivity of the Hippocampus

The hippocampus is a relatively straightforward circuit which takes information from the cortex, processed by the entorhinal cortex, and feeds it back to the cortex following its own processing. Though the circuit is simple, it is critical to understand its architecture in order to understand how it's able to process information largely unilaterally, and why perturbations seen in diseases like Alzheimer's disease could lead to functional consequences. Below, I will outline the specific circuit architecture of the hippocampus, summarized in **Figure 1.1**, as well as the function of each of its four sub-regions, with specific focus on the primary excitatory output cells, pyramidal neurons (PNs).

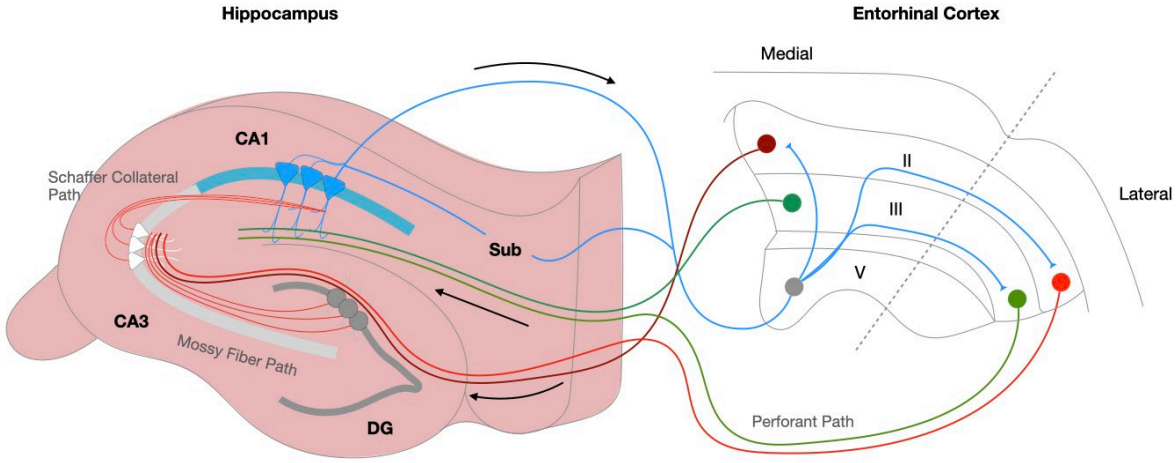

Figure 1.1. Excitatory Hippocampal Anatomy & Connectivity
Inputs projecting from layer II of the medial and lateral entorhinal cortex (red) synapse onto the dentate gyrus via the perforant path as well as CA3. The dentate gyrus then sends axonal projections along the mossy fiber path to CA3. CA3 sends its axonal projections along the Schaffer Collateral pathway to the apical oblique dendrites of CA1 PNs. CA1 PNs also receive direct inputs from layer III of the medial and lateral entorhinal cortex (green). CA1 PNs then send their axonal projects back to layer V of the entorhinal cortex, completing the trisynaptic loop (blue).

The hippocampus can be anatomically and functionally divided into four distinct subregions: the dentate gyrus (DG) and the CA3, CA2, and CA1 regions. Information flows into the hippocampus through direct inputs from the entorhinal cortex (EC; Basu and Siegelbaum 2015). Specifically, layer II of the lateral entorhinal cortex (LEC) and medial entorhinal cortex (MEC) send excitatory, glutamatergic projects to the DG via the perforant path where they will form synapses onto the dendrites of granule cells (Basu and Siegelbaum 2015). While the entorhinal cortex itself receives inputs from primary and higher sensory cortical areas, the MEC provides mostly spatial information to the hippocampus, while the LEC provides more specific sensory information, such as object identity, smells, sights, taste, time, etc. (Mallory and Giocomo 2018). One of the many interesting features of the hippocampus is that the dendritic arbors of most neurons within all four regions receive presynaptic inputs in a spatially regulated manner. For example, inputs from the LEC synapse onto the outermost dendrites of granule cells within the stratum moleculare (SM) of the DG, while inputs from the MEC synapse onto the middle third of the dendrites (Fernandez-Ruiz et al. 2021). Functionally, the DG is primarily thought to be involved in pattern separation, receiving information from the EC where it will split otherwise similar information into individual, unique concepts (Jonas & Lisman 2014; Lamothe-Molina et al. 2022; Hainmueller & Bartos 2020) where it is then passed forward to CA3. Interestingly, the DG is one of the only regions of the brain where adult

neurogenesis is thought to occur (Zhao et al. 2008; Tuncdemir et al. 2019; Nakashiba et al. 2012), with the role that these adult born granule cells might play in memory formation and consolidation still currently being explored.

Information from the DG is passed to area CA3 through granule cell axonal projections, known as mossy fibers, which synapse onto the proximal apical dendrites in the stratum lucidum (SL) of CA3. CA3 also receives direct inputs from layer II of both the LEC and the MEC, which synapse onto the distal apical tuft dendrites found in the stratum lacunosum moleculare (SLM) (Basu and Siegelbaum 2015; Rebola et al. 2017). CA3 also contains significant recurrent connectivity, in which CA3 neurons will send axonal projections to other CA3 neurons both ipsilaterally and contralaterally, where they will synapse onto the apical oblique dendrites of CA3 neurons found in the stratum radiatum (SR) as well as the basal dendrites found in the stratum oriens (SO) (Rebola et al. 2017; Basu and Siegelbaum 2015). The CA3 region of the hippocampus has been associated with many different functions, including rapid encoding of new information, spatial information, novelty and associational detection, and pattern completion (Kesner, 2007).

Pyramidal neurons from CA3 send their axonal projections via the Schaffer collateral pathway to the CA1 subregion of the hippocampus, which is the main output of the hippocampus itself and focus of this thesis. Critically, CA3 axons terminate in both the basal and apical oblique dendrites of CA1 neurons, found in SO and SR respectively (Basu and Siegelbaum 2015). However, CA1 PNs also receive inputs directly from Layer III of the MEC and the LEC, which synapse onto the distal apical tuft dendrites found in the SLM. CA1 PNs are unique in this aspect, receiving indirect input from the EC, which has been processed through the DG, CA3, and CA2 (see below), as well as direct, unfiltered input from the EC (Basu and Siegelbaum 2015). It is this unique architecture of indirect and direct inputs to CA1 that has led many to hypothesize the role of CA1 PNs in part is to compare relatively direct sensory input arriving from the environment through the EC to existing representations and experiences stored in CA3 or the other parts of the hippocampus (see Chapter 2 and 3 for more details). CA1 PNs can then make a computational comparison of these two experiences, either in conflict or agreement, and ultimately output that calculation to downstream brain regions, including back to the EC where their axons terminate in Layer V/VI, as well as in the subiculum, lateral septum, and neocortex (Basu and Siegelbaum 2015).

Not to be overlooked, however, is area CA2 of the hippocampus, which is a relatively small region between CA3 and CA1. When it comes to connectivity of this region, it is quite similar to CA3 in that it receives input via the mossy fibers from the DG, inputs from CA3 directly, contains recurrent CA2-to-CA2 projections, and sends some projection back to CA3 as well as forward to CA1. Interestingly, CA2 axonal projections to CA1 terminate almost exclusively in the basal dendrites located in the SR, providing even more nuance to the compartmentalization of CA1 PNs (see Chapter 2 and 3 for more details). Functionally, CA2 seems to be a hub for social memory, providing social context and representations to CA1 (Donegan et al., 2020; Hitti and Siegelbaum, 2014).

Overall, the hippocampus forms a tri-synaptic loop, where the main inputs come from the EC, making their way through the DG and CA3/CA2, and the main output is from CA1 back to the EC. Perhaps most interestingly and important for the research discussed in this thesis, each region of the hippocampus receives unique, spatially restricted inputs onto sub-compartments of their dendritic arbors. Though the molecular targeting for such compartmentalization is relatively understood (Jarsky et al., 2005; Takahashi & Magee, 2009; Sando et al. 2019; Blockus et al. 2021), the consequences of this input specificity on function remains largely unexplored. Importantly, however, is the hypothesis that this connectivity could explain in part how individual PNs within CA1 become spatially tuned, which I will explore further below. Even more intriguing, perhaps, is that some of these sub compartments of CA1 PNs remain selectively vulnerable to perturbations such as AD-dependent synaptotoxicity (Mairet-Coello et al. 2013; Lee et al. 2022). Unraveling the underlying mechanisms of this selective vulnerability as well as the intracellular compartmentalization that reflects the intercellular compartmentalized inputs is the primary focus of Chapters 2 and 3 of this thesis, while understanding the consequences of compartmentalized synaptic loss on cellular and circuit function is the focus of Chapter 4.

1.3 Spatial Selectivity within the Hippocampal-Entorhinal Cortical Circuit

As mentioned in the previous section, one of the most well-documented roles of the hippocampus is in forming and maintaining a cognitive map of an animal's environment. Specifically, individual neurons within the hippocampus and the entorhinal cortex are spatially tuned, such that their firing rates correspond to specific physical locations within an animal's environment. In the following section, I will explore further the different types of spatially and non-spatially tuned cells within the entorhinal cortex and hippocampus,

focusing mostly on PNs within CA1, as well as the potential mechanisms through which these place cells become spatially tuned.

1.3.1 Spatially tuned cells in the Entorhinal Cortex

The entorhinal cortex, as the main input to the hippocampus, contains both spatially tuned and non-spatially tuned cells, largely corresponding to the MEC and LEC respectively (Hafting et al., 2005; Moser et al., 2008). Within the MEC lies one of the other most well-known and well-studied spatially tuned cells in the brain: grid cells. These cells, like place cells, reliably increase their firing rate in specific locations within an animal's physical environment. However, unlike place cells, grid cells do not have singular firing fields—rather, individual grid cells will form a hexagonal array of spatially tuned locations often spanning the entire environment, with variable distances between these multiple fields, orientations, and x-y displacements (Hafting et al., 2005; Moser et al., 2008). Like place cells, a population of these individual grid cells will tile the entire environment, though not in a topographical manner, unlike other feature selective populations of neurons within the cortex. Grid cells, along with other spatially tuned and non-spatially tuned cells within the MEC project to CA1 PNs, as discussed above, potentially giving rise to spatial tuning in CA1 (as discussed below). In addition to grid cells, the MEC also contains border cells and head direction cells (Mallory and Giocomo, 2018). Border cells, as their name suggests, increase their firing rate when encountering the border or edge of an animal's environment. Head direction cells, as their name also suggests, increase their firing rate in an orientation-specific manner, firing more as the head of the animal is facing one specific direction within an environment. Though the LEC does not contain spatially tuned cells, many non-spatially tuned cells have been identified, including time cells, odor sensitive cells, and cells that specifically respond to the presence or absence of objects within an environment (Tsao et al., 2018; Leitner et al., 2016; Xu and Wilson, 2012; Deshmukh & Knierim, 2011; Tsao et al., 2013). The inputs to the hippocampus arriving from the EC provide both spatially tuned and non-spatially tuned context information either directly or indirectly to all regions of the hippocampus. However, whether or not these inputs are required and to what extent they are required for CA1 PN spatial tuning remains unclear, with the current consensus hypothesizing that the EC controls aspects of CA1 place cell dynamics, but is not wholly necessary for spatial tuning (Brun et al., 2008; Van Cauter et al., 2008; Mallory & Giocomo, 2018; Rueckemann et al., 2016).

1.3.2 Spatially tuned cells in the Hippocampus

As mentioned previously, place cells in CA1 of the hippocampus are spatially tuned pyramidal neurons that encode physical locations within an animal's environment, summarized briefly in **Figure 1.2**. Following their discovery many decades ago, we have since learned a significant amount about what they are, how they function, and how they're formed. Because the focus of most of the work in this thesis is on CA1 neurons, and specifically place cells, I will not be discussing place cells found in other parts of the hippocampus, such as spatially tuned inputs arriving from CA3. Rather, I will discuss below what CA1 place cells are, how CA1 PNs encode non-spatial information, place cell remapping and enrichment, and the hypothesized mechanisms of place cell formation.

What are place cells? As already highlighted, place cells are defined largely by their selectivity to physical locations within an organism's environment. Specifically, place cells reliably increase their firing rates when an animal enters the often small area of the environment for which that cell is tuned, also known as the place field. While place cells can encode for multiple place fields, these events are rather rare, make up an insignificant portion of place cells, and will not be discussed. Place cells or synonymous spatially tuned neurons have been identified now in many species, including bats (Ulanovsky & Moss, 2007), birds (Payne et al., 2021), non-human primates (Rueckemann & Buffalo, 2017), and humans (Tsitsiklis et al., 2020), implying relatively strong evolutionary conservation.

What is driving the increase in firing rate for an individual place cell is often a combination of many different environmental cues, including sensory cues such as visual information, olfactory information, auditory information, and mechanosensory information, and, importantly, where and when those cues are arriving within the environment. However, place cells, like grid cells discussed previously, are not topographically organized with in CA1 of the hippocampus—that is, the environment is not coded in cognitive space as it is in physical space, and so neighboring PNs that are spatially tuned may not reflect neighboring points within the environment (Moser et al. 2008). Because less than half of PNs in CA1 are reported to be spatially tuned and thus place cells (anywhere between 10-40% depending on the imaging and/or behavioral methods used and reported), most CA1 PNs are not in fact spatially tuned or place cells at a given moment. Instead, CA1 PNs may be responsive to specific trajectories, objects and/or goals within an environment and the distances to those cues, as well as the temporal order in which various odors, objects, etc. occur,

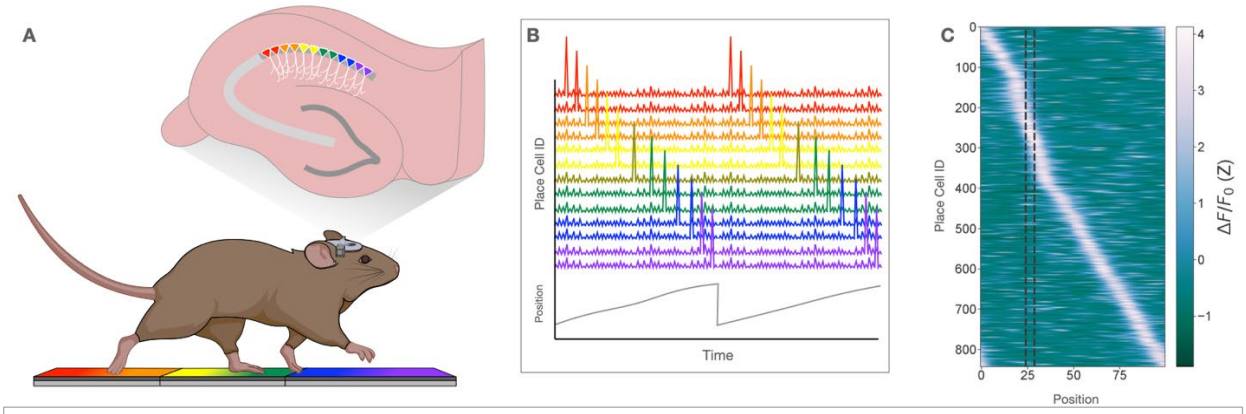

Figure 1.2. Place Cells are spatially tuned neurons within CA1 of the hippocampus and tile an animal's entire environment
A) As a mouse navigates an environment, such as a linear track (represented by a rainbow of colors) a population of cells within CA1 of the hippocampus will become spatially tuned to that environment, such that the population of these place cells will tile or represent the entire population. **B**) Example activity traces from individual place cells that are spatially tuned for specific locations within the mouse's environment—red cells having spatially tuned place fields at the red section of the track, orange for the orange, etc.—compared to the position of the mouse along the belt. **C**) Example data in which a population of spatially tuned CA1 neurons (y-axis) recorded using in vivo two-photon Ca^{2+} imaging from a mouse navigating a cued belt (position on the x-axis) are sorted according to peak activity. The population not only represents the entire environment, but in the case in which a reward has been placed within a fixed location (dashed line), place fields are enriched.

or PNs may just be silent (Mallory & Giocomo, 2018). However, that does not preclude spatially non-responsive neurons from becoming spatially tuned and therefore become place cells—interestingly, silent cells, defined as cells that do not exhibit any somal firing activity during a given recording window, can seemingly spontaneously become spatially tuned through yet to be determined mechanisms discussed below.

Place cells are also variable themselves, both in their reliability and their stability. Within individual trials, place cells may not fire every time an animal passes through that cells place field, or the place cell my fire outside of the place field, though to a lesser degree than within the place field. Place cells may also lose their spatial tuning, failing at a certain point to reliably fire within their place field and therefore losing their identity as a place cell. Across trials, the same is true. Recent advancements in longitudinal imaging of the same place cells over days or weeks using multi-photon-based techniques rather than electrode-based techniques have indicated that place cells can either encode the same location across weeks, remaining very stable, or they can either shift the location of encoding or lose their place fields across days (Grosmark et al., 2021; Ziv et al., 2013). However, the exact mechanisms leading to the differences in stability or reliability are unclear.

Yet another interesting facet of place cell identity is the ability of a place cell to change or remap their place fields. When animals are moved from one environment to another, or subtle changes are made to an existing environment, place cells tend to either remap their place fields in the new location, or show preferential spatial tuning in one of the two environments (Muller & Kubie, 1987; Quirk et al., 1990; Bostock et al., 1991; Colgin et al., 2008; Priestley et al., 2022). In this case, remapping can be defined in two ways: either a change in the response rate for a given place field in different environments, or through completely changing the place field itself. Place cells within CA1 have also exhibited remapping within the same environment under different motivational and/or behavioral contexts (Colgin et al., 2008; Markus et al., 1995). Whether its contextual or behavioral, place cells display remarkable flexibility in how they encode an environment. This is further demonstrated in experiments in which a salient feature is introduced into an animal's environment while recording place cell activity. Interestingly, place cells will tend to aggregate or enrich their place fields around the salient feature—be it a reward or an aversive cue (Hollup et al., 2001; Kaufman et al., 2020; Zaremba et al., 2017). This enrichment around a specific zone within the environment can occur through two different means: either the existing place cell population, which tiles the entire environment, remaps their existing place fields such that there's an enrichment around the salient cue, or new place cells can form at the salient location, thus enriching place fields at that location. The mechanisms underlying which of these methods is preferentially used in various contexts remains unclear, as well as the mechanisms underlying the remapping and enrichment itself. What is clear from the ability of place cells to remap and specifically enrich around salient information is that these cells retain an incredible amount of flexibility in their feature selectivity. The flexibility of a population to encode an input as variable as the environments that an animal may encounter appears critical for the ability of an animal to appropriately navigate many similar and dissimilar environments, and specifically to emphasize within those environments, objects or locations that provide danger or provide refuge. The flexibility or plasticity with which these place cells can encode the environment may come down to the plasticity of individual neurons themselves; however, the exact mechanisms through which place cells are formed is itself unclear.

1.3.3 Mechanisms of Spatial Selectivity in the Hippocampus

Many of the earliest hypotheses regarding place cell formation focused on integration of grid cell inputs, as the EC is the primary input to the hippocampus broadly and to CA1 specifically (Bush et al., 2014). However,

it has become clear largely through ablation or chemo- and opto-genetic inhibition experiments targeting grid cell inputs to CA1 that place cell formation is retained in the absence of grid cell activity (Brandon et al., 2015; Sasaki et al., 2015). Rather, emerging evidence suggests that specific forms of plasticity within CA1 PNs integrate location-specific information from CA3 inputs with location- and non-location specific information from EC inputs, the precise timing of which results in potentiation and selective tuning.

In order for an organism to form long-term associations at a cellular and ultimately behavioral level, long-lasting changes must occur within the individual components of the circuits driving those learned behavior (Hebb, 1949; Abbott & Blum, 1996). Through decades of work, we now know that the primary means through which long-term changes are embedded into cells and circuits is through a process of strengthening (and/or weakening) individual synapses, thus improving the efficacy of communication between neurons, through activity-dependent molecular mechanisms known as synaptic plasticity (Bliss & Lømo 1973; Pinsker et al., 1970; Kandel & Schwartz, 1982). Much of what is known about synaptic plasticity has been through experiments in CA1 of the hippocampus, and synaptic plasticity can come in two opposing forms: long-term potentiation (LTP; Bliss & Lømo, 1973; Citri & Malenka, 2008) and long-term depression (LTD; Massey & Bashir, 2007; Markram et al., 1997). Through coincidental activation—meaning presynaptic activation of a neuron during postsynaptic depolarization—a specific receptor, called an N-Methyl-D-Aspartate (NMDA) receptor, will open, allowing calcium influx into the neuron, triggering a molecular cascade that ultimately results in more efficient synaptic transmission postsynaptically (Citri & Malenka, 2008). Alternatively, when a presynaptic input fires out of sync with postsynaptic depolarization, rather than a coincidental event resulting in increased efficacy, the converse events occur—molecular mechanisms lead to decreased postsynaptic transmission efficacy, termed LTD (Massey & Bashir, 2007; Markram et al., 1997). The importance of these mechanisms in circuit function cannot be overemphasized, as they provide the basis upon which events that are related are more strongly connected, while events that are unrelated are less connected—essentially, these mechanisms outline the mechanisms of learning and memory. Critically, it is these very fundamental mechanisms that are thought to be at play in the establishment of place cells themselves.

In place cells, a novel form of plasticity has been described recently and has won significant support as a potential mechanism of place cell formation called behavioral time-scale synaptic plasticity (BTSP;

Bittner et al. 2015, Bittner et al. 2017). This form of plasticity requires two very basic processes in order for a place cell to form: a dendritic plateau event coinciding with spatially tuned CA3 inputs. In essence, a CA1 PN receives spatially tuned information from thousands of CA3 cells onto its basal and apical oblique dendrites. In a non-selective condition, a CA1 PN is not spatially tuned and therefore will not reliably fire within a specific place field or location within the environment. However, when a dendritic plateau occurs—which is a large, dendritic spike event in the apical tuft dendrites, often resulting in somal spiking, likely consisting of many high amplitude dendritic firing events and a massive influx of calcium—any active, spatially tuned presynaptic inputs arriving onto those CA1 PNs will be selectively potentiated. There are two particularly remarkable aspects of BTSP: the limited number of events required in order to induce potentiation and therefore produce a place cell, and the time-frame over which potentiation occurs versus depotentiation. In classical spike-timing dependent plasticity, tens to hundreds of coincidental spiking events are often required in order to induce potentiation. However, in BTSP, often only a single coincidental event—a dendritic plateau paired with spatially tuned presynaptic release—is required for potentiation to occur and a place field to form (Bittner et al. 2015; Bittner et al. 2017). This very rapid form of plasticity allows for very rapid formation of environmental representation, which is often necessary, and reflected by how quickly an entire environment is tuned for within a couple laps in a given environment experimentally. In addition to the rapid onset of potentiation, the window for potentiation in BTSP is closer to multiple seconds (~3 seconds) before and after postsynaptic depolarization. Interestingly, this so-called plasticity kernel is asymmetric in nature, with a slightly longer tale prior to depolarization than after, producing a characteristic backward shift in spatial potentiation, potentially allowing for a predictive representation (Bittner et al. 2017; Priestley et al. 2022). Similar to spike-timing dependent plasticity, any presynaptic input that closely preceded or followed the CA1 PN's plasticity kernel are de-potentiated, refining the spatial tuning that can occur from the BTSP event (Milstein et al., 2021). It is important to note, while place cells can be induced either optogenetically or through active depolarization (Rolotti et al. 2022), the mechanisms of dendritic plateaus themselves, including their initiation, is not clear, and the cellular and molecular mechanisms of BTSP are not yet obvious. That said, BTSP provides a clear basis upon which to examine how place cells may be formed, and confirm the importance of the spatially compartmentalized inputs to CA1 PNs for their function. What is less clear is the relative contribution that these inputs play in plasticity

of CA1 PNs, and whether removing either CA3 inputs or EC inputs to CA1, and thus removing one of the apparently critical aspects of CA1 place cell formation, would have an impact on place cell formation or place cell function itself. Recently, work from the Polleux lab has demonstrated that reducing the fraction of CA3 inputs to CA1 PNs, specifically localizing to the basal and apical oblique compartments, is sufficient to reduce the fraction of cells that are place cells and compromises the function of existing place cells that could form (Blockus et al. 2021). This line of research will not only shed additional light on the mechanisms of place cell formation, and thus the importance of connectivity (and to an extent intracellular effectors) to this process, but may also shed light on whether, how, and why place cells are compromised in diseases such as Alzheimer's disease, where significant synaptic loss in CA1 PNs is observed in the earliest stages, and individuals with Alzheimer's exhibit significant spatial memory and navigation deficits.

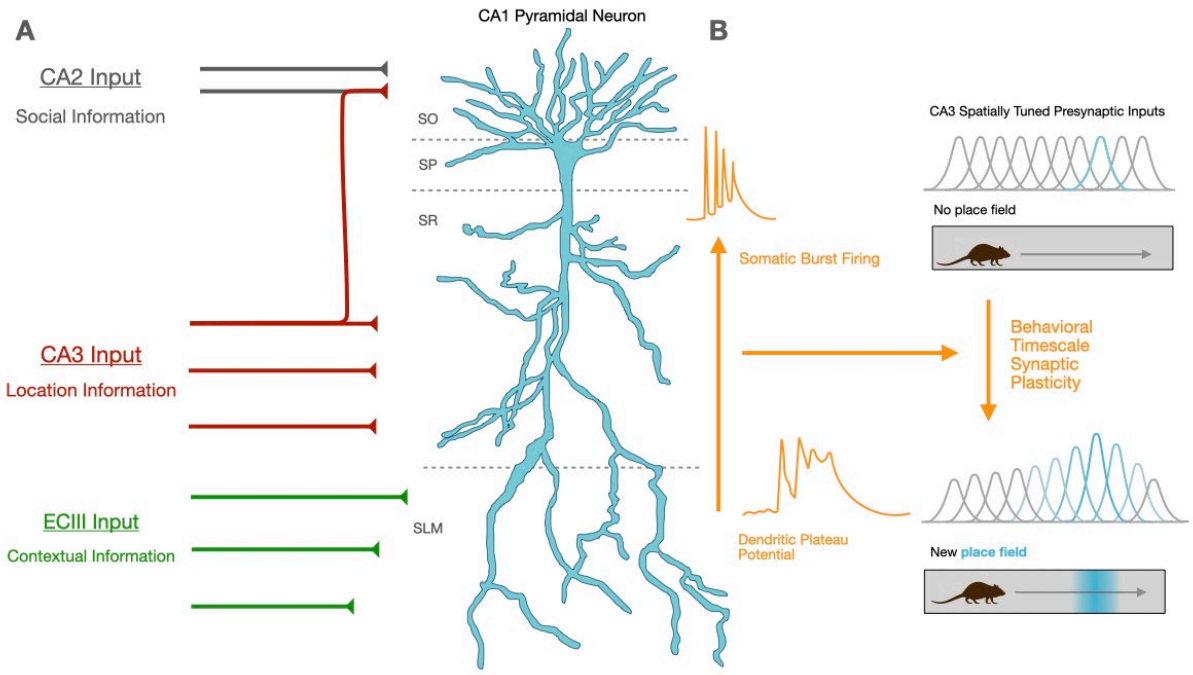

Figure 1.3. Proposed mechanism of place cell formation
A) CA1 PNs receive spatially compartmentalized inputs from the other regions of the hippocampus or from the entorhinal cortex directly—CA2 inputs terminate onto the basal dendrites in the SO region, CA3 inputs terminate onto the apical oblique dendrites in the SR region, and EC inputs from Layer III terminate onto the distal apical tuft dendrites in the SLM region. Importantly, CA3 presynaptic inputs carry spatially tuned information. **B**) Through unknown mechanisms, a large depolarization event called a dendritic plateau will trigger synaptic burst firing within a CA1 PN. Any spatially tuned inputs that were active within seconds of this dendritic plateau are thought to undergo a very rapid form of potentiation, known as behavioral timescale synaptic plasticity, causing those spatially tuned inputs to become stronger/more efficient, leading to formation of a place field at that specific location for that (previously non-spatially tuned) CA1 PN.

1.4 Alzheimer's disease & its Impact on Cellular Function

1.4.1 Alzheimer's disease: Clinical & Pathological Features

As mentioned throughout, Alzheimer's disease is a memory disorder that impacts the brain over decades, ultimately resulting in the deterioration of an individual's capacity to function in the world. It is a devastating disease both personally, interpersonally, and for society. Though no cure exists, it remains one of the most well-funded, well-researched disorders on the planet. Below I will discuss the prevalence and impact of AD, both internationally and nationally, and what AD is both clinically and pathologically.

Alzheimer's disease (AD) is progressive, neurodegenerative disease that primarily impacts memory and cognition in humans, and accounts for the majority (60-70%) of all dementia cases (WHO, 2023). Approximately 55 million individuals have dementia worldwide, 60% of whom live in low- or middle-income countries, with this number expected to grow to 78 million by 2030 and 139 million in 2050 (WHO, 2023). In the United States, as of 2023, an estimated 6.7 million people are living with AD (Rajan et al. 2021), with that number expected to grow to 7.2 million by 2025 and 13.8 million by 2060, in large part due to the rapidly aging population (Rajan et al. 2021). Almost two-thirds of American's living with AD are women, while non-Hispanic Black and Latine individuals over 65 are disproportionately more likely to have AD or other dementias (Dilworth-Anderson et al. 2008; Manly & Mayeux 2004; Demirovic et al. 2003; Harwood & Ownby 2000; Perkins et al. 1997; Steenland et al. 2016; Power et al. 2021). Though the disease is undoubtedly devastating both personally and interpersonally, it also poses a significant public health threat as one of the most financially costly conditions to society, with the estimated total cost for 2023 for all individuals with AD approaching $345 billion, including Medicare, Medicaid, and out-of-pocket care costs (Alzheimer's Association, 2023; Lewin Group, 2016). This cost for AD care is projected to increase to just under $1 trillion by 2050 (Alzheimer's Association, 2023; Lewin Group 2016). This does not, of course, account for the approximately 18.5 billion hours spent caring for AD patients by family, friends, nurses, and other unpaid carers (Alzheimer's Association, 2023; Rabarison et al. 2018), a disproportionate number of whom are women (Kasper et al. 2011; Rabarison et al. 2018), which amounts to an estimated $573 billion in unpaid labor. AD is not only a personally devastating disease, impacting the ability of individuals to live full and fulfilling lives as well as those around the patients who care for them, but a significant economic and healthcare burden with few treatments and no cure.

Clinically, AD is categorized into five broader stages, summarized in **Figure 1.4**, depending on the severity of the pathology and therefore cognitive and functional impairment: pre-symptomatic, mild cognitive impairment (MCI), mild AD, moderate AD, and severe AD. At pre-symptomatic stages of AD, individuals may experience little to no behavioral, cognitive, or functional deficits associated with the disease. Rather, pathological changes are impacting cells and circuits of the brains, especially in the hippocampus and to some extent the cortex (explored in depth below) up to 20 years before the disease begins to manifest as deficits in memory, cognition, or behavior. Individuals with MCI suffer from more subtle memory loss and deficits in cognition, beyond what can occur through natural aging, though they generally live independently with daily activities remaining largely unaffected. These two first stages are considered pre-clinical AD, as they lack most clinical symptoms often associated with the disease and patients live relatively normal lives. During mild or early AD, patients begin to notice difficulties in daily life, largely associated with a loss of concentration and episodic memory, disorientation of place and time, which can cause wandering and getting lost, mood changes, and depression (Wattmo et al. 2016; Hope et al. 1994). It is at this stage that most individuals are diagnosed. As the disease progresses to moderate AD, more significant brain loss has occurred in the cortex as the disease spreads, and patients exhibit greater memory deficits, including an inability to reliably recall family members and friends, continued behavioral changes, including a lack of impulse control, and difficulty reading, writing, and speaking (Kumar et al. 2021). Finally, during late-stage or severe AD, at which point disease pathology has spread to the majority of the cortex, with significant accumulation of neuritic plaques and neurofibrillary tangles (described below), major atrophy of the brain has occurred, along with detrimental cognitive and functional deficits, resulting often in a complete inability to recognize family, hospitalization, and confinement to a bed (Apostolova 2016; De-Paula 2012; Weintraub et al. 2012; Scheltens et al. 2016). Ultimately, complications due to severe AD will result in death.

Pathologically, AD is characterized at both a macroscopic and microscopic level and follows a relatively stereotypic progression (Jack et al. 2010; Sperling et al. 2011; Kant et al. 2019). Macroscopically, AD patients exhibit significant atrophy of the cortex and the hippocampus. Specifically, the frontal and

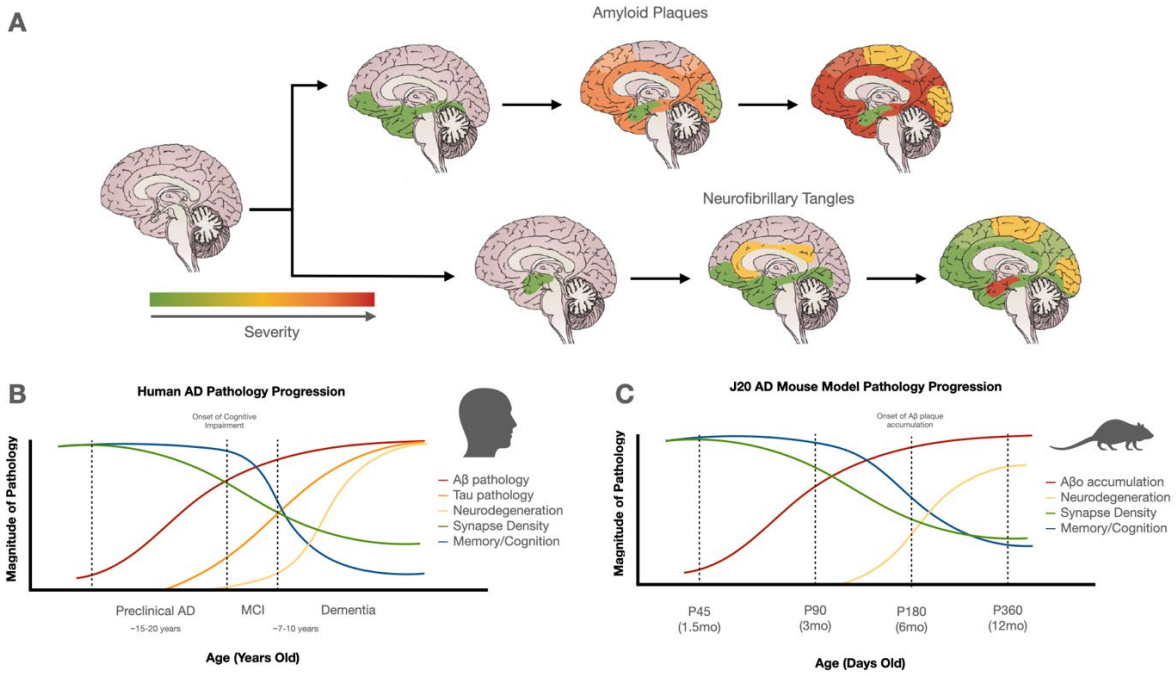

Figure 1.4. Alzheimer's disease pathological progression in humans and the J20 mouse model
A) Typical spread of amyloid plaques (top) and neurofibrillary tangles (bottom) in patients diagnosed with Alzheimer's disease across time and brain regions by severity (Figure adapted from Masters et al. 2015 from Braak and Braak 1991). **B**) Various pathological hallmarks and their magnitude of change across time in patients diagnosed with Alzheimer's disease. **C**) Various pathological hallmarks and their magnitude of change across age in the J20 mouse model of AD.

temporal cortices are more effected than the motor or somatosensory cortices. Microscopically, AD brains accumulate misfolded or improperly processed plaques of a protein called amyloid-β (Aβ) extracellularly, and neurofibrillary triangles (NFTs) intracellularly, composed of an aggregated, hyperphosphorylated microtubule-associated protein, Tau. When it comes to a pathological timeline, Aβ accumulation begins first, up to 20 years before neuronal death or cognitive decline characterizing MCI, prior to neurodegeneration, synaptic loss, glial activation, or tau hyperphosphorylation and tangling. Starting in the neocortex of the brain, Aβ next spreads to CA1 of the hippocampus and the entorhinal cortex (Thal et al. 2002; Grothe et al. 2017; Kant et al. 2019; Serrano-Pozo et al. 2011). Aβ then accumulates in subcortical regions, including the thalamus and hypothalamus, basal forebrain, caudate nucleus, etc. before spreading into the midbrain/brain stem and ending in the cerebellum (Thal et al. 2002; Grothe et al. 2017; Kant et al. 2019; Serrano-Pozo et al. 2011). Tau accumulation begins closer to the onset of MCI, starting first in the trans-entorhinal cortex, specifically layer 2, before quickly spreading to the medial temporal lobe and specifically CA1 of the hippocampus. Next, tau spreads to the limbic structures such as the subiculum of

the hippocampus and the amygdala, thalamus, and claustrum. Finally, tau pathology spreads to the majority of the neocortex, with associative areas more affected, while the primary sensory, motor, and visual areas mostly spared (Serrano-Pozo et al. 2011; Arnold et al. 1991; Braak and Braak 1991; Braak et al. 2006). Neurodegeneration often follows accumulation of NFTs in a similar pattern through which it is spread, primarily occurring in layers II, III and IV of the entorhinal cortex (EC), CA1 and the subiculum of the hippocampus, and layers II and V of the neocortex (Serrano-Pozo et al. 2011; Hyman et al. 1984; Arnold et al. 1991; Braak and Braak 1991).

1.4.2 Alzheimer's disease: the Role of Aβ

Though an overwhelming amount of time, effort, and money has been poured into determining the causes of AD, the scientific and medical communities still do not have a concrete answer. However, decades of research have reached a consensus that Aβ processing (summarized in **Figure 1.5**) and toxicity does seem to play a causative role in the disease, especially during the early stages—from causing synaptic loss, instigating hyperactivity, or leading to intracellular abnormalities like mitochondrial dysfunction and autophagic and/or calcium imbalance. In the following section, I will discuss the genetics associated with Aβ processing in AD, the amyloid-β cascade hypothesis, which is the assertion that Aβ is instigating the cascade of disease pathology seen in AD, and mouse models currently used to study AD, with specific attention paid to the J20 mouse model which is used throughout this thesis.

Much of what is known about the potential causes of AD and specifically the role that Aβ plays in AD pathology comes from the heritable, dominant mutations found in cases of early onset AD, most of which affect either the amyloid precursor protein itself (APP) or the catalytic proteins that process APP, Presenilin 1 (PS1) or Presenilin 2 (PS2) (Selkoe & Hardy, 2016). In non-amyloidogenic, physiological conditions—that is to say, non-diseased or pathologic states—APP, which is a transmembrane protein, is first cleaved by α-secretase to produce a cytoplasmic, soluble unit, called sAPPα, and a membrane-remaining unit, called the CTFα (carboxyl terminal fragment). Interestingly, sAPPα appears to have a neuroprotective function, having been shown to be involved in neural stem cell proliferation and CNS development (Caille et al. 2004; Ohsawa et al. 1999), and prevent excitotoxicity (Furukawa et al. 1996; Mattson, 1997). The function of CTFα, as a more intermediate protein seldom seen alone, is poorly understood. Following cleavage by α-secretase, the remaining membrane-localized CTFα protein is

cleaved again by γ-secretase within the transmembrane segment, producing two products: p3 and AICD (APP intracellular domain). p3 is released into the cytoplasm and rapidly degraded, with no known function, while AICD is released intracellularly and can in part initiate transcription of multiple genes (von Rotz et al. 2004) or function to activate apoptosis and/or recruit other proteins to the full-length transmembrane APP protein (Giliberto et al. 2008; Kinoshita et al. 2002). In amyloidogenic, AD pathological conditions, rather than APP being first processed by α-secretase, it is instead cleaved by β-secretase, creating sAPPβ and CTFβ. Subsequently, CTFβ is processed by γ-secretase to produce AICD and Aβ. Importantly, γ-secretase-mediated cleavage of CTFβ tends to produce at least two isoforms of Aβ: Aβ40 and Aβ42. While Aβ40 is the majority isoform produced via γ-secretase cleavage, and is not considered to be the toxic isoform, increases in the ratio of Aβ42 to Aβ40 is strongly linked to AD pathology, and specifically associated with APP and Presenilin mutations in familial AD.

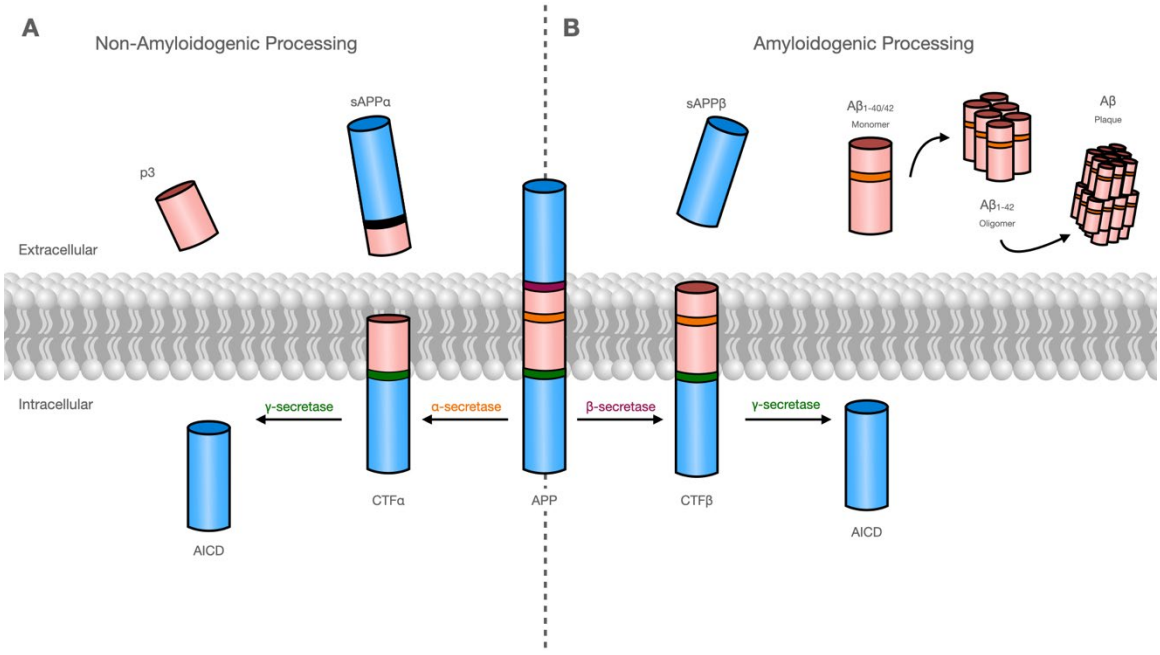

Figure 1.5. APP processing under physiological conditions and during Alzheimer's disease
A) During non-amyloidogenic processing of APP, α-secretase cleaves APP, creating sAPPα and CTFα, which is further cleaved by γ-secretase to release p3 extracellularly and AICD intracellularly. **B**) During amyloidogenic processing of APP in AD, β-secretase (rather than α-) cleaves APP creating sAPPβ and CTFβ, which is further cleaved by γ-secretase to release either $Aβ_{1-40}$ or $Aβ_{1-42}$ depending on the length of the final product and cleavage site. $Aβ_{1-42}$, which is fairly hydrophobic, forms dimers, trimers, and oligomers, which are the most toxic species of this protein aggregate, ultimately resulting in large Aβ plaques.

Aβ42 is a hydrophobic protein, prone to aggregation and fibrillization (Burdick et al. 1998). As a consequence, Aβ42 exists not only as monomers through amyloidogenic processing of APP, but as dimers, trimers, oligomers, and plaques (Sheng et al. 2012). It is critical to note that soluble Aβ42 oligomers, rather than plaques, appear to be the most significantly toxic species of Aβ according to cellular, animal, and human experiments, and remains one of the most widely supported contributors to AD pathology (Lambert et al., 1998; Kayed et al., 2003; Hsia et al. 1999; Lue et al. 1999; McLean et al. 1999; Hartley et al. 1999; DeKosky & Scheff, 1990; DeKosky et al. 1996; Serrano-Pozo et al., 2011; Terry et al., 1987; Terry et al., 1991). There is now a wide breadth of research indicating that soluble Aβ42 oligomers (Aβ42o) are directly responsible for excitatory, glutamatergic synaptic loss prior to Aβ plaque deposition in cortical and hippocampal PNs, and are therefore one of the earliest and most significant effectors in the pathology of AD (Hong et al., 2016; Mairet-Coello et al., 2013; Masliah et al., 2001; Moolman et al., 2004; Shankar et al., 2007; Jin et al., 2011; Lacor et al., 2004; Lacor et al., 2007; Shankar et al., 2008). In addition to structural synaptotoxicity, Aβ42o have also been implicated in disrupting the electrophysiological properties of synapses, including inhibiting long-term potentiation/plasticity itself (Mattson, 1997; Chapman et al., 1999; Walsh et al., 2002). The mechanisms of action of Aβ42o-mediated synaptic loss remain unclear, however recent work, including the work in Chapter 1 of this thesis, has tied the mechanism to increased Ca^{2+} flux through NMDA receptors and excitotoxicity (discussed further below) (Paoletti et al., 2013; Kamenetz et al., 2003). Essentially, Aβ42o induces increased Ca^{2+} influx, leading to hyperactivity, which can in turn lead to increase Aβ42 production and further synaptic loss. Ultimately, the accumulation of Aβ, specifically the toxic oligomeric forms, is what is causing the many disease phenotypes observed in the amyloid cascade hypothesis (Hardy et al. 2006; Selko and Hardy, 2016)

Importantly, however, the role that Aβ plays in the various facets of AD pathology is still widely contested and significant research has questioned the validity of the amyloid cascade hypothesis. First, there is little correlation between the levels of Aβ plaques within the brain and the severity of dementia in AD (Teich & Arancio, 2012; Sorrentino et al., 2014), with a significant fraction of non-demented individuals who are otherwise neurotypical exhibiting significant accumulation of Aβ plaques upon post-mortem analyses (Lippa & Morris, 2006; Aizenstein et al., 2008). Second, the majority of anti-amyloid plaque clinical interventions have failed to effectively prevent either cognitive decline in patients following treatment or

significantly slow the progression of the pathology (Cummings et al. 2019; Lippa & Morris, 2006) For example, Bapineuzumab, an anti-Aβ drug which has been shown to effectively reduce Aβ (Blennow et al., 2012) has failed to slow cognitive decline, and, in fact, shows significant negative side effects (Salloway et al., 2014; Castellani & Perry, 2012). Finally, many mutations associated with sporadic or non-familial AD do not seem to impact Aβ itself or impact other aspects of the disease, such as microglial and immune responses, tau, oxidative stress, etc. One rebuttal to the first major critique, which seems to have significant support, is that plaques themselves are not the toxic species of Aβ causing AD symptoms—rather, soluble Aβ42 oligomers are the toxic species, and thus examining the ratio of Aβ42 to Aβ40 is much more instructive and tends to better correlate with cognitive decline. Importantly, the most significant correlate with cognitive decline, as pointed out above, is not Aβ plaque density, neuronal loss, or even NFT density, but severity of synaptic loss (DeKosky & Scheff, 1990; Terry et al., 1991). While it true that the majority of treatments for AD have failed, three different Aβ antibody treatments, Solanezumab, Crenezumab, and Aducanumab, have shown promising reductions in both Aβ deposits as well as in the progression of cognitive decline (Cummings et al. 2014; Doody et al., 2014; Sevigny et al., 2015).

Despite contradictions in basic research, and significant failure to clinically translate findings from rodents to humans, the amyloid cascade hypothesis remains the leading hypothesis today. However, most AD researchers would agree that significantly more work needs to be done to address the other contributing factors to the clearly multimodal AD pathology.

1.4.3 Alzheimer's disease: Mouse Models

In order to better understand the pathology of AD, most researchers have turned to animal models of the disease, ranging from *Caenorhabditis elegans*, *Drosophila melanogaster*, and zebra fish, to the more popular rats and mice. Because of their physiological similarities to humans, breadth of genetic and behavioral tools, ease of breeding, and relatively short life-spans, transgenic mice have occupied the majority of AD-relevant research. As such, the majority of transgenic lines fall into one or more of three categories: human APP expressing lines, human PSEN1 expressing lines, or human Tau expressing lines (Wisniewski & Sigurdsson, 2010; Boutajangout & Wisniewski, 2014; Dujardin et al. 2015; Puzzo et al., 2015). Recently, there has been a push not only to produce mouse models of AD in which other relevant human genes expressing AD-mutations are over expressed, but to also use CRISPR/Cas9 to knock in

these human genes to better replicate disease pathology. Similarly, pushes to diversify the genetic backgrounds of models to better capture the diversity of disease penetrance has recently been explored with promising, though complicated, results (Neuner et al. 2018). Most human APP expressing mouse models of AD recapitulate many different aspects of AD pathology found in humans, including elevated human Aβ, Aβ plaques, neuronal death, synaptic loss, gliosis, vasculature deficits, circuit and network dysfunction, and cognitive and behavioral deficits (Ashe & Zahs, 2010). However, most models fail to fully capture the entire breadth of the disease, with most failing to exhibit NFTs. It is for this reason, perhaps, that many individuals question the validity of using these specific mouse models to study such a human-specific, complex disease like AD. Nevertheless, despite their shortcomings, mouse models have and continue to provide the basis for most of what we have discovered about the causes of Aβ- and Tau-dependent neuronal and cognitive deficits.

For this thesis, I used the J20 AD mouse model to study the mechanisms of Aβ-dependent synaptotoxicity and the resulting effects on hippocampal circuit deficits. The J20 model, also known as B6.Cg-Zbtb20$^{Tg(PDGFB-APPSwe/Ind)20Lms}$/2Mmjax, overexpresses human APP carrying two familial AD-associated mutations—K670N/M671L known as the Swedish mutation, and V717F known as the Indiana mutation—via the PDGF-β promoter (Mucke et al. 2000). One of the advantages of using mouse lines in general, but specifically the J20 mouse line, is how stereotypic the pathology progresses in these mice and how closely this pathology reflects what is observed in patients with sporadic or familial AD, which is summarized in **Figure 1.4**. Specifically, J20 mice exhibit increased Aβ42 levels as early as six weeks (1.3 months) of age which increases through 9 months, moderate cell death in CA1 beginning around 12 weeks (2.7 months) which increases in severity up to 9 months, deficits in long-term potentiation specifically between CA3 and CA1 synapses starting at 3 months, significant synaptic loss in the hippocampus starting around 3 months, with no differences seen at 1 month, indicating no developmental deficits due to Aβ overexpression, Aβ plaque deposition beginning first in the hippocampus and neocortex around 5-7 months and becoming widespread by 8-10 months, and significant activation of microglial cells starting around 5 months (Hong et al., 2016; Mucke et al., 2000; Pozueta et al., 2013; Wright et al., 2013; Saganich et al., 2006). Critically, however, J20 mice completely lack NFTs, making them an imperfect model for AD, though simplifying the potential pathways through which any deficits seen could be attributed to NFTs rather than

Aβ (Mucke et al. 2000). On top of the pathological hallmarks, J20 mice also exhibit cognitive and behavioral deficits characteristic of AD, including spatial memory deficits as measured by Morris water maze and radial arm maze as early as 4 months (Wright et al. 2014; Cheng et al. 2007). Recently, the J20 mouse model has been used to measure circuit deficits within the cortex and hippocampus, which will be explored further below.

1.5 Functional effects of Alzheimer's disease

As discussed above, one of the most significant pathological deficits seen in AD is the loss of excitatory synapses. While tremendous effort has gone into understanding how synaptotoxicity occurs and progresses, there remains a fundamental disconnect between synaptic dysfunction and synaptic loss in AD, and the cellular, circuit, and behavioral deficits observed. Below, I will not only further explore the broader effects of Aβ on synapses, plasticity, and neuronal function, but how these changes in synaptic density and/or function could be producing functional and/or circuit deficits. As part of this section, I will also expand upon the current literature surrounding cortical and hippocampal circuit deficits in AD specifically.

1.5.1 Synaptic dysfunction and hyperexcitability in AD

Aβ itself is a neurotoxic peptide. As has been demonstrated *in vitro* and *in vivo*, application of Aβ, often Aβ42 or human-derived, soluble Aβ, can directly induce neuronal apoptosis (De Strooper & Karran, 2016). This can occur either through direct interaction with receptors on the neuronal membrane surface, or through disruption of oxidative pathways and/or calcium dysregulation, all of which can result in significant DNA damage and cell death (Kayed & Lasagna-Reeves, 2012). However, neuronal loss is an, as of yet, irreversible stage of AD and other neurodegenerative diseases that result in cell death. Because of this, focusing instead on the aspects of neuronal dysfunction that precede neuronal death, often by years or decades, is critical as they provide a means through which clinical intervention may have a significant impact.

At a cellular level, Aβ induces deficits in synaptic, cellular, and circuit function prior to degeneration (Palop & Mucke, 2010). Because the cellular deficits of AD are explored in depth in Chapter 2, specifically highlighting the mechanisms through which cellular deficits lead to synaptic loss, I will not cover them here, and focus instead on the synaptic and contributing cellular/circuit functional deficits in AD for this section. As reported previously, the degree of synaptic loss within brain regions such as the cortex or hippocampus

is currently the best correlate for cognitive decline—over plaques, NFTs, or cell death—highlighting the importance of understanding the mechanisms of synaptic loss, and how loss might result either directly or indirectly in functional decline. Neurons exposed to Aβ either *in vitro* or *in vivo* exhibit significant dendritic shortening, structural irregularities, fragmentation, and decreases in postsynaptic density across cortical and hippocampal neurons (Spires & Hyman, 2004; Koffie et al., 2009; Mairet-Coello et al. 2013; D'Amore et al., 2003; Tsai et al., 2004; Spires, 2005; Garcia-Alloza et al., 2006; Meyer-Luehmann et al., 2008; Bittner et al., 2012; Zou et al., 2016; Blazquez-Llorca et al., 2017). With significant reductions in synapses, there is an accompanying decrease in connections between presynaptic and postsynaptic partners within these circuits (DeKosky & Scheff, 1990; Scheff et al. 1990; Scheff & Price, 1993; Scheff et al., 2007; Ye et al. 2022). A combination of decreased synaptic density and decreases in neuritic length itself has been linked to increased intrinsic excitability both experimentally and computationally in an AD context, potentially linking these synaptic changes to functional changes (Šišková et al., 2014). It is important to note, a significant number of *in vivo* investigations into Aβ-dependent synaptic loss, during which researchers simultaneously image Aβ plaques and dendritic spine density as a function of distance from plaques, have found that proximity to plaques strongly predicts the degree of dendritic spine loss (Bittner et al., 2010, 2012; Grutzendler et al., 2007; Penzes et al., 2011). However, whether this is the result of the plaques themselves, or the presence of high concentrations of soluble Aβ42 oligomers which surround these plaques is unclear, and could explain why when plaques themselves are cleared do not often prevent synapse loss, as oligomers are still present, often at higher numbers.

In addition to synaptic loss, Aβ can directly impact remaining synaptic function. Exposure of neurons to Aβ *in vitro* leads to increases in both AMPA and NMDA receptors as well as spontaneous excitatory postsynaptic potentials (Sanchez-Mejia et al., 2008; Um et al., 2012). Similarly, exposing hippocampal slices to Aβ directly elicits increased action potential firing in CA1 PNs (Kurudenkandy et al., 2014). In living mouse models of AD, similar phenomena have been reported: hyperactive and hypoactive populations of PNs have been reported both pre and post plaque development, measured as a significant increase in the number of action potential-elicited calcium transients *in vivo* (Chin et al., 2005; Palop et al., 2007; Busche et al., 2008; Grienberger et al., 2012; Rudinskiy et al., 2012). Complementary studies have been carried out in humans, where PET imaging of AD patients has shown increase glucose metabolism,

indicative of increased neuronal activity, closer to Aβ plaques (Cohen et al., 2009; Johnson et al., 2014; Oh et al., 2014). So, while Aβ does directly lead to synaptic loss, it can also lead to increased activity in existing synapses. Conversely, Aβ has been shown to simultaneously lead to synaptic depression (Chapman et al., 1999; Kamenetz et al., 2003; Hsieh et al., 2006; Shankar et al., 2007; Palop & Mucke, 2010). The means through which this process occurs is less understood, but research has shown that Aβ40 and Aβ42 can promote glutamate release and prevent glutamate re-uptake respectively, resulting in AMPA- and NMDA-dependent desensitization and ultimately synaptic depression (Li et al. 2009; Fogel et al., 2014; Hsieh et al., 2006). Though seemingly contradictory, the evidence above highlights that Aβ is playing a negative role in synaptic health, specifically leading to either synaptic depression and/or hyperexcitability, culminating eventually in synaptic loss. This theory corresponds well with the hypothesis that AD is primarily a disease of the synapses which becomes a disease of the mind (Selkoe, 2002). How exactly these disruptions of synaptic function and synaptic loss ultimately lead to circuit dysfunction remains much less clear and will be explored further below as well as in Chapter 4 of this thesis.

One thing that is very evident in AD models, and especially in humans, is the reliable degree to which hippocampal activity is at first hyperactive, and then severely depressed through disease progression. Using longitudinal fMRI, researchers have found that, in humans, there is a significant increase in activity within the hippocampal region (Dickerson et al., 2005; O'Brien et al., 2010). Importantly, this hyperactivity precedes any severe clinical AD symptoms, indicating this overactivity within the hippocampus is a primary symptom of the disease and has been seen in pre-symptomatic patients carrying familial AD mutations, patients with abnormal Aβ plaque development and no cognitive decline, and patients with MCI—a precursor to AD (2). Upon further progression of the disease, similar longitudinal fMRI studies have shown that hippocampal activity becomes significantly depressed (Celone et al., 2006; Persson et al., 2008; Sperling et al., 2009). What is unclear from these insights is whether the hypoactivity of the hippocampus is a pathological progression of the disease itself or a failure of the hippocampus to respond due to significant disease-dependent degeneration and deficits, therefore becoming more of a symptom than a driver of behavioral deficits (Putcha et al., 2011; Bakker et al., 2012, 2015).

1.5.2 Circuit deficits in AD

One question that remains given these symptoms of hyperactivity and/or hypoactivity is whether this dysfunctional activity can be directly linked to functional deficits at a cellular or circuit level and, subsequently, behavioral deficits. One remarkable paper has shown, in the visual cortex of an AD mouse model, that hyperactivity alone is sufficient to predict orientation tuning deficits (Grienberger et al. 2012). In this longitudinal, *in vivo* two-photon experiment, both spontaneous and visual tuning behavior was recorded within the visual cortex of AD mice. As the Aβ plaque burden developed, not only did a sub-population of cortical PNs become hyperactive during spontaneous activity, but their proximity to plaques increased the likelihood that they would be hyperactive. When subsequently recording response properties of PNs within the visual cortex to visual stimuli, only the previously identified hyperactive neurons showed degraded visual tuning, indicating deterioration of their function. Additionally, this increase in hyperactivity and subsequent deterioration of feature selectivity within this population was strongly correlated with a decrease in visual pattern discrimination in these mice (Grienberger et al. 2012). These studies strongly indicate a direct correlation between Aβ-dependent hyperactivity, functional deficits at a circuit and cellular level, and behavioral deficits.

In addition to cortical studies on neuronal functional deficits in AD mouse models, there has been a recent increase in the number of papers studying the functional impact of AD pathology on hippocampal circuit properties. The work done in this specific field can be split into several different categories: First, whether or not the experiments were carried out using microelectrode-based electrophysiological recording or using *in vivo* two-photon calcium recording; second, whether the experiments took place before and/or after Aβ plaque accumulation in the given model that was being used; third, whether the experimenters measured hippocampal and/or EC activity while the mouse was awake and behaving in either an open field or linear track. Because of the relevance of this relatively limited body of literature to this thesis, and specifically to Chapter 4, I'll be highlighting the findings of a select number of papers that fit various criteria outlined above.

Very few studies have examined hippocampal cellular and circuit function in a pre-plaque stage of AD. However, one such study that focused exclusively on pre-plaque AD pathology used microelectrode-based electrophysiological recording in a 3xTg model of AD (APP^{Swe}, Tau^{P301L}, $PS1^{M146V}$) while mice navigated a linear track (Mably et al. 2017). Interestingly, they found a decrease in transient firing properties

in CA1 PNs and a corresponding decrease in nearly all spatial tuning properties, including reduced spatial information, place field stability, and peak/mean firing rates, but no changes in place field width or the number of place fields per place cell. Other studies have examined CA1 activity at timepoints both pre- and post-plaque formation, allowing for more comparative analyses between two pathologically distinct stages of the disease. In Cacucci et al. 2008 and Ying et al. 2022, both of which used microelectrode-based electrophysiological recording in awake mice navigating an open field, both groups found no changes in CA1 PN firing rate before or after Aβ plaque accumulation. While both labs used human APP carrying Swedish mutations overexpression models, Cacucci et al. used the Tg2576 line while Ying et al. used the J20 line, which carries both the Swedish and Indiana mutations. Importantly, Caccuci et al. do report deficits in spatial properties of CA1 PNs post-plaque formation, specifically noting deficits in spatial information encoding as well as increased place field size, indicating a disruption in the precision of place cells in CA1 at this stage of the disease. Ying et al., on the other hand, found no significant changes in place cell properties before or after plaque development. However, they did find that grid cell function in the EC was significant disrupted, with a reduction in the total number of grid cells as well as reduced spatial periodicity, though only after plaque development.

In Busche et al. 2012, we see use of *in vivo* two-photon calcium imaging—something relatively rare in this field of study—using a dye-based calcium reporter in the APP-PS1 mouse model of AD pre- and post-plaque development. Interestingly, Busche et al. recorded not only from the hippocampus, but also measured cortical activity within the same mice prior to craniotomy and cannula implantation for hippocampal analysis. When recording from the cortex, they found no significant changes in cortical PN function at either stage of the disease. Conversely, they did find a significant increase in the number of hyperactive cells and an increase in the mean frequency at both stages of the disease in the hippocampus. However, only post-plaque did they find a significant increase in the number of silent neurons. One very significant caveat to this work is the failure to record cell function while the animal was awake and behaving, limiting the any possible conclusions to spontaneous CA1 activity.

The majority of other reports in CA1 function in an AD model focus exclusively on post-plaque stages of the disease. Four such papers have examined CA1 activity using microelectrode-based electrophysiological recording in mice navigating linear tracks, open fields, or both (Zhao et al. 2014; Prince

et al. 2021; Cayzac et al. 2015; Jun et al. 2020). In Zhao et al. 2014, they examined CA1 PN activity in a familiar and novel linear track using a forebrain-exclusive APP^{Swe} overexpression model. Though they found no changes in basic transient properties in CA1 PNs, they did find significant deficits in overall place cell tuning, especially in familiar contexts or in repeated exposure to novel contexts. Specifically, they find that spatial information is reduced while place field width increases after a mouse is exposed multiple times to a novel environment, becoming familiarized. In already familiar environments, however, they see decreases in spatial information encoding, place field stability, peak firing rate within the place field, and precision, with an increase in place field width. Overall, these data indicate deficits in spatial tuning in CA1 PNs is dependent on familiarity to an environment. In Prince et al. 2021, they examined CA1 PN activity in a virtual-reality linear track paradigm using the 5xFAD mouse model ($APP^{Swe,F,L}$ $PS1^{M146L-L286V}$). While they do report decreases in peak firing rate, spatial information, and synchrony with oscillations, only the decreases in synchrony are considered significant. These authors, like many others, report more significant changes in hippocampal oscillations and sharp wave ripples than specific place cell function, something I will not discuss in this thesis (Villette et al. 2010; Scott et al. 2011; Rubio et al. 2012; Davis et al. 2014; Ittner et al. 2014; Schneider et al. 2014; Busche et al. 2015; Gillespie et al. 2016; Iaccarino et al. 2016; Stolijkovic et al. 2016; Witton et al. 2016; Jones et al. 2019; Stolijkovic et al. 2019; Funane et al. 2022). Cayzac et al. 2015, rather than examining place cell activity in CA1 PNs in a linear track, did so using an open field using the APP-PS1 mouse model. Here, they see similar spatial tuning deficits to the previous papers outlined: decreased spatial information encoding, increased place field width, a decrease in the coherence, and a decrease for the first time in the number of cells that are considered place cells. Jun et al. 2020, while recording from open field, also record from linear tracks. In addition, these authors opt to use a recently generated APP knock-in line, claiming more physiological relevance than existing overexpression models used by the majority of the field. Despite using this model, they focus almost exclusively on pathological timepoints after plaque development, though do so at “young” (3-5 month) and “old” (7-13 month) ages. These authors recorded both grid cell properties and place cell properties in their knock-in mice, ultimately reporting that grid cell dysfunction precedes any place cell dysfunction. Specifically, they find decreases in peak CA1 PN firing rate within place fields, the number of neurons that are place cells, as well as a decrease in the spatial information encoded. However, they only find these changes occur in their “older” population

of mice. In addition to recording basic transient and place cell properties, Jun et al. also took advantage of a multi-linear belt imaging paradigm, which allowed them to compare the ability of place cells to remap. Interestingly, they found that, in “older” mice, only the AD mice showed invariability in their spatial representations between the two unique environments, implying a failure to remap. This is the first such example, to my knowledge, of a lab measuring remapping properties of CA1 PNs in an AD mouse model—something I expand upon greatly in Chapter 4 of this thesis.

Finally, there are two papers that have measured CA1 activity in an AD mouse model post plaque development exclusively, this time using *in vivo* two-photon calcium imaging (Inayat et al. 2022; Takamura et al. 2021). Both papers utilized the APP-KI mouse model that was been crossed to either a Thy1-GCaMP6s or -GCaMP7f line to constitutively express a fluorescent calcium reporter in PNs. Though Inayat et al. find only subtle decreases in the mean firing rate of CA1 PNs, with no changes in distance or time encoding, Takamura et al. find significant differences in transient and place cell properties at both timepoints they measured. In their younger time-point of 4 months, which is still post-plaque development, Takamura report increases in the mean firing rate, but a decrease in the number of active cells and a decrease in the spatial stability. At 7 months, these same measurements are exacerbated, while they record additive increases in place cell width and additive decreases in the fraction of neurons that are place cells, as well as decreases in place field enrichment at a reward zone. This specific study, similar to Jun et al. 2020, is the first to my knowledge to examine whether place field enrichment is affected in an AD mouse model. As with remapping, I expand on these analyses in Chapter 4 of this thesis.

Overall, this handful of papers, examining the functional deficits in CA1 PNs, find largely similar trends—decreases in the overall spatial tuning of this population through pathological progression of AD. However, many of these reports either find no changes in the mean firing rate (Cacucci et al. 2008; Ying et al. 2022; Jun et al. 2020; Zhao et al. 2014; Ciupek et al. 2013), an increase in the mean firing rate, implying hyperactivity (Busche et al. 2012; Takamura et al. 2021), or a decrease in the mean firing rate, implying hypoactivity (Mably et al. 2017; Inayat et al. 2022; Prince et al. 2021; Cheng & Ji 2013). These contradictions could be explained in part by the experimental method used—two-photon versus electrophysiology, or open field versus head-fixed linear tracks—, the pathological timepoints of their specific AD models, and/or the AD models themselves. Regardless, the heterogeneity in these findings

indicates a strong need to investigate multiple timepoints in multiple AD models, and to not limit the data to simple analyses such as basic transient properties or even basic place cell properties. Instead, as in Jun et al. 2020 and Takamura et al. 2021, we should be fine-tuning the scope of our analyses to better understand not only how place cells are functioning in a diseased context generally, but specifically how these diseased neurons might be producing dysfunctional circuit and/or network properties. Further, whether or not cellular deficits leading to circuit deficits relates in any way to behavioral deficits is significantly lacking in hippocampal AD analysis presented here.

Chapter 2: Aβ42 oligomers trigger synaptic loss through CAMKK2-AMPK-dependent effectors coordinating mitochondrial fission and mitophagy

Annie Lee*, Chandana Kondapalli*, **Daniel M. Virga***, Tommy L. Lewis Jr., So Yeon Koo, Archana Ashok, Georges Mairet-Coello, Sebastian Herzig, Marc Foretz, Benoit Viollet, Reuben Shaw, Andrew Sproul, and Franck Polleux. 2022. *Nature Communications 13:4444*.

https://doi.org/10.1038/s41467-022-32130-5

2.1 Chapter Introduction

Alzheimer's disease is notoriously a multimodal disease, with autophagy, mitochondrial dysfunction, calcium dysregulation, aberrant glial activity, vascular atrophy, and many other cellular deficits being implicated. Though extensive work has aimed to clarify individual facets of this disease, few have managed to bring together some of these disparate phenotypes. Here, we discovered that Aβ-dependent synaptic loss is driven by CAMKK2-AMPK-dependent mitochondrial fission and degradation *in vitro* and *in vivo*.

Aβ42o drives an influx of Ca^{2+}, leading to overactivation of CAMKK2. This in part leads to overactivation of AMPK, both *in vivo* and *in vitro*, in mouse and human neurons. If AMPK is removed, Aβ42o-mediated synaptic loss is prevented. Two important initial findings of this work were that 1) Aβ-mediated synaptic loss *in vivo* is spatially restricted to the distal tuft dendrites in CA1, and 2) mitochondria in the distal tuft, which are abnormally long compared to more proximal dendrites (explored in Chapter 3), are selectively impacted in an AD mouse model. Not only does removing AMPK prevent synaptic loss in the distal tuft, but it also prevents mitochondrial fragmentation and degradation in the tufts.

It was previously known that AMPK functions in part to promote mitochondrial fission via direct MFF phosphorylation and autophagy through ULK1/2 phosphorylation. Here, we demonstrated that removing MFF or preventing AMPK from phosphorylating MFF is sufficient to prevent both Aβ-dependent mitochondrial fragmentation and synaptic loss, *in vitro* and *in vivo*. Similarly, by removing ULK2 only (ULK1 is interestingly not involved in this pathway) or preventing ULK2 from being phosphorylated by AMPK, we could prevent 1) mitochondrial degradation, but not fragmentation, and 2) synaptic loss.

Finally, we were able to show that this novel mitochondrial fragmentation and degradation is Tau dependent, as expressing a Tau isoform that cannot be hyperphosphorylated by AMPK is sufficient to prevent both mitochondrial fragmentation (and thus degradation) as well as synaptic loss.

Overall, this work managed to pull together calcium dysregulation, mitochondrial disfunction, and aberrant autophagy along wit Aβ and Tau into a single, unifying molecular pathway to explain synaptotoxicity in AD. It also directly led to the research in Chapters 3 and 4 of this thesis.

All human differentiated neuronal work, *in vivo* MFF, Tau, and spine characterization work was done by myself (**Figures 6, S3, S9, S10**), with the rest of the manuscript forming the basis for the thesis of a previous graduate student, Dr. Annie Lee. I also performed all of the revision experiments, revised the entire manuscript, and led the effort to ensure the paper made it through the two+ year peer review process. The paper was published in its entirety in *Nature Communication* in 2022.

2.2 Abstract

During the early stages of Alzheimer's disease (AD) in both mouse models and human patients, soluble forms of Amyloid-β 1–42 oligomers (Aβ42o) trigger loss of excitatory synapses (synaptotoxicity) in cortical and hippocampal pyramidal neurons (PNs) prior to the formation of insoluble amyloid plaques. In a transgenic AD mouse model, we observed a spatially restricted structural remodeling of mitochondria in the apical tufts of CA1 PNs dendrites corresponding to the dendritic domain where the earliest synaptic loss is detected *in vivo*. We also observed AMPK over-activation as well as increased fragmentation and loss of mitochondrial biomass in Ngn2-induced neurons derived from a new $APP^{Swe/Swe}$ knock-in human ES cell line. We demonstrate that Aβ42o-dependent over-activation of the CAMKK2-AMPK kinase dyad mediates synaptic loss through coordinated phosphorylation of MFF-dependent mitochondrial fission and ULK2-dependent mitophagy. Our results uncover a unifying stress-response pathway causally linking Aβ42o-dependent structural remodeling of dendritic mitochondria to synaptic loss.

2.3 Introduction

Alzheimer's disease (AD) is the most prevalent form of dementia in humans, leading to socially devastating cognitive defects with poorly effective treatments. AD is characterized by two hallmark lesions, including extracellular amyloid plaques composed of fibrillar forms of Amyloid-β (Aβ) and intracellular neurofibrillary tangles (NFTs) composed of aggregated, hyperphosphorylated Tau. Before the formation of amyloid plaques and NFTs, amyloidogenic processing of amyloid precursor protein (APP) by β-and γ-secretase produces abnormal accumulation of a 42-amino acid-long amyloid-beta (Aβ42) peptide. Aβ42 peptides have a strong ability to oligomerize and form dimers, trimers, and higher order oligomers that ultimately fibrillate to form Aβ plaques[1]. Oligomeric forms of Aβ42 (Aβ42o) lead to early loss of excitatory synapses (synaptotoxic effects) in cortical and hippocampal pyramidal neurons (PNs) before plaque formation, strongly suggesting that synaptotoxicity is an early event in the disease progression, triggered by soluble Aβ42o[2–6]. This phenotype has been observed in various AD mouse models, including the J20 transgenic mouse model ($hAPP^{Swe,Ind}$), where progressive loss of excitatory synaptic connections occurs prior to Aβ plaque formation[2,7,8]. Soluble Aβ42o, extracted biochemically from AD patients or produced synthetically, also leads to rapid synaptic loss in PNs *in vitro*[2,5,6,9–11].

A second phenotype observed at the early stages of AD progression is structural abnormalities of mitochondria. Because of the terminal postmitotic status and extreme degree of compartmentalization of neurons of the central nervous system (CNS), maintaining mitochondrial homeostasis in neurons is highly dependent on the dynamic balance of fission/fusion and the efficient autophagic degradation of aged and damaged mitochondria[12–17]. Mitochondrial fission is carried out by a GTPase protein called Drp1 that needs to be recruited to the outer mitochondrial membrane (OMM) by various proteins, including MFF, Fis1, MiD49, and MiD51. The fusion machinery includes Mfn1/2, which is involved in the fusion of the OMM, and OPA1, which is involved in inner mitochondrial membrane fusion[18–20]. PNs show strikingly compartmentalized morphology of their mitochondria in the somato-dendritic versus axonal domains[14]. In most cells, mitochondria play critical physiological functions that might differ between dendrites and axons, such as ATP production, Ca^{2+} buffering, and lipid biosynthesis[13,14,21]. Recent evidence points to significant structural remodeling of dendritic mitochondria in hippocampal neurons in multiple AD mouse models and in AD patients[18,22–27], the hippocampus being one of the earliest affected brain regions in AD in mouse models and in AD patients[28–33]. However, the role played by changes in mitochondria structure and/or function in the disease's progression *in vivo*, especially in relation to synaptic loss, remains untested. Moreover, the molecular mechanisms causally linking changes in mitochondria structure/function and synaptic loss remain unknown in the context of AD pathophysiology.

Results from our lab, as well as others, have demonstrated that, in hippocampal and cortical PNs, Aβ42 oligomers over-activate AMP-activated kinase (AMPK) in a Ca^{2+}/calmodulin kinase kinase protein 2 (CAMKK2)-dependent manner, and preventing CAMKK2 or AMPK overactivation, either pharmacologically or genetically, protects hippocampal neurons from Aβ42o-dependent synaptic loss *in vitro* and *in vivo* in the $hAPP^{Swe,Ind}$ transgenic mouse model (J20)[2,34–36]. Importantly, AMPK is overactivated in the brain of AD patients where catalytically active AMPK accumulates in pyramidal neurons of the cortex and hippocampus[37,38].

In non-neuronal cells, AMPK is a key metabolic sensor that is catalytically activated upon increasing levels of AMP/ADP (when ATP levels drop) and regulates various downstream effectors involved in maintaining mitochondrial integrity in part via two recently identified downstream effectors: mitochondrial fission factor (MFF) and Unc-51 like autophagy activating kinases 1 and 2 (ULK1/2)[39]. MFF is an outer

mitochondrial protein with two identified AMPK phosphorylation sites. Upon AMPK activation, MFF enhances the recruitment of the fission protein Drp1, which is important for efficient fragmentation of mitochondria[40], a step thought to be required for efficient mitophagy through adaptation of mitochondria size to autophagosomes. The second, coordinated step regulated by AMPK activation is through the ULK proteins. ULK1 (also called Atg1) has multiple AMPK phosphorylation sites and functions in an evolutionarily conserved process called autophagy. Autophagy is involved in degrading cytoplasmic components via lysosomes, often under nutrient stress to obtain energy. Importantly, autophagy is the only known mechanism for degrading organelles, including mitochondria (mitophagy). Mounting evidence has also implicated altered autophagy in the pathogenesis of AD, as abnormal autophagic vacuoles (AV) build up in neurites of AD patients, at least at late stages of the disease progression[41].Therefore, we wanted to test if the CAMKK2-AMPK pathway could be the first pathway identified to coherently regulate the major AD phenotypes, and, more precisely, if Aβ42o-dependent overactivation of AMPK triggers synaptic loss through its ability to mediate mitochondrial structural remodeling.

In this study, we first reveal that hippocampal CA1 PNs display remarkably compartmentalized structural remodeling of dendritic mitochondria in the J20 AD mouse model *in vivo*: we observe the significant loss of mitochondrial biomass only in the apical tuft dendrites of CA1 PNs which, most significantly, corresponds to the dendritic compartment in the hippocampus where the loss of excitatory synapses can be first observed in this and other AD mouse models[42]. We next demonstrate that Aβ42o application induces sequential mitochondrial fission and loss of mitochondrial biomass through mitophagy in dendrites of cortical PNs via coordinated phosphorylation and activation of two critical AMPK effectors: MFF and ULK2. Importantly, individual manipulation of either MFF or ULK2 prevents Aβ42o-dependent dendritic spine loss, demonstrating a causal link between Aβ42o-dependent mitochondria structural remodeling and synaptic maintenance. Finally, we previously identified that Aβ42o-dependent AMPK phosphorylates Tau at Serine 262, and preventing S262 phosphorylation by AMPK protects cortical PNs from Aβ42oinduced synaptic loss. Interestingly, we show that the expression of Tau-S262A is protective towards Aβ42o-induced dendritic mitochondrial remodeling and synaptic loss in cortical PNs. Our results (1) demonstrate that the CAMKK2-AMPK stress-response pathway mediates Aβ42o-dependent synaptic loss through Tau-S262 and MFF-ULK2-dependent remodeling of dendritic mitochondria, (2) provide the

first “unifying” stress-response pathway triggering many of the cellular defects reported in AD mouse models and in the brain of AD patients during the early stages of the disease progression, such as Aβ42o-dependent Tau phosphorylation, defects in Ca^{2+} homeostasis, increased autophagy, and defective mitochondrial integrity (reviewed in ref. 1) and (3) provide the first causal link between Aβ- and Tau-dependent dendritic mitochondrial remodeling and synaptic loss.

2.4 Results

2.4.1 Spatially restricted structural remodeling of mitochondria and synaptic loss in apical tufts dendrites of CA1 hippocampal PNs in the $APP^{Swe, Ind}$ mouse model

The J20 mouse line is a powerful model to study the effect of amyloidosis in AD pathogenesis, as it expresses the human Amyloid Precursor Protein (APP) carrying two mutations found in familial forms of AD ($APP^{Swe,Ind}$ i.e., KM670/671NL and V717F called J20 model hereafter), and shows Aβ42o accumulation in the hippocampus[8].Forthisstudy, we chose to focus on the analysis of mitochondrial morphology and dendritic spine density in CA1 hippocampal neurons, which are among the first and the most affected in AD patients and AD mouse models[33,42–44]. Using sparse in utero hippocampal or cortical electroporation (E15 to P21), we were able to visualize dendritic mitochondria morphology and spine density in optically isolated dendritic segments of hippocampal CA1 PNs or layer 2/3 pyramidal neurons *in vivo* (Supplementary Fig. S1). Interestingly, in WT mice, both fluorescent labeling approaches[14] and serial EM reconstructions[45] demonstrate that layer 2/3 cortical PNs display elongated and fused dendritic mitochondria, forming a complex network throughout the entire dendritic arbor (Supplementary Fig. S1a, f, h). In sharp contrast, CA1 PNs display a high degree of compartmentalization of mitochondrial morphology in dendrites of WT mice: in basal and apical oblique dendrites, mitochondria are mostly small and punctate, whereas the distal apical dendrites contain elongated and fused mitochondria (Supplementary Fig. S1a–c, e, g). The transition between these two types of mitochondrial morphologies is sharp and corresponds to the boundary between the hippocampal layer stratum radiatum (SR; receiving primarily inputs from CA3 PNs; Supplementary Fig. S1b) and stratum lacunosum moleculare (SLM; receiving presynaptic inputs from the medial entorhinal cortex MEC directly; Supplementary Fig. S1b).

Figure 1

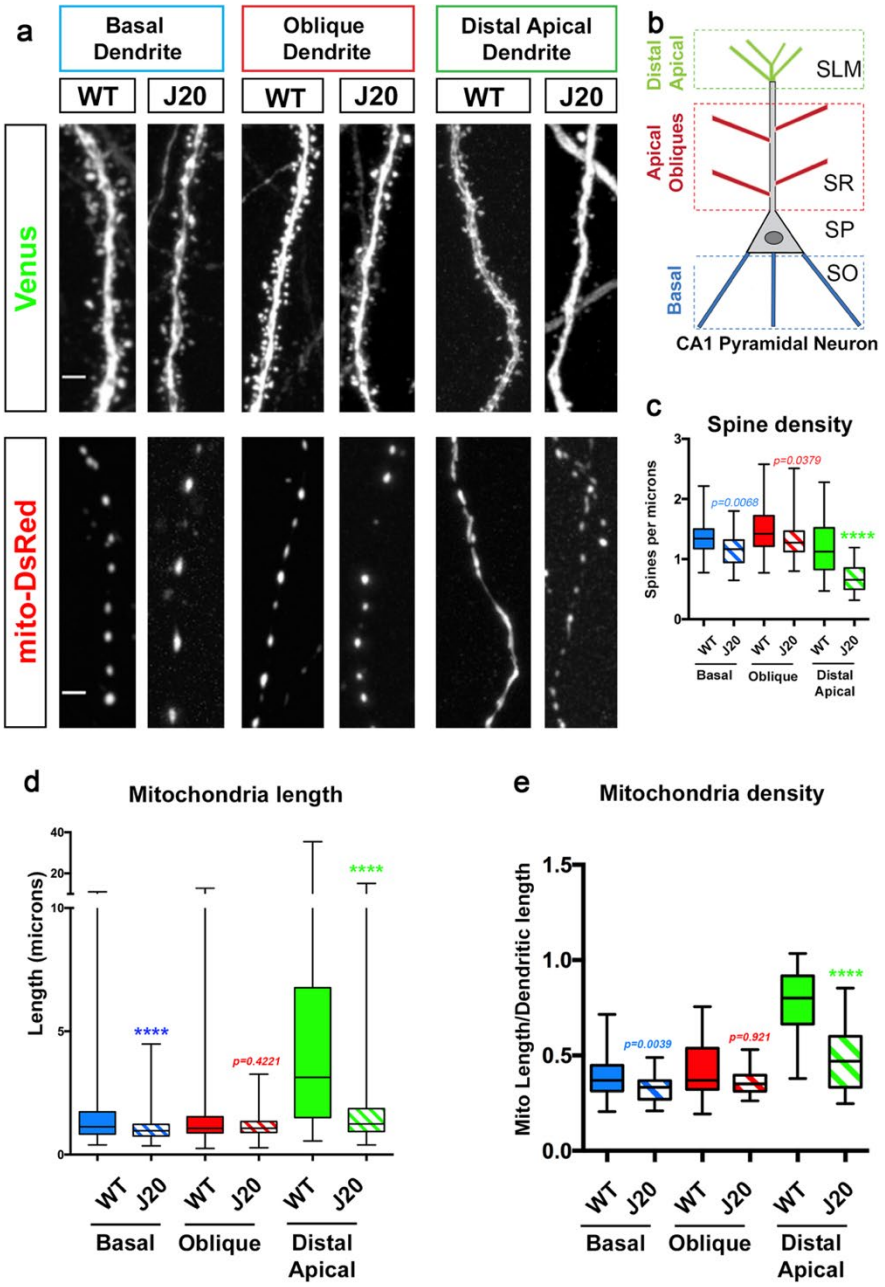

Figure 2.1. In an AD mouse model (J20), CA1 pyramidal neurons display spatially restricted loss of mitochondrial biomass and dendritic spine loss in distal apical tufts.

a, b Representative images of CA1 PN dendritic segments from different layers of WT control and J20 mice. CA1 PNs were electroporated with pCAG-Venus and pCAG-mito-DsRed by in utero electroporation in E15.5 WT and J20 mouse embryos. Both mouse groups were fixed and imaged at 3-months postnatal (P90). Dendrites from basal, oblique, and distal apical are magnified to show spine density and mitochondrial morphology. The three types of dendritic segments were imaged in three distinct layers as depicted in b for both WT and J20 mice. **c–e** Quantification of spine density (**c**), individual mitochondrial length (**d**), and mitochondrial density (**e**), measured as the fraction of a dendritic segment length occupied by mitochondria. In panels **c–e**, data are represented by box plots displaying minimum to maximum values, with the box denoting 25th, 50th (median), and 75th percentiles from at least three independent in utero electroporated mice. $n_{Basal\ WT}$ = 47 dendrites, 595 mitochondria; $n_{Basal\ J20}$ = 32 dendrites, 495 mitochondria; $n_{Oblique\ WT}$ = 46 dendrites, 630 mitochondria; $n_{Oblique\ J20}$ = 33 dendrites, 507 mitochondria; $n_{Distal\ WT}$ = 39 dendrites, 284 mitochondria; $n_{Distal\ J20}$ = 32 dendrites; 426 mitochondria. All of the analyses were done blind to the experimental conditions and were manually counted using FIJI. Statistical analyses were performed using Mann–Whitney test (c–e). Exact *P* values are indicated on the figure when available through Prism software, otherwise, the test significance is provided using the following criteria: ***$P < 0.001$; ****$P < 0.0001$. Scale bar = 2 µm.

We applied the same experimental approach in both WT and J20 littermate mice, and examined mitochondrial morphology and spine density in 3-month-old mice, a time point where abundant Aβ42o can be detected, but preceding appearance of amyloid plaques[8]. This analysis revealed that, consistent with what we observed in the hippocampus of WT mice at P21 (Supplementary Fig. S1), 3-month-old WT and J20 mice both display mostly small, punctate mitochondria, visualized by labeling the mitochondrial matrix, in basal and apical oblique dendrites (Fig. 1a). This is accompanied by a trending, though not significant, decrease in spine density in basal and apical oblique dendrites in the J20 mice (Fig. 1a, c). However, the distal apical dendrites of the J20 mice showed a dramatic and significant reduction of both mitochondrial length and density/biomass, as well as a significant decrease in spine density compared to WT littermates (Fig. 1a, d, e). These results reveal (1) a striking and unique degree of compartmentalization of mitochondrial morphology in dendrites of CA1 PNs not observed in cortical layer 2/3 PNs, and (2) a spatially restricted loss of mitochondrial biomass and spine density specifically in the apical tuft dendrites of CA1 PNs in the J20 mouse model. This co-occurrence of mitochondrial remodeling and decreased spine density raised the possibility, tested below, of a potential causal relationship between Aβ42o-dependent mitochondrial remodeling and synaptic maintenance.

2.4.2 Aβ42o induces synaptic loss and dendritic mitochondrial remodeling in the same time frame

In order to examine the temporal relationship between mitochondrial remodeling and decreased spine density, we adopted an *in vitro* model allowing us to control the timing of Aβ42o application. We turned to long-term *in vitro* cortical PNs cultures[2], which are synaptically connected and display uniformly fused mitochondria throughout their dendritic arbor *in vitro* (Fig. 2) as observed *in vivo* (Supplementary Fig. S1). We observed significant, time-dependent changes in dendritic mitochondrial structure following acute Aβ42o application, including both a reduction of their length and a reduction in mitochondrial density/biomass (lower panels in Fig. 2a–c and Fig.2d, e). In the same neurons, we observed a progressive reduction in dendritic spine density in Aβ42o-treated neurons between 14 and 24 h following Aβ42o application (upper panels in Fig. 2a–c and Fig.2f). No significant changes in mitochondria morphology were observed in the soma or the axon of the same neurons or, as previously reported, when control inverted peptide (INV42) were applied at similar concentrations as Aβ42o (300–450 nM; Supplementary Fig. S2)[2,5,6,10,11]. We previously reported that, at this dose and duration, Aβ42o application

Figure 2

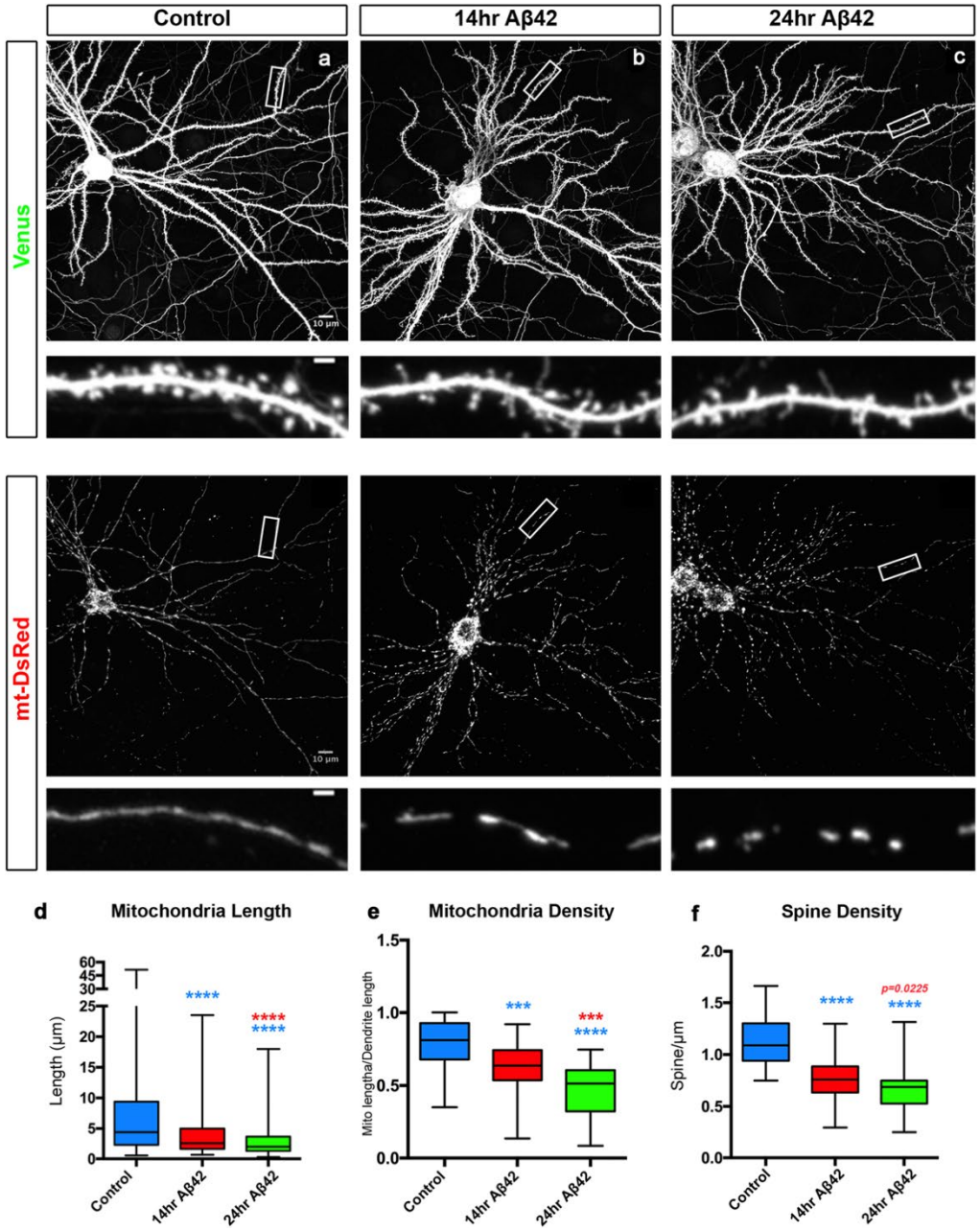

Figure 2.2. Aβ42o induces dendritic mitochondrial fragmentation and dendritic spine loss within the same time frame. **a–c** Representative images of primary cortical neurons at 21 days *in vitro* (DIV). Neurons express via ex utero electroporation pCAG-mVenus (upper panels in **a–c**) and pCAG-mito-DsRed (lower panels in **a–c**) to assess spine density and mitochondrial morphology, respectively. At 20 DIV, neurons were treated with either a vehicle control for 24 h or with Aβ42o (300–450 nM, see "Methods" for details) for either 14 or 24 h. High magnification of secondary dendrites is shown below the low magnification of the whole neurons. **d** Quantification of dendritic mitochondrial length. **e** Quantification of dendritic mitochondrial density. Dendritic mitochondrial density was calculated by summing the length of all the mitochondria then dividing that cumulative length by the length of the dendritic segment in which the mitochondria were quantified. **f** Quantification of dendritic spine density, calculated by dividing the number of spines by the length of the dendrite segment in which the spines were quantified. All of the analyses were done blind to the experimental conditions and were done by manual counting using FIJI. In panels **d–f**, data are represented by box plots displaying minimum to maximum values, with the box denoting 25th, 50th (median), and 75th percentiles from three independent experiments. $n_{control}$ = 53 dendrites, 278 mitochondria; $n_{14hr\ A\beta42o}$ = 47 dendrites; 380 mitochondria; $n_{24hrA\beta42o}$ = 51 dendrites, 400 mitochondria. Statistical analyses were performed using Mann–Whitney test in (**d–f**). Exact *P* values are indicated on the figure when available through Prism software, otherwise, the test significance is provided using the following criteria: ***$P < 0.001$; ****$P < 0.0001$. Colors of significance symbols correspond to groups being compared. Scale bar for high-magnification dendritic segments = 2 µm.

does not affect neuronal viability, strongly suggesting that the effects we observe are not a secondary consequence of compromising neuronal survival[2]. Taken together, our results highlight that Aβ42o application triggers a significant degree of time-dependent, structural remodeling of dendritic mitochondria, including a reduction of mitochondrial biomass concomitant with a reduction in spine density, which is a reliable index of excitatory synapse number in dendrites of PNs[46,47].

2.4.3 Aβ42o induces mitochondrial structural remodeling and AMPK overactivation in human pyramidal neurons

These results show that *in vivo* exposure of CA1 hippocampal PNs to Aβ42o resulting from overexpression of $APP^{Swe,Ind}$ in the J20 AD mouse model, or direct application of synthetic Aβ42o at 300–450 nM for 24 h in mature cortical PNs *in vitro*, leads to striking loss of dendritic mitochondrial biomass and to synaptotoxicity. However, we wanted to overcome two potential limitations of these approaches: (1) both use mouse models, which could differ from the way human neurons might respond to Aβ42o, and (2) both approaches rely on exposure of cortical or hippocampal PNs to high levels of Aβ42o. In order to address both points, we generated a novel human embryonic stem cell (hESC) $APP^{Swe/Swe}$ homozygous knock-in model. CRISPR-Cas9-mediated genome engineering was used to introduce the APP^{Swe} mutation into both alleles of the H9 hESC cell line (WA09, WiCell). Previous knock-in of the Swedish mutation into a human PSC line demonstrated increased endogenous APP processing and generation of Aβ42oinanallelic dose-dependent manner[48].

$APP^{Swe/Swe}$ knock-in hESCs and their isogenic H9 parent control line were transdifferentiated into glutamatergic cortical neurons (iNs) using doxycycline-inducible Neurogenin2 (Ngn2) expression[49]. Following efficient Ngn2-P2A-EGFP-induced neuronal differentiation (see “Methods”), we transiently transfected these neurons in a sparse manner with a mitochondrial fluorescent reporter (mito-DsRed) and quantified dendritic mitochondrial morphology in control H9 and isogenic $APP^{Swe/Swe}$-derived neurons (Supplementary Fig. S3). Our results demonstrate a significant reduction in dendritic mitochondrial density (Supplementary Fig. S3b) and mitochondrial length (Supplementary Fig. S3c) in $APP^{Swe/Swe}$ human neurons compared to isogenic control neurons. As previously observed in cortical and hippocampal mouse neurons *in vitro* and *in vivo*[2], we also found increased AMPK activation in $APP^{Swe/Swe}$ neurons compared to isogenic control neurons, as measured biochemically by the ratio of phosphorylated AMPK-T172 to total AMPK

(Supplementary Fig. S3d, e). These results demonstrate that endogenous levels of Amyloid-β generated by the processing of mutated APP^{Swe} in human neurons can trigger dendritic mitochondrial remodeling and loss of biomass as well as AMPK overactivation as observed in mouse cortical and hippocampal neurons *in vitro* and *in vivo*, respectively.

2.4.4 Acute Aβ42o application induces local mitophagy in dendrites

We next tested whether the loss of mitochondrial biomass induced by Aβ42o is triggered in dendrites of PNs by local mitophagy. To that end, we examined the dynamics of autophagosomes, lysosomes, and autolysosomes, as well as changes in mitochondrial biomass in cortical PNs upon Aβ42o treatment, using sparse ex utero electroporation of plasmids encoding mito-mTagBFP2, LAMP1-mEmerald, and RFP-LC3 to visualize mitochondria, lysosomes, and autophagosomes, respectively. Cortical PNs were cultured for at least 21DIV in high-density cultures, when they display mature synapses[2], and imaged live using time-lapse confocal microscopy every 15 min for 14 h following treatment with either control (vehicle) or Aβ42o (Fig. 3).

In contrast, upon Aβ42o treatment, we observed a significant accumulation of both LC3+ and LAMP1+ puncta in dendrites over time (Fig. 3a–d). In dendrites exposed to Aβ42o, many of the LC3+ puncta become co-localized with LAMP1+, suggesting these autolysosomes can accumulate locally in dendrites. LC3+/LAMP1+ autolysosomes do form occasionally in control dendrites (Fig. 3a–d and quantified in Fig. 3e). As quantified in Fig. 3e, treatment with Aβ42o leads to an almost fivefold increase in the percentage of dendritic segments with increased LC3+ /LAMP1+ autolysosome accumulation compared to control-treated PNs. Both LC3 and LAMP1 normalized fluorescence intensity showed time-dependent increases upon Aβ42o application, highlighting local biogenesis of autophagic vacuoles and their coalescence with lysosomes in dendritic shafts upon Aβ42o treatment, respectively (Fig. 3). We also observed a significant reduction in mitochondria fluorescence (measured via mito-mTAGBFP2, (Fig. 3b–d)) in a spatially restricted area close to LC3+/LAMP1+ puncta as indicated by yellow arrows in the representative image (Fig. 3b) and the kymograph (Fig. 3c). Not all LC3+ /LAMP1+ puncta correlated with loss of mitochondria within 14 h of time-lapse imaging, however, as indicated by the red arrow in the representative image and kymograph (Fig. 3a–c). However, our approach of monitoring autolysosome formation and determining if they engage in mitophagy events (as opposed to autophagy of other cargoes

Figure 3

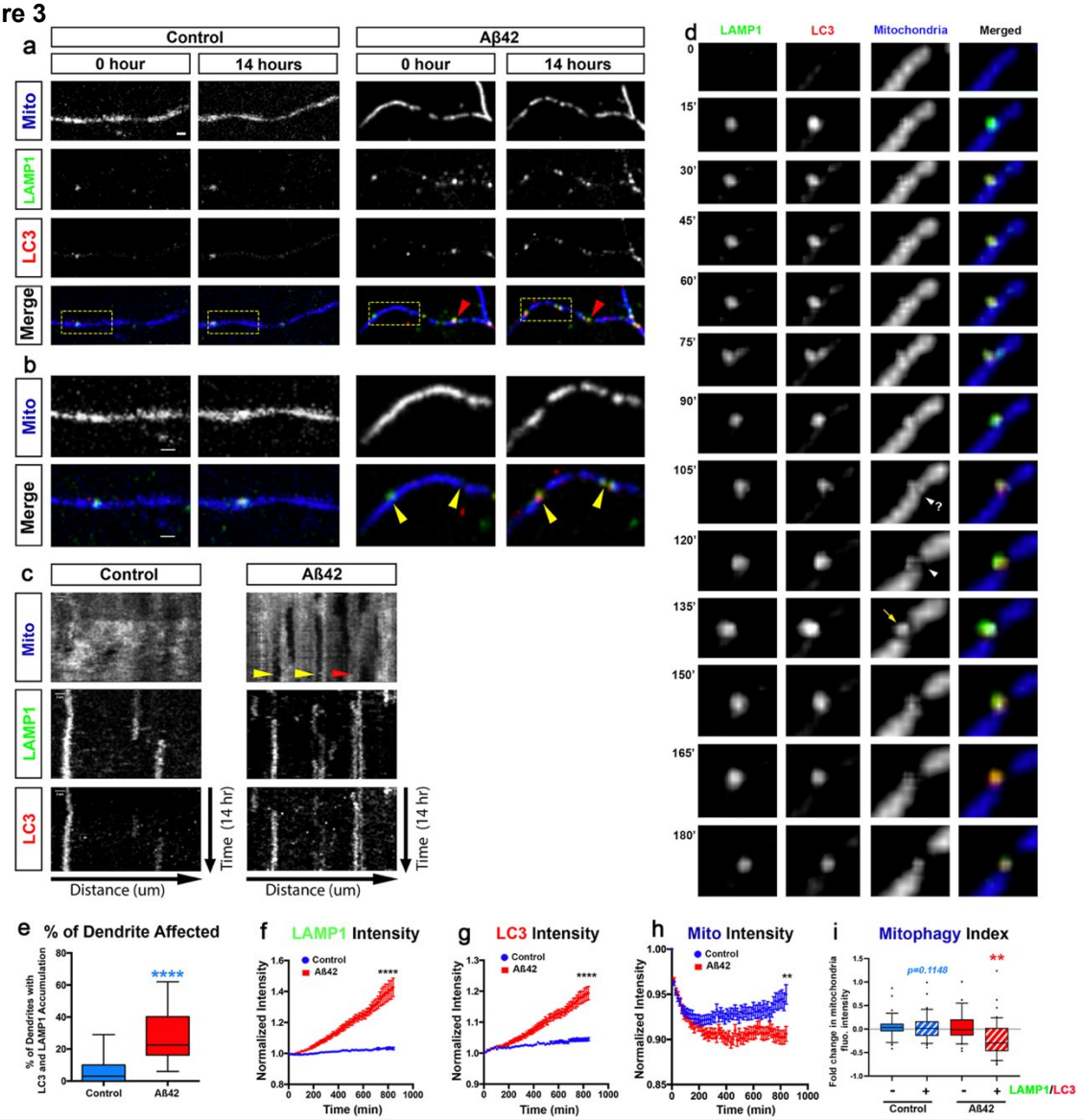

Figure 2.3. Aβ42o treatment induces local mitophagy in dendrites.

a, b Secondary dendritic segments from primary cortical PNs at 21–25 DIV, ex utero electroporated at E15.5 with pCAG-mito-mTagBFP2, pCAG-LAMP1-mEmerald, and pCAG-RFP-LC3 to visualize mitochondria, lysosomes, and autophagosomes, respectively (**a**). At 21 DIV, neurons were treated with either a vehicle control or Aβ42o and imaged live using time-lapse microscopy every 15 min for 14 h. The yellow boxes label the magnified areas shown in **b** illustrating that, in control-treated neurons, there is no significant change in LAMP1 + (lysosomes), LC3 + (autophagosomes), or LC3-LAMP1 double- positive (autolysosomes) vesicle dynamics and/or accumulation (see Supplementary Movies S1 and S2). In contrast, in dendrites of Aβ42o-treated cortical PNs, sites of LAMP1-LC3 double-positive autolysosome accumulation often result in loss of mitochondria as indicated by yellow arrows in panel **b**. **c** Representative kymographs of mitochondria, lysosomes, and autophagosomes from dendrites in panel a. The yellow arrows point to loss of mitochondrial fluorescent signal, deemed mitophagy events. The red arrow indicates no decrease in mitochondrial signal, despite LAMP1 and LC3 signal, indicating an incomplete mitophagy event. **d** Detail of an autolysosome engulfing a fragment of mitochondria (135′) following a mitochondrial fission event (105′−120′). **e** The percentage of dendritic segments showing accumulation of both LC3 + autophagosomes, LAMP1 + lysosomes, or LC3-LAMP1 double-positive autolysosomes. Data are represented by box plots displaying minimum to maximum values, with the box denoting 25th, 50th (median), and 75th percentiles from three independent experiments. $n_{control}$ = 15 neurons; $n_{Aβ42o}$ = 24 neurons. **f–i** Quantification of **f** LAMP1 intensity, **g** LC3 intensity, and **h** Mitochondrial intensity for dendritic segments over the course of the 14 h following treatments. **i** Mitophagy index defined as the change in mitochondrial fluorescence intensity in dendritic segment with (+) or without (−) LC3-LAMP1 double-positive puncta (autophagosomes) at 14 h. In panels **f–i**, data are represented as mean + /− SEM based on $n_{Control}$ = 33 dendrites; $n_{Aβ42o}$ = 44 dendrites. Statistical significance was performed using a Mann–Whitney test. Exact *P* values are indicated on the figure when available through Prism software, otherwise, the test significance is provided using the following criteria: ***P* < 0.01; *****P* < 0.0001. Scale bar = 2 μm.

or organelles) is validated by careful examination of these time-lapse videos. As shown in Fig. 3d, the formation and recruitment of an autolysosome (LC3+/LAMP1+) near a mitochondrion is temporally separated from fission events and actual engulfment of a mitochondrial fragment, demonstrating that these events actually correspond to mitophagosomes.

To quantify spatial dynamics of mitophagy, we defined a 'mitophagy index' along segments of dendrites by measuring the intensity of mito-mTagBFP2 fluorescence using line scan intensity measurements in regions of interest (ROI) with or without LC3+/LAMP1+ puncta. This index reflects the probability of loss of mitochondrial biomass inside versus outside of areas where autophagosomes and lysosomes coalesce to generate autolysosomes. In control conditions, the formation of LC3+/LAMP1+ puncta is not only a rare event (Fig. 3a, e), but the presence of LC3+/LAMP1+ puncta did not result in loss of mitochondria biomass, suggesting basal levels of mitophagy are low in dendrites of cortical PNs in these conditions (Fig. 3e, f). In contrast, upon Aβ42o treatment, we frequently observed spatially restricted mitophagy events (shown in Fig. 3d), only found in dendritic segments containing LC3+/LAMP1+ autolysosomes, demonstrating significant levels of mitophagy occur locally in dendrites of cortical PNs upon Aβ42o treatment (Fig. 3e–i).

2.4.5 Aβ42o-dependent mitochondrial fragmentation and synaptotoxicity are mediated by CAMKK2-AMPK overactivation

We have previously shown that Aβ42o-dependent overactivation of the CAMKK2-AMPK kinase dyad mediates excitatory synaptic loss both in primary cortical PNs in culture and in hippocampal PNs in the J20 AD mouse model[2]. Since AMPK is a central regulator of mitochondrial homeostasis[39], we tested if the CAMKK2-AMPK pathway was required for Aβ42o-induced dendritic mitochondrial remodeling in primary cortical PNs cultures *in vitro* using a conditional double-floxed mouse line for the two genes encoding catalytic subunits (α1 and α2) of the AMPK heterotrimers (AMPKα1$^{F/F}$/α2$^{F/F}$ [50]). We performed ex utero cortical electroporation of AMPKα1$^{F/F}$/α2$^{F/F}$ E15.5 embryos (targeting progenitors generating layer 2/3 PNs) with (1) a control plasmid lacking Cre recombinase or a plasmid expressing Cre recombinase, (2) a Venus fluorescent protein to visualize spine morphology, and (3) mito-DsRed to examine mitochondrial morphology (Fig. 4). Quantitative analysis indicated that, in basal conditions, AMPKα1/α2 null PNs have spine and mitochondrial densities indistinguishable from wild-type neurons (Fig. 4a–d). Strikingly,

Figure 4

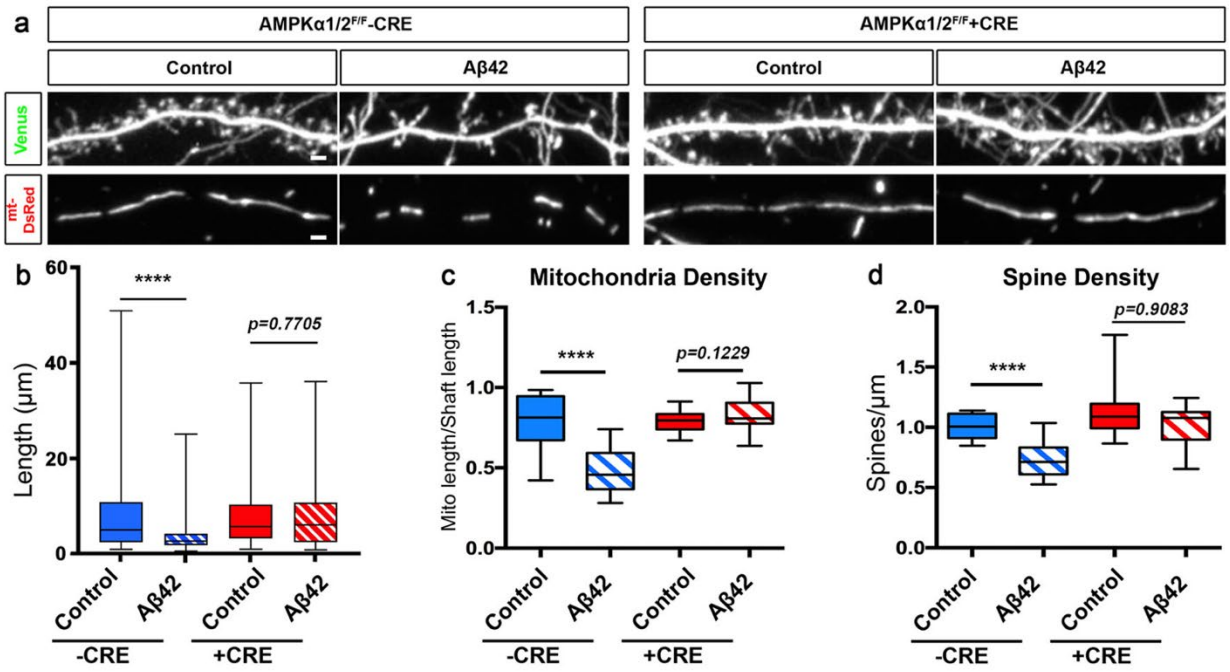

Figure 2.4. Oligomeric Aβ42-induced synaptotoxicity and dendritic mitochondrial fragmentation is AMPK-dependent.
a Secondary dendritic segments of primary cortical PNs at 21 DIV. Embryos from AMPK*α*1/*α*2 double conditional knockout (AMPK$\alpha1^{F/F}/\alpha2^{F/F}$) were ex utero electroporated at E15.5 with pCAG-mVenus, pCAG-mito-DsRed, and either scrambled pCAG-Cre (control) or pCAG-Cre recombinase. Neurons were treated at 20 DIV with either a vehicle control or A*β*42o for 24 h. **b–d** Quantification of **b** mitochondria length, **c** mitochondrial density, and **d** spine density in individual dendritic segments. All of the analyses were done blind to the experimental conditions and were done by manual counting using FIJI. Data is represented by box plots displaying minimum to maximum values, with the box denoting 25th, 50th (median), and 75th percentiles from three independent experiments. $n_{CreNegative\ Control}$ = 27 dendrites, 128 mitochondria; $n_{CreNegative A\beta42o}$ = 29 dendrites, 204 mitochondria; $n_{CrePositive\ Control}$ = 29 dendrites, 143 mitochondria; $n_{CrePositive\ A\beta42o}$ = 24 dendrites, 112 mitochondria. Statistical significance was performed using a Mann–Whitney test. Exact *P* values are indicated on the figure when available through Prism software, otherwise, the test significance is provided using the following criteria: ***P* < 0.01; *****P* < 0.0001. Scale bar = 2 *µ*m.

AMPKα1/α2 null neurons are completely protected from Aβ42oinduced mitochondrial density reduction (Fig. 4a–c) as well as dendritic spine loss (Fig. 4a–d) as previously reported[2].This demonstrates that overactivation of AMPK is required for both Aβ42o-induced mitochondria structural remodeling and spine loss in dendrites of PNs.

AMPK has two upstream regulatory kinases, namely LKB1 and CAMKK2, which phosphorylate the AMPKα subunit on T172, significantly increasing its catalytic activity[51]. However, in cortical PNs, CAMKK2 has been identified as the primary upstream regulator of AMPK[2,35,52]. Therefore, we assessed if pharmacologically blocking CAMKK2 acutely interfered with Aβ42o effects on mitochondrial structural remodeling and dendritic spine loss. Pretreatment of primary neuronal cultures with STO-609, a specific CAMKK2 inhibitor[53], completely blocked Aβ42o-induced mitochondrial structural remodeling (Supplementary Fig. S4a–c) as well as synaptotoxicity (Supplementary Fig. S4d) as previously published[2].

2.4.6 Aβ42o-induced MFF overactivation causally links mitochondrial fragmentation and synaptic loss

In non-neuronal cells, AMPK has been identified as a major metabolic sensor regulating ATP homeostasis upon induction of metabolic stress through its ability to phosphorylate many downstream effectors involved in various aspects of metabolic homeostasis[39,52]. As part of this metabolic stress response, AMPK regulates mitochondrial fission through direct phosphorylation of mitochondrial fission factor (MFF), which enhances its ability to recruit Drp1 to the outer mitochondrial membrane and promotes mitochondrial fission[40]. To that end, we tested if MFF is the effector mediating AMPK-dependent Aβ42o-induced mitochondrial fission, and if blocking MFF-dependent fission can prevent synaptic loss. Upon exposure to Aβ42o, cortical PNs *in vitro* that express MFF shRNA (knockdown efficacy validated in ref. 14) are protected from loss of mitochondrial biomass in dendrites (Fig. 5a–c) and from synaptic loss (Fig. 5a, d). Strikingly, knockdown of MFF in basal conditions does not affect dendritic mitochondrial length and density (Fig. 5a–c) or dendritic spine density (Fig. 5a, d), strongly suggesting that the signaling pathway we have identified is a bona fide stress-response pathway in dendrites upon Aβ42o exposure, as we have previously hypothesized[54,55]. Altogether, these results suggest a causal relationship between Aβ42o-induced MFF-dependent dendritic mitochondrial fission and dendritic spine loss.

Figure 5

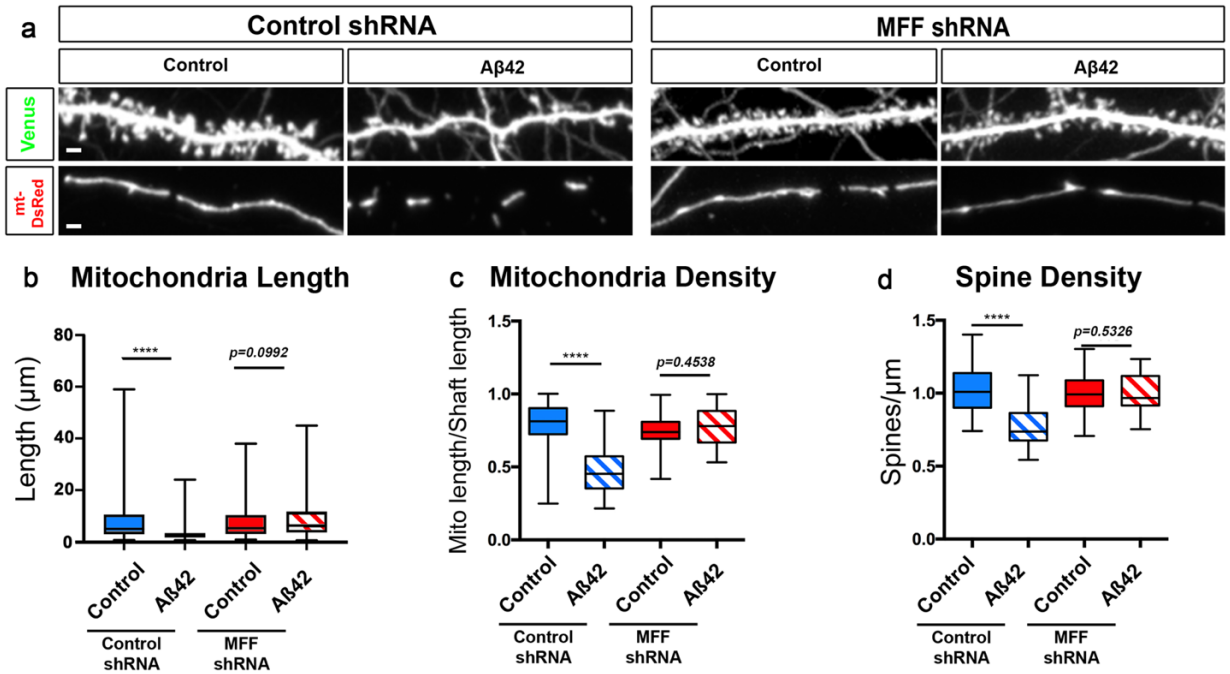

Figure 2.5. MFF is required for Aβ42o-induced dendritic mitochondrial fragmentation and dendritic spine loss *in vitro*.
a Representative images of secondary dendritic segments of primary cortical PNs at 21 DIV. Embryos at E15.5 were ex utero electroporated with pCAG-mVenus, pCAG-mito-DsRed, and either with control shRNA or an shRNA specific for mouse MFF (MFF shRNA). Neurons were treated at 20 DIV with either a vehicle control or Aβ42o for 24 h. Knockdown of MFF blocks both dendritic mitochondrial fragmentation and subsequent degradation as well as dendritic spine loss. **b–d** Quantification of dendritic mitochondrial length (**b**), dendritic mitochondrial density (**c**), and dendritic spine density (**d**). All of the analyses were done blind to the experimental conditions and were done by manual counting using FIJI. Data are represented by box plots displaying minimum to maximum values, with the box denoting 25th, 50th (median), and 75th percentiles from three independent experiments. $n_{pLKO\ Control}$ = 36 dendrites, 188 mitochondria; $n_{pLKO\ Aβ42o}$ = 41 dendrites, 300 mitochondria; $n_{MFFshRNA\ Control}$ = 36 dendrites, 167 mitochondria; $n_{MFFshRNA\ Aβ42o}$ = 30 dendrites, 125 mitochondria. Statistical analyses were performed using a Mann–Whitney test in (**b–d**). Exact *P* values are indicated on the figure when available through Prism software, otherwise, the test significance is provided using the following criteria: ****$P < 0.0001$. Scale bar for magnified dendritic segments = 2 µm.

2.4.7 MFF knockdown prevents spatially restricted mitochondrial fragmentation and reduced synaptic density in distal apical tufts in CA1 PNs of an AD mouse model *in vivo*

The results from the *in vitro* rescue experiments presented in Fig. 5 strongly suggest that blocking MFF-dependent mitochondrial fission in cortical PNs prevents spine loss mediated by acute exposure to Aβ42o. We wanted to extend this observation *in vivo* and for CA1 PNs. To achieve this, we performed hippocampal in utero electroporation targeting specifically CA1 PNs in wild-type or J20 ($APP^{Swe, Ind}$) mouse littermates[55] with plasmids expressing a mitochondrial matrix marker (mito-YFP), a cell filler (tdTomato), and either a control shRNA or an shRNA knocking down MFF[14] (Fig. 6a). As reported in Fig. 1, we observed both a significant reduction of spine density in apical tufts dendrites of CA1 PNs and a reduction of mitochondrial volume in J20 mice compared to wild-type littermates at 3 months (Fig. 6b–d). Strikingly, shRNA-mediated knockdown of MFF prevented loss of mitochondrial volume in the apical tufts dendrites of J20 mice (Fig. 6a, c) and also rescued spine loss in the same dendritic segments (Fig. 6a, d). Because these experiments are performed at very low transfection efficiency *in vivo*, these rescue effects are not only cell-autonomous, they are postsynaptic-autonomous since close to 100% of the axonal inputs to these CA1 PNs where we knockdown MFF are either wild-type in the wild-type littermates or pathologically unmodified in the J20 APP-expressing mice as they have no MFF knockdown. We conclude that Aβ42o-mediated mitochondrial structural remodeling in apical tufts of CA1 PNs *in vivo* are causally linked to the postsynaptic loss of spines *in vivo*.

2.4.8 Aβ42o-induced MFF phosphorylation by AMPK is required for dendritic mitochondrial fragmentation and synaptic loss

To determine if MFF is phosphorylated by Aβ42o-dependent AMPK overactivation in neurons, we measured and compared AMPK-mediated phosphorylation of MFF at Serine 146 (S146; one of the AMPK phosphorylation sites of Isoform 3 enriched in the brain[56]) to total MFF in primary cortical neurons treated with Aβ42o or a control (Supplementary Fig. S5). As a positive control to show that the MFF S146 site is regulated by AMPK activation, we overexpressed the human isoform of MFF in Neuro2A (N2A) neuroblastoma cells and treated with Metformin, a potent activator of AMPK[40], or a vehicle control

Figure 6

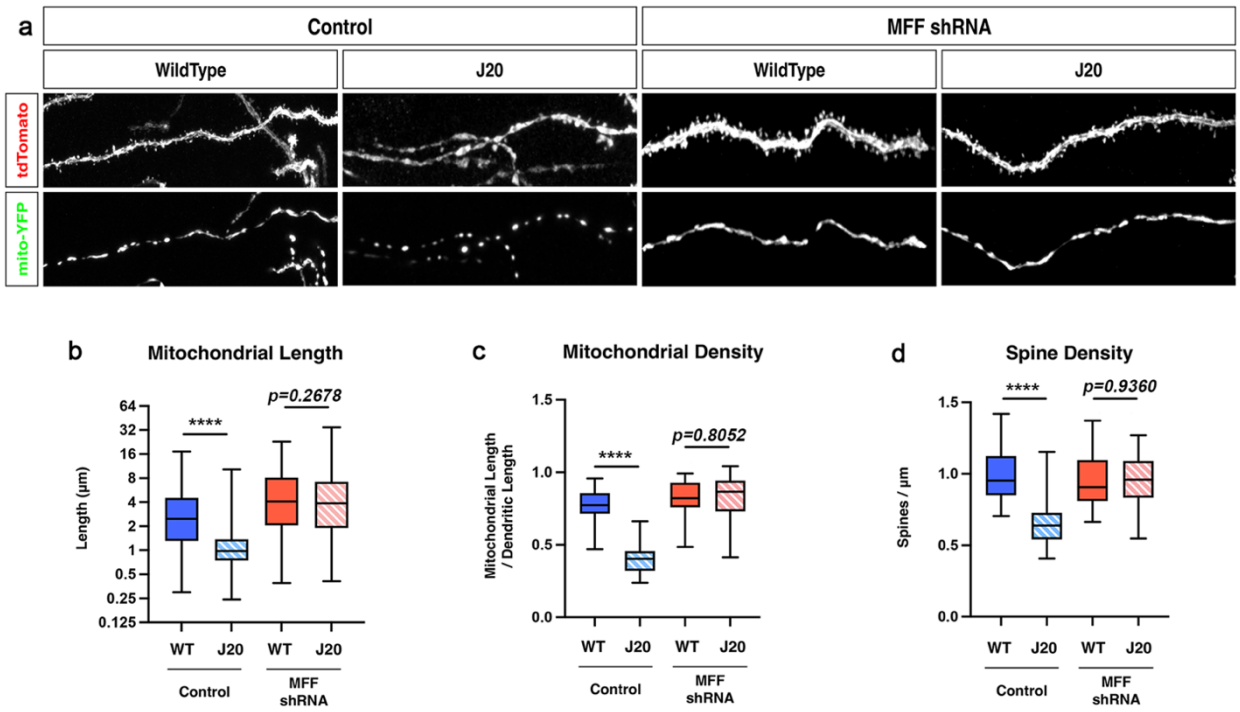

Figure 2.6. MFF is required for Aβ42o-induced dendritic mitochondrial fragmentation and spine loss in apical tufts of CA1 PNs *in vivo*.

a High-magnification images of dendritic segments in stratum lacunosum moleculare (SLM) of CA1 PNs of 3-months-old WT or J20 mice. CA1 PNs were co-electroporated in utero at E15.5 with plasmids expressing a cell filler (tdTomato), a mitochondrial matrix marker (mito-YFP) and either control (scrambled) shRNA or shRNA targeting mouse MFF. **b–d** Quantification of dendritic mitochondrial length (**b**), dendritic mitochondrial density (**c**), and dendritic spine density (**d**). Data are represented by box plots displaying minimum to maximum values, with the box denoting 25th, 50th (median), and 75th percentiles from at least three independent in utero electroporated mice. $n_{Control/WT}$ = 21 dendrites, 157 mitochondria; $n_{Control/J20Het}$ = 22 dendrites, 327 mitochondria; $n_{shMFF/WT}$ = 14 dendrites, 102 mitochondria; $n_{shMFF/J20Het}$ = 36 dendrites, 256 mitochondria. All of the analyses were done blind to the experimental conditions and were manually counted using FIJI. Statistical analyses were performed using a Mann–Whitney test in **b–d**. Exact *P* values are indicated on the figure when available through Prism software, other- wise, the test significance is provided using the following criteria: ****$P < 0.0001$. Scale bar for magnified dendritic segments = 2 µm.

(Supplementary Fig. S5a, b). First, Aβ42o application for 24 h on long-term cortical PNs cultures showed a significant increase in AMPK phosphorylation at T172 site as previously reported[2,36] (Supplementary Fig. S5a, b). As a consequence of AMPK activation, we observe an increase in phosphorylation of MFF at S146 in cortical neurons upon Aβ42o application that is comparable to Metformin treatment of N2A cells (Supplementary Fig. S5a, b). This experiment demonstrates that Aβ42o triggers phosphorylation of MFF via AMPK in cortical PNs, which is also observed in AD patients brains[37].

To test if AMPK-dependent phosphorylation of MFF is required for Aβ42o-dependent mitochondrial remodeling, we took a gene replacement approach by knocking down mouse MFF and expressing either wild-type human MFF (hMFF-WT) or human MFF that cannot be phosphorylated by AMPK (hMFF-AA) in primary cortical PNs. Low expression levels of hMFF-WT (not targeted by mouse-specific MFF shRNA) and hMFF-AA, which carries two point mutations (S155A and S172A), previously shown to abolish AMPK-mediated MFF function in mitochondrial fission[40], when combined with mouse-specific MFF shRNA, does not lead to mitochondrial fragmentation in control conditions, i.e., does not lead to MFF overexpression which was previously shown to be sufficient to induce dendritic mitochondrial fragmentation[40]. Primary cortical PNs expressing these titrated levels of hMFF-WT showed both mitochondrial and spine loss following 24 h of Aβ42o treatment (Fig. 7a–d) to levels comparable to control neurons exposed to Aβ42o, whereas neurons expressing titrated levels of hMFF-AA were protected from Aβ42o-induced mitochondrial structural remodeling and spine loss (Fig. 7a–d). These results demonstrate a causal role of Aβ42o-triggered mitochondrial remodeling, induced by AMPK-mediated phosphorylation of MFF, and synaptic loss.

2.4.9 Activation of ULK2 by AMPK leads to loss of mitochondrial biomass following MFF-dependent mitochondrial fission

In non-neuronal cells under conditions of metabolic stress, AMPK activation not only triggers increased mitochondrial fission through phosphorylation and activation, but also triggers mitophagy by directly phosphorylating the autophagy initiating kinase, ULK1 (Atg1)[57]. Since we observed (1) increased mitophagy in dendrites exposed to Aβ42o, (2) a significant decrease in mitochondrial biomass following increased AMPK-MFF-dependent fission between 14–24 h of Aβ42o treatment (Figs. 2 and 3) and (3) previous results show AMPK robustly activates ULK kinases in neurons[58], we hypothesized that over-activation of AMPK

Figure 7

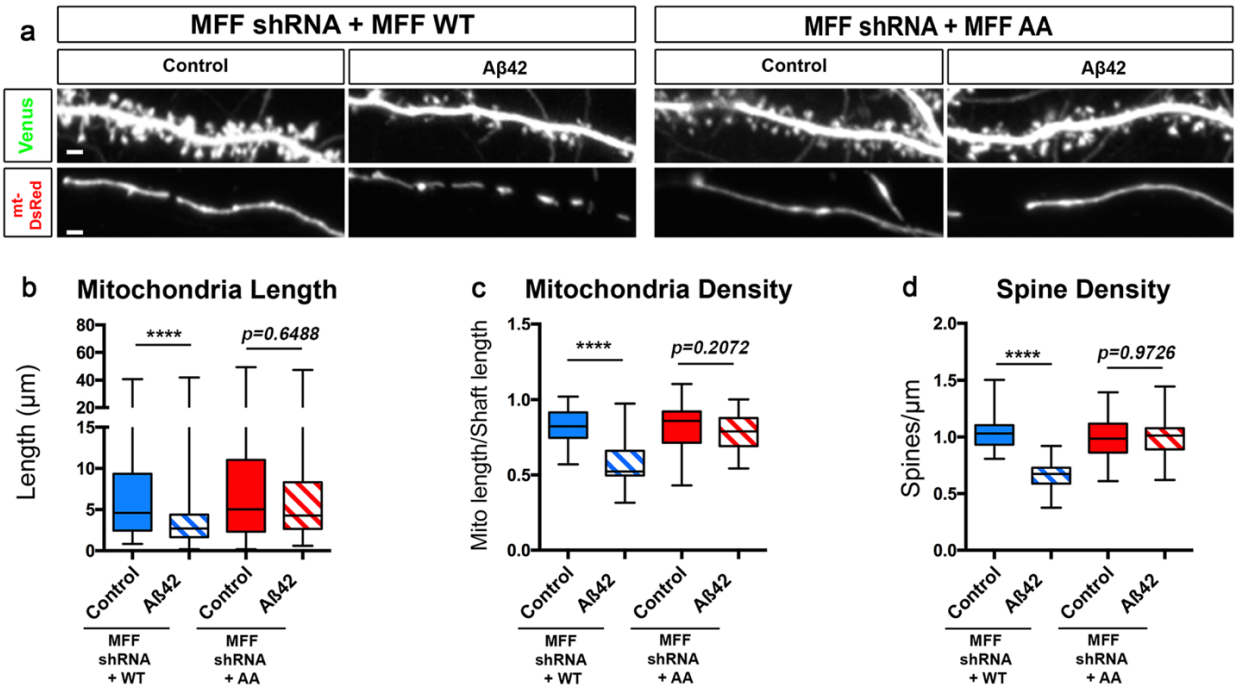

Figure 2.7. Aβ42o induces AMPK-dependent MFF phosphorylation at two serine sites required for Aβ42o-dependent dendritic mitochondrial fragmentation and spine loss.

a Representative images of secondary dendritic segments of primary cortical PNs at 21 DIV. Embryos at E15.5 were ex utero electroporated with pCAG-Venus, pCAG-mito-DsRed, MFF shRNA, and low levels of either pCAG-MFF-WT cDNA or phospho-dead pCAG-MFF-AA. At 20DIV, the neurons were treated with either a vehicle control or Aβ42o for 24 h. Gene replacement with a form of MFF that cannot be phosphorylated by AMPK (MFF shRNA + MFF-AA) blocks dendritic mitochondrial fragmentation and subsequent spine loss. **b–d** Quantification of **b** dendritic mitochondrial length, **c** dendritic mitochondrial density, and **d** spine density. All of the analyses were done blind to the experimental conditions and performed by manual counting using FIJI. Data are represented by box plots displaying minimum to maximum values, with the box denoting 25th, 50th (median), and 75th percentiles from three independent experiments. $n_{MFFshRNA + MFFWT\ Control}$ = 31 dendrites, 166 mitochondria; $n_{MFFshRNA + MFFWT\ Aβ42o}$ = 29 dendrites, 228 mitochondria; $n_{MFFshRNA + MFFAA\ Control}$ = 35 dendrites, 164 mitochondria; $n_{MFFshRNA + MFFAA\ Aβ42o}$ = 28 dendrites, 137 mitochondria. Statistical analyses were performed using a Mann–Whitney test in **b–d**. Exact *P* values are indicated on the figure when available through Prism software, otherwise, the test significance is provided using the following criteria: ****$P < 0.0001$. Scale bar in **a**: 2 μm.

by Aβ42o also mediates the observed increased levels of mitophagy by activating ULK1 and/or ULK2, two isoforms of ULK implicated in autophagy and, in particular, mitophagy and are highly expressed in developing and adult cortical neurons[57,59].

We first tested if either one or both isoforms of ULK mediate Aβ42o-induced synaptotoxicity by performing shRNA-mediated knockdown of either ULK1 or ULK2 (Supplementary Fig. S6). Interestingly, we found that knockdown of ULK2, but not ULK1, protected cortical PNs from Aβ42o-induced spine loss at 24 h of Aβ42o treatment *in vitro* (Supplementary Fig. S6a, c). We further validated that ULK2 knockdown can block the increased autophagy induced by Aβ42o treatment in cortical PNs: immunofluorescent detection of SQSTM1/p62 is significantly increased in the soma of cortical PNs treated with Aβ42o for 24 h compared to vehicle alone (DMSO) (Supplementary Fig. S7). Knockdown of ULK2 using shRNA blocks the increase in p62 accumulation induced by treatment with Aβ42o (Supplementary Fig. S7).

We then tested if loss of ULK2 could protect Aβ42o-treated neurons from loss of mitochondrial biomass. We sparsely expressed Cre recombinase using ex utero electroporation in primary cortical PNs isolated from a conditional ULK2 mouse line ($ULK2^{F/F}$)[60] along with Venus to visualize dendritic spines, and mito-dsRed to visualize mitochondria. Loss of ULK2 completely blocks Aβ42o-induced loss of mitochondrial biomass which is compatible with blocking ULK2-mediated mitophagy (Fig. 8a–c); interestingly, however, dendritic mitochondria remain fragmented compared to the controls (Fig. 8a–c), compatible with the Aβ42o-induced AMPK-MFF-dependent induction of mitochondrial fission being intact in these ULK2-deficient cortical PNs. This further supports the idea that mitochondrial fission and mitophagy are coupled events, such that mitochondrial fragmentation must precede mitophagy[16,19]. Importantly, preservation of mitochondrial density/biomass upon ULK2 conditional deletion was sufficient to rescue Aβ42o-induced synaptotoxicity (Fig. 8a–d). Therefore, our data suggest that these two parallel effectors (MFF-dependent fission and ULK2-dependent mitophagy), coincidentally activated by AMPK, act in a concerted manner to couple fission and mitophagy in neuronal dendrites, and, most importantly, that loss of dendritic mitochondria biomass triggered by Aβ42o is causally linked to synaptic loss.

Figure 8

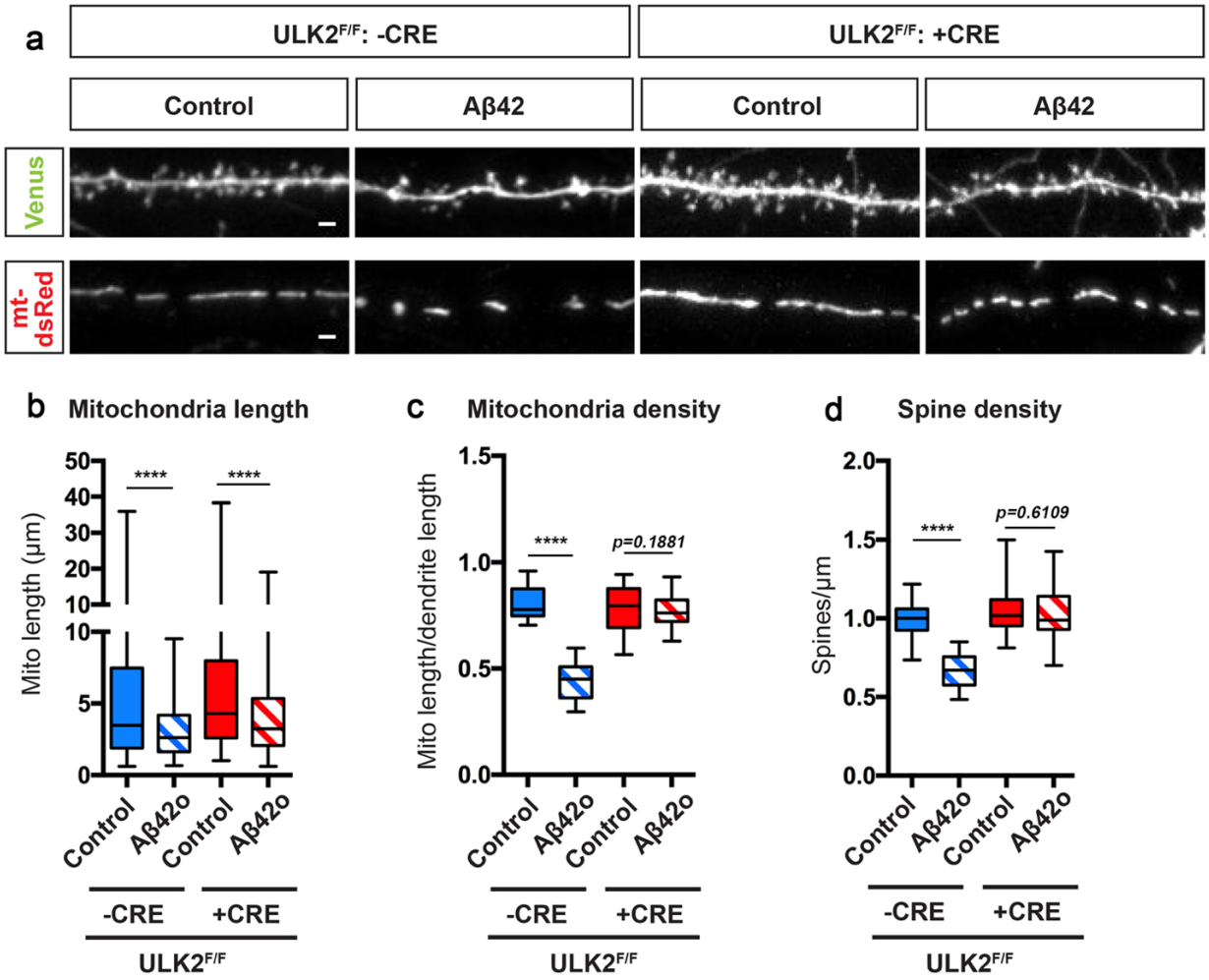

Figure 2.8. ULK2 acts in a concerted manner with MFF and leads to loss of mitochondrial biomass following MFF-dependent mitochondrial fragmentation.

a Representative images of secondary dendritic segments of primary cortical PNs at 21DIV. ULK2$^{F/F}$ embryos were ex utero electroporated at E15.5 with pCAG-Venus, pCAG-mito-DsRed, and without (-Cre) or with pCAG-Cre recombinase (+Cre). Neurons were treated at 20 DIV with either a vehicle control or Aβ42o for 24 h. Deletion of ULK2 in cortical PNs blocks Aβ42o-induced loss of dendritic spines and loss of mitochondrial biomass, but does not prevent a decrease in mitochondrial length. **b–d** Quantification of **b** dendritic mitochondrial length, **c** dendritic mitochondrial density, and **d** dendritic spine density. Analyses were done blind to the experimental conditions and were done by manual counting using FIJI. Data are represented by box plots displaying minimum to maximum values, with the box denoting 25th, 50th (median), and 75th percentiles from three independent experiments. $n_{CreNegative\ Control}$ = 36 dendrites, 193 mitochondria; $n_{CreNegative\ Aβ42o}$ = 38 dendrites, 254 mitochondria; $n_{CrePositive\ Control}$ = 36 dendrites, 186 mitochondria; $n_{CrePositive\ Aβ42o}$ = 35 dendrites, 435 mitochondria. Statistical analyses were performed using a Mann–Whitney test in **b–d**. Exact *P* values are indicated on the figure when available through Prism software, otherwise, the test significance is provided using the following criteria: ****$P < 0.0001$. Scale bar for magnified dendritic segments = 2 μm.

2.4.10 AMPK phosphorylation of ULK2 is required for Aβ42o-induced dendritic mitophagy and synaptic loss

We next tested if AMPK-mediated phosphorylation of ULK2 is required for Aβ42o-dependent synaptotoxic effects in cortical PNs. Extensive studies in nonneuronal cells have established that the closest ortholog of ULK2, ULK1, is phosphorylated and thereby catalytically activated by AMPK and plays a key role in regulating mitophagy[57,59]. Although the two orthologs seem to have redundant functions in non-neuronal cells, the above results uncovered that, in cortical PNs, only downregulation of ULK2, but not ULK1, blocks Aβ42-mediated synaptotoxicity (Supplementary Fig. S6). Therefore, we performed a sequence homology analysis of candidate AMPK phosphorylation sites identified in ULK1 and compared them to ULK2. Two independent groups collectively reported six AMPK-mediated phosphorylation sites on ULK1[57,59]. Using primary sequence alignment between human and mouse ULK1 and ULK2, we found that four of these ULK1 phosphorylation sites are conserved in ULK2 and are predicted as bona fide AMPK consensus phosphorylation sites (Fig. 9a and Supplementary Fig. S8; S309/T441/ S528/S547).

To validate that these four S/T residues are the most prevalent AMPK target sites in ULK2, we mutated these four candidate S/T residues to alanine in ULK2 (ULK2–4SA) and overexpressed them in HEK293T cells. We then performed immunoprecipitation (IP) of Flag-tagged ULK2-WT and ULK2–4SA from cells that were either treated with DMSO or AMPK direct agonist 991. Overexpression of constitutively active AMPK (ca-AMPK) in the presence of ULK2-WT or ULK2–4SA mutant conditions were used as a positive control. Immunoprecipitated Flag-ULK2-WT or Flag-ULK2–4SA were then immunoblotted with an antibody recognizing the optimal AMPK phospho-substrate motif. We observed basal levels of phosphorylation of ULK2-WT in control cells which increases upon AMPK activation via 991 treatment or when co-expressed with ca-AMPK (Fig. 9b). Importantly, AMPK-mediated phosphorylation of ULK2 was completely abolished in the 4SA mutant (Fig. 9b), strongly suggesting that these four S/T sites are the main AMPK phosphorylation sites in ULK2.

Finally, we tested if ULK2 phosphorylation by AMPK is required for the loss of mitochondrial biomass and synaptic loss induced by Aβ42o. We performed gene replacement experiments taking advantage of $ULK2^{F/F}$ primary cortical PNs co-electroporated with Cre and either ULK2-WT (positive control), ULK2–4SA, or kinase-inactive ULK2 (ULK2-KI, as negative control). We found that expression of

Figure 9

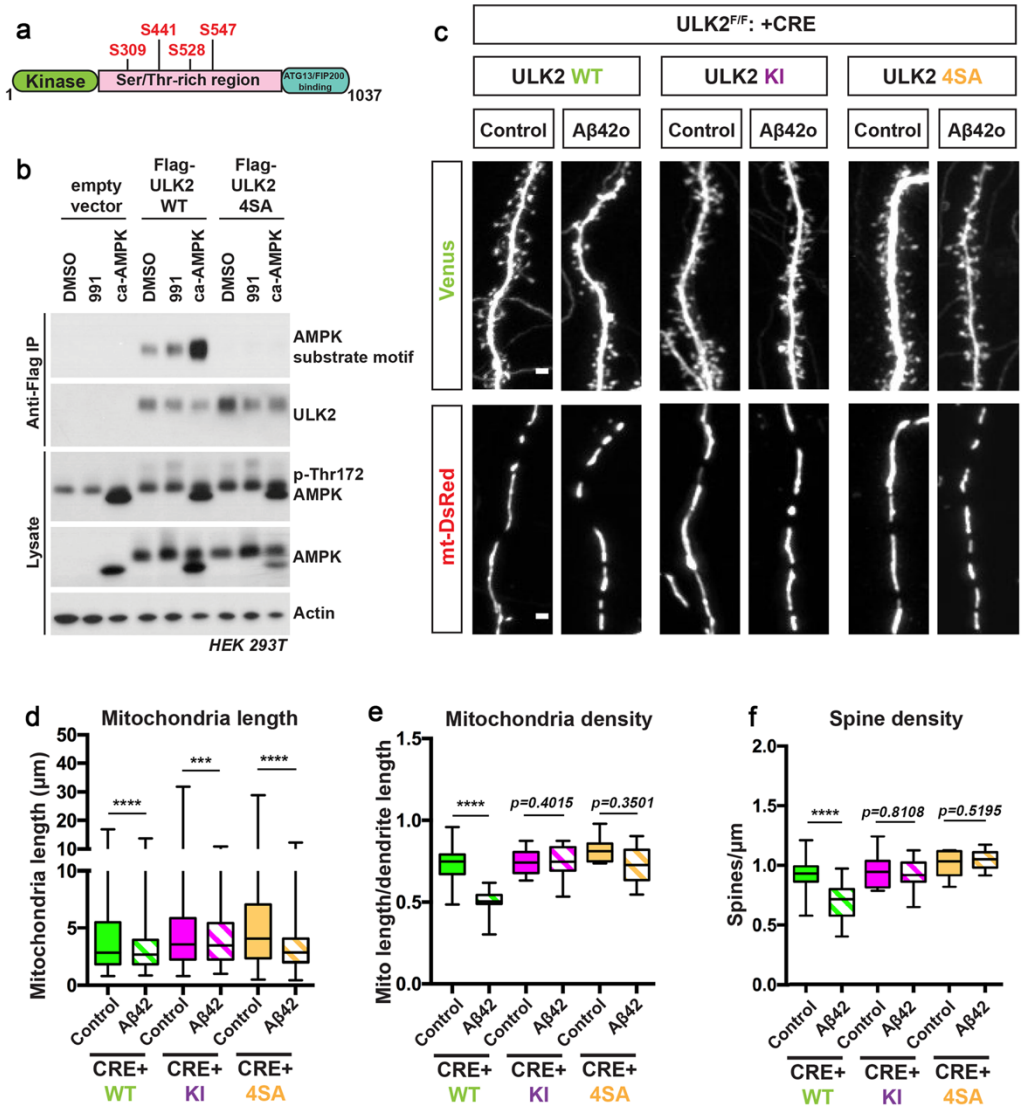

Figure 2.9. AMPK-mediated phosphorylation of ULK2 is crucial for oligomeric Aβ42-induced synaptotoxicity and loss of mitochondrial biomass.

a Schematic of ULK2 domain structure highlighting the four predicted AMPK-mediated phosphorylation sites (see Supplementary Fig. S8) conserved in ULK1 and ULK2. **b** Flag- mULK2 WT or Flag-mULK2 4SA (the four conserved phosphorylation sites shown in Supplementary Fig. S8b are mutated to alanine) was overexpressed in HEK293T cells co-expressing either GST or GST-ca-AMPKα1(1–312) (constitutively active AMPK). Cells were treated with DMSO or 50 μM of compound 991 for 1 h. Blots were probed with AMPK substrate motif antibody, Flag M2 monoclonal antibody, total ULK2, p-Thr172 AMPK, total AMPK, and actin antibodies. **c** Representative high-magnification images of secondary dendritic segments showing dendritic spines in the upper panel and mitochondria in the lower panel. ULK2$^{F/F}$ embryos were ex utero electroporated at E15.5 with pCAG-mVenus, pCAG- mito-DsRed, either a scrambled pCAG-Cre (Control, no Cre), or pCAG-Cre recombinase. The pCAG-Cre recombinase conditions in which ULK2 is genetically removed were also co-electroporated with either pCAG-mULK2 WT (Wild type), pCAG-mULK2 KI (K39I) (Kinase inactive), or pCAG-mULK2 4SA (Kinase dead, see Supplementary Fig. S8). Neurons were treated at 20DIV with either a vehicle control or Aβ42o for 24 h. **d–f** Quantification of **d** dendritic mitochondrial length, **e** dendritic mitochondrial density, and **f** spine density. Analyses were done blind to the experimental conditions and done by manual counting using FIJI. For western blot in panel **b**, the same results were obtained for three independent experiments. In panels **d–f**, data are represented by box plots displaying minimum to maximum values, with the box denoting 25th, 50th (median), and 75th percentiles from three independent experiments. $n_{ULK2WT\ Control}$ = 32 dendrites, 194 mitochondria; $n_{ULK2WT\ A\beta42o}$ = 30 dendrites, 289 mitochondria; $n_{ULK2KI\ Control}$ = 36 dendrites, 183 mitochondria; $n_{ULK2KI\ A\beta42o}$ = 34 dendrites, 449 mitochondria; $n_{ULK24SA\ Control}$ = 34 dendrites, 198 mitochondria; $n_{ULK24SA\ A\beta42o}$ = 32 dendrites, 472 mitochondria. Statistical analyses were performed using a Mann–Whitney test in (d–f). Exact *P* values are indicated on the figure when available through Prism software, otherwise, the test significance is provided using the following criteria: *P < 0.001; ****P < 0.0001. Scale bar for magnified dendritic segments = 2 μm.

ULK2-WT in ULK2-null cortical PNs enabled both loss of mitochondrial biomass and synaptic loss induced by Aβ42o, but expression of ULK2-KI or ULK2–4SA in the ULK2-null neurons resulted in no reduction in mitochondrial biomass and did prevent dendritic spine loss upon treatment with Aβ42o (Fig. 9c–f). These results confirm that AMPK-mediated phosphorylation and activation of ULK2 mediate Aβ42o-dependent synaptic loss through its ability to induce mitophagy and loss of mitochondrial biomass.

2.4.11 Phosphorylation of Tau on serine 262 is required for Aβ42oinduced mitochondrial remodeling and synaptotoxicity

We and others have previously shown that AMPK phosphorylates human Tau (hTau) on the KGxS motif present at serine 262 embedded within the R1 microtubule binding domain[2,36],and that over-expressing a form of hTau that cannot be phosphorylated at S262 (hTau-S262A) blocked Aβ42o-induced synaptic loss in cortical and hippocampal PNs[2,61]. Since hTau phosphorylation has been involved in Drp1-mediated mitochondrial fission in multiple fly and mouse AD models[62,63], we tested specifically if AMPK-dependent hTauS262 phosphorylation could link Aβ42o-induced mitochondrial remodeling and synaptotoxicity. Indeed, the expression of hTau-S262A (but not wild-type hTau) protected neurons from Aβ42o-induced mitochondrial remodeling and synaptotoxicity (Supplementary Fig. S9a–d). This result strongly suggests that AMPK-dependent Tau phosphorylation on S262[2,36] participates in the MFF-ULK2-dependent mitochondrial remodeling and synaptic loss triggered by Aβ42o.

2.4.12 Reduction of AMPK expression slows the rate of Amyloid-β plaque accumulation in the hippocampus of J20 mice

Finally, since (1) there is clear evidence for circuit hyperactivity at early stages in various AD mouse models (reviewed in ref. 64), (2) increased neuronal activity is sufficient to activate AMPK in a CAMKK2-dependent manner[2], and (3) amyloidogenic APP processing into Aβ42 is activity dependent[65], we tested if part of the protective effect of reducing AMPK in the context of AD pathophysiology could be due to decreased APP processing and Aβ42 production. To do this, we monitored the accumulation of Aβ42 (using the 6E10 antibody detecting Aβ42) into plaques in wild-type, J20, AMPKα1$^{+/-}$ x J20, or AMPKα1$^{-/-}$ x J20 mice, the latter two of which have either heterozygous (AMPKα1$^{+/-}$) or homozygous (AMPKα1$^{-/-}$), constitutive knockdown of the α1 subunit of AMPK (Supplementary Fig. S11). Our results show that only complete

knockout of AMPKα1significantly reduces Aβ plaque coverage and plaque size compared to 5 months J20 mice (Supplementary Fig. S11a, b). These results suggest that AMPK overactivation observed in the J20 AD mouse model[2] participates in increased APP processing into Aβ42.

2.5 Discussion

Loss of excitatory glutamatergic synapses in cortical and hippocampal PNs has been reported as an early event in AD progression, primarily driven by soluble Aβ42o and Tau hyperphosphorylation[5,6,8,11,66–69]; reviewed in ref. 1). This loss of connectivity is thought to be responsible for the early cognitive defects characterizing AD patients, including defective learning and memory[1,70]. Recently, mitochondrial remodeling and dysfunction in PNs have emerged as prominent cellular phenotypes in AD[24,25,27,37,71–73]. However, whether structural remodeling of dendritic mitochondria is causally linked to excitatory synaptic loss was unknown, in part because the molecular mechanisms mediating Aβ42o-dependent mitochondrial remodeling were unknown.

AMPK is best-characterized as a metabolic sensor in non-neuronal cells[39]. Importantly, in AD patients, catalytically active AMPK is abnormally accumulated in the cytoplasm of PNs of CA1, the entorhinal cortex, and the neocortex[37,38]. AMPK overactivation has been consistently reported in AD patient brain samples[37,38], in various AD mouse models[2,34,35], as well as *in vitro* upon acute treatment with Aβ42o[2,34,36,74].

The CAMKK2-AMPK signaling pathway is unique in its involvement in multiple phenotypes observed during the progression of AD. The present study and previous reports collectively implicate this signaling pathway as the first to unify multiple phenotypes reported in the brain of AD patients and in AD mouse models, including Ca^{2+} homeostasis disruption, APP processing, hTau phosphorylation, mitochondrial remodeling, increased autophagy, and synaptic loss[1,75,76]. There is growing evidence that one of the earliest events upon Aβ42o application is disrupted cytoplasmic Ca^{2+} homeostasis, which drives PNs hyperexcitability (see below)[29,77–81]. This increased Ca^{2+} accumulation precedes spine morphological changes[77], strongly suggesting that Ca^{2+}-dependent signaling pathways, including the CAMKK2-AMPK pathway, occur early in the disease progression and play a critical role in reduced synaptic plasticity (reduced LTP-augmented LTD) through abnormal trafficking and post-translational modification of Ca^{2+} permeable AMPA receptors as well as NMDA receptors[66,82–85]. Importantly, recent work demonstrated that

preventing AMPK-overactivation blocks the synaptic plasticity defects triggered by Aβ42o application through the ability of AMPK to regulate eukaryotic elongation factor 2 (eEF2) and its kinase's, eEF2K, control of protein translation[34].

Interestingly, Aβ42o-induced AMPK overactivation has been found to induce a vicious cycle of increased Aβ42o production via activation of JNK3-dependent APP processing[74]. In line with the results in ref. 74, we found that part of the protective effect of preventing Aβ42o-mediated AMPK overactivation might also be to reduce APP processing and Aβ42 production. However, the main results from our current study and previously published work are that AMPK links the two key players of AD: Aβ42o and Tau[2]. Catalytically active AMPK has been shown to co-localize with phosphorylated-S262 hTau in brains of AD patients[38], and previous work highlights that hyperactivation of AMPK by Aβ42o and/or other AMPK-like kinases such as NUAK1 leads to Tau phosphorylation on two of its serine residues (S262 and S356[2,86]) embedded in the R1 and R4 microtubule binding domains, respectively[87]. These results identified for the first time the CAMKK2-AMPK signaling pathway as a critical link between Aβ42o and Tau phosphorylation in the induction of synaptic loss[54].

In this paper, we identified two new critical effectors of AMPK mediating the effects of Aβ42o on synaptic loss. We show that AMPK overactivation by Aβ42o coordinates multiple aspects of mitochondrial remodeling by co-regulating mitochondrial fission and mitophagy through its activation of MFF and ULK2, respectively. For the first time, we demonstrate that Aβ42o mediated loss of excitatory synapses in cortical PNs *in vitro* and in CA1 PNs *in vivo* requires AMPK-mediated activation of MFF-ULK2-dependent mitochondrial fission and mitophagy, respectively. We cannot formally exclude the possibility that Aβ42o-mediated spine loss require ULK2-mediated autophagy events of cargoes other than mitochondria. However, this is unlikely since we also show that preventing MFF-dependent mitochondrial fission, which blocks subsequent loss of mitochondrial biomass (Figs. 5–7), also prevents Aβ42o-mediated spine loss *in vitro* and *in vivo*.

We have also identified that Aβ42o-mediated AMPK overactivation also signals through phosphorylation of Tau on S262 in conjunction with MFF-ULK2 phosphorylation/activation, leading to dendritic mitochondrial remodeling and synapse loss. Further work will be required to understand if Aβ42o-induced AMPK-Tau signaling plays a direct role in mitochondrial fission and/or mitophagy machinery, or if

it plays an indirect role through its postsynaptic signaling function[67,88] and/or its ability to regulate microtubule dynamics[89].

Lastly, what makes this molecular mechanism attractive for the development of new therapeutic approaches is that CAMKK2-AMPK is a bona fide stress-response signaling pathway[54], i.e., these AMPK-dependent pathways are dispensable for normal neuronal development and/or synaptic maintenance in adult cortical and hippocampal neurons[54,90].

Mitochondrial remodeling and dysfunction are converging mechanisms of disease pathogenesis shared by multiple neurodegenerative diseases (ND). This is in part explained by the disruptions of mitochondrial homeostasis, motility, and dynamics observed in various NDs, as well as by genetic evidence suggesting a strong association between genes involved in mitochondrial function and various adult onset ND syndromes[88,91].In AD specifically, altered mitochondrial dynamics have been implicated by changes of mitochondrial fission and fusion protein expression levels in AD patient brains[24] and in various AD mouse models[25], as well as altered post-translational modification of Drp1, which is thought to disrupt mitochondrial dynamics[24,71,73]. In line with our results, Wang and colleagues[24,73] also observe that, in the presence of Aβ42o, dendritic mitochondria decrease in length and density, which is correlated with reduced spine density. Interestingly, a recent study suggested a significant degree of mitochondrial structural remodeling in CA1 of the hippocampal region in various AD mouse models and in AD patients using 3D EM reconstructions[27]. Our present study further corroborates these observations and provides a molecular mechanism mediating Aβ42odependent mitochondrial remodeling and synaptic loss during the early stages of AD.

A second cellular defect thought to contribute to several neurodegenerative diseases, including AD, is a disruption of the autophagocytic–lysosomal pathway[41,76]. Although the cellular and molecular mechanisms of autophagy have largely been examined using nonneuronal cells[92], recent results demonstrated unique, compartment-specific regulation of autophagy in neurons. Local biogenesis of autophagosomes has been observed in distal axons, which are then trafficked retrogradely towards the soma in order to fuse with lysosomes, whereas autophagosomes in the soma are more stationary[93]. The dynamics of autophagy in dendrites, however, remain largely unexplored. Much of what we know about neuronal autophagy has been primarily focused on axonal and presynaptic autophagy dynamics, where it

mediates efficient synaptic transmission by regulating the turnover of synaptic proteins[94,95]. Autophagy has received significant attention in AD research, in part due to the abnormal accumulation of autophagosomes and autolysosomes in dystrophic neurites of AD patients[76]. Moreover, familial mutations and polymorphisms associated with AD are linked to dysfunction of the autophagocytic–lysosomal pathway. Mutations of the Presenilin 1 and 2 proteins have been shown to disrupt lysosomal acidification and autophagy[96,97]. AD associated genes such as PICALM, BIN1, RAB11, and VPS34 are involved in various initiation, sorting, and trafficking processes of autophagy[98–101]. However, the majority of the cellular phenotypes involving autophagosome and autolysosome buildup in neurons have been described at late stages of AD progression when neurodegeneration involving neuronal cell loss occurs[76]. More recent results suggested that, in AD mouse models, autophagic flux is disrupted[35] and the expression level of mitophagy-associated genes are elevated during the early stages of AD[102].

A recent study confirmed that AMPK is overactivated in brains of AD human patients and is accompanied by increased MFF phosphorylation on S146 confirming our present observations[37]. However, the same study reported reduced ULK1 activation, increased mitochondria damage but reduced mitophagy[37]. One possibility to explain the potential differences between our results and the results of ref. 37 is that in their study, ULK1 expression/activation and mitophagy were assessed on whole brain tissue which includes neurons and non-neuronal cells, including astrocytes and microglial cells where mitophagy might be differentially altered than in neurons. Another potential difference between our present results and ref. 37 results is that our *in vitro* and *in vivo* results examine the influence of Aβ42o-mediated spine loss using acute (24 h) exposure *in vitro* or early stages of Aβ42o accumulation in the J20 model (3 months i.e., before amyloid plaque appearance) whereas the Fang et al. paper examine mostly ULK1 and mitophagy events in “late” AD patients at a point where neuronal viability and therefore autophagosome clearance might be compromised[41]. Future experiments will need to address the timing and cell-type specificity of mitophagy activation or downregulation in both mouse models and human AD patients at early versus late stages of the disease progression.

Overall, our results demonstrate that Aβ42o triggers an AMPK-ULK2-dependent increase in mitophagy cell-autonomously in cortical and hippocampal mouse and human neurons, resulting in significant local degradation of dendritic mitochondria. We developed a direct way to visualize mitophagy

using quantifications of mitochondria “degradation” in time-lapse analysis where genetically encoded mitochondrial markers disappeared in location where LAMP1 + lysosome and LC3+ autophagosome fused. We computed a “mitophagy index” which reflects mitochondria biomass loss at location where autophagolysosomes emerge, however, this index might also be influenced by local mitochondria dynamics, including fission events followed by mitochondria transport independent of mitophagy events. Despite this potential limitation, our rescue experiments in PNs performed by gene replacement strategies reinforces that MFF-dependent fission coupled with ULK2-dependent autophagy is causally linked with dendritic spine loss induced by Aβ42o. Altogether, our results strongly argue that at least during the early stages of the disease progression, Aβ42o-induced overactivation of CAMKK2-AMPK mediates synaptic loss through drastic structural remodeling and loss of biomass of dendritic mitochondria.

Our *in vivo* analyses also reveal a striking and previously unknown degree of compartmentalization of mitochondria morphology in dendrites of CA1 PNs: in basal and apical oblique dendrites, mitochondria are small and punctate, whereas the distal apical dendrites contain elongated and fused mitochondria (Supplementary Fig. S1). The transition between these two types of mitochondrial morphology is sharp and corresponds to the transition between two hippocampal layers, stratum radiatum (SR) and stratum lacunosum moleculare (SLM), where the earliest excitatory synaptic loss is observed in this mouse model. This is particularly relevant because the synapses made between medial entorhinal cortical inputs and the apical tufts of CA1 PNs in SLM has been described as one of the central synapses defective in late-onset forms of AD[103]. Future investigations will need to determine why this synapse is particularly vulnerable during early stages of AD progression.

As discussed above, disruption of Ca^{2+} homeostasis has been observed in various AD mouse models[29,78,80,104], in wild-type PNs exposed to acute treatment of oligomeric Aβ42 *in vivo*[77], and neuronal cultures exposed to Aβ42o *in vitro*[105,106]. Recent results suggested that disruption of Ca^{2+} dynamics is largely due to Aβ42o, as immune-depletion of Aβ42o can prevent this phenotype77 and decrease the population of hyperactive neurons[29,78]. Possible explanations of this increased cytoplasmic Ca^{2+} accumulation include increased mobilization of Ca^{2+} from the extracellular space through NMDAR and VGCC, increased leakage of Ca^{2+} from intracellular Ca^{2+} storing organelles such as the ER, and loss of Ca^{2+} buffering capacity by the neurons. Currently, there is evidence supporting the hypothesis that excess

Ca^{2+} is derived from the extracellular influx of Ca^{2+} via NMDA Receptors[1,77], as well as from the ER via the IP3 and Ryanodine receptors[107,108]. Future experiments will need to address the exact source of intracellular Ca^{2+} increase (NMDA/VGCC only and/or ER-mitochondria dependent intracellular stores/buffering) leading to CAMKK2 overactivation by Aβ42o. The fact that ER-mitochondria contacts have been shown to be disrupted in response to Aβ42o (ref. 109 and reviewed in ref. 110) argues in favor of disruption of ER-dependent Ca^{2+} or reduced mitochondrial Ca^{2+} buffering. Regardless of the Ca^{2+} source, the current model is that PNs ultimately experience an increase in frequency and/or amplitude of intracellular Ca^{2+} that can activate Ca^{2+}-dependent signaling pathways, including overactivation of the CAMKK2-AMPK pathway. There may be a complex, positive feed-forward loop where Aβ42o-dependent, fast NMDAR-dependent Ca^{2+} influx[77] over-activates the CAMKK2-AMPK pathway[2], resulting in the reduction of mitochondrial biomass, i.e., mitochondrial matrix volume, which in turn reduces Ca^{2+} buffering capacity, further increasing cytoplasmic Ca^{2+} accumulation and CAMKK2 overactivation. Future work will need to address if the striking but spatially restricted degree of Aβ42odependent reduction in dendritic mitochondrial biomass and subsequent reduction in spine density identified in the present study in the apical tuft dendrites of CA1 PNs in the J20 AD mouse model contributes to the degradation of the spatial tuning properties of these neurons at early stages of the disease progression.

2.6 Supplemental Figures

Supplemental Figure S1

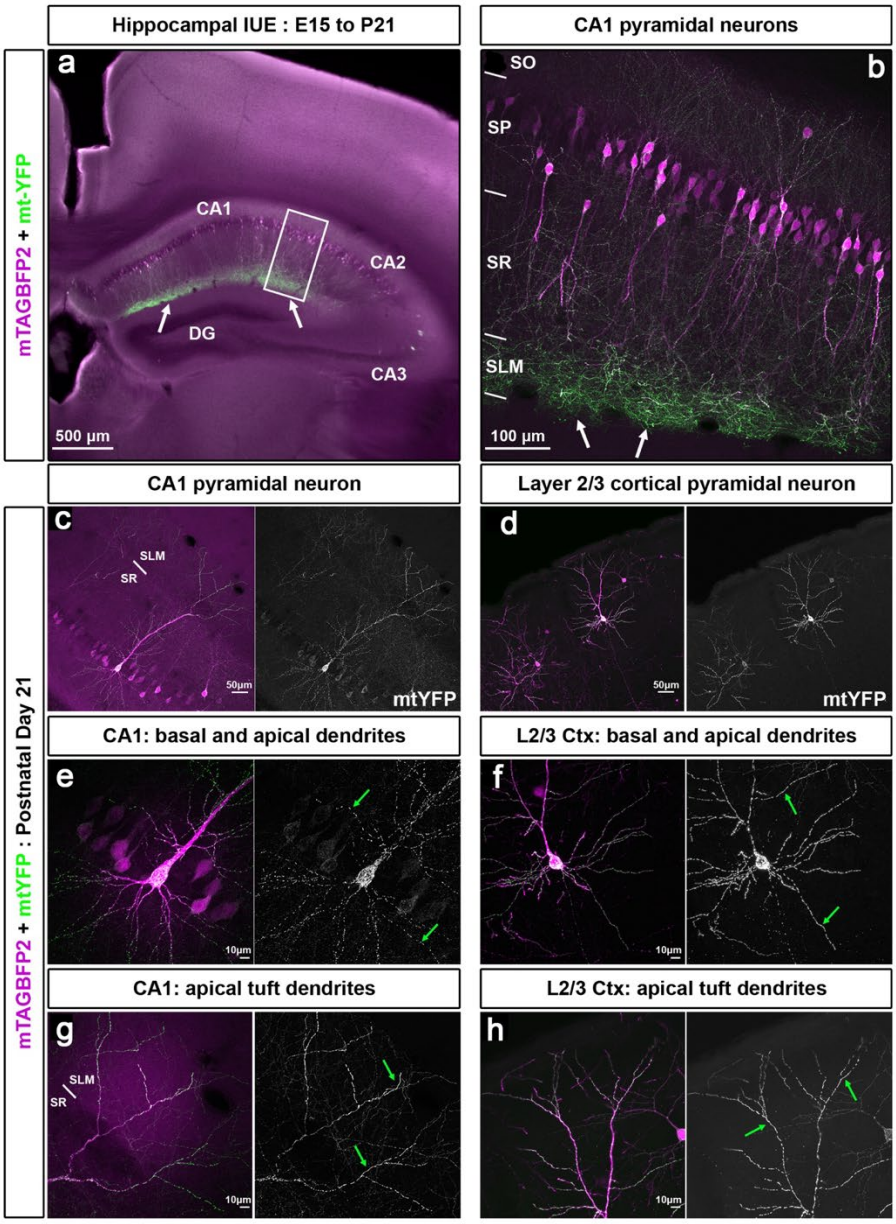

Supplemental Figure S2.1. Hippocampal CA1 pyramidal neurons are characterized by highly compartmentalized dendritic mitochondria morphology compared to layer 2/3 cortical pyramidal neurons.
(**a**) Low magnification image of hippocampal CA1 pyramidal neurons *in utero* electroporated at E15.5 with pCAG-mTagBFP2 (purple) and pCAG-mito-YFP (green) imaged at P21. (**b**) High magnification image of inset in panel **a**, highlighting that the distal apical tuft dendrites in the SLM layer contain a high density of mitochondria compared to the basal and oblique dendrites (in SO and SR respectively). (**c**) Low magnification of a single optically isolated CA1 pyramidal neuron, and (**e**, **g**) high magnification of its proximal dendrites (basal and apical oblique in **e**) as well as apical tuft dendrites (panel **g**) highlighting that mitochondria in the basal and oblique dendrites are small and fragmented (green arrows in **e**) in proximal dendrites whereas mitochondria in apical tuft of the same CA1 PN are fused (green arrows in **g**). (**d**) Low magnification of a single optically isolated cortical layer 2/3 PN, and (**f**, **h**) high magnification images of its proximal dendrites (basal and apical oblique in panel **f**) and apical tuft (panel **h**), highlighting that mitochondria morphology is homogenously elongated and fused throughout the dendritic arbor (green arrows in **f**, **h**) of layer 2/3 PNs. Each image shown has been observed in at least 3 independent in utero electroporated brains and quantification of mitochondria morphology for CA1 hippocampal neurons is shown in Figure 1. Abbreviations: SLM: stratum lacunosum moleculare; SR: stratum radiatum; SO: stratum oriens; SP: stratum pyramidalis.

Supplemental Figure S2

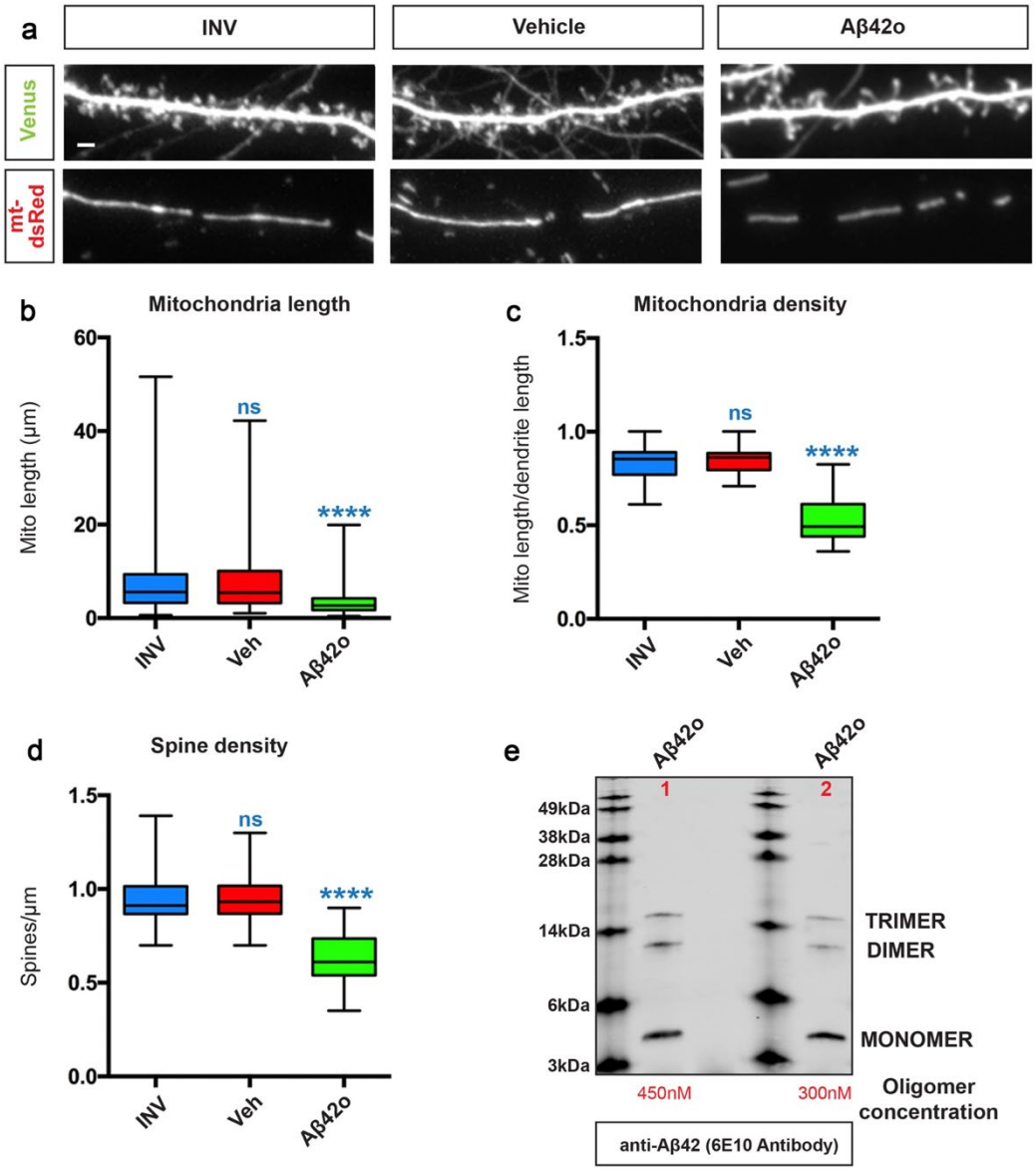

Supplemental Figure S2.2. Treatment with control inverse oligomeric Aβ42 does not influence mitochondrial morphology or spine density.

(**a**) Representative high magnification images of dendritic segments showing dendritic spines in the upper panel and mitochondria in the lower panel. Treatment with inverse Aβ42o does not affect spine density or mitochondrial morphology, and similar to DMSO treated neurons. (**b**) Mitochondrial length for inverse Aβ42o is comparable to DMSO treated neurons, while Aβ42 oligomer treatment significantly reduces mitochondrial length. (**c**) Mitochondrial density for inverse Aβ42o is comparable to DMSO treated neurons while Aβ42 oligomer treatment significantly reduces mitochondrial density. (**d**) Spine density quantification for inverse Aβ42o is comparable to DMSO treated neurons, while Aβ42 oligomer treatment significantly reduces spine density. All analyses were done blind to the experimental conditions, and were done by manual counting using FIJI. Data is represented by box plots displaying minimum to maximum values, with the box denoting 25$^{th.}$, 50th(median) and 75th percentiles from three independent experiments. nINV = 41 dendrites, 243 mitochondria; nVeh = 31 dendrites; 178 mitochondria; nAβ42o = 33 dendrites, 245 mitochondria. Statistical analysis was performed using Kruskal-Wallis test followed by Dunn's post-hoc test in (**b-d**). The test was considered significant when $p<0.05$ with the following criteria: * $p<0.05$; ** $p<0.01$; ***$p<0.001$; ****$p<0.0001$; ns, not significant. Scale bar= 2µm. (**e**) 16.5% Tris-Tricine SDS-PAGE was performed to resolve Aβ42 oligomers from the peptide monomer that were generated as described in Material and Methods. Immuno-blotting was performed with 6E10 antibody which shows a mixture of monomers, dimers and trimers in lane one and two (two independent oligomerization experiments). For quantifying the relative oligomer/monomer concentration in lane one and two, near-infrared fluorescence signal intensity was measured for dimer plus trimer, and monomer using an Odyssey Imager. Optical density for Lane 1: Dimer + Trimer: 1510; Monomer: 1830. Signal intensity values for Lane 2: Dimer + Trimer: 736; Monomer: 1720.

Supplemental Figure S3

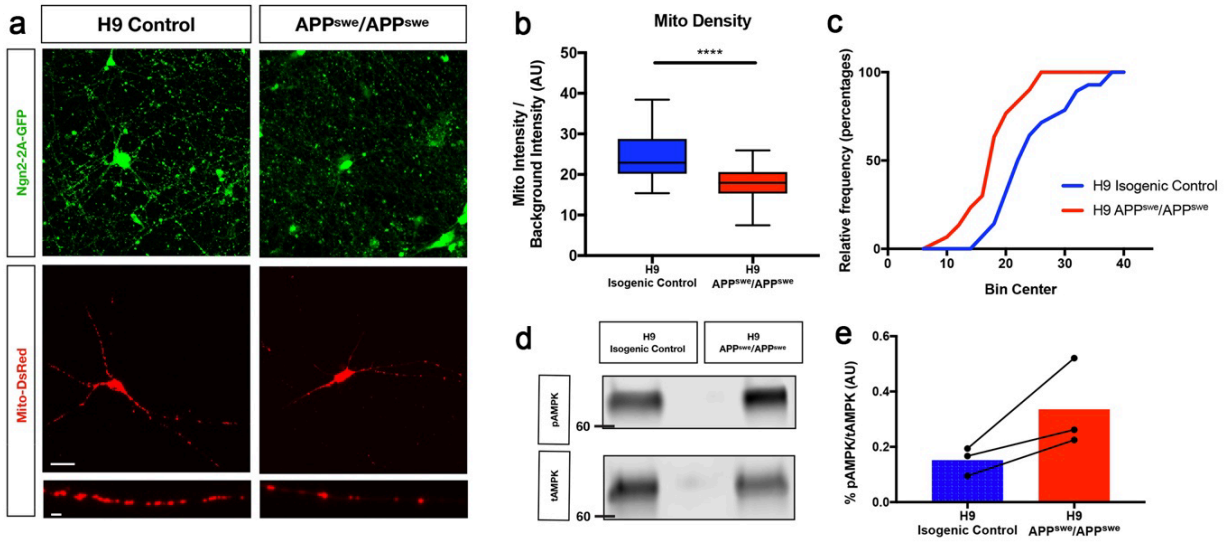

Supplemental Figure S2.3. Human ES-derived cortical-like pyramidal neurons expressing endogenous APP^{swe} mutations exhibit decreases in mitochondrial density and increased AMPK activation.

(**a**) Representative low and high magnification images of neurons transdifferentiated from control human H9 embryonic stem (hES) cells and APP$^{swe/swe}$ knock-in hES cells at 24 DIV. hES-derived cortical-like neurons were induced using a Ngn2-dependent neural induction and were lipofected at 21DIV with a pCAG-mito-DsRed reporter gene to label mitochondria, fixed at 24 DIV, and imaged by confocal microscopy. Endogenous expression of the APP^{swe}/APP^{swe} mutation alone is sufficient to induce a significant decrease in mitochondrial density in their dendrites (bottom high magnification panels). (**b**) Quantification of neuritic mitochondrial density shows a significant decrease in the mitochondrial density in the H9 APP^{swe}/APP^{swe} cells compared to the H9 isogenic controls. All of the analyses were done by kymographic fluorescent density measurement in Nikon Elements software and blind to genotype. (**c**) Cumulative frequency distribution of mitochondrial density in Ngn2-induced cortical-like neurons derived from control isogenic H9- hES cells (blue) and APP^{swe}/APP^{swe} hES cells (red) confirms a decrease in mitochondrial density in cells expressing APP^{swe}/APP^{swe}. (**d**) Sample western blot of H9 isogenic control versus H9 APP^{swe}/APP^{swe} demonstrates an increase in phosphorylated AMPK in APP^{swe}/APP^{swe} expressing cells. 50µg of immunoprecipitated cell lysate was immunoblotted with phospho-AMPK (T172, CST) to confirm activation of AMPK under endogenous expression of APP^{swe} mutations. (**e**) Quantification of increased phospho- AMPK, representing mean with all three paired values represented by individual points. In panel b, data represented by box plots are displaying minimum to maximum values, with the box denoting 25th, 50th (median), and 75th percentiles from three independent experiments. In a-c: nH9control = 227 neurites, 70 neurons; nAPPswe = 203 neurites, 73 neurons. Statistical analyses in b were performed using one-way ANOVA followed by Kruskal-Wallis post-hoc. The test was considered significant when $p < 0.05$ with the following criteria: **** $p < 0.0001$; ns, not significant. Scale bars in panels **a**: low magnification panels: 20 microns; high magnification panels (bottom): 2 microns.

Supplemental Figure S4

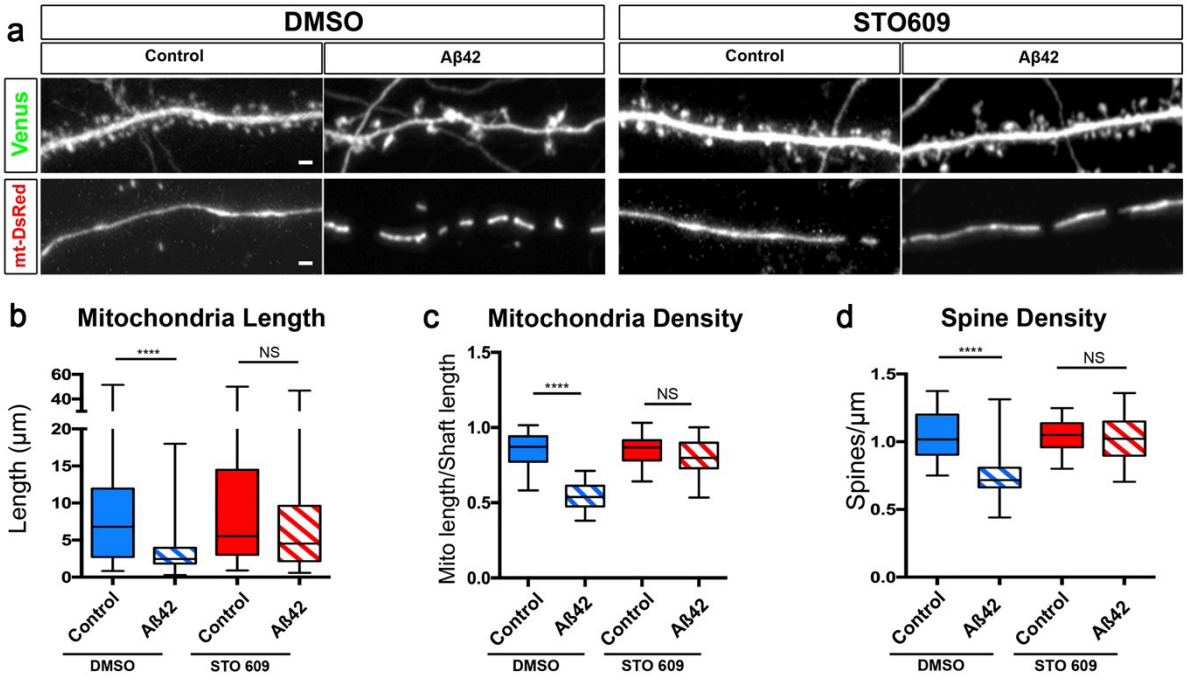

Supplemental Figure S2.4. Oligomeric Aβ42 induced synaptotoxicity and dendritic mitochondrial fragmentation is CAMKK2 dependent.

(**a**) Secondary dendritic segments of primary cortical neuron at 21 DIV. Embryos at E15.5 were *ex utero* electroporated with pCAG-Venus and pCAG-mito-DsRed. At 20 DIV, neurons were pre-treated with either DMSO or STO609 (2.5µM) for 2 hours before being treated with either control or Aβ42 oligomers for 24 hours. (**b**) Quantification of dendritic mitochondrial length, (**c**) dendritic mitochondrial density, and (**d**) spine density show that blocking CAMKK2 activity via STO609 blocks both dendritic mitochondrial remodeling and synaptotoxicity. All the analyses were done blind to the experimental conditions, and were done by manual counting using FIJI. Data is represented by box plots displaying minimum to maximum values, with the box denoting 25th, 50th (median), and 75th percentiles from three independent experiments. nDMSO Control = 37 dendrites, 163 mitochondria; nDMSO Aβ42o = 31 dendrites, 248 mitochondria; nSTO609 Control = 37 dendrites, 163 mitochondria; nSTO609 Aβ42o = 35 dendrites, 157 mitochondria. Statistical analyses were performed using Kruskal-Wallis test followed by Dunn's post-hoc test in (b-d). The test was considered significant when p<0.05 with the following criteria: * p<0.05; ** p<0.01; ***p<0.001; ****p<0.0001; ns, not significant. Scalebar = 2µm.

Supplemental Figure S5

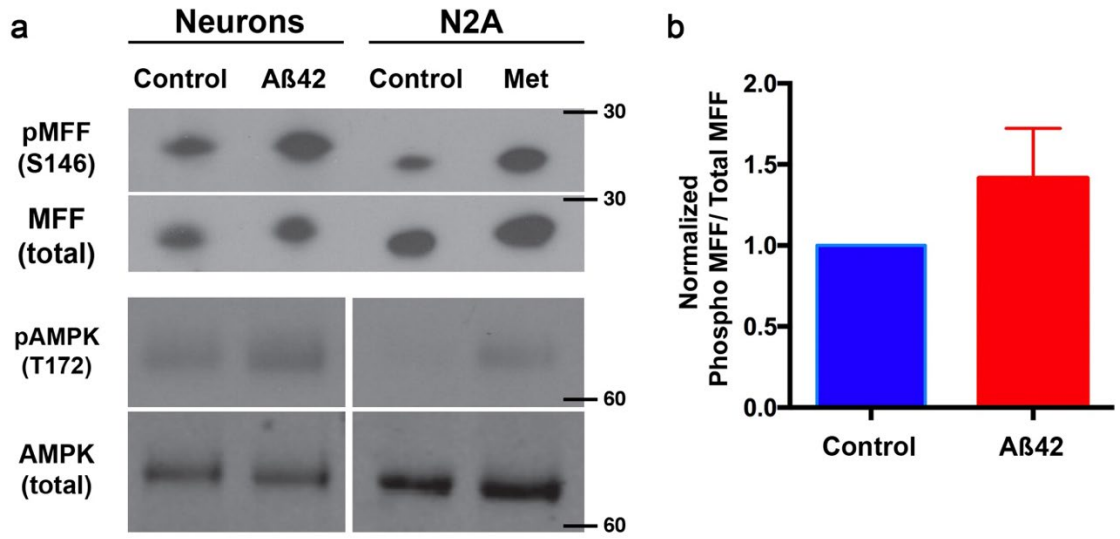

Supplemental Figure S2.5. Aβ42o-dependent increase in MFF phosphorylation.
(**a**) Cortical PNs maintained in dissociated culture were treated at 20DIV with either a control vehicle or Aβ42o for 24 hours (left two lanes). N2A cells were treated with either DMSO or 2mM of Metformin for 5 hours as a positive control for AMPK-dependent MFF phosphorylation[2] (right two lanes). 80µg of whole cell lysate was immunoprecipitated with MFF antibody (Progen) and immunoblotted with either MFF antibody or phospho-MFF antibody (S146, CST). Whole cell lysates were also immunoblotted with either AMPK or phospho-AMPK (T172, CST) to confirm activation of AMPK under both Aβ42o for 24 hours [1] and metformin treatment for 5 hours [2]. (**b**) Quantification of immunoblot phospho-MFF band intensity normalized to total MFF levels demonstrate an increase in phospho-MFF in neurons treated with Aβ42o (n=3 independent cultures).

Supplemental Figure S6

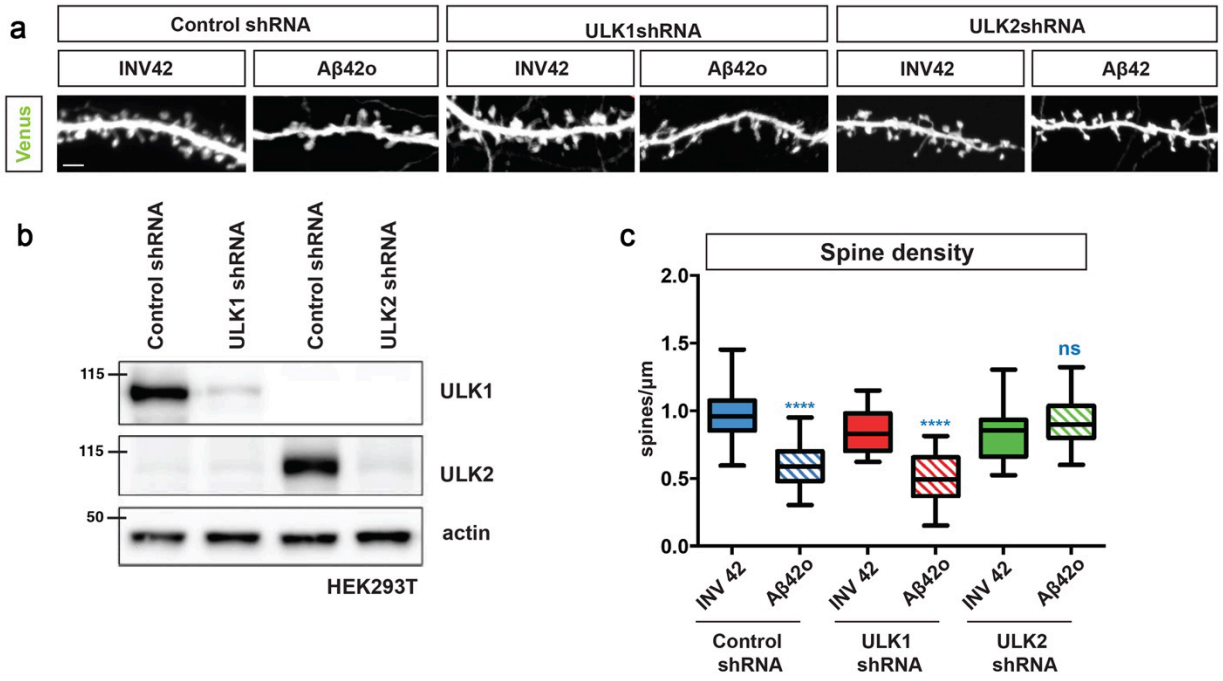

Supplemental Figure S2.6. ULK2 but not ULK1 is required for Aβ42o-dependent synaptotoxic effects.
(**a**) Representative images of secondary dendritic segments of primary cortical PNs treated with either control or Aβ42o at 21DIV for 24 hours. Embryos were subjected to *ex utero* electroporation at E15.5 with pCAG-Venus and either a control shRNA or an shRNA specific for the kinase ULK1 or ULK2. Knockdown of ULK2, but not ULK1 kinase, blocks Aβ42o-induced synaptotoxicity. (**b**) Western blot showing validation of both the ULK1 and ULK2 shRNAs, and the specificity of the shRNAs for their respective isoform. HEK 293T cells were transiently co-transfected with either control shRNA or ULK1/ULK2 shRNA, along with myc-mULK1 or Flag-mULK2 respectively, and western blotting was performed with 25µg of lysate with the indicated antibody. The same results were obtained for three independent cell cultures. (**c**) Quantification of spine density for panel a. All of the analyses were done blind to the experimental conditions and were done by manual counting using FIJI. In panel c, data is represented by box plots displaying minimum to maximum values, with the box denoting 25th, 50th (median) and 75th percentile from three independent experiments. nPLKO control = 31 dendrites; nPLKO Aβ42o = 27 dendrites; nULK1shRNA Control = 27 dendrites; nULK1shRNA Aβ42o = 24 dendrites; nULK2shRNA Control = 33 dendrites; nULK2shRNA Aβ42o = 35 dendrites. Statistical analyses were performed using Kruskal-Wallis test followed by Dunn's post-hoc test in panel c. The test was considered significant when $p<0.05$ with the following criteria: * $p<0.05$; ** $p<0.01$; ***$p<0.001$; ****$p<0.0001$; ns, not significant. Scale bar = 2µm.

Supplemental Figure S7

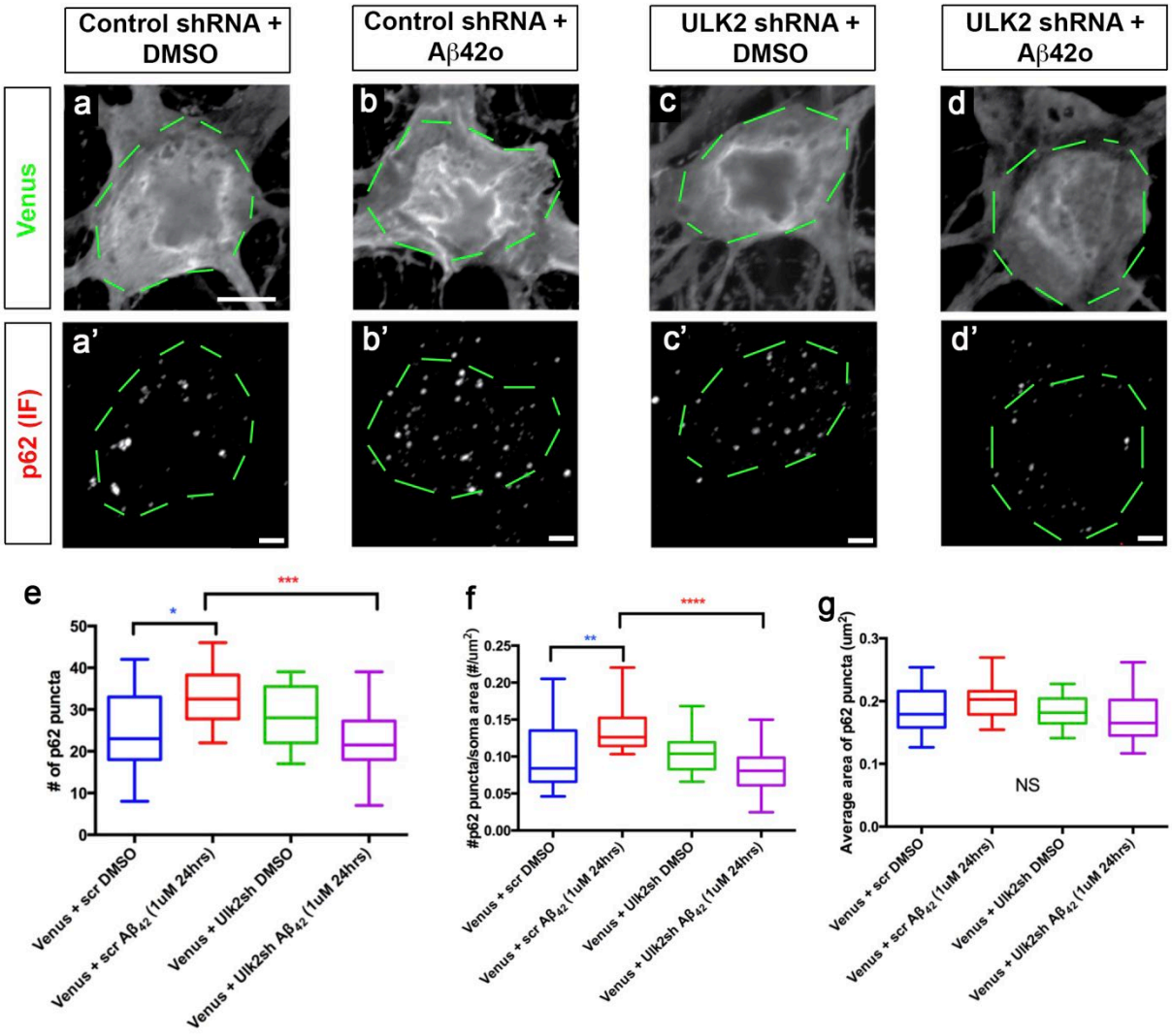

Supplemental Figure S2.7. Knocking down ULK2 prevents the increased in p62 autophagosomes density induced by Aβ42 oligomers in cortical pyramidal neurons.

(**a-d'**) Images of soma from cortical layer 2/3 PNs cultured for 21DIV following ex utero electroporation with Venus as a cell filler in combination with control (scrambled) shRNA (**a-a'** and **c-c'**) or ULK2 shRNA (see Fig. 6B for validation) (**b-b'** and **d-d'**). Cultures were treated for 24h prior to fixation with either vehicle (DMSO) or Aβ42 oligomers prepared as in Fig. S1. Following fixation, cultures were stained by immunofluorescence for p62 (also called SQSTM1), a ubiquitin- binding protein degraded marking autophagosomes. (**e-g**) Quantification of number of p62 puncta per soma (**e**), number of p62+ puncta normalized to soma area (**f**) and area of p62 puncta found over soma (**g**). In panels **e-g**, data is represented by box plots displaying minimum to maximum values, with the box denoting 25th, 50th (median) and 75th percentile from three independent experiments. Each experiment quantified was performed in triplicate of independent cultures. Number of cells analyzed: nVenus+control shRNA+DMSO =21; nVenus+control shRNA+Aβ42o=18; nVenus+ULK2shRNA+DMSO=21; nVenus+ULK2 shRNA+Aβ42o=22. Statistical analysis was performed using Kruskal-Wallis test followed by Dunn's post-hoc test. * p<0.05 **p<0.01; *** p< 0.005;
****p<0.001. Scale bars in **a-d'**: 2 microns.

Supplemental Figure S8

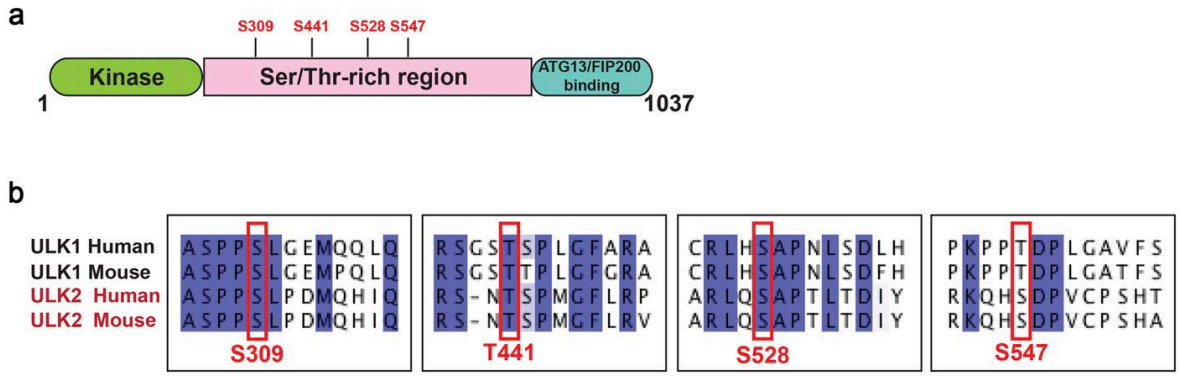

Supplemental Figure S2.8. Schematic of conserved AMPK-mediated phosphorylation sites in ULK2.
(**a**) Schematic of mULK2 domain structure highlighting the four predicted AMPK-mediated phosphorylation sites. (b) ClustalW multiple sequence alignment of human and mouse ULK1 and ULK2 showing a high degree of conservation of four AMPK-mediated phosphorylation sites in ULK2 which were previously reported in ULK1[3].

Supplemental Figure S9

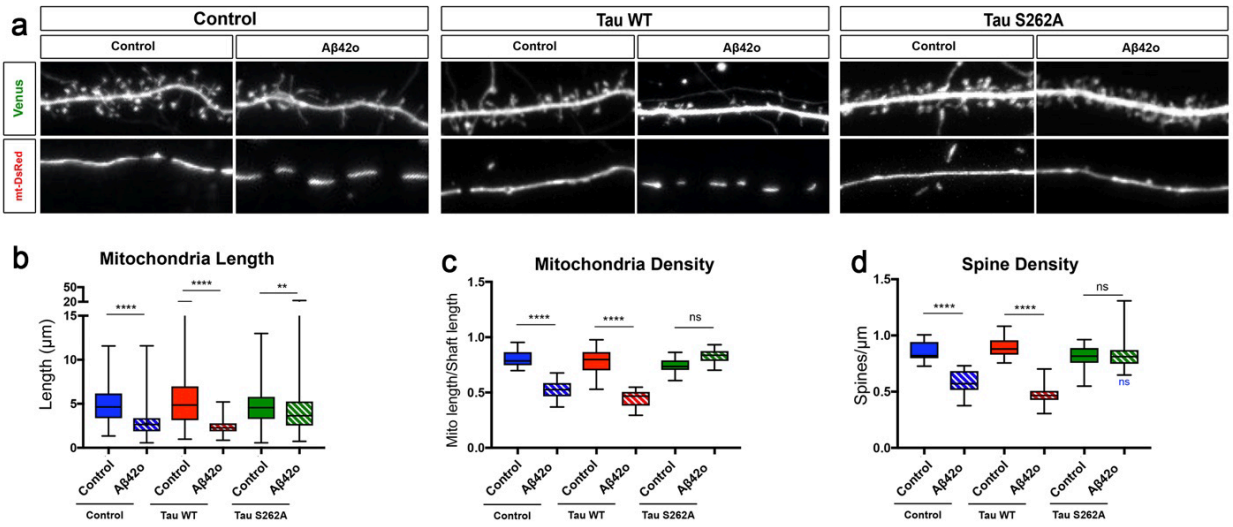

Supplemental Figure S2.9. Tau phosphorylation at S262 is required for Aβ42o-induced dendritic mitochondrial remodeling. (**a**) Representative images of secondary dendritic segments of primary cortical PNs at 21 DIV. E15.5 mouse embryos were *ex utero* electroporated with mVenus, mito-DsRed only or in combination with either wildtype hTau (isoform 4R2N) or a non-phosphorylatable mutant hTau-S262A. Neurons were treated at 20 DIV with either a vehicle or Aβ42o for 24 hours. Overexpression of hTau in the presence of Aβ42o decreases spine density, mitochondrial length, and mitochondrial density, while over expression of hTauS262A blocked oligomer-induced spine loss and mitochondrial density decrease, but not mitochondrial fragmentation. (**b**) Quantification of dendritic mitochondrial length, (**c**) dendritic mitochondrial density, and (**d**) dendritic spine density. All of the analyses were done blind to the experimental conditions and were done by manual counting in FIJI. In panels **b-d**, data is represented by box plots displaying minimum to maximum values, with the box denoting 25th, 50th (median) and 75th percentile from three to six independent experiments. ncontrol= 81 dendrites, 593 mitochondria; ncontrol Aβ42o = 105 dendrites, 645 mitochondria; nhTauWT Control = 38 dendrites, 258 mitochondria; nhTauWT Aβ42o = 79 dendrites, 725 mitochondria; nhTauS262A Control = 81 dendrites, 555 mitochondria; nhTauS262A Aβ42o = 89 dendrites, 756 mitochondria. Statistical analyses were performed using One-way ANOVA followed by Kruskal-Wallis Multiple Comparisons in (b-d). The test was considered significant when $p < 0.05$ with the following criteria: * $p < 0.05$; ** $p < 0.01$; *** $p < 0.001$; **** $p < 0.0001$; ns, not significant.

Supplemental Figure S10

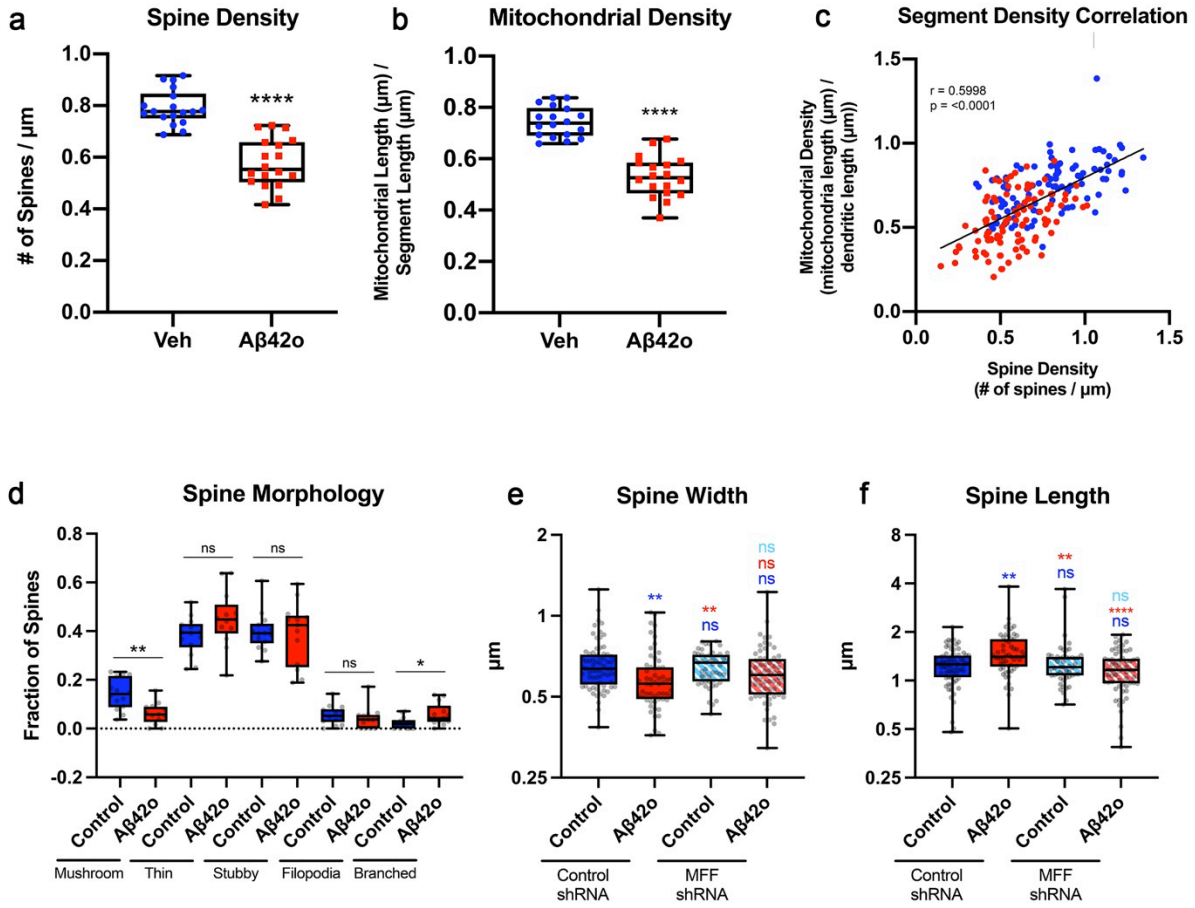

Supplemental Figure S2.10. Correlation between degree of dendritic mitochondrial remodeling and spine densities and morphological features of dendritic spines induced by Aβ42o are rescued by MFF knockdown.
(**a-b**) Quantification spine density (**a**) and mitochondrial density (**b**) in secondary dendritic segments of primary cortical PNs at 21DIV following 24 hours of treatment with either a vehicle control (blue) or Aβ42o (red values). (**c**) Correlation between dendritic mitochondrial density (volume of dendrite occupied by mitochondria) and spine density in individual secondary dendritic segments treated with either a vehicle control (blue points) or Aβ42o (red points). Non-parametric Spearman correlation coefficient (r) is highly significant. (**d**) Categorization of spine morphology for primary cortical PNs treated with either a vehicle control or Aβ42o. (**e-f**) Quantification of dendritic spine width (**e**) and dendritic spine width (**f**) for primary cortical PNs *ex utero* electroporated with pCAG-mVenus, pCAG-mito-DsRed, and either a control shRNA or MFF shRNA, treated with either a vehicle control or Aβ42o. In all panels (except panel **c**), data is represented by box plots displaying minimum to maximum values, with the box denoting 25th, 50th (median), and 75th percentile, with each data point representing an individual dendritic segment. Statistical analyses were performed using a Mann-Whitney test. The data was quantified using three to six biological replicates, nVeh = 99 dendritic segments, 750 mitochondria; nAβ42o = 101 dendritic segments, 840 mitochondria; nControlshRNA Veh = 13 dendritic segments, 600 spines; nControlshRNA Aβ42o = 12 dendritic segments, 490 spines; nMFFshRNA Veh = 8 dendritic segments, 360 spines; nMFFshRNA Aβ42o = 9 dendritic segments, 394 spines. All of the analyses were done blind to the experimental conditions, using dendritic segments of similar length (43µm on average), and were done by manual counting using Fiji. The tests were considered significant when $p<0.05$ with the following criteria: *$p<0.05$; ** $p<0.01$, *** $p<0.001$, **** $p<0.0001$.

Supplemental Figure S11

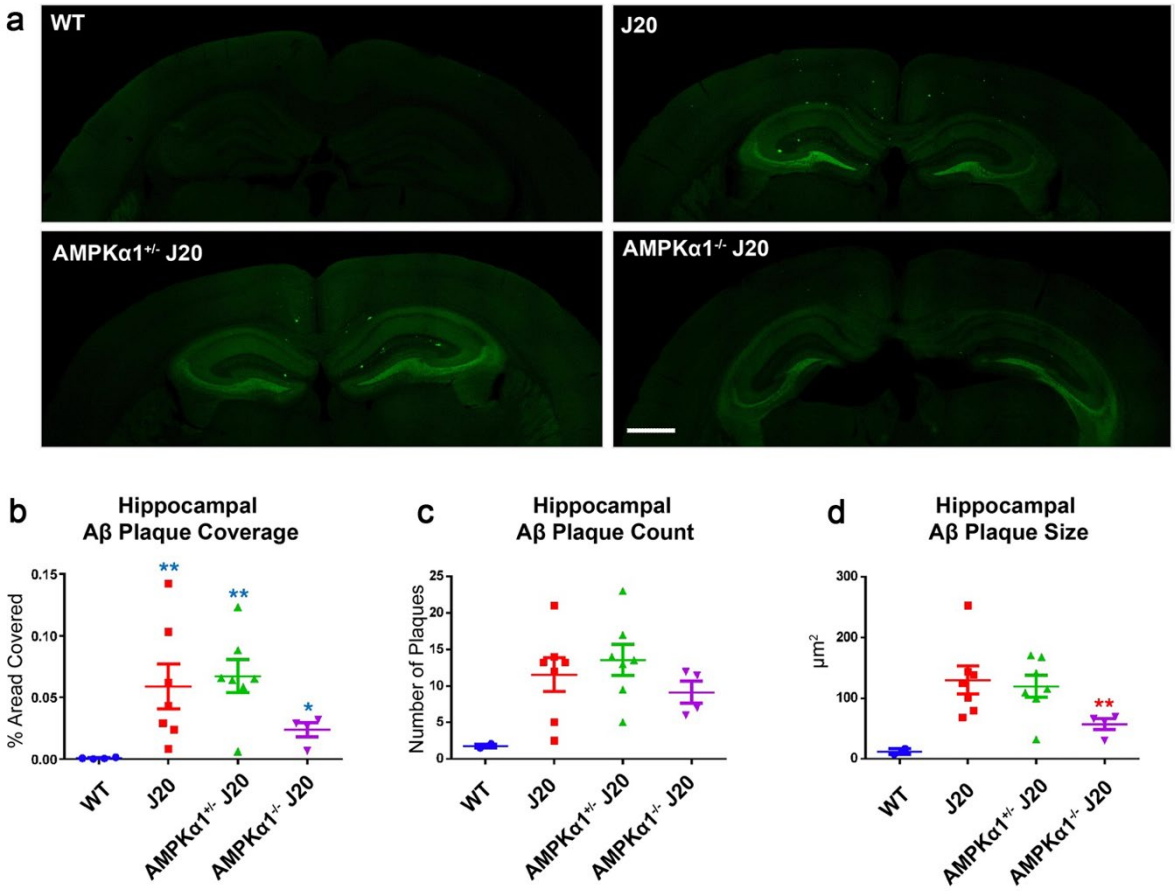

Supplemental Figure S2.11. Aβ plaque load is decreased in the hippocampus of 5 months-old AMPKα1-/- J20 mice.
(**a**) Coronal sections from 5-month-old WT, J20 (Hets), AMPKα1$^{+/-}$(Het) x J20(Hets) and AMPKα1$^{-/-}$ (KO) x J20(Hets) mice immunolabeled with 6E10 antibody (detecting Aβ42 oligomers) reveals amyloid plaques. (**b**) The area covered by amyloid plaques, (**c**) the number of amyloid plaques, and (**d**) their sizes were measured in the hippocampus. These quantifications suggest that Aβ plaque coverage and Aβ plaque size is reduced in the J20 mouse when AMPKα1 expression is reduced in a dose-dependent manner, although the number of plaques does not seem to be decreased. Statistical analyses were performed using Mann-Whitney test between each genotype versus WT (blue stars) or J20 (red stars). In panels **b-d**, bar graph represent mean +/- S.E.M. The tests were considered significant when $p<0.05$ with the following criteria: * $p<0.05$; ** $p<0.01$. n = 4-7 animals per genotype. Scale bar in panels **a**: 200 microns.

2.7 Methods

Animals

Mice were used according to protocols approved by the Institutional Animal Care and Use Committee (IACUC) at Columbia University and in accordance with National Institutes of Health guidelines. Time-pregnant CD1 females were purchased from Charles Rivers. 129/SvJ, C57Bl/6J non-transgenic mice and hemizygous transgenic mice from line B6.Cg-*Zbtb20*$^{Tg(PDGFB-APPSwInd)20Lms}$/2Mmjax (hereafter referred as J20) (The Jackson Laboratory stock #006293) were maintained in a 12-hour light/dark cycle. J20 mice express human APP carrying the Swedish and Indiana mutations under a PDGFβ promoter [8,111]. AMPKα1$^{F/F}$α2$^{F/F}$ double conditional knockout mice were generated by Drs. Foretz and Viollet [50]. Ulk2$^{F/F}$ mice were obtained from The Jackson Laboratory stock #017977 [60]. Timed-pregnant females were obtained by overnight breeding with males of the same strain. Noon the day after the breeding was considered as E0.5. Mice of both sexes were used for each experiment and no sex difference was detected.

All mouse strains were maintained in a 12h dark/12h light cycle in rooms with constant humidity and temperature control in a barrier SPF housing facility.

Synthetic Aβ42 oligomers preparation

Aβ42 (rPeptide or Creative Peptide) was processed to generate Aβ42 oligomers as described in [2]. Briefly, lyophilized Aβ42 peptide was dissolved in hexafluoro-2-propanol (HFIP; Sigma-Aldrich) for 2 hours to allow monomerization. HFIP was removed by speed vacuum, and the monomers were stored in -80°C. Aβ42 monomers were dissolved in anhydrous dimethyl sulfoxide (DMSO) to make a 5mM solution, then added to cold phenol red-free F12 medium (Life Technology) to make a 100uM solution. The solution was incubated at 4°C for two days and centrifuged at 12,000 x g for 10 min at 4°C in order to discard the fibrils. The supernatant containing the 4°C oligomers were assayed for protein content using the BCA kit (Thermo Fisher Scientific). For control experiments, vehicle treatment corresponded to the same volume of DMSO and F12 media used for Aβ42o treatment and for Figure S02, a peptide corresponding to the inverted sequence of Aβ42 (INV42; rPeptide and Creative Peptide) was processed as for Aβ42 oligomerization. For western blotting of Aβ42 oligomers, 16.5% Tris-Tricine SDS-PAGE was performed. Synthetic Aβ42 oligomers were prepared in 2X Tricine sample buffer (BIORAD) without reducing agent and resolved by SDS-PAGE. The separated proteins were transferred onto Immobilin-FL PVDF membrane (EMD Millipore),

blocked for 1 hour with Odyssey blocking buffer (LICOR) and probed with 6E10 monoclonal antibody (Covance) overnight at 4°C. Secondary antibody incubation was performed for 1 hour at room temperature with IRDye 680RD goat anti-mouse secondary (LICOR) and the blot was visualized using the Odyssey Imaging system. To estimate the relative concentration of synthetic Aβ42 peptide monomer versus oligomers (dimers and trimers), we performed quantitative western blotting (see Fig. S2E) and measured the ratio of optical density measured for the monomeric peptide versus the dimer/trimer bands. Using this approach, we estimated that a 1μM concentration of oligomerized peptide contains approximately 300-450nM of effective dimers/trimers (Fig. S2E).

Primary cortical culture and *ex utero* electroporation

Cortices from E15.5 mouse embryos were dissected followed by dissociation in complete Hank's balanced salt solution (cHBSS) containing papain (Worthington) and DNase I (100ug/mL, Sigma) for 15 minutes at 37°C, washed three times, and manually triturated in DNase I (100ug/mL) containing neurobasal medium (Life Technology) supplemented with B27 (1x, Thermo Fischer Scientific,), FBS (2.5%, Gibson), N2 (1x, Thermo Fischer Scientific), and glutaMAX (2mM, Gibco). Cells were plated at 10.0 X 10^4 cells per 35 mm glass bottom dish (Mattek) that has been coated with poly-D-lysine (1mg/mL, Sigma) overnight. One-third of the medium was changed every 5 days thereafter with non-FBS containing medium and maintained for 20-25 days in 5% CO_2 incubator at 37°C. *Ex utero* electroporation was performed as previously published [112]. See the Supplemental Experimental Procedures for details and constructs. Plasmids used for *ex utero* electroporation where all in pCAG vector backbone [113] expressing the following cDNAs: LAMP1-mEmerald[114], mito-DsRed and Venus [112], mRFP-LC3 (originally from https://www.addgene.org/21075/ and subcloned into pCAG backbone). pSCV2-Venus and pCAG-mito-dsRed were described in a previous publication [114]. pLKO-MFFsh specific for mouse was obtained from Sigma Aldrich (TRCN0000174665). Validation of the MFF shRNA knockdown efficiency was done elsewhere[14]. cDNA encoding Renalin, MFF WT (Uniprot Q9GZY8 isoform 5), and MFF AA were described in [40] and subcloned in the pCAG plasmid backbone 3' to the CAG promoter using PCR. 0.25μg/mL of individual constructs were used for the MFF rescue experiments. pCAG-Cre, pCAG-Scrambled Cre, pCIG-hTau (isoform 4R2N), and non-phosphorylatable hTau-S262A were described in previous publications [112]. pcDNA3-flag-ULK2 specific for mouse was obtained from Addgene (#27637) and was used to generate the kinase-inactive (K39I) and

serine-to-alanine 4SA mutant (S309/T441/S528/S547A) using Quickchange II site-directed mutagenesis kit (Agilent technologies) and were subcloned into pCAG vector backbone using PCR. pSUPER-scrambled, ULK1 shRNA and ULK2 shRNA constructs were validated in a previous study [115]. Sequences for ULK1 shRNA: 5′-ATCCCCAGACTCCTGTGACACAGATTTCAAGAGAATCTGTGTCAC A G G A GTCTTTTTTA-3′ and for ULK2 shRNA: 5′-ATCCCCTGCCTAGTATTCCCAGAGATTCAAGAGATC T C T G G G A A T ACTAGGCATTTTTA-3′.

***In utero* hippocampal electroporation**

In utero electroporation targeting the hippocampus was performed as previously described [2,116,117] with slight modifications as described in [55,118] to target the embryonic hippocampus at E15.5. See Supplemental Experimental Procedures for more details. In brief, a mix of endotoxin-free plasmid preparation was injected into both lateral hemispheres of E15.5 embryos using a picospritzer. Electroporation was performed with a triple electrode to target hippocampal progenitors in E15.5 embryos by placing the two anodes (positively charged) on either side of the head and the cathode on top of the head at a 0° angle to the horizontal plane. Four pulses of 45V for 50ms with 500ms interval were used for the electroporation.

Microscopy

Imaging on dissociated neurons was performed between 20-25 DIV in 1,024 x 1,024 resolution with a Nikon Ti-E microscope equipped with A1R laser-scanning confocal microscope using the Nikon software NIS-Element (Version 4.3;Nikon, Melville, NY, USA). We used the following objective lenses (Nikon): 10x PlanApo; NA 0.45 (for images of hippocampal slices), 60X Apo TIRF; NA 1.49 (for analysis of spine density and mitochondrial morphology in cultured neurons), 100x H-TIRF; and NA 1.49 (for analysis of spine densities and mitochondrial morphology in brain slices). Dendritic spine density was quantified on secondary or tertiary dendritic branches that were proximal to the cell body, on z projections for cultured neurons and in the depth of the z stack for slices, using FIJI software (ImageJ; NIH). See Supplemental Experimental Procedures for more details.

hESC culture

H9 (WA09; WiCell) and its genome edited derivatives were maintained on StemFlex (Life) and Cultrex substrate (Biotechne), and routinely split approximately twice a week with ReLeSR (Stem Cell Technologies) in the presence of ROCKi (Y-27632; Selleckchem). H9 is a commercially available hESC

line on the NIH Registry (# 0062), and Dr. Sproul has approval to genome edit and differentiate this hESC line by the Columbia University Human Embryonic and Human Embryonic Stem Cell Research Committee.

APP^{Swe} knockin hESC line generation

The APP^{Swe} mutation (KM670/671NL) was knocked into both alleles of H9 using CRISPR/Cas9, bi-allelic knockin of APP^{Swe} has been demonstrated to have increased Aβ42 production relatively to monoallelic knockin in a control iPSC line [48]. In brief, a sgRNA targeting Exon16 of *APP* was designed and subcloned into the MLM3636 vector, a gift from Keith Joung (Addgene plasmid # 43860; http://www.addgene.com/43860). An ssDNA HDR template (IDT) was designed in which the APP^{Swe} mutation disrupted the PAM and introduced a *de novo* Xba1 restriction site. The sgRNA, Cas9-GFP (a gift from Kiran Musunuru (Addgene plasmid # 44719; http://www.addgene.org/44719/), and ssDNA HDR template were electroporated (Lonza nucleofector) into feeder-free H9 hESCs, followed by cell sorting on GFP signal and plating at low density on MEFs (MTI-GlobalStem). Individual clones were manually picked into a 96 well format, subsequently split into duplicate plates, one of which were used to generate sgDNA as had been done previously (Paquet et al., 2016). For each clone, exon 16 of *APP* was amplified and initially screened by restriction digest with Xba1 (NEB). Sanger sequencing was used to confirm the mutation, and successful knockin clones were expanded and banked. Potential off-target effects of CRISPR/Cas9 cleavage were analyzed by Sanger sequencing of the top 5 predicted off-target genomic locations [https://mit.crispr.edu], which demonstrated a lack of indels for multiple clones. One APP$^{Swe/}$APP^{Swe} knockin line was analyzed and demonstrated to have a normal karyotype (G-banding, Columbia University Clinical Cytology Laboratory), and was used in the present work (Cl. 160).

Transdifferentiation of hESCs into cortical-like pyramidal neurons

pLV-TetO-hNGN2-eGFP-Puro was generously provided by Kristen Brennand [119] and FUdeltaGW-rtTA was a gift from Konrad Hochedlinger (Addgene plasmid #19780; http://www.addgene.org/19780/) [120]. Concentrated lentiviruses for these two plasmids were made using Lenti-X concentrator (Takara) as has been done previously [121]. Permanent doxycycline inducible Ngn2-eGFP lines were generated by reverse infecting H9 and H9:APP$^{Swe/Swe}$ hESC lines with Ngn2-eGFP and rtTA and subsequent selection by puromycin.

For transdifferentiation of these two lines of hESCs into cortical neurons (iNs; [49]), H9 and H9:APP$^{Swe/Swe}$ lines were plated at ~165,000 cells per 12 well-well in N2/B27 medium on PEI (0.1% Sigma)/laminin (10 ug/mL, Biotechne) coated plates, supplemented with 1 ug/mL doxycycline (Sigma),10 ng/mL BDNF and NT3 (Biotechne) and 1 ug/mL laminin (Biotechne). BDNF, NT3 and laminin were added at similar levels for all subsequent feeds for the duration of the experiment. One day post plating cells were treated with puromycin (1ug/mL, Fisher). The following day cells were treated with 2 uM AraC (Biotechne) for 4 days, and 100 ng/mL on subsequent feeds. One week post infection, cells were transitioned into BrainPhys (Stem Cell Technologies). Two weeks post infection, 10% mouse astrocyte conditioned media (ACM; ScienCell) was also added to the medium. Transfection of mitoDsRed2 was done at day 21-23 post infection using Lipofectamine 3000 (Life), and cells were fixed and analyzed 4 days later. A full media change (1/2 saved conditioned media) was performed approximately 6h post transfection. Note that iNs had poor survival from Lipofectamine transfection without either ACM or primary mouse glia present.

Cell Lysis and Immunoprecipitation

Neuron and differentiated hESC cultures were washed with cold PBS and lysed in Triton Lysis Buffer: 20mM HEPES (pH 7.5), 150mM NaCl, 1 mM EDTA, 1 mM EGTA, 1% Triton X-100, 0.25M Sucrose, Complete™protease inhibitor (Roche), and phosphoSTOP (Roche). Lysates were incubated at 4°C for 15 minutes and cleared at 15,000 x g for 15 minutes at 4°C. Total protein was normalized using Bio-rad Protein Assay Dye (Bio-rad).

For western blotting of phospho-T172 AMPK and total AMPK, equal amounts of lysates were loaded on a Mini-Protean TGX (4-20%) SDS-PAGE (Bio-rad). The separated proteins were transferred onto polyvinylidene difluoride membrane (PVDF, Bio-Rad), blocked for 1 hour with blocking buffer containing 5% fat-free dry milk in TBS-T. Membranes were then incubated overnight at 4°C with different primary antibodies diluted in the same blocking buffer. Incubations with HRP conjugated secondary antibodies were performed for 1 hour at room temperature, and visualization was performed by chemiluminescence.

For phospho-T172 AMPK and total AMPK for eSC experiments, equal amounts of lysates (50µg) were immunoprecipitated with phospho-T172 AMPKα or total AMPKα to enhance AMPK proteins. Lysates from H9-Control and H9APP lines were incubated overnight at 4ºC in a rotator with either phospho-T172 AMPK or total AMPK primary antibodies. Protein A-Agarose beads (Sigma) were washed three times with

PBS and added to the immuno-bound lysates for at least 1 hr at 4ºC. The lysates and beads were then washed thrice with lysis buffer and eluted in SDS lysis buffer for 5 minutes at 95ºC and resolved by loading equal amounts of eluted protein on a Mini-Protean TGX (4-20%) SDS-PAGE (Bio-rad). The separated proteins were transferred onto polyvinylidene difluoride membrane (PVDF, Bio-Rad), and blocked for 1 hour with Odyssey Blocking Buffer (PBS). Membranes were then incubated overnight at 4°C with phospho-T172 AMPK or total AMPK primary antibodies diluted in the same blocking buffer. Incubations with Li-Cor fluorescence-coupled secondary antibodies were performed for 1 hour at room temperature, and visualization was performed by Li-Cor Odyssey Blot Imager.

For phospho-MFF and MFF immunodetection, equal amounts of lysates (80µg) were immunoprecipitated with MFF or HA (as negative control for specific binding) to enhance MFF proteins. SureBeads™ Protein A Magnetic Beads were washed three times with lysis buffer and added to equilibrated lysates for 1 hour at 4°C. The beads were washed 2 times with lysis buffer, two times with lysis buffer without Triton X-100, and then eluted by boiling in SDS lysis buffer for 5 minutes at 95°C and resolved by SDS-PAGE (Bio-rad) gel. The separated proteins were transferred onto polyvinylidene difluoride membrane (PVDF, Bio-Rad), blocked for 1 hour with blocking buffer containing 5% BSA in Tris-buffered saline solution. Membranes were incubated overnight at 4°C with either phospho or total MFF primary antibodies diluted in the same blocking buffer. Clean-Blot™ IP Detection Kit (Thermo Fisher Scientific) was used to detect the bands of interest without the detection of denatured IgG as MFF protein size is close to both heavy and light chain. After overnight primary antibody incubation, membranes were incubated with Dilute Clean-Blot IP Detection Reagent at 1:100 for 1 hour at room temperature and visualization was performed by enhanced chemiluminescence.

For phospho-ULK2 experiments, HEK293T cells (ATCC #CRL-3216) were transfected using Lipofectamine 2000 (Life Technologies) according to manufacturer's instructions with pcDNA3 plasmids encoding flag tagged WT ULK2, flag tagged K39I ULK2 (ULK2 KI) or flag tagged S309A, T441A, S528A, S547A ULK2 (SA4). Where indicated, cells were co-transfected with a constitutively active truncated version of AMPKα1 (caAMPK). Transfected cell lysates were harvested 40-48 hours post transfection. 1 hour after changing the media with fresh media containing vehicle or 50µM compound 991 (Glixx laboratories, Inc.), cells were washed with cold PBS and lysed in lysis buffer: 20 mM Tris pH 7.5, 150 mM

NaCl, 1 mM EDTA, 1mM EGTA, 1% Triton X-100, 2.5 mM pyrophosphate, 50 mM NaF, 5 mM β-glycero-phosphate, 50 nM calyculin A, 1 mM Na3VO4, and protease inhibitors (Roche). Lysates were incubated at 4°C for 15 minutes and cleared at 16,000g for 15 minutes at 4°C. Total protein was normalized using BCA protein kit (Pierce) and lysates were resolved on SDS-PAGE gel. Immunoprecipitations were performed by adding magnetic M2 FLAG beads (Sigma) to equilibrated lysates for 2 hours at 4°C. The beads were washed three times with lysis buffer and then eluted by boiling in SDS lysis buffer for 5 minutes and resolved by SDS-PAGE.

Antibodies used in this study: anti-phospho-T172-AMPKα (40H9, 1:1000, Cell Signaling); anti-AMPKα1/2 (1:1000, Cell Signaling Technology); MFF (1:1000, Proteintech); phospho-S146/172-MFF (1:1000, CST); pAMPK motif (Cell Signaling Technology, #5759S); total AMPKα (Cell Signaling Technology, #2532), p62/SQSTM1 (Cell Signaling #5114); Flag M2 (Sigma, F7425), pAMPK (Cell Signaling Technology, #2535), actin (Sigma, A5441). HRP-coupled secondary antibodies to mouse (AP124P) or rabbit (AP132P) were from Millipore. Li-Cor Fluorescence-coupled secondary antibodies to mouse or rabbit were from Li-Cor Biosciences.

Tissue slice preparation and Immunofluorescence

Animals were sacrificed 3 months after birth by terminal transcardial perfusion of 4% paraformaldehyde (PFA, Electron Microscopy Sciences) followed by overnight post-fixation in 4% PFA. Brains were washed 3X with PBS for 5 minutes and sectioned at 100μm thickness using vibratome (Leica). Sections were permeabilized with 0.2% Triton X-100 3X for 5 minutes, blocked in PBS based blocking buffer with 5% BSA and 0.2% Triton, and stained with chicken anti-GFP (Aves, 1:1000) and rabbit anti-RFP (Abcam, 1:1000) for enhancement of PSCV2-mVenus and pCAG-mitoDsRed, respectively overnight at 4°C. Sections were washed with 0.2% Triton buffer 3X for 5 minutes and incubated with Alexa488- and Alexa 555- labeled secondary antibodies for PSCV2-mVenus and pCAG-mitoDsRed, respectively overnight at 4°C. Sections were washed with 0.2% Triton buffer 3X for 10 minutes each and mounted using VectaShield® Mounting Medium (Vector Laboratory).

Drug Treatments

Neuronal cells at 20-25 DIV were treated with STO609 (2.5μM, Millipore), a CAMKK2 inhibitor, 2.5 hours prior to Aβ42 treatment. N2A cells were transfected with pCAG-MFF-WT construct using the recommended

protocol from FuGENE®HD Transfection Reagent overnight. Cells were treated with either DMSO or Metformin (2mM, Sigma) for 5 hours before cells were lysed using Triton lysis buffer as described under Cell Lysis and Immunoprecipitation.

Analysis of Spine Density and Mitochondrial Morphology

Dendritic spine densities were quantified on secondary or tertiary dendritic branches for cultured neurons and in the depth of the z stack for slices, using FIJI software (ImageJ, NIH). The length of the dendritic segment was measured on the z projection, which implies the density could be overestimated. To limit this issue, only dendrites that were parallel to the plane of the slices were analyzed. Spines were quantified over an average of 40μm in cultures (between 2-3 segments per cell) and 40μm *in vivo* (between 2-3 segments per cell). Spine density was defined as the number of quantified spines divided by the length over which the spines were quantified. The criteria for measuring mitochondrial length for each dendritic segment were the same as above. Mitochondrial density was defined as the total sum of all the mitochondria divided by the length over which the mitochondria lengths were measured.

Analysis of Mitophagy Events

For quantifications in Figure 3, manual counting of the total number of dendrites and number of dendrites showing accumulation of fluorescently-tagged LC3-RFP and LAMP1-mEmerald was performed for all imaged neurons. To confirm both LC3 and LAMP1 accumulation over time following Aβ42o application using an independent quantification approach, we selectively examined all of the 251 dendritic segments categorized as showing LC3+/LAMP1+ accumulation upon Aβ42o application and measured the intensities of LC3 and LAMP1 fluorescence (within an ROI ranging from 20-30μm in length) over time. All the dendrites that showed accumulation of LC3 and LAMP1 in control conditions were also analyzed, as well as randomly selected dendritic segments that did not show detectable accumulation of LC3 and LAMP1. Optical density of LAMP1-mEmerald and LC3-RFP fluorescence were normalized to the initial starting fluorescence intensities at t_0 ($\Delta F/F_0$). For these selected dendrites, mito-mTagBFP2 intensities were also measured over time for Fig. 3E. To measure local mitophagy events as indicated in Fig. 3F, random dendrites analyzed in Fig. 3B were selected for each condition. For a given dendritic segment, intensity line scan analysis (pixel neighborhood-1 pixel) was performed where two vertical lines were drawn: one along the region of dendrite without LC3/LAMP1 puncta and one along the region with LC3/LAMP1 puncta. The fold change of

mitochondrial intensity from time point zero to 14 hours after respective treatment was calculated as illustrated in Fig. 3F.

Analysis of Mitochondrial Density in hES cell-derived cortical neurons

For Figure S3B-C, lines of equal thickness and of an average length of ~40μm were drawn along the neurites of differentiated hES cell-derived cortical neurons in Nikon NIS-Elements Software. A kymograph was subsequently created from each drawn line, for which the mean fluorescence intensity of the mitochondria as a function of area was calculated and normalized to the background fluorescence intensity of the image.

Statistics

Statistical analyses were performed with Prizm 9.0.4 (GraphPad Software, LLC). The statistical tests applied for data analysis are indicated in the corresponding figure legend. Experimental groups with Gaussian/normal distributions were assessed using the unpaired t-test for two-population comparison. For groups that deviated significantly from normal distributions, non-parametric test (Mann-Whitney U test for two-population comparisons was used. Unless otherwise noted, data are expressed as mean ± SEM. For dendritic spine and mitochondrial morphology analysis, all data were obtained from at least three independent experiments or at least three individual mice of each genotype. The test was considered significant when $p<0.05$. For all analyses, the following apply: * $p<0.05$; ** $p<0.01$; *** $p<0.001$; **** $p<0.0001$; ns, not significant with $p > 0.05$.

2.8 Acknowledgements

We thank members of the Polleux lab for feedback and discussion, as well as Karen Duff, Ulrich Hengst, and Carol Troy for critically evaluating the manuscript. We thank Fan Wang (Duke University) for providing ULK1 and ULK2 shRNA constructs. We thank Qiaolian Lu and Miyako Hirabayashi for the excellent management of our mouse colony. This work was supported by grants from the NIH (NS089456) (F.P.), a F31 Award from NIH (A.L.), a K99 award (NS091526) (T.L.L.), the Thompson Foundation (TAME-AD) (A.S.), the Henry and Marilyn Taub Foundation (A.S.), the Ludwig Foundation (F.P., A.S., and A.M.V.), and an award from the Fondation Roger De Sproelberch (F.P.). Georges Mairet-Coello is affiliated with UCB Biopharma (Belgium) but has no other competing interests to declare.

2.9 Author Contributions

A.S., C.K., D.M.V., T.L.L. R.S., and F.P. contributed to the conceptualization of this manuscript. A.L., C.K., D.M.V., S.H., A.S., and F.P. contributed to the methodology of this manuscript. A.S., C.K., D.M.V., T.L.L., G.M-C., S.Y.K., A.A., M.F., B.V., and A.S. contributed to the investigation presented in this manuscript. A.S., C.K., D.M.V., and F.P. participated in the writing of this manuscript. A.S., R.S., and F.P. secured funding for the work presented in this manuscript. A.S., R.S., and B.V. provided resources which enabled the work presented in this manuscript.

2.10 References

1. Sheng, M., Sabatini, B. L. & Sudhof, T. C. Synapses and Alzheimer's disease. *Cold Spring Harb Perspect Biol* **4**, doi:10.1101/cshperspect.a005777 (2012).
2. Mairet-Coello, G. *et al.* The CAMKK2-AMPK kinase pathway mediates the synaptotoxic effects of Abeta oligomers through Tau phosphorylation. *Neuron* **78**, 94-108, doi:10.1016/j.neuron.2013.02.003 (2013).
3. Masliah, E. *et al.* Altered expression of synaptic proteins occurs early during progression of Alzheimer's disease. *Neurology* **56**, 127-129 (2001).
4. Moolman, D. L., Vitolo, O. V., Vonsattel, J. P. & Shelanski, M. L. Dendrite and dendritic spine alterations in Alzheimer models. *J Neurocytol* **33**, 377-387, doi:10.1023/B:NEUR.0000044197.83514.64 (2004).
5. Shankar, G. M. *et al.* Natural oligomers of the Alzheimer amyloid-beta protein induce reversible synapse loss by modulating an NMDA-type glutamate receptor-dependent signaling pathway. *J Neurosci* **27**, 2866-2875, doi:10.1523/JNEUROSCI.4970-06.2007 (2007).
6. Shankar, G. M. *et al.* Amyloid-beta protein dimers isolated directly from Alzheimer's brains impair synaptic plasticity and memory. *Nat Med* **14**, 837-842, doi:10.1038/nm1782 (2008).
7. Jacobsen, J. S. *et al.* Early-onset behavioral and synaptic deficits in a mouse model of Alzheimer's disease. *Proc Natl Acad Sci U S A* **103**, 5161-5166, doi:10.1073/pnas.0600948103 (2006).
8. Mucke, L. *et al.* High-level neuronal expression of abeta 1-42 in wild-type human amyloid protein precursor transgenic mice: synaptotoxicity without plaque formation. *J Neurosci* **20**, 4050-4058 (2000).
9. Jin, M. *et al.* Soluble amyloid beta-protein dimers isolated from Alzheimer cortex directly induce Tau hyperphosphorylation and neuritic degeneration. *Proc Natl Acad Sci U S A* **108**, 5819-5824, doi:10.1073/pnas.1017033108 (2011).

10. Lacor, P. N. *et al.* Synaptic targeting by Alzheimer's-related amyloid beta oligomers. *J Neurosci* **24**, 10191-10200, doi:10.1523/JNEUROSCI.3432-04.2004 (2004).
11. Lacor, P. N. *et al.* Abeta oligomer-induced aberrations in synapse composition, shape, and density provide a molecular basis for loss of connectivity in Alzheimer's disease. *J Neurosci* **27**, 796-807, doi:10.1523/JNEUROSCI.3501-06.2007 (2007).
12. Ashrafi, G. & Schwarz, T. L. PINK1- and PARK2-mediated local mitophagy in distal neuronal axons. *Autophagy* **11**, 187-189, doi:10.1080/15548627.2014.996021 (2015).
13. Lewis, T. L., Jr., Courchet, J. & Polleux, F. Cell biology in neuroscience: Cellular and molecular mechanisms underlying axon formation, growth, and branching. *J Cell Biol* **202**, 837-848, doi:10.1083/jcb.201305098 (2013).
14. Lewis, T. L., Jr., Kwon, S. K., Lee, A., Shaw, R. & Polleux, F. MFF-dependent mitochondrial fission regulates presynaptic release and axon branching by limiting axonal mitochondria size. *Nat Commun* **9**, 5008, doi:10.1038/s41467-018-07416-2 (2018).
15. Rangaraju, V. *et al.* Pleiotropic Mitochondria: The Influence of Mitochondria on Neuronal Development and Disease. *J Neurosci* **39**, 8200-8208, doi:10.1523/JNEUROSCI.1157-19.2019 (2019).
16. Schwarz, T. L. Mitochondrial trafficking in neurons. *Cold Spring Harb Perspect Biol* **5**, doi:10.1101/cshperspect.a011304 (2013).
17. Lee, A., Hirabayashi, Y., Kwon, S. K., Lewis, T. L., Jr. & Polleux, F. Emerging roles of mitochondria in synaptic transmission and neurodegeneration. *Curr Opin Physiol* **3**, 82-93, doi:10.1016/j.cophys.2018.03.009 (2018).
18. Burte, F., Carelli, V., Chinnery, P. F. & Yu-Wai-Man, P. Disturbed mitochondrial dynamics and neurodegenerative disorders. *Nat Rev Neurol* **11**, 11-24, doi:10.1038/nrneurol.2014.228 (2015).
19. Chan, D. C. Mitochondria: dynamic organelles in disease, aging, and development. *Cell* **125**, 1241-1252, doi:10.1016/j.cell.2006.06.010 (2006).
20. Youle, R. J. & van der Bliek, A. M. Mitochondrial fission, fusion, and stress. *Science* **337**, 1062-1065, doi:10.1126/science.1219855 (2012).

21. Kwon, S. K. *et al.* LKB1 Regulates Mitochondria-Dependent Presynaptic Calcium Clearance and Neurotransmitter Release Properties at Excitatory Synapses along Cortical Axons. *PLoS Biol* **14**, e1002516, doi:10.1371/journal.pbio.1002516 (2016).
22. Du, H. *et al.* Early deficits in synaptic mitochondria in an Alzheimer's disease mouse model. *PNAS* **107**, 18670-18675 (2010).
23. Itoh, K., Nakamura, K., Iijima, M. & Sesaki, H. Mitochondrial dynamics in neurodegeneration. *Trends Cell Biol* **23**, 64-71, doi:10.1016/j.tcb.2012.10.006 (2013).
24. Wang, X. *et al.* Impaired balance of mitochondrial fission and fusion in Alzheimer's disease. *J Neurosci* **29**, 9090-9103, doi:10.1523/JNEUROSCI.1357-09.2009 (2009).
25. Wang, X. *et al.* Amyloid Beta overproduction causes abnormal mitochondrial dynamics via differential modulation of mitochondrial fission/fusion proteins. *PNAS* **105**, 19318-19323 (2008).
26. Xie, H. *et al.* Mitochondrial alterations near amyloid plaques in an Alzheimer's disease mouse model. *J Neurosci* **33**, 17042-17051, doi:10.1523/JNEUROSCI.1836-13.2013 (2013).
27. Zhang, L. *et al.* Altered brain energetics induces mitochondrial fission arrest in Alzheimer's Disease. *Sci Rep* **6**, 18725, doi:10.1038/srep18725 (2016).
28. Arriagada, P. V., Marzloff, K. & Hyman, B. T. Distribution of Alzheimer-type pathologic changes in nondemented elderly individuals matches the pattern in Alzheimer's disease. *Neurology* **42**, 1681-1688 (1992).
29. Busche, M. A. *et al.* Critical role of soluble amyloid-beta for early hippocampal hyperactivity in a mouse model of Alzheimer's disease. *Proc Natl Acad Sci U S A* **109**, 8740-8745, doi:10.1073/pnas.1206171109 (2012).
30. David, D. C. *et al.* Proteomic and functional analyses reveal a mitochondrial dysfunction in P301L tau transgenic mice. *J Biol Chem* **280**, 23802-23814, doi:10.1074/jbc.M500356200 (2005).
31. Eckert, A. *et al.* Oligomeric and fibrillar species of beta-amyloid (A beta 42) both impair mitochondrial function in P301L tau transgenic mice. *J Mol Med (Berl)* **86**, 1255-1267, doi:10.1007/s00109-008-0391-6 (2008).

32. Rhein, V. *et al.* Amyloid-beta and tau synergistically impair the oxidative phosphorylation system in triple transgenic Alzheimer's disease mice. *Proc Natl Acad Sci U S A* **106**, 20057-20062, doi:10.1073/pnas.0905529106 (2009).
33. Serrano-Pozo, A., Frosch, M. P., Masliah, E. & Hyman, B. T. Neuropathological alterations in Alzheimer disease. *Cold Spring Harb Perspect Med* **1**, a006189, doi:10.1101/cshperspect.a006189 (2011).
34. Ma, T. *et al.* Inhibition of AMP-activated protein kinase signaling alleviates impairments in hippocampal synaptic plasticity induced by amyloid beta. *J Neurosci* **34**, 12230-12238, doi:10.1523/JNEUROSCI.1694-14.2014 (2014).
35. Son, S. M., Jung, E. S., Shin, H. J., Byun, J. & Mook-Jung, I. Abeta-induced formation of autophagosomes is mediated by RAGE-CaMKKbeta-AMPK signaling. *Neurobiol Aging* **33**, 1006 e1011-1023, doi:10.1016/j.neurobiolaging.2011.09.039 (2012).
36. Thornton, C., Bright, N. J., Sastre, M., Muckett, P. J. & Carling, D. AMP-activated protein kinase (AMPK) is a tau kinase, activated in response to amyloid beta-peptide exposure. *Biochem J* **434**, 503-512, doi:10.1042/BJ20101485 (2011).
37. Fang, E. F. *et al.* Mitophagy inhibits amyloid-beta and tau pathology and reverses cognitive deficits in models of Alzheimer's disease. *Nat Neurosci* **22**, 401-412, doi:10.1038/s41593-018-0332-9 (2019).
38. Vingtdeux, V., Davies, P., Dickson, D. W. & Marambaud, P. AMPK is abnormally activated in tangle- and pre-tangle-bearing neurons in Alzheimer's disease and other tauopathies. *Acta Neuropathol* **121**, 337-349, doi:10.1007/s00401-010-0759-x (2011).
39. Herzig, S. & Shaw, R. J. AMPK: guardian of metabolism and mitochondrial homeostasis. *Nat Rev Mol Cell Biol* **19**, 121-135, doi:10.1038/nrm.2017.95 (2018).
40. Toyama, E. *et al.* AMP-activated protein kinase mediates mitochondrial fission in response to energy stress. *Science* **351**, 275-281 (2016).
41. Nixon, R. A. The role of autophagy in neurodegenerative disease. *Nat Med* **19**, 983-997, doi:10.1038/nm.3232 (2013).
42. Siskova, Z. *et al.* Dendritic structural degeneration is functionally linked to cellular hyperexcitability in a mouse model of Alzheimer's disease. *Neuron* **84**, 1023-1033, doi:10.1016/j.neuron.2014.10.024 (2014).

43. Perez-Cruz, C. *et al.* Reduced spine density in specific regions of CA1 pyramidal neurons in two transgenic mouse models of Alzheimer's disease. *J Neurosci* **31**, 3926-3934, doi:10.1523/JNEUROSCI.6142-10.2011 (2011).
44. Pozueta, J. *et al.* Caspase-2 is required for dendritic spine and behavioural alterations in J20 APP transgenic mice. *Nat Commun* **4**, 1939, doi:10.1038/ncomms2927 (2013).
45. Turner, N. L. *et al.* Multiscale and multimodal reconstruction of cortical structure and function. *bioRxiv* (2020).
46. Harnett, M. T., Makara, J. K., Spruston, N., Kath, W. L. & Magee, J. C. Synaptic amplification by dendritic spines enhances input cooperativity. *Nature* **491**, 599-602, doi:10.1038/nature11554 (2012).
47. Iascone, D. M. *et al.* Whole-Neuron Synaptic Mapping Reveals Spatially Precise Excitatory/Inhibitory Balance Limiting Dendritic and Somatic Spiking. *Neuron* **106**, 566-578 e568, doi:10.1016/j.neuron.2020.02.015 (2020).
48. Paquet, D. *et al.* Efficient introduction of specific homozygous and heterozygous mutations using CRISPR/Cas9. *Nature* **533**, 125-129, doi:10.1038/nature17664 (2016).
49. Zhang, Y. *et al.* Rapid single-step induction of functional neurons from human pluripotent stem cells. *Neuron* **78**, 785-798, doi:10.1016/j.neuron.2013.05.029 (2013).
50. Boudaba, N. *et al.* AMPK Re-Activation Suppresses Hepatic Steatosis but its Downregulation Does Not Promote Fatty Liver Development. *EBioMedicine* **28**, 194-209, doi:10.1016/j.ebiom.2018.01.008 (2018).
51. Garcia, D. & Shaw, R. J. AMPK: Mechanisms of Cellular Energy Sensing and Restoration of Metabolic Balance. *Mol Cell* **66**, 789-800, doi:10.1016/j.molcel.2017.05.032 (2017).
52. Hardie, D. G., Ross, F. A. & Hawley, S. A. AMPK: a nutrient and energy sensor that maintains energy homeostasis. *Nat Rev Mol Cell Biol* **13**, 251-262, doi:10.1038/nrm3311 (2012).
53. Tokumitsu, H. *et al.* STO-609, a specific inhibitor of the Ca(2+)/calmodulin-dependent protein kinase kinase. *J Biol Chem* **277**, 15813-15818, doi:10.1074/jbc.M201075200 (2002).
54. Mairet-Coello, G. & Polleux, F. Involvement of 'stress-response' kinase pathways in Alzheimer's disease progression. *Curr Opin Neurobiol* **27**, 110-117, doi:10.1016/j.conb.2014.03.011 (2014).

55. Blockus, H. *et al.* Synaptogenic activity of the axon guidance molecule Robo2 underlies hippocampal circuit function. *Cell Rep* **37**, 109828, doi:10.1016/j.celrep.2021.109828 (2021).
56. Ducommun, S. *et al.* Motif affinity and mass spectrometry proteomic approach for the discovery of cellular AMPK targets: identification of mitochondrial fission factor as a new AMPK substrate. *Cell Signal* **27**, 978-988, doi:10.1016/j.cellsig.2015.02.008 (2015).
57. Egan, D. F. *et al.* Phosphorylation of ULK1 (hATG1) by AMP-activated protein kinase connects energy sensing to mitophagy. *Science* **331**, 456-461, doi:10.1126/science.1196371 (2011).
58. Domise, M. *et al.* Neuronal AMP-activated protein kinase hyper-activation induces synaptic loss by an autophagy-mediated process. *Cell Death Dis* **10**, 221, doi:10.1038/s41419-019-1464-x (2019).
59. Kim, J., Kundu, M., Viollet, B. & Guan, K. L. AMPK and mTOR regulate autophagy through direct phosphorylation of Ulk1. *Nat Cell Biol* **13**, 132-141, doi:10.1038/ncb2152 (2011).
60. Cheong, H., Lindsten, T., Wu, J., Lu, C. & Thompson, C. Ammonia-induced autophagy is independent of ULK1/ULK2 kinases. *PNAS* **108**, 11121-11126, doi:10.1073/pnas.1115120108 (2011).
61. Domise, M. *et al.* AMP-activated protein kinase modulates tau phosphorylation and tau pathology in vivo. *Sci Rep* **6**, 26758, doi:10.1038/srep26758 (2016).
62. DuBoff, B., Gotz, J. & Feany, M. B. Tau promotes neurodegeneration via DRP1 mislocalization in vivo. *Neuron* **75**, 618-632, doi:10.1016/j.neuron.2012.06.026 (2012).
63. Manczak, M. & Reddy, P. H. Abnormal interaction between the mitochondrial fission protein Drp1 and hyperphosphorylated tau in Alzheimer's disease neurons: implications for mitochondrial dysfunction and neuronal damage. *Hum Mol Genet* **21**, 2538-2547, doi:10.1093/hmg/dds072 (2012).
64. Zott, B., Busche, M. A., Sperling, R. A. & Konnerth, A. What Happens with the Circuit in Alzheimer's Disease in Mice and Humans? *Annu Rev Neurosci* **41**, 277-297, doi:10.1146/annurev-neuro-080317-061725 (2018).
65. Das, U. *et al.* Activity-induced convergence of APP and BACE-1 in acidic microdomains via an endocytosis-dependent pathway. *Neuron* **79**, 447-460, doi:10.1016/j.neuron.2013.05.035 (2013).
66. Hsieh, H. *et al.* AMPAR removal underlies Abeta-induced synaptic depression and dendritic spine loss. *Neuron* **52**, 831-843, doi:10.1016/j.neuron.2006.10.035 (2006).

67. Ittner, L. M. *et al.* Dendritic function of tau mediates amyloid-beta toxicity in Alzheimer's disease mouse models. *Cell* **142**, 387-397, doi:10.1016/j.cell.2010.06.036 (2010).
68. Roberson, E. D. *et al.* Amyloid-beta/Fyn-induced synaptic, network, and cognitive impairments depend on tau levels in multiple mouse models of Alzheimer's disease. *J Neurosci* **31**, 700-711, doi:10.1523/JNEUROSCI.4152-10.2011 (2011).
69. Roberson, E. D. *et al.* Reducing endogenous tau ameliorates amyloid beta-induced deficits in an Alzheimer's disease mouse model. *Science* **316**, 750-754, doi:10.1126/science.1141736 (2007).
70. Terry, R. D. *et al.* Physical basis of cognitive alterations in Alzheimer's disease: synapse loss is the major correlate of cognitive impairment. *Ann Neurol* **30**, 572-580, doi:10.1002/ana.410300410 (1991).
71. Cho, D.-H. *et al.* S-Nitrosylation of Drp1 Mediates β-Amyloid Related Mitochondrial Fission and Neuronal Injury. *Science* **324**, 102-105 (2009).
72. Wang, L. *et al.* Synaptosomal Mitochondrial Dysfunction in 5xFAD Mouse Model of Alzheimer's Disease. *PLoS One* **11**, e0150441, doi:10.1371/journal.pone.0150441 (2016).
73. Wang, X. *et al.* The role of abnormal mitochondrial dynamics in the pathogenesis of Alzheimer's disease. *J Neurochem* **109 Suppl 1**, 153-159, doi:10.1111/j.1471-4159.2009.05867.x (2009).
74. Yoon, S. O. *et al.* JNK3 perpetuates metabolic stress induced by Abeta peptides. *Neuron* **75**, 824-837, doi:10.1016/j.neuron.2012.06.024 (2012).
75. Marinangeli, C. *et al.* AMP-Activated Protein Kinase Is Essential for the Maintenance of Energy Levels during Synaptic Activation. *iScience* **9**, 1-13, doi:10.1016/j.isci.2018.10.006 (2018).
76. Nixon, R. A. Endosome function and dysfunction in Alzheimer's disease and other neurodegenerative diseases. *Neurobiol Aging* **26**, 373-382, doi:10.1016/j.neurobiolaging.2004.09.018 (2005).
77. Arbel-Ornath, M. *et al.* Soluble oligomeric amyloid-beta induces calcium dyshomeostasis that precedes synapse loss in the living mouse brain. *Mol Neurodegener* **12**, 27, doi:10.1186/s13024-017-0169-9 (2017).
78. Grienberger, C. *et al.* Staged decline of neuronal function in vivo in an animal model of Alzheimer's disease. *Nat Commun* **3**, 774, doi:10.1038/ncomms1783 (2012).

79. Kuchibhotla, K. V. *et al.* Abeta plaques lead to aberrant regulation of calcium homeostasis in vivo resulting in structural and functional disruption of neuronal networks. *Neuron* **59**, 214-225, doi:10.1016/j.neuron.2008.06.008 (2008).
80. Lerdkrai, C. *et al.* Intracellular Ca(2+) stores control in vivo neuronal hyperactivity in a mouse model of Alzheimer's disease. *Proc Natl Acad Sci U S A*, doi:10.1073/pnas.1714409115 (2018).
81. Palop, J. J. & Mucke, L. Amyloid-beta-induced neuronal dysfunction in Alzheimer's disease: from synapses toward neural networks. *Nat Neurosci* **13**, 812-818, doi:10.1038/nn.2583 (2010).
82. Guntupalli, S. *et al.* GluA1 subunit ubiquitination mediates amyloid-beta-induced loss of surface alpha-amino-3-hydroxy-5-methyl-4-isoxazolepropionic acid (AMPA) receptors. *J Biol Chem* **292**, 8186-8194, doi:10.1074/jbc.M116.774554 (2017).
83. Malinow, R. New developments on the role of NMDA receptors in Alzheimer's disease. *Curr Opin Neurobiol* **22**, 559-563, doi:10.1016/j.conb.2011.09.001 (2012).
84. Sanderson, J. L., Freund, R. K., Gorski, J. A. & Dell'Acqua, M. L. β-Amyloid disruption of LTP/LTD balance is mediated by AKAP150-anchored PKA and Calcineurin regulation of Ca(2+)-permeable AMPA receptors. *Cell Rep* **37**, 109786, doi:10.1016/j.celrep.2021.109786 (2021).
85. Whitcomb, D. J. *et al.* Intracellular oligomeric amyloid-beta rapidly regulates GluA1 subunit of AMPA receptor in the hippocampus. *Sci Rep* **5**, 10934, doi:10.1038/srep10934 (2015).
86. Lasagna-Reeves, C. A. *et al.* Reduction of Nuak1 Decreases Tau and Reverses Phenotypes in a Tauopathy Mouse Model. *Neuron* **92**, 407-418, doi:10.1016/j.neuron.2016.09.022 (2016).
87. Buee, L., Bussiere, T., Buee-Scherrer, V., Delacourte, A. & Hof, P. R. Tau protein isoforms, phosphorylation and role in neurodegenerative disorders. *Brain Res Brain Res Rev* **33**, 95-130 (2000).
88. Ittner, L. M. & Gotz, J. Amyloid-beta and tau--a toxic pas de deux in Alzheimer's disease. *Nat Rev Neurosci* **12**, 65-72, doi:10.1038/nrn2967 (2011).
89. Qu, X. *et al.* Stabilization of dynamic microtubules by mDia1 drives Tau-dependent Abeta1-42 synaptotoxicity. *J Cell Biol* **216**, 3161-3178, doi:10.1083/jcb.201701045 (2017).
90. Williams, T., Courchet, J., Viollet, B., Brenman, J. E. & Polleux, F. AMP-activated protein kinase (AMPK) activity is not required for neuronal development but regulates axogenesis during metabolic stress. *Proc Natl Acad Sci U S A* **108**, 5849-5854, doi:10.1073/pnas.1013660108 (2011).

91. Schon, E. A. & Przedborski, S. Mitochondria: the next (neurode)generation. *Neuron* **70**, 1033-1053, doi:10.1016/j.neuron.2011.06.003 (2011).
92. Mizushima, N. & Komatsu, M. Autophagy: renovation of cells and tissues. *Cell* **147**, 728-741, doi:10.1016/j.cell.2011.10.026 (2011).
93. Maday, S. & Holzbaur, E. L. Compartment-Specific Regulation of Autophagy in Primary Neurons. *J Neurosci* **36**, 5933-5945, doi:10.1523/JNEUROSCI.4401-15.2016 (2016).
94. Birdsall, V. & Waites, C. L. Autophagy at the synapse. *Neurosci Lett* **697**, 24-28, doi:10.1016/j.neulet.2018.05.033 (2019).
95. Uytterhoeven, V. *et al.* Hsc70-4 Deforms Membranes to Promote Synaptic Protein Turnover by Endosomal Microautophagy. *Neuron* **88**, 735-748, doi:10.1016/j.neuron.2015.10.012 (2015).
96. Lee, J. H. *et al.* Presenilin 1 Maintains Lysosomal Ca(2+) Homeostasis via TRPML1 by Regulating vATPase-Mediated Lysosome Acidification. *Cell Rep* **12**, 1430-1444, doi:10.1016/j.celrep.2015.07.050 (2015).
97. Lee, J. H. *et al.* Lysosomal proteolysis and autophagy require presenilin 1 and are disrupted by Alzheimer-related PS1 mutations. *Cell* **141**, 1146-1158, doi:10.1016/j.cell.2010.05.008 (2010).
98. Ando, K. *et al.* Level of PICALM, a key component of clathrin-mediated endocytosis, is correlated with levels of phosphotau and autophagy-related proteins and is associated with tau inclusions in AD, PSP and Pick disease. *Neurobiol Dis* **94**, 32-43, doi:10.1016/j.nbd.2016.05.017 (2016).
99. Miyagawa, T. *et al.* BIN1 regulates BACE1 intracellular trafficking and amyloid-beta production. *Hum Mol Genet* **25**, 2948-2958, doi:10.1093/hmg/ddw146 (2016).
100. Morel, E. *et al.* Phosphatidylinositol-3-phosphate regulates sorting and processing of amyloid precursor protein through the endosomal system. *Nat Commun* **4**, 2250, doi:10.1038/ncomms3250 (2013).
101. Udayar, V. *et al.* A paired RNAi and RabGAP overexpression screen identifies Rab11 as a regulator of beta-amyloid production. *Cell Rep* **5**, 1536-1551, doi:10.1016/j.celrep.2013.12.005 (2013).
102. Sorrentino, V. *et al.* Enhancing mitochondrial proteostasis reduces amyloid-beta proteotoxicity. *Nature* **552**, 187-193, doi:10.1038/nature25143 (2017).

103. Small, S. A., Schobel, S. A., Buxton, R. B., Witter, M. P. & Barnes, C. A. A pathophysiological framework of hippocampal dysfunction in ageing and disease. *Nat Rev Neurosci* **12**, 585-601, doi:10.1038/nrn3085 (2011).

104. LaFerla, F. M. Calcium dyshomeostasis and intracellular signalling in Alzheimer's disease. *Nat Rev Neurosci* **3**, 862-872, doi:10.1038/nrn960 (2002).

105. Demuro, A. *et al.* Calcium dysregulation and membrane disruption as a ubiquitous neurotoxic mechanism of soluble amyloid oligomers. *J Biol Chem* **280**, 17294-17300, doi:10.1074/jbc.M500997200 (2005).

106. Guo, Q. *et al.* Increased vulnerability of hippocampal neurons to excitotoxic necrosis in presenilin-1 mutant knock-in mice. *Nat Med* **5**, 101-106, doi:10.1038/4789 (1999).

107. Chan, S. L., Mayne, M., Holden, C. P., Geiger, J. D. & Mattson, M. P. Presenilin-1 mutations increase levels of ryanodine receptors and calcium release in PC12 cells and cortical neurons. *J Biol Chem* **275**, 18195-18200, doi:10.1074/jbc.M000040200 (2000).

108. Stutzmann, G. E., Caccamo, A., LaFerla, F. M. & Parker, I. Dysregulated IP3 signaling in cortical neurons of knock-in mice expressing an Alzheimer's-linked mutation in presenilin1 results in exaggerated Ca2+ signals and altered membrane excitability. *J Neurosci* **24**, 508-513, doi:10.1523/JNEUROSCI.4386-03.2004 (2004).

109. Calvo-Rodriguez, M., Hernando-Perez, E., Nunez, L. & Villalobos, C. Amyloid beta Oligomers Increase ER-Mitochondria Ca(2+) Cross Talk in Young Hippocampal Neurons and Exacerbate Aging-Induced Intracellular Ca(2+) Remodeling. *Front Cell Neurosci* **13**, 22, doi:10.3389/fncel.2019.00022 (2019).

110. Area-Gomez, E. & Schon, E. A. Mitochondria-associated ER membranes and Alzheimer disease. *Curr Opin Genet Dev* **38**, 90-96, doi:10.1016/j.gde.2016.04.006 (2016).

111. Palop, J. J. *et al.* Aberrant excitatory neuronal activity and compensatory remodeling of inhibitory hippocampal circuits in mouse models of Alzheimer's disease. *Neuron* **55**, 697-711, doi:10.1016/j.neuron.2007.07.025 (2007).

112. Courchet, J. *et al.* Terminal axon branching is regulated by the LKB1-NUAK1 kinase pathway via presynaptic mitochondrial capture. *Cell* **153**, 1510-1525, doi:10.1016/j.cell.2013.05.021 (2013).

113. Guerrier, S. *et al.* The F-BAR domain of srGAP2 induces membrane protrusions required for neuronal migration and morphogenesis. *Cell* **138**, 990-1004, doi:10.1016/j.cell.2009.06.047 (2009).

114. Lewis, T. L., Jr., Turi, G. F., Kwon, S. K., Losonczy, A. & Polleux, F. Progressive Decrease of Mitochondrial Motility during Maturation of Cortical Axons In Vitro and In Vivo. *Curr Biol* **26**, 2602-2608, doi:10.1016/j.cub.2016.07.064 (2016).

115. Zhou, X. *et al.* Unc-51-like kinase 1/2-mediated endocytic processes regulate filopodia extension and branching of sensory axons. *Proc Natl Acad Sci U S A* **104**, 5842-5847, doi:10.1073/pnas.0701402104 (2007).

116. Hand, R. & Polleux, F. Neurogenin2 regulates the initial axon guidance of cortical pyramidal neurons projecting medially to the corpus callosum. *Neural Dev* **6**, 30, doi:10.1186/1749-8104-6-30 (2011).

117. Meyer-Dilhet, G. & Courchet, J. In Utero Cortical Electroporation of Plasmids in the Mouse Embryo. *STAR Protoc* **1**, 100027, doi:10.1016/j.xpro.2020.100027 (2020).

118. Szczurkowska, J. *et al.* Targeted in vivo genetic manipulation of the mouse or rat brain by in utero electroporation with a triple-electrode probe. *Nat Protoc* **11**, 399-412, doi:10.1038/nprot.2016.014 (2016).

119. Ho, S. M. *et al.* Rapid Ngn2-induction of excitatory neurons from hiPSC-derived neural progenitor cells. *Methods* **101**, 113-124, doi:10.1016/j.ymeth.2015.11.019 (2016).

120. Maherali, N. *et al.* A high-efficiency system for the generation and study of human induced pluripotent stem cells. *Cell Stem Cell* **3**, 340-345, doi:10.1016/j.stem.2008.08.003 (2008).

121. Sun, J. *et al.* CRISPR/Cas9 editing of APP C-terminus attenuates beta-cleavage and promotes alpha-cleavage. *Nat Commun* **10**, 53, doi:10.1038/s41467-018-07971-8 (2019).

Chapter 3: Activity-dependent subcellular compartmentalization of dendritic mitochondria structure in CA1 pyramidal neurons

Daniel M. Virga*, Stevie Hamilton*, Bertha Osei, Abigail Morgan, Emiliano Zamponi. Natalie J. Park, Victoria L. Hewitt, David Zhang, Kevin C. Gonzalez, Erik Bloss, Franck Polleux, and Tommy L. Lewis Jr

https://www.biorxiv.org/content/10.1101/2023.03.25.534233v1

3.1 Chapter Introduction

CA1 pyramidal neurons, the major output cell-type of the hippocampus, receive remarkably spatially restricted inputs from the entorhinal cortex. The proximal dendrites of these neurons receive indirect inputs from the entorhinal cortex, having first to filter through the dentate gyrus, CA3, and CA2 of the hippocampus. The distal dendrites of CA1 pyramidal neurons, however, receive direct inputs from the entorhinal cortex. Interestingly, it was found in our previous work (Chapter 2) that mitochondrial morphology reflects the exact same spatial input structure, with proximal dendrites of CA1 pyramidal neurons containing short, punctate mitochondria, while distal dendrites contain long, tubular mitochondria that occupy most of the dendritic branch. What was not known, however, is how this compartmentalized mitochondrial morphology was maintained.

In this section of the thesis, we determined the molecular effectors responsible for mitochondrial compartmentalization in CA1 pyramidal neurons. First, I confirmed that this compartmentalization was true in a live, adult hippocampus to bypass any potential fixation artifacts using *in vivo* two-photon microscopy and single-cell electroporation. Next, we discovered that removing CA1 pyramidal neurons from their context and culturing them disrupts the mitochondrial compartmentalized morphologies, implying cell non-autonomous factors may be important. We confirmed this by removing over half of the inputs from CA3 to the proximal dendrites and showed elongation of the mitochondria. We also effectively silenced these neurons through hyperpolarization and show a similar elongation.

Next, we determined the downstream molecular effectors responsible for biasing proximal dendrites toward fusion. By knocking down or out CAMKK2, AMPK, MFF, or MTFR1L, we show that each of these proteins is necessary to some extent in maintaining mitochondrial morphology in CA1 pyramidal neurons, as removing them elongates mitochondria primarily in the basal and apical oblique dendrites.

Finally, we demonstrated that this pathway of mitochondrial compartmentalization is activity dependent by stimulating neurons *in vitro* and measuring CAMKK2, AMPK, MFF, and MTFR1L activity in the presence or absence of CAMKK2 inhibitors. Overall, this provides the first molecular pathway that is connecting activity to mitochondrial morphology in a sub-compartment manner.

I carried out and quantified all *in vivo* experiments outlined in this chapter (**Figures 1, 3, 4, 5, 6, S1**), with the exception of the Lphn/Kir2.1 experiments, including imaging and quantifying all of the two-photon experiments. I also configured all of the above listed figures, and drafted the original manuscript. This paper was published on bioRxiv in March 2023, and is in submission at *Nature Communication* as of the publication of this thesis.

3.2 Abstract

Neuronal mitochondria play important roles beyond ATP generation, including Ca^{2+} uptake, and therefore have instructive roles in synaptic function and neuronal response properties. Mitochondrial morphology differs significantly in the axon and dendrites of a given neuronal subtype, but in CA1 pyramidal neurons (PNs) of the hippocampus, mitochondria within the dendritic arbor also display a remarkable degree of subcellular, layer-specific compartmentalization. In the dendrites of these neurons, mitochondria morphology ranges from highly fused and elongated in the apical tuft, to more fragmented in the apical oblique and basal dendritic compartments, and thus occupy a smaller fraction of dendritic volume than in the apical tuft. However, the molecular mechanisms underlying this striking degree of subcellular compartmentalization of mitochondria morphology are unknown, precluding the assessment of its impact on neuronal function. Here, we demonstrate that this compartment-specific morphology of dendritic mitochondria requires activity-dependent, CAMKK2-dependent activation of AMPK and its ability to phosphorylate two direct effectors: the pro-fission Drp1 receptor MFF and the recently identified anti-fusion, Opa1-inhibiting protein, MTFR1L. Our study uncovers a new activity- dependent molecular mechanism underlying the extreme subcellular compartmentalization of mitochondrial morphology in dendrites of neurons *in vivo* through spatially precise regulation of mitochondria fission/fusion balance.

3.3 Introduction

Neurons are among the largest, most complex and highly polarized cell types found in nature. The two main neuronal compartments, dendrites and the axon, differ dramatically in their overall architecture, morphology and functional properties. This striking degree of polarization requires differential targeting of mRNA and proteins, differences in organelle composition, such as specific classes of endosomes, as well as compartment-specific organelle morphology and dynamics [1-5]. Two of the most abundant and complex organelles found in neurons, mitochondria and the endoplasmic reticulum, display a remarkable degree of morphological specialization between axonal and dendritic compartments [5-10]: in the axon of long-projecting mammalian cortical pyramidal neurons (PNs), mitochondria are small (~1 micron in length) and selectively localized to presynaptic boutons, whereas in the dendrites of the same neurons, mitochondria are long and tubular, filling a large fraction of the dendritic volume.

This high degree of polarization not only applies to these two broad neuronal compartments, but also to sub-compartments within axons and dendrites. Our recent work has identified a dramatic sub-cellular compartmentalization of mitochondrial morphology within the dendrites of CA1 PNs of the hippocampus *in vivo*[11]. Unlike other classes of PNs, such as cortical layer 2/3 PNs for example [7], CA1 PNs dendritic mitochondria are small and relatively uniform in shape in the dendritic compartments proximal to the soma (basal and apical oblique dendrites) but are significantly more tubular and occupy a larger fraction of the distal apical tuft compartment [11]. Interestingly, this subcellular compartmentalization of mitochondrial morphology corresponds directly to the spatial segregation of presynaptic inputs received by CA1 PNs: basal dendrites in stratum oriens (SO) receive presynaptic inputs from CA2 and CA3 PNs, apical oblique dendrites in the stratum radiatum (SR) receive presynaptic inputs from CA3 PNs, while distal apical tuft dendrites in the stratum lacunosum moleculare (SLM) receive inputs from the entorhinal cortex (EC).

Mitochondrial morphology in dendrites of pyramidal neurons was previously shown to be regulated by synaptic activity such that neuronal depolarization increased dendritic mitochondria fission through Ca^{2+}-dependent activation of the small-GTPase Dynamin-related protein 1 (Drp1) [12-15]. However, most of these results were obtained *in vitro* and therefore their relevance for mitochondrial morphology of specific neuronal subtypes *in vivo* is largely unknown. In addition, Drp1 was recently shown to also be involved in regulating endocytosis in neurons [16,17] obscuring the interpretation of these earlier results and leaving the molecular mechanisms whereby neuronal depolarization and/or synaptic activity could regulate dendritic mitochondrial morphology *in vivo* unresolved. Drp1 is a cytoplasmic protein recruited to the outer mitochondrial membrane (OMM) in order to promote constriction and fission in concert with so-called Drp1 'receptors' present at the OMM including mitochondrial fission factor (MFF), fission 1 (Fis1), and mitochondrial dynamics proteins of 49 and 51 kDA (MiD49/MiD51) [18-20], with MFF being the most dominant and universal Drp1 receptor in mammalian cells. AMP-activated kinase (AMPK, also called Protein kinase AMP-activated or Prka) is a heterotrimer composed of a catalytic α subunit, an adaptor subunit β and the γ subunit that binds to AMP/ADP. In most cells, AMPK plays a central role as a metabolic sensor activated when ATP levels drop in cells (i.e., when AMP/ADP levels increase), and once activated AMPK phosphorylates many downstream substrates involved in restoring ATP levels and/or decreasing activity of pathways that consume significant levels of ATP such as protein synthesis [21,22]. In the context of metabolic

stress, AMPK promotes mitochondrial fission by directly phosphorylating MFF[23]. Interestingly, in mammalian neurons AMPK is not only a metabolic sensor but also an activity-regulated kinase being phosphorylated and catalytically activated by Calcium/calmodulin dependent protein kinase kinase 2 (CAMKK2), which is induced by increases in intracellular Ca^{2+} levels following either opening of voltage-gated Ca^{2+} channels (VGCC) induced by neuronal depolarization, or activation of N-methyl D-aspartate (NMDA) receptors [11,24,25]. We have recently shown that Aβ42 oligomers trigger overactivation of CAMKK2 leading to excessive activation of AMPK which phosphorylates MFF to trigger dendritic mitochondrial fission in apical tufts of CA1 PNs dendrites *in vivo* [11].

However, the physiological, developmental, and molecular mechanisms underlying this striking degree of mitochondrial compartmentalization in dendrites of CA1 PNs *in vivo* are largely unknown, preventing the exploration of its functional significance. Here, we report that the compartmentalized morphology of dendritic mitochondria characterizing CA1 PNs *in vivo* is present early in development, refined during postnatal maturation of CA1 PNs dendrites and requires activity-dependent and input-specific regulation of the CAMKK2-AMPK kinase dyad. The relationship between activity and mitochondrial dynamics differs across the dendrites, as, in proximal dendrites, but not in apical tuft dendrites, high levels of activity-dependent CAMKK2-mediated AMPK phosphorylates two direct effectors (MFF and MTFR1L) that respectively promote mitochondrial fission and oppose fusion. Thus, our results identify a novel activity-dependent molecular pathway regulating the compartment-specific morphology of dendritic mitochondria of CA1 PNs *in vivo*.

3.4 Results

3.4.1 CA1 hippocampal pyramidal neurons display sub-cellular, compartment specific dendritic mitochondria morphology *in vivo*

In order to visualize mitochondrial morphology in adult CA1 PNs *in vivo* in unfixed and fixed conditions, we used two complementary electroporation techniques: single cell electroporation (SCE; **Fig. 1B**) and *in utero* electroporation (IUE; **Fig. 1A**). Both techniques enable the labeling of mitochondria to visualize their morphology with enough sparsity for optical isolation of single CA1 PNs *in vivo*. The SCE approach has the advantage of enabling *in vivo* live 2-photon imaging of mitochondria in an anesthetized mouse, preventing

any potential artifact of fixation which can affect mitochondria morphology [26]. IUE also allows for sparse expression of mitochondrial markers *in vivo* and is coupled with fixation and imaging with confocal microscopy on brain slices. In both techniques, we co-electroporated a cytoplasmic fluorescent protein (tdTomato, mGreenLantern or mTagBFP2) and a mitochondrial matrix-targeted fluorescent protein (mt-YFP, mt-DsRed or mt-mTAGBFP2) allowing us to visualize single mitochondrial matrices in optically isolated dendrites in developing or adult CA1 PNs.

As previously reported [11], quantitative measurement of mitochondrial matrix size and dendritic occupancy following fixation of IUE CA1 PNs shows a remarkable degree of subcellular compartmentalization corresponding with spatially restricted afferents arriving onto distinct portions of the dendritic arbor (**Fig. 1C-D, H-J**). In basal dendrites (SO) of CA1 PNs located, mitochondria are short (1.065 µm ± 0.029), occupy a third of the dendritic segments (33.01% ± 1.84%), and are uniform in length (mean intra-segment variability: 0.4736 µm ± 0.030). In apical oblique dendrites located in SR, mitochondria are also short, though nearly 1.5 times longer than in SO (1.569 µm ± 0.104), occupy just under half of the dendritic processes (42.38% ± 2.98%), and are rather uniform (mean intra-segment variability: 0.9169 µm ± 0.149). In apical tuft dendrites located in SLM, mitochondria are significantly more elongated (6.562 µm ± 0.437) than in SO or SR, occupy a larger proportion of dendritic segments (84.19% ± 1.44%), and vary significantly more in size within individual dendritic segments (mean intra-segment variability, 5.695 µm ± 0.552).

To exclude the possibility that this compartment-specific morphology of dendritic mitochondria could be the result of fixation [26], we turned to SCE to image dendritic mitochondria of CA1 PNs in living mice. Two to three days following SCE with a cytoplasmic and mitochondrial matrix marker, mice were placed under isoflurane anesthesia while individual dendritic segments from all three compartments—basal, apical oblique, and apical tuft—were imaged using 2-photon microscopy. Despite different imaging conditions, quantitative measurements of size, occupancy, and intra-segment variability show conserved relationships between all three compartments with both approaches (**Fig. 1D, E-G**). These results demonstrate that the striking degree of compartmentalization of dendritic mitochondria characterizing CA1 PNs *in vivo* is not the result of fixation artifacts.

Figure 1

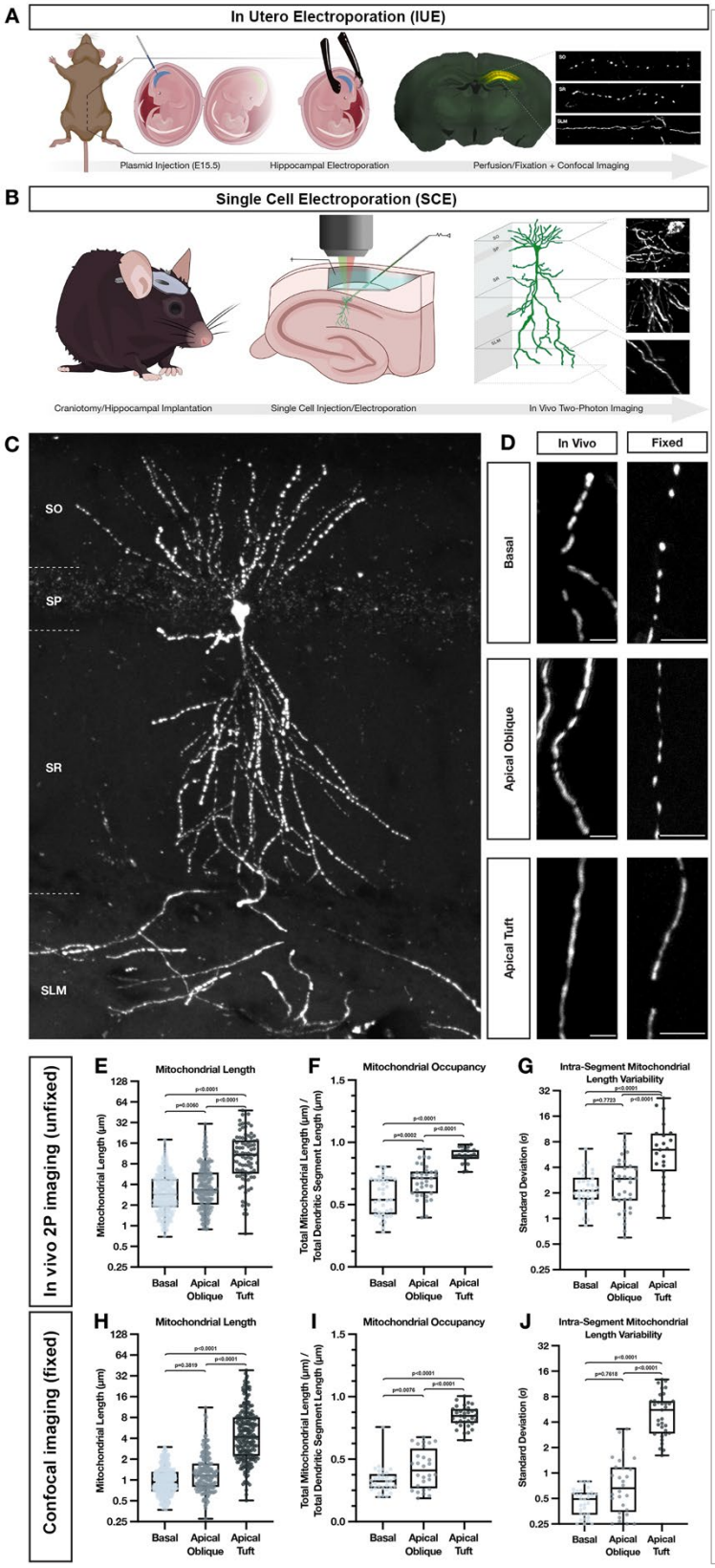

Figure 3.1. Mitochondria display highly compartmentalized, layer-specific, morphology in dendrites of CA1 PNs *in vivo*.

(**A**) Schematic of *in utero* electroporation (IUE) procedure used to sparsely express fluorescent reporters, cDNAs or shRNAs in CA1 PNs of the hippocampus. (**B**) Schematic of single cell electroporation (SCE), used to express fluorescent reporters into single adult CA1 pyramidal neurons in the hippocampus. This method allows for rapid expression of plasmid DNA and *in vivo* two-photon visualization of individual neurons in an adult anesthetized mouse *in vivo*. (**C**) Representative image of a single CA1 PN expressing a mitochondrial matrix reporter (mt-YFP) via SCE following fixation and re-imaged using confocal microscopy on a single vibratome section. (**D**) High-magnification representative images of dendrites from the three hippocampal compartments—basal (SO), apical oblique (SR), and apical tuft (SLM)—expressing a mitochondrial matrix marker (mt-YFP or mt- DsRed) imaged either *in vivo* using two-photon microscopy (left) or post-fixation with confocal microscopy (right). Scale bar, 5 µm. (**E-G**) Quantification of individual mitochondrial length (**E**), mitochondrial segment occupancy (**F**), and intra- segment mitochondrial length variability (**G**) from basal, apical oblique, and apical tuft dendrites captured *in vivo*. (Basal: n = 422 mitochondria; n = 37 dendritic segments; mean length = 3.621 µm ± 0.124 (SEM); mean occupancy = 56.11% ± 2.49% (SEM); mean intra-segment variability = 2.420 µm ± 0.198 (SEM); Apical Oblique: n = 263 mitochondria; n = 35 dendritic segments; mean length = 4.719 µm ± 0.249 (SEM); mean occupancy = 68.82% ± 2.20% (SEM); mean intra-segment variability = 3.185 µm ± 0.370 (SEM); Apical Tuft: n = 90 mitochondria; n = 23 dendritic segments; mean length = 13.02 µm ± 1.041 (SEM); mean occupancy = 89.26% ± 1.24% (SEM); mean intra-segment variability = 8.018 µm ± 6.359 (SEM)). (**H-J**) Quantification of individual mitochondrial length (**H**), mitochondrial segment occupancy (**I**), and intra- segment mitochondrial length variability (**J**) from basal, apical oblique, and apical tuft dendrites following fixation. (Basal: n = 313 mitochondria; n = 32 dendritic segments; mean length = 1.065 µm ± 0.029 (SEM); mean occupancy = 33.01% ± 1.84% (SEM); mean intra-segment variability = 0.4736 µm ± 0.030 (SEM); Apical Oblique: n = 184 mitochondria; n = 28 dendritic segments; mean length = 1.569 µm ± 0.104 (SEM); mean occupancy = 42.38% ± 2.98% (SEM); mean intra-segment variability = 0.9169 µm ± 0.149 (SEM); Apical Tuft: n = 226 mitochondria; n = 33 dendritic segments; mean length = 6.562 µm ± 0.437 (SEM); mean occupancy = 84.19% ± 1.44% (SEM); mean intra-segment variability = 5.695 µm ± 0.552 (SEM)).

Because the above observations were made using mitochondrial matrix-targeted fluorescent reporters, we repeated the IUE experiments, this time expressing fluorescent proteins targeted to both the mitochondrial matrix (mt-mTAGBFP2 or mt-YFP) and the outer mitochondrial membrane (OMM; ActA-mCherry-HA). Quantification of both mitochondrial size and occupancy using both OMM and matrix markers confirmed the above observations. Interestingly, however, values obtained with the OMM marker were significantly longer in all three compartments than their respective matrix measurements, while still maintaining significantly compartmentalized differences (**Fig. S1A-C**).

This result indicates that individual mitochondria defined by OMM markers can contain fragmented matrix sub- volumes, which can be challenging to resolve using diffraction-limited light microscopy. Previous work has reported that in neuronal dendrites, the IMM can undergo repetitive constriction events, termed CoMIC, independently of OMM membrane dynamics [27]. In order to determine the ultrastructural features of mitochondria in CA1 PNs dendrites *in vivo*, and to confirm if dendritic mitochondria in SLM and SR adopted distinct morphology with an independent imaging approach, we took advantage of a serial EM dataset previously published for connectomic analysis [28]. In this dataset, mitochondria located in the apical dendrites of CA1 PNs located in SLM and SR were reconstructed in 3D (**Fig. S1D-H**) and our analysis confirms striking differences in mitochondria morphology between these two dendritic compartments. In SR, mitochondria adopt a unique morphology with thin constrictions (often <100nm in diameter; arrow in **Fig. S1E**) and bulging of the matrix (arrowheads in **Fig. S1E**). This unique ultrastructural feature is seen much less frequently in mitochondria found in SLM which presents a more uniformly tubular morphology (see multiple examples in **Fig. S1H**). This morphological difference results in a significant reduction in the volume of dendrite occupied by mitochondria in SR compared to SLM (**Fig. S1I**).

Overall, our light and electron microscopy approaches converge to show that mitochondrial morphology differs significantly in specific dendritic compartments of CA1 PNs *in vivo* with highly elongated and tubular morphology in SLM and progressively more fragmented matrix compartments in SR and SO.

3.4.2 Compartment-specific dendritic mitochondria morphology is present early in the development of CA1 PNs *in vivo* but is absent *in vitro*

To determine the developmental timeframe for the appearance of compartmentalized mitochondria morphology described above in adult CA1 PNs *in vivo,* we collected *in utero* electroporated brains at postnatal days seven, ten, fourteen and twenty-one (P7, P10, P14 and P21). At all stages of development, we observed that mitochondria are significantly shorter in the basal dendrites located in SO than in the apical tuft dendrites located in SLM (**Fig. S2A**). Interestingly, while this compartment-specific mitochondrial morphology is clearly present at each developmental timepoint, mitochondria increase in both size (**Fig. S2B**) and dendritic occupancy (**Fig. S2C**) in both domains throughout maturation and reach adult-like values by P21.

To determine whether compartmentalized mitochondrial morphology characterizing CA1 PNs *in vivo* is regulated by cues intrinsic to the dendrites or cues extrinsic to the cell, we performed IUE to label mitochondria of CA1 PNs at E15.5 as above but at E18.5, the hippocampi of electroporated embryos were collected, enzymatically dissociated, and maintained in 2-dimensional (2D) cultures *in vitro* (**Fig. S3A-B**). Following culture for ten, fourteen or eighteen days *in vitro* (DIV10, 14, 18), we observed either no significant difference in mitochondrial length or occupancy (10, 18DIV), or opposite results to those found *in vivo*: mitochondria were slightly but significantly longer with higher occupancy values in the proximal dendrites compared to distal dendrites (14DIV) (**Fig. S3C-D**). These results suggest that factors extrinsic to the cell, including local activity patterns, might drive the formation of the compartment specific mitochondrial morphology observed *in vivo*.

3.4.3 Neuronal activity and domain-specific synaptic inputs regulate the formation of compartmentalized mitochondrial morphology of CA1 PNs *in vivo*

Previous results obtained *in vitro* suggest that synaptic activity induces local Drp1-dependent mitochondrial fission events in the context of synaptic plasticity induction [12]. To test if the compartmentalized morphology of dendritic mitochondria observed in CA1 PNs *in vivo* is regulated by neuronal activity, we first performed IUE to express the inward rectifying potassium channel 2.1 (Kir2.1) which hyperpolarizes neurons to

Figure 2

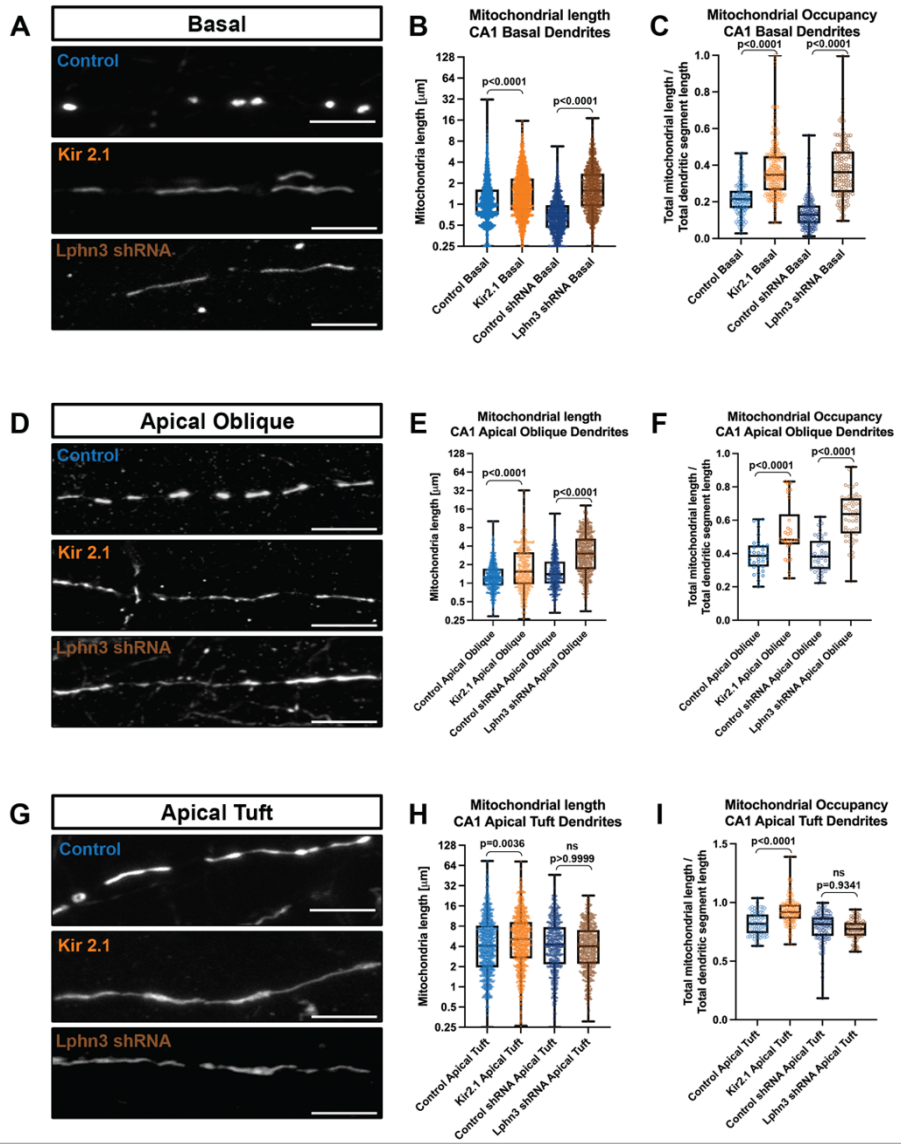

Figure 3.2. Neuronal activity regulates mitochondrial size in a compartment specific manner in CA1 pyramidal neurons *in vivo*. (**A-I**) High magnification representative images of mitochondrial morphology within isolated secondary or tertiary hippocampal CA1 (**A**) basal, (**D**) apical oblique, and (**G**) apical tuft dendrites in which a mitochondrial matrix-targeted fluorescent protein (mt-YFP) was IUE along with either a control plasmid (pCAG tdTomato) or pCAG Kir2.1-T2A-tdTomato), or either control shRNA or Lphn3 shRNA plasmid. Quantification of mitochondrial length and occupancy in the (**B-C**) basal, (**E-F**) apical oblique, and (**H-I**) apical tuft dendritic compartments following Kir2.1 over-expression or shRNA-mediated knockdown of Lphn3. Quantification of mitochondrial length (**B**, **E,** and **H**) and mitochondrial occupancy (**C**, **F** and **I**) in basal dendrites (**B-C**), apical oblique (**E-F**) and apical tuft (**H-I**) demonstrates that both Kir2.1 over-expression and Lphn3 knockdown significantly increases mitochondrial length and occupancy in basal (**B-C**) and apical oblique dendrites (**E-F**). $Control_{tdTomato\text{-}basal}$ = 127 segments, 2154 mitochondria, mean length = 1.42µm ± 0.03µm (SEM), mean occupancy = 21.8% ± 0.9% (SEM); $Control_{tdTomato\text{-}apical\ oblique}$ = 34 segments, 748 mitochondria, mean length = 1.49µm ± 0.04µm, mean occupancy = 39.4% ± 1.0%; $Control_{tdTomato\text{-}apical\ tuft}$ = 75 segments, 1036 mitochondria, mean length = 6.48µm ± 0.23µm, mean occupancy = 81.9% ± 1.1%; $Kir2.1_{tdTomato\text{-}basal}$ = 206 segments, 2278 mitochondria, mean length = 1.87µm ± 0.03µm, mean occupancy = 37.8% ± 1.0%; $Kir2.1_{tdTomato\text{-}apical\ oblique}$ = 30 segments, 435 mitochondria, mean length = 2.54µm ± 0.14µm, mean occupancy = 53.5% ± 2.9%; $Kir2.1_{tdTomato\text{-}apical\ tuft}$ = 128 segments, 965 mitochondria, mean length = 7.19µm ± 0.22µm, mean occupancy = 92.7% ± 1.0%; $Control_{shRNA\text{-}basal}$ = 169 segments, 1344 mitochondria, mean length = 0.81µm ± 0.01µm, mean occupancy = 13.8% ± 0.6%; $Control_{shRNA\text{-}apical\ oblique}$ = 45 segments, 633 mitochondria, mean length = 1.84µm ± 0.05µm, mean occupancy = 39% ± 1.6%; $Control_{shRNA\text{-}apical\ tuft}$ = 106 segments, 617 mitochondria, mean length = 5.81µm ± 0.20µm, mean occupancy = 78.6% ± 1.2%; $Lphn3_{shRNA\text{-}basal}$ = 129 segments, 1169 mitochondria, mean length = 2.11µm ± 0.04µm, mean occupancy = 37.4% ± 1.3%; $Lphn3_{shRNA\text{-}apical\ oblique}$ = 53 segments, 573 mitochondria, mean length = 3.92µm ± 0.12µm, mean occupancy = 62.5% ± 1.9%; $Lphn3_{shRNA\text{-}apical\ tuft}$ = 84 segments, 561 mitochondria, mean length = 5.1µm ± 0.16µm, mean occupancy = 75.2% ± 0.9%. p values are indicated in the figure a following Kruskal-Wallis tests. Data are shown as individual points on box plots with 25th, 50th and 75th percentiles indicated with whiskers indicating min and max values. Scale bar, 5 µm.

~-90mV and drastically reduces their excitability and ability to fire action potentials [29,30]. Strikingly, Kir2.1 overexpression in CA1 PNs *in vivo* through development strongly reduced the compartment-specific differences in mitochondria morphology. Dendritic mitochondria in Kir2.1 expressing CA1 PNs became significantly longer and occupied a higher percentage of the dendrites in SO (basal dendrites, **Fig. 2A-C**), SR (apical obliques, **Fig. 2D-F**), and SLM (apical tufts, **Fig. 2G-I**) compared to control. This result demonstrates that neuronal activity is required for the proper maturation of compartmentalized morphology of dendritic mitochondria in CA1 PNs *in vivo*.

We next perturbed the synaptic inputs received by CA1 PNs in compartment-specific manner by downregulating Latrophilin 3 (Lphn3, **Fig. S4**), a postsynaptic adhesion molecule recently shown to be required for the ability of CA3 axons to form ~50% of synapses onto dendrites of CA1 PNs specifically in the SO and SR compartments, but not for synapses made by EC axons in SLM [31]. This synapse-specific manipulation results in a reduction by ~50% of miniature excitatory potential synaptic currents (mEPSC) in CA1 PNs [31]. We confirmed that shRNA-mediated knockdown of Lhpn3 (**Fig. S4A-B**) by IUE of CA1 PNs leads to ~40% reduction in spine density in SO but not in SLM (**Fig. S4C-D**).

Interestingly, this reduction of presynaptic input mediated by Lphn3 knockdown in CA1 PNs led to a striking and significant increase in mitochondria size and occupancy in dendritic compartments receiving CA3 inputs (SO and SR; **Fig. 2A-F**), while mitochondria morphology in the apical tuft (SLM) of the same CA1 PNs were unaffected (**Fig. 2G-I**). These results show that (1) local synaptic activity is a major regulator of mitochondria morphology in dendrites of CA1 PNs and (2) suggests that an activity-dependent signaling mechanism promotes the small mitochondria morphology in SO and SR *in vivo,* potentially by promoting mitochondria fission and/or inhibiting mitochondria fusion in basal and apical dendrites but not in the apical tuft.

3.4.4 Compartmentalized mitochondrial morphology in CA1 PNs requires CAMKK2 and AMPK *in vivo*

We and others previously showed that the kinase dyad CAMKK2 and AMPK are regulated by neuronal activity since both neuronal depolarization, activation of VGCCs by depolarization, or activation of NMDA receptors can activate AMPK in a CAMKK2-dependent manner in cortical and hippocampal neurons [24,32].

Figure 3

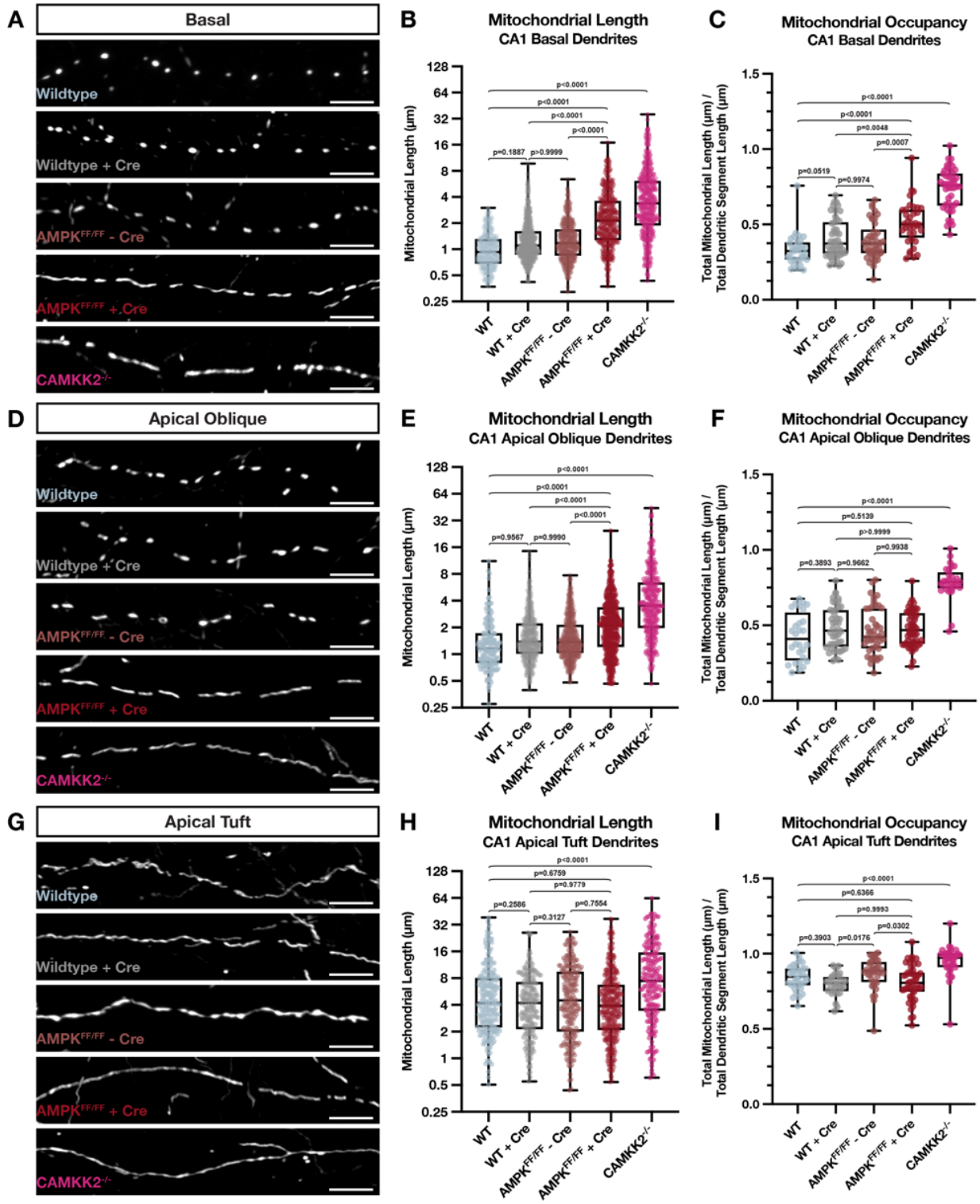
A
Basal
Wildtype
Wildtype + Cre
AMPK^FF/FF - Cre
AMPK^FF/FF + Cre
CAMKK2^-/-
B
Mitochondrial Length
CA1 Basal Dendrites
Mitochondrial Length (µm)
p<0.0001
p<0.0001
p<0.0001
p<0.0001
p=0.1887
p>0.9999
C
Mitochondrial Occupancy
CA1 Basal Dendrites
Total Mitochondrial Length (µm) / Total Dendritic Segment Length (µm)
p<0.0001
p<0.0001
p=0.0048
p=0.0007
p=0.0519
p=0.9974
D
Apical Oblique
E
Mitochondrial Length
CA1 Apical Oblique Dendrites
p=0.9567
p=0.9990
F
Mitochondrial Occupancy
CA1 Apical Oblique Dendrites
p<0.0001
p=0.5139
p>0.9999
p=0.9938
p=0.3893
p=0.9662
G
Apical Tuft
H
Mitochondrial Length
CA1 Apical Tuft Dendrites
p<0.0001
p=0.6759
p=0.9779
p=0.2586
p=0.3127
p=0.7554
I
Mitochondrial Occupancy
CA1 Apical Tuft Dendrites
p<0.0001
p=0.6366
p=0.9993
p=0.3903
p=0.0176
p=0.0302
WT
WT + Cre
AMPK^FF/FF - Cre
AMPK^FF/FF + Cre
CAMKK2^-/-

Figure 3 Cont…

Figure 3.3. CAMKK2 and AMPK are required for the compartment-specific mitochondrial morphology in CA1 PNs *in vivo*. (**A-I**) High magnification representative images of mitochondrial morphology within isolated secondary or tertiary hippocampal CA1 (**A**) basal, (**D**) apical oblique, and (**G**) apical tuft dendrites in which a mitochondrial matrix-targeted fluorescent protein (mt-YFP or mt-DsRed) and cell fill (tdTomato or mGreenLantern—not pictured) were co-expressed by IUE with or without Cre recombinase (+/-Cre). AMPKα1$^{F/F}$α2$^{F/F}$ double conditional mice were *in utero* electroporated with the same mitochondrial markers/cell fills and either no Cre (AMPK$^{FF/FF}$ - Cre) or Cre (AMPK$^{FF/FF}$ + Cre). CAMKK2$^{-/-}$ constitutive knock-out mice were electroporated with the same mitochondrial markers/cell fills as above (CAMKK2$^{-/-}$). Quantification of mitochondrial length and occupancy in the (**B-C**) basal, (**E-F**) apical oblique, and (**H-I**) apical tuft dendritic compartments reveals a significant increase in mitochondrial length (**B**) and occupancy (**C**) in basal dendrites when knocking out AMPK or CAMKK2 when compared to their controls, with CAMKK2 KO having a much bigger effect (WT: n = 32 dendritic segments, 313 individual mitochondria, mean length = 1.065 µm ± 0.029 (SEM), mean occupancy = 33.01% ± 1.84%; WT + Cre: n = 46 dendritic segments, 627 individual mitochondria, mean length = 1.437 µm ± 0.040 (SEM), mean occupancy = 40.95% ± 1.94%; AMPK$^{FF/FF}$ - Cre: n = 42 dendritic segments, 463 individual mitochondria, mean length = 1.418 µm ± 0.039 (SEM), mean occupancy = 39.24% ± 1.89%; AMPK$^{FF/FF}$ + Cre: n = 36 dendritic segments, 381 individual mitochondria, mean length = 2.832 µm ± 0.116 (SEM), mean occupancy = 50.72% ± 2.36%, length increase = 97.08%, occupancy increase = 23.86%; CAMKK2$^{-/-}$: n = 46 dendritic segments, 449 individual mitochondria, mean length = 4.975 µm ± 0.233 (SEM), mean occupancy = 73.36% ± 2.03%, length increase = 367%, occupancy increase = 122%). A significant increase in mitochondrial length (**E**) and occupancy (**F**) is also seen in apical oblique dendrites when knocking out CAMKK2, but only an increase in length is seen when knocking out AMPK. (WT: n = 28 dendritic segments, 184 individual mitochondria, mean length = 1.569 µm ± 0.104 (SEM), mean occupancy = 42.38% ± 2.98%; WT + Cre: n = 44 dendritic segments, 525 individual mitochondria, mean length = 1.791 µm ± 0.052 (SEM), mean occupancy = 48.50% ± 2.12%; AMPK$^{FF/FF}$ - Cre: n = 45 dendritic segments, 440 individual mitochondria, mean length = 1.885 µm ± 0.075 (SEM), mean occupancy = 45.82% ± 2.29%; AMPK$^{FF/FF}$ + Cre: n = 52 dendritic segments, 499 individual mitochondria, mean length = 2.645 µm ± 0.098 (SEM), mean occupancy = 47.79% ± 1.62%, length increase = 47.68%; CAMKK2$^{-/-}$: n = 29 dendritic segments, 288 individual mitochondria, mean length = 5.366 µm ± 0.346 (SEM), mean occupancy = 78.64% ± 2.07%, length increase = 242%, occupancy increase = 85.56%). Note that in CAMKK2-null CA1 PNs we observe a significant increase in mitochondrial length (**H**) and occupancy (**I**) in the apical tuft compared to WT controls (WT: n = 33 dendritic segments, 226 individual mitochondria, mean length = 6.562 µm ± 0.437 (SEM), mean occupancy = 84.19% ± 1.44%; WT + Cre: n = 29 dendritic segments, 189 individual mitochondria, mean length = 5.206 µm ± 0.052 (SEM), mean occupancy = 79.40% ± 1.38%; AMPK$^{FF/FF}$ - Cre: n = 38 dendritic segments, 229 individual mitochondria, mean length = 6.498 µm ± 0.368 (SEM), mean occupancy = 87.00% ± 1.67%; AMPK$^{FF/FF}$ + Cre: n = 47 dendritic segments, 370 individual mitochondria, mean length = 5.723 µm ± 0.300 (SEM), mean occupancy = 80.65% ± 1.71%; CAMKK2$^{-/-}$: n = 35 dendritic segments, 199 individual mitochondria, mean length = 11.14 µm ± 0.758 (SEM), mean occupancy = 95.03% ± 1.73%, length increase = 69.77%, occupancy increase = 12.88%). Scale bar, 5 µm.

Furthermore, we also demonstrated that CAMKK2-dependent AMPK over-activation mediates excessive mitochondrial fission through direct phosphorylation of MFF in apical dendrites of CA1 PNs [11,23]. Therefore, we hypothesized that synaptic activity could regulate mitochondrial compartmentalization in a CAMKK2-AMPK-dependent manner whereby low CAMKK2-AMPK activity in apical tufts of CA1 PNs leads to fusion-dominant mitochondrial elongation in SLM and higher activity in basal and apical oblique dendrites leads to fission-dominant smaller mitochondrial morphology in SO and SR.

To test this in CA1 PNs *in vivo*, we performed CA1-targeted IUE in a constitutive *CAMKK2* knockout mouse, as well as in a conditional *AMPK*α*1*$^{F/F}$α*2*$^{F/F}$ mouse (AMPK cDKO) and measured mitochondrial length and occupancy using a mitochondrial matrix-targeted fluorescent protein (mt-YFP, mt-DsRed) (**Fig. 3**). By electroporating Cre recombinase with a Cre-dependent reporter (FLEX-tdTomato, FLEX-mGreenLantern) in the AMPK cDKO, we could delete AMPK only from a subset of CA1 PNs. Using these approaches, we found that AMPK-null CA1 PNs display significantly increased mitochondria length and occupancy in basal (SO, **Fig. 3A-C**) and apical oblique (SR, **Fig. 3D-F**), but not in the apical tuft (SLM, **Fig. 3G-I**) dendritic compartments. Similarly, CAMKK2-null CA1 PNs show a remarkably similar increase in mitochondrial size and occupancy in both SO and SR dendritic compartments (**Fig. 3A-F**). One interesting difference is that CAMKK2-null CA1 PNs display a small but significant increase in mitochondria size and occupancy in the apical tuft compartment (SLM) not observed in the AMPK-null CA1 PNs. These results overall demonstrate that CAMKK2 and AMPK are both required for the compartmentalized morphology of dendritic mitochondria observed *in vivo* and are specifically required for the small mitochondria size and dendritic occupancy in SO and SR dendritic compartments of CA1 PNs *in vivo*.

3.4.5 Compartmentalized mitochondrial morphology in CA1 PNs requires MTFR1L-dependent inhibition of Opa1

Previous results identified two direct effectors phosphorylated by AMPK mediating mitochondrial fission: the Drp1-receptor MFF [23] and the anti-fusion, Opa1-inhibiting protein Mitochondrial Fission Regulator 1-Like (MTFR1L)[33]. We performed CA1-targeted IUE with cytoplasmic fluorescent proteins (tdTomato, mGreenLantern) and mitochondrial matrix-targeted fluorescent proteins (mt-YFP, mt-DsRed) in combination with either a control, non-targeting shRNA (shNT) or an shRNA targeting *MTFR1L* (**Fig. 4**). The shRNA selected to knockdown MTFR1L is validated in **Fig. S5A-B**. We found that knocking down

Figure 4

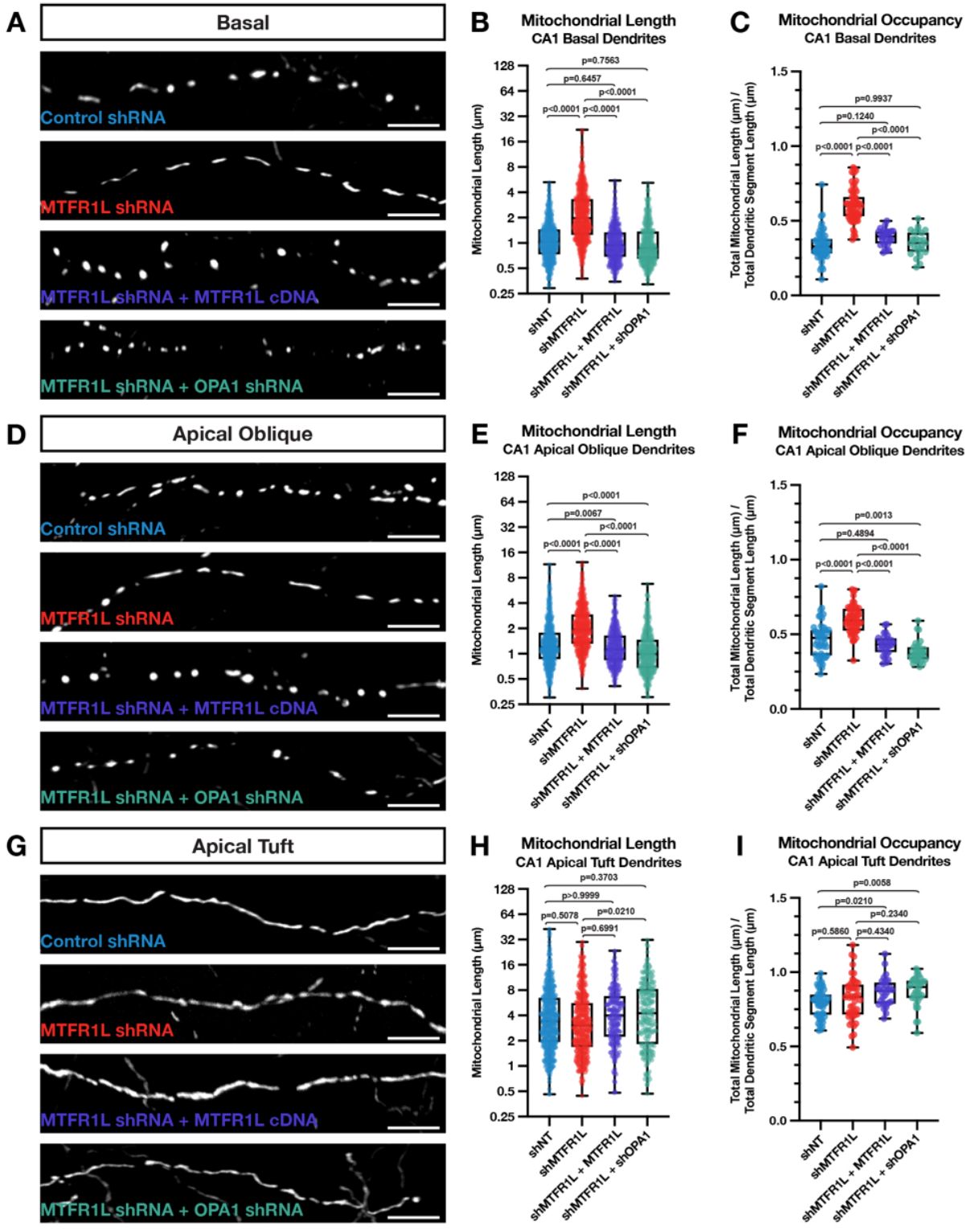
A
Basal
Control shRNA
MTFR1L shRNA
MTFR1L shRNA + MTFR1L cDNA
MTFR1L shRNA + OPA1 shRNA
B
Mitochondrial Length
CA1 Basal Dendrites
Mitochondrial Length (µm)
p=0.7563
p=0.6457
p<0.0001
p<0.0001
p<0.0001
C
Mitochondrial Occupancy
CA1 Basal Dendrites
Total Mitochondrial Length (µm) / Total Dendritic Segment Length (µm)
p=0.9937
p=0.1240
p<0.0001
p<0.0001
p<0.0001
shNT
shMTFR1L
shMTFR1L + MTFR1L
shMTFR1L + shOPA1
D
Apical Oblique
Control shRNA
MTFR1L shRNA
MTFR1L shRNA + MTFR1L cDNA
MTFR1L shRNA + OPA1 shRNA
E
Mitochondrial Length
CA1 Apical Oblique Dendrites
Mitochondrial Length (µm)
p<0.0001
p=0.0067
p<0.0001
p<0.0001
p<0.0001
F
Mitochondrial Occupancy
CA1 Apical Oblique Dendrites
Total Mitochondrial Length (µm) / Total Dendritic Segment Length (µm)
p=0.0013
p=0.4894
p<0.0001
p<0.0001
p<0.0001
G
Apical Tuft
Control shRNA
MTFR1L shRNA
MTFR1L shRNA + MTFR1L cDNA
MTFR1L shRNA + OPA1 shRNA
H
Mitochondrial Length
CA1 Apical Tuft Dendrites
Mitochondrial Length (µm)
p=0.3703
p>0.9999
p=0.5078
p=0.0210
p=0.6991
I
Mitochondrial Occupancy
CA1 Apical Tuft Dendrites
Total Mitochondrial Length (µm) / Total Dendritic Segment Length (µm)
p=0.0058
p=0.0210
p=0.2340
p=0.5860
p=0.4340

Figure 4 Cont…

Figure 3.4. MTFR1L restricts hippocampal CA1 PN basal and apical oblique dendritic morphology through inhibition of Opa1
High magnification representative images of mitochondrial morphology within isolated secondary or tertiary hippocampal CA1 **A**) basal, **D**) apical oblique, and **G**) apical tuft dendrites in which a mitochondrial matrix- targeted fluorescent protein (mt-YFP or mt-DsRed) and cell fill (tdTomato or mGreenLantern—not pictured) was *in utero* electroporated along with either a control shRNA (shNT), *MTFR1L* shRNA (shMTFR1L), *MTFR1L* shRNA with full-length hMTFR1L cDNA (shMTFR1L + hMTFR1L), or *MTFR1L* shRNA and *Opa1* shRNA (shMTFR1L + shOpa1). Quantification of mitochondrial length and occupancy in the (**B-C**) basal, (**E-F**) apical oblique, and (**H- I**) apical tuft dendritic compartments reveals a significant increase in mitochondrial length (**B**) and occupancy (**C**) in basal dendrites when knocking down MTFR1L, which is rescued when re-expressing full-length hMTFR1L or knocking down Opa1 (shNT: n = 51 dendritic segments, 670 individual mitochondria, mean length = 1.225 µm ± 0.028 (SEM), mean occupancy = 33.95% ± 1.46%; shMTFR1L: n = 60 dendritic segments, 773 individual mitochondria, mean length = 2.721 µm ± 0.085 (SEM), mean occupancy = 60.36% ± 1.46%, length increase = 122%, occupancy increase = 77.79%; shMTFR1L + hMTFR1L: n = 28 dendritic segments, 511 individual mitochondria, mean length = 1.113 µm ± 0.029 (SEM), mean occupancy = 39.10% ± 1.02%; shMTFR1L + shOpa1: n = 25 dendritic segments, 515 individual mitochondria, mean length = 1.126 µm ± 0.032 (SEM), mean occupancy = 35.08% ± 1.61%). A significant increase in mitochondrial length (**E**) and occupancy (**F**) is also seen in apical dendrites when knocking down MTFR1L, which is similarly rescued when either expressing full-length hMTFR1L or additionally knocking down Opa1 (shNT: n = 48 dendritic segments, 669 individual mitochondria, mean length = 1.584 µm ± 0.059 (SEM), mean occupancy = 46.34% ± 1.72%; shMTFR1L: n = 54 dendritic segments, 683 individual mitochondria, mean length = 2.390 µm ± 0.061 (SEM), mean occupancy = 59.86% ± 1.29%, length increase = 50.88%, occupancy increase = 29.18%; shMTFR1L + hMTFR1L: n = 29 dendritic segments, 490 individual mitochondria, mean length = 1.352 µm ± 0.034 (SEM), mean occupancy = 42.92% ± 1.25%; shMTFR1L + shOpa1: n = 32 dendritic segments, 514 individual mitochondria, mean length = 1.248 µm ± 0.038 (SEM), mean occupancy = 38.28% ± 1.23%). There's no significant effect of knocking down MTFR1L in the apical tuft dendrites in either mitochondrial length (**H**) or occupancy **(I**) compared to control neurons (shNT: n = 53 dendritic segments, 472 individual mitochondria, mean length = 5.177 µm ± 0.250 (SEM), mean occupancy = 79.14% ± 1.29%; shMTFR1L: n = 46 dendritic segments, 388 individual mitochondria, mean length = 4.665 µm ± 0.236 (SEM), mean occupancy = 82.35% ± 2.17%; shMTFR1L + hMTFR1L: n = 30 dendritic segments, 219 individual mitochondria, mean length = 5.186 µm ± 0.280 (SEM), mean occupancy = 86.65% ± 1.75%; shMTFR1L + shOpa1: n = 34 dendritic segments, 215 individual mitochondria, mean length = 5.872 µm ± 0.352 (SEM), mean occupancy = 87.36% ± 1.72%). Scale bar, 5 µm.

MTFR1L in CA1 PNs significantly elongates mitochondria and increases mitochondrial occupancy in the basal (SO; **Fig. 4A-C**) and apical oblique (SR; **Fig. 4D-F**) dendritic compartments, but not in apical tuft (SLM) dendrites (**Fig. 4H**). To confirm the specificity of our *MTFR1L*-targeting shRNA, we co-expressed it together with a shRNA-resistant human cDNA expressing hMTFR1L. We found, as expected, that expression of hMTFR1L is sufficient to rescue mitochondrial length (**Fig. 4B,E**) and occupancy (**Fig. 4C,F**) back to levels observed in SO and SR dendritic compartments of control shRNA expressing CA1 PNs. Recent work demonstrated that MTFR1L exerts its effects on mitochondria size by inhibiting the pro-fusion protein Opa1, and that functionally, MTFR1L represents a novel class of 'anti-fusion' mitochondrial proteins because of its ability to oppose fusion and thereby enable MFF-dependent fission [33]. Based on these previously published results, we hypothesized that the mitochondrial elongation mediated by knocking down MTFR1L should be rescued by simultaneously knocking down Opa1 in CA1 PNs. Therefore, we performed IUEs with shRNAs targeting both *MTFR1L* and *Opa1* (see validation in **Fig. S5E-F**). Knocking down Opa1 completely rescues the effect of knocking down MTFR1L and re-establishes short mitochondria and low occupancy in both basal and apical oblique dendrites to levels observed in control CA1 PNs (**Fig. 4A-F**) No significant effects were observed in dual knockdown of MTFR1L and Opa1 in the apical tuft of the same neurons compared to knockdown of MTFR1L alone or control shRNA expressing neurons (**Fig. 4H,I**). Overall, these results demonstrate that MTFR1L is required for the compartmentalized morphology of mitochondria observed in the basal and apical oblique dendritic domains of CA1 PNs *in vivo* through inhibition of Opa1.

3.4.6 Compartmentalized mitochondrial morphology in CA1 PNs requires MFF

AMPK has also been shown to regulate mitochondrial morphology through direct phosphorylation of the OMM localized Drp1 receptor MFF [19,23]. To test if MFF is required for the compartmentalized morphology of mitochondria in dendrites of CA1 PNs, we repeated the same IUE experiments using an shRNA targeting *MFF* (shMFF) previously characterized [7], and validated the shRNA efficiently knocks down all isoforms of MFF (**Fig. S5C-D**). Upon knocking down MFF in CA1 PNs using IUE, we observe a significant increase in mitochondrial length and occupancy in all three dendritic compartments (**Fig. 5A-I**). Since knockdown of either MTFR1L or MFF leads to similar phenotypes on mitochondria morphology, especially in basal and apical oblique dendritic domains of CA1 PNs, we tested if these two proteins have redundant or only partially

Figure 5

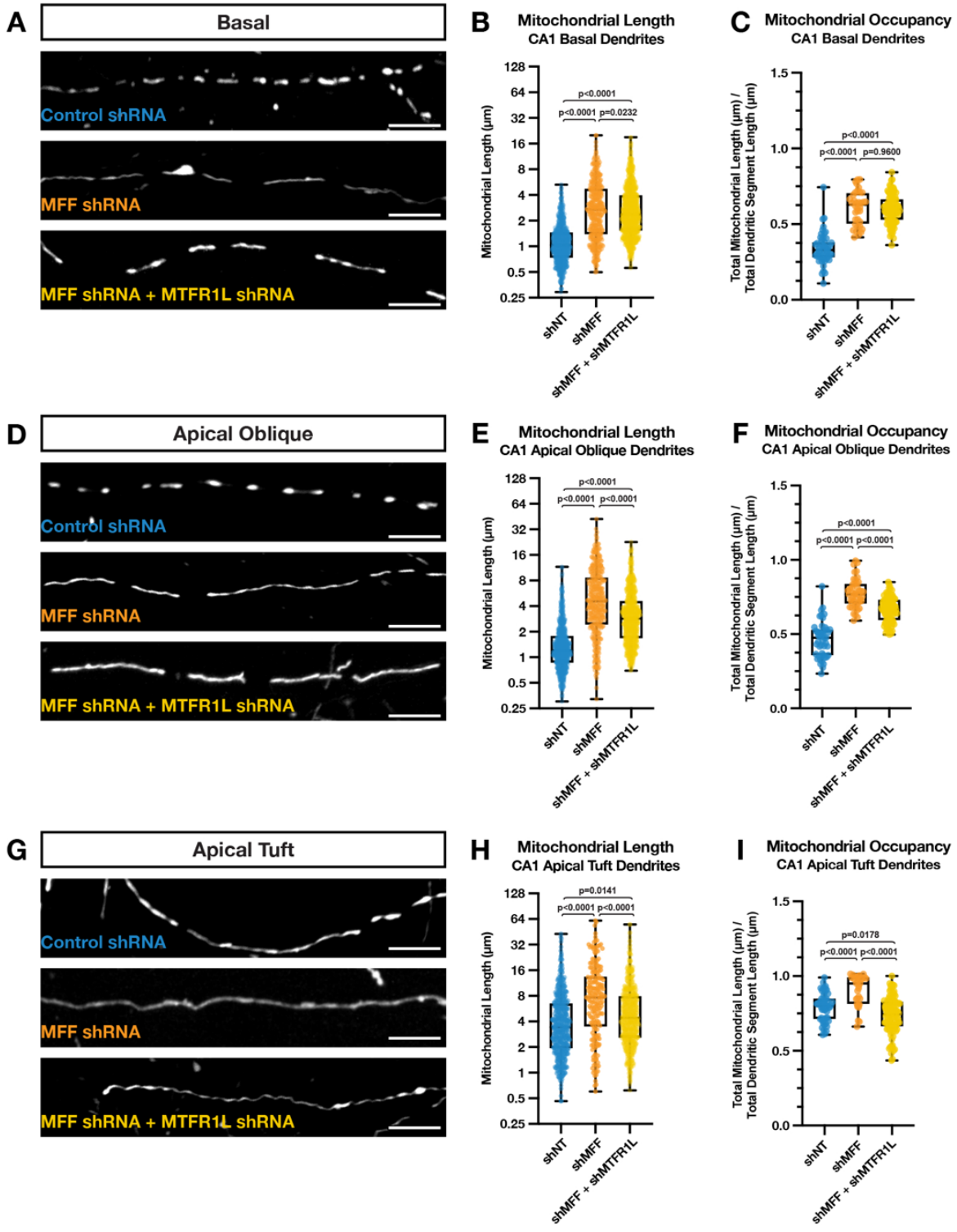
A
Basal
Control shRNA
MFF shRNA
MFF shRNA + MTFR1L shRNA
B
Mitochondrial Length
CA1 Basal Dendrites
Mitochondrial Length (µm)
p<0.0001
p<0.0001 p=0.0232
C
Mitochondrial Occupancy
CA1 Basal Dendrites
Total Mitochondrial Length (µm) / Total Dendritic Segment Length (µm)
p<0.0001
p<0.0001 p=0.9600
D
Apical Oblique
E
Mitochondrial Length
CA1 Apical Oblique Dendrites
p<0.0001
p<0.0001 p<0.0001
F
Mitochondrial Occupancy
CA1 Apical Oblique Dendrites
G
Apical Tuft
H
Mitochondrial Length
CA1 Apical Tuft Dendrites
p=0.0141
p<0.0001 p<0.0001
I
Mitochondrial Occupancy
CA1 Apical Tuft Dendrites
p=0.0178
p<0.0001 p<0.0001
shNT
shMFF
shMFF + shMTFR1L

Figure 5 Cont…

Figure 3.5. MFF restricts hippocampal CA1 PN basal, apical oblique, and apical tuft dendritic morphology
High magnification representative images of mitochondrial morphology within isolated secondary or tertiary hippocampal CA1 **A**) basal, **D**) apical oblique, and **G**) apical tuft dendrites in which a mitochondrial matrix- targeted fluorescent protein (mt-YFP or mt-DsRed) and cell fill (tdTomato or mGreenLantern—not pictured) was *in utero* electroporated along with either a control shRNA (shNT), *MFF* shRNA (shMFF), or *MFF* and *MTFR1L* shRNA (shMFF + shMTFR1L). Quantification of mitochondrial length and occupancy in the (**B-C**) basal, (**E-F**) apical oblique, and (**H-I**) apical tuft dendritic compartments reveals a significant increase in mitochondrial length (**B**) and occupancy (**C**) in basal dendrites when knocking down MFF, which does not show an additive effect when also knocking down MTFR1L (shNT: n = 51 dendritic segments, 670 individual mitochondria, mean length = 1.225 µm ± 0.028 (SEM), mean occupancy = 33.95% ± 1.46%; shMFF: n = 36 dendritic segments, 380 individual mitochondria, mean length = 3.530 µm ± 0.152 (SEM), mean occupancy = 60.83% ± 1.86%, length increase = 188%, occupancy increase = 79.18%; shMFF + shMTFR1L: n = 92 dendritic segments, 1004 individual mitochondria, mean length = 3.180 µm ± 0.078 (SEM), mean occupancy = 59.94% ± 0.99%, length increase = 160%, occupancy increase = 76.55%). A significant increase in mitochondrial length (**E**) and occupancy (**F**) is also seen in apical dendrites when knocking down MFF, but to a significantly less degree when knocking down both MFF and MTFR1L (shNT: n = 48 dendritic segments, 669 individual mitochondria, mean length = 1.584 µm ± 0.059 (SEM), mean occupancy = 46.34% ± 1.72%; shMFF: n = 44 dendritic segments, 371 individual mitochondria, mean length = 6.445 µm ± 0.300 (SEM), mean occupancy = 77.34% ± 1.46%, length increase = 307%, occupancy increase = 66.90%; shMFF + shMTFR1L: n = 85 dendritic segments, 829 individual mitochondria, mean length = 3.728 µm ± 0.106 (SEM), mean occupancy = 66.63% ± 0.93%, length increase = 135%, occupancy increase = 43.79%). While there is a significant increase mitochondrial length (**H**) and occupancy (**I**) in the apical tuft when knocking down MFF alone, this increase largely goes away when knocking down both MFF and MTFR1L (shNT: n = 53 dendritic segments, 472 individual mitochondria, mean length = 5.177 µm ± 0.250 (SEM), mean occupancy = 79.14% ± 1.29%; shMFF: n = 31 dendritic segments, 199 individual mitochondria, mean length = 10.78 µm ± 0.757 (SEM), mean occupancy = 90.44% ± 1.86%, length increase = 109%, occupancy increase = 14.28%; shMFF + shMTFR1L: n = 95 dendritic segments, 708 individual mitochondria, mean length = 6.326 µm ± 0.236 (SEM), mean occupancy = 73.79% ± 1.27%, length increase = 22.19%). Scale bar, 5 µm.

overlapping functions in regulating dendritic mitochondrial morphology in these neurons. Interestingly, we found that knocking down both MTFR1L and MFF does not lead to additive effects compared to knocking down MFF or MTFR1L separately (**Fig. 5A-F**), strongly arguing that they play redundant functions or that they regulate their mutual abundance at OMM. In fact, we discovered that knockdown of either MFF or MTFR1L significantly decreased protein abundance of the other; however, knockdown of MFF had a stronger impact on MTFR1L expression (**Fig. S5G-H**). These results explain the observations that MFF knockdown has a greater effect on mitochondrial compartmentalization *in vivo*, and that no synergistic effect was seen upon simultaneous knockdown of both MFF and MTFR1L.

3.4.7 CAMKK2 regulates compartmentalization of dendritic mitochondria in CA1 PNs through AMPK-dependent MTFR1L phosphorylation

We next tested whether the kinase dyad CAMKK2-AMPK regulates the compartment-specific morphology of mitochondria in CA1 PNs through phosphorylation of MTFR1L. We used two experimental approaches to test this. First, we performed biochemical analysis in mouse hippocampal neurons *in vitro* to test if MTFR1L phosphorylation by AMPK is regulated by neuronal activity, and, whether activity-dependent regulation of MTFR1L phosphorylation is CAMKK2-dependent. To this end, we treated hippocampal neurons maintained in dissociated cultures for 3 weeks to a high potassium chloride (KCl) concentration (switch from 5 to 40mM) for a short time period (15min) to induce strong membrane depolarization and effectively open VGCCs leading to increased intracellular Ca^{2+} in hippocampal neurons [34]. As shown previously [24,32], western blot analysis revealed that neuronal depolarization induces increased AMPK phosphorylation on T172 in a CAMKK2- dependent manner since it was blocked by a CAMKK2-specific inhibitor STO609 [24,32] (**Fig. 6A**). In the same lysates, KCl-mediated neuronal depolarization induced a significant increase in MTFR1L phosphorylation on S103, one of the two serine residues phosphorylated by AMPK [33] that was also blocked by STO609 (**Fig. 6A**). These results demonstrate that, in hippocampal neurons, MTFR1L is phosphorylated by AMPK in an activity- and CAMKK2-dependent manner.

Next, we tested whether CAMKK2-dependent MTFR1L phosphorylation by AMPK required for the compartmentalized mitochondrial morphology characterizing CA1 PNs *in vivo*. Previous work demonstrated that AMPK phosphorylates two conserved serine residues on MTFR1L (positions S103 and S238), and that a phosphomimetic form of $MTFR1L^{S103D/238D}$ (hereafter referred to as $MTFR1L^{S2D}$) is sufficient to rescue

Figure 6

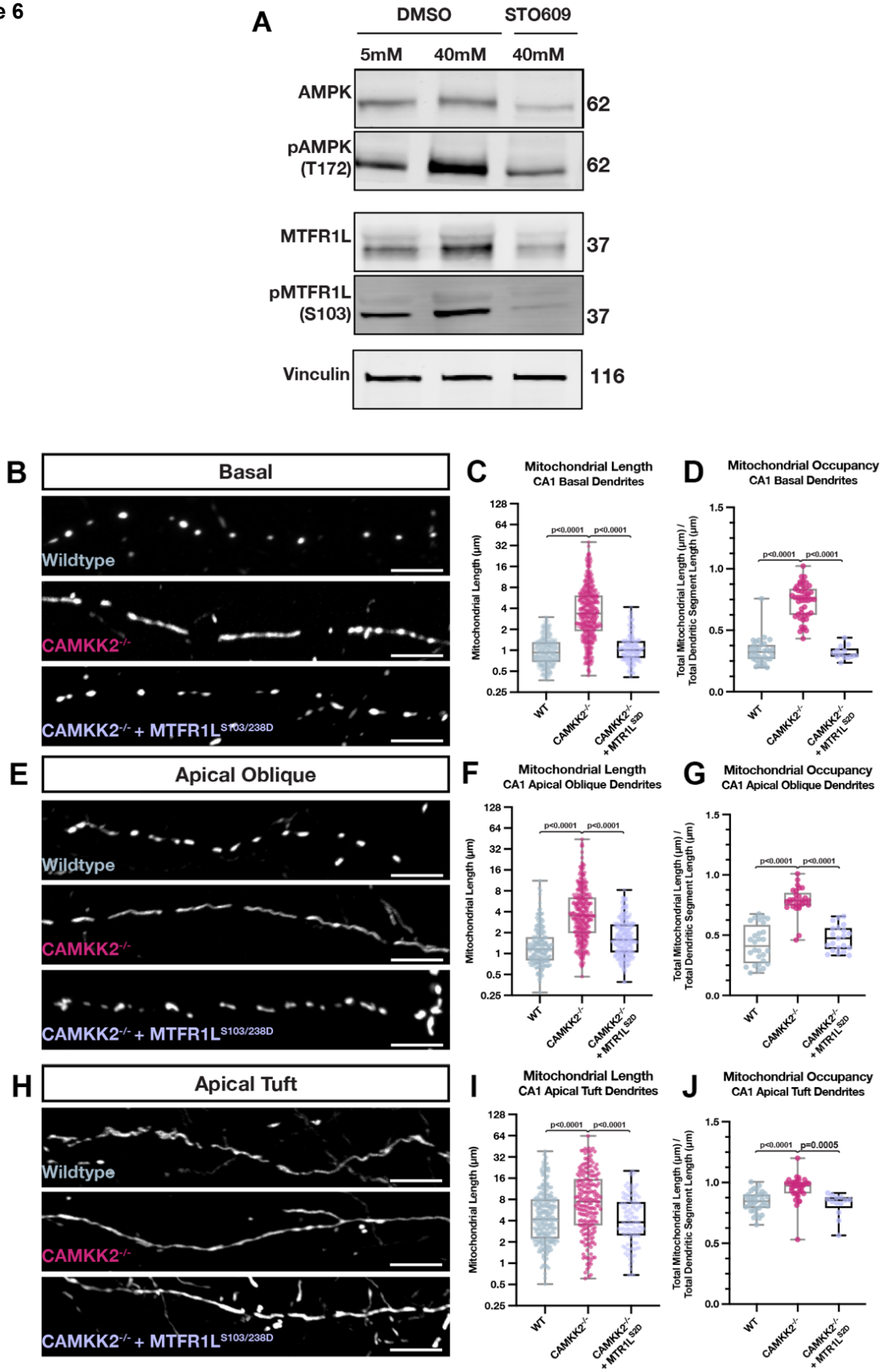
A
DMSO
STO609
5mM
40mM
40mM
AMPK
62
pAMPK (T172)
62
MTFR1L
37
pMTFR1L (S103)
37
Vinculin
116
B
Basal
Wildtype
CAMKK2-/-
CAMKK2-/- + MTFR1LS103/238D
C
Mitochondrial Length
CA1 Basal Dendrites
Mitochondrial Length (µm)
p<0.0001
p<0.0001
WT
CAMKK2-/-
CAMKK2-/- + MTR1LS2D
D
Mitochondrial Occupancy
CA1 Basal Dendrites
Total Mitochondrial Length (µm) / Total Dendritic Segment Length (µm)
E
Apical Oblique
F
Mitochondrial Length
CA1 Apical Oblique Dendrites
G
Mitochondrial Occupancy
CA1 Apical Oblique Dendrites
H
Apical Tuft
I
Mitochondrial Length
CA1 Apical Tuft Dendrites
J
Mitochondrial Occupancy
CA1 Apical Tuft Dendrites
p=0.0005

Figure 6 Cont…

Figure 3.6. Activity-dependent and CAMKK2-dependent phosphorylation of MTFR1L by AMPK mediates compartmentalized mitochondria morphology in dendrites of CA1 PNs *in vivo*.
(**A**) Western blots of whole cell lysates from mouse hippocampal neurons maintained in culture for 18- 21DIV and treated for 5 min with physiological (5mM) extracellular potassium chloride (KCl) (first column) or high KCl (40mM) inducing membrane depolarization (columns 2 & 3) in the presence (column 3) or absence (columns 1&2) of the CAMKK2 inhibitor STO609. These results demonstrate that phosphorylation of AMPKα catalytic subunit on T172 is increased by neuronal depolarization which is blocked by STO609. In turn, AMPK phosphorylation of its substrate MTFR1L on S103 [33] is increased by depolarization which is CAMKK2- dependent since it is blocked by STO609. (**B-J**) Rescue experiments showing that phosphomimetic form of MTFR1L (MTFR1L^{S2D}) mimicking phosphorylation by AMPK [33] is sufficient to rescue compartmentalized mitochondria morphology in basal (B-D), apical oblique (**E-G**) and apical tufts (**H-J**) dendrites of CA1 PNs *in vivo*. CA1 PNs from wild-type (WT) or *CAMKK2*$^{-/-}$ constitutive knockout mice were IUE with the same mitochondrial markers/cell fills as in Figure 3 (WT and CAMKK2$^{-/-}$) and a plasmid cDNA expressing phosphomimetic mutant on the two serine residues phosphorylated by AMPK (S103D and S238D) of MTFR1L (MTFR1L^{S2D}) [33]. Data and quantifications from WT and CAMKK2$^{-/-}$ are the same as in Figure 3. Basal Dendrites (WT: n = 32 dendritic segments, 313 individual mitochondria, mean length = 1.065 µm ± 0.029 (SEM), mean occupancy = 33.01% ± 1.84%; CAMKK2$^{-/-}$: n = 46 dendritic segments, 449 individual mitochondria, mean length = 4.975 µm ± 0.233 (SEM), mean occupancy = 73.36% ± 2.03%, length increase = 367%, occupancy increase = 122%; CAMKK2$^{-/-}$ + MTFR1L^{S2D}: n = 13 dendritic segments, 171 individual mitochondria, mean length = 1.187 µm ± 0.051 (SEM), mean occupancy = 31.89% ± 1.49%) Apical Oblique Dendrites (WT: n = 28 dendritic segments, 184 individual mitochondria, mean length = 1.569 µm ± 0.104 (SEM), mean occupancy = 42.38% ± 2.98%; CAMKK2$^{-/-}$: n = 29 dendritic segments, 288 individual mitochondria, mean length = 5.366 µm ± 0.346 (SEM), mean occupancy = 78.64% ± 2.07%, length increase = 242%, occupancy increase = 85.56%; CAMKK2$^{-/-}$ + MTFR1L^{S2D}: n = 21 dendritic segments, 223 individual mitochondria, mean length = 2.030 µm ± 0.092 (SEM), mean occupancy = 47.45% ± 2.28%) Apical Tuft Dendrites (WT: n = 33 dendritic segments, 226 individual mitochondria, mean length = 6.562 µm ± 0.437 (SEM), mean occupancy = 84.19% ± 1.44%; CAMKK2$^{-/-}$: n = 35 dendritic segments, 199 individual mitochondria, mean length = 11.14 µm ± 0.758 (SEM), mean occupancy = 95.03% ± 1.73%, length increase = 69.77%, occupancy increase = 12.88%; CAMKK2$^{-/-}$ + MTFR1L^{S2D}: n = 13 dendritic segments, 110 individual mitochondria, mean length = 5.419 µm ± 0.402 (SEM), mean occupancy = 81.83% ± 2.71%). Scale bar, 5 µm.

mitochondria morphology in AMPK-null cells [33]. Therefore, we reasoned that if CAMKK2 regulates the dendritic compartmentalization of mitochondrial morphology in CA1 PNs by AMPK-dependent phosphorylation of MTFR1L, expression of phosphomimetic MTFR1L^{S2D} should rescue the mitochondrial morphology defects observed in CAMKK2-null CA1 PNs *in vivo*. Indeed, we found that expression of MTFR1L^{S2D} in CAMKK2-null CA1 PNs rescues the morphology of dendritic mitochondria both in SR and SO compartments back to levels observed in wild-type mice (**Fig. 6B-J**).

3.5 Discussion

In this study, we identified novel molecular and cellular effectors that enable synaptic activity to shape the compartment-specific morphology of mitochondria in neuronal dendrites. In the apical tufts (SLM) of CA1 pyramidal neurons, mitochondria are elongated, tubular, and fill a high fraction of the dendritic volume; in contrast, the mitochondria found in more proximal dendritic compartments are short and occupy a significantly smaller fraction of dendritic volume. This striking compartmentalization of mitochondria morphology corresponds to dendritic domains receiving different presynaptic inputs, from the entorhinal cortex in SLM and from CA2/3 in SR and SO. Collectively, our results (summarized in **Fig. 7**) demonstrate that the mitochondrial morphology observed in the SR and SO dendritic compartments is shaped by synaptic activity via CAMKK2- dependent AMPK phosphorylation of the pro-fission Drp1 receptor MFF [11,23] and phosphorylation of the anti- fusion MTFR1L [33], a protein antagonizing Opa1.

The most parsimonious interpretation of our results is that mitochondrial fusion is dominant in dendrites, and constitutes the 'default', as the elongated mitochondria morphology observed in the apical tufts (SLM) of CA1 PNs is present across the entire dendritic arbor in the absence of or under low levels of synaptic activity (**Fig. 7**). In support of this concept, experimentally reducing neuronal activity through expression of Kir2.1 or cell- autonomously reducing by ~50% the number of CA3 inputs received by individual CA1 PNs (**Fig. 2**), is sufficient to induce tubular and fused mitochondria morphology in the SO and SR dendritic compartments *in vivo* (**Fig. 2**). Therefore, our data suggests that presynaptic activity and cytoplasmic Ca^{2+} dynamics in basal and apical oblique dendrites of CA1 PNs drives the CAMKK2 dependent pathway to trigger high levels of AMPK kinase activity and phosphorylation of the anti-fusion effector MTFR1L (**Fig. 4;** [33]) and pro-fission MFF (**Fig. 5;** [11,23]). In the apical tuft, we hypothesize that lower levels of synaptic activity and/or lower levels of cytoplasmic Ca^{2+} levels due to lower amplitude and/or

frequency of Ca^{2+} transients than in SO/SR compartments leads to low levels of CAMKK2/AMPK activity and therefore low levels of MFF and MTFR1L activity (**Fig. 7B**). Our biochemical and rescue experiments (**Fig. 6**) strongly argue in favor of a model whereby MTFR1L phosphorylation by AMPK is increased by neuronal depolarization (which activates VGCCs and increases intracellular Ca^{2+}; [34]) in a CAMKK2-dependent manner.

What could be the functional consequence of this striking compartmentalized mitochondrial morphology in dendrites of CA1 PNs? As mitochondria buffer a significant fraction of the Ca^{2+} released from the ER in dendrites of CA1 PNs [35], one potential consequence of the reduced mitochondrial volume in SR/SO dendrites would be that mitochondria in these compartments have a reduced capacity to buffer Ca^{2+}, therefore representing a positive-feedback loop allowing more cytoplasmic Ca^{2+} to accumulate in these compartments upon synaptic activity, further increasing CAMKK2/AMPK activity. In the apical tufts of the same neurons, lower synaptic activity (spine density is ~40% lower in SLM than in SO/SR dendrites [28,36]), might trigger lower amplitude/frequency of Ca^{2+} transients and therefore lower levels of CAMKK2/AMPK activity allowing mitochondrial fusion to dominate over MFF-dependent fission.

The novel molecular effectors identified in the present study will enable future investigations of the functional impact of this striking degree of compartmentalization of mitochondrial morphology on dendritic integration properties, synaptic plasticity, and circuit properties of CA1 PNs *in vivo* [35].

Figure 7

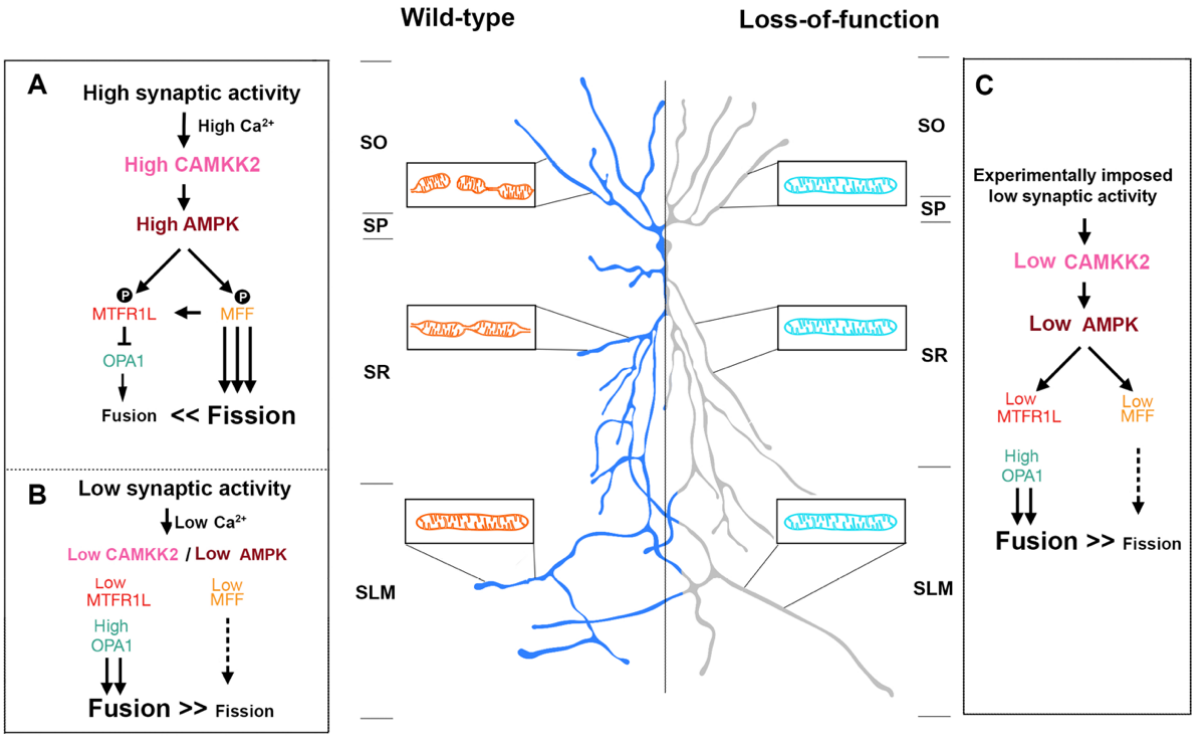

Figure 3.7. Summary of the main findings.
In wild-type mouse CA1 PNs, dendritic mitochondria display a striking degree of compartmentalized morphology, being long and fused in the apical tufts (SLM) with progressive fragmentation and occupancy of a smaller volume of the dendritic segments in SR and SO respectively. We demonstrate using loss-of-function as well as rescue experiments that this compartmentalization of dendritic mitochondria morphology requires (1) neuronal activity (blocked by neuronal hyperpolarization following over-expression of Kir2.1) or by reducing the number of presynaptic inputs from CA3 by ~50% (shRNA Lphn3) *in vivo*, (2) requires activity-dependent activation of AMPK mediated by CAMKK2 and (3) requires the AMPK-dependent phosphorylation of the pro- fission Drp1 receptor MFF and the anti-fusion protein MTFR1L though its ability to suppress the pro-fusion Opa1 protein. These results demonstrate that mitochondrial fusion dominates over fission in apical tuft dendrites (SLM) and that fission dominates fusion in both SO and SR dendritic compartments. See Discussion for details.

3.6 Supplemental Figures

Supplemental Figure S1

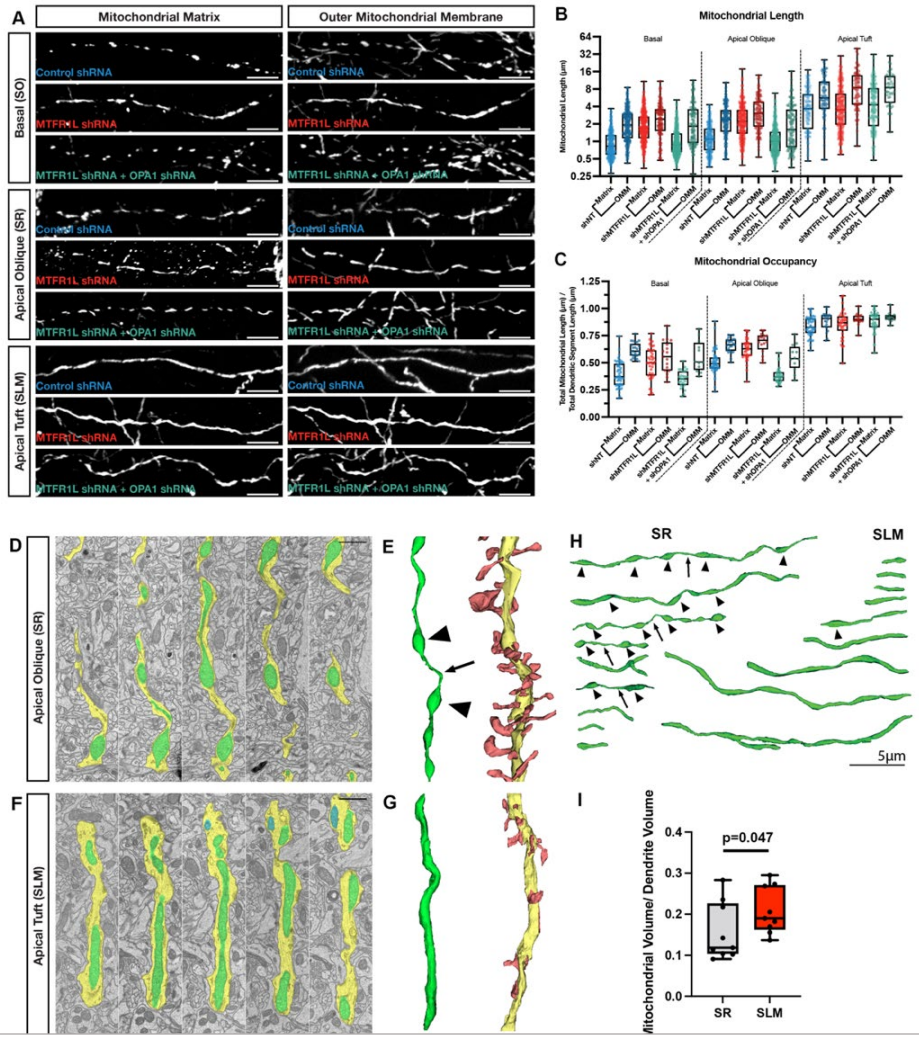

Supplemental Figure S3.1: Compartmentalized mitochondrial morphology visualized using fluorescent OMM and matrix markers as well as 3D serial electron microscopy (3D-SEM).

(**A-C**) High magnification representative images of mitochondrial morphology within isolated secondary or tertiary hippocampal CA1 basal, apical oblique, and apical tuft dendrites in which a mitochondrial matrix-targeted fluorescent protein (mt-mTAGBFP2 or mt-YFP), an outer mitochondrial matrix (OMM)-targeted fluorescent protein (mt-ActAmCherry-HA), and cell fill (mGreenLantern or mTAGBFP2—not pictured) were *in utero* electroporated along with either a control shRNA (shNT), *MTFR1L* shRNA (shMTFR1L), or *MTFR1L* and *Opa1* shRNA (shMTFR1L + shOpa1). (**A**) Quantification of mitochondrial length and occupancy in the basal, apical oblique, and apical tuft dendritic compartments reveals a significant increase in mitochondrial matrix length (**B**) and occupancy (**C**) in basal and apical oblique dendrites when knocking down MTFR1L, which is rescued when also knocking down Opa1 (**Fig. S5E-F**). Note the significant increase in OMM length (**B**) and occupancy (**C**) in all conditions in all dendritic compartments when comparing against mitochondrial matrix length and occupancy. Nevertheless, knocking down shMTFR1L continues to moderately, but significantly, increase the length (**B**) and occupancy (C**)** of the OMM when knocking down MTFR1L, which is rescued when simultaneously knocking down Opa1. There are no significant differences between shNT, shMTFR1L, or shMTFR1L + Opa1 matrix lengths (**B**) or occupancies (**C**), nor between OMM lengths or occupancies. Scale bar: 5 µm. (**D-G**) Serial transmission electron microscopy images from the apical oblique dendrites (SR, panel D) and the apical tuft (SLM, panel F) where the cytoplasm is annotated in yellow and mitochondria in green. Three dimensional reconstructions of the dendritic segments shown in D and F are shown in panels E and G where the mitochondria are highlighted in green (left) and the dendritic shaft in yellow with dendritic spines in red. In panel E, arrowheads indicate matrix bulges along the continuous mitochondria and the arrow points to a constriction separating two matrix bulges. (**H**) Multiple examples of 3D reconstructed, individual dendritic mitochondria displaying various morphologies and length from SR (left) and SLM (right). Note the presence of frequent matrix bulges (arrowheads) and thin constrictions (arrows) in mitochondria from SR dendritic segments that are rarely observed in SLM dendritic segments. (**I**) Quantification of mitochondrial occupancy defined by volume of dendritic segments reconstructed occupied divided by volume occupied by mitochondria in SR and SO. * p=0.047 according to one-tailed Mann-Whitney non-parametric test (U=21). Number of dendritic segments and mitochondria reconstructed: SR, n=76 individual mitochondria along 9 dendritic segments. SLM, n=101 mitochondria along 9 dendritic segments.

Supplemental Figure S2

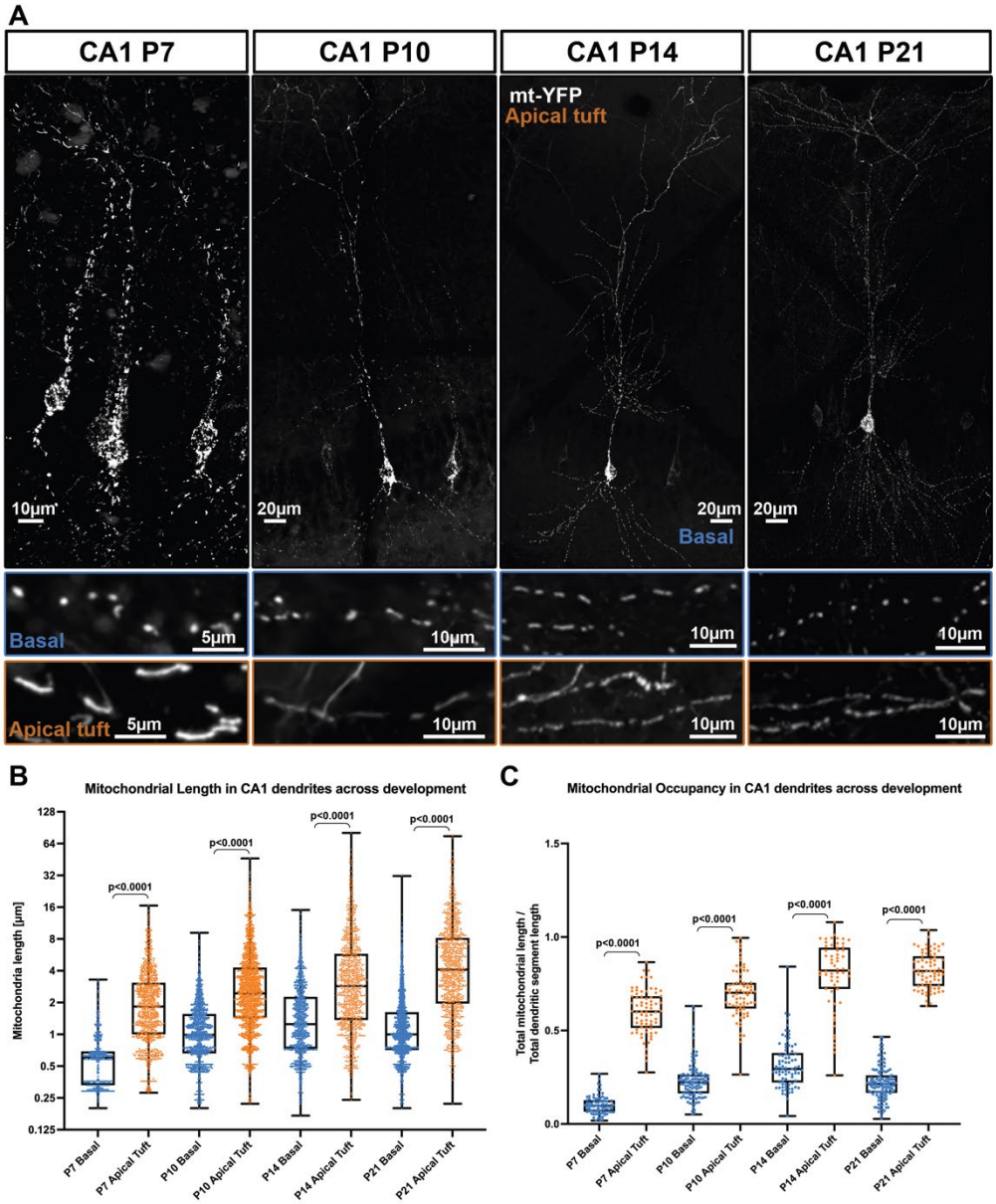

Supplemental Figure S3.2: *In vivo* time course of mitochondrial size and occupancy in CA1 pyramidal neurons.
(**A**) Top: Low magnification representative images of mitochondrial morphologies across CA1 pyramidal neurons at the indicated stages of development following IUE of pCAG mtYFP-P2A- tdTomato at E15.5. Bottom: Higher magnification boxes of mitochondria morphologies from basal (blue) or apical tuft (orange) dendrites at the developmental stage indicated. **(B-C**) Quantification of mitochondrial length (B) and occupancy (C) in the basal and apical tufts at the indicated timepoints showing clear, distinct regulation of mitochondrial size and occupancy in the basal dendrites and apical tuft dendrites early in development that is maintained into adulthood. $P7_{basal}$ = 79 segments, 759 mitochondria, mean length = 0.63µm ± 0.05µm (SEM), mean occupancy = 10.2% ± 0.5% (SEM); $P7_{apical\ tuft}$ = 72 segments, 1119 mitochondria, mean length = 2.45µm ±0.06µm, mean occupancy = 60.1% ± 1.4%; $P10_{basal}$ = 108 segments, 1622 mitochondria, mean length = 1.23µm ±0.02µm, mean occupancy = 23% ± 0.9%; $P10_{apical\ tuft}$ = 73 segments, 2141 mitochondria, mean length = 3.56µm ± 0.08µm, mean occupancy = 69.5% ± 1.5%; $P14_{basal}$ = 82 segments, 1265 mitochondria, mean length = 1.79µm ± 0.05µm, mean occupancy = 31.6% ± 1.4%; $P14_{apical\ tuft}$ = 59 segments, 1022 mitochondria, mean length = 5.1µm ± 0.22µm, mean occupancy = 79.6% ± 2.4%; $P21_{basal}$ = 127 segments, 2154 mitochondria, mean length = 1.42µm ±0.03µm, mean occupancy = 21.8% ± 0.7%; $P21_{apical\ tuft}$ = 75 segments, 1036 mitochondria mean length = 6.48µm ±0.23µm, mean occupancy = 81.9% ± 1.1%. P21 data is the same as the control$_{tdTomato}$ set used in Figure 2. p values are displayed within the figure. Data are shown as individual points on min to max box plots with 25th, 50th and 75th percentiles.

Supplemental Figure S3

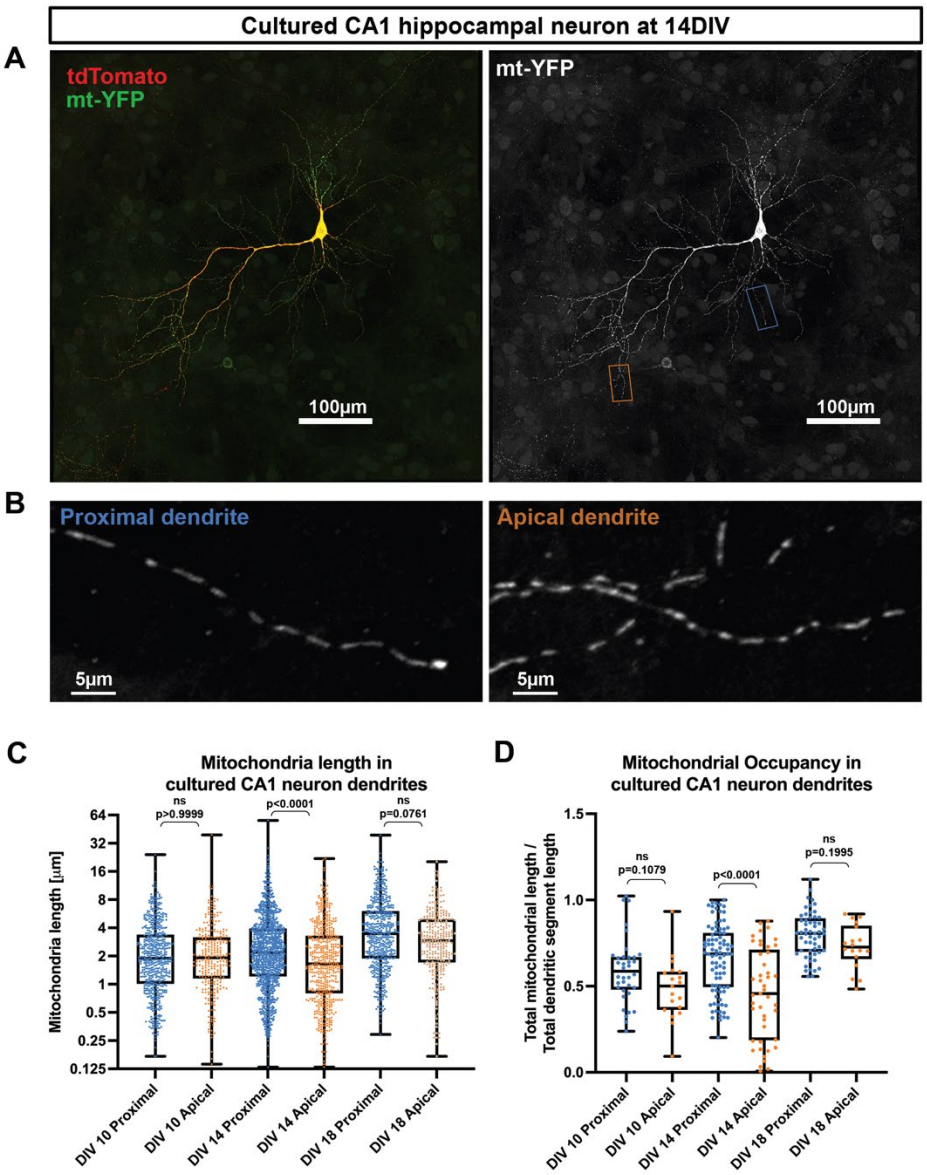

Supplemental Figure S3.3: Dendritic mitochondria morphology observed in CA1 pyramidal neurons *in vivo* are not conserved in cultured CA1 PNs *in vitro*.
(**A**) Low magnification representative images of mitochondrial morphology across a hippocampal neuron in culture following IUE of pCAG mtYFP-P2A-tdTomato at E15.5, followed by culture at E18.5. (**B**) Higher magnification of the indicated boxes in **A**. (**C-D**) Quantification of mitochondrial length (**C**) and occupancy (**D**) in the proximal and apical dendrites at the indicated timepoints showing that in culture the distinct mitochondrial populations observed *in vivo* are absent. $10DIV_{proximal}$ = 36 segments, 580 mitochondria, mean length = 2.64µm ±0.1µm (SEM), mean occupancy = 59% ± 3.2% (SEM); $10DIV_{apical}$ = 19 segments, 275 mitochondria, mean length = 2.58µm ± 0.18µm, mean occupancy = 48.4% ± 4.1%; $14DIV_{proximal}$ = 88 segments, 1199 mitochondria, mean length = 3.2µm ± 0.1µm, mean occupancy = 65.7% ± 2.1%; $14DIV_{apical}$ = 45 segments, 527 mitochondria, mean length = 2.56µm ±0.12µm, mean occupancy = 45.5% ± 3.9%; $18DIV_{proximal}$ = 56 segments, 572 mitochondria, mean length = 4.74µm ± 0.18µm, mean occupancy = 79.7% ± 1.7%; 18 DIV_{apical} = 18 segments, 300 mitochondria mean length = 3.7µm ± 0.17µm, mean occupancy = 72.9% ± 3%. p values are shown in the figure. Data are shown as individual points on min to max box plots with 25th, 50th and 75th percentiles.

Supplemental Figure S4

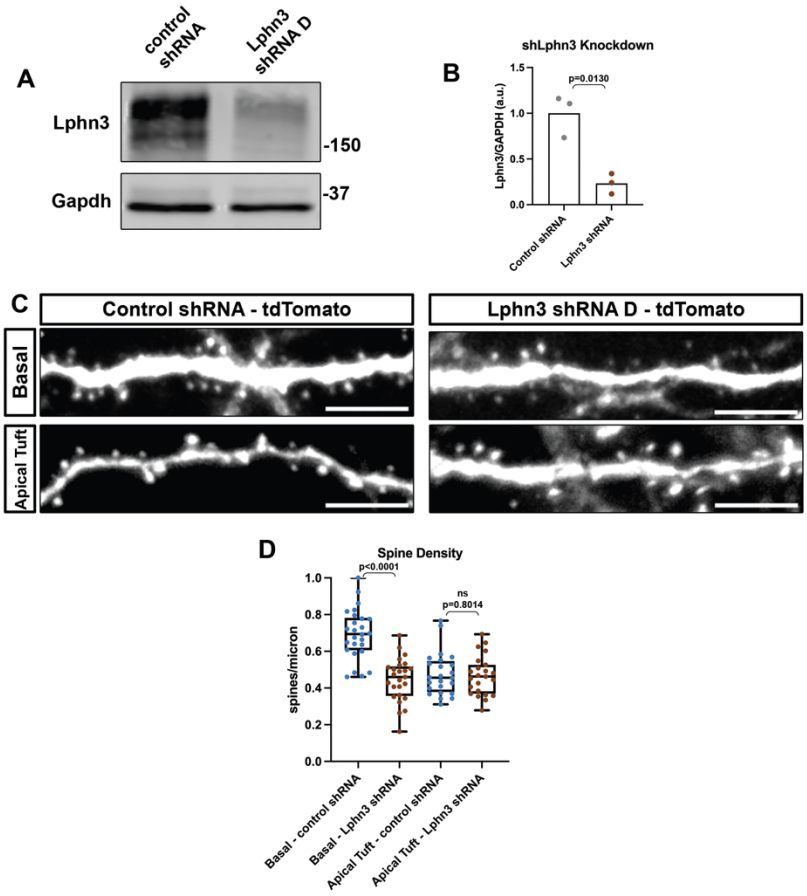

Supplemental Figure S3.4: Validation of Lphn3 shRNA knockdown construct.

(**A**) Western blot using a mouse Lphn3 antibody (R&D research, top panel) on samples from HEK cells that were transfected with mouse Lphn3 cDNA and either a control or *Lphn3* shRNA construct. Gapdh (Cell Signaling Technologies, bottom panel) was used as a loading control. (**B**) Relative Lphn3 expression following 72hrs knockdown from 3 independent experiments. Paired t test. p value indicated in the figure. **C**) High magnification representative images of P21 CA1 dendrite segments electroporated at E15.5 with tdTomato and either control shRNA (left) or Lphn3 shRNA D (right) from basal dendrites in SO (top) or apical tuft dendrites (bottom). **E**) Quantification of spine density following IUE with control shRNA or Lphn3 shRNA D at P21 demonstrating that Lphn3 knockdown throughout development results in decreased spine density on basal dendrites but not apical tuft dendrites. Control $shRNA_{basal}$ = 26 dendrite segments, mean spine density = 0.69 ± 0.03 spines/micron (SEM), Control $shRNA_{apical\ tuft}$ = 24 dendrite segments, mean spine density = 0.48 ± 0.02 spines/micron, Lphn3 $shRNA_{basal}$ = 25 dendrite segments, mean spine density = 0.45 ± 0.02 spines/micron, Lphn3 $shRNA_{apical\ tuft}$ = 23 dendrite segments, mean spine density = 0.47 ± 0.02 spines/micron. p values are shown in the figure. Data are shown as individual points on min to max box plots with 25th, 50th and 75th percentiles. Scale bars are 5 microns.

Supplemental Figure S5

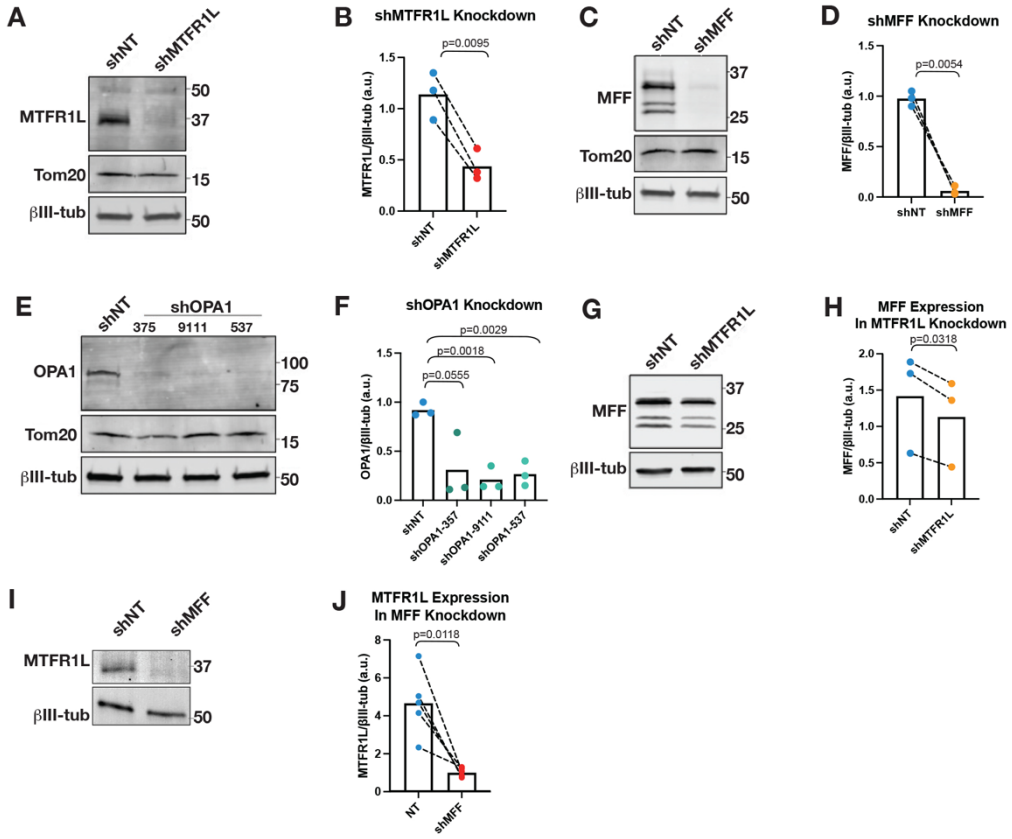

Supplemental Figure S3.5: Validation of MTFR1L, MFF, and Opa1 shRNA constructs.

(**A-B**) Western blot demonstrating shMTFR1L significantly knocks down MTFR1L (37kDa) compared to control shNT in neuronal cultures. β-Tubulin III (βIII-tub, 50kDa) was stained as a control for neuronal content and Tom20 (15kDa) to control for mitochondrial content and quantification (B) of shMTFR1L knockdown measuring fluorescence intensity of anti-MTFR1L normalized to anti-βIII-tub. (**C-D**) Western blot demonstrating shMFF significantly knocks down MFF (37-25kDa) compared to control shNT and quantification (D) of shMFF knockdown measuring fluorescence intensity of anti- MFF normalized to anti-βIII-tub. (**E-F**) Western blot demonstrating three separate shOpa1s (357, 9111, 537) significantly knocks down Opa1 (78kDa) compared to control shNT and quantification (F) of shOpa1 knockdowns measuring fluorescence intensity of anti-Opa1 normalized to anti-βIII-tub. (**G-H**) Western blot probing for MFF in control shRNA and MTFR1L shRNA treated neurons and quantification (**H**) of fluorescence intensity of anti-MFF compared to anti-βIII-tub from **G**. (**I-J**) Western blot probing for MTFR1L in control shRNA and MFF shRNA treated neurons and quantification (**J**) of fluorescence intensity of anti-MTFR1L compared to anti-βIII-tub from **I**.

3.7 Methods

Animals

All experiments involving mice were done according to protocols approved by the Institutional Animal Care and Use Committee (IACUC) at Columbia University, Oklahoma Medical Research Foundation (OMRF) and in accordance with National Institutes of Health guidelines. Animal health and welfare were supervised by a designated veterinarian. All mice were maintained in Columbia University or OMRF animal facilities that comply with all appropriate standards of care, including cage conditions, space per animal, temperature, humidity, food, water, and 12-hour light/dark cycles.

Timed-pregnant hybrid F1 control females were obtained by mating inbred *129/SvJ* females (Charles River) and *C57BL/6J* males in house. Homozygous double conditional knockout (cKO) lines AMPKα1$^{F/F}$α2$^{F/F}$ [37] were provided by Dr Benoit Viollet (INSERM, Institut Cochin- Paris, France) and homozygous *CAMKK2*$^{-/-}$ [38] were obtained from Dr. Talal Chatila (Harvard Medical School, Boston). Both AMPKα1$^{F/F}$ 2$^{F/F}$ double cKO and *CAMKK2*$^{-/-}$ timed-pregnant females were obtained by mating homozygous males with females of the same genotype. CD-1 IGS mice (Strain Code: 022) were purchased from Charles River Laboratories.

Cell and Tissue Lysis and Western Blotting

Human Embryonic Kidney 293T/17 (HEK293T) cells were purchased from ATCC (CRL-11268). 1x10^5 HEK cells were resuspended in media (DMEM, Gibco) with penicillin/streptomycin (0.5×; Gibco) and FBSL(Sigma) and seeded in 6 well plates (Corning). Transfection with plasmid DNA (1 mg/mL) using jetPRIME® reagent (Polyplus) according to manufacturer protocol was performed 24 hours after seeding. 72 hours following transfection, cells were carefully washed with 1xPBS (Gibco) then collected into RIPA buffer with protease inhibitor cocktail.

Aliquots of the collected samples were separated by SDS-PAGE and then transferred to a polyvinylidene difluoride (PVDF) membrane (Amersham). After transfer, the membrane was washed 3X in Tris Buffer Saline (10 mM Tris-HCl pH 7.4, 150 mM NaCl) with 0.1% of Tween 20 (T-TBS), blocked for 1 hr at room temperature in Odyssey Blocking Buffer (TBS, LI-COR), followed by 4°C overnight incubation with the appropriate primary antibody in the above buffer. The following day, the membrane was washed 3X in T-TBS, incubated at room temperature for 1 hr with IRDye secondary antibodies (LI-COR) at 1:10,000 dilution in Odyssey Blocking Buffer (TBS), followed by 3X T-TBS washes. Visualization was performed by

quantitative fluorescence using an Odyssey CLx imager (LI-COR). Signal intensity was quantified using Image Studio software (LI-COR). Primary antibody used for Western blotting was mouse anti-LPHN3 (R&D Systems MAB5916) and rabbit anti-GAPDH (CST 2118). Total protein was assessed using the Revert 700 Total protein stain (LI-COR 926-11010).

Activity Assay

Cell Culture and Lysis: Embryos were harvested at E15.5 and chilled in Hank's Balanced Salt Solution (HBSS, Thermo Fisher Scientific) while medial portion of the dorsal telencephalon (presumptive hippocampi) were dissected out. Isolated hippocampi were incubated in papain for 15 minutes at 37°C. After three washes of HBSS, hippocampi were manually dissociated with a pipette into Neurobasal (Thermo Fisher Scientific) supplemented with FBS (Gemini Bio-Products), GlutaMAX (Thermo Fisher Scientific), penicillin/streptomycin (Thermo Fisher Scientific), B27 (Fisher Scientific), and N2 (Thermo Fisher Scientific). Dissociated cells were plated into the wells of 6 well plates (Corning) (7.5×10^5 cells/well) that were previously coated in Poly-D- Lysine (Thermo Fisher Scientific) and incubated at 37°C with 5% CO2. Cells were fed every 3-4 days by removing 0.75mL of media and replenished with 1mL of fresh Neurobasal containing GlutaMAX, B27 and N2 only. Cells were brought to 21 days *in vitro* (DIV) and then treated with either DMSO (2.5μM, Santa Cruz Biotechnology), STO609 (2.5μM, Sigma-Aldrich), or Compound 991 (50μM, Selleck Chem) for 2.5 hours. Neurobasal media was then switched out for 5K Tyrode Solution containing TTX (1μM, Hello Bio) to block sodium channels, NMDA antagonist AP5 (10μM, Hello Bio), and AMPA antagonist NBQX (50μM, Hello Bio) for 30 minutes to dampen cell activity. Media was then switched out for either a second incubation in 5K or 40K Tyrode Solution for 15 minutes. Drug treatments were maintained throughout every incubation step. Tyrode Solution was removed, and cells were lysed on ice with 100μl of N-PER (Thermo Fisher Scientific) containing phosphatase inhibitors (Sigma Aldrich), protease inhibitor (Sigma Aldrich), and benzonase (EMD Millipore). Lysates were then denatured in 4x Laemmli Buffer (BioRad) and 2-Mercaptoethanol (BioRad) at 95°C for 5 minutes.

Western Blotting: Equal amounts of lysates were loaded onto Mini-Protean TGX (4-20%) SDS-PAGE gels (BioRad). All blots except phospho-MTFR1L were transferred to nitroceullose membranes (BioRad) with a Trans-Blot Turbo and blocked for one hour in Intercept Buffer (Li-COR). Membranes were then incubated in their respective primary antibodies in blocking buffer at 4°C overnight. Blots probing for phospho-MTFR1L

we transferred to polyvinylidene difluoride membranes (PVDF, Immobilion) and blocked in 5% fat-free dry milk in TBS-T for 1 hour before primary antibody incubation for four days at 4°C. Membranes were incubated in Li-Cor fluorescence-coupled secondary antibodies for 1 hour at room temperature prior to visualization with a Li-Cor Odyssey Blot Imager.

Antibodies: AMPKα (Cell Signaling, #2532S, 1:2000); phospho-AMPKα (Cell Signaling, #2535S, 1:2000); MFF (Proteintech #17090-1-AP, 1:1000); phospho-MFF (Affinity Bioscience #AF2365, 1:2000), MTFR1L (Atlas Antibodies #HPA027124, 1:2000); phospho-MTFR1L (Gift from the Graham Hardie Lab, S103 and S235, 1:500; characterized in [33])

Lentiviral particle production and transduction

Lentiviral particles were generated as described before (https://www.addgene.org/protocols/lentivirus-production/). Briefly, freshly thawed HEK293T cells (ATCC, CRL-3216) were seeded in a 10 cm dish containing DMEM (GIBCO, 12430-054) supplemented with 10% FBS (Thermo Scientific, 16141002), 1% GlutaMax (GIBCO, 35050061), 1% Sodium Pyruvate (GIBCO, 11360070), and 1% Pen / Strep (Life Technologies, 15140-122), and grown at 37°C, 5% CO2 for ~ 48 hours. Once confluent, cells were detached from the dish by trypsinization (GIBCO, 25200072), split into 15 cm dishes, and grown to ~80 % confluence. Before transfection, cultures were treated with 25 µM chloroquine diphosphate for 5 h, supplemented in fresh growth media. For one 15 cm dish, the transfection reaction was assembled in two separate tubes, each containing 1.5 ml serum-free DMEM. The plasmid mixture, composed of pMD2.G (Addgene, #12259), psPAX2 (Addgene, #12260), and a designated transfer vector, was added to the first tube, and the transfection reagent Polyethylenimine (PEI) to the second tube. Both halves were mixed and incubated at RT for 20 min, time after which the reaction was added dropwise to the dish. Cultures were incubated with the transfection reaction for 24 h and then replaced by fresh growth media. Media containing lentiviral particles was collected 72 h after transfection and spun down for 5 min at 2000 g to pellet cell debris. The supernatant was filtered through a 0.45 µm pore, aliquoted in 1.5 ml Eppendorf tubes, and centrifuged for 2 h at 16000 g at 4°C. The supernatant was discarded, and dry viral pellets were stored at -80°C until use. For neuronal transduction, viral pellets were resuspended in serum-free Neurobasal medium (GIBCO, 21103049), added to neuronal cultures, and incubated for 5-7 days before sample collection.

Single Cell Electroporation (SCE) of CA1 PNs

SCEs were performed as previously described in detail[35,39]. Briefly, DNA plasmid constructs were diluted to 50ng/µL and electroporated into single dorsal hippocampal CA1-area pyramidal neurons, guided by two-photon microscopy at 920 nm excitation. Successfully electroporated cells were imaged 48-72h post SCE.

In utero electroporation (IUE) targeting CA1 PNs

In utero electroporation targeting the dorsal hippocampus was performed using a triple-electrode setup as previously described [36,40,41] in E15.5 mouse embryos in order to target the dividing progenitors generating CA1 pyramidal neurons. Briefly, endotoxin-free plasmids were injected into the lateral ventricle (1 µg/µL) followed by 5 pulses at 45V (50ms duration, 500ms inter-pulse interval) using two anodes (positively charged) laterally on either side of the head and one cathode (negatively charged) rostrally at a 0º angle to the horizontal plane. Mice were perfused transcardially with ice cold PFA (2-4%) and glutaraldehyde (0.075%) at P21, post-fixed overnight in the same solution at 4C, and then sectioned at 110-125 µm on a vibratome (Leica). Sections were mounted with Fluoromount-G aqueous mounting medium (ThermoFisher Scientific) and imaged on a Nikon Ti- E A1R laser-scanning confocal microscope using a 40x or 60x NA1.49 objective, or a Zeiss LSM 880 confocal microscope controlled by Zeiss Black software. Imaging required two lasers 488nm and 561nm together with Zeiss objectives 20x (1.2NA) with 2x zoom, or 100x oil (1.25NA) with 3x zoom. Neuronal processes were visualized by Z-stacking that was later processed into Maximum Intensity Projection (MIP). MIP 2D images were then used for analysis of mitochondrial length and occupancy using NIS Elements software (Nikon) or Fiji (Image J).

Primary neuronal culture

Following *in utero* electroporation, at E18.5 embryonic mouse cortices were dissected in Hank's Balanced Salt Solution (HBSS) supplemented with HEPES (10LmM, pH 7.4), and incubated in HBSS containing papain (Worthington; 14LU/mL) and DNase I (100Lµg/mL) for 15Lmin at 37L°C with a gentle flick between incubation. Samples were washed with HBSS three times and dissociated by pipetting on the fourth wash. Cells were counted using Countess™ (Invitrogen) and cell suspension was plated on poly-D-lysine (1Lmg/mL, Sigma)-coated glass bottom dishes (MatTek) or poly-D-lysine/laminin coated coverslips (BD bioscience) in Neurobasal media (Gibco) containing FBS (2.5%) (Sigma), B27 (1LX) (Gibco), and Glutamax

(1LX) (Gibco). After 7 days, media was changed with supplemented Neurobasal media without FBS, and 1/3 of the media replaced every 3 days.

Fixation for primary neuron culture

Culture dishes were fixed with 2% PFA (PFA Alfa Aesar)/0.075% GA (Electron Microscopy Science, EMS) in 1x PBS (Sigma) for 10 minutes. Dishes were washed three times following fixation with 1x PBS (Sigma) for 10 minutes.

Immunohistochemistry

Following fixation and washing, brains were embedded in 3% low melt agarose (RPI, A20070) in 1x PBS. Brains in agarose cubes were sectioned using a vibratome (Leica VT1200) to 120 µm thick sections. Sections/coverslips were then incubated with primary antibodies (chicken anti-GFP Aves Lab 1:4000, rabbit anti-dsRed Abcam 1:4000) that were diluted in the Blocking buffer (1%BSA, 0.2%TritonX-100, 5%NGS in PBS) at 4 °C for 48h. Subsequently sections were washed 6 times for 10 min in PBS and incubated with secondary antibodies (Alexa conjugated goat anti-chicken488 and goat anti-rabbit568 1:4000) at 4 °C for 48h. The excess of secondary antibodies was removed by six, 10min washes in 1xPBS. Sections were then mounted on slides and coverslipped with Aqua PolyMount (PolyMount Sciences, Inc.) and kept at 4°C.

Analysis of spine density and mitochondrial morphology

Dendritic spine and mitochondrial morphology quantification was carried out by first identifying 2º or 3º dendritic segments in the basal, apical oblique, or apical tuft dendritic compartments using the cell fill channel only, blinding the experimenter to mitochondrial morphology and density, removing potential bias during segment selection. Individual dendritic segments were then measured in their length manually using Fiji or NIS-Elements software (ImageJ; NIH or Nikon), with each individual mitochondria length in each dendritic segment subsequently measured manually. The same was done for dendritic spines in a select number of segments. In order to calculate mitochondrial occupancy, the sum of an individual dendritic segment's mitochondria is divided by the total length of the dendritic segment itself. Spine density similarly is calculated by dividing the total number of dendritic spines by the total length of the dendritic segment.

Plasmids

pCAG:Cre (Addgene: Cat#13775), pEF1α:flex-tdTomato (Addgene: Cat#28306), pCAG:mito-YFP (Addgene; Cat# 168508) [42], pCAG:mito-dsRed [43], pCAG:tdTomato [42], pCAG:mGreenLantern (Addgene:

Cat#164469), pCAG:mtYFP-P2A-tdTomato [42], pCAG:Kir2.1-T2A-tdTomato was a gift from Massimo Scanziani (Addgene plasmid #60598), pLKO.1:shMTFR1L (GAGTGGAGTGTATCTGCTTAAGGGG) [33], pCAG:MTFR1L^{WT} [33], pCAG:MTFR1L$^{S103D/S238D}$ [33], pLKO.1:shMFF (CCGGGATCGTGGTTACAGGAAATAA – TRCN0000174665) [7], pLKO.1:shOPA1 (CCGACACAAAGGAAACTATTT – TRCN0000091111), pLKO.1:shNT (CGTTAATCGCGTATAATACGCGTAT) [33]. pCMV6 Lphn3 (MR212027), pGFP-C-shLenti scrambled negative control (TR30021), and pGFP-C-shLenti Lphn3 shRNA-D (GTATGTTGGCTTCGCCTTGACACCTACTT, custom) were purchased from Origene.

***In Vivo* two-photon Imaging**

We used the same imaging system as described previously 35,36. All images were acquired using a Nikon 40 x NIR water-immersion objective (0.8 NA, 3.5 mm WD) in distilled milliQ water. For excitation, we used a Chameleon, Ultra II (Coherent) laser tuned to 920 nm. We continuously acquired red (tdTomato) and green (mt-YFP) channels separated by an emission cube set (green: HQ525/70 m-2p; red: HQ607/45 m-2p; 575dcxr, Chroma Technology) at 512 x 512 pixels covering 330 µm x 330 µm at 30 Hz with photomultiplier tubes (green mt-YFP fluorescence, GaAsP PMT, Hamamatsu Model 7422-40; red tdTomato fluorescence, GaAsP PMT Hamamatsu).

3.8 Acknowledgements

We thank past and present members of the Polleux and Lewis labs for feedback and discussion along the way. We thank Nelson Spruston (HHMI-Janelia) for sharing the CA1 serial EM dataset generated while EB was in his laboratory. We thank Grahame Hardie (Univ. Dundee- UK) and Julien Prudent (Univ. Cambridge-UK) for generously sharing the phospho-specific MTFR1L antibody. We thank Patrycja Szybowska, Joshua Weertman, Klaudia Strucinska, Qiaolian Liu and Rhythm Sharma for technical help. This research was supported by grants NIGMS R35GM137921 (TL), NIGMS P20GM103636-06 sub-project 2 (TL), Presbyterian Health Foundation (TL), NINDS R35 NS127232 (FP) and NINDS NS107483 (FP).

3.9 Author Contributions

Conceptualization: DMV, FP, TL. Formal analysis: DMV, SH, BO, EZ, NP, VH, DZ, KG, FP, TL. Funding acquisition: FP, TL. Investigation: DMV, SH, BO, AM, EZ, NP, VH, DZ, KG, EB, FP, TL. Methodology: DMV, SH, BO, EZ, KG, EB, FP, TL. Project administration: FP, TL. Resources: EB, FP, TL. Supervision: FP, TL.

Visualization: DMV, SH, BO, FP, TL. Writing – original draft: DMV, SH, FP, TL. Writing – review & editing: DMV, SH, BO, EB, FP, TL.

3.10 References

1. Barnes, A.P., and Polleux, F. (2009). Establishment of axon-dendrite polarity in developing neurons. Annu Rev Neurosci *32*, 347-381. 10.1146/annurev.neuro.31.060407.125536.
2. Gumy, L.F., and Hoogenraad, C.C. (2018). Local mechanisms regulating selective cargo entry and long-range trafficking in axons. Curr Opin Neurobiol *51*, 23-28. 10.1016/j.conb.2018.02.007.
3. Horton, A.C., and Ehlers, M.D. (2003). Neuronal polarity and trafficking. Neuron *40*, 277-295. 10.1016/s0896-6273(03)00629-9.
4. Lewis, T.L., Jr., Courchet, J., and Polleux, F. (2013). Cell biology in neuroscience: Cellular and molecular mechanisms underlying axon formation, growth, and branching. J Cell Biol *202*, 837-848. 10.1083/jcb.201305098.
5. Wu, Y., Whiteus, C., Xu, C.S., Hayworth, K.J., Weinberg, R.J., Hess, H.F., and De Camilli, P. (2017). Contacts between the endoplasmic reticulum and other membranes in neurons. Proc Natl Acad Sci U S A *114*, E4859-E4867. 10.1073/pnas.1701078114.
6. Lee, A., Hirabayashi, Y., Kwon, S.K., Lewis, T.L., Jr., and Polleux, F. (2018). Emerging roles of mitochondria in synaptic transmission and neurodegeneration. Curr Opin Physiol *3*, 82-93. 10.1016/j.cophys.2018.03.009.
7. Lewis, T.L., Jr., Kwon, S.K., Lee, A., Shaw, R., and Polleux, F. (2018). MFF-dependent mitochondrial fission regulates presynaptic release and axon branching by limiting axonal mitochondria size. Nat Commun *9*, 5008. 10.1038/s41467-018-07416-2.
8. Faitg, J., Lacefield, C., Davey, T., White, K., Laws, R., Kosmidis, S., Reeve, A.K., Kandel, E.R., Vincent, A.E., and Picard, M. (2021). 3D neuronal mitochondrial morphology in axons, dendrites, and somata of the aging mouse hippocampus. Cell Rep *36*, 109509. 10.1016/j.celrep.2021.109509.
9. Terasaki, M. (2018). Axonal endoplasmic reticulum is very narrow. J Cell Sci *131*. 10.1242/jcs.210450.

10. Turner, N.L., Macrina, T., Bae, J.A., Yang, R., Wilson, A.M., Schneider-Mizell, C., Lee, K., Lu, R., Wu, J., Bodor, A.L., et al. (2022). Reconstruction of neocortex: Organelles, compartments, cells, circuits, and activity. Cell *185*, 1082-1100 e1024. 10.1016/j.cell.2022.01.023.

11. Lee, A., Kondapalli, C., Virga, D.M., Lewis, T.L., Jr., Koo, S.Y., Ashok, A., Mairet-Coello, G., Herzig, S., Foretz, M., Viollet, B., et al. (2022). Abeta42 oligomers trigger synaptic loss through CAMKK2-AMPK- dependent effectors coordinating mitochondrial fission and mitophagy. Nat Commun *13*, 4444. 10.1038/s41467-022-32130-5.

12. Divakaruni, S.S., Van Dyke, A.M., Chandra, R., LeGates, T.A., Contreras, M., Dharmasri, P.A., Higgs, H.N., Lobo, M.K., Thompson, S.M., and Blanpied, T.A. (2018). Long-Term Potentiation Requires a Rapid Burst of Dendritic Mitochondrial Fission during Induction. Neuron *100*, 860-875 e867. 10.1016/j.neuron.2018.09.025.

13. Li, Z., Okamoto, K., Hayashi, Y., and Sheng, M. (2004). The importance of dendritic mitochondria in the morphogenesis and plasticity of spines and synapses. Cell *119*, 873-887. 10.1016/j.cell.2004.11.003.

14. Han, X.J., Lu, Y.F., Li, S.A., Kaitsuka, T., Sato, Y., Tomizawa, K., Nairn, A.C., Takei, K., Matsui, H., and Matsushita, M. (2008). CaM kinase I alpha-induced phosphorylation of Drp1 regulates mitochondrial morphology. J Cell Biol *182*, 573-585. 10.1083/jcb.200802164.

15. Brustovetsky, T., Li, V., and Brustovetsky, N. (2009). Stimulation of glutamate receptors in cultured hippocampal neurons causes Ca^{2+}-dependent mitochondrial contraction. Cell Calcium *46*, 18-29. 10.1016/j.ceca.2009.03.017.

16. Itoh, K., Murata, D., Kato, T., Yamada, T., Araki, Y., Saito, A., Adachi, Y., Igarashi, A., Li, S., Pletnikov, M., et al. (2019). Brain-specific Drp1 regulates postsynaptic endocytosis and dendrite formation independently of mitochondrial division. Elife *8*. 10.7554/eLife.44739.

17. Li, H., Alavian, K.N., Lazrove, E., Mehta, N., Jones, A., Zhang, P., Licznerski, P., Graham, M., Uo, T., Guo, J., et al. (2013). A Bcl-xL-Drp1 complex regulates synaptic vesicle membrane dynamics during endocytosis. Nat Cell Biol *15*, 773-785. 10.1038/ncb2791.

18. Loson, O.C., Song, Z., Chen, H., and Chan, D.C. (2013). Fis1, MFF, MiD49, and MiD51 mediate Drp1 recruitment in mitochondrial fission. Mol Biol Cell *24*, 659-667. 10.1091/mbc.E12-10-0721.

19. Otera, H., Wang, C., Cleland, M.M., Setoguchi, K., Yokota, S., Youle, R.J., and Mihara, K. (2010). MFF is an essential factor for mitochondrial recruitment of Drp1 during mitochondrial fission in mammalian cells. J Cell Biol *191*, 1141-1158. 10.1083/jcb.201007152.

20. Shen, Q., Yamano, K., Head, B.P., Kawajiri, S., Cheung, J.T., Wang, C., Cho, J.H., Hattori, N., Youle, R.J., and van der Bliek, A.M. (2014). Mutations in Fis1 disrupt orderly disposal of defective mitochondria. Mol Biol Cell *25*, 145-159. 10.1091/mbc.E13-09-0525.

21. Herzig, S., and Shaw, R.J. (2018). AMPK: guardian of metabolism and mitochondrial homeostasis. Nat Rev Mol Cell Biol *19*, 121-135. 10.1038/nrm.2017.95.

22. Steinberg, G.R., and Hardie, D.G. (2022). New insights into activation and function of the AMPK. Nat Rev Mol Cell Biol. 10.1038/s41580-022-00547-x.

23. Toyama, E.Q., Herzig, S., Courchet, J., Lewis, T.L., Jr., Loson, O.C., Hellberg, K., Young, N.P., Chen, H., Polleux, F., Chan, D.C., and Shaw, R.J. (2016). Metabolism. AMP-activated protein kinase mediates mitochondrial fission in response to energy stress. Science *351*, 275-281. 10.1126/science.aab4138.

24. Mairet-Coello, G., Courchet, J., Pieraut, S., Courchet, V., Maximov, A., and Polleux, F. (2013). The CAMKK2-AMPK kinase pathway mediates the synaptotoxic effects of Abeta oligomers through Tau phosphorylation. Neuron *78*, 94-108. 10.1016/j.neuron.2013.02.003.

25. Racioppi, L., and Means, A.R. (2012). Calcium/calmodulin-dependent protein kinase kinase 2: roles in signaling and pathophysiology. J Biol Chem *287*, 31658-31665. 10.1074/jbc.R112.356485.

26. Kim, S.Y., Strucinska, K., Osei, B., Han, K., Kwon, S.K., and Lewis, T.L., Jr. (2022). Neuronal mitochondrial morphology is significantly affected by both fixative and oxygen level during perfusion. Front Mol Neurosci *15*, 1042616. 10.3389/fnmol.2022.1042616.

27. Cho, B., Cho, H.M., Jo, Y., Kim, H.D., Song, M., Moon, C., Kim, H., Kim, K., Sesaki, H., Rhyu, I.J., et al. (2017). Constriction of the mitochondrial inner compartment is a priming event for mitochondrial division. Nat Commun *8*, 15754. 10.1038/ncomms15754.

28. Bloss, E.B., Cembrowski, M.S., Karsh, B., Colonell, J., Fetter, R.D., and Spruston, N. (2018). Single excitatory axons form clustered synapses onto CA1 pyramidal cell dendrites. Nat Neurosci *21*, 353-363. 10.1038/s41593-018-0084-6.

29. Cancedda, L., Fiumelli, H., Chen, K., and Poo, M.M. (2007). Excitatory GABA action is essential for morphological maturation of cortical neurons in vivo. J Neurosci *27*, 5224-5235. 10.1523/JNEUROSCI.5169-06.2007.

30. Xue, M., Atallah, B.V., and Scanziani, M. (2014). Equalizing excitation-inhibition ratios across visual cortical neurons. Nature *511*, 596-600. 10.1038/nature13321.

31. Sando, R., Jiang, X., and Sudhof, T.C. (2019). Latrophilin GPCRs direct synapse specificity by coincident binding of FLRTs and teneurins. Science *363*. 10.1126/science.aav7969.

32. Thornton, C., Bright, N.J., Sastre, M., Muckett, P.J., and Carling, D. (2011). AMP-activated protein kinase (AMPK) is a tau kinase, activated in response to amyloid beta-peptide exposure. Biochem J *434*, 503-512. 10.1042/BJ20101485.

33. Tilokani, L., Russell, F.M., Hamilton, S., Virga, D.M., Segawa, M., Paupe, V., Gruszczyk, A.V., Protasoni, M., Tabara, L.C., Johnson, M., et al. (2022). AMPK-dependent phosphorylation of MTFR1L regulates mitochondrial morphology. Sci Adv *8*, eabo7956. 10.1126/sciadv.abo7956.

34. Bading, H., Ginty, D.D., and Greenberg, M.E. (1993). Regulation of gene expression in hippocampal neurons by distinct calcium signaling pathways. Science *260*, 181-186. 10.1126/science.8097060.

35. O'Hare, J.K., Gonzalez, K.C., Herrlinger, S.A., Hirabayashi, Y., Hewitt, V.L., Blockus, H., Szoboszlay, M., Rolotti, S.V., Geiller, T.C., Negrean, A., et al. (2022). Compartment-specific tuning of dendritic feature selectivity by intracellular Ca(2+) release. Science *375*, eabm1670. 10.1126/science.abm1670.

36. Blockus, H., Rolotti, S.V., Szoboszlay, M., Peze-Heidsieck, E., Ming, T., Schroeder, A., Apostolo, N., Vennekens, K.M., Katsamba, P.S., Bahna, F., et al. (2021). Synaptogenic activity of the axon guidance molecule Robo2 underlies hippocampal circuit function. Cell Rep *37*, 109828. 10.1016/j.celrep.2021.109828.

37. Boudaba, N., Marion, A., Huet, C., Pierre, R., Viollet, B., and Foretz, M. (2018). AMPK Re-Activation Suppresses Hepatic Steatosis but its Downregulation Does Not Promote Fatty Liver Development. EBioMedicine *28*, 194-209. 10.1016/j.ebiom.2018.01.008.

38. Ageta-Ishihara, N., Takemoto-Kimura, S., Nonaka, M., Adachi-Morishima, A., Suzuki, K., Kamijo, S., Fujii, H., Mano, T., Blaeser, F., Chatila, T.A., et al. (2009). Control of cortical axon elongation by a GABA-driven Ca^{2+}/calmodulin-dependent protein kinase cascade. J Neurosci *29*, 13720-13729. 10.1523/JNEUROSCI.3018-09.2009.

39. Rolotti, S.V., Ahmed, M.S., Szoboszlay, M., Geiller, T., Negrean, A., Blockus, H., Gonzalez, K.C., Sparks, F.T., Solis Canales, A.S., Tuttman, A.L., et al. (2022). Local feedback inhibition tightly controls rapid formation of hippocampal place fields. Neuron *110*, 783-794 e786. 10.1016/j.neuron.2021.12.003.

40. Hand, R., and Polleux, F. (2011). Neurogenin2 regulates the initial axon guidance of cortical pyramidal neurons projecting medially to the corpus callosum. Neural Dev *6*, 30. 10.1186/1749-8104-6-30.

41. Meyer-Dilhet, G., and Courchet, J. (2020). In Utero Cortical Electroporation of Plasmids in the Mouse Embryo. STAR Protoc *1*, 100027. 10.1016/j.xpro.2020.100027.

42. Lewis, T.L., Jr., Turi, G.F., Kwon, S.K., Losonczy, A., and Polleux, F. (2016). Progressive Decrease of Mitochondrial Motility during Maturation of Cortical Axons In Vitro and In Vivo. Curr Biol *26*, 2602-2608. 10.1016/j.cub.2016.07.064.

43. Courchet, J., Lewis, T.L., Jr., Lee, S., Courchet, V., Liou, D.Y., Aizawa, S., and Polleux, F. (2013). Terminal axon branching is regulated by the LKB1-NUAK1 kinase pathway via presynaptic mitochondrial capture. Cell *153*, 1510-1525. 10.1016/j.cell.2013.05.021.

Chapter 4: Hippocampal circuit deficits in a mouse model of Alzheimer's disease

Daniel M. Virga, Justin K. O'Hare, Attila Losonczy, Franck Polleux

4.1 Chapter Introduction

Much of what we know about Alzheimer's disease is restricted to the cellular and molecular phenotypes and hallmarks of the disease, as well as the clinical, behavioral and cognitive deficits reported in humans. Very little work, if any, has managed to branch the synaptic and cellular deficits observed in Alzheimer's disease with functional, circuit, and behavioral deficits. Recently, however, labs have begun to probe these more complex circuit deficits in Alzheimer's disease model. In this chapter, I did exactly that: determined the circuit deficits within CA1 of the hippocampus at two distinct pathological timepoints in the J20 Alzheimer's disease mouse model.

Much of the limited work that has been published regarding hippocampal CA1 activity in an Alzheimer's disease model have reported, to some extent, spatial encoding deficits and neuronal hyperactivity. However, there is not a clear consensus due in part to the limited number of papers published, and the variability in ages and techniques. Using *in vivo* two-photon calcium imaging at two pathologically distinct time-points in disease progression, I was able to demonstrate that hippocampal encoding deficits largely arise due to population rigidity, while individual place cell properties and basic transient properties remain mostly intact.

I conceived of and carried out every experiment in this project, with analysis support from Dr. Justin O'Hare. The entire manuscript, including the figures, was drafted by me.

4.2 Abstract

Alzheimer's disease (AD) is a progressive, currently irreversible neurodegenerative disease that causes significant deficits in cognition, learning, and memory. Though significant progress has been made to uncover the molecular and cellular mechanisms of amyloid β-driven synaptic loss and ultimately neuronal loss in AD, the circuit defects characterizing cortical or hippocampal circuits during AD progression are still poorly characterized. Here, we probed functional properties of the CA1 region of the hippocampus in a J20 ($APP^{SWE,IND}$) mouse model of AD. *In vivo* longitudinal 2-photon Ca^{2+} imaging in awake, behaving mice during two navigational and behavioral tasks demonstrates that CA1 pyramidal neurons (CA1 PNs) exhibit increased rigidity in spatial representations throughout disease progression, in addition to remapping deficits, despite limited changes in basic place cell properties. These results provide an extensive characterization of population-level hippocampal circuit dysfunction throughout the progression of AD, and emphasize the importance of establishing clear, circuit-level readouts for AD mouse models.

4.3 Introduction

Spatial memory and navigation deficits are some of the first symptoms reported in individuals with Alzheimer's disease, with the majority of AD patients exhibiting spatial memory deficits (Wattmo et al. 2018; Hope et al. 1994). Despite significant research on the molecular, cellular, and synaptic mechanisms of amyloid-β (Aβ) pathology in AD, little is known about how neuronal circuits are impacted in the disease, and specifically how circuit dysfunction could lead to spatial memory loss and broader behavioral and cognitive deficits.

Extensive work has uncovered the importance of the entorhinal cortex and hippocampal circuits in spatial memory and navigation, both in humans and in rodents (O'Keefe and Dostrovsky 1971; O'Keefe and Nadel 1978; Ekstrom et al. 2003; Moser et al. 2015; Tsitsiklis et al. 2020). Specifically, grid cells in the medial entorhinal cortex and place cells in the hippocampus are populations of neurons selectively tuned for spatial location, such that as an animal navigates an environment, external sensory cues ultimately lead to reliable firing of individual neurons at specific locations in the environment. In the dorsal CA1 region of the hippocampus, place cell ensembles are formed as an animal becomes familiar with and forms a representation of the contextual environment (Moser et al. 2008). A balance between stability and flexibility of this spatial representation must also be maintained in order to retain cognitive flexibility. Though

significant progress has been made to understand how CA1 PNs contribute to building and maintaining cognitive spatial maps, how these cells are impacted in AD and therefore whether and when CA1 PNs dysfunction could account for spatial memory deficits is still unclear.

In order to probe this question, we recorded activity from place cells in the hippocampus of the J20 transgenic AD mouse model using *in vivo* two-photon Ca^{2+} imaging (Mucke et al. 2000). This model of AD expresses a mutant form of the human amyloid precursor protein (APP) carrying both the familial Swedish and Indiana ($APP^{SWE,IND}$) mutations which drastically increases its processing through the amyloidogenic pathway leading to increased production and extracellular accumulation of pathogenic Aβ42 peptides. These extracellular Aβ42 peptides form first soluble oligomers (dimers and trimers mostly) that ultimately aggregate into larger insoluble fibrils and amyloid plaques (Sheng et al. 2012). During early stages of the disease, when soluble Aβ42 oligomers (Aβ42o) are present and before plaques are detected, Aβ42o triggers excitatory (E) synapse loss (Jacobsen et al. 2006; Mairet-Coello et al. 2013; Mucke et al. 2000). Importantly, we tested two pathologically distinct timepoints for our experiments: 3 and 6 months. At 3 months, J20 mice exhibit elevated levels of soluble Aβ42 oligomers throughout the cortex and the hippocampus which strongly correlates with excitatory synaptic loss, but critically lack Aβ plaques or fibrils; at 6 months, J20 mice exhibit not only elevated levels of soluble Aβ42, but fibrils and plaques, in addition to increased neuronal loss and spatial memory deficits (Hong et al. 2016; Mucke et al. 2000; Wright et al. 2013; Cheng et al. 2007; Mairet-Coello et al. 2013).

Here, we report that basic transient properties are largely spared across pathological timepoints in J20 mice, with no differences in basic place cell properties observed. However, we find increased rigidity in spatial tuning at a population level in J20 mice that progresses with disease pathology and correlates with unreliability in place cell remapping and behavior. Together, these large-scale deficits in CA1 circuit properties indicate a defect in hippocampal spatial encoding that represents a circuit-level readout of early AD pathology.

4.4 Results

4.4.1 Basic transient and place cell-specific properties of CA1 pyramidal neurons are largely spared across age in J20 mice

To determine whether functional deficits occur in the hippocampus of a mouse model of Alzheimer's disease, we first characterized whether there were any differences in basic transient properties in CA1 pyramidal neurons (PNs) at 3 months and 6 months. To test this, we used *in vivo* two-photon microscopy-based calcium (Ca^{2+}) imaging of CA1 PNs in head-fixed, awake and behaving wild-type (WT; non-transgenic, littermate controls) and J20 (hemizygously expressing $hAPP^{Swe/Ind}$) mice (**Figure 1A-B**).

First, we used in utero electroporation (IUE) at E15.5 allowing expression of a cytoplasmic fluorescent reporter (tdTomato) in pyramidal neurons in the dorsal CA1 region of the hippocampus. We used this cell filler in order to validate synaptic loss in J20 mice following all experiments (**Figure 1C**). We confirm and extend previous analyses (Mairet-Coello et al. 2013; Lee et al. 2022) demonstrating a significant loss of ~30% of dendritic spines at 3 months and 6 months in the J20 compared to WT littermates (**Figure 1C**).

Next, we stereotactically injected dorsal CA1 of either WT or J20 mice with a recombinant adeno-associated virus (rAAV) expressing the genetically encoded Ca^{2+} indicator, GCaMP6f, in order to record neuronal activity at either P75 (15 days before 3 months) or P165 (15 days before 6 months). Following injection, a cannula was implanted immediately dorsal to CA1 and a metal head-post attached to the skull for visualization via 2-photon (2P) microscopy. Using this technique, we were able to record longitudinally hundreds of CA1 PNs simultaneously in the stratum pyramidale (SP) (**Figure 1A**). We then habituated and trained water-deprived mice to run on a linear track while randomly providing water rewards, known as random foraging and described previously (Danielson et al. 2016, Blockus et al. 2021, O'Hare et al. 2022), for 14 consecutive days. Following training, at which point mice were running at least 15 laps per session for a single, randomly dispersed water reward, we began six days of 2P Ca^{2+} imaging of CA1 PNs as the mice navigated a novel track, decorated with spatial cues as landmarks (**Figure 1B**).

We first analyzed basic transient properties of CA1 PNs, including somatic Ca^{2+} transient frequency—how often the neurons exhibited Ca^{2+} transients (**Figure 2A**), duration—how long Ca^{2+} transients lasted (**Figure 2B**), and amplitude—the average peak of each Ca^{2+} transient (**Figure 2C**). When

Figure 1

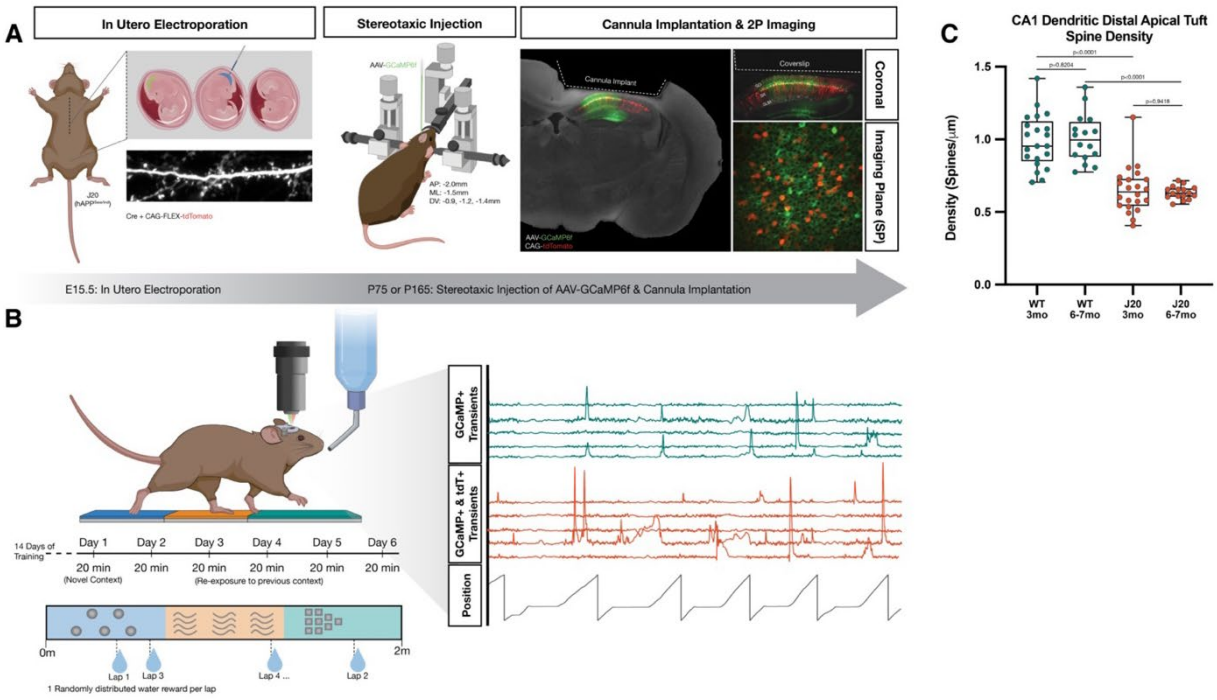

Figure 4.1: *In vivo* two-photon calcium imaging in an awake behaving mouse model of Alzheimer's disease.
(**A**) Schematic of experimental design. In utero electroporation (left) sparsely targets CA1 of the hippocampus. Once P75 or P165, mice were injected with AAV-GCaMP6f (middle) and implanted with a cannula and metal headpost. Representative images (right) of craniotomy and cannula implantation, highlighting removal of the cortex, placement of coverslip over CA1, and the imaging plane during two-photon imaging. (**B**) Schematic of imaging and random foraging behavioral paradigm. Mice are water deprived and trained, head-fixed, on decreasing quantities of water rewards while running on a cue-less linear track for two weeks following injection with AAV-GCaMP. Mice are then imaged daily for twenty minutes using two-photon Ca^{2+} imaging while running on a cue-rich belt for a single water reward randomly dispersed once per lap. Position and Ca^{2+} transients are simultaneously recorded. (**C**) Quantification of postsynaptic synapse density in the distal apical tuft dendrites of WT and J20 mice at 3 and 6-7 months following in utero electroporation and *in vivo* two-photon imaging. There is a significant decrease in apical tuft spine density at 3 months in J20 mice which persists through to 6 months, but does not get significantly worse.

comparing WT and J20 mice, we found, at 3 months, there was a significant increase in transient frequency in J20 animals, but no significant differences in duration or amplitude. When averaging across the entire population of imaged neurons across all WT or J20 mice, we find a moderate but significant increase in transient frequency in J20 animals compared to WT, as well as a significant decrease in transient duration and amplitude in J20 animals. At 6 months, we found no significant changes in transient properties between WT and J20 mice. However, we observed moderate but significant increases in transient frequency and decreases in transient duration and transient amplitude in J20 mice when averaging across the entire population of imaged neurons. These data imply that CA1 PNs are generally hyperactive at 3 months, but not at 6 months, which are in accordance with previous reports in mice and patients (Šišková et al. 2014; Chin et al. 2005; Palop et al. 2007; Bushe et al. 2008; Grienberger et al. 2012; Rudinskiy et al. 2012).

We next measured more specific place cell properties of CA1 PNs, including place cell probability—the fraction of all imaged cells that had spatially-tuned activity (place fields; **Figure 2D**), place field width (**Figure 2E**), sensitivity—the probability of detecting Ca^{2+} events during each of place field transversal (**Figure 2F**), specificity—the fraction of all detected Ca^{2+} events occurring inside versus outside the place field (**Figure 2G**), and spatial information—the amount of spatial information each place cell encodes (**Figure 2H**). We detected no significant differences in place cell properties when comparing WT and J20 mice at either 3 months or 6 months. However, when averaging across the population of imaged PNs, we found subtle but significant increases in place cell probability, specificity, sensitivity, and spatial information at 3 months in J20 mice, decreases in place field width in J20 mice compared to WT at 3 months, and increases in only place cell fraction and spatial information in J20 compared to WT only at 6 months. Together, these data demonstrate that basic place cell properties are largely spared in J20 mice across age and pathological progression. Overall, analyses of both transient and place cell properties indicate that, despite significant excitatory synaptic loss, most basic neuronal properties and spatial tuning properties of CA1 PNs remain largely unaffected in the J20 AD mouse model.

Figure 2

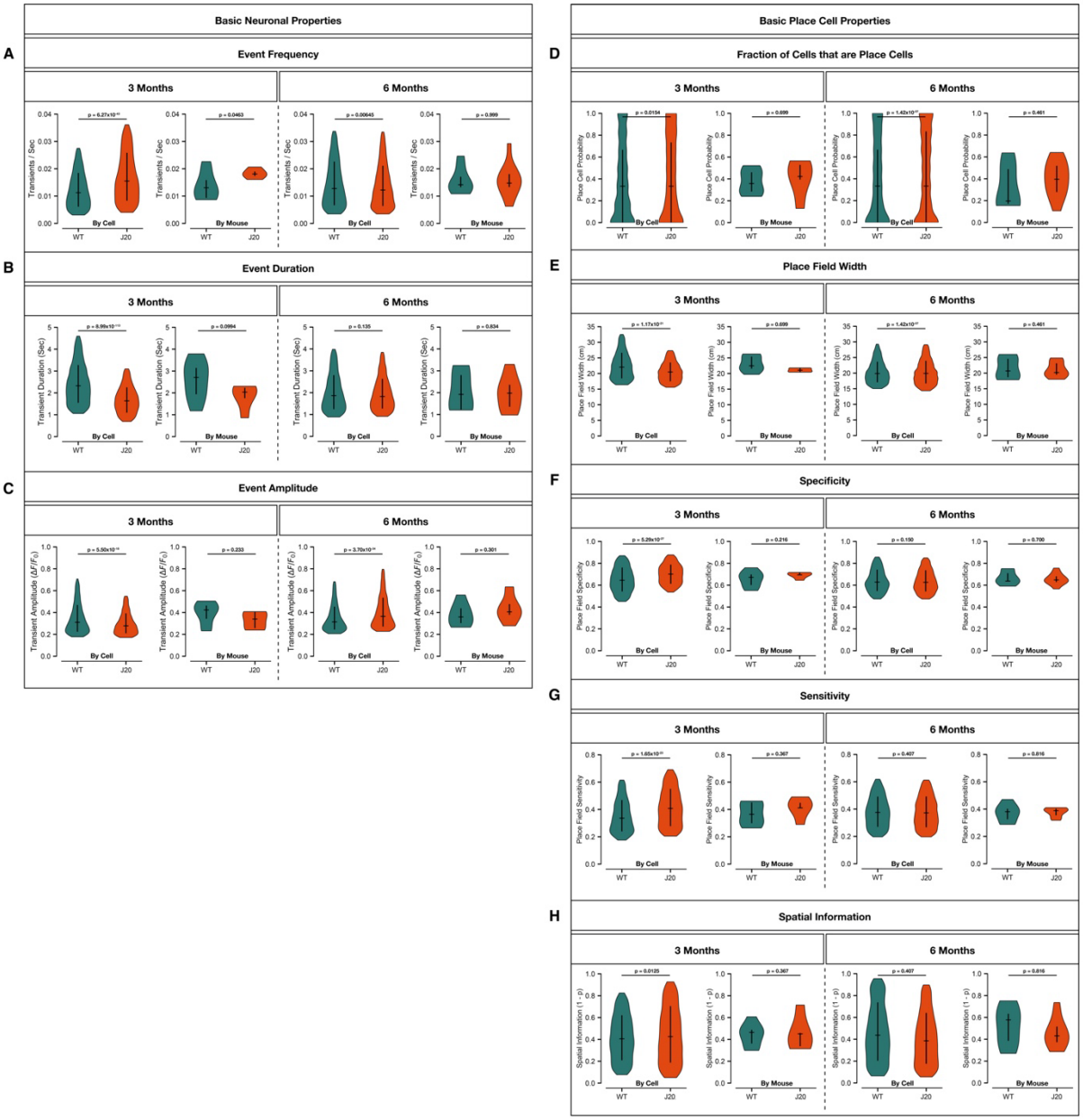

Figure 4.2: Basic transient and place cell-specific properties remain mostly unchanged at 3 and 6 months in CA1 of the hippocampus of a J20 mouse model.

(**A-C**) Basic neuronal properties in WT and J20 mice at three and six months, grouped as an entire population of neurons (left) or as individual mice (right). N = 3617 WT cells and 2195 J20 cells at 3mo from 13 mice (8 WT, 5 J20); N = 2731 WT cells and 4964 J20 cells at 6 months from 18 mice (7 WT, 11 J20). At three months, J20 mice exhibit a significant increase (p=0.0463) in calcium transient frequency at a population and animal levels (A), while transient duration (B) and amplitude (C) are significantly altered at a population level. At 6 months, there are no significant differences between J20 and WT mice at an animal level, while a significant trend in transient frequency and amplitude are detected at a cell population level. (**D-H**) Basic place cell properties in WT and J20 mice at 3 and 6 months, grouped as the entire cell population imaged (left) or as individual mice (right). N = 2570 place cells detected in WT and 1524 place cells detected in J20 mice at 3 months from 13 mice (8 WT, 5 J20); N = 1827 WT cells and 3497 J20 cells at 6 months from 18 mice (7 WT, 11 J20). At 3 months, there are no significant differences between J20 and WT mice when testing all mice, but significant increases in the fraction of place cells (D), specificity (F), sensitivity (G), and spatial information (H), and a decrease in place field width (E) at a population level. At 6 months, there are no significant differences between J20 and WT mice when considering all mice imaged—however, there is a significant increase in the place cell fraction (D) and decrease in spatial information (H) at a population level. Error bars represent SEM. Violin plots represent the median (middle), 1st, and 3rd quartiles, clipped at the 10th and 90th.

4.4.2 Place cells in J20 mice exhibit increased stability that strengthens with pathological progression.

Having established that basic transient and spatial tuning properties remain largely unaffected in J20 animals at 3 and 6 months, we next analyzed the flexibility of spatially tuned cells across time. It is known that spatial representations in CA1 drift over time as mice are exploring an environment (Ziv et al. 2013; Keinarth et al. 2022; Driscoll et al. 2022). Because we captured the same field of view each day of imaging, we could faithfully record activity from the same neurons longitudinally across all six days of imaging, allowing us to quantify place cell remapping across days through repeated exposure to the same cue-rich belt. To do this, we first identified all cells that were place cells on Day 1 of imaging in WT or J20 mice at either 3 or 6 months, and sorted them by peak activity (**Figure S1A,C**). When recording a large enough sample of dorsal CA1 PNs, spatially-tuned place cells tile the entire two-meter linear belt as previously reported (Wilson & McNaugton 1993; Franck et al. 2004; Sheffield et al. 2017; Zhao et al. 2020). Interestingly, however, when we use the same spatial sorting on Day 1 and subsequently map the activity of those same CA1 PNs across Days 2-6, we observe that the population of place cells in J20 mice qualitatively display less remapping than in WT mice (**Figure S1A,C**). To quantify this, we calculated the tuning curve correlations of all cells across the six days of imaging, quantitatively capturing how stable the spatial representation of their environment is at the population level across days (**Figure S1B,D**). As expected, in WT mice, we observe a gradual decline in the tuning curve (TC) correlations across days of recording—a direct reflection of representational drift in CA1. Interestingly, in J20 mice, at both 3 months and 6 months, we observed significantly increased TC correlations when compared to WT mice of the same age. These results indicate that spatial representation in dorsal CA1 of J20 mice is significantly more rigid (i.e., less flexible) than in WT littermates.

To further examine this increased rigidity in the J20 mice, we next calculated the population vector correlations for each location bin of the linear track across all six days of imaging (**Figure 3**). In essence, population vector correlations are a measure of how the activity of the entire neuronal population encodes each location, and, as a consequence, how spatial representation of each location of the environment remains stable or changes across time. Similar to the tuning curve correlations, analysis of population

Figure 3

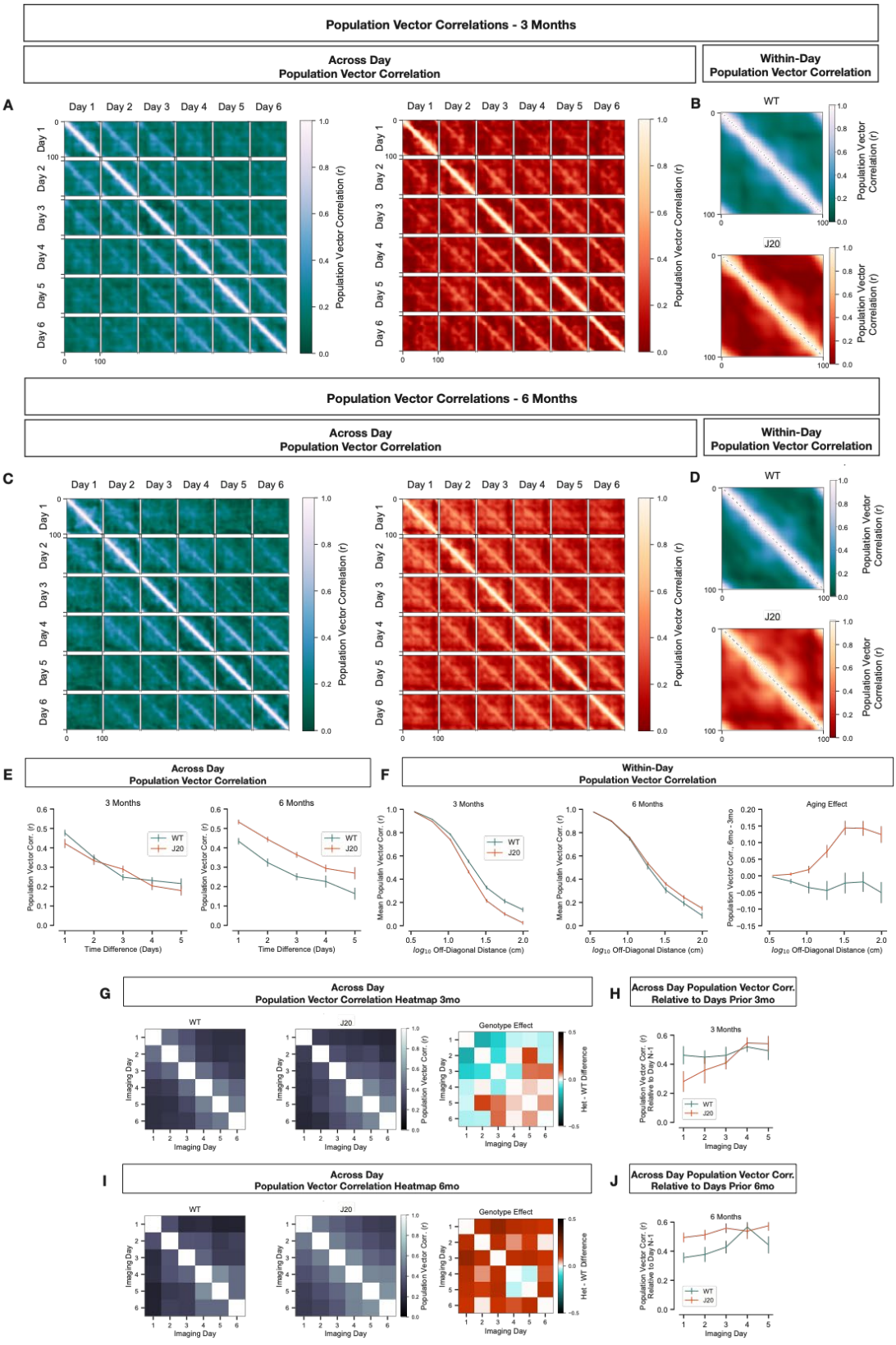
Population Vector Correlations - 3 Months
Across Day
Population Vector Correlation
Within-Day
Population Vector Correlation
A
B
WT
J20
Day 1
Day 2
Day 3
Day 4
Day 5
Day 6
Population Vector Correlation (r)
Population Vector Correlations - 6 Months
Across Day
Population Vector Correlation
Within-Day
Population Vector Correlation
C
D
E
Across Day
Population Vector Correlation
3 Months
6 Months
Population Vector Corr. (r)
Time Difference (Days)
WT
J20
F
Within-Day
Population Vector Correlation
3 Months
6 Months
Aging Effect
Mean Population Vector Corr. (r)
log10 Off-Diagonal Distance (cm)
Population Vector Corr., 6mo - 3mo
G
Across Day
Population Vector Correlation Heatmap 3mo
H
Across Day Population Vector Corr.
Relative to Days Prior 3mo
WT
J20
Genotype Effect
Imaging Day
Het - WT Difference
Population Vector Corr. (r)
Population Vector Corr. Relative to Day N-1
I
Across Day
Population Vector Correlation Heatmap 6mo
J
Across Day Population Vector Corr.
Relative to Days Prior 6mo

Figure 3 Cont…

Figure 4.3: Place cells in APP mice exhibit increased stability that strengthens with pathological progression.
(**A,C**) Population vector correlation heat-map matrix across all six days of imaging at 3 months (A) and 6 months (C) in WT (left) and J20 (right) mice. For each location (100, 2 cm bins), a population vector correlation is calculated and plotted against that same location within and across days. (**B,D**) Population vector correlation within-day heat-maps aggregating all days of imaging at 3 months (B) and 6 months (D) in WT (top) and J20 (bottom) mice. For each location (100, 2 cm bins), a population vector correlation is calculated and plotted against that same location within days and averaged across all days. (**E**) Absolute population vector correlations at 3 (left) and 6 (right) months. A significant, uniform decrease in correlation occurs the larger the time difference at both timepoints, with no difference in correlations at 3 months between WT and J20 mice, but a significant increase in correlation in J20 mice at 6 months. Two-way ANOVAs, 3mo: disease effect: $F_{(1,58)} = 0.85$, $p = 0.36$; time effect: $F_{(4,54)} = 15.49$, $p < 0.0001$; no interaction; 6mo: disease effect: $F_{(1,80)} = 20.081$, $p < 0.0001$; time effect: $F_{(4,80)} = 18.13$, $p < 0.0001$; no interaction. (**F**) Within-day population vector correlation off-diagonal distance at 3 and 6 months, and the subsequent differences between the two time points (6mo - 3mo). There's a significant decrease in mean population vector correlation over time in both WT and J20 mice at both timepoints. At 3 months, J20 mice exhibit overall smaller mean population vector correlations, which shifts to a higher correlation at 6 months, while WT mice have a consistent correlation at both time points, as seen by a large positive when subtracting the two timepoints in J20 mice. Two-way ANOVAs, 3mo: disease effect: $F_{(1,525)} = 8.15\text{x}10^{-12}$, $p = 1.00$; distance effect: $F_{(7,525)} = 4.46\text{x}10^{3}$, $p < 0.0001$; interaction: $F_{(7,525)} = 1.83$, $p < 0.001$; 6mo: disease effect: $F_{(1,707)} = 1.50\text{x}10^{-12}$, $p = 1.00$; distance effect: $F_{(7,707)} = 3.15\text{x}10^{3}$, $p < 0.0001$; interaction: $F_{(7,525)} = 2.71$, $p = 0.0088$. Three-way ANOVA, Aging diff: disease effect: $F_{(1,1232)} = 11.75$, $p = 0.00063$; distance effect: $F_{(7,1232)} = 6309.21$, $p < 0.0001$; age effect: $F_{(1,1232)} = 14.30$, $p = 0.00016$; 3-way interaction: $F_{(22,1232)} = 6.50$, $p < 0.0001$; (**G, I**) Matrices of across-day population vector correlations at G) 3 and I) 6 months in WT and J20 mice, and a difference matrix between WT and J20 matrices. (**H, J**) Across-day population vector correlations relative to the number of days prior. For WT mice, at 3 and 6 months, there's a uniform correlation across days. For J20 mice, there's an increase in correlation across imaging days at 3mo, which shifts to a stable correlation across days at 6mo. Similar to E and F, J20 mice at 6mo exhibit a significant increase in population vector correlation. Two-way ANOVAs, 3mo: disease effect: $F_{(1,58)} = 1.81$, $p = 0.18$; time effect: $F_{(4,58)} = 1.99$, $p = 0.11$; no interaction; 6mo: disease effect: $F_{(1,80)} = 13.70$, $p = 0.00039$; time effect: $F_{(4,58)} = 2.32$, $p = 0.064$; no interaction.

vector correlations for each day reveals that the spatial representation gradually becomes less correlated in WT mice at both 3 and 6 months (**Figure 3A,C**). In essence, the CA1 PN population is encoding the same locations in space less and less similarly over time. However, when comparing the population vector correlation between Day 1 and subsequent days in J20 mice, they appear more correlated, especially at 6 months. To quantify this, we compared how similar the population vector correlations were between each subsequent day, as a function of absolute time (**Figure 3E**). This analysis revealed a significant decrease in the population vector correlations for both WT and J20 mice as you increase the time difference at both 3 and 6 months. When comparing WT and J20 mice at 3 months, we find no significant difference in the population vector correlations, regardless of the time difference measured. However, at 6 months, we observe a significant increase in the population vector correlations at all time-points in the J20 mice only, meaning the representation of each location held by the population is more similar across days in J20 mice at 6 months compared to WT mice. Again, this implies that the spatial representation within the CA1 PN population becomes much more rigid in the J20 mice as AD pathology progresses.

Because these previous measurements were examining correlations across days, we next wanted to determine within individual days, how the population encodes space. To do this, we took a similar approach as previously, this time collapsing all six days into an average population vector correlation for the environment at both 3 and 6 months, visualized as a correlation heatmap (**Figure 3B,D**). Here, the more refined the population encoding is, the tighter the population correlation will be—i.e., the population vector correlation will more steeply decline as you move away from the diagonal, which represents perfect correlation, as the population will encode one spatial bin significantly differently than the spatial bin immediately preceding or following. To quantify this, we measured the mean population vector correlation as a function of the distance from the diagonal (**Figure 3F**). As expected from the qualitative heatmaps, the closer you are to the diagonal, the higher the mean population vector correlation, and the further you get from the diagonal, the smaller the mean population vector correlation. In essence, the population is encoding positions that are further away from each other much differently than neighboring locations. Interestingly, however, we find that the mean population vector correlation is lower in J20 mice than in WT mice at 3 months, and higher in J20 mice than in WT mice at 6 months. To better visualize these changes over the progression of the disease, we subtracted the 3 month values from the 6 month values to create

a fold-change difference between these two time-points. When quantifying the changes in mean population vector correlation as a fold-change, dependent on pathological time-point, we find a significant positive change in correlation in the J20 mice at the two pathological stages, and a nearly stable correlation in the WT mice (**Figure 3F**). Again, these data, in addition to the across day population vector analyses, indicate that, as a whole, the CA1 PN population becomes increasingly rigid in its representation of space in J20 mice when compared to WT mice between 3 and 6 months.

In order to better understand how the population vector correlation changes across behavior and genotype, we extracted the correlations for each day as individual values, and re-plotted them as their own matrices at both 3 and 6 months (**Figure 3G,I**). This then allowed us to subtract the correlations values between WT and J20 mice to produce a difference matrix dependent now on the genotype of the animal—i.e, whether the mouse has AD or not. What this qualitatively revealed, and was confirmed through quantification (**Figure 3H,J**) was at 3 months, J20 mice start off with more distinct population vectors, but through repeated exposure to the same environment, the population vector increases in correlation. This phenomenon of increasing rigidity within the six days of imaging is not seen in the WT animals, where the population vector correlation is stable across days of imaging. Interestingly, at 6 months, the J20 animals have significantly higher correlations across all days of imaging compared to WT mice, and their representations do not change through repeated exposure. These data indicate that WT mice retain a homogeneously flexible representation of their environment across ages, while J20 mice through pathological progression start out with increasingly rigid representations that ultimately result in very stable spatial representations. Overall, these data indicate that J20 mice, especially at 6 months, are forming increasingly rigid or inflexible representations of their environments compared to WT mice, which could have significant implications for context discrimination and behavioral performance.

4.4.3 Spatial encoding rigidity correlates with symmetric past and future decoding reliability

Given the decreased spatial tuning flexibility of the CA1 PN population in J20 mice, we next examined whether these differences in spatial coding properties would alter the spatial representation encoded by the population using a decoding approach. To do this, we trained a support vector machine (SVM) model on either WT or J20 population neuronal data at 3 and 6 months and tested how reliably the decoder predicted the physical location of a mouse compared to the actual recorded position of the mouse (**Figure 4**). Across

Figure 4

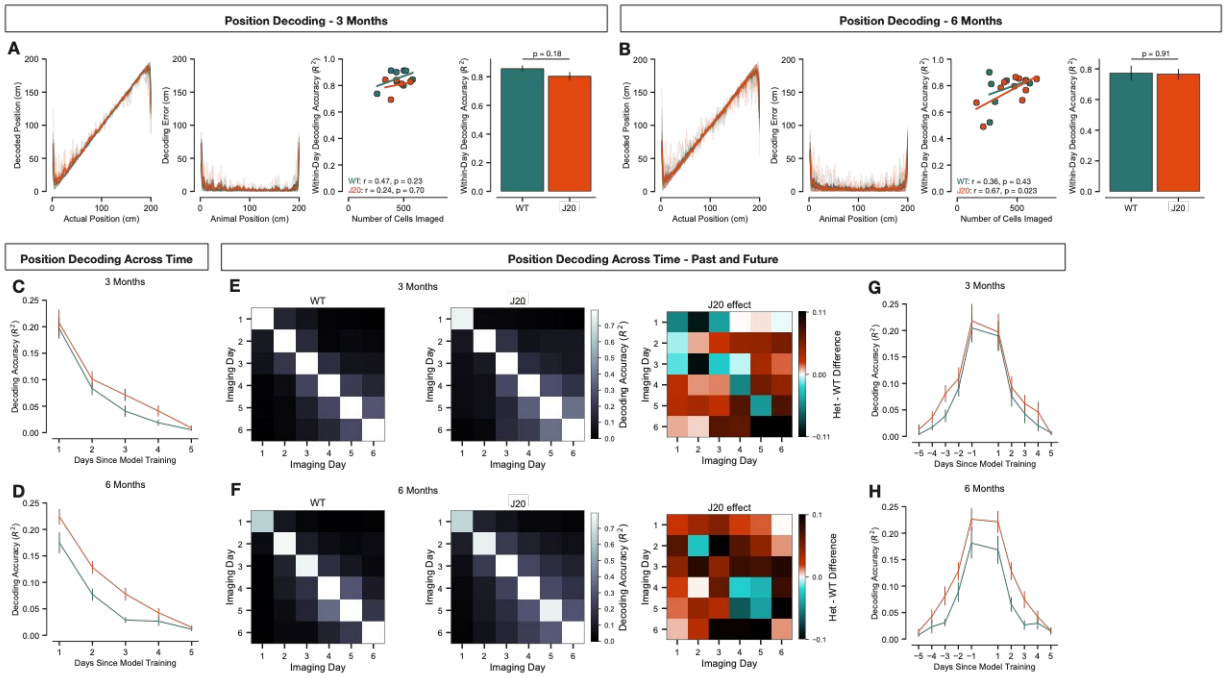

Figure 4.4: Position decoding reliability is not significantly different between WT and J20 animals across time

(**A-B**) Decoding performance of animal position at A) 3 and B) 6 months. Decoding by a model trained on population data is similarly reliable between WT and J20 mice at both ages, with a slight but insignificant decrease in reliability at 3 months, regardless of the number of cells used in training. (**C-D**) Decoding accuracy as a function of absolute days since training the model. Decoding accuracy significantly decreases the larger the difference in time from training to prediction, in both WT and J20 mice at 3 months (C) and 6 months (D), with reliability being slightly higher in J20 mice at 3 months, and significantly higher at 6 months. Two-way ANOVAs, 3mo: disease effect: $F_{(1,364)} = 2.00$, $p = 0.16$; time effect: $F_{(4,364)} = 35.39$, $p < 0.0001$; no interaction; 6mo: disease effect: $F_{(1,500)} = 17.82$, $p < 0.0001$; time effect: $F_{(4,500)} = 48.89$, $p < 0.0001$; no interaction. (**E-F**) Matrices of decoding accuracy as a function of days before or after training input at both E) 3 and F) 6 months in WT and J20 mice, and a difference matrix between WT and J20 matrices. (**G-H**) Decoding accuracy as a function of days before or after training input at both 3 months (G) and 6 months (H). At both time points, decoding accuracy significantly decreases in both WT and J20 mice the further away in time. At 3 months, both WT and J20 mice exhibit slightly, though insignificantly, increased reliability of decoding when testing the model against days prior to the training day when compared to testing against days after the training day (G). At 6 months, while decoding accuracy remains slightly higher when testing against days prior to the training day in WT mice, in J20 mice, decoding accuracy for days prior to or after training days is more equally accurate, though again not significantly (H). J20 mice exhibit significantly higher overall decoding accuracy at 6 months than WT mice. Three-way ANOVAs, 3mo: disease effect: $F_{(1,363)} = 2.00$, $p = 0.16$; time effect: $F_{(4,363)} = 35.37$, $p < 0.0001$; past/future effect: $F_{(1,363)} = 0.76$, $p = 0.38$; no interaction; 6mo: disease effect: $F_{(1,499)} = 17.79$, $p < 0.0001$; time effect: $F_{(4,499)} = 48.83$, $p < 0.0001$; past/future effect: $F_{(1,499)} = 0.35$, $p = 0.55$; no interactions.

both time points, 3 and 6 months, decoding reliability was consistent between both WT and J20 mice with minimal error (**Figure 4A-B**). When quantifying reliability as a measure of absolute time from the day on which the model was trained, we found first a characteristic decline in accuracy the further from the training day you test the model, which is expected, in both WT and J20 mice (**Figure 4C-D**). Interestingly, the model consistently performs significantly better when predicting the mouse's location in J20 mice compared to WT mice at 6 months, potentially due to the increased rigidity in the population representation of the environment. Importantly, the number of cells fed to the model for training did not impact the performance of the model (**Figure S2**). In order to better understand this phenomenon, we split the comparison of training versus prediction day into either days prior or days following that training input (**Figure 4E-H**). At 3 months, when measuring the decoding accuracy of the model backward or forward in time—i.e., how well does the model when trained on a specific day decode the position of the mouse on days prior or on subsequent days—we found a similar asymmetric decoding reliability in WT and J20 mice, such that the model was more accurate at decoding the location of the mice when testing against days prior to the day on which the model was trained. At 6 months, this asymmetric decoding trend holds in the WT animals; interestingly, however, J20 mice exhibit a more symmetric decoding reliability at this later time-point—i.e., the model is equally as reliable at predicting the location of the mouse when testing against days that occurred prior to or after the training input day. In summary, these data suggest that, because the population of place cells are more rigid in their tuning in J20 mice than in WT mice, it is marginally easier to predict the location of these mice and potentially as easy to predict the location in the past as in the future.

4.4.4 Place field remapping deficits during goal-oriented learning fail to correlate with behavior in aged J20 mice

J20 mice, similarly to humans with AD, exhibit significant spatial memory and navigation early in the disease pathology, often measured through the Morris Water Maze assay (Cheng et al. 2007; Meilandt et al. 2008), which persists throughout pathology progression (Palop et al. 2003; Galvan et al. 2006; Sanchez-Mejia et al. 2008; Cissé et al. 2011; Sanchez et al. 2011). To determine whether J20 mice exhibit any changes in behavior due in part to the increased rigidity of the spatial representation in CA1, we used a goal-oriented learning paradigm (**Figure 5**) while recording CA1 PN activity using *in vivo* 2P Ca^{2+} imaging (Danielson et al. 2016; Turi et al. 2019; Zaremba et al. 2017).

Briefly, in goal-oriented learning, the mice run on a cue-rich linear belt with a single reward at a fixed position on the belt. The mice undergo three, 20 minute long imaging sessions where the reward is in the first zone, at which point the location of the reward was switched to a new, fixed zone at a different location along the belt for the final three days of imaging (**Figure 5A**). This paradigm, unlike random foraging, requires the mice to learn the first reward location along the belt in order to receive a water reward on the first three days, but then 'forget' and learn the location of a new reward for the final three days Previous work showed that, within a few training sessions, mice learn the location of the reward along the belt which is manifested by (1) decreasing their running speed immediately prior to the reward location, and (2) increasing their licking frequency immediately prior to and within the reward location, limiting residual licking outside the reward zone.

At both 3 and 6 months of age, WT and J20 mice successfully learned the location of the first reward by Day 3 as demonstrated by deceleration at the reward location and licking in anticipation of and within the reward zones (**Figures 5B,D; S3C-F, S4A-H**) with no significant difference in velocity or number of laps run (**Figure S4I-J**). However, we noticed that at 3 months, J20 mice tend to lick significantly more outside the reward location at Day 3 and Day 6 compared to WT mice, and that at Day 6, J20 mice still display significantly more licks in the previous reward location (**Figure 5B**), strongly suggesting that the J20 mice learn the locations of the first and second rewards less precisely, at least based on licking behavior. When quantifying two features of goal-oriented learning—anticipatory licking and deceleration—we find that, at 3 months, J20 mice barely perform better than chance when it comes to anticipatory licking, whereas WT mice increase their rate of anticipatory licking at both reward locations, increasing in reliability through repeated exposure to the same reward zone (**Figure 5C**). This same trend is reflected to a lesser degree in the anticipatory deceleration, where both WT and J20 mice increasingly decelerate, especially once the reward position is changed to a new location. However, J20 mice are slightly, though significantly, worse at slowing down than WT mice (**Figure 5D-E**). At 6 months, although we observed relatively similar behavioral performances with anticipatory licking and deceleration in WT mice, J20 mice perform nearly as well as WT mice at the first reward zone, but are more negatively impacted when the reward is shifted to a new location. J20 mice exhibit a much steeper decline in anticipatory licking on Imaging Day 4 and a

Figure 5

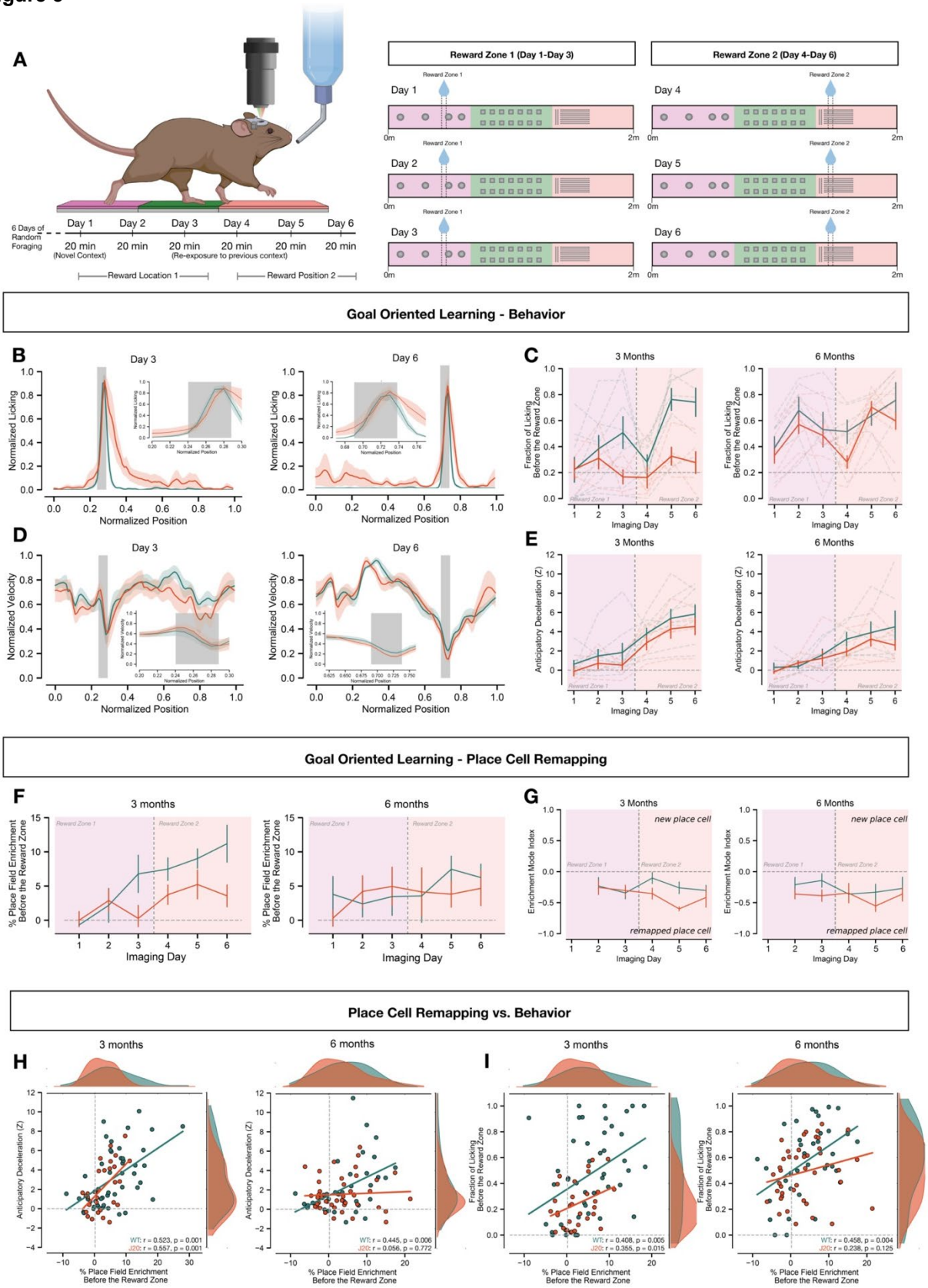
A
6 Days of Random Foraging
Day 1
Day 2
Day 3
Day 4
Day 5
Day 6
20 min (Novel Context)
20 min
20 min (Re-exposure to previous context)
20 min
20 min
20 min
Reward Location 1
Reward Position 2
Reward Zone 1 (Day 1-Day 3)
Reward Zone 2 (Day 4-Day 6)
Reward Zone 1
Reward Zone 2
0m
2m
Goal Oriented Learning - Behavior
B
Day 3
Day 6
Normalized Licking
Normalized Position
C
3 Months
6 Months
Fraction of Licking Before the Reward Zone
Imaging Day
D
Normalized Velocity
E
Anticipatory Deceleration (Z)
Goal Oriented Learning - Place Cell Remapping
F
3 months
6 months
% Place Field Enrichment Before the Reward Zone
G
Enrichment Mode Index
new place cell
remapped place cell
Place Cell Remapping vs. Behavior
H
I
WT: r = 0.523, p = 0.001
J20: r = 0.557, p = 0.001
WT: r = 0.445, p = 0.006
J20: r = 0.056, p = 0.772
WT: r = 0.408, p = 0.005
J20: r = 0.355, p = 0.015
WT: r = 0.458, p = 0.004
J20: r = 0.238, p = 0.125

Figure 5 Continued…

Figure 4.5: J20 mice show deficits in goal-oriented learning at 3 months which correlates with a decrease in place field enrichment.

(**A**) Schema of goal-oriented learning behavioral paradigm. Following fourteen days of training and six days of random foraging, WT and J20 mice are imaged daily for 20 minutes using two-photon Ca^{2+} imaging while they navigate a novel, cue-rich linear belt for a single water reward dispensed per lap at a fixed location. Following the first three days of imaging, the reward location is moved to a second fixed position for the final three days. (**B**) Representative normalized licking plots from all WT and J20 mice undergoing goal-oriented learning at 3 months, specifically Day 3 (the final day of imaging in Reward Zone 1—shaded region) and Day 6 (the final day in Reward Zone 2—shaded region). Inset are the same graphs, re-plotted to focus exclusively on the region immediately before and after the reward zone. Licking peaks in the reward zone on both days, with residual licking outside the reward zone present mostly in J20 mice. (**C**) Quantification of the fraction of licking before the reward zone at 3 (left) and 6 (right) months in WT and J20 mice. At 3 and 6 months, WT mice show increased licking before the reward zone across days, which decreases the first day the reward is moved to a new position (Imaging Day 4). At 3 months, J20 mice do not lick before the reward zone more than chance, but do at 6 months, showing significantly worse performance than WT mice at 6 months. Three-way ANOVAs 3mo: disease effect: $F_{(1,71)} = 15.26$, $p = 0.00021$; time effect: $F_{(2,71)} = 7.58$, $p = 0.0010$; reward context effect: $F_{(1,71)} = 5.71$, $p = 0.020$; no interactions; 6mo: disease effect: $F_{(1,75)} = 3.29$, $p = 0.074$; time effect: $F_{(2,75)} = 11.50$, $p < 0.0001$; reward context effect: $F_{(1,75)} = 2.76$, $p = 0.100$; no interactions. (**D**) Representative normalized velocity plots from all WT and J20 mice undergoing goal-oriented learning at 3 months, specifically Day 3 (the final day of imaging in Reward Zone 1–shaded region) and Day 6 (the final day in Reward Zone 2–shaded region). Inset are the same graphs, re-plotted to focus exclusively on the region immediately before and after the reward zone. Velocity reaches its lowest values in the reward zone on both days, with significant deceleration seen mostly in the second reward zone in both J20 and WT mice. (**E**) Quantification of mice velocity and in particular anticipatory deceleration before the reward zone at 3 (left panel) and 6 months (right panel) in WT and J20 mice. At 3 and 6 months, both WT and J20 mice exhibit a significant decrease in velocity before the reward location across days, though to a slightly, but significantly, less degree in J20 mice than WT mice at 3 months. All mice learn significantly better when exposed to the second reward location. Three-way ANOVAs 3mo: disease effect: $F_{(1,73)} = 4.75$, $p = 0.033$; time effect: $F_{(2,73)} = 3.80$, $p = 0.027$; reward context effect: $F_{(1,73)} = 62.6$, $p < 0.0001$; no interactions; 6mo: disease effect: $F_{(1,75)} = 2.94$, $p = 0.091$; time effect: $F_{(2,75)} = 2.69$, $p = 0.074$; reward context effect: $F_{(1,75)} = 35.90$, $p < 0.0001$; no interactions. (**F**) Quantification of the fraction of place cells that are enriched before the reward zone at 3 (left) and 6 (right) months in WT and J20 mice. At 3 months, WT mice significantly and increasingly enrich place cells before the reward zone across all days, while J20 mice exhibit significantly less enrichment comparatively. At 6 months, there is equal enrichment of place cells before the reward zone in both positions, across all days, in WT and J20 mice. Three-way ANOVAs 3mo: disease effect: $F_{(1,73)} = 7.25$, $p = 0.0088$; time effect: $F_{(2,73)} = 2.74$, $p = 0.071$; reward context effect: $F_{(1,73)} = 18.03$, $p < 0.0001$; no interactions; 6mo: disease effect: $F_{(1,75)} = 0.37$, $p = 0.55$; time effect: $F_{(2,75)} = 0.69$, $p = 0.51$; reward context effect: $F_{(1,75)} = 1.45$, $p = 0.23$; no interactions. (**G**) Quantification of the enrichment mode index, a measure of whether de novo place cells at the reward zone were remapped from an existing location or novel place cells during each day of goal-oriented learning at 3 (left) and 6 (right) months in WT and J20 mice. In both WT and J20 mice, there's a significant preference to remap existing place cells to the reward zone rather than form new place cells. J20 mice at 3 and 6 months slightly, though insignificantly, are biased toward remapping place cells rather than forming new place cells compared to WT mice. Three-way ANOVAs 3mo: disease effect: $F_{(1,55)} = 3.66$, $p = 0.061$; time effect: $F_{(2,55)} = 3.99$, $p = 0.024$; reward context effect: $F_{(1,55)} = 6.27$, $p = 0.015$; 3-way interaction: $F_{(7,55)} = 2.43$, $p = 0.030$; 6mo: disease effect: $F_{(1,60)} = 3.29$, $p = 0.075$; time effect: $F_{(2,60)} = 0.43$, $p = 0.65$; reward context effect: $F_{(1,60)} = 1.97$, $p = 0.166$; no interactions. (**H**) Place field enrichment as a function of anticipatory deceleration at 3 (left) and 6 (right) months in WT and J20 mice. There's a strong, significant, positive correlation between enrichment and deceleration at 3 months in both WT and J20 mice, which goes away only in J20 mice at 6 months, with the correlation remaining significantly positive in WT mice. (**I**) Place field enrichment as a function of anticipatory licking at 3 (left) and 6 (right) months in WT and J20 mice. There's a strong, significant, positive correlation between enrichment and anticipatory licking at 3 months in both WT and J20 mice that decreases only in J20 mice at 6 months, persisting in WT mice.

decrease in deceleration that does not recover to the same extent as WT mice at this crucial point in which the reward is relocated.

It has been well-established that, when performing a task such as goal-oriented learning, the fraction of place fields encoding the reward location increases during learning, which represents a form of neuronal plasticity associated with spatial learning (Hollup et al. 2001; Zaremba et al. 2017; Kaufman et al. 2020). Therefore, we next quantified place cell enrichment at the reward zones in WT and J20 mice at 3 and 6 months (**Figure S3A-B**; **Figure 5F-G**). First, we quantified the fraction of place fields that were enriched prior to the reward zone and found that, at 3 months, WT mice increase enrichment across all days of imaging, while J20 mice have significantly lower fraction of place cell enrichment across all days of imaging (**Figure 5F**). Interestingly, at 6 months, both WT and J20 mice exhibit similar degrees of place field enrichment before the reward locations.

Two potential mechanisms have been proposed to explain place cell enrichment at the reward location during goal-oriented learning (Hollup et al. 2001; Zaremba et al. 2017; Sheffield et al. 2017; Dong et al. 2021): (1) new place cells can emerge at the reward location, i.e., emergence of spatially tuned CA1 PNs which were previously not spatially tuned, and/or (2) remapping of previously existing place cells via a significant shift in the place field to the reward zone. In order to differentiate between these two mechanisms, we developed an enrichment mode index, with positive numbers reflecting the addition of new place cells at the reward zone and negative numbers reflecting remapping of existing place cells (**Figure 5G**). We found that both WT and J20 mice, at 3 and 6 months, preferentially remap existing place fields within their population of spatially tuned cells rather than forming new place cells. Overall, these data indicate, at 3 months, J20 mice have significant remapping deficits compared to WT mice, but these deficits are not detected by 6 months.

Though place field enrichment around a reward is often temporally correlated with learning the reward location, few studies have explored whether enrichment is necessary for behavioral performance (Kaufman et al. 2021). We designed a new type of analysis to determine whether any correlation exists between place field remapping and behavioral performance in WT and J20 mice at 3 and 6 months (**Figure 5H-I**). Interestingly, we find that, though the degree of place field enrichment strongly correlates with both anticipatory deceleration and licking at the reward locations at 3 months in both WT and J20 mice, there is

a strong decorrelation at 6 months in J20 but not in WT mice. In other words, an increase in place field enrichment positively correlates with behavioral performance in the context of spatial learning in both WT and J20 at 3 months, but not at 6 months for the J20 mice. This implies that, contrary to expectations, there is a strong decoupling of behavioral performance with remapping, and thus J20 mice in more advanced stages of disease progression could be using alternative circuit mechanisms to accomplish these behavioral task. Overall, these data indicate there are significant deficits in both behavior and in place field remapping in J20 mice at 3 and 6 months of age.

4.5 Discussion

In order to characterize hippocampal circuit deficits occurring in an AD model, we recorded populations of CA1 PNs from J20 mice at two time points. We found that basic transient neuronal properties are largely unaffected, but that hippocampal neurons are hyperactive at the earliest stages of the disease. The increase in the mean firing rate of CA1 PNs can arise through many potential mechanisms present in AD. First, this increase in CA1 PNs activity could be due to a loss of interneurons as previously reported (Xu et al. 2020), leading to a decrease in inhibitory feedback received by CA1 PNs. An additional explanation, which is also consistent with previous data, is that structural changes to the neurons, including synaptic loss and dendritic shortening, are increasing their intrinsic excitability (Šišková et al., 2014). Finally, Aβ itself has been shown to increase neuronal firing rate, possibly through increases in synaptic AMPA and NMDA receptors (Sanchez-Mejia et al., 2008; Um et al., 2012; Kurudenkandy et al., 2014).

While a significant portion of the literature is in line with our data, implicating hyperactivity as a key early phenotype in AD, both in mice and in humans (Quiroz et al., 2010; Sepulveda-Falla et al. 2012; Filippini et al., 2009; Sperling et al., 2009; Dickerson et al., 2005; Celone et al., 2006; Bakker et al., 2012), there is limited consensus in the field of hippocampal circuit analyses in AD mouse models. While some papers report increases in neuronal activity in CA1 PNs (Busche et al. 2012; Takamura et al. 2021), others report no changes or report hypoactivity (Caccuci et al. 2008; Ying et al. 2022; Zhao et al. 2014; Mably et al. 2017). There are several potential explanations for the differences reported between these previous studies: (1) Most of these previous reports are using different mouse models of AD, with only Ying et al. 2022 using the J20 mouse as described in our paper; (2) several of these previous studies performed recordings of hippocampal activity at different time-points, before or after amyloid plaques formation; (3)

while most of the papers are using microelectrode-based recording techniques, a very small number of studies used *in vivo* two-photon Ca^{2+} imaging, with remarkably different numbers of recorded cells; (4) most papers are using different behavioral paradigms when recording neuronal activity in the hippocampus, including head-fixed linear tracks with or without visual cues, open fields, or recordings under anesthesia.

When examining basic place cell properties, we found no significant differences between WT and J20 mice. Specifically, we found no significant changes in the fraction of place cells, place field width, specificity, selectivity, and spatial information between WT and J20 mice at either 3 or 6 month time points. This indicates, in part, that the hippocampal network is retaining its basic output functions, despite CA1 PNs losing nearly half of inputs from the entorhinal cortex to the apical tuft dendrites (Mairet-Coello 2013; Lee et al. 2022). When comparing our data to the most similar paper previously published (Ying et al. 2022), using the J20 mouse at nearly the same ages, our data is in alignment, as they find only grid cell impairment in J20 mice. The only two place cell property measurements that are widely examined and have achieved near consensus across other papers is spatial information and place field width, with a decrease in spatial information and an increase in width reported in several previous reports (Mably et al. 2017; Cacucci et al. 2008; Jun et al. 2020; Zhao et al. 2014; Cayzac et al. 2015), though in the cases of Mably et al. 2017 and Jun et al. 2020, no changes in place field width were observed. One potential explanation for internal differences in the data is that the two papers in which place field width increases were not observed, the mice were navigating a linear belt, similar to this study, while the other three reports used an open field behavioral paradigm. One potential explanation for why our data differs is the use of two-photon Ca^{2+} imaging rather than microelectrode-based recording in addition to a head-fixed, linear belt. Alternatively, spatial encoding properties at an individual level may occur later in the disease development, and so recording CA1 PNs in a 9-12 month old J20 mouse might yield significant changes in these properties.

When examining the population as a whole, however, we found that CA1 PNs were more rigid in their spatial representations, and this rigidity strengthened as pathology progressed. This rigidity in the spatial encoding manifested in slightly more reliable location prediction when training a model on neuronal activity. Work from Jun et al. 2020, who used an APP-Knocking AD mouse model and microelectrode-based recording, showed that place cells in post-plaque mice exhibit a failure to remap their place fields when moved from linear belt to a different linear belt, implying a rigidity in the tuning properties of this

population of neurons. The implications of this rigidity is particularly interesting, because it occurs even in the absence of basic tuning properties and could explain the subtlety with which many AD patients experience spatial memory and/or navigation deficits. If the population is abstracting the same spatial representation of a given environment to other, similar spaces, it is easy to infer how subtle context discrimination between these different contexts could be missed.

Finally, we found that though place field remapping is largely compromised in pre-plaque J20 mice, and this correlates with deficits in anticipatory behavior and therefore learning, these deficits lose their correlation with behavioral performance at later stages of the disease. In 3 month J20 mice, one simple explanation is that failure to enrich could be in part responsible for diminished performance—if an animal cannot over-represent a salient feature within the environment, its behavior suffers. However, at 6 months, we fail to see a correlation in the J20 mice only, indicating perhaps that these mice, through significant disruption of their hippocampal network, rely on alternative external, potentially hippocampal-independent cues, to achieve the task, such as olfaction or sound. Recent work (Takamura et al. 2021) has shown that, through *in vivo* two-photon Ca^{2+} imaging of an APP-Knock-in AD mouse model, there is a significant deficit in place field enrichment around a reward zone, which is in line with our data. It is currently unclear how and why place cells enrich around a salient feature, and to what extent that enrichment does or does not predict behavior. Together, these data show that hippocampal network flexibility is compromised in early AD pathology, which can correlate with behavioral deficits.

Overall, our data point to a critical need to carefully and stringently examine cellular and circuit function in models of AD. As we collect more and more data to understand how precisely neurons are affected at an intracellular level, we must also begin collecting more data to understand how individual neuronal deficits may or may not contribute to broader circuit and system deficits, and how these circuit deficits may or may not impact behavior.

4.6 Supplemental Figures

Supplemental Figure S1

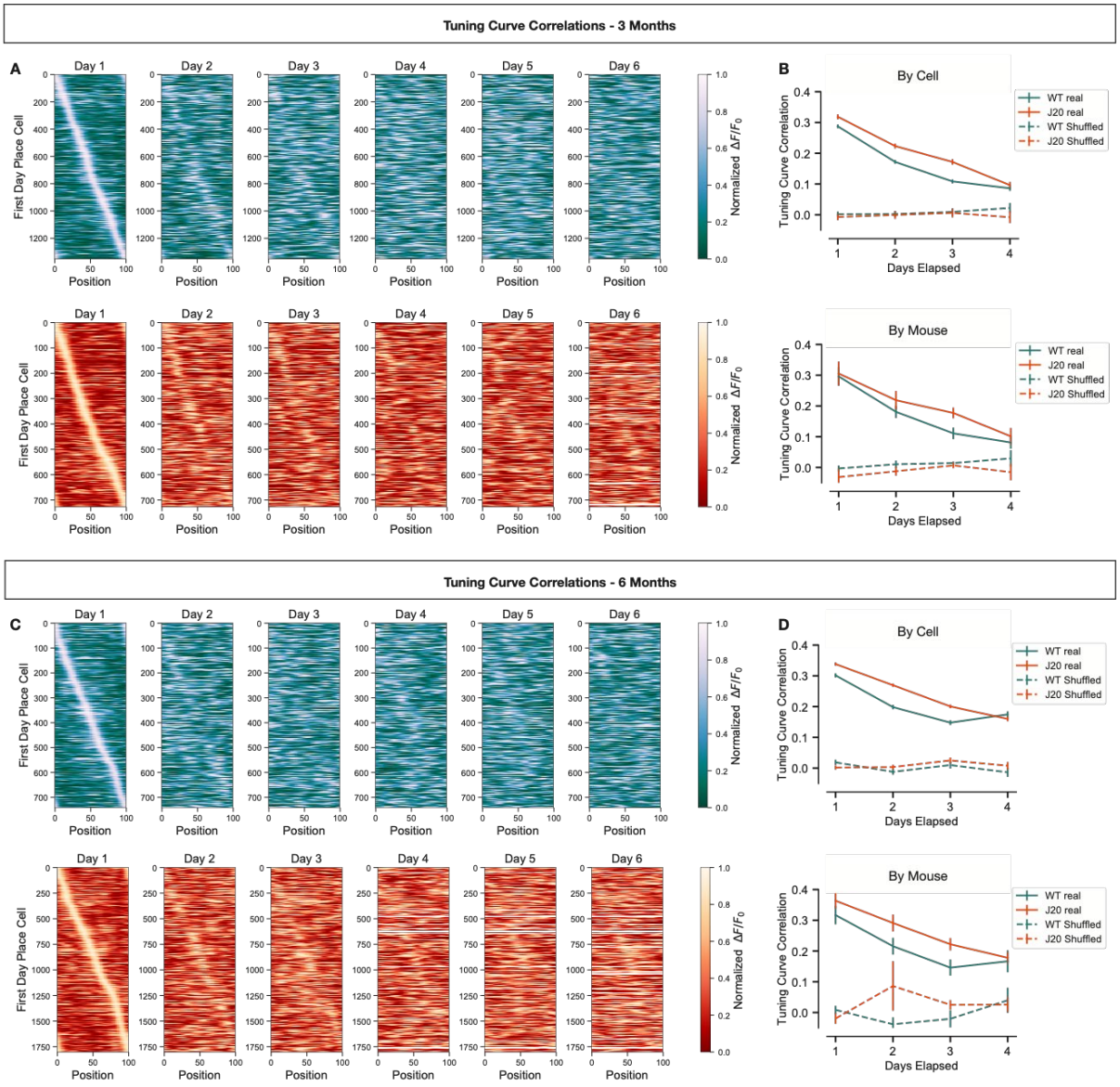

Supplemental Figure S4.1: Place cells in APP mice display increased stability that strengthens with pathological progression. **A**) Tuning curve correlation heat-maps of all cells that are place cells on day one of imaging, sorted by peak activity on day one, and tracked on each subsequent day of imaging in WT (top) and J20 (bottom) mice at 3 months. **B**) Tuning curve correlations between place cells as a measure of days elapsed from first recording—real correlations vs. randomly shuffled correlations—plotted by population (top) or by individual mouse (bottom). Tuning curve correlations significantly decrease across days in both J20 and WT mice. J20 mice have significantly higher tuning curve correlations across days compared to WT mice at a population level. Two-way ANOVAs, By Cell: disease effect: $F_{(1,13660)} = 52.93$, $p < 0.0001$; time effect: $F_{(3,13660)} = 286.72$, $p < 0.0001$; interaction: $F_{(3,13660)} = 4.13$, $p = 0.0062$; By Mouse: disease effect: $F_{(1,46)} = 3.38$, $p = 0.072$; time effect: $F_{(3,46)} = 25.73$, $p < 0.0001$; no interaction. **C**) Tuning curve correlation heat-maps of all cells that are place cells on day one of imaging, sorted by peak activity on day one, and tracked on each subsequent day of imaging in WT (top) and J20 (bottom) mice at 6 months. **D**) Tuning curve correlations between place cells as a measure of days elapsed from first recording—real correlations vs. randomly shuffled correlations—plotted by population (top) or by individual mouse (bottom). Tuning curve correlations significantly decrease across days in both J20 and WT mice. J20 mice have higher tuning curve correlations across days compared to WT mice at population and mouse levels. Two-way ANOVAs, By Cell: disease effect: $F_{(1,18116)} = 60.93$, $p < 0.0001$; time effect: $F_{(3,18116)} = 232.23$, $p < 0.0001$; interaction: $F_{(3,18116)} = 12.32$, $p < 0.0001$; By Mouse: disease effect: $F_{(1,63)} = 7.92$, $p = 0.0065$; time effect: $F_{(3,63)} = 17.90$, $p < 0.0001$; no interaction.

Supplemental Figure S2

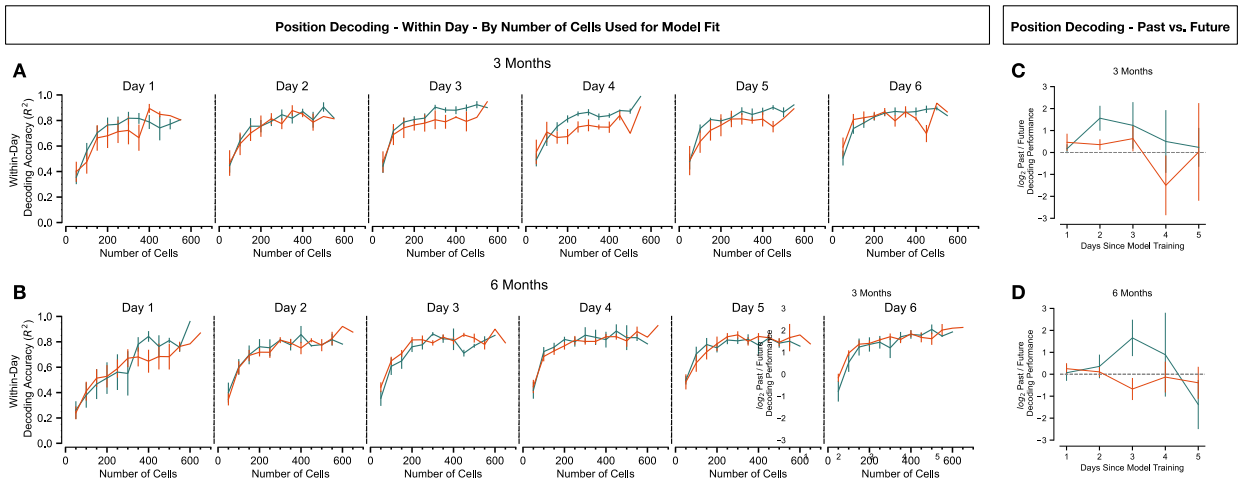

Supplemental Figure S4.2: Position decoding reliability is not significantly impacted by the number of cells used to a model between WT and J20 mice

A-B) Decoding performance of mouse position at A) 3 and B) 6 months as a function of the number of cells used to train a model for WT and J20 mice. Though providing a model fewer cells results in significantly less reliable decoding than feeding it more cells, the model is equally as reliable at predicting location regardless of the number of inputs at 3 and 6 months in WT and J20 mice. Three-way ANOVAs, 3mo: disease effect: $F_{(1,622)} = 12.47$, $p = 0.00044$; # of cells effect: $F_{(10,622)} = 58.70$, $p < 0.0001$; time effect: $F_{(5,622)} = 10.20$, $p < 0.0001$; no interactions; 6mo: disease effect: $F_{(1,701)} = 28.23$, $p < 0.0001$; # of cells effect: $F_{(12,701)} = 54.82$, $p < 0.0001$; time effect: $F_{(5,701)} = 12.86$, $p < 0.0001$; 3-way interaction: $F_{(137,701)} = 3.27$, $p < 0.0001$. **C-D**) Decoding accuracy fold-difference when testing a model on data prior to or following a training day in WT and J20 mice at C) 3 and D) 6 months. At 3 months and 6 months, WT mice show consistently better performance when testing on data from days prior to training, with J20 mice showing marginal fold-differences at six months.

Supplemental Figure S3

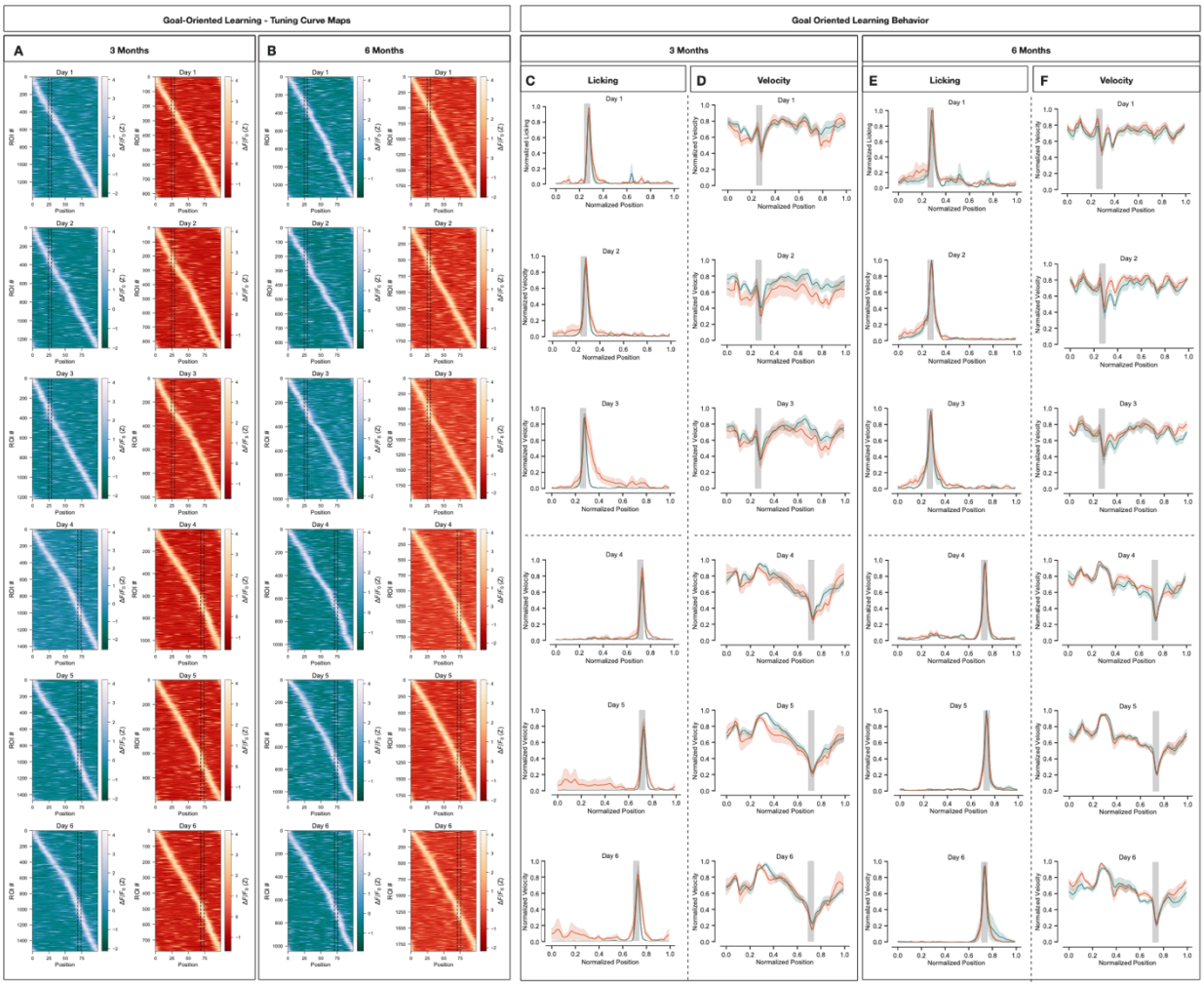

Supplemental Figure S4.3: Goal-oriented learning tuning curve maps and behavior
A-B) All place cells imaged during goal-oriented learning at A) 3 and B) 6 months in WT and J20 mice, sorted by peak firing rate. Dashed line represents the location of the fixed reward for the first three days and the final three days. **C,E**) Quantification of normalized licking from all WT and J20 mice undergoing goal-oriented learning at C) 3 and E) 6 months, across all six days of imaging, including Reward Zone 1 (Days 1-3, shaded regions), and Reward Zone 2 (Days 4-6, shaded regions). **D,F**) Quantification of normalized velocity from all WT and J20 mice undergoing goal-oriented learning at D) 3 and F) 6 months, across all six days of imaging, including Reward Zone 1 (Days 1-3, shaded regions), and Reward Zone 2 (Days 4-6, shaded regions).

Supplemental Figure S4

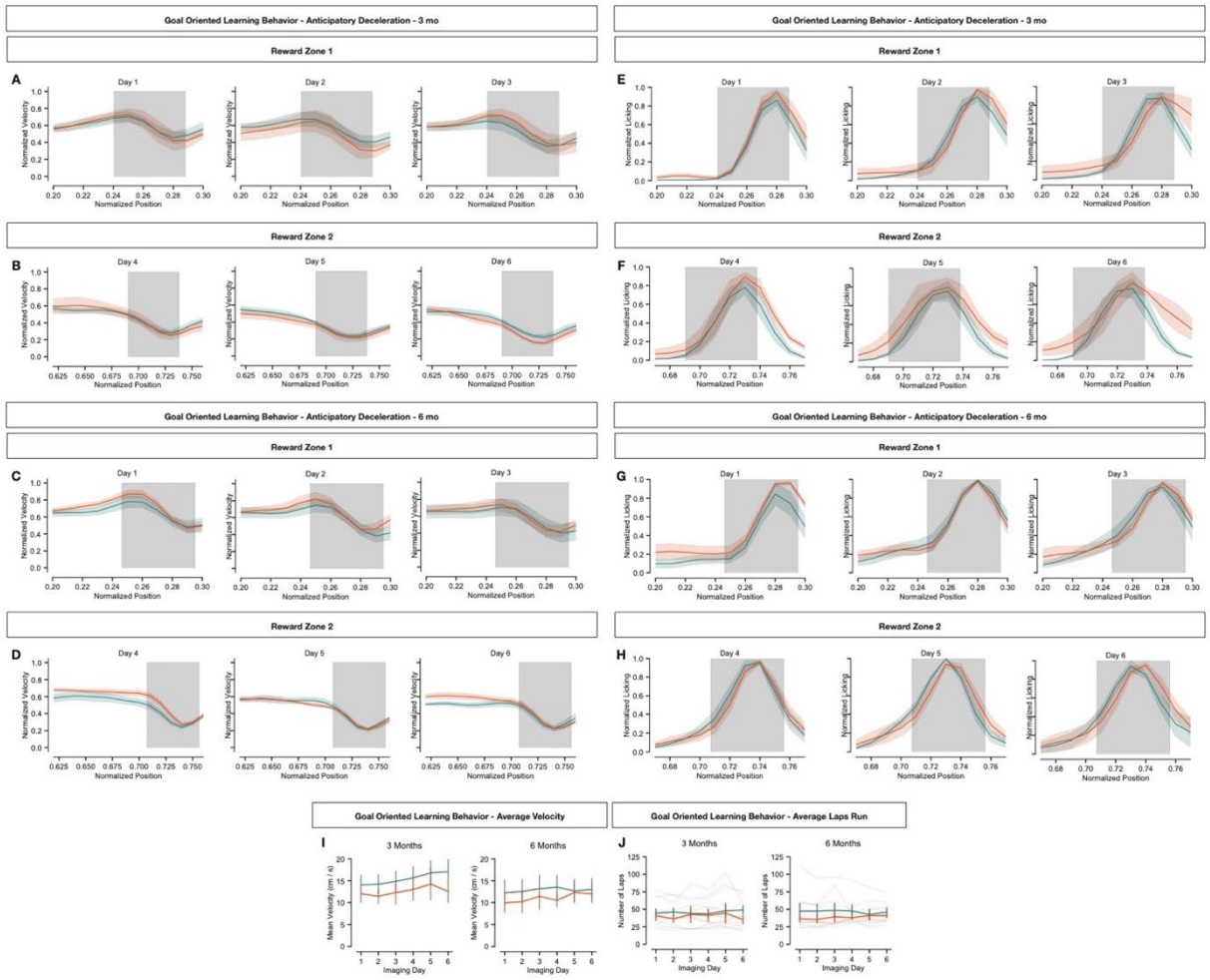

Supplemental Figure S4.4: Goal-oriented learning anticipatory behavior
A-D) Normalized mouse velocity immediately before and after the reward zone at A-B) 3 and C-D) 6 months in WT and J20 mice. **E-H**) Normalized mouse licking immediately before and after the reward zone at E-F) 3 and G-H) 6 months in WT and J20 mice. **I**) Quantification of the average velocity for all six days of goal-oriented learning for all WT and J20 mice at 3 (left) and 6 (right) months. Both WT and J20 mice run slightly less at 6 months than at 3 months, but consistently across days. Three-way ANOVAs 3mo: disease effect: $F_{(1,73)} = 3.46$, $p = 0.067$; time effect: $F_{(2,73)} = 0.073$, $p = 0.93$; reward context effect: $F_{(1,73)} = 1.51$, $p = 0.22$; no interactions; 6mo: disease effect: $F_{(1,75)} = 1.62$, $p = 0.21$; time effect: $F_{(2,75)} = 0.14$, $p = 0.87$; reward context effect: $F_{(1,73)} = 0.082$, $p = 0.78$; no interactions. **J**) Quantification of the average number of laps run for all six days of goal-oriented learning for all WT and J20 mice at 3 (left) and 6 (right) months. There are no significant differences in the number of laps run between WT and J20 animals at either age. Three-way ANOVAs 3mo: disease effect: $F_{(1,73)} = 1.53$, $p = 0.22$; time effect: $F_{(2,73)} = 0.037$, $p = 0.96$; reward context effect: $F_{(1,73)} = 0.082$, $p = 0.78$; no interactions; 6mo: disease effect: $F_{(1,75)} = 3.75$, $p = 0.056$; time effect: $F_{(2,75)} = 0.081$, $p = 0.92$; reward context effect: $F_{(1,75)} = 0.014$, $p = 0.91$; no interactions.

4.7 Methods

Animals

All animals used and experiments conducted were handled according to protocols approved by the Columbia University Institutional Animal Care and Use Committee (IACUC) and in accordance with National Institutes of Health guidelines. The health and welfare of the animals was supervised by a designated veterinarian. The Columbia University animal facilities comply with all appropriate standards—ie. cages, space per animal, temperature, 12h light/dark cycles, humidity, food, water. Both males and females were used for all experiments, no differences were reported between sexes of individual mice for any of the parameters analyzed in this study.

c129/SvJ, C57Bl/6J (referred to as F1) nontransgenic mice, hemizygous transgenic mice from line B6.Cg-Zbtb20$^{Tg(PDGFB-APPSwInd)20Lms}$/2Mmjax (referred to as J20) mice were maintained in a 12-hour light/dark cycle. J20 mice express human APP carrying the Swedish and Indiana (APP^{SWE,IND}) mutations under a PDGFβ promoter (Mucke et al. 2000, Lacor et al. 2007).

In utero hippocampal electroporation and spine analysis

In utero electroporation targeting the hippocampus was performed using a triple-electrode setup as previously described (Hand and Polleux 2011, Meyer-Dilhet and Courchet 2020; Blockus et al. 2020) to target hippocampal CA1 pyramidal neuron progenitors at E15.5. Briefly, endotoxin-free plasmids were injected into the lateral ventricle (pCAG-Cre::mRuby (Blockus et al. 2021): 1 µg/µL, pEF1α::FLEX-tdTomato (Iascone et al. 2020): 1 µg/µL followed by 5 pulses at 45V (50 ms duration, 500 ms inter-pulse interval) using two anodes (positively charged) laterally on either side of the head and one cathode (negatively charged) rostrally at a 0º angle to the horizontal plane.

Mice were perfused transcardially with PFA (4%) and glutaraldehyde (0.075%) in PBS at either 3 months (~P90) or 6 months (~P180) or immediately following 2P imaging at the same times and sectioned at 110 µm on a vibratome (Leica). Sections were mounted on slides with Fluoromount-G aqueous mounting medium (ThermoFisher Scientific) and imaged for spine analyses on a Nikon Ti-E A1R laser-scanning confocal using the following objectives (Nikon): 60x App TIRF;NA 1.49 or 100x H-TIRF; NA 1.49.

Dendritic spine density analysis was carried out by quantifying, in an experimentally blind manner, the number of spines (identified through expression of the tdTomato cell fill) on distal tuft dendritic branches.

Spines were counted by hand by scrolling through a 0.5-1.0 μm step Z-stack using Fiji software (ImageJ; NIH) and the density calculated by dividing the total spine count by the length of the segment quantified.

Stereotactic virus injection, craniotomy

For *in vivo* imaging experiments, recombinant adeno-associated viruses (AAV) carrying the GCaMP6f gene were obtained from the Penn Vector Core (AAV1.pSyn.GCaMP6f.WPRE.SV40) with a titer of 1-2 x 10^{23}. Dorsal CA1 was stereotactically injected at —2.0 mm AP; —1.5 mm ML; and —0.9, —1.2, and —1.4 mm DV relative to the cortical surface. Mice were then surgically implanted with an imaging window over the left dorsal CA1 and implanted with a stainless-steel headpost for head fixation during 2P imaging experiments.

***In vivo* two-photon calcium imaging**

We used the same imaging system as described previously (Blockus et al. 2020, O'Hare et al. 2022). All images were acquired using a Nikon 40 x NIR water-immersion objective (0.8 NA, 3.5 mm WD) in distilled milliQ water. For excitation, we used a Chameleon, Ultra II (Coherent) laser tuned to 920 nm. We continuously acquired red (tdTomato) and green (GCaMP6f) channels separated by an emission cube set (green: HQ525/70 m-2p; red: HQ607/45 m-2p; 575dcxr, Chroma Technology) at 512 x 512 pixels covering 330 μm x 330 μm at 30 Hz with photomultiplier tubes (green GCaMPF6f fluorescence, GaAsP PMT, Hamamatsu Model 7422-40; red tdTomato fluorescence, GaAsP PMT Hamamatsu).

For training, mice were water restricted (>90% pre-deprivation weight) and trained to run on a cue-poor burlap treadmill belt for 10 days and a cue-rich multi-textured belt for 4 days for a non-operantly delivered water reward. We applied a progressively restrictive water reward schedule, with mice initially receiving 10 randomly placed rewards per lap and ultimately receiving 1 randomly placed reward per lap. Mice were habituated to optical instrumentation, then trained for 20 min daily until they regularly ran at least one lap per minute. During imaging sessions, mice received either one randomly placed or one fixed reward per lap, with water delivered for every subsequent lick inside the reward zone being rewarded for a maximum of 2.5 s.

Behavioral Analysis

All behavioral measures were time-locked to image acquisition. Where indicated, these measures were binned (100 bins) by animal position on a lap-by-lap basis and smoothed with a 1-bin Gaussian filter for

further analysis. For goal-oriented learning experiments, anticipatory licking and deceleration were calculated from the 40 cm (20 position bins) preceding the reward zone.

Ca^{2+} Imaging Preprocessing

For each animal and behavioral paradigm (random foraging and goal-oriented learning), individual datasets were concatenated across days. Concatenated datasets were processed using the Suite2P software package (Pachitariu et al. 2017) in three steps: (1) non-rigid 2-dimensional motion correction, (2) Cellpose-based ROI segmentation (Stringer et al. 2021) based on the motion-corrected, time-averaged field of view ('anatomical mode' in Suite2P), and (3) signal extraction with built-in neuropil decontamination. Cellpose-based ROI segmentation was chosen over an activity-based approach to guard against potential bias: silent neurons, which are not detected using activity-based segmentation, may differ in prevalence between groups. Following signal extraction, individual datasets were repopulated with corresponding signals from cross-registered datasets. To quantify the quality of cross-registration, i.e. how well fields of view were aligned across days, motion-corrected time-averaged fields of view were then recalculated for each individual dataset using stored displacement values from the bulk motion correction. A template dataset was then chosen for each animal per behavioral paradigm, and time-averaged fields of view were compared to that of the template dataset. Prior to image comparison, time-averaged fields of view were preprocessed by clipping pixel values to 5^{th} and 95^{th} percentiles and applying histogram equalization along an 8 x 8 grid. Alignment was then calculated using the Enhanced Correlation Coefficient (ECC) (Evangelidis et al. 2008), implemented in the Python-based OpenCV software library (opencv.org). Datasets were manually inspected for obvious drops in cross-day alignment; no datasets were excluded according to within-animal ECC values.

Ca^{2+} signal processing and event detection

Ca^{2+} signal processing and event detection were carried out as previously described for population imaging (O'Hare et al. 2022). In brief, signal baselines were calculated using a rolling max-min filter with a 30-s window. $\Delta F/F_0$ was calculated from the baseline and smoothed over a 2-frame window before detrending over a 60-s window. Ca^{2+} transients were identified based on z-score relative to baseline and duration, validated based as previously described (Lovett-Barron et al. 2014), and iteratively recalculated three times while masking events from baseline calculation Ca^{2+} signals were then transformed into binary vectors

using the OASIS event deconvolution software package (Friedrich et al. 2016) for subsequent spatial tuning analysis.

Spatial tuning analysis

Spatial tuning curves, spatial information, place field properties, and spontaneous place field formation events were calculated as previously reported for population imaging data[4] with the exception that silent ROIs were never excluded from analyses. For goal-oriented learning experiments, place fields were considered to be near the reward zone if they fell within the 40 cm (20% of the treadmill belt) preceding the reward zone. This "enrichment window" corresponds to that used to identify anticipatory behaviors that indicate that the animal has learned where to expect reward delivery. To determine place field enrichment mechanisms, we classified place fields within the enrichment window as having remapped toward the reward zone or formed *de novo*. A place field was considered to have remapped if the CA1 PN expressed a place field in a different location on the previous day. A place field was considered to have formed *de novo* if the CA1 PN did not express a place field on the previous day or if the place field formed on the first imaging day. To compare the rates of remapping and *de novo* formation, we used an "enrichment mode index":

$$\frac{(N_{new} - N_{remapped})}{(N_{new} + N_{remapped}}),$$

where a value of 1 indicated that all PFs formed *de novo* and a value of -1 indicated that all place fields remapped from a prior location toward the reward zone.

Spatial tuning stability analyses

Stability of CA1 PN spatial tuning across days was assessed using two metrics: tuning curve correlations and population vector correlations. To be included in either analysis, CA1 PNs were required to display a place field on one of the two days being compared. While deconvolved events were used for spatial tuning analyses, $\Delta F/F_0$ was used for population vector correlations to prevent silent cells from having NaN values that would corrupt correlation coefficient calculations. As with spatial tuning analysis, only "running frames", i.e. imaging frames corresponding to animal velocity ≥ 1.0 cm/s, were included.

Spatial tuning curve correlations were calculated by calculating the Pearson's correlation coefficient between tuning curves for a given CA1 PN across two given days. Population vector correlations were

calculated by first binning population activity across all N ROIs from a given field of view into 100 position bins and normalizing bin values to position occupancy time. The resultant N x 100 population tuning matrices were smoothed with a Gaussian window of 3 position bins. To compare population-level tuning across two given days, population vectors were correlated (Pearson's correlation) between every possible pair of position bins to generate a 100 x 100 matrix of correlation coefficients describing how similarly the imaged population of CA1 PNs represented different position bins (**Figure 3B, D**). This process was repeated for all pairwise combinations of imaging days (**Figure 3A, C**). Population vector correlations were calculated by correlating the diagonals of two population tuning matrices corresponding to separate days. This correlation coefficient reflects how similar spatial tuning across an entire imaged field of view is between two given days (**Figure 3G-J**).

Spatial tuning precision analysis

To determine the precision with which an entire imaged population of CA1 PNs encodes an animal's environment, we used the 100 x 100 matrices described above from population vector analyses to quantify, within a given day, how population vector correlations varies as a function of their off-diagonal distance. In other words, from the cross-day matrix M shown in **Figure 3A**, submatrices $M_{i,i}$ were averaged across days to generate **Figure 3B**. A high-precision population-level spatial code should show rapidly decreasing population vector correlations away from the diagonal since even proximal position bins should be represented in relatively orthogonal fashion. A low-precision code would show a broader distribution of high population vector correlations around the diagonal. Thus, for each day, population vector correlations were binned (8 bins) by their minimum Euclidean distances from the diagonal of the population vector correlation matrix for each animal. Data were clipped at an off-diagonal distance of 100 cm prior to binning because, at longer distances, positions become more similarly represented due to the circular nature of the treadmill belt.

Position decoding

Animal position was decoded from CA1 PN population activity by training an ensemble of support vector machine classifiers (scikit-learn.org) to predict an animal's position bin based on lap-by-lap tuning curves of all imaged ROIs. For each cell, we generated an occupancy-normalized, lap-by-lap heatmap of ROI $\Delta F/F_0$ along 100 position bins. These N_{lap} x 100 heatmaps were flattened and stacked into M_{ROI} x ($N\text{-}1_{lap}$ x

P_{bins}) matrices and used to predict animal position across all laps and position bins using a circular leave-one-out approach. To determine how the number of ROIs available for model training impacted model performance, and therefore how any differences in numbers of ROIs imaged per group might impact group-wise comparisons, we also iteratively decoded animal position using Ns from 50 ROIs up to the full N imaged, in 50-ROI intervals. As an alternative strategy to assess cross-day stability of population-level spatial tuning, we also decoded animal position on a given imaging day using models trained on each of all other imaging days for a given animal.

Statistical tests

For all pairwise group comparisons, two-sided *t* tests with Welch's correction for heteroscedasticity or two-tailed Mann-Whitney *U* tests were used depending on the normality of the underlying distributions, as determined using the Kolmogorov-Smirnoff test. Non-normal distributions were described by median ± inter-quartile range and normal data by mean ± standard error of the mean. ANOVAs were used for multi-way comparisons (statsmodels.org).

4.8 Acknowledgements

The authors would like to thank Qiaolian Liu for technical assistance in managing the mouse colony, setting up all breeding, and preparing all timed pregnancies—a true hero of every Polleux Lab manuscript. We would also like to thank members of the Polleux Lab for providing feedback through the many years of this project's development. This work was supported by: NINDS R35 NS127232 (FP) and NINDS K99 GG017969 (JKO).

4.9 Author Contributions

Conceptualization: DMV, FP; Methodology: DMV, FP; Software: JKO; Formal Analysis: DMV, JKO; Investigation: DMV; Visualization: DMV, JKO; Data Curation: DMV, JKO; Writing — original draft: DMV; Writing — review and editing: DMV, JKO, FP; Resources: AL, FP; Supervision: FP; Project administration: FP; Funding acquisition: FP, JKO.

4.10 References

Bakker, A., Krauss, G. L., Albert, M. S., Speck, C. L., Jones, L. R., Stark, C. E., Yassa, M. A., Bassett, S. S., Shelton, A. L., & Gallagher, M. (2012). Reduction of hippocampal hyperactivity improves cognition in amnestic mild cognitive impairment. *Neuron*, *74*(3), 467–474. https://doi.org/10.1016/j.neuron.2012.03.023

Blockus, H., Rolotti, S. V., Szoboszlay, M., Peze-Heidsieck, E., Ming, T., Schroeder, A., Apostolo, N., Vennekens, K. M., Katsamba, P. S., Bahna, F., Mannepalli, S., Ahlsen, G., Honig, B., Shapiro, L., de Wit, J., Losonczy, A., & Polleux, F. (2021). Synaptogenic activity of the axon guidance molecule Robo2 underlies hippocampal circuit function. *Cell Reports*, *37*(3), 109828. https://doi.org/10.1016/j.celrep.2021.109828

Busche, M. A., Eichhoff, G., Adelsberger, H., Abramowski, D., Wiederhold, K.-H., Haass, C., Staufenbiel, M., Konnerth, A., & Garaschuk, O. (2008). Clusters of hyperactive neurons near amyloid plaques in a mouse model of Alzheimer's disease. *Science (New York, N.Y.)*, *321*(5896), 1686–1689. https://doi.org/10.1126/science.1162844

Cacucci, F., Yi, M., Wills, T. J., Chapman, P., & O'Keefe, J. (2008). Place cell firing correlates with memory deficits and amyloid plaque burden in Tg2576 Alzheimer mouse model. *Proceedings of the National Academy of Sciences*, *105*(22), 7863–7868. https://doi.org/10.1073/pnas.0802908105

Celone, K. A., Calhoun, V. D., Dickerson, B. C., Atri, A., Chua, E. F., Miller, S. L., DePeau, K., Rentz, D. M., Selkoe, D. J., Blacker, D., Albert, M. S., & Sperling, R. A. (2006). Alterations in memory networks in mild cognitive impairment and Alzheimer's disease: An independent component analysis. *The Journal of Neuroscience: The Official Journal of the Society for Neuroscience*, *26*(40), 10222–10231. https://doi.org/10.1523/JNEUROSCI.2250-06.2006

Cheng, I. H., Scearce-Levie, K., Legleiter, J., Palop, J. J., Gerstein, H., Bien-Ly, N., Puoliväli, J., Lesné, S., Ashe, K. H., Muchowski, P. J., & Mucke, L. (2007). Accelerating amyloid-beta fibrillization reduces oligomer levels and functional deficits in Alzheimer disease mouse models. *The Journal of Biological Chemistry*, *282*(33), 23818–23828. https://doi.org/10.1074/jbc.M701078200

Chin, J., Palop, J. J., Puoliväli, J., Massaro, C., Bien-Ly, N., Gerstein, H., Scearce-Levie, K., Masliah, E., & Mucke, L. (2005). Fyn kinase induces synaptic and cognitive impairments in a transgenic mouse model of Alzheimer's disease. *The Journal of Neuroscience: The Official Journal of the Society for Neuroscience*, *25*(42), 9694–9703. https://doi.org/10.1523/JNEUROSCI.2980-05.2005

Cissé, M., Halabisky, B., Harris, J., Devidze, N., Dubal, D. B., Sun, B., Orr, A., Lotz, G., Kim, D. H., Hamto, P., Ho, K., Yu, G.-Q., & Mucke, L. (2011). Reversing EphB2 depletion rescues cognitive functions in Alzheimer model. *Nature*, *469*(7328), 47–52. https://doi.org/10.1038/nature09635

Danielson, N. B., Kaifosh, P., Zaremba, J. D., Lovett-Barron, M., Tsai, J., Denny, C. A., Balough, E. M., Goldberg, A. R., Drew, L. J., Hen, R., Losonczy, A., & Kheirbek, M. A. (2016). Distinct Contribution of Adult-Born Hippocampal Granule Cells to Context Encoding. *Neuron*, *90*(1), 101–112. https://doi.org/10.1016/j.neuron.2016.02.019

Dickerson, B. C., Salat, D. H., Greve, D. N., Chua, E. F., Rand-Giovannetti, E., Rentz, D. M., Bertram, L., Mullin, K., Tanzi, R. E., Blacker, D., Albert, M. S., & Sperling, R. A. (2005). Increased hippocampal activation in mild cognitive impairment compared to normal aging and AD. *Neurology*, *65*(3), 404–411. https://doi.org/10.1212/01.wnl.0000171450.97464.49

Dong, C., Madar, A. D., & Sheffield, M. E. J. (2021). Distinct place cell dynamics in CA1 and CA3 encode experience in new environments. *Nature Communications*, *12*(1), Article 1. https://doi.org/10.1038/s41467-021-23260-3

Driscoll, L. N., Duncker, L., & Harvey, C. D. (2022). Representational drift: Emerging theories for continual learning and experimental future directions. *Current Opinion in Neurobiology*, *76*, 102609. https://doi.org/10.1016/j.conb.2022.102609

Ekstrom, A. D., Kahana, M. J., Caplan, J. B., Fields, T. A., Isham, E. A., Newman, E. L., & Fried, I. (2003). Cellular networks underlying human spatial navigation. *Nature*, *425*(6954), 184–188. https://doi.org/10.1038/nature01964

Filippini, N., MacIntosh, B. J., Hough, M. G., Goodwin, G. M., Frisoni, G. B., Smith, S. M., Matthews, P. M., Beckmann, C. F., & Mackay, C. E. (2009). Distinct patterns of brain activity in young carriers of the APOE-ε4 allele. *Proceedings of the National Academy of Sciences*, *106*(17), 7209–7214. https://doi.org/10.1073/pnas.0811879106

Frank, L. M., Stanley, G. B., & Brown, E. N. (2004). Hippocampal plasticity across multiple days of exposure to novel environments. *The Journal of Neuroscience: The Official Journal of the Society for Neuroscience*, *24*(35), 7681–7689. https://doi.org/10.1523/JNEUROSCI.1958-04.2004

Galvan, V., Gorostiza, O. F., Banwait, S., Ataie, M., Logvinova, A. V., Sitaraman, S., Carlson, E., Sagi, S. A., Chevallier, N., Jin, K., Greenberg, D. A., & Bredesen, D. E. (2006). Reversal of Alzheimer's-like pathology and behavior in human APP transgenic mice by mutation of Asp664. *Proceedings of the National Academy of Sciences*, *103*(18), 7130–7135. https://doi.org/10.1073/pnas.0509695103

Grienberger, C., Rochefort, N. L., Adelsberger, H., Henning, H. A., Hill, D. N., Reichwald, J., Staufenbiel, M., & Konnerth, A. (2012). Staged decline of neuronal function in vivo in an animal model of Alzheimer's disease. *Nature Communications*, *3*(1), Article 1. https://doi.org/10.1038/ncomms1783

Hollup, S. A., Molden, S., Donnett, J. G., Moser, M.-B., & Moser, E. I. (2001). Accumulation of Hippocampal Place Fields at the Goal Location in an Annular Watermaze Task. *Journal of Neuroscience*, *21*(5), 1635–1644. https://doi.org/10.1523/JNEUROSCI.21-05-01635.2001

Hong, S., Beja-Glasser, V. F., Nfonoyim, B. M., Frouin, A., Li, S., Ramakrishnan, S., Merry, K. M., Shi, Q., Rosenthal, A., Barres, B. A., Lemere, C. A., Selkoe, D. J., & Stevens, B. (2016). Complement and microglia mediate early synapse loss in Alzheimer mouse models. *Science (New York, N.Y.)*, *352*(6286), 712–716. https://doi.org/10.1126/science.aad8373

Hope, T., Tilling, K. M., Gedling, K., Keene, J. M., Cooper, S. D., & Fairburn, C. G. (1994). The structure of wandering in dementia. *International Journal of Geriatric Psychiatry*, *9*(2), 149–155. https://doi.org/10.1002/gps.930090209

Jacobsen, J. S., Wu, C.-C., Redwine, J. M., Comery, T. A., Arias, R., Bowlby, M., Martone, R., Morrison, J. H., Pangalos, M. N., Reinhart, P. H., & Bloom, F. E. (2006). Early-onset behavioral and synaptic deficits in a mouse model of Alzheimer's disease. *Proceedings of the National Academy of Sciences*, *103*(13), 5161–5166. https://doi.org/10.1073/pnas.0600948103

Jun, H., Bramian, A., Soma, S., Saito, T., Saido, T. C., & Igarashi, K. M. (2020). Disrupted Place Cell Remapping and Impaired Grid Cells in a Knockin Model of Alzheimer's Disease. *Neuron*, *107*(6), 1095-1112.e6. https://doi.org/10.1016/j.neuron.2020.06.023

Kaufman, A. M., Geiller, T., & Losonczy, A. (2020). A Role for the Locus Coeruleus in Hippocampal CA1 Place Cell Reorganization during Spatial Reward Learning. *Neuron*, *105*(6), 1018-1026.e4. https://doi.org/10.1016/j.neuron.2019.12.029

Keinath, A. T., Mosser, C.-A., & Brandon, M. P. (2022). The representation of context in mouse hippocampus is preserved despite neural drift. *Nature Communications*, *13*(1), Article 1. https://doi.org/10.1038/s41467-022-30198-7

Kurudenkandy, F. R., Zilberter, M., Biverstål, H., Presto, J., Honcharenko, D., Strömberg, R., Johansson, J., Winblad, B., & Fisahn, A. (2014). Amyloid-β-Induced Action Potential Desynchronization and Degradation of Hippocampal Gamma Oscillations Is Prevented by Interference with Peptide Conformation Change and Aggregation. *Journal of Neuroscience*, *34*(34), 11416–11425. https://doi.org/10.1523/JNEUROSCI.1195-14.2014

Lee, A., Kondapalli, C., Virga, D. M., Lewis, T. L., Koo, S. Y., Ashok, A., Mairet-Coello, G., Herzig, S., Foretz, M., Viollet, B., Shaw, R., Sproul, A., & Polleux, F. (2022). Aβ42 oligomers trigger synaptic loss through CAMKK2-AMPK-dependent effectors coordinating mitochondrial fission and mitophagy. *Nature Communications*, *13*(1), Article 1. https://doi.org/10.1038/s41467-022-32130-5

Mably, A. J., Gereke, B. J., Jones, D. T., & Colgin, L. L. (2017). Impairments in spatial representations and rhythmic coordination of place cells in the 3xTg mouse model of Alzheimer's disease. *Hippocampus*, *27*(4), 378–392. https://doi.org/10.1002/hipo.22697

Meilandt, W. J., Yu, G.-Q., Chin, J., Roberson, E. D., Palop, J. J., Wu, T., Scearce-Levie, K., & Mucke, L. (2008). Enkephalin Elevations Contribute to Neuronal and Behavioral Impairments in a Transgenic Mouse Model of Alzheimer's Disease. *The Journal of Neuroscience*, *28*(19), 5007–5017. https://doi.org/10.1523/JNEUROSCI.0590-08.2008

Moser, E. I., Kropff, E., & Moser, M.-B. (2008). Place cells, grid cells, and the brain's spatial representation system. *Annual Review of Neuroscience*, *31*, 69–89. https://doi.org/10.1146/annurev.neuro.31.061307.090723

Moser, M.-B., Rowland, D. C., & Moser, E. I. (2015). Place cells, grid cells, and memory. *Cold Spring Harbor Perspectives in Biology*, *7*(2), a021808. https://doi.org/10.1101/cshperspect.a021808

Mucke, L., Masliah, E., Yu, G. Q., Mallory, M., Rockenstein, E. M., Tatsuno, G., Hu, K., Kholodenko, D., Johnson-Wood, K., & McConlogue, L. (2000). High-level neuronal expression of abeta 1-42 in wild-type human amyloid protein precursor transgenic mice: Synaptotoxicity without plaque formation. *The Journal of Neuroscience: The Official Journal of the Society for Neuroscience*, *20*(11), 4050–4058. https://doi.org/10.1523/JNEUROSCI.20-11-04050.2000

O'Hare, J. K., Gonzalez, K. C., Herrlinger, S. A., Hirabayashi, Y., Hewitt, V. L., Blockus, H., Szoboszlay, M., Rolotti, S. V., Geiller, T. C., Negrean, A., Chelur, V., Polleux, F., & Losonczy, A. (2022). Compartment-

specific tuning of dendritic feature selectivity by intracellular Ca2+ release. *Science*, *375*(6586), eabm1670. https://doi.org/10.1126/science.abm1670

O'Keefe, J., & Dostrovsky, J. (1971). The hippocampus as a spatial map. Preliminary evidence from unit activity in the freely-moving rat. *Brain Research*, *34*(1), 171–175. https://doi.org/10.1016/0006-8993(71)90358-1

O'Keefe, J., & Nadel, L. (1979). The hippocampus as a cognitive map. *Behavioral and Brain Sciences*, *2*(4), 487–494. https://doi.org/10.1017/S0140525X00063949

Palop, J. J., Chin, J., Roberson, E. D., Wang, J., Thwin, M. T., Bien-Ly, N., Yoo, J., Ho, K. O., Yu, G.-Q., Kreitzer, A., Finkbeiner, S., Noebels, J. L., & Mucke, L. (2007). Aberrant Excitatory Neuronal Activity and Compensatory Remodeling of Inhibitory Hippocampal Circuits in Mouse Models of Alzheimer's Disease. *Neuron*, *55*(5), 697–711. https://doi.org/10.1016/j.neuron.2007.07.025

Palop, J. J., Jones, B., Kekonius, L., Chin, J., Yu, G.-Q., Raber, J., Masliah, E., & Mucke, L. (2003). Neuronal depletion of calcium-dependent proteins in the dentate gyrus is tightly linked to Alzheimer's disease-related cognitive deficits. *Proceedings of the National Academy of Sciences of the United States of America*, *100*(16), 9572–9577. https://doi.org/10.1073/pnas.1133381100

Quiroz, Y. T., Budson, A. E., Celone, K., Ruiz, A., Newmark, R., Castrillón, G., Lopera, F., & Stern, C. E. (2010). Hippocampal hyperactivation in presymptomatic familial Alzheimer's disease. *Annals of Neurology*, *68*(6), 865–875. https://doi.org/10.1002/ana.22105

Rudinskiy, N., Hawkes, J. M., Betensky, R. A., Eguchi, M., Yamaguchi, S., Spires-Jones, T. L., & Hyman, B. T. (2012). Orchestrated experience-driven Arc responses are disrupted in a mouse model of Alzheimer's disease. *Nature Neuroscience*, *15*(10), 1422–1429. https://doi.org/10.1038/nn.3199

Sanchez, P. E., Zhu, L., Verret, L., Vossel, K. A., Orr, A. G., Cirrito, J. R., Devidze, N., Ho, K., Yu, G.-Q., Palop, J. J., & Mucke, L. (2012). Levetiracetam suppresses neuronal network dysfunction and reverses synaptic and cognitive deficits in an Alzheimer's disease model. *Proceedings of the National Academy of Sciences of the United States of America*, *109*(42), E2895–E2903. https://doi.org/10.1073/pnas.1121081109

Sanchez-Mejia, R. O., Newman, J. W., Toh, S., Yu, G.-Q., Zhou, Y., Halabisky, B., Cissé, M., Scearce-Levie, K., Cheng, I. H., Gan, L., Palop, J. J., Bonventre, J. V., & Mucke, L. (2008). Phospholipase A2 reduction ameliorates cognitive deficits in a mouse model of Alzheimer's disease. *Nature Neuroscience*, *11*(11), Article 11. https://doi.org/10.1038/nn.2213

Sepulveda-Falla, D., Glatzel, M., & Lopera, F. (2012). Phenotypic profile of early-onset familial Alzheimer's disease caused by presenilin-1 E280A mutation. *Journal of Alzheimer's Disease: JAD*, *32*(1), 1–12. https://doi.org/10.3233/JAD-2012-120907

Sheffield, M. E. J., Adoff, M. D., & Dombeck, D. A. (2017). Increased Prevalence of Calcium Transients across the Dendritic Arbor during Place Field Formation. *Neuron*, *96*(2), 490-504.e5. https://doi.org/10.1016/j.neuron.2017.09.029

Sheng, M., Sabatini, B. L., & Südhof, T. C. (2012). Synapses and Alzheimer's disease. *Cold Spring Harbor Perspectives in Biology*, *4*(5), a005777. https://doi.org/10.1101/cshperspect.a005777

Šišková, Z., Justus, D., Kaneko, H., Friedrichs, D., Henneberg, N., Beutel, T., Pitsch, J., Schoch, S., Becker, A., von der Kammer, H., & Remy, S. (2014). Dendritic structural degeneration is functionally linked to cellular hyperexcitability in a mouse model of Alzheimer's disease. *Neuron*, *84*(5), 1023–1033. https://doi.org/10.1016/j.neuron.2014.10.024

Sperling, R. A., Laviolette, P. S., O'Keefe, K., O'Brien, J., Rentz, D. M., Pihlajamaki, M., Marshall, G., Hyman, B. T., Selkoe, D. J., Hedden, T., Buckner, R. L., Becker, J. A., & Johnson, K. A. (2009). Amyloid deposition is associated with impaired default network function in older persons without dementia. *Neuron*, *63*(2), 178–188. https://doi.org/10.1016/j.neuron.2009.07.003

Takamura, R., Mizuta, K., Sekine, Y., Islam, T., Saito, T., Sato, M., Ohkura, M., Nakai, J., Ohshima, T., Saido, T. C., & Hayashi, Y. (2021). Modality-Specific Impairment of Hippocampal CA1 Neurons of Alzheimer's Disease Model Mice. *The Journal of Neuroscience: The Official Journal of the Society for Neuroscience*, *41*(24), 5315–5329. https://doi.org/10.1523/JNEUROSCI.0208-21.2021

Tsitsiklis, M., Miller, J., Qasim, S. E., Inman, C. S., Gross, R. E., Willie, J. T., Smith, E. H., Sheth, S. A., Schevon, C. A., Sperling, M. R., Sharan, A., Stein, J. M., & Jacobs, J. (2020). Single-Neuron Representations of Spatial Targets in Humans. *Current Biology: CB*, *30*(2), 245-253.e4. https://doi.org/10.1016/j.cub.2019.11.048

Turi, G. F., Li, W.-K., Chavlis, S., Pandi, I., O'Hare, J., Priestley, J. B., Grosmark, A. D., Liao, Z., Ladow, M., Zhang, J. F., Zemelman, B. V., Poirazi, P., & Losonczy, A. (2019). Vasoactive Intestinal Polypeptide-Expressing Interneurons in the Hippocampus Support Goal-Oriented Spatial Learning. *Neuron*, *101*(6), 1150-1165.e8. https://doi.org/10.1016/j.neuron.2019.01.009

Um, J. W., Nygaard, H. B., Heiss, J. K., Kostylev, M. A., Stagi, M., Vortmeyer, A., Wisniewski, T., Gunther, E. C., & Strittmatter, S. M. (2012). Alzheimer amyloid-β oligomer bound to postsynaptic prion protein activates Fyn to impair neurons. *Nature Neuroscience*, *15*(9), 1227–1235. https://doi.org/10.1038/nn.3178

Wattmo, C., Minthon, L., & Wallin, Å. K. (2016). Mild versus moderate stages of Alzheimer's disease: Three-year outcomes in a routine clinical setting of cholinesterase inhibitor therapy. *Alzheimer's Research & Therapy*, *8*(1), 7. https://doi.org/10.1186/s13195-016-0174-1

Wilson, M. A., & McNaughton, B. L. (1993). Dynamics of the hippocampal ensemble code for space. *Science (New York, N.Y.)*, *261*(5124), 1055–1058. https://doi.org/10.1126/science.8351520

Wright, A. L., Zinn, R., Hohensinn, B., Konen, L. M., Beynon, S. B., Tan, R. P., Clark, I. A., Abdipranoto, A., & Vissel, B. (2013). Neuroinflammation and neuronal loss precede Aβ plaque deposition in the hAPP-J20 mouse model of Alzheimer's disease. *PloS One*, *8*(4), e59586. https://doi.org/10.1371/journal.pone.0059586

Ying, J., Keinath, A. T., Lavoie, R., Vigneault, E., El Mestikawy, S., & Brandon, M. P. (2022). Disruption of the grid cell network in a mouse model of early Alzheimer's disease. *Nature Communications*, *13*(1), Article 1. https://doi.org/10.1038/s41467-022-28551-x

Zaremba, J. D., Diamantopoulou, A., Danielson, N. B., Grosmark, A. D., Kaifosh, P. W., Bowler, J. C., Liao, Z., Sparks, F. T., Gogos, J. A., & Losonczy, A. (2017). Impaired hippocampal place cell dynamics in a mouse model of the 22q11.2 deletion. *Nature Neuroscience*, *20*(11), Article 11. https://doi.org/10.1038/nn.4634

Zhao, R., Fowler, S. W., Chiang, A. C. A., Ji, D., & Jankowsky, J. L. (2014). Impairments in experience-dependent scaling and stability of hippocampal place fields limit spatial learning in a mouse model of Alzheimer's disease. *Hippocampus*, *24*(8), 963–978. https://doi.org/10.1002/hipo.22283

Zhao, X., Wang, Y., Spruston, N., & Magee, J. C. (2020). Membrane potential dynamics underlying context-dependent sensory responses in the hippocampus. *Nature Neuroscience*, *23*(7), 881–891. https://doi.org/10.1038/s41593-020-0646-2

Ziv, Y., Burns, L. D., Cocker, E. D., Hamel, E. O., Ghosh, K. K., Kitch, L. J., Gamal, A. E., & Schnitzer, M. J. (2013). Long-term dynamics of CA1 hippocampal place codes. *Nature Neuroscience*, *16*(3), Article 3. https://doi.org/10.1038/nn.3329

Chapter 5: Discussion

5.1 Overview

In this thesis I set out to essentially answer three questions that revolved exclusively around a subset of pyramidal neurons within the hippocampus. Specifically, I set out to determine at a cellular level, what is causing their synaptic vulnerability in Alzheimer's disease, how this is dependent on a remarkably unique intracellular asymmetric distribution of its mitochondrial network, and the functional impact of synaptic loss on neuronal function at cellular and population levels. These CA1 PNs are selectively vulnerable in Alzheimer's disease, being one of the first affected by disease pathology and most significantly impacted. These neurons are also responsible in part for an animal's ability to form spatial memories and to reliably navigate an environment. Incidentally, these exact same hippocampal functions are deficient early in Alzheimer's disease pathology. What was not clear prior to these findings was a defined, molecular pathway linking Aβ exposure directly to synaptic loss, and how synaptic loss in CA1 PNs could causatively explain spatial memory and navigation deficits in AD models.

Here, I described how Aβ directly causes spatially-restricted synaptic loss through overactivation of the kinase dyad, CAMKK2-AMPK, and subsequent mitochondrial fragmentation and degradation in apical tuft dendrites via AMPK phosphorylation of MFF and ULK2. I then described the molecular mechanism necessary to establish and maintain the unique, compartmentalized mitochondrial network in CA1 PNs, which is activity dependent and requires CAMKK-AMPK activation of MFF and MTFR1L. Finally, I described the functional impact on CA1 PNs and the CA1 population in an AD mouse model *in vivo*, highlighting a functional rigidity encoded at the population level which subsequently results in deficits in place field enrichment at a reward zone and behavioral deficits.

Below, I will specifically explore the main findings of each chapter of this thesis in order, followed by potential outstanding questions and future directions for each.

5.2 Summary of Findings & Future Directions

5.2.1 What are the molecular mechanisms driving synaptic loss in the hippocampus during Alzheimer's disease?

In Chapter 2, I investigated the molecular mechanisms responsible for synaptic loss using *in vitro* and *in vivo* models of AD. I used a mixture of *in utero* and *ex utero* electroporation of genetically engineered autophagy, mitochondria, and cytoplasmic reporters to determine that mitochondrial fragmentation and degradation, triggered by Aβ, is necessary for synaptic loss.

Specifically, my findings included:

1. **CA1 PNs exhibit remarkable spatially-compartmentalized dendritic mitochondrial morphology**, with proximal dendrites in the SR and SO regions containing small, punctate mitochondria and distal tuft dendrites in SLM containing long, tubular mitochondria.
2. **Aβ-dependent synaptotoxicity in CA1 PNs is largely compartmentalized**, with distal tuft dendrites exhibiting the most significant decreases in synaptic density, while proximal dendrites exhibit moderately significant decreases.
3. Aβ42o-dependent **over-activation of AMPK leads to mitochondrial fragmentation and degradation** in the distal tuft dendrites of CA1 PNs in a J20 mouse model, in cortical PNs *in vitro*, and in hESC-derived cortical neurons *in vitro*. Knocking out AMPK is sufficient to prevent mitochondrial biomass loss and subsequently prevent spine loss *in vitro*.
4. Aβ42o-dependent **over-activation of AMPK leads to mitochondria fragmentation via phosphorylation of MFF**. Knocking down MFF via shRNA *in vitro* or *in vivo* or preventing AMPK phosphorylation by expressing a mutated MFF which cannot be phosphorylated by AMPK *in vitro* is sufficient to prevent both AMPK-dependent mitochondrial fragmentation and synaptic loss.
5. Treating cortical PNs *in vitro* with **Aβ42o leads to increased local dendritic mitophagy through AMPK-dependent phosphorylation of ULK2**, but not ULK1. By knocking out ULK2, but not ULK1, or preventing phosphorylation by AMPK through point mutations, accumulation of LC3+ and LAMP+ puncta at sites of mitochondrial degradation is prevented. Importantly, preventing ULK2-mediated mitophagy induced by AMPK hyperactivity does not prevent mitochondrial fragmentation, but does prevent synaptic loss, indicating mitochondrial biomass loss is the driving force behind synaptotoxicity.

6. **Mitochondrial degradation is required for synaptic loss** in models of AD, as preventing mitophagy and thus a decrease in mitochondrial density or preventing mitochondrial fragmentation, a necessary step for mitophagy, through inhibiting AMPK, MFF, or ULK2, is sufficient to prevent synaptotoxicity.
7. **Aβ42o-dependent mitochondrial fragmentation and subsequent degradation is Tau-dependent**. By expressing a mutant form of Tau *in vitro* which cannot be phosphorylated by AMPK, we blocked MFF-mediated mitochondrial fragmentation as well as synaptic loss.
8. **Preventing synaptic loss in an AD context rescues spine morphology.** By knocking down MFF *in vivo* in a mouse model of AD and subsequently preventing spine loss in CA1 PNs, we demonstrated that the rescued synapses retain their spine width and spine length, indicating they may retain their functionality.
9. Constitutive **knockdown of AMPK is sufficient to decrease the degree of Aβ plaque deposition in an AD mouse model**. By crossing a homozygous AMPKα1$^{-/-}$ mouse to an AMPKα1$^{-/-}$-J20 mouse and measuring Aβ plaque deposition within the hippocampus, we showed that both plaque count, size, and distribution is reduced only in homozygous AMPK knockout, but not in heterozygous knockouts.

These findings highlight several avenues for future exploration. One of the most obvious places for future research is continuing to pursue this newly identified pathway to its end, synaptic loss. Because we have found that mitochondrial fragmentation and subsequent degradation via mitophagy is necessary for synaptic loss, there is an implication that mitochondria are necessary for maintaining synapses—both in CA1 PNs *in vivo* and in layer 2/3 cortical PNs *in vitro*. What is unclear from these data is how the removal of mitochondria is leading to synaptic loss—could it be through supplying ATP or regulating cytosolic Ca^{2+}? One attractive hypothesis is that, due to the nature of the distal tuft dendrites being elongated and occupying most of the dendritic compartment, they are selectively vulnerable to mitochondrial biomass loss. If these dendrites are under different functional constraints than the basal and apical oblique dendrites, which may very well be true given their differential inputs, disrupting these mitochondria could preferentially harm distal tuft synapses through some Ca^{2+} overload. The more complete the model, the more precise any potential therapeutic interventions that take advantage of such a pathway could be.

Yet another remaining question is whether or not the existing mitochondria in the diseased neurons or in the rescued neurons are functionally different than physiological, non-diseased conditions. One could imagine that the mitochondria present following Aβ exposure are either fully functional mitochondria that are just occupying less of the dendritic space, or the Aβ exposure and subsequent cellular changes have negative impacts on those remaining mitochondria—be it a decrease in ATP production, changes in membrane potential, excess ROS signaling, greater sensitivity to Ca^{2+}, etc. Additionally, these effects could be independent of the biomass loss, meaning "rescuing" the mitochondrial fragmentation and/or degradation might not have a preventative effect on mitochondrial dysfunction. Understanding how these organelles are impacted functionally, rather than just structurally, is critical or understanding whether simply preventing their loss is sufficient to prevent further pathological issues.

A broader question left from these results is to what extent preventing synaptic loss in CA1 PNs rescues synaptic and cellular function. One of the most important findings in this chapter is that preventing mitochondrial fragmentation or degradation through preventing activation of CAMKK, AMPK, MFF, or ULK2 is sufficient in every case to prevent Aβ-mediated synaptic loss. Because synaptic loss is such a strong indicator for cognitive decline, this is a significant advancement in the potential treatment for AD. These data are so important in part because the neurons are still intact—as mentioned in the introduction to this thesis, dead cells cannot be rescued. It is critical not only to prevent cell loss, but as this study shows, synaptic loss. What is left unanswered and warrants further research, though, is whether or not synapses that are maintained *in vitro* or *in vivo* in these AD models retain their physiological activity. One could imagine two situations: either, the rescued synapses retain physiological levels of excitability, connectivity, plasticity, and function and thus support neuronal function like synapses in non-diseased cells; or, these rescued synapses could be dysfunctional in some capacity—be it diminished LTP or LTD, decreased efficiency, disrupted connectivity, etc. Evaluating to what extent rescued synapses are still functional is critical for evaluating whether preventing synaptic loss in this context is a viable therapeutic avenue or not.

One of the less obvious questions that is not explicitly related to lead us directly into Chapter 3 of this thesis: what are the mechanisms that are leading to spatially-regulated compartmentalization of dendritic mitochondrial morphology in CA1 PNs? And, further, why are the mitochondria

compartmentalized? Is it simply a consequence of cellular activity, or is it playing a more essential role in the function of the neuron?

Overall, the data in this chapter represents for the first time a singular, unifying molecular pathway which links several of the previous disparate hallmarks of AD: Aβ, mitochondrial dysfunction, calcium disregulation, autophagy imbalance, Tau, and synapse loss. This pathway could represent a very attractive therapeutic target for future AD drug therapies, providing a very clear mechanism to target in order to selectively prevent synaptic loss in early AD. These data also generally provide an important link between a cell's mitochondrial network and synaptic maintenance generally, implicating the necessity even in physiological, non-diseased conditions for robust mitochondria in neuronal maintenance and function.

5.2.1 What are the effectors responsible for maintaining hippocampal intracellular organization under physiological conditions?

In Chapter 3, I sought to determine which mechanisms are causing the compartmentalized mitochondrial morphology in CA1 PNs discovered in Chapter 2 using a combination of biochemistry, *in utero* electroporation, and *in vivo* two-photon imaging. I found that local inputs are driving mitochondrial fission in proximal dendrites through activity-dependent activation of CAMKK2 and AMPK and its downstream effectors, MFF and MTFR1L.

Specifically, my findings included:

1. **Imaging of mitochondria in CA1 PNs *in vivo* confirms dendritic mitochondrial compartmentalized morphology**, with dendritic mitochondria in SO and SR significantly smaller and occupying less dendritic volume than dendritic mitochondria in SLM, which are long, tubular, and occupy most of dendritic volume. Using single cell electroporation for the first time to visualize organelles, we were able to image mitochondria within CA1 PNs in a live, anesthetized mouse.
2. **Proximal dendritic mitochondria in CA1 PNs contain constricted mitochondrial matrices and contiguous OMMs**, though length and occupancy as measured by OMM retains the previously observed compartmentalization phenotype. By expressing an OMM-targeted fluorophore in addition to a mitochondrial matrix-targeted fluorophore, we were able to measure both mitochondrial lengths and occupancies within CA1 PNs. This revealed that, in basal dendrites, several matrices can be part of a single "mitochondrion" through a single OMM. Similarly, in apical oblique dendrites, several longer

matrices can be encompassed by a single longer OMM. In the tuft, there is very limited matrix constriction in the absence of OMM constriction.

3. **Compartmentalized dendritic mitochondrial morphology in CA1 PNs is present very early in development** and maintained throughout adulthood. By expressing mitochondrial reporters via IUE at early developmental stages (P7, P10, P14, and P21) we were able to determine that even in the earliest stages of development during synaptic connectivity, mitochondria are compartmentalized.
4. Removing CA1 PNs from their context and **culturing CA1 hippocampal PNs results in de-compartmentalized mitochondrial morphology**. Rather than retaining short mitochondrial matrices in proximal dendrites and long mitochondrial matrices in distal tuft dendrites, CA1 PNs in culture, dissociated from the hippocampus, exhibit moderate to longer phenotypes more reminiscent of distal tuft dendrites or cortical PNs. This implies two things: 1) cell non-autonomous effectors, such as inputs, are driving compartmentalization *in vivo* as their context matter for mitochondrial morphology, and 2) the default cell autonomous mitochondrial phenotype is fusion over fission, as mitochondria appear long and tubular.
5. **Domain-specific inputs to CA1 PNs are required for mitochondrial compartmentalization in proximal dendrites**. By selectively limiting the number of inputs arriving to basal and apical oblique dendrites by ~50% using an shRNA against Lphn3, we could sufficiently prevent mitochondrial fission in these compartments, elongating mitochondria to more closely resemble the distal tuft dendrites *in vivo* or cortical dendrites *in vitro*.
6. **Restricting activity within CA1 PNs is sufficient to prevent mitochondrial compartmentalization in proximal dendrites**. By over-expressing an inward-rectifying potassium pump, Kir2.1, thus hyperpolarizing the cell and preventing neuronal activity, we could prevent mitochondrial fission in basal and apical oblique dendrites, leading to mitochondrial elongation in these proximal dendrites. This implies that not only are inputs to these two compartments necessary for mitochondrial morphology, but the activity driven by these inputs is also necessary and unique from the distal tuft.
7. **Dendritic mitochondrial morphology in CA1 PNs is regulated by CAMKK2 and AMPK *in vivo***. By constitutively or conditionally knocking out CAMKK2 or AMPK respectively *in vivo* using IUE, we showed that getting rid of either protein is sufficient to prevent mitochondrial fission in the basal and

apical oblique dendritic compartments, resulting in significant elongation. This implies that the increased activity in these proximal dendrites is leading to increased activity of the CAMKK2-AMPK pathway via increased cytosolic Ca^{2+} in these dendrites compared to distal tuft dendrites.

8. **Dendritic mitochondrial morphology in CA1 PNs is regulated by MTFR1L *in vivo*.** By knocking down MTFR1L *in vivo* using IUE, we showed that mitochondrial fission in basal and apical oblique dendrites of CA1 PNs requires MTFR1L activity, which can be rescued by expressing shRNA-resistant MTFR1L cDNA. Additionally, knocking down OPA1 is sufficient to prevent shMTFR1L-mediated elongation, confirming that MTFR1L restricts mitochondrial size in proximal dendrites through inhibition of the pro-fusion protein OPA1.
9. **Dendritic mitochondrial morphology in CA1 PNs is regulated by MFF *in vivo*.** By knocking down MFF *in vivo* using IUE, we should that mitochondrial fission in basal and apical oblique dendrites of CA1 PNs also requires MFF. Interestingly, distal apical tuft dendrites also, to some extent, required MFF to maintain their length, as knocking down MFF elongates tuft mitochondria as well. We also find that knocking down MFF and MTFR1L simultaneously *in vivo* does not result in an additive effect, indicating redundant but non-overlapping functions. MFF knockdown is more effective, however, which could be explained by biochemistry showing that MFF more strongly regulates MTFR1L expression than MTFR1L regulates MFF expression.
10. **Activity-dependent activation of CAMKK2 leads to mitochondrial vision via AMPK-mediated MTFR1L phosphorylation in CA1 PNs**. Using a combination of biochemistry and IUE, we showed that activating hippocampal neurons *in vitro* is sufficient to induce CAMKK2, AMPK, and MTFR1L phosphorylation, all of which can be prevented in the presence of a pharmacological inhibitor of CAMKK2. To further prove the dependence of MTFR1L activation in an activity-dependent, CAMKK2-dependent pathway, we expressed a constitutively active mutant form of MTFR1L in a constitutive CAMKK2 knockout mouse using IUE and showed over-activation of MTFR1L, even if the absence of CAMKK2, is sufficient to prevent mitochondrial elongation in the proximal dendrites of CA1 PNs.

These data, while complete in their description of the molecular pathways necessary to maintain compartmentalized dendritic mitochondrial morphology in CA1 PNs, raise even more potential questions

worth pursuing. The biggest question, of course, is the extent to which mitochondria structural compartmentalization is necessary for CA1 PN function. So, if this compartmentalization is disrupted, either through fragmentation in the distal tuft dendrites (as we observe in AD as mentioned in Chapter 2) or elongation of the basal and apical oblique dendrites (as we achieve through multiple means in this chapter), does this have an impact on basic neuronal properties? And, further, because CA1 PNs are great models for selective tuning and circuit function as place cells, does this impact CA1 PNs specifically from becoming or functioning as spatially tuned neurons? One could imagine that disrupting this compartmentalization in either direction—elongating the proximal dendritic mitochondria or fragmenting the distal dendritic mitochondria—could bias the cells in either two opposing directions or the same direction. For basic neuronal properties, I anticipate that the two different perturbations would lead to opposite effects—in essence, elongating the mitochondrial network could limit the amount of cytosolic Ca^{2+} levels, decreasing amplitudes and durations of firing events, potentially limiting frequency, and negatively impacting spatial tuning properties; fragmenting the tuft, however, has less clear potential outcomes, though due to the nature of the tuft as the source of dendritic plateau events, whether or how these elongated mitochondria might be necessary in some way for this event and therefore for place cell formation would be interesting to explore. However, these hypotheses rest upon a current unknown: whether or not increasing mitochondrial length corresponds to a relative increase in ER-mitochondrial contact sites, which are critical for ER Ca^{2+} buffering. Another assumption is that the primary function of the mitochondria in neuronal function is to regulate Ca^{2+} homeostasis. Relatively simple experiments limiting mitochondrial Ca^{2+} uptake in a condition in which mitochondria are elongated could quickly answer this concern, however. Understanding the extent to which mitochondrial compartmentalization plays a role in spatial tuning within CA1 would not only allow us to better understand how CA1 PNs, but potentially how they are formed.

Another very important question that is left unanswered in this chapter is to what extent these different dendritic compartments in CA1 PNs—basal, apical oblique, and apical tuft—are functionally different from each other. One major assumption made in this project, which is built directly into the foundation of the model, is that basal and apical oblique dendrites are undergoing local firing events at higher rates than distal tuft dendrites. As noted previously, these two different compartments receive either CA3 (and CA2) inputs or direct inputs from the EC. It is entirely possible, therefore, that these two

populations of neurons are firing at different rates and therefore biasing these compartments in one way or the other. However, we do not currently know whether basal and apical oblique dendrites have higher baseline cytoplasmic Ca^{2+}, or whether the limited mitochondrial biomass in these compartments results in higher amplitude, longer duration Ca^{2+} transients. Understanding how these different dendritic compartments might be functionally different could help explain how they are able to receive and compare distinct information, outputting an ultimate response.

One broader question that follows from this work is expanding our view outward and asking to what extent this mitochondrial compartmentalization is unique to CA1 PNs. We know that Layer 2/3 PNs in the somatosensory and motor cortex do not display similar mitochondrial morphologies, as mentioned. However, whether or not CA3, CA2, or DG neurons, which have similarly compartmentalized inputs as CA1, have similarly compartmentalized mitochondrial morphology is unclear. Additionally, are there other neuronal cell types within the brain but outside of the hippocampus that contain similarly interesting mitochondrial sub-cellular compartmentalization?

Overall, these data represent for the first time a pathway in which localized inputs drive a sub-dendritic, asymmetric mitochondrial network in an activity dependent manner. Though activity had previously been linked to mitochondrial structure, such a robust and stark sub-cellular compartmentalization of an organelle like what is seen in CA1 PNs is rarely seen. These data strongly indicate a need for neuroscientists, especially those focused on understanding neuronal function, circuits, and systems, to seriously consider intracellular organelle dynamics in the shaping of neuronal function and plasticity.

5.2.1 How does Alzheimer's disease progression affect the hippocampal circuit?

In Chapter 4, I aimed to determine when and how the hippocampal circuit is disrupted in AD. Using *in vivo* two-photon Ca^{2+} microscopy at two pathologically distinct time-points in the J20 AD mouse model, I was able to determine that basic neuronal properties and place cell properties in CA1 PNs are largely unaffected, while the population as a whole is inflexible in its encoding properties, manifesting in part in behavioral deficits.

Specifically, my findings included:

1. **CA1 PNs exhibit hyperactivity at early timepoints in AD pathology, but not in later timepoints**. By measuring basic neuronal properties, such as event frequency, duration, and amplitude, I found that

only in 3 month old J20 mice recorded during random foraging was there any significant change in basic neuronal properties, in this case an increase in the event frequency. Though significant at a population level, likely due to the incredibly large numbers of neurons recorded, no other basic neuronal property was significantly different from littermate controls.

2. **CA1 PNs do not exhibit any significant place cell property differences at early or late stages of disease pathology**. By measuring the fraction of cells that are place cells, the place field width, the specificity and sensitivity, and the amount of spatial information, I was able to determine that, at an individual mouse level, there are no significant deficits or changes in place cell properties at 3 or 6 months in J20 mice.
3. **Place cells in CA1 of J20 mice exhibit significant increases in tuning curve correlations across AD pathology**. Tuning curve correlations are how similar individual neurons' spatial tuning, or firing within a specific area within an environment, changes across days of recording. Though it is expected to see a gradual decline in correlation across time, J20 animals have persistently higher correlation, indicating rigidity in the encoding of individual place cells.
4. **At a population level, place cells in J20 are more rigid, which is exacerbated through AD pathology progression**. By performing population vector correlations, which is examining how the entire population of CA1 PNs encodes each position within the environment, I was able to determine that, within days and across days, there is an increase in the population vector correlations at both 3 and 6 months, with 6 months being significantly higher than 3 months. This implies that, not only are individual place cells more rigid in their firing, but the entire population is rigid/inflexible.
5. Due largely to their increased rigidity, **it is easier to predict a J20 animal's position using CA1 place cell information**. By training a model on CA1 place cell data, we could then test the decoding accuracy of this model to determine whether training the model on J20 place cell information resulted in any differences in decoding accuracy than from WT littermate place cell data. Ultimately, we found lack of flexibility in the place cell encoding in J20 mice increased reliability for the model.
6. **Decoding position of J20 mice is equally as reliable in the past as it is in the future**, due to the inflexibly of the population. Because of the rigidity of the spatial information in J20 animals, the information present at Day 1 of recording was represented in a more similar way on Day 6 of recording

in J20 mice than in WT mice. This meant that using data from Day 1 to predict location in the future (Days 2-6) was equally as reliable as using data from Day 6 to predict location in the past (Days 1-5). One would expect in WT conditions, as we observe in our data, an asymmetry in the ability to reliably decode position, with the reliability increasing when using data to predict location in the past due to that residual information existing within the population code.

7. **J20 animals at more advanced stages AD pathology can reliably learn a spatial memory task**. Unlike many previous experiments, we do not report deficits in the ability of J20 mice to reliably learn a spatial memory task. When putting the mice through a goal-oriented learning behavioral regime, J20 mice learned the location of the reward better than chance at 6 months. However, we do note significant deficits in the J20 mice at 3 months, with anticipatory licking no greater than chance.
8. **Place cell remapping is significantly disrupted at early AD time-points and relies on an increase in the number of new place fields at later time-points**. By measuring the amount of place field enrichment occurring at or around the reward zone in a goal-oriented behavioral paradigm, we observed a significant deficit in enrichment in 3 month J20 mice only. This correlated significantly with deficits in ability of the mice to anticipate the reward and lick prior to the reward zone itself. However, at 6 months, J20 mice exhibit significantly better enrichment, relying almost exclusively on an increase in the number of new place cells rather than remapping.
9. **Though place cell enrichment at a reward zone correlates with behavioral performance in WT animals, there's a significant de-correlation in enrichment and behavioral performance in J20 mice**. In WT mice at 3 and 6 months, by correlating place field enrichment with anticipatory behavior, we found a positive correlation between the two, indicating enrichment could be a predictor for behavioral performance. However, in J20 mice, there was no correlation between enrichment and behavior.

These data represent for the first time a more complete, circuit and population level assessment of how AD-dependent pathology affects the hippocampus at multiple stages. However, it leaves many potential avenues of research to investigate. First, the project is limited in its ability to report how the circuit changes over time in the same animals. Though testing two pathologically distinct time-points gives significant insight

into what is going wrong pre-plaque development and post-plaque development, expressing a genetically encoded Ca2+ sensor rather than injecting an AAV-GCaMP virus could provide a more longitudinal approach to this experiment, allowing you to track the same mice across the development of the disease. This would give a much more nuanced description of the disease and how it changes throughout pathological progression.

Another facet to this project which was left unexplored was the extent to which synaptic loss is necessary for the circuit deficits we observe. One outstanding question which has yet to be directly answered in this field is what at a cellular level is leading to functional deficits. One hypothesis is that synaptic loss is directly responsible, as removing a significant number of excitatory inputs, disrupting the excitatory/inhibitory balance of these neurons, could be the driving force behind changes in neuronal properties. This is supported by the notion that synapse loss is currently the greatest correlate with cognitive decline we have. In order to test this, one could utilize the insight we uncovered in Chapter 2 regarding the molecular mechanisms necessary for Aβ-dependent synaptic loss in CA1 to selectively and cell-autonomously prevent synapse loss. By using a conditional AMPK mouse line crossed to the J20 mouse line for example, you could prevent synaptic loss and subsequently record place cell activity in diseased animals to determine if rescuing synapses alone is sufficient to prevent circuit deficits. In fact, I collected significant data to this point, in utero electroporating AMPK$\alpha1^{F/F}\alpha2^{F/F}$-J20 mice with Cre and then raising them to the defined timepoints (3 and 6 months) and putting them through the exact same tests described in Chapter 4. Because we see limited effects on basic transient properties, it's difficult to make conclusions about whether preventing synapse loss prevents any functional changes at a single cell level. However, we do observe potential changes in tuning curve correlations in cells that are AMPK KO compared to those that are not within individual J20 animals. Similarly, preventing AMPK-mediated synaptic loss seems to have a general neuroprotective role, specifically leading to an increase in place field enrichment. These data are unpublished and preliminary, in large part due to the low numbers of animals and cells and thus lack of statistical power due to the incredible difficulty of the experiment itself.

One question that arises additionally from this research is the extent to which rescuing synapses themselves rescues synaptic connectivity and function, as briefly mentioned in the discussion above regarding Chapter 2. One potential experiment that would be important to interpreting any functional rescue

experiments would be to determine whether preventing synaptic loss in an AMPK knockout for example prevents any deficits in connectivity. By using monosynaptic rabies-tracing, one would not only be able to determine whether and how connectivity to CA1 PNs is disrupted in AD mouse models, but preventing synaptic loss, you could also determine if that is sufficient to prevent any connectivity deficits.

Overall, these data indicate that, in CA1 PNs, circuit rigidity is a primary hallmark of AD pathology in a mouse model. These data indicate that, rather than individual neuronal deficits, the spatial code in AD mice is being abstracted uniformly across environments at a population level. If this is true, it implies that mice are less likely to distinguish subtle differences between environments—a phenotype that is highly reminiscent of the behavioral and cognitive deficits seen in patients with moderate to advanced AD. Therefore, interventions which could destabilize the spatial encoding of the hippocampal network, restoring flexibility in the population, may function to rescue any behavioral deficits that can occur from circuit rigidity. Additionally, because basic neuronal properties are largely spared, these data indicate a strong need to also evaluate circuit readouts of complex diseases such as AD at higher orders, considering the population in addition to individual neurons. Regardless, we are in the early stages of establishing clear circuit readouts for AD models, the value of which is hard to overstate for the next stages of therapeutic research into this devastating disease.

5.3 Conclusion

Alzheimer's disease is a complex, devastating disease that continues to impact millions of individuals and their families, with only more to be affected as the population continues to age. Most researchers who study AD know too well the discussion had with almost every member of the public when learning about our work—a recount of a family member or friend of theirs who suffered from this disease. Watching, often excruciatingly slowly, the person they know slip away from themselves and from everyone else. It is as important as ever to focus on new, innovative ways to approach this disease in order to hopefully make any headway in finding a treatment or cure. To me, that includes birding the gaps currently in the field by linking molecular and cellular changes in AD to functional changes and subsequently behavioral changes. Hopefully, through the discoveries in this thesis and the potential work that it inspires, I have moved the field forward, even if incrementally, by attempting to do exactly that: better understanding the underlying

mechanisms of AD and the cells that are most vulnerable, and how specific cellular deficits can manifest into circuit and behavioral deficits.

References

2023 Alzheimer's disease facts and figures. (2023). *Alzheimer's & Dementia*, alz.13016. https://doi.org/10.1002/alz.13016

Abbott, L. F., & Blum, K. I. (1996). Functional significance of long-term potentiation for sequence learning and prediction. *Cerebral Cortex (New York, N.Y.: 1991)*, *6*(3), 406–416. https://doi.org/10.1093/cercor/6.3.406

Ageta-Ishihara, N., Takemoto-Kimura, S., Nonaka, M., Adachi-Morishima, A., Suzuki, K., Kamijo, S., Fujii, H., Mano, T., Blaeser, F., & Chatila, T. A. (2009). Control of cortical axon elongation by a GABA-driven Ca^{2+}/calmodulin-dependent protein kinase cascade. *J Neurosci*, *29*, 13720–13729. https://doi.org/10.1523/JNEUROSCI.3018-09.2009.

Aizenstein, H. J., Nebes, R. D., Saxton, J. A., Price, J. C., Mathis, C. A., Tsopelas, N. D., Ziolko, S. K., James, J. A., Snitz, B. E., Houck, P. R., Bi, W., Cohen, A. D., Lopresti, B. J., DeKosky, S. T., Halligan, E. M., & Klunk, W. E. (2008). Frequent amyloid deposition without significant cognitive impairment among the elderly. *Archives of Neurology*, *65*(11), 1509–1517. https://doi.org/10.1001/archneur.65.11.1509

Anderson, N. B., Bulatao, R. A., Cohen, B., & National Research Council (US) Panel on Race, E. (2004). Ethnic Differences in Dementia and Alzheimer's Disease. In *Critical Perspectives on Racial and Ethnic Differences in Health in Late Life*. National Academies Press (US). https://www.ncbi.nlm.nih.gov/books/NBK25535/

Ando, K., Tomimura, K., Sazdovitch, V., Suain, V., Yilmaz, Z., Authelet, M., Ndjim, M., Vergara, C., Belkouch, M., Potier, M.-C., Duyckaerts, C., & Brion, J.-P. (2016). Level of PICALM, a key component of clathrin-mediated endocytosis, is correlated with levels of phosphotau and autophagy-related proteins and is associated with tau inclusions in AD, PSP and Pick disease. *Neurobiology of Disease*, *94*, 32–43. https://doi.org/10.1016/j.nbd.2016.05.017

Apostolova, L. G. (2016). Alzheimer Disease. *Continuum : Lifelong Learning in Neurology*, *22*(2 Dementia), 419–434. https://doi.org/10.1212/CON.0000000000000307

Arbel-Ornath, M., Hudry, E., Boivin, J. R., Hashimoto, T., Takeda, S., Kuchibhotla, K. V., Hou, S., Lattarulo, C. R., Belcher, A. M., Shakerdge, N., Trujillo, P. B., Muzikansky, A., Betensky, R. A., Hyman, B. T., & Bacskai, B. J. (2017). Soluble oligomeric amyloid-β induces calcium dyshomeostasis that precedes synapse loss in the living mouse brain. *Molecular Neurodegeneration*, *12*(1), 27. https://doi.org/10.1186/s13024-017-0169-9

Area-Gomez, E., & Schon, E. A. (2016). Mitochondria-associated ER membranes and Alzheimer disease. *Curr Opin Genet Dev*, *38*, 90-96. https://doi.org/10.1016/j.gde.2016.04.006

Arnold, S. E., Hyman, B. T., Flory, J., Damasio, A. R., & Van Hoesen, G. W. (1991). The topographical and neuroanatomical distribution of neurofibrillary tangles and neuritic plaques in the cerebral cortex of patients with Alzheimer's disease. *Cerebral Cortex (New York, N.Y.: 1991)*, *1*(1), 103–116. https://doi.org/10.1093/cercor/1.1.103

Arriagada, P. V., Marzloff, K., & Hyman, B. T. (1992). Distribution of Alzheimer-type pathologic changes in nondemented elderly individuals matches the pattern in Alzheimer's disease. *Neurology*, *42*, 1681–1688.

Ashe, K. H., & Zahs, K. R. (2010). Probing the biology of Alzheimer's disease in mice. *Neuron*, *66*(5), 631–645. https://doi.org/10.1016/j.neuron.2010.04.031

Ashrafi, G., & Schwarz, T. L. (2015). PINK1- and PARK2-mediated local mitophagy in distal neuronal axons. *Autophagy*, *11*, 187-189. https://doi.org/10.1080/15548627.2014.996021

Bading, H., Ginty, D. D., & Greenberg, M. E. (1993). Regulation of gene expression in hippocampal neurons by distinct calcium signaling pathways. *Science*, *260*, 181–186. https://doi.org/10.1126/science.8097060.

Bakker, A., Albert, M. S., Krauss, G., Speck, C. L., & Gallagher, M. (2015). Response of the medial temporal lobe network in amnestic mild cognitive impairment to therapeutic intervention assessed by fMRI and memory task performance. *NeuroImage. Clinical*, *7*, 688–698. https://doi.org/10.1016/j.nicl.2015.02.009

Bakker, A., Krauss, G. L., Albert, M. S., Speck, C. L., Jones, L. R., Stark, C. E., Yassa, M. A., Bassett, S. S., Shelton, A. L., & Gallagher, M. (2012). Reduction of hippocampal hyperactivity improves cognition in amnestic mild cognitive impairment. *Neuron*, *74*(3), 467–474. https://doi.org/10.1016/j.neuron.2012.03.023

Barnes, A. P., & Polleux, F. (2009). Establishment of axon-dendrite polarity in developing neurons. *Annu Rev Neurosci*, *32*, 347–381. https://doi.org/10.1146/annurev.neuro.31.060407.125536.

Basu, J., & Siegelbaum, S. A. (2015). The Corticohippocampal Circuit, Synaptic Plasticity, and Memory. *Cold Spring Harbor Perspectives in Biology*, *7*(11), a021733. https://doi.org/10.1101/cshperspect.a021733

Benna, M. K., & Fusi, S. (2021). Place cells may simply be memory cells: Memory compression leads to spatial tuning and history dependence. *Proceedings of the National Academy of Sciences*, *118*(51), e2018422118. https://doi.org/10.1073/pnas.2018422118

Birdsall V., & Waites C. L. (2019). Autophagy at the synapse. *Neurosci Lett*, *697*, 24-28. https://doi.org/10.1016/j.neulet.2018.05.033

Bittner, K. C., Grienberger, C., Vaidya, S. P., Milstein, A. D., Macklin, J. J., Suh, J., Tonegawa, S., & Magee, J. C. (2015). Conjunctive input processing drives feature selectivity in hippocampal CA1 neurons. *Nature Neuroscience*, *18*(8), Article 8. https://doi.org/10.1038/nn.4062

Bittner, K. C., Milstein, A. D., Grienberger, C., Romani, S., & Magee, J. C. (2017). Behavioral time scale synaptic plasticity underlies CA1 place fields. *Science (New York, N.Y.)*, *357*(6355), 1033–1036. https://doi.org/10.1126/science.aan3846

Bittner, T., Burgold, S., Dorostkar, M. M., Fuhrmann, M., Wegenast-Braun, B. M., Schmidt, B., Kretzschmar, H., & Herms, J. (2012). Amyloid plaque formation precedes dendritic spine loss. *Acta Neuropathologica*, *124*(6), 797–807. https://doi.org/10.1007/s00401-012-1047-8

Bittner, T., Fuhrmann, M., Burgold, S., Ochs, S. M., Hoffmann, N., Mitteregger, G., Kretzschmar, H., LaFerla, F. M., & Herms, J. (2010). Multiple Events Lead to Dendritic Spine Loss in Triple Transgenic Alzheimer's Disease Mice. *PLOS ONE*, *5*(11), e15477. https://doi.org/10.1371/journal.pone.0015477

Blazquez-Llorca, L., Valero-Freitag, S., Rodrigues, E. F., Merchán-Pérez, Á., Rodríguez, J. R., Dorostkar, M. M., DeFelipe, J., & Herms, J. (2017). High plasticity of axonal pathology in Alzheimer's disease mouse models. *Acta Neuropathologica Communications*, *5*(1), 14. https://doi.org/10.1186/s40478-017-0415-y

Blennow, K., Zetterberg, H., Rinne, J. O., Salloway, S., Wei, J., Black, R., Grundman, M., Liu, E., & AAB-001 201/202 Investigators. (2012). Effect of immunotherapy with bapineuzumab on cerebrospinal

fluid biomarker levels in patients with mild to moderate Alzheimer disease. *Archives of Neurology*, *69*(8), 1002–1010. https://doi.org/10.1001/archneurol.2012.90

Bliss, T. V., & Lomo, T. (1973). Long-lasting potentiation of synaptic transmission in the dentate area of the anaesthetized rabbit following stimulation of the perforant path. *The Journal of Physiology*, *232*(2), 331–356. https://doi.org/10.1113/jphysiol.1973.sp010273

Blockus, H., Rolotti, S. V., Szoboszlay, M., Peze-Heidsieck, E., Ming, T., Schroeder, A., Apostolo, N., Vennekens, K. M., Katsamba, P. S., Bahna, F., Mannepalli, S., Ahlsen, G., Honig, B., Shapiro, L., de Wit, J., Losonczy, A., & Polleux, F. (2021). Synaptogenic activity of the axon guidance molecule Robo2 underlies hippocampal circuit function. *Cell Reports*, *37*(3), 109828. https://doi.org/10.1016/j.celrep.2021.109828

Bloss, E. B., Cembrowski, M. S., Karsh, B., Colonell, J., Fetter, R. D., & Spruston, N. (2018). Single excitatory axons form clustered synapses onto CA1 pyramidal cell dendrites. *Nat Neurosci*, *21*, 353–363. https://doi.org/10.1038/s41593-018-0084-6.

Bostock, E., Muller, R. U., & Kubie, J. L. (1991). Experience-dependent modifications of hippocampal place cell firing. *Hippocampus*, *1*(2), 193–205. https://doi.org/10.1002/hipo.450010207

Boudaba, N., Marion, A., Huet, C., Pierre, R., Viollet, B., & Foretz, M. (2018). AMPK Re-Activation Suppresses Hepatic Steatosis but its Downregulation Does Not Promote Fatty Liver Development. *EBioMedicine*, *28*, 194–209. https://doi.org/10.1016/j.ebiom.2018.01.008.

Boutajangout, A., & Wisniewski, T. (2014). Tau-based therapeutic approaches for Alzheimer's disease—A mini-review. *Gerontology*, *60*(5), 381–385. https://doi.org/10.1159/000358875

Braak, H., Alafuzoff, I., Arzberger, T., Kretzschmar, H., & Del Tredici, K. (2006). Staging of Alzheimer disease-associated neurofibrillary pathology using paraffin sections and immunocytochemistry. *Acta Neuropathologica*, *112*(4), 389–404. https://doi.org/10.1007/s00401-006-0127-z

Braak, H., & Braak, E. (1991). Neuropathological stageing of Alzheimer-related changes. *Acta Neuropathologica*, *82*(4), 239–259. https://doi.org/10.1007/BF00308809

Brandon, M. P., Koenig, J., Leutgeb, J. K., & Leutgeb, S. (2014). New and distinct hippocampal place codes are generated in a new environment during septal inactivation. *Neuron*, *82*(4), 789–796. https://doi.org/10.1016/j.neuron.2014.04.013

Brun, V. H., Solstad, T., Kjelstrup, K. B., Fyhn, M., Witter, M. P., Moser, E. I., & Moser, M.-B. (2008). Progressive increase in grid scale from dorsal to ventral medial entorhinal cortex. *Hippocampus*, *18*(12), 1200–1212. https://doi.org/10.1002/hipo.20504

Brustovetsky, T., Li, V., & Brustovetsky, N. (2009). Stimulation of glutamate receptors in cultured hippocampal neurons causes Ca^{2+}-dependent mitochondrial contraction. *Cell Calcium*, *46*, 18–29. https://doi.org/10.1016/j.ceca.2009.03.017.

Buee, L., Bussiere, T., Buee-Scherrer, V., Delacourte, A., & Hof, P. R. (2000). Tau protein isoforms, phosphorylation and role in neurodegenerative disorders. *Brain Res Brain Res Rev*, *33*, 95–130.

Burdick, D., Soreghan, B., Kwon, M., Kosmoski, J., Knauer, M., Henschen, A., Yates, J., Cotman, C., & Glabe, C. (1992). Assembly and aggregation properties of synthetic Alzheimer's A4/beta amyloid peptide analogs. *The Journal of Biological Chemistry*, *267*(1), 546–554.

Burte, F., Carelli, V., Chinnery, P. F., & Yu-Wai-Man, P. (2015). Disturbed mitochondrial dynamics and neurodegenerative disorders. *Nat Rev Neurol*, *11*, 11-24. https://doi.org/10.1038/nrneurol.2014.228

Busche, M. A., Chen, X., Henning, H. A., Reichwald, J., Staufenbiel, M., Sakmann, B., & Konnerth, A. (2012). Critical role of soluble amyloid-β for early hippocampal hyperactivity in a mouse model of Alzheimer's disease. *Proceedings of the National Academy of Sciences*, *109*(22), 8740–8745. https://doi.org/10.1073/pnas.1206171109

Busche, M. A., Eichhoff, G., Adelsberger, H., Abramowski, D., Wiederhold, K.-H., Haass, C., Staufenbiel, M., Konnerth, A., & Garaschuk, O. (2008). Clusters of hyperactive neurons near amyloid plaques in a mouse model of Alzheimer's disease. *Science (New York, N.Y.)*, *321*(5896), 1686–1689. https://doi.org/10.1126/science.1162844

Busche, M. A., Kekuš, M., Adelsberger, H., Noda, T., Förstl, H., Nelken, I., & Konnerth, A. (2015). Rescue of long-range circuit dysfunction in Alzheimer's disease models. *Nature Neuroscience*, *18*(11), Article 11. https://doi.org/10.1038/nn.4137

Bush, D., Barry, C., & Burgess, N. (2014). What do grid cells contribute to place cell firing? *Trends in Neurosciences*, *37*(3), 136–145. https://doi.org/10.1016/j.tins.2013.12.003

Buzsáki, G., & Tingley, D. (2018). Space and Time: The Hippocampus as a Sequence Generator. *Trends in Cognitive Sciences*, *22*(10), 853–869. https://doi.org/10.1016/j.tics.2018.07.006

Cacucci, F., Yi, M., Wills, T. J., Chapman, P., & O'Keefe, J. (2008). Place cell firing correlates with memory deficits and amyloid plaque burden in Tg2576 Alzheimer mouse model. *Proceedings of the National Academy of Sciences*, *105*(22), 7863–7868. https://doi.org/10.1073/pnas.0802908105

Caillé, I., Allinquant, B., Dupont, E., Bouillot, C., Langer, A., Müller, U., & Prochiantz, A. (2004). Soluble form of amyloid precursor protein regulates proliferation of progenitors in the adult subventricular zone. *Development (Cambridge, England)*, *131*(9), 2173–2181. https://doi.org/10.1242/dev.01103

Calvo-Rodriguez, M., Hernando-Perez, E., Nunez, L., & Villalobos, C. (2019). Amyloid beta Oligomers Increase ER-Mitochondria Ca^{2+} Cross Talk in Young Hippocampal Neurons and Exacerbate Aging-Induced Intracellular Ca^{2+} Remodeling. *Front Cell Neurosci*, *13*, 22. https://doi.org/10.3389/fncel.2019.00022

Cancedda, L., Fiumelli, H., Chen, K., & Poo, M. M. (2007). Excitatory GABA action is essential for morphological maturation of cortical neurons in vivo. *J Neurosci*, *27*, 5224–5235. https://doi.org/10.1523/JNEUROSCI.5169-06.2007.

Castellani, R. J., & Perry, G. (2012). Pathogenesis and disease-modifying therapy in Alzheimer's disease: The flat line of progress. *Archives of Medical Research*, *43*(8), 694–698. https://doi.org/10.1016/j.arcmed.2012.09.009

Cayzac, S., Mons, N., Ginguay, A., Allinquant, B., Jeantet, Y., & Cho, Y. H. (2015). Altered hippocampal information coding and network synchrony in APP-PS1 mice. *Neurobiology of Aging*, *36*(12), 3200–3213. https://doi.org/10.1016/j.neurobiolaging.2015.08.023

Celone, K. A., Calhoun, V. D., Dickerson, B. C., Atri, A., Chua, E. F., Miller, S. L., DePeau, K., Rentz, D. M., Selkoe, D. J., Blacker, D., Albert, M. S., & Sperling, R. A. (2006). Alterations in memory networks in mild cognitive impairment and Alzheimer's disease: An independent component analysis. *The Journal of Neuroscience: The Official Journal of the Society for Neuroscience*, *26*(40), 10222–10231. https://doi.org/10.1523/JNEUROSCI.2250-06.2006

Chan, D. C. (2006). Mitochondria: Dynamic organelles in disease, aging, and development. *Cell*, *125*, 1241-1252. https://doi.org/10.1016/j.cell.2006.06.010

Chan, S. L., Mayne, M., Holden, C. P., Geiger, J. D., & Mattson, M. P. (2000). Presenilin-1 mutations increase levels of ryanodine receptors and calcium release in PC12 cells and cortical neurons. *J Biol Chem*, *275*, 18195-18200. https://doi.org/10.1074/jbc.M000040200

Chapman, P. F., White, G. L., Jones, M. W., Cooper-Blacketer, D., Marshall, V. J., Irizarry, M., Younkin, L., Good, M. A., Bliss, T. V., Hyman, B. T., Younkin, S. G., & Hsiao, K. K. (1999). Impaired synaptic plasticity and learning in aged amyloid precursor protein transgenic mice. *Nature Neuroscience*, *2*(3), 271–276. https://doi.org/10.1038/6374

Cheng, I. H., Scearce-Levie, K., Legleiter, J., Palop, J. J., Gerstein, H., Bien-Ly, N., Puoliväli, J., Lesné, S., Ashe, K. H., Muchowski, P. J., & Mucke, L. (2007). Accelerating amyloid-beta fibrillization reduces oligomer levels and functional deficits in Alzheimer disease mouse models. *The Journal of Biological Chemistry*, *282*(33), 23818–23828. https://doi.org/10.1074/jbc.M701078200

Cheng, J., & Ji, D. (2013). Rigid firing sequences undermine spatial memory codes in a neurodegenerative mouse model. *ELife*, *2*, e00647. https://doi.org/10.7554/eLife.00647

Cheong, H., Lindsten, T., Wu, J., Lu, C., & Thompson, C. (2011). Ammonia-induced autophagy is independent of ULK1/ULK2 kinases. *PNAS*, *108*, 11121-11126. https://doi.org/10.1073/pnas.1115120108

Chin, J., Palop, J. J., Puoliväli, J., Massaro, C., Bien-Ly, N., Gerstein, H., Scearce-Levie, K., Masliah, E., & Mucke, L. (2005). Fyn kinase induces synaptic and cognitive impairments in a transgenic mouse model of Alzheimer's disease. *The Journal of Neuroscience: The Official Journal of the Society for Neuroscience*, *25*(42), 9694–9703. https://doi.org/10.1523/JNEUROSCI.2980-05.2005

Cho, B., Cho, H. M., Jo, Y., Kim, H. D., Song, M., Moon, C., Kim, H., Kim, K., Sesaki, H., & Rhyu, I. J. (2017). Constriction of the mitochondrial inner compartment is a priming event for mitochondrial division. *Nat Commun*, *8*, 15754. https://doi.org/10.1038/ncomms15754.

Cho, D.-H., Nakamura, T., Fang, J., Cieplak, P., Godzik, A., Gu, Z., & Lipton, S. A. (2009). S-nitrosylation of Drp1 mediates beta-amyloid-related mitochondrial fission and neuronal injury. *Science (New York, N.Y.)*, *324*(5923), 102–105. https://doi.org/10.1126/science.1171091

Cissé, M., Halabisky, B., Harris, J., Devidze, N., Dubal, D. B., Sun, B., Orr, A., Lotz, G., Kim, D. H., Hamto, P., Ho, K., Yu, G.-Q., & Mucke, L. (2011). Reversing EphB2 depletion rescues cognitive functions in Alzheimer model. *Nature*, *469*(7328), 47–52. https://doi.org/10.1038/nature09635

Citri, A., & Malenka, R. C. (2008). Synaptic plasticity: Multiple forms, functions, and mechanisms. *Neuropsychopharmacology: Official Publication of the American College of Neuropsychopharmacology*, *33*(1), 18–41. https://doi.org/10.1038/sj.npp.1301559

Ciupek, S. M., Cheng, J., Ali, Y. O., Lu, H.-C., & Ji, D. (2015). Progressive Functional Impairments of Hippocampal Neurons in a Tauopathy Mouse Model. *The Journal of Neuroscience*, *35*(21), 8118–8131. https://doi.org/10.1523/JNEUROSCI.3130-14.2015

Cohen, A. D., Price, J. C., Weissfeld, L. A., James, J., Rosario, B. L., Bi, W., Nebes, R. D., Saxton, J. A., Snitz, B. E., Aizenstein, H. A., Wolk, D. A., Dekosky, S. T., Mathis, C. A., & Klunk, W. E. (2009). Basal cerebral metabolism may modulate the cognitive effects of Abeta in mild cognitive impairment: An example of brain reserve. *The Journal of Neuroscience: The Official Journal of the Society for Neuroscience*, *29*(47), 14770–14778. https://doi.org/10.1523/JNEUROSCI.3669-09.2009

Colgin, L. L., Moser, E. I., & Moser, M.-B. (2008). Understanding memory through hippocampal remapping. *Trends in Neurosciences*, *31*(9), 469–477. https://doi.org/10.1016/j.tins.2008.06.008

Corkin, S. (2002). What's new with the amnesic patient H.M.? *Nature Reviews. Neuroscience*, *3*(2), 153–160. https://doi.org/10.1038/nrn726

Courchet, J., Lewis, T. L., Jr., Lee, S., Courchet, V., Liou, D. Y., Aizawa, S., & Polleux, F. (2013). Terminal axon branching is regulated by the LKB1-NUAK1 kinase pathway via presynaptic mitochondrial capture. *Cell*, *153*, 1510–1525. https://doi.org/10.1016/j.cell.2013.05.021.

Cummings, J. L., Morstorf, T., & Zhong, K. (2014). Alzheimer's disease drug-development pipeline: Few candidates, frequent failures. *Alzheimer's Research & Therapy*, *6*(4), 37. https://doi.org/10.1186/alzrt269

Cummings, J. L., Tong, G., & Ballard, C. (2019). Treatment Combinations for Alzheimer's Disease: Current and Future Pharmacotherapy Options. *Journal of Alzheimer's Disease: JAD*, *67*(3), 779–794. https://doi.org/10.3233/JAD-180766

D'Amore, J. D., Kajdasz, S. T., McLellan, M. E., Bacskai, B. J., Stern, E. A., & Hyman, B. T. (2003). In vivo multiphoton imaging of a transgenic mouse model of Alzheimer disease reveals marked thioflavine-S-associated alterations in neurite trajectories. *Journal of Neuropathology and Experimental Neurology*, *62*(2), 137–145. https://doi.org/10.1093/jnen/62.2.137

Danielson, N. B., Kaifosh, P., Zaremba, J. D., Lovett-Barron, M., Tsai, J., Denny, C. A., Balough, E. M., Goldberg, A. R., Drew, L. J., Hen, R., Losonczy, A., & Kheirbek, M. A. (2016). Distinct Contribution of Adult-Born Hippocampal Granule Cells to Context Encoding. *Neuron*, *90*(1), 101–112. https://doi.org/10.1016/j.neuron.2016.02.019

Das, U., Scott, D. A., Ganguly, A., Koo, E. H., Tang, Y., & Roy, S. (2013). Activity-Induced Convergence of APP and BACE-1 in Acidic Microdomains via an Endocytosis-Dependent Pathway. *Neuron*, *79*(3), 447–460. https://doi.org/10.1016/j.neuron.2013.05.035

David, D. C., Hauptmann, S., Scherping, I., Schuessel, K., Keil, U., Rizzu, P., Ravid, R., Dröse, S., Brandt, U., Müller, W. E., Eckert, A., & Götz, J. (2005). Proteomic and Functional Analyses Reveal a Mitochondrial Dysfunction in P301L Tau Transgenic Mice*. *Journal of Biological Chemistry*, *280*(25), 23802–23814. https://doi.org/10.1074/jbc.M500356200

Davis, K. E., Fox, S., & Gigg, J. (2014). Increased Hippocampal Excitability in the 3xTgAD Mouse Model for Alzheimer's Disease In Vivo. *PLOS ONE*, *9*(3), e91203. https://doi.org/10.1371/journal.pone.0091203

De Strooper, B., & Karran, E. (2016). The Cellular Phase of Alzheimer's Disease. *Cell*, *164*(4), 603–615. https://doi.org/10.1016/j.cell.2015.12.056

DeKosky, S. T., & Scheff, S. W. (1990). Synapse loss in frontal cortex biopsies in Alzheimer's disease: Correlation with cognitive severity. *Annals of Neurology*, *27*(5), 457–464. https://doi.org/10.1002/ana.410270502

DeKosky, S. T., Scheff, S. W., & Styren, S. D. (1996). Structural correlates of cognition in dementia: Quantification and assessment of synapse change. *Neurodegeneration: A Journal for Neurodegenerative Disorders, Neuroprotection, and Neuroregeneration*, *5*(4), 417–421. https://doi.org/10.1006/neur.1996.0056

Demirovic, J., Prineas, R., Loewenstein, D., Bean, J., Duara, R., Sevush, S., & Szapocznik, J. (2003). Prevalence of dementia in three ethnic groups: The South Florida program on aging and health. *Annals of Epidemiology*, *13*(6), 472–478. https://doi.org/10.1016/s1047-2797(02)00437-4

Demuro, A., Mina, E., Kayed, R., Milton, S. C., Parker, I., & Glabe, C. G. (2005). Calcium Dysregulation and Membrane Disruption as a Ubiquitous Neurotoxic Mechanism of Soluble Amyloid Oligomers*. *Journal of Biological Chemistry*, *280*(17), 17294–17300. https://doi.org/10.1074/jbc.M500997200

De-Paula, V. J., Radanovic, M., Diniz, B. S., & Forlenza, O. V. (2012). Alzheimer's disease. *Sub-Cellular Biochemistry*, *65*, 329–352. https://doi.org/10.1007/978-94-007-5416-4_14

Deshmukh, S. S., & Knierim, J. J. (2011). Representation of non-spatial and spatial information in the lateral entorhinal cortex. *Frontiers in Behavioral Neuroscience*, *5*, 69. https://doi.org/10.3389/fnbeh.2011.00069

Dickerson, B. C., Salat, D. H., Greve, D. N., Chua, E. F., Rand-Giovannetti, E., Rentz, D. M., Bertram, L., Mullin, K., Tanzi, R. E., Blacker, D., Albert, M. S., & Sperling, R. A. (2005). Increased hippocampal activation in mild cognitive impairment compared to normal aging and AD. *Neurology*, *65*(3), 404–411. https://doi.org/10.1212/01.wnl.0000171450.97464.49

Dilworth-Anderson, P., Hendrie, H. C., Manly, J. J., Khachaturian, A. S., Fazio, S., & Social, Behavioral and Diversity Research Workgroup of the Alzheimer;s Association. (2008). Diagnosis and assessment of Alzheimer's disease in diverse populations. *Alzheimer's & Dementia: The Journal of the Alzheimer's Association*, *4*(4), 305–309. https://doi.org/10.1016/j.jalz.2008.03.001

Disability and Care Needs of Older Americans by Dementia Status: An Analysis of the 2011 National Health and Aging Trends Study. (n.d.). ASPE. Retrieved April 11, 2023, from https://aspe.hhs.gov/reports/disability-care-needs-older-americans-dementia-status-analysis-2011-national-health-aging-trends-1

Divakaruni, S. S., Dyke, A. M., Chandra, R., LeGates, T. A., Contreras, M., Dharmasri, P. A., Higgs, H. N., Lobo, M. K., Thompson, S. M., & Blanpied, T. A. (2018). Long-Term Potentiation Requires a Rapid Burst of Dendritic Mitochondrial Fission during Induction. *Neuron*, *100*, 860-875 867. https://doi.org/10.1016/j.neuron.2018.09.025.

Domise, M., Didier, S., Marinangeli, C., Zhao, H., Chandakkar, P., Buée, L., Viollet, B., Davies, P., Marambaud, P., & Vingtdeux, V. (2016). AMP-activated protein kinase modulates tau phosphorylation and tau pathology in vivo. *Scientific Reports*, *6*(1), Article 1. https://doi.org/10.1038/srep26758

Domise, M., Sauvé, F., Didier, S., Caillerez, R., Bégard, S., Carrier, S., Colin, M., Marinangeli, C., Buée, L., & Vingtdeux, V. (2019). Neuronal AMP-activated protein kinase hyper-activation induces synaptic loss by an autophagy-mediated process. *Cell Death & Disease*, *10*(3), Article 3. https://doi.org/10.1038/s41419-019-1464-x

Donegan, M. L., Stefanini, F., Meira, T., Gordon, J. A., Fusi, S., & Siegelbaum, S. A. (2020). Coding of social novelty in the hippocampal CA2 region and its disruption and rescue in a 22q11.2 microdeletion mouse model. *Nature Neuroscience*, *23*(11), 1365–1375. https://doi.org/10.1038/s41593-020-00720-5

Dong, C., Madar, A. D., & Sheffield, M. E. J. (2021). Distinct place cell dynamics in CA1 and CA3 encode experience in new environments. *Nature Communications*, *12*(1), Article 1. https://doi.org/10.1038/s41467-021-23260-3

Doody, R. S., Thomas, R. G., Farlow, M., Iwatsubo, T., Vellas, B., Joffe, S., Kieburtz, K., Raman, R., Sun, X., Aisen, P. S., Siemers, E., Liu-Seifert, H., Mohs, R., Alzheimer's Disease Cooperative Study Steering Committee, & Solanezumab Study Group. (2014). Phase 3 trials of solanezumab for mild-to-moderate Alzheimer's disease. *The New England Journal of Medicine*, *370*(4), 311–321. https://doi.org/10.1056/NEJMoa1312889

Driscoll, L. N., Duncker, L., & Harvey, C. D. (2022). Representational drift: Emerging theories for continual learning and experimental future directions. *Current Opinion in Neurobiology*, *76*, 102609. https://doi.org/10.1016/j.conb.2022.102609

Du, H., Guo, L., Yan, S., Sosunov, A. A., McKhann, G. M., & Yan, S. S. (2010). Early deficits in synaptic mitochondria in an Alzheimer's disease mouse model. *Proceedings of the National Academy of Sciences of the United States of America*, *107*(43), 18670–18675. https://doi.org/10.1073/pnas.1006586107

DuBoff, B., Gotz, J., & Feany, M. B. (2012). Tau promotes neurodegeneration via DRP1 mislocalization in vivo. *Neuron*, *75*, 618-632. https://doi.org/10.1016/j.neuron.2012.06.026

Ducommun, S., Deak, M., Sumpton, D., Ford, R. J., Núñez Galindo, A., Kussmann, M., Viollet, B., Steinberg, G. R., Foretz, M., Dayon, L., Morrice, N. A., & Sakamoto, K. (2015). Motif affinity and mass spectrometry proteomic approach for the discovery of cellular AMPK targets: Identification of mitochondrial fission factor as a new AMPK substrate. *Cellular Signalling*, *27*(5), 978–988. https://doi.org/10.1016/j.cellsig.2015.02.008

Dujardin, S., Colin, M., & Buée, L. (2015). Invited review: Animal models of tauopathies and their implications for research/translation into the clinic. *Neuropathology and Applied Neurobiology*, *41*(1), 59–80. https://doi.org/10.1111/nan.12200

Eckert, A., Hauptmann, S., Scherping, I., Meinhardt, J., Rhein, V., Dröse, S., Brandt, U., Fändrich, M., Müller, W. E., & Götz, J. (2008). Oligomeric and fibrillar species of β-amyloid (Aβ42) both impair mitochondrial function in P301L tau transgenic mice. *Journal of Molecular Medicine*, *86*(11), 1255–1267. https://doi.org/10.1007/s00109-008-0391-6

Egan, D. F., Shackelford, D. B., Mihaylova, M. M., Gelino, S., Kohnz, R. A., Mair, W., Vasquez, D. S., Joshi, A., Gwinn, D. M., Taylor, R., Asara, J. M., Fitzpatrick, J., Dillin, A., Viollet, B., Kundu, M., Hansen, M., & Shaw, R. J. (2011). Phosphorylation of ULK1 (hATG1) by AMP-Activated Protein Kinase Connects Energy Sensing to Mitophagy. *Science*, *331*(6016), 456–461. https://doi.org/10.1126/science.1196371

Eichenbaum, H. (2017). On the Integration of Space, Time, and Memory. *Neuron*, *95*(5), 1007–1018. https://doi.org/10.1016/j.neuron.2017.06.036

Ekstrom, A. D., Kahana, M. J., Caplan, J. B., Fields, T. A., Isham, E. A., Newman, E. L., & Fried, I. (2003). Cellular networks underlying human spatial navigation. *Nature*, *425*(6954), 184–188. https://doi.org/10.1038/nature01964

Evangelidis, G. D., & Psarakis, E. Z. (2008). Parametric Image Alignment Using Enhanced Correlation Coefficient Maximization. *IEEE Transactions on Pattern Analysis and Machine Intelligence*, *30*(10), 1858–1865. https://doi.org/10.1109/TPAMI.2008.113

Faitg, J., Lacefield, C., Davey, T., White, K., Laws, R., Kosmidis, S., Reeve, A. K., Kandel, E. R., Vincent, A. E., & Picard, M. (2021). 3D neuronal mitochondrial morphology in axons, dendrites, and somata of the aging mouse hippocampus. *Cell Rep*, *36*, 109509. https://doi.org/10.1016/j.celrep.2021.109509.

Fang, E. F., Hou, Y., Palikaras, K., Adriaanse, B. A., Kerr, J. S., Yang, B., Lautrup, S., Hasan-Olive, M. M., Caponio, D., Dan, X., Rocktäschel, P., Croteau, D. L., Akbari, M., Greig, N. H., Fladby, T., Nilsen, H., Cader, M. Z., Mattson, M. P., Tavernarakis, N., & Bohr, V. A. (2019). Mitophagy inhibits amyloid-β and tau pathology and reverses cognitive deficits in models of Alzheimer's disease. *Nature Neuroscience*, *22*(3), Article 3. https://doi.org/10.1038/s41593-018-0332-9

Fernández-Ruiz, A., Oliva, A., Soula, M., Rocha-Almeida, F., Nagy, G. A., Martin-Vazquez, G., & Buzsáki, G. (2021). Gamma rhythm communication between entorhinal cortex and dentate gyrus neuronal assemblies. *Science (New York, N.Y.)*, *372*(6537), eabf3119. https://doi.org/10.1126/science.abf3119

Filippini, N., MacIntosh, B. J., Hough, M. G., Goodwin, G. M., Frisoni, G. B., Smith, S. M., Matthews, P. M., Beckmann, C. F., & Mackay, C. E. (2009). Distinct patterns of brain activity in young carriers of the APOE-ε4 allele. *Proceedings of the National Academy of Sciences*, *106*(17), 7209–7214. https://doi.org/10.1073/pnas.0811879106

Fogel, H., Frere, S., Segev, O., Bharill, S., Shapira, I., Gazit, N., O'Malley, T., Slomowitz, E., Berdichevsky, Y., Walsh, D. M., Isacoff, E. Y., Hirsch, J. A., & Slutsky, I. (2014). APP homodimers transduce an amyloid-β-mediated increase in release probability at excitatory synapses. *Cell Reports*, *7*(5), 1560–1576. https://doi.org/10.1016/j.celrep.2014.04.024

Frank, L. M., Stanley, G. B., & Brown, E. N. (2004). Hippocampal plasticity across multiple days of exposure to novel environments. *The Journal of Neuroscience: The Official Journal of the Society for Neuroscience*, *24*(35), 7681–7689. https://doi.org/10.1523/JNEUROSCI.1958-04.2004

Friedrich, J., & Paninski, L. (2016). Fast Active Set Methods for Online Spike Inference from Calcium Imaging. *Advances in Neural Information Processing Systems*, *29*. https://papers.nips.cc/paper_files/paper/2016/hash/fc2c7c47b918d0c2d792a719dfb602ef-Abstract.html

Funane, T., Jun, H., Sutoko, S., Saido, T. C., Kandori, A., & Igarashi, K. M. (2022). Impaired sharp-wave ripple coordination between the medial entorhinal cortex and hippocampal CA1 of knock-in model of Alzheimer's disease. *Frontiers in Systems Neuroscience*, *16*. https://www.frontiersin.org/articles/10.3389/fnsys.2022.955178

Furukawa, K., Sopher, B. L., Rydel, R. E., Begley, J. G., Pham, D. G., Martin, G. M., Fox, M., & Mattson, M. P. (1996). Increased activity-regulating and neuroprotective efficacy of alpha-secretase-derived secreted amyloid precursor protein conferred by a C-terminal heparin-binding domain. *Journal of Neurochemistry*, *67*(5), 1882–1896. https://doi.org/10.1046/j.1471-4159.1996.67051882.x

Galvan, V., Gorostiza, O. F., Banwait, S., Ataie, M., Logvinova, A. V., Sitaraman, S., Carlson, E., Sagi, S. A., Chevallier, N., Jin, K., Greenberg, D. A., & Bredesen, D. E. (2006). Reversal of Alzheimer's-like pathology and behavior in human APP transgenic mice by mutation of Asp664. *Proceedings of the National Academy of Sciences*, *103*(18), 7130–7135. https://doi.org/10.1073/pnas.0509695103

Garcia, D., & Shaw, R. J. A. M. P. K. (2017). Mechanisms of Cellular Energy Sensing and Restoration of Metabolic Balance. *Mol Cell*, *66*, 789-800. https://doi.org/10.1016/j.molcel.2017.05.032

Garcia-Alloza, M., Robbins, E. M., Zhang-Nunes, S. X., Purcell, S. M., Betensky, R. A., Raju, S., Prada, C., Greenberg, S. M., Bacskai, B. J., & Frosch, M. P. (2006). Characterization of amyloid deposition in the APPswe/PS1dE9 mouse model of Alzheimer disease. *Neurobiology of Disease*, *24*(3), 516–524. https://doi.org/10.1016/j.nbd.2006.08.017

Giliberto, L., Zhou, D., Weldon, R., Tamagno, E., De Luca, P., Tabaton, M., & D'Adamio, L. (2008). Evidence that the Amyloid beta Precursor Protein-intracellular domain lowers the stress threshold

of neurons and has a “regulated” transcriptional role. *Molecular Neurodegeneration*, *3*, 12. https://doi.org/10.1186/1750-1326-3-12

Gillespie, A. K., Jones, E. A., Lin, Y.-H., Karlsson, M. P., Kay, K., Yoon, S. Y., Tong, L. M., Nova, P., Carr, J. S., Frank, L. M., & Huang, Y. (2016). Apolipoprotein E4 Causes Age-Dependent Disruption of Slow Gamma Oscillations during Hippocampal Sharp-Wave Ripples. *Neuron*, *90*(4), 740–751. https://doi.org/10.1016/j.neuron.2016.04.009

Grienberger, C., Rochefort, N. L., Adelsberger, H., Henning, H. A., Hill, D. N., Reichwald, J., Staufenbiel, M., & Konnerth, A. (2012). Staged decline of neuronal function in vivo in an animal model of Alzheimer’s disease. *Nature Communications*, *3*(1), Article 1. https://doi.org/10.1038/ncomms1783

Grosmark, A. D., Sparks, F. T., Davis, M. J., & Losonczy, A. (2021). Reactivation predicts the consolidation of unbiased long-term cognitive maps. *Nature Neuroscience*, *24*(11), Article 11. https://doi.org/10.1038/s41593-021-00920-7

Grothe, M. J., Heinsen, H., Amaro, E., Jr, Grinberg, L. T., Teipel, S. J., & for the Alzheimer’s Disease Neuroimaging Initiative. (2016). Cognitive Correlates of Basal Forebrain Atrophy and Associated Cortical Hypometabolism in Mild Cognitive Impairment. *Cerebral Cortex*, *26*(6), 2411–2426. https://doi.org/10.1093/cercor/bhv062

Grutzendler, J., Helmin, K., Tsai, J., & Gan, W.-B. (2007). Various dendritic abnormalities are associated with fibrillar amyloid deposits in Alzheimer’s disease. *Annals of the New York Academy of Sciences*, *1097*, 30–39. https://doi.org/10.1196/annals.1379.003

Guerrier, S., Coutinho-Budd, J., Sassa, T., Gresset, A., Jordan, N. V., Chen, K., Jin, W.-L., Frost, A., & Polleux, F. (2009). The F-BAR Domain of srGAP2 Induces Membrane Protrusions Required for Neuronal Migration and Morphogenesis. *Cell*, *138*(5), 990–1004. https://doi.org/10.1016/j.cell.2009.06.047

Gumy, L. F., & Hoogenraad, C. C. (2018). Local mechanisms regulating selective cargo entry and long-range trafficking in axons. *Curr Opin Neurobiol*, *51*, 23–28. https://doi.org/10.1016/j.conb.2018.02.007.

Guntupalli, S., Jang, S. E., Zhu, T., Huganir, R. L., Widagdo, J., & Anggono, V. (2017). GluA1 subunit ubiquitination mediates amyloid-β-induced loss of surface α-amino-3-hydroxy-5-methyl-4-isoxazolepropionic acid (AMPA) receptors. *Journal of Biological Chemistry*, *292*(20), 8186–8194. https://doi.org/10.1074/jbc.M116.774554

Guo, Q., Fu, W., Sopher, B. L., Miller, M. W., Ware, C. B., Martin, G. M., & Mattson, M. P. (1999). Increased vulnerability of hippocampal neurons to excitotoxic necrosis in presenilin-1 mutant knock-in mice. *Nature Medicine*, *5*(1), Article 1. https://doi.org/10.1038/4789

Hafting, T., Fyhn, M., Molden, S., Moser, M.-B., & Moser, E. I. (2005). Microstructure of a spatial map in the entorhinal cortex. *Nature*, *436*(7052), Article 7052. https://doi.org/10.1038/nature03721

Hainmueller, T., & Bartos, M. (2020). Dentate gyrus circuits for encoding, retrieval and discrimination of episodic memories. *Nature Reviews. Neuroscience*, *21*(3), 153–168. https://doi.org/10.1038/s41583-019-0260-z

Han, X. J., Lu, Y. F., Li, S. A., Kaitsuka, T., Sato, Y., Tomizawa, K., Nairn, A. C., Takei, K., Matsui, H., & Matsushita, M. (2008). CaM kinase I alpha-induced phosphorylation of Drp1 regulates mitochondrial morphology. *J Cell Biol*, *182*, 573–585. https://doi.org/10.1083/jcb.200802164.

Hand, R., & Polleux, F. (2011). Neurogenin2 regulates the initial axon guidance of cortical pyramidal neurons projecting medially to the corpus callosum. *Neural Dev*, *6*, *30*. https://doi.org/10.1186/1749-8104-6-30

Hardie, D. G., Ross, F. A., & Hawley, S. A. (2012). AMPK: a nutrient and energy sensor that maintains energy homeostasis. *Nat Rev Mol Cell Biol*, *13*, 251-262. https://doi.org/10.1038/nrm3311

Hardy, J. (2006). Alzheimer's disease: The amyloid cascade hypothesis: An update and reappraisal. *Journal of Alzheimer's Disease*, *9*(s3), 151–153. https://doi.org/10.3233/JAD-2006-9S317

Harnett, M. T., Makara, J. K., Spruston, N., Kath, W. L., & Magee, J. C. (2012). Synaptic amplification by dendritic spines enhances input cooperativity. *Nature*, *491*, 599-602. https://doi.org/10.1038/nature11554

Hartley, D. M., Walsh, D. M., Ye, C. P., Diehl, T., Vasquez, S., Vassilev, P. M., Teplow, D. B., & Selkoe, D. J. (1999). Protofibrillar intermediates of amyloid beta-protein induce acute electrophysiological changes and progressive neurotoxicity in cortical neurons. *The Journal of Neuroscience: The Official Journal of the Society for Neuroscience*, *19*(20), 8876–8884. https://doi.org/10.1523/JNEUROSCI.19-20-08876.1999

Harwood, D. G., Barker, W. W., Ownby, R. L., & Duara, R. (2000). Relationship of behavioral and psychological symptoms to cognitive impairment and functional status in Alzheimer's disease. *International Journal of Geriatric Psychiatry*, *15*(5), 393–400. https://doi.org/10.1002/(sici)1099-1166(200005)15:5<393::aid-gps120>3.0.co;2-o

Hebb, D. O. (1949). *The organization of behavior; a neuropsychological theory* (pp. xix, 335). Wiley.

Herzig, S., & Shaw, R. J. (2018). AMPK: guardian of metabolism and mitochondrial homeostasis. *Nat Rev Mol Cell Biol*, *19*, 121-135. https://doi.org/10.1038/nrm.2017.95

Hitti, F. L., & Siegelbaum, S. A. (2014). The hippocampal CA2 region is essential for social memory. *Nature*, *508*(7494), Article 7494. https://doi.org/10.1038/nature13028

Ho, S.-M., Hartley, B. J., Tcw, J., Beaumont, M., Stafford, K., Slesinger, P. A., & Brennand, K. J. (2016). Rapid Ngn2-induction of excitatory neurons from hiPSC-derived neural progenitor cells. *Methods*, *101*, 113–124. https://doi.org/10.1016/j.ymeth.2015.11.019

Hollup, S. A., Molden, S., Donnett, J. G., Moser, M.-B., & Moser, E. I. (2001). Accumulation of Hippocampal Place Fields at the Goal Location in an Annular Watermaze Task. *Journal of Neuroscience*, *21*(5), 1635–1644. https://doi.org/10.1523/JNEUROSCI.21-05-01635.2001

Hong, S., Beja-Glasser, V. F., Nfonoyim, B. M., Frouin, A., Li, S., Ramakrishnan, S., Merry, K. M., Shi, Q., Rosenthal, A., Barres, B. A., Lemere, C. A., Selkoe, D. J., & Stevens, B. (2016). Complement and microglia mediate early synapse loss in Alzheimer mouse models. *Science (New York, N.Y.)*, *352*(6286), 712–716. https://doi.org/10.1126/science.aad8373

Hope, T., Tilling, K. M., Gedling, K., Keene, J. M., Cooper, S. D., & Fairburn, C. G. (1994). The structure of wandering in dementia. *International Journal of Geriatric Psychiatry*, *9*(2), 149–155. https://doi.org/10.1002/gps.930090209

Horton, A. C., & Ehlers, M. D. (2003). Neuronal polarity and trafficking. *Neuron*, *40*, 277–295. https://doi.org/10.1016/s0896-6273(03)00629-9.

Hsia, A. Y., Masliah, E., McConlogue, L., Yu, G. Q., Tatsuno, G., Hu, K., Kholodenko, D., Malenka, R. C., Nicoll, R. A., & Mucke, L. (1999). Plaque-independent disruption of neural circuits in Alzheimer's

disease mouse models. *Proceedings of the National Academy of Sciences of the United States of America*, *96*(6), 3228–3233. https://doi.org/10.1073/pnas.96.6.3228

Hsieh, H., Boehm, J., Sato, C., Iwatsubo, T., Tomita, T., Sisodia, S., & Malinow, R. (2006). AMPAR removal underlies Aβ-induced synaptic depression and dendritic spine loss. *Neuron*, *52*(5), 831–843. https://doi.org/10.1016/j.neuron.2006.10.035

Hyman, B. T., Van Hoesen, G. W., Damasio, A. R., & Barnes, C. L. (1984). Alzheimer's disease: Cell-specific pathology isolates the hippocampal formation. *Science (New York, N.Y.)*, *225*(4667), 1168–1170. https://doi.org/10.1126/science.6474172

Iaccarino, H. F., Singer, A. C., Martorell, A. J., Rudenko, A., Gao, F., Gillingham, T. Z., Mathys, H., Seo, J., Kritskiy, O., Abdurrob, F., Adaikkan, C., Canter, R. G., Rueda, R., Brown, E. N., Boyden, E. S., & Tsai, L.-H. (2016). Gamma frequency entrainment attenuates amyloid load and modifies microglia. *Nature*, *540*(7632), Article 7632. https://doi.org/10.1038/nature20587

Iascone, D. M., Li, Y., Sümbül, U., Doron, M., Chen, H., Andreu, V., Goudy, F., Blockus, H., Abbott, L. F., Segev, I., Peng, H., & Polleux, F. (2020). Whole-Neuron Synaptic Mapping Reveals Spatially Precise Excitatory/Inhibitory Balance Limiting Dendritic and Somatic Spiking. *Neuron*, *106*(4), 566-578.e8. https://doi.org/10.1016/j.neuron.2020.02.015

Inayat, S., McAllister, B. B., Chang, H., Lacoursiere, S. G., Whishaw, I. Q., Sutherland, R. J., & Mohajerani, M. H. (2022). *Generation of a hybrid AppNL-G-F/NL-G-F×Thy1-GCaMP6s+/- Alzheimer disease mouse mitigates the behavioral and hippocampal encoding deficits of APP knock-in mutations of AppNL-G-F/NL-G-F mice* (p. 2022.11.18.517152). bioRxiv. https://doi.org/10.1101/2022.11.18.517152

Insausti, R. (1993). Comparative anatomy of the entorhinal cortex and hippocampus in mammals. *Hippocampus*, *3*(S1), 19–26. https://doi.org/10.1002/hipo.1993.4500030705

Itoh, K., Murata, D., Kato, T., Yamada, T., Araki, Y., Saito, A., Adachi, Y., Igarashi, A., Li, S., & Pletnikov, M. (2019). Brain-specific Drp1 regulates postsynaptic endocytosis and dendrite formation independently of mitochondrial division. *Elife*, *8*, 10 7554 44739. https://doi.org/10.7554/eLife.44739

Itoh, K., Nakamura, K., Iijima, M., & Sesaki, H. (2013). Mitochondrial dynamics in neurodegeneration. *Trends Cell Biol*, *23*, 64-71. https://doi.org/10.1016/j.tcb.2012.10.006

Ittner, A. A., Gladbach, A., Bertz, J., Suh, L. S., & Ittner, L. M. (2014). P38 MAP kinase-mediated NMDA receptor-dependent suppression of hippocampal hypersynchronicity in a mouse model of Alzheimer's disease. *Acta Neuropathologica Communications*, *2*, 149. https://doi.org/10.1186/s40478-014-0149-z

Ittner, L. M. (2010). Dendritic function of tau mediates amyloid-beta toxicity in Alzheimer's disease mouse models. *Cell*, *142*, 387-397. https://doi.org/10.1016/j.cell.2010.06.036

Ittner, L. M., & Gotz, J. (2011). Amyloid-beta and tau–a toxic pas de deux in Alzheimer's disease. *Nat Rev Neurosci*, *12*, 65-72. https://doi.org/10.1038/nrn2967

Ittner, L. M., Ke, Y. D., Delerue, F., Bi, M., Gladbach, A., van Eersel, J., Wölfing, H., Chieng, B. C., Christie, M. J., Napier, I. A., Eckert, A., Staufenbiel, M., Hardeman, E., & Götz, J. (2010). Dendritic Function of Tau Mediates Amyloid-β Toxicity in Alzheimer's Disease Mouse Models. *Cell*, *142*(3), 387–397. https://doi.org/10.1016/j.cell.2010.06.036

Jack, C. R., Knopman, D. S., Jagust, W. J., Shaw, L. M., Aisen, P. S., Weiner, M. W., Petersen, R. C., & Trojanowski, J. Q. (2010). Hypothetical model of dynamic biomarkers of the Alzheimer's pathological cascade. *The Lancet. Neurology*, *9*(1), 119–128. https://doi.org/10.1016/S1474-4422(09)70299-6

Jacobsen, J. S., Wu, C.-C., Redwine, J. M., Comery, T. A., Arias, R., Bowlby, M., Martone, R., Morrison, J. H., Pangalos, M. N., Reinhart, P. H., & Bloom, F. E. (2006). Early-onset behavioral and synaptic deficits in a mouse model of Alzheimer's disease. *Proceedings of the National Academy of Sciences*, *103*(13), 5161–5166. https://doi.org/10.1073/pnas.0600948103

Jarsky, T., Roxin, A., Kath, W. L., & Spruston, N. (2005). Conditional dendritic spike propagation following distal synaptic activation of hippocampal CA1 pyramidal neurons. *Nature Neuroscience*, *8*(12), 1667–1676. https://doi.org/10.1038/nn1599

Jin, M., Shepardson, N., Yang, T., Chen, G., Walsh, D., & Selkoe, D. J. (2011). Soluble amyloid beta-protein dimers isolated from Alzheimer cortex directly induce Tau hyperphosphorylation and neuritic degeneration. *Proceedings of the National Academy of Sciences of the United States of America*, *108*(14), 5819–5824. https://doi.org/10.1073/pnas.1017033108

Johnson, S. C., Christian, B. T., Okonkwo, O. C., Oh, J. M., Harding, S., Xu, G., Hillmer, A. T., Wooten, D. W., Murali, D., Barnhart, T. E., Hall, L. T., Racine, A. M., Klunk, W. E., Mathis, C. A., Bendlin, B. B., Gallagher, C. L., Carlsson, C. M., Rowley, H. A., Hermann, B. P., … Sager, M. A. (2014). Amyloid burden and neural function in people at risk for Alzheimer's Disease. *Neurobiology of Aging*, *35*(3), 576–584. https://doi.org/10.1016/j.neurobiolaging.2013.09.028

Jonas, P., & Lisman, J. (2014). Structure, function, and plasticity of hippocampal dentate gyrus microcircuits. *Frontiers in Neural Circuits*, *8*, 107. https://doi.org/10.3389/fncir.2014.00107

Jones, E. A., Gillespie, A. K., Yoon, S. Y., Frank, L. M., & Huang, Y. (2019). Early Hippocampal Sharp-Wave Ripple Deficits Predict Later Learning and Memory Impairments in an Alzheimer's Disease Mouse Model. *Cell Reports*, *29*(8), 2123-2133.e4. https://doi.org/10.1016/j.celrep.2019.10.056

Jun, H., Bramian, A., Soma, S., Saito, T., Saido, T. C., & Igarashi, K. M. (2020). Disrupted Place Cell Remapping and Impaired Grid Cells in a Knockin Model of Alzheimer's Disease. *Neuron*, *107*(6), 1095-1112.e6. https://doi.org/10.1016/j.neuron.2020.06.023

Kamenetz, F., Tomita, T., Hsieh, H., Seabrook, G., Borchelt, D., Iwatsubo, T., Sisodia, S., & Malinow, R. (2003). APP processing and synaptic function. *Neuron*, *37*(6), 925–937. https://doi.org/10.1016/s0896-6273(03)00124-7

Kandel, E. R., & Schwartz, J. H. (1982). Molecular biology of learning: Modulation of transmitter release. *Science (New York, N.Y.)*, *218*(4571), 433–443. https://doi.org/10.1126/science.6289442

Kaufman, A. M., Geiller, T., & Losonczy, A. (2020). A Role for the Locus Coeruleus in Hippocampal CA1 Place Cell Reorganization during Spatial Reward Learning. *Neuron*, *105*(6), 1018-1026.e4. https://doi.org/10.1016/j.neuron.2019.12.029

Kayed, R., Head, E., Thompson, J. L., McIntire, T. M., Milton, S. C., Cotman, C. W., & Glabe, C. G. (2003). Common structure of soluble amyloid oligomers implies common mechanism of pathogenesis. *Science (New York, N.Y.)*, *300*(5618), 486–489. https://doi.org/10.1126/science.1079469

Kayed, R., & Lasagna-Reeves, C. A. (2013). Molecular mechanisms of amyloid oligomers toxicity. *Journal of Alzheimer's Disease*, *33*(SUPPL. 1), S67–S78. https://doi.org/10.3233/JAD-2012-129001

Keinath, A. T., Mosser, C.-A., & Brandon, M. P. (2022). The representation of context in mouse hippocampus is preserved despite neural drift. *Nature Communications*, *13*(1), Article 1. https://doi.org/10.1038/s41467-022-30198-7

Kesner, R. P. (2007). Behavioral functions of the CA3 subregion of the hippocampus. *Learning & Memory (Cold Spring Harbor, N.Y.)*, *14*(11), 771–781. https://doi.org/10.1101/lm.688207

Kim, J., Kundu, M., Viollet, B., & Guan, K. L. (2011). AMPK and mTOR regulate autophagy through direct phosphorylation of Ulk1. *Nat Cell Biol*, *13*, 132-141. https://doi.org/10.1038/ncb2152

Kim, S. Y., Strucinska, K., Osei, B., Han, K., Kwon, S. K., & Lewis, T. L., Jr. (2022). Neuronal mitochondrial morphology is significantly affected by both fixative and oxygen level during perfusion. *Front Mol Neurosci*, *15*, 1042616. https://doi.org/10.3389/fnmol.2022.1042616.

Kinoshita, A., Whelan, C. M., Berezovska, O., & Hyman, B. T. (2002). The gamma secretase-generated carboxyl-terminal domain of the amyloid precursor protein induces apoptosis via Tip60 in H4 cells. *The Journal of Biological Chemistry*, *277*(32), 28530–28536. https://doi.org/10.1074/jbc.M203372200

Koffie, R. M., Meyer-Luehmann, M., Hashimoto, T., Adams, K. W., Mielke, M. L., Garcia-Alloza, M., Micheva, K. D., Smith, S. J., Kim, M. L., Lee, V. M., Hyman, B. T., & Spires-Jones, T. L. (2009). Oligomeric amyloid beta associates with postsynaptic densities and correlates with excitatory synapse loss near senile plaques. *Proceedings of the National Academy of Sciences of the United States of America*, *106*(10), 4012–4017. https://doi.org/10.1073/pnas.0811698106

Kuchibhotla, K. V. (2008). Aβ plaques lead to aberrant regulation of calcium homeostasis in vivo resulting in structural and functional disruption of neuronal networks. *Neuron*, *59*, 214-225. https://doi.org/10.1016/j.neuron.2008.06.008

Kumar, A., Sidhu, J., Goyal, A., & Tsao, J. W. (2023). Alzheimer Disease. In *StatPearls*. StatPearls Publishing. http://www.ncbi.nlm.nih.gov/books/NBK499922/

Kurudenkandy, F. R., Zilberter, M., Biverstål, H., Presto, J., Honcharenko, D., Strömberg, R., Johansson, J., Winblad, B., & Fisahn, A. (2014). Amyloid-β-Induced Action Potential Desynchronization and Degradation of Hippocampal Gamma Oscillations Is Prevented by Interference with Peptide Conformation Change and Aggregation. *Journal of Neuroscience*, *34*(34), 11416–11425. https://doi.org/10.1523/JNEUROSCI.1195-14.2014

Kwon, S.-K., Iii, R. S., Lewis, T. L., Hirabayashi, Y., Maximov, A., & Polleux, F. (2016). LKB1 Regulates Mitochondria-Dependent Presynaptic Calcium Clearance and Neurotransmitter Release Properties at Excitatory Synapses along Cortical Axons. *PLOS Biology*, *14*(7), e1002516. https://doi.org/10.1371/journal.pbio.1002516

Lacor, P. N., Buniel, M. C., Chang, L., Fernandez, S. J., Gong, Y., Viola, K. L., Lambert, M. P., Velasco, P. T., Bigio, E. H., Finch, C. E., Krafft, G. A., & Klein, W. L. (2004). Synaptic targeting by Alzheimer's-related amyloid beta oligomers. *The Journal of Neuroscience: The Official Journal of the Society for Neuroscience*, *24*(45), 10191–10200. https://doi.org/10.1523/JNEUROSCI.3432-04.2004

Lacor, P. N., Buniel, M. C., Furlow, P. W., Clemente, A. S., Velasco, P. T., Wood, M., Viola, K. L., & Klein, W. L. (2007). Aβ oligomer-induced aberrations in synapse composition, shape, and density provide a molecular basis for loss of connectivity in Alzheimer's disease. *The Journal of Neuroscience: The Official Journal of the Society for Neuroscience*, *27*(4), 796–807. https://doi.org/10.1523/JNEUROSCI.3501-06.2007

LaFerla, F. M. (2002). Calcium dyshomeostasis and intracellular signalling in Alzheimer's disease. *Nat Rev Neurosci*, *3*, 862-872. https://doi.org/10.1038/nrn960

Lambert, M. P., Barlow, A. K., Chromy, B. A., Edwards, C., Freed, R., Liosatos, M., Morgan, T. E., Rozovsky, I., Trommer, B., Viola, K. L., Wals, P., Zhang, C., Finch, C. E., Krafft, G. A., & Klein, W. L. (1998). Diffusible, nonfibrillar ligands derived from Abeta1-42 are potent central nervous system neurotoxins. *Proceedings of the National Academy of Sciences of the United States of America*, *95*(11), 6448–6453. https://doi.org/10.1073/pnas.95.11.6448

Lamothe-Molina, P. J., Franzelin, A., Beck, L., Li, D., Auksutat, L., Fieblinger, T., Laprell, L., Alhbeck, J., Gee, C. E., Kneussel, M., Engel, A. K., Hilgetag, C. C., Morellini, F., & Oertner, T. G. (2022). ΔFosB accumulation in hippocampal granule cells drives cFos pattern separation during spatial learning. *Nature Communications*, *13*(1), Article 1. https://doi.org/10.1038/s41467-022-33947-w

Lasagna-Reeves, C. A., de Haro, M., Hao, S., Park, J., Rousseaux, M. W. C., Al-Ramahi, I., Jafar-Nejad, P., Vilanova-Velez, L., See, L., De Maio, A., Nitschke, L., Wu, Z., Troncoso, J. C., Westbrook, T. F., Tang, J., Botas, J., & Zoghbi, H. Y. (2016). Reduction of Nuak1 Decreases Tau and Reverses Phenotypes in a Tauopathy Mouse Model. *Neuron*, *92*(2), 407–418. https://doi.org/10.1016/j.neuron.2016.09.022

Lee, A., Hirabayashi, Y., Kwon, S. K., Lewis, T. L., Jr., & Polleux, F. (2018). Emerging roles of mitochondria in synaptic transmission and neurodegeneration. *Curr Opin Physiol*, *3*, 82-93. https://doi.org/10.1016/j.cophys.2018.03.009

Lee, A., Kondapalli, C., Virga, D. M., Lewis, T. L., Koo, S. Y., Ashok, A., Mairet-Coello, G., Herzig, S., Foretz, M., Viollet, B., Shaw, R., Sproul, A., & Polleux, F. (2022). Aβ42 oligomers trigger synaptic loss through CAMKK2-AMPK-dependent effectors coordinating mitochondrial fission and mitophagy. *Nature Communications*, *13*(1), Article 1. https://doi.org/10.1038/s41467-022-32130-5

Lee, J. H. (2010). Lysosomal proteolysis and autophagy require presenilin 1 and are disrupted by Alzheimer-related PS1 mutations. *Cell*, *141*, 1146-1158. https://doi.org/10.1016/j.cell.2010.05.008

Lee, J.-H., McBrayer, M. K., Wolfe, D. M., Haslett, L. J., Kumar, A., Sato, Y., Lie, P. P. Y., Mohan, P., Coffey, E. E., Kompella, U., Mitchell, C. H., Lloyd-Evans, E., & Nixon, R. A. (2015). Presenilin 1 Maintains Lysosomal Ca^{2+} Homeostasis via TRPML1 by Regulating vATPase-Mediated Lysosome Acidification. *Cell Reports*, *12*(9), 1430–1444. https://doi.org/10.1016/j.celrep.2015.07.050

Leitner, F. C., Melzer, S., Lütcke, H., Pinna, R., Seeburg, P. H., Helmchen, F., & Monyer, H. (2016). Spatially segregated feedforward and feedback neurons support differential odor processing in the lateral entorhinal cortex. *Nature Neuroscience*, *19*(7), 935–944. https://doi.org/10.1038/nn.4303

Lerdkrai, C., Asavapanumas, N., Brawek, B., Kovalchuk, Y., Mojtahedi, N., Olmedillas del Moral, M., & Garaschuk, O. (2018). Intracellular Ca^{2+} stores control in vivo neuronal hyperactivity in a mouse model of Alzheimer's disease. *Proceedings of the National Academy of Sciences*, *115*(6), E1279–E1288. https://doi.org/10.1073/pnas.1714409115

Lewis, T. L., Jr., Courchet, J., & Polleux, F. (2013). Cell biology in neuroscience: Cellular and molecular mechanisms underlying axon formation, growth, and branching. *J Cell Biol*, *202*, 837-848. https://doi.org/10.1083/jcb.201305098

Lewis, T. L., Jr., Kwon, S. K., Lee, A., Shaw, R., & Polleux, F. (2018). MFF-dependent mitochondrial fission regulates presynaptic release and axon branching by limiting axonal mitochondria size. *Nat Commun*, *9*, 5008. https://doi.org/10.1038/s41467-018-07416-2

Lewis, T. L., Jr., Turi, G. F., Kwon, S. K., Losonczy, A., & Polleux, F. (2016). Progressive Decrease of Mitochondrial Motility during Maturation of Cortical Axons In Vitro and In Vivo. *Curr Biol*, *26*, 2602-2608. https://doi.org/10.1016/j.cub.2016.07.064

Li, H., Alavian, K. N., Lazrove, E., Mehta, N., Jones, A., Zhang, P., Licznerski, P., Graham, M., Uo, T., & Guo, J. (2013). A Bcl-xL-Drp1 complex regulates synaptic vesicle membrane dynamics during endocytosis. *Nat Cell Biol*, *15*, 773–785. https://doi.org/10.1038/ncb2791.

Li, S., Hong, S., Shepardson, N. E., Walsh, D. M., Shankar, G. M., & Selkoe, D. (2009). Soluble oligomers of amyloid Beta protein facilitate hippocampal long-term depression by disrupting neuronal glutamate uptake. *Neuron*, *62*(6), 788–801. https://doi.org/10.1016/j.neuron.2009.05.012

Li, Z., Okamoto, K., Hayashi, Y., & Sheng, M. (2004). The importance of dendritic mitochondria in the morphogenesis and plasticity of spines and synapses. *Cell*, *119*, 873–887. https://doi.org/10.1016/j.cell.2004.11.003.

Lippa, C. F., & Morris, J. C. (2006). Alzheimer neuropathology in nondemented aging: Keeping mind over matter. *Neurology*, *66*(12), 1801–1802. https://doi.org/10.1212/01.wnl.0000234879.82633.f3

Loson, O. C., Song, Z., Chen, H., & Chan, D. C. (2013). Fis1, MFF, MiD49, and MiD51 mediate Drp1 recruitment in mitochondrial fission. *Mol Biol Cell*, *24*, 659–667. https://doi.org/10.1091/mbc.E12-10-0721.

Lovett-Barron, M., Kaifosh, P., Kheirbek, M. A., Danielson, N., Zaremba, J. D., Reardon, T. R., Turi, G. F., Hen, R., Zemelman, B. V., & Losonczy, A. (2014). Dendritic Inhibition in the Hippocampus Supports Fear Learning. *Science*, *343*(6173), 857–863. https://doi.org/10.1126/science.1247485

Lue, L. F., Kuo, Y. M., Roher, A. E., Brachova, L., Shen, Y., Sue, L., Beach, T., Kurth, J. H., Rydel, R. E., & Rogers, J. (1999). Soluble amyloid beta peptide concentration as a predictor of synaptic change in Alzheimer's disease. *The American Journal of Pathology*, *155*(3), 853–862. https://doi.org/10.1016/s0002-9440(10)65184-x

Ma, T., Chen, Y., Vingtdeux, V., Zhao, H., Viollet, B., Marambaud, P., & Klann, E. (2014). Inhibition of AMP-Activated Protein Kinase Signaling Alleviates Impairments in Hippocampal Synaptic Plasticity Induced by Amyloid β. *Journal of Neuroscience*, *34*(36), 12230–12238. https://doi.org/10.1523/JNEUROSCI.1694-14.2014

Mably, A. J., Gereke, B. J., Jones, D. T., & Colgin, L. L. (2017). Impairments in spatial representations and rhythmic coordination of place cells in the 3xTg mouse model of Alzheimer's disease. *Hippocampus*, *27*(4), 378–392. https://doi.org/10.1002/hipo.22697

Maday, S., & Holzbaur, E. L. (2016). Compartment-Specific Regulation of Autophagy in Primary Neurons. *J Neurosci*, *36*, 5933-5945. https://doi.org/10.1523/JNEUROSCI.4401-15.2016

Maherali, N., Ahfeldt, T., Rigamonti, A., Utikal, J., Cowan, C., & Hochedlinger, K. (2008). A High-Efficiency System for the Generation and Study of Human Induced Pluripotent Stem Cells. *Cell Stem Cell*, *3*(3), 340–345. https://doi.org/10.1016/j.stem.2008.08.003

Mairet-Coello, G., Courchet, J., Pieraut, S., Courchet, V., Maximov, A., & Polleux, F. (2013). The CAMKK2-AMPK kinase pathway mediates the synaptotoxic effects of Abeta oligomers through Tau phosphorylation. *Neuron*, *78*, 94–108. https://doi.org/10.1016/j.neuron.2013.02.003.

Mairet-Coello, G., & Polleux, F. (2014). Involvement of "stress-response" kinase pathways in Alzheimer's disease progression. *Curr Opin Neurobiol*, *27*, 110-117. https://doi.org/10.1016/j.conb.2014.03.011

Malinow, R. (2012). New developments on the role of NMDA receptors in Alzheimer's disease. *Curr Opin Neurobiol*, *22*, 559-563. https://doi.org/10.1016/j.conb.2011.09.001

Mallory, C. S., & Giocomo, L. M. (2018). Heterogeneity in hippocampal place coding. *Current Opinion in Neurobiology*, *49*, 158–167. https://doi.org/10.1016/j.conb.2018.02.014

Manczak, M., & Reddy, P. H. (2012). Abnormal interaction between the mitochondrial fission protein Drp1 and hyperphosphorylated tau in Alzheimer's disease neurons: Implications for mitochondrial dysfunction and neuronal damage. *Hum Mol Genet*, *21*, 2538-2547. https://doi.org/10.1093/hmg/dds072

Marinangeli, C., Didier, S., Ahmed, T., Caillerez, R., Domise, M., Laloux, C., Bégard, S., Carrier, S., Colin, M., Marchetti, P., Ghesquière, B., Balschun, D., Buée, L., Kluza, J., & Vingtdeux, V. (2018). AMP-Activated Protein Kinase Is Essential for the Maintenance of Energy Levels during Synaptic Activation. *IScience*, *9*, 1–13. https://doi.org/10.1016/j.isci.2018.10.006

Markram, H., Lübke, J., Frotscher, M., & Sakmann, B. (1997). Regulation of synaptic efficacy by coincidence of postsynaptic APs and EPSPs. *Science (New York, N.Y.)*, *275*(5297), 213–215. https://doi.org/10.1126/science.275.5297.213

Markus, E. J., Qin, Y. L., Leonard, B., Skaggs, W. E., McNaughton, B. L., & Barnes, C. A. (1995). Interactions between location and task affect the spatial and directional firing of hippocampal neurons. *Journal of Neuroscience*, *15*(11), 7079–7094. https://doi.org/10.1523/JNEUROSCI.15-11-07079.1995

Masliah, E., Mallory, M., Alford, M., DeTeresa, R., Hansen, L. A., McKeel, D. W., & Morris, J. C. (2001). Altered expression of synaptic proteins occurs early during progression of Alzheimer's disease. *Neurology*, *56*(1), 127–129. https://doi.org/10.1212/wnl.56.1.127

Massey, P. V., & Bashir, Z. I. (2007). Long-term depression: Multiple forms and implications for brain function. *Trends in Neurosciences*, *30*(4), 176–184. https://doi.org/10.1016/j.tins.2007.02.005

Masters, C. L., Masters, C. L., Bateman, R., Blennow, K., Rowe, C. C., Sperling, R. A., & Cummings, J. L. (2015). Alzheimer's disease. *Nature Reviews Disease Primers*, *1*(1), Article 1. https://doi.org/10.1038/nrdp.2015.56

Mattson, M. P. (1997). Cellular actions of beta-amyloid precursor protein and its soluble and fibrillogenic derivatives. *Physiological Reviews*, *77*(4), 1081–1132. https://doi.org/10.1152/physrev.1997.77.4.1081

McLean, C. A., Cherny, R. A., Fraser, F. W., Fuller, S. J., Smith, M. J., Beyreuther, K., Bush, A. I., & Masters, C. L. (1999). Soluble pool of Abeta amyloid as a determinant of severity of neurodegeneration in Alzheimer's disease. *Annals of Neurology*, *46*(6), 860–866. https://doi.org/10.1002/1531-8249(199912)46:6<860::aid-ana8>3.0.co;2-m

Meilandt, W. J., Yu, G.-Q., Chin, J., Roberson, E. D., Palop, J. J., Wu, T., Scearce-Levie, K., & Mucke, L. (2008). Enkephalin Elevations Contribute to Neuronal and Behavioral Impairments in a Transgenic Mouse Model of Alzheimer's Disease. *The Journal of Neuroscience*, *28*(19), 5007–5017. https://doi.org/10.1523/JNEUROSCI.0590-08.2008

Meyer-Dilhet, G., & Courchet, J. (2020). In Utero Cortical Electroporation of Plasmids in the Mouse Embryo. *STAR Protoc*, *1, 100027*. https://doi.org/10.1016/j.xpro.2020.100027

Meyer-Luehmann, M., Spires-Jones, T. L., Prada, C., Garcia-Alloza, M., de Calignon, A., Rozkalne, A., Koenigsknecht-Talboo, J., Holtzman, D. M., Bacskai, B. J., & Hyman, B. T. (2008). Rapid

appearance and local toxicity of amyloid-beta plaques in a mouse model of Alzheimer's disease. *Nature*, *451*(7179), 720–724. https://doi.org/10.1038/nature06616

Milstein, A. D., Li, Y., Bittner, K. C., Grienberger, C., Soltesz, I., Magee, J. C., & Romani, S. (2021). Bidirectional synaptic plasticity rapidly modifies hippocampal representations. *ELife*, *10*, e73046. https://doi.org/10.7554/eLife.73046

Miyagawa, T., Ebinuma, I., Morohashi, Y., Hori, Y., Young Chang, M., Hattori, H., Maehara, T., Yokoshima, S., Fukuyama, T., Tsuji, S., Iwatsubo, T., Prendergast, G. C., & Tomita, T. (2016). BIN1 regulates BACE1 intracellular trafficking and amyloid-β production. *Human Molecular Genetics*, *25*(14), 2948–2958. https://doi.org/10.1093/hmg/ddw146

Mizushima, N., & Komatsu, M. (2011). Autophagy: Renovation of cells and tissues. *Cell*, *147*, 728-741. https://doi.org/10.1016/j.cell.2011.10.026

Moolman, D. L., Vitolo, O. V., Vonsattel, J. P., & Shelanski, M. L. (2004). Dendrite and dendritic spine alterations in Alzheimer models. *J Neurocytol*, *33*, 377-387. https://doi.org/10.1023/B:NEUR.0000044197.83514.64

Morel, E. (2013). Phosphatidylinositol-3-phosphate regulates sorting and processing of amyloid precursor protein through the endosomal system. *Nat Commun*, *4*, 2250. https://doi.org/10.1038/ncomms3250

Morris, R. G. M., Garrud, P., Rawlins, J. N. P., & O'Keefe, J. (1982). Place navigation impaired in rats with hippocampal lesions. *Nature*, *297*(5868), Article 5868. https://doi.org/10.1038/297681a0

Moser, E. I., Kropff, E., & Moser, M.-B. (2008). Place cells, grid cells, and the brain's spatial representation system. *Annual Review of Neuroscience*, *31*, 69–89. https://doi.org/10.1146/annurev.neuro.31.061307.090723

Moser, M.-B., Rowland, D. C., & Moser, E. I. (2015). Place cells, grid cells, and memory. *Cold Spring Harbor Perspectives in Biology*, *7*(2), a021808. https://doi.org/10.1101/cshperspect.a021808

Mucke, L., Masliah, E., Yu, G. Q., Mallory, M., Rockenstein, E. M., Tatsuno, G., Hu, K., Kholodenko, D., Johnson-Wood, K., & McConlogue, L. (2000). High-level neuronal expression of abeta 1-42 in wild-type human amyloid protein precursor transgenic mice: Synaptotoxicity without plaque formation. *The Journal of Neuroscience: The Official Journal of the Society for Neuroscience*, *20*(11), 4050–4058. https://doi.org/10.1523/JNEUROSCI.20-11-04050.2000

Muller, R. U., & Kubie, J. L. (1987). The effects of changes in the environment on the spatial firing of hippocampal complex-spike cells. *The Journal of Neuroscience: The Official Journal of the Society for Neuroscience*, *7*(7), 1951–1968. https://doi.org/10.1523/JNEUROSCI.07-07-01951.1987

Nakashiba, T., Cushman, J. D., Pelkey, K. A., Renaudineau, S., Buhl, D. L., McHugh, T. J., Rodriguez Barrera, V., Chittajallu, R., Iwamoto, K. S., McBain, C. J., Fanselow, M. S., & Tonegawa, S. (2012). Young dentate granule cells mediate pattern separation, whereas old granule cells facilitate pattern completion. *Cell*, *149*(1), 188–201. https://doi.org/10.1016/j.cell.2012.01.046

Neuner, S. M., Heuer, S. E., Huentelman, M. J., O'Connell, K. M. S., & Kaczorowski, C. C. (2019). Harnessing Genetic Complexity to Enhance Translatability of Alzheimer's Disease Mouse Models: A Path toward Precision Medicine. *Neuron*, *101*(3), 399-411.e5. https://doi.org/10.1016/j.neuron.2018.11.040

Nixon, R. A. (2005). Endosome function and dysfunction in Alzheimer's disease and other neurodegenerative diseases. *Neurobiol Aging*, *26*, 373-382. https://doi.org/10.1016/j.neurobiolaging.2004.09.018

Nixon, R. A. (2013). The role of autophagy in neurodegenerative disease. *Nat Med*, *19*, 983-997. https://doi.org/10.1038/nm.3232

O'Brien, J. L., O'Keefe, K. M., LaViolette, P. S., DeLuca, A. N., Blacker, D., Dickerson, B. C., & Sperling, R. A. (2010). Longitudinal fMRI in elderly reveals loss of hippocampal activation with clinical decline. *Neurology*, *74*(24), 1969–1976. https://doi.org/10.1212/WNL.0b013e3181e3966e

Oh, H., Habeck, C., Madison, C., & Jagust, W. (2014). Covarying alterations in Aβ deposition, glucose metabolism, and gray matter volume in cognitively normal elderly. *Human Brain Mapping*, *35*(1), 297–308. https://doi.org/10.1002/hbm.22173

O'Hare, J. K., Gonzalez, K. C., Herrlinger, S. A., Hirabayashi, Y., Hewitt, V. L., Blockus, H., Szoboszlay, M., Rolotti, S. V., Geiller, T. C., Negrean, A., Chelur, V., Polleux, F., & Losonczy, A. (2022). Compartment-specific tuning of dendritic feature selectivity by intracellular Ca^{2+} release. *Science*, *375*(6586), eabm1670. https://doi.org/10.1126/science.abm1670

Ohsawa, I., Takamura, C., Morimoto, T., Ishiguro, M., & Kohsaka, S. (1999). Amino-terminal region of secreted form of amyloid precursor protein stimulates proliferation of neural stem cells. *The European Journal of Neuroscience*, *11*(6), 1907–1913. https://doi.org/10.1046/j.1460-9568.1999.00601.x

O'Keefe, J., & Dostrovsky, J. (1971). The hippocampus as a spatial map. Preliminary evidence from unit activity in the freely-moving rat. *Brain Research*, *34*(1), 171–175. https://doi.org/10.1016/0006-8993(71)90358-1

O'Keefe, J., & Nadel, L. (1979). The hippocampus as a cognitive map. *Behavioral and Brain Sciences*, *2*(4), 487–494. https://doi.org/10.1017/S0140525X00063949

Otera, H., Wang, C., Cleland, M. M., Setoguchi, K., Yokota, S., Youle, R. J., & Mihara, K. (2010). MFF is an essential factor for mitochondrial recruitment of Drp1 during mitochondrial fission in mammalian cells. *J Cell Biol*, *191*, 1141–1158. https://doi.org/10.1083/jcb.201007152.

Pachitariu, M., Stringer, C., Dipoppa, M., Schröder, S., Rossi, L. F., Dalgleish, H., Carandini, M., & Harris, K. D. (2017). *Suite2p: Beyond 10,000 neurons with standard two-photon microscopy* (p. 061507). bioRxiv. https://doi.org/10.1101/061507

Palop, J. J., Chin, J., Roberson, E. D., Wang, J., Thwin, M. T., Bien-Ly, N., Yoo, J., Ho, K. O., Yu, G.-Q., Kreitzer, A., Finkbeiner, S., Noebels, J. L., & Mucke, L. (2007). Aberrant Excitatory Neuronal Activity and Compensatory Remodeling of Inhibitory Hippocampal Circuits in Mouse Models of Alzheimer's Disease. *Neuron*, *55*(5), 697–711. https://doi.org/10.1016/j.neuron.2007.07.025

Palop, J. J., Jones, B., Kekonius, L., Chin, J., Yu, G.-Q., Raber, J., Masliah, E., & Mucke, L. (2003). Neuronal depletion of calcium-dependent proteins in the dentate gyrus is tightly linked to Alzheimer's disease-related cognitive deficits. *Proceedings of the National Academy of Sciences of the United States of America*, *100*(16), 9572–9577. https://doi.org/10.1073/pnas.1133381100

Palop, J. J., & Mucke, L. (2010). Amyloid-beta-induced neuronal dysfunction in Alzheimer's disease: From synapses toward neural networks. *Nat Neurosci*, *13*, 812-818. https://doi.org/10.1038/nn.2583

Paoletti, P., Bellone, C., & Zhou, Q. (2013). NMDA receptor subunit diversity: Impact on receptor properties, synaptic plasticity and disease. *Nature Reviews. Neuroscience*, *14*(6), 383–400. https://doi.org/10.1038/nrn3504

Paquet, D., Kwart, D., Chen, A., Sproul, A., Jacob, S., Teo, S., Olsen, K. M., Gregg, A., Noggle, S., & Tessier-Lavigne, M. (2016). Efficient introduction of specific homozygous and heterozygous mutations using CRISPR/Cas9. *Nature*, *533*(7601), Article 7601. https://doi.org/10.1038/nature17664

Payne, H. L., Lynch, G. F., & Aronov, D. (2021). Neural representations of space in the hippocampus of a food-caching bird. *Science (New York, N.Y.)*, *373*(6552), 343–348. https://doi.org/10.1126/science.abg2009

Penzes, P., Cahill, M. E., Jones, K. A., VanLeeuwen, J.-E., & Woolfrey, K. M. (2011). Dendritic spine pathology in neuropsychiatric disorders. *Nature Neuroscience*, *14*(3), Article 3. https://doi.org/10.1038/nn.2741

Perez-Cruz, C., Nolte, M. W., Gaalen, M. M. van, Rustay, N. R., Termont, A., Tanghe, A., Kirchhoff, F., & Ebert, U. (2011). Reduced Spine Density in Specific Regions of CA1 Pyramidal Neurons in Two Transgenic Mouse Models of Alzheimer's Disease. *Journal of Neuroscience*, *31*(10), 3926–3934. https://doi.org/10.1523/JNEUROSCI.6142-10.2011

Perkins, P., Annegers, J. F., Doody, R. S., Cooke, N., Aday, L., & Vernon, S. W. (1997). Incidence and prevalence of dementia in a multiethnic cohort of municipal retirees. *Neurology*, *49*(1), 44–50. https://doi.org/10.1212/wnl.49.1.44

Persson, J., Lind, J., Larsson, A., Ingvar, M., Sleegers, K., Van Broeckhoven, C., Adolfsson, R., Nilsson, L.-G., & Nyberg, L. (2008). Altered deactivation in individuals with genetic risk for Alzheimer's disease. *Neuropsychologia*, *46*(6), 1679–1687. https://doi.org/10.1016/j.neuropsychologia.2008.01.026

Pinsker, H., Kupfermann, I., Castellucci, V., & Kandel, E. (1970). Habituation and dishabituation of the gill-withdrawal reflex in Aplysia. *Science (New York, N.Y.)*, *167*(3926), 1740–1742. https://doi.org/10.1126/science.167.3926.1740

Power, M. C., Bennett, E. E., Turner, R. W., Dowling, N. M., Ciarleglio, A., Glymour, M. M., & Gianattasio, K. Z. (2021). Trends in Relative Incidence and Prevalence of Dementia Across Non-Hispanic Black and White Individuals in the United States, 2000-2016. *JAMA Neurology*, *78*(3), 275–284. https://doi.org/10.1001/jamaneurol.2020.4471

Pozueta, J., Lefort, R., Ribe, E. M., Troy, C. M., Arancio, O., & Shelanski, M. (2013). Caspase-2 is required for dendritic spine and behavioural alterations in J20 APP transgenic mice. *Nature Communications*, *4*(1), Article 1. https://doi.org/10.1038/ncomms2927

Priestley, J. B., Bowler, J. C., Rolotti, S. V., Fusi, S., & Losonczy, A. (2022). Signatures of rapid plasticity in hippocampal CA1 representations during novel experiences. *Neuron*, *110*(12), 1978-1992.e6. https://doi.org/10.1016/j.neuron.2022.03.026

Prince, S. M., Paulson, A. L., Jeong, N., Zhang, L., Amigues, S., & Singer, A. C. (2021). Alzheimer's pathology causes impaired inhibitory connections and reactivation of spatial codes during spatial navigation. *Cell Reports*, *35*(3), 109008. https://doi.org/10.1016/j.celrep.2021.109008

Putcha, D., Brickhouse, M., O'Keefe, K., Sullivan, C., Rentz, D., Marshall, G., Dickerson, B., & Sperling, R. (2011). Hippocampal hyperactivation associated with cortical thinning in Alzheimer's disease signature regions in non-demented elderly adults. *The Journal of Neuroscience: The Official*

Journal of the Society for Neuroscience, *31*(48), 17680–17688. https://doi.org/10.1523/JNEUROSCI.4740-11.2011

Puzzo, D., Gulisano, W., Palmeri, A., & Arancio, O. (2015). Rodent models for Alzheimer's disease drug discovery. *Expert Opinion on Drug Discovery*, *10*(7), 703–711. https://doi.org/10.1517/17460441.2015.1041913

Qu, X., Yuan, F. N., Corona, C., Pasini, S., Pero, M. E., Gundersen, G. G., Shelanski, M. L., & Bartolini, F. (2017). Stabilization of dynamic microtubules by mDia1 drives Tau-dependent Aβ1–42 synaptotoxicity. *Journal of Cell Biology*, *216*(10), 3161–3178. https://doi.org/10.1083/jcb.201701045

Quirk, G. J., Muller, R. U., & Kubie, J. L. (1990). The firing of hippocampal place cells in the dark depends on the rat's recent experience. *The Journal of Neuroscience: The Official Journal of the Society for Neuroscience*, *10*(6), 2008–2017. https://doi.org/10.1523/JNEUROSCI.10-06-02008.1990

Quiroz, Y. T., Budson, A. E., Celone, K., Ruiz, A., Newmark, R., Castrillón, G., Lopera, F., & Stern, C. E. (2010). Hippocampal hyperactivation in presymptomatic familial Alzheimer's disease. *Annals of Neurology*, *68*(6), 865–875. https://doi.org/10.1002/ana.22105

Rabarison, K. M., Bouldin, E. D., Bish, C. L., McGuire, L. C., Taylor, C. A., & Greenlund, K. J. (2018). The Economic Value of Informal Caregiving for Persons With Dementia: Results From 38 States, the District of Columbia, and Puerto Rico, 2015 and 2016 BRFSS. *American Journal of Public Health*, *108*(10), 1370–1377. https://doi.org/10.2105/AJPH.2018.304573

Racioppi, L., & Means, A. R. (2012). Calcium/calmodulin-dependent protein kinase kinase 2: Roles in signaling and pathophysiology. *J Biol Chem*, *287*, 31658–31665. https://doi.org/10.1074/jbc.R112.356485.

Rajan, K. B., Weuve, J., Barnes, L. L., McAninch, E. A., Wilson, R. S., & Evans, D. A. (2021). Population Estimate of People with Clinical AD and Mild Cognitive Impairment in the United States (2020–2060). *Alzheimer's & Dementia : The Journal of the Alzheimer's Association*, *17*(12), 1966. https://doi.org/10.1002/alz.12362

Rangaraju, V., Lewis, T. L., Hirabayashi, Y., Bergami, M., Motori, E., Cartoni, R., Kwon, S.-K., & Courchet, J. (2019). Pleiotropic Mitochondria: The Influence of Mitochondria on Neuronal Development and Disease. *Journal of Neuroscience*, *39*(42), 8200–8208. https://doi.org/10.1523/JNEUROSCI.1157-19.2019

Rebola, N., Carta, M., & Mulle, C. (2017). Operation and plasticity of hippocampal CA3 circuits: Implications for memory encoding. *Nature Reviews Neuroscience*, *18*(4), Article 4. https://doi.org/10.1038/nrn.2017.10

Rhein, V., Song, X., Wiesner, A., Ittner, L. M., Baysang, G., Meier, F., Ozmen, L., Bluethmann, H., Dröse, S., Brandt, U., Savaskan, E., Czech, C., Götz, J., & Eckert, A. (2009). Amyloid-β and tau synergistically impair the oxidative phosphorylation system in triple transgenic Alzheimer's disease mice. *Proceedings of the National Academy of Sciences*, *106*(47), 20057–20062. https://doi.org/10.1073/pnas.0905529106

Roberson, E. D., Halabisky, B., Yoo, J. W., Yao, J., Chin, J., Yan, F., Wu, T., Hamto, P., Devidze, N., Yu, G.-Q., Palop, J. J., Noebels, J. L., & Mucke, L. (2011). Amyloid-β/Fyn–Induced Synaptic, Network, and Cognitive Impairments Depend on Tau Levels in Multiple Mouse Models of Alzheimer's Disease. *Journal of Neuroscience*, *31*(2), 700–711. https://doi.org/10.1523/JNEUROSCI.4152-10.2011

Roberson, E. D., Scearce-Levie, K., Palop, J. J., Yan, F., Cheng, I. H., Wu, T., Gerstein, H., Yu, G.-Q., & Mucke, L. (2007). Reducing Endogenous Tau Ameliorates Amyloid ß-Induced Deficits in an Alzheimer's Disease Mouse Model. *Science*, *316*(5825), 750–754. https://doi.org/10.1126/science.1141736

Robinson, N. T. M., Descamps, L. A. L., Russell, L. E., Buchholz, M. O., Bicknell, B. A., Antonov, G. K., Lau, J. Y. N., Nutbrown, R., Schmidt-Hieber, C., & Häusser, M. (2020). Targeted Activation of Hippocampal Place Cells Drives Memory-Guided Spatial Behavior. *Cell*, *183*(6), 1586-1599.e10. https://doi.org/10.1016/j.cell.2020.09.061

Rolotti, S. V., Ahmed, M. S., Szoboszlay, M., Geiller, T., Negrean, A., Blockus, H., Gonzalez, K. C., Sparks, F. T., Solis Canales, A. S., Tuttman, A. L., Peterka, D. S., Zemelman, B. V., Polleux, F., & Losonczy, A. (2022). Local feedback inhibition tightly controls rapid formation of hippocampal place fields. *Neuron*, *110*(5), 783-794.e6. https://doi.org/10.1016/j.neuron.2021.12.003

Rubio, S. E., Vega-Flores, G., Martínez, A., Bosch, C., Pérez-Mediavilla, A., Río, J. del, Gruart, A., Delgado-García, J. M., Soriano, E., & Pascual, M. (2012). Accelerated aging of the GABAergic septohippocampal pathway and decreased hippocampal rhythms in a mouse model of Alzheimer's disease. *The FASEB Journal*, *26*(11), 4458–4467. https://doi.org/10.1096/fj.12-208413

Rudinskiy, N., Hawkes, J. M., Betensky, R. A., Eguchi, M., Yamaguchi, S., Spires-Jones, T. L., & Hyman, B. T. (2012). Orchestrated experience-driven Arc responses are disrupted in a mouse model of Alzheimer's disease. *Nature Neuroscience*, *15*(10), 1422–1429. https://doi.org/10.1038/nn.3199

Rueckemann, J. W., & Buffalo, E. A. (2017). Spatial responses, immediate experience, and memory in the monkey hippocampus. *Current Opinion in Behavioral Sciences*, *17*, 155–160. https://doi.org/10.1016/j.cobeha.2017.08.008

Rueckemann, J. W., DiMauro, A. J., Rangel, L. M., Han, X., Boyden, E. S., & Eichenbaum, H. (2016). Transient optogenetic inactivation of the medial entorhinal cortex biases the active population of hippocampal neurons. *Hippocampus*, *26*(2), 246–260. https://doi.org/10.1002/hipo.22519

Saganich, M. J., Schroeder, B. E., Galvan, V., Bredesen, D. E., Koo, E. H., & Heinemann, S. F. (2006). Deficits in synaptic transmission and learning in amyloid precursor protein (APP) transgenic mice require C-terminal cleavage of APP. *The Journal of Neuroscience: The Official Journal of the Society for Neuroscience*, *26*(52), 13428–13436. https://doi.org/10.1523/JNEUROSCI.4180-06.2006

Salloway, S., Sperling, R., Fox, N. C., Blennow, K., Klunk, W., Raskind, M., Sabbagh, M., Honig, L. S., Porsteinsson, A. P., Ferris, S., Reichert, M., Ketter, N., Nejadnik, B., Guenzler, V., Miloslavsky, M., Wang, D., Lu, Y., Lull, J., Tudor, I. C., … Brashear, H. R. (2014). Two Phase 3 Trials of Bapineuzumab in Mild-to-Moderate Alzheimer's Disease. *New England Journal of Medicine*, *370*(4), 322–333. https://doi.org/10.1056/NEJMoa1304839

Sanchez, P. E., Zhu, L., Verret, L., Vossel, K. A., Orr, A. G., Cirrito, J. R., Devidze, N., Ho, K., Yu, G.-Q., Palop, J. J., & Mucke, L. (2012). Levetiracetam suppresses neuronal network dysfunction and reverses synaptic and cognitive deficits in an Alzheimer's disease model. *Proceedings of the National Academy of Sciences of the United States of America*, *109*(42), E2895–E2903. https://doi.org/10.1073/pnas.1121081109

Sanchez-Mejia, R. O., Newman, J. W., Toh, S., Yu, G.-Q., Zhou, Y., Halabisky, B., Cissé, M., Scearce-Levie, K., Cheng, I. H., Gan, L., Palop, J. J., Bonventre, J. V., & Mucke, L. (2008). Phospholipase A2 reduction ameliorates cognitive deficits in a mouse model of Alzheimer's disease. *Nature Neuroscience*, *11*(11), Article 11. https://doi.org/10.1038/nn.2213

Sanderson, J. L., Freund, R. K., Gorski, J. A., & Dell'Acqua, M. L. (2021). Beta-Amyloid disruption of LTP/LTD balance is mediated by AKAP150-anchored PKA and Calcineurin regulation of Ca(2+)-permeable AMPA receptors. *Cell Rep*, *37, 109786*. https://doi.org/10.1016/j.celrep.2021.109786

Sando, R., Jiang, X., & Sudhof, T. C. (2019). Latrophilin GPCRs direct synapse specificity by coincident binding of FLRTs and teneurins. *Science*, *363*. https://doi.org/10.1126/science.aav7969.

Sasaki, T., Leutgeb, S., & Leutgeb, J. K. (2015). Spatial and memory circuits in the medial entorhinal cortex. *Current Opinion in Neurobiology*, *32*, 16–23. https://doi.org/10.1016/j.conb.2014.10.008

Scheff, S. W., DeKosky, S. T., & Price, D. A. (1990). Quantitative assessment of cortical synaptic density in Alzheimer's disease. *Neurobiology of Aging*, *11*(1), 29–37. https://doi.org/10.1016/0197-4580(90)90059-9

Scheff, S. W., & Price, D. A. (1993). Synapse loss in the temporal lobe in Alzheimer's disease. *Annals of Neurology*, *33*(2), 190–199. https://doi.org/10.1002/ana.410330209

Scheff, S. W., Price, D. A., Schmitt, F. A., DeKosky, S. T., & Mufson, E. J. (2007). Synaptic alterations in CA1 in mild Alzheimer disease and mild cognitive impairment. *Neurology*, *68*(18), 1501–1508. https://doi.org/10.1212/01.wnl.0000260698.46517.8f

Scheltens, P., Blennow, K., Breteler, M. M. B., de Strooper, B., Frisoni, G. B., Salloway, S., & Van der Flier, W. M. (2016). Alzheimer's disease. *Lancet (London, England)*, *388*(10043), 505–517. https://doi.org/10.1016/S0140-6736(15)01124-1

Schneider, F., Baldauf, K., Wetzel, W., & Reymann, K. G. (2014). Behavioral and EEG changes in male 5xFAD mice. *Physiology & Behavior*, *135*, 25–33. https://doi.org/10.1016/j.physbeh.2014.05.041

Schon, E. A., & Przedborski, S. (2011). Mitochondria: The next (neurode)generation. *Neuron*, *70*, 1033-1053. https://doi.org/10.1016/j.neuron.2011.06.003

Schwarz, T. L. (2013). Mitochondrial trafficking in neurons. *Cold Spring Harb Perspect Biol*, *5*. https://doi.org/10.1101/cshperspect.a011304

Scott, L., Feng, J., Kiss, T., Needle, E., Atchison, K., Kawabe, T. T., Milici, A. J., Hajós-Korcsok, É., Riddell, D., & Hajós, M. (2012). Age-dependent disruption in hippocampal theta oscillation in amyloid-β overproducing transgenic mice. *Neurobiology of Aging*, *33*(7), 1481.e13-1481.e23. https://doi.org/10.1016/j.neurobiolaging.2011.12.010

Scoville, W. B., & Milner, B. (1957). Loss of Recent Memory After Bilateral Hippocampal Lesions. *Journal of Neurology, Neurosurgery & Psychiatry*, *20*(1), 11–21. https://doi.org/10.1136/jnnp.20.1.11

Selkoe, D. J. (2002). Alzheimer's Disease Is a Synaptic Failure. *Science*, *298*(5594), 789–791. https://doi.org/10.1126/science.1074069

Selkoe, D. J., & Hardy, J. (2016). The amyloid hypothesis of Alzheimer's disease at 25 years. *EMBO Molecular Medicine*, *8*(6), 595–608. https://doi.org/10.15252/emmm.201606210

Sepulveda-Falla, D., Glatzel, M., & Lopera, F. (2012). Phenotypic profile of early-onset familial Alzheimer's disease caused by presenilin-1 E280A mutation. *Journal of Alzheimer's Disease: JAD*, *32*(1), 1–12. https://doi.org/10.3233/JAD-2012-120907

Serrano-Pozo, A., Frosch, M. P., Masliah, E., & Hyman, B. T. (2011). Neuropathological alterations in Alzheimer disease. *Cold Spring Harb Perspect Med*, *1, a006189*. https://doi.org/10.1101/cshperspect.a006189

Sevigny, J., Chiao, P., Bussière, T., Weinreb, P. H., Williams, L., Maier, M., Dunstan, R., Salloway, S., Chen, T., Ling, Y., O'Gorman, J., Qian, F., Arastu, M., Li, M., Chollate, S., Brennan, M. S., Quintero-Monzon, O., Scannevin, R. H., Arnold, H. M., … Sandrock, A. (2016). The antibody aducanumab reduces Aβ plaques in Alzheimer's disease. *Nature*, *537*(7618), 50–56. https://doi.org/10.1038/nature19323

Shankar, G. M., Bloodgood, B. L., Townsend, M., Walsh, D. M., Selkoe, D. J., & Sabatini, B. L. (2007). Natural oligomers of the Alzheimer amyloid-beta protein induce reversible synapse loss by modulating an NMDA-type glutamate receptor-dependent signaling pathway. *The Journal of Neuroscience: The Official Journal of the Society for Neuroscience*, *27*(11), 2866–2875. https://doi.org/10.1523/JNEUROSCI.4970-06.2007

Shankar, G. M., Li, S., Mehta, T. H., Garcia-Munoz, A., Shepardson, N. E., Smith, I., Brett, F. M., Farrell, M. A., Rowan, M. J., Lemere, C. A., Regan, C. M., Walsh, D. M., Sabatini, B. L., & Selkoe, D. J. (2008). Amyloid-β protein dimers isolated directly from Alzheimer's brains impair synaptic plasticity and memory. *Nature Medicine*, *14*(8), Article 8. https://doi.org/10.1038/nm1782

Sheffield, M. E. J., Adoff, M. D., & Dombeck, D. A. (2017). Increased Prevalence of Calcium Transients across the Dendritic Arbor during Place Field Formation. *Neuron*, *96*(2), 490-504.e5. https://doi.org/10.1016/j.neuron.2017.09.029

Shen, Q., Yamano, K., Head, B. P., Kawajiri, S., Cheung, J. T., Wang, C., Cho, J. H., Hattori, N., Youle, R. J., & Bliek, A. M. (2014). Mutations in Fis1 disrupt orderly disposal of defective mitochondria. *Mol Biol Cell*, *25*, 145–159. https://doi.org/10.1091/mbc.E13-09-0525.

Sheng, M., Sabatini, B. L., & Südhof, T. C. (2012). Synapses and Alzheimer's disease. *Cold Spring Harbor Perspectives in Biology*, *4*(5), a005777. https://doi.org/10.1101/cshperspect.a005777

Šišková, Z., Justus, D., Kaneko, H., Friedrichs, D., Henneberg, N., Beutel, T., Pitsch, J., Schoch, S., Becker, A., von der Kammer, H., & Remy, S. (2014). Dendritic structural degeneration is functionally linked to cellular hyperexcitability in a mouse model of Alzheimer's disease. *Neuron*, *84*(5), 1023–1033. https://doi.org/10.1016/j.neuron.2014.10.024

Small, S. A., Schobel, S. A., Buxton, R. B., Witter, M. P., & Barnes, C. A. (2011). A pathophysiological framework of hippocampal dysfunction in ageing and disease. *Nat Rev Neurosci*, *12*, 585-601. https://doi.org/10.1038/nrn3085

Son, S. M., Jung, E. S., Shin, H. J., Byun, J., & Mook-Jung, I. (2012). Abeta-induced formation of autophagosomes is mediated by RAGE-CaMKKbeta-AMPK signaling. *Neurobiol Aging*, *33*, 1006 1011-1023. https://doi.org/10.1016/j.neurobiolaging.2011.09.039

Sorrentino, P., Iuliano, A., Polverino, A., Jacini, F., & Sorrentino, G. (2014). The dark sides of amyloid in Alzheimer's disease pathogenesis. *FEBS Letters*, *588*(5), 641–652. https://doi.org/10.1016/j.febslet.2013.12.038

Sorrentino, V., Romani, M., Mouchiroud, L., Beck, J. S., Zhang, H., D'Amico, D., Moullan, N., Potenza, F., Schmid, A. W., Rietsch, S., Counts, S. E., & Auwerx, J. (2017). Enhancing mitochondrial proteostasis reduces amyloid-β proteotoxicity. *Nature*, *552*(7684), Article 7684. https://doi.org/10.1038/nature25143

Sperling, R. A., Aisen, P. S., Beckett, L. A., Bennett, D. A., Craft, S., Fagan, A. M., Iwatsubo, T., Jack, C. R., Kaye, J., Montine, T. J., Park, D. C., Reiman, E. M., Rowe, C. C., Siemers, E., Stern, Y., Yaffe, K., Carrillo, M. C., Thies, B., Morrison-Bogorad, M., … Phelps, C. H. (2011). Toward defining the preclinical stages of Alzheimer's disease: Recommendations from the National Institute on Aging-Alzheimer's Association workgroups on diagnostic guidelines for Alzheimer's disease. *Alzheimer's*

& Dementia: The Journal of the Alzheimer's Association, *7*(3), 280–292. https://doi.org/10.1016/j.jalz.2011.03.003

Sperling, R. A., Laviolette, P. S., O'Keefe, K., O'Brien, J., Rentz, D. M., Pihlajamaki, M., Marshall, G., Hyman, B. T., Selkoe, D. J., Hedden, T., Buckner, R. L., Becker, J. A., & Johnson, K. A. (2009). Amyloid deposition is associated with impaired default network function in older persons without dementia. *Neuron*, *63*(2), 178–188. https://doi.org/10.1016/j.neuron.2009.07.003

Spires, T. L., & Hyman, B. T. (2004). Neuronal structure is altered by amyloid plaques. *Reviews in the Neurosciences*, *15*(4), 267–278. https://doi.org/10.1515/revneuro.2004.15.4.267

Spires, T. L., Meyer-Luehmann, M., Stern, E. A., McLean, P. J., Skoch, J., Nguyen, P. T., Bacskai, B. J., & Hyman, B. T. (2005). Dendritic spine abnormalities in amyloid precursor protein transgenic mice demonstrated by gene transfer and intravital multiphoton microscopy. *The Journal of Neuroscience: The Official Journal of the Society for Neuroscience*, *25*(31), 7278–7287. https://doi.org/10.1523/JNEUROSCI.1879-05.2005

Squire, L. R. (1986). Mechanisms of memory. *Science (New York, N.Y.)*, *232*(4758), 1612–1619. https://doi.org/10.1126/science.3086978

Squire, L. R. (2009). Memory and Brain Systems: 1969–2009. *Journal of Neuroscience*, *29*(41), 12711–12716. https://doi.org/10.1523/JNEUROSCI.3575-09.2009

Stachenfeld, K. L., Botvinick, M. M., & Gershman, S. J. (2017). The hippocampus as a predictive map. *Nature Neuroscience*, *20*(11), Article 11. https://doi.org/10.1038/nn.4650

Steenland, K., Goldstein, F. C., Levey, A., & Wharton, W. (2016). A Meta-Analysis of Alzheimer's Disease Incidence and Prevalence Comparing African-Americans and Caucasians. *Journal of Alzheimer's Disease: JAD*, *50*(1), 71–76. https://doi.org/10.3233/JAD-150778

Steinberg, G. R., & Hardie, D. G. (2022). New insights into activation and function of the AMPK. *Nat Rev Mol Cell Biol*. https://doi.org/10.1038/s41580-022-00547-x.

Stoiljkovic, M., Kelley, C., Hajós, G. P., Nagy, D., Koenig, G., Leventhal, L., & Hajós, M. (2016). Hippocampal network dynamics in response to α7 nACh receptors activation in amyloid-β overproducing transgenic mice. *Neurobiology of Aging*, *45*, 161–168. https://doi.org/10.1016/j.neurobiolaging.2016.05.021

Stoiljkovic, M., Kelley, C., Stutz, B., Horvath, T. L., & Hajós, M. (2019). Altered Cortical and Hippocampal Excitability in TgF344-AD Rats Modeling Alzheimer's Disease Pathology. *Cerebral Cortex (New York, NY)*, *29*(6), 2716–2727. https://doi.org/10.1093/cercor/bhy140

Stringer, C., Wang, T., Michaelos, M., & Pachitariu, M. (2021). Cellpose: A generalist algorithm for cellular segmentation. *Nature Methods*, *18*(1), Article 1. https://doi.org/10.1038/s41592-020-01018-x

Stutzmann, G. E., Caccamo, A., LaFerla, F. M., & Parker, I. (2004). Dysregulated IP3 signaling in cortical neurons of knock-in mice expressing an Alzheimer's-linked mutation in presenilin1 results in exaggerated Ca^{2+} signals and altered membrane excitability. *J Neurosci*, *24*, 508-513. https://doi.org/10.1523/JNEUROSCI.4386-03.2004

Sun, J., Carlson-Stevermer, J., Das, U., Shen, M., Delenclos, M., Snead, A. M., Koo, S. Y., Wang, L., Qiao, D., Loi, J., Petersen, A. J., Stockton, M., Bhattacharyya, A., Jones, M. V., Zhao, X., McLean, P. J., Sproul, A. A., Saha, K., & Roy, S. (2019). CRISPR/Cas9 editing of APP C-terminus attenuates β-cleavage and promotes α-cleavage. *Nature Communications*, *10*(1), Article 1. https://doi.org/10.1038/s41467-018-07971-8

Szczurkowska, J., Cwetsch, A. W., dal Maschio, M., Ghezzi, D., Ratto, G. M., & Cancedda, L. (2016). Targeted in vivo genetic manipulation of the mouse or rat brain by in utero electroporation with a triple-electrode probe. *Nature Protocols*, *11*(3), Article 3. https://doi.org/10.1038/nprot.2016.014

Takahashi, H., & Magee, J. C. (2009). Pathway interactions and synaptic plasticity in the dendritic tuft regions of CA1 pyramidal neurons. *Neuron*, *62*(1), 102–111. https://doi.org/10.1016/j.neuron.2009.03.007

Takamura, R., Mizuta, K., Sekine, Y., Islam, T., Saito, T., Sato, M., Ohkura, M., Nakai, J., Ohshima, T., Saido, T. C., & Hayashi, Y. (2021). Modality-Specific Impairment of Hippocampal CA1 Neurons of Alzheimer's Disease Model Mice. *The Journal of Neuroscience: The Official Journal of the Society for Neuroscience*, *41*(24), 5315–5329. https://doi.org/10.1523/JNEUROSCI.0208-21.2021

Teich, A. F., & Arancio, O. (2012). Is the amyloid hypothesis of Alzheimer's disease therapeutically relevant? *The Biochemical Journal*, *446*(2), 165–177. https://doi.org/10.1042/BJ20120653

Terasaki, M. (2018). Axonal endoplasmic reticulum is very narrow. *J Cell Sci*, *131*. https://doi.org/10.1242/jcs.210450.

Terry, R. D., Hansen, L. A., DeTeresa, R., Davies, P., Tobias, H., & Katzman, R. (1987). Senile dementia of the Alzheimer type without neocortical neurofibrillary tangles. *Journal of Neuropathology and Experimental Neurology*, *46*(3), 262–268. https://doi.org/10.1097/00005072-198705000-00003

Terry, R. D., Masliah, E., Salmon, D. P., Butters, N., DeTeresa, R., Hill, R., Hansen, L. A., & Katzman, R. (1991). Physical basis of cognitive alterations in Alzheimer's disease: Synapse loss is the major correlate of cognitive impairment. *Annals of Neurology*, *30*(4), 572–580. https://doi.org/10.1002/ana.410300410

Thal, D. R., Rüb, U., Orantes, M., & Braak, H. (2002). Phases of A beta-deposition in the human brain and its relevance for the development of AD. *Neurology*, *58*(12), 1791–1800. https://doi.org/10.1212/wnl.58.12.1791

Thornton, C., Bright, N. J., Sastre, M., Muckett, P. J., & Carling, D. (2011). AMP-activated protein kinase (AMPK) is a tau kinase, activated in response to amyloid beta-peptide exposure. *Biochem J*, *434*, 503-512. https://doi.org/10.1042/BJ20101485

Tilokani, L., Russell, F. M., Hamilton, S., Virga, D. M., Segawa, M., Paupe, V., Gruszczyk, A. V., Protasoni, M., Tabara, L. C., & Johnson, M. (2022). AMPK-dependent phosphorylation of MTFR1L regulates mitochondrial morphology. *Sci Adv*, *8, eabo7956*. https://doi.org/10.1126/sciadv.abo7956.

Tokumitsu, H. (2002). STO-609, a specific inhibitor of the Ca(2+)/calmodulin-dependent protein kinase kinase. *J Biol Chem*, *277*, 15813-15818. https://doi.org/10.1074/jbc.M201075200

Tolman, E. C. (1948). Cognitive maps in rats and men. *Psychological Review*, *55*, 189–208. https://doi.org/10.1037/h0061626

Toyama, E. Q., Herzig, S., Courchet, J., Lewis, T. L., Jr., Loson, O. C., Hellberg, K., Young, N. P., Chen, H., Polleux, F., Chan, D. C., & Shaw, R. J. (2016). Metabolism. AMP-activated protein kinase mediates mitochondrial fission in response to energy stress. *Science*, *351*, 275–281. https://doi.org/10.1126/science.aab4138.

Tsai, J., Grutzendler, J., Duff, K., & Gan, W.-B. (2004). Fibrillar amyloid deposition leads to local synaptic abnormalities and breakage of neuronal branches. *Nature Neuroscience*, *7*(11), 1181–1183. https://doi.org/10.1038/nn1335

Tsao, A., Moser, M.-B., & Moser, E. I. (2013). Traces of experience in the lateral entorhinal cortex. *Current Biology: CB*, *23*(5), 399–405. https://doi.org/10.1016/j.cub.2013.01.036

Tsao, A., Sugar, J., Lu, L., Wang, C., Knierim, J. J., Moser, M.-B., & Moser, E. I. (2018). Integrating time from experience in the lateral entorhinal cortex. *Nature*, *561*(7721), 57–62. https://doi.org/10.1038/s41586-018-0459-6

Tsitsiklis, M., Miller, J., Qasim, S. E., Inman, C. S., Gross, R. E., Willie, J. T., Smith, E. H., Sheth, S. A., Schevon, C. A., Sperling, M. R., Sharan, A., Stein, J. M., & Jacobs, J. (2020). Single-Neuron Representations of Spatial Targets in Humans. *Current Biology: CB*, *30*(2), 245-253.e4. https://doi.org/10.1016/j.cub.2019.11.048

Tuncdemir, S. N., Lacefield, C. O., & Hen, R. (2019). Contributions of adult neurogenesis to dentate gyrus network activity and computations. *Behavioural Brain Research*, *374*, 112112. https://doi.org/10.1016/j.bbr.2019.112112

Turi, G. F., Li, W.-K., Chavlis, S., Pandi, I., O'Hare, J., Priestley, J. B., Grosmark, A. D., Liao, Z., Ladow, M., Zhang, J. F., Zemelman, B. V., Poirazi, P., & Losonczy, A. (2019). Vasoactive Intestinal Polypeptide-Expressing Interneurons in the Hippocampus Support Goal-Oriented Spatial Learning. *Neuron*, *101*(6), 1150-1165.e8. https://doi.org/10.1016/j.neuron.2019.01.009

Turner, N. L. (2020). *Multiscale and multimodal reconstruction of cortical structure and function: Vol. bioRxiv*.

Turner, N. L., Macrina, T., Bae, J. A., Yang, R., Wilson, A. M., Schneider-Mizell, C., Lee, K., Lu, R., Wu, J., & Bodor, A. L. (2022). Reconstruction of neocortex: Organelles, compartments, cells, circuits, and activity. *Cell*, *185*, 1082-1100 1024. https://doi.org/10.1016/j.cell.2022.01.023.

Udayar, V., Buggia-Prévot, V., Guerreiro, R. L., Siegel, G., Rambabu, N., Soohoo, A. L., Ponnusamy, M., Siegenthaler, B., Bali, J., Guerreiro, R., Brás, J., Sassi, C., Gibbs, J. R., Hernandez, D., Lupton, M. K., Brown, K., Morgan, K., Powell, J., Singleton, A., … Rajendran, L. (2013). A Paired RNAi and RabGAP Overexpression Screen Identifies Rab11 as a Regulator of β-Amyloid Production. *Cell Reports*, *5*(6), 1536–1551. https://doi.org/10.1016/j.celrep.2013.12.005

Ulanovsky, N., & Moss, C. F. (2007). Hippocampal cellular and network activity in freely moving echolocating bats. *Nature Neuroscience*, *10*(2), 224–233. https://doi.org/10.1038/nn1829

Um, J. W., Nygaard, H. B., Heiss, J. K., Kostylev, M. A., Stagi, M., Vortmeyer, A., Wisniewski, T., Gunther, E. C., & Strittmatter, S. M. (2012). Alzheimer amyloid-β oligomer bound to postsynaptic prion protein activates Fyn to impair neurons. *Nature Neuroscience*, *15*(9), 1227–1235. https://doi.org/10.1038/nn.3178

Uytterhoeven, V., Lauwers, E., Maes, I., Miskiewicz, K., Melo, M. N., Swerts, J., Kuenen, S., Wittocx, R., Corthout, N., Marrink, S.-J., Munck, S., & Verstreken, P. (2015). Hsc70-4 Deforms Membranes to Promote Synaptic Protein Turnover by Endosomal Microautophagy. *Neuron*, *88*(4), 735–748. https://doi.org/10.1016/j.neuron.2015.10.012

Van Cauter, T., Poucet, B., & Save, E. (2008). Unstable CA1 place cell representation in rats with entorhinal cortex lesions. *The European Journal of Neuroscience*, *27*(8), 1933–1946. https://doi.org/10.1111/j.1460-9568.2008.06158.x

van der Kant, R., Goldstein, L. S. B., & Ossenkoppele, R. (2020). Amyloid-β-independent regulators of tau pathology in Alzheimer disease. *Nature Reviews. Neuroscience*, *21*(1), 21–35. https://doi.org/10.1038/s41583-019-0240-3

Villette, V., Poindessous-Jazat, F., Simon, A., Léna, C., Roullot, E., Bellessort, B., Epelbaum, J., Dutar, P., & Stéphan, A. (2010). Decreased rhythmic GABAergic septal activity and memory-associated theta oscillations after hippocampal amyloid-beta pathology in the rat. *The Journal of Neuroscience: The Official Journal of the Society for Neuroscience*, *30*(33), 10991–11003. https://doi.org/10.1523/JNEUROSCI.6284-09.2010

Vingtdeux, V., Davies, P., Dickson, D. W., & Marambaud, P. (2011). AMPK is abnormally activated in tangle- and pre-tangle-bearing neurons in Alzheimer's disease and other tauopathies. *Acta Neuropathol*, *121*, 337-349. https://doi.org/10.1007/s00401-010-0759-x

von Rotz, R. C., Kohli, B. M., Bosset, J., Meier, M., Suzuki, T., Nitsch, R. M., & Konietzko, U. (2004). The APP intracellular domain forms nuclear multiprotein complexes and regulates the transcription of its own precursor. *Journal of Cell Science*, *117*(Pt 19), 4435–4448. https://doi.org/10.1242/jcs.01323

Walsh, D. M., Klyubin, I., Fadeeva, J. V., Cullen, W. K., Anwyl, R., Wolfe, M. S., Rowan, M. J., & Selkoe, D. J. (2002). Naturally secreted oligomers of amyloid beta protein potently inhibit hippocampal long-term potentiation in vivo. *Nature*, *416*(6880), 535–539. https://doi.org/10.1038/416535a

Wang, L. (2016). Synaptosomal Mitochondrial Dysfunction in 5xFAD Mouse Model of Alzheimer's Disease. *PLoS One*, *11, e0150441*. https://doi.org/10.1371/journal.pone.0150441

Wang, X., Su, B., Lee, H., Li, X., Perry, G., Smith, M. A., & Zhu, X. (2009). Impaired Balance of Mitochondrial Fission and Fusion in Alzheimer's Disease. *Journal of Neuroscience*, *29*(28), 9090–9103. https://doi.org/10.1523/JNEUROSCI.1357-09.2009

Wang, X., Su, B., Siedlak, S. L., Moreira, P. I., Fujioka, H., Wang, Y., Casadesus, G., & Zhu, X. (2008). Amyloid-beta overproduction causes abnormal mitochondrial dynamics via differential modulation of mitochondrial fission/fusion proteins. *Proceedings of the National Academy of Sciences of the United States of America*, *105*(49), 19318–19323. https://doi.org/10.1073/pnas.0804871105

Wattmo, C., Minthon, L., & Wallin, Å. K. (2016). Mild versus moderate stages of Alzheimer's disease: Three-year outcomes in a routine clinical setting of cholinesterase inhibitor therapy. *Alzheimer's Research & Therapy*, *8*(1), 7. https://doi.org/10.1186/s13195-016-0174-1

Weintraub, S., Wicklund, A. H., & Salmon, D. P. (2012). The neuropsychological profile of Alzheimer disease. *Cold Spring Harbor Perspectives in Medicine*, *2*(4), a006171. https://doi.org/10.1101/cshperspect.a006171

Whitcomb, D. J., Hogg, E. L., Regan, P., Piers, T., Narayan, P., Whitehead, G., Winters, B. L., Kim, D.-H., Kim, E., St George-Hyslop, P., Klenerman, D., Collingridge, G. L., Jo, J., & Cho, K. (2015). Intracellular oligomeric amyloid-beta rapidly regulates GluA1 subunit of AMPA receptor in the hippocampus. *Scientific Reports*, *5*(1), Article 1. https://doi.org/10.1038/srep10934

Williams, T., Courchet, J., Viollet, B., Brenman, J. E., & Polleux, F. (2011). AMP-activated protein kinase (AMPK) activity is not required for neuronal development but regulates axogenesis during metabolic stress. *Proc Natl Acad Sci U S A*, *108*, 5849-5854. https://doi.org/10.1073/pnas.1013660108

Wilson, M. A., & McNaughton, B. L. (1993). Dynamics of the hippocampal ensemble code for space. *Science (New York, N.Y.)*, *261*(5124), 1055–1058. https://doi.org/10.1126/science.8351520

Wisniewski, T., & Sigurdsson, E. M. (2010). Murine models of Alzheimer's disease and their use in developing immunotherapies. *Biochimica Et Biophysica Acta*, *1802*(10), 847–859. https://doi.org/10.1016/j.bbadis.2010.05.004

Witton, J., Staniaszek, L. E., Bartsch, U., Randall, A. D., Jones, M. W., & Brown, J. T. (2016). Disrupted hippocampal sharp-wave ripple-associated spike dynamics in a transgenic mouse model of dementia. *The Journal of Physiology*, *594*(16), 4615–4630. https://doi.org/10.1113/jphysiol.2014.282889

Wright, A. L., Zinn, R., Hohensinn, B., Konen, L. M., Beynon, S. B., Tan, R. P., Clark, I. A., Abdipranoto, A., & Vissel, B. (2013). Neuroinflammation and neuronal loss precede Aβ plaque deposition in the hAPP-J20 mouse model of Alzheimer's disease. *PloS One*, *8*(4), e59586. https://doi.org/10.1371/journal.pone.0059586

Wu, Y., Whiteus, C., Xu, C. S., Hayworth, K. J., Weinberg, R. J., Hess, H. F., & Camilli, P. (2017). Contacts between the endoplasmic reticulum and other membranes in neurons. *Proc Natl Acad Sci U S A*, *114*, 4859–4867. https://doi.org/10.1073/pnas.1701078114.

Xie, H., Guan, J., Borrelli, L. A., Xu, J., Serrano-Pozo, A., & Bacskai, B. J. (2013). Mitochondrial Alterations near Amyloid Plaques in an Alzheimer's Disease Mouse Model. *Journal of Neuroscience*, *33*(43), 17042–17051. https://doi.org/10.1523/JNEUROSCI.1836-13.2013

Xu, W., & Wilson, D. A. (2012). Odor-evoked activity in the mouse lateral entorhinal cortex. *Neuroscience*, *223*, 12–20. https://doi.org/10.1016/j.neuroscience.2012.07.067

Xue, M., Atallah, B. V., & Scanziani, M. (2014). Equalizing excitation-inhibition ratios across visual cortical neurons. *Nature*, *511*, 596–600. https://doi.org/10.1038/nature13321.

Ye, Q., Gast, G., Su, X., Saito, T., Saido, T. C., Holmes, T. C., & Xu, X. (2022). Hippocampal neural circuit connectivity alterations in an Alzheimer's disease mouse model revealed by monosynaptic rabies virus tracing. *Neurobiology of Disease*, *172*, 105820. https://doi.org/10.1016/j.nbd.2022.105820

Ying, J., Keinath, A. T., Lavoie, R., Vigneault, E., El Mestikawy, S., & Brandon, M. P. (2022). Disruption of the grid cell network in a mouse model of early Alzheimer's disease. *Nature Communications*, *13*(1), Article 1. https://doi.org/10.1038/s41467-022-28551-x

Yoon, S. O., Park, D. J., Ryu, J. C., Ozer, H. G., Tep, C., Shin, Y. J., Lim, T. H., Pastorino, L., Kunwar, A. J., Walton, J. C., Nagahara, A. H., Lu, K. P., Nelson, R. J., Tuszynski, M. H., & Huang, K. (2012). JNK3 Perpetuates Metabolic Stress Induced by Aβ Peptides. *Neuron*, *75*(5), 824–837. https://doi.org/10.1016/j.neuron.2012.06.024

Youle, R. J., & Bliek, A. M. (2012). Mitochondrial fission, fusion, and stress. *Science*, *337*, 1062-1065. https://doi.org/10.1126/science.1219855

Zaremba, J. D., Diamantopoulou, A., Danielson, N. B., Grosmark, A. D., Kaifosh, P. W., Bowler, J. C., Liao, Z., Sparks, F. T., Gogos, J. A., & Losonczy, A. (2017). Impaired hippocampal place cell dynamics in a mouse model of the 22q11.2 deletion. *Nature Neuroscience*, *20*(11), Article 11. https://doi.org/10.1038/nn.4634

Zhang, L., Trushin, S., Christensen, T. A., Bachmeier, B. V., Gateno, B., Schroeder, A., Yao, J., Itoh, K., Sesaki, H., Poon, W. W., Gylys, K. H., Patterson, E. R., Parisi, J. E., Diaz Brinton, R., Salisbury, J. L., & Trushina, E. (2016). Altered brain energetics induces mitochondrial fission arrest in Alzheimer's Disease. *Scientific Reports*, *6*(1), Article 1. https://doi.org/10.1038/srep18725

Zhang, Y., Pak, C., Han, Y., Ahlenius, H., Zhang, Z., Chanda, S., Marro, S., Patzke, C., Acuna, C., Covy, J., Xu, W., Yang, N., Danko, T., Chen, L., Wernig, M., & Südhof, T. C. (2013). Rapid Single-Step Induction of Functional Neurons from Human Pluripotent Stem Cells. *Neuron*, *78*(5), 785–798. https://doi.org/10.1016/j.neuron.2013.05.029

Zhao, C., Deng, W., & Gage, F. H. (2008). Mechanisms and functional implications of adult neurogenesis. *Cell*, *132*(4), 645–660. https://doi.org/10.1016/j.cell.2008.01.033

Zhao, R., Fowler, S. W., Chiang, A. C. A., Ji, D., & Jankowsky, J. L. (2014). Impairments in experience-dependent scaling and stability of hippocampal place fields limit spatial learning in a mouse model of Alzheimer's disease. *Hippocampus*, *24*(8), 963–978. https://doi.org/10.1002/hipo.22283

Zhao, X., Wang, Y., Spruston, N., & Magee, J. C. (2020). Membrane potential dynamics underlying context-dependent sensory responses in the hippocampus. *Nature Neuroscience*, *23*(7), 881–891. https://doi.org/10.1038/s41593-020-0646-2

Zhou, X., Babu, J. R., da Silva, S., Shu, Q., Graef, I. A., Oliver, T., Tomoda, T., Tani, T., Wooten, M. W., & Wang, F. (2007). Unc-51-like kinase 1/2-mediated endocytic processes regulate filopodia extension and branching of sensory axons. *Proceedings of the National Academy of Sciences*, *104*(14), 5842–5847. https://doi.org/10.1073/pnas.0701402104

Ziv, Y., Burns, L. D., Cocker, E. D., Hamel, E. O., Ghosh, K. K., Kitch, L. J., Gamal, A. E., & Schnitzer, M. J. (2013). Long-term dynamics of CA1 hippocampal place codes. *Nature Neuroscience*, *16*(3), Article 3. https://doi.org/10.1038/nn.3329

Zott, B., Busche, M. A., Sperling, R. A., & Konnerth, A. (2018). What Happens with the Circuit in Alzheimer's Disease in Mice and Humans? *Annu Rev Neurosci*, *41*, 277-297. https://doi.org/10.1146/annurev-neuro-080317-061725

Zou, C., Crux, S., Marinesco, S., Montagna, E., Sgobio, C., Shi, Y., Shi, S., Zhu, K., Dorostkar, M. M., Müller, U. C., & Herms, J. (2016). Amyloid precursor protein maintains constitutive and adaptive plasticity of dendritic spines in adult brain by regulating D-serine homeostasis. *The EMBO Journal*, *35*(20), 2213–2222. https://doi.org/10.15252/embj.201694085

Appendix A: AMPK-dependent phosphorylation of MTFR1L regulates mitochondrial morphology

Lisa Tilokani, Fiona M. Russell*, Stevie Hamilton*, **Daniel M. Virga***, Mayuko Segawa, Vincent Paupe, Anja V. Gruszczyk, Margherita Protasoni, Luis-Carlos Tabara, Mark Johnson, Hanish Anand, Michael P. Murphy, D. Grahame Hardie, Franck Polleux, Julien Prudent (2022) Sci Adv 8, eabo7956.
https://doi.org/10.1126/sciadv.abo7956

MTFR1L is a mitochondrial associated protein that, prior to this work, had not been characterized beyond its activation via AMPK. Here, we fully characterized the function of this protein as a novel mitochondrial anti-fusion protein, functioning to promote fission by limiting fusion in mitochondria via OPA1 *in vitro* and *in vivo*.

For this study, I performed all of the *in vivo* murine experiments (Figure 6), quantified those experiments, and helped with configuring the figure and drafting the manuscript where it relates to this experiment. This work was published in its entirety in Science Advances in 2022.

Abstract

Mitochondria are dynamic organelles that undergo membrane remodeling events in response to metabolic alterations to generate an adequate mitochondrial network. Here, we investigated the function of mitochondrial fission regulator 1-like protein (MTFR1L), an uncharacterized protein that has been identified in phosphoproteomic screens as a potential AMP-activated protein kinase (AMPK) substrate. We showed that MTFR1L is an outer mitochondrial membrane–localized protein modulating mitochondrial morphology. Loss of MTFR1L led to mitochondrial elongation associated with increased mitochondrial fusion events and levels of the mitochondrial fusion protein, optic atrophy 1. Mechanistically, we show that MTFR1L is phosphorylated by AMPK, which thereby controls the function of MTFR1L in regulating mitochondrial morphology both in mammalian cell lines and in murine cortical neurons in vivo. Furthermore, we demonstrate that MTFR1L is required for stress-induced AMPK-dependent mitochondrial fragmentation. Together, these findings identify MTFR1L as a critical mitochondrial protein transducing AMPK-dependent metabolic changes through regulation of mitochondrial dynamics.

Introduction

Mitochondria form a dynamic and interconnected network, which is constantly remodeled by cycles of membrane fission and fusion to ensure adequate shape, size, and cellular distribution (*1*). This dynamic regulation of mitochondrial structure underlies remarkable functional adaptations of this unique organelle: in general, mitochondria adopting a highly tubular and connected network display high oxidative phosphorylation (OXPHOS), whereas fragmented and small mitochondria tend to be associated with lower OXPHOS capacity and low adenosine triphosphate (ATP) production (*2*). Mitochondrial fission, or division, encompasses a complex multistep series of events mediated by cooperation between core members of the mitochondrial fission machinery and that of other organelles (*3*–*5*). The large guanosine triphosphatase (GTPase) dynamin-related protein-1, Drp1, the principal player in mitochondrial division, is recruited to mitochondrial constriction sites, which are induced by close association with the endoplasmic reticulum (ER) (*6*), through its outer mitochondrial membrane (OMM) receptors such as mitochondrial fission factor (MFF) (*7*) and/or mitochondrial dynamics protein of 49 kDa (MiD49) (*8*) and protein of 51 kDa (MiD51) (*9*). At these mitochondrial constriction sites, Drp1 oligomerizes, constricting the membrane and inducing mitochondrial division in a guanosine triphosphate (GTP)–dependent manner (*10*–*12*), with the contribution

of lysosomes (*13*) and trans-Golgi network vesicles (*14*). In contrast, mitochondrial fusion is a coordinated two-step mechanism executed sequentially by OMM fusion, followed by inner mitochondrial membrane (IMM) fusion (*15*, *16*). OMM fusion is mainly mediated by homo- or heterotypic interactions of the large GTPases mitofusin 1 and 2 (Mfn1/2) (*17*), which upon GTP hydrolysis and conformational change drive membrane fusion (*18*). This event is followed by fusion of the IMM, which is regulated by the heterotypic interaction between the large GTPase optic atrophy 1 (OPA1) and cardiolipin at the contact site of opposing membranes (*19*). An imbalance between these two opposing processes of mitochondrial division and fusion has been reported across multiple disorders from cancer to neurodegeneration (*20*), which highlights their physiological relevance and the need to elucidate their mechanisms of regulation.

These dynamic shape transitions of the mitochondrial network represent a crucial response to cellular needs and are adaptations to energetic stress (*2*). While these two antagonistic processes are spatiotemporally coordinated and regulated (*21*–*23*), the underlying signaling pathways that regulate these events have not been fully elucidated. Adenosine 5′-monophosphate (AMP)–activated protein kinase (AMPK), an essential kinase that senses cellular metabolites, is activated upon decreases in cellular energy status or nutrient availability, initiating cascades of phosphorylation reactions that act to restore energy homeostasis, by inhibiting anabolism and promoting catabolic processes (*24*). With an array of substrates involved in different functions, AMPK has been shown to localize to different subcellular compartments, including to the surface of the OMM (*25*–*27*). Increasing numbers of mitochondrial substrates for AMPK, involved in stimulation of mitochondrial biogenesis, regulation of mitochondrial quality control and motility, calcium homeostasis, and dynamics, have now been identified (*28*). These findings highlight AMPK as a crucial regulator of mitochondrial homeostasis. For example, during mitochondrial stress induced by electron transport chain (ETC) dysfunction and a decline in ATP production, activated AMPK phosphorylates MFF, leading to enhanced recruitment of Drp1 to mitochondria (*29*). This leads to mitochondrial fragmentation (*29*), which is thought to increase mitochondrial turnover through mitophagy and allow increased mitochondrial biogenesis (*28*). In addition, Armadillo repeat containing protein 10 (ARMC10) has recently been shown to be an additional substrate of AMPK involved in the regulation of mitochondrial morphology (*30*), revealing the critical and complex role of AMPK signaling in the regulation of mitochondrial dynamics.

Recent high-throughput phosphoproteomic screens have identified potential AMPK substrates including an uncharacterized protein of unknown function, called mitochondrial fission regulator 1-like (MTFR1L) or FAM54B (*25*, *30*, *31*). In these studies, two potential AMPK phosphorylation sites at conserved residues Ser^{103} (*31*) and Ser^{238} (*30*) have been identified. However, their validation and characterization of their functional relevance have not been performed. Phylogenetic analysis of protein sequences revealed that MTFR1L belongs to the MTFR1 family of proteins, alongside mitochondrial-localized members MTFR1 and MTFR2, with MTFR1L being the most divergent member (*32*). MTFR1 has been implicated in regulating not only mitochondrial division, cristae architecture, and mitochondrial bioenergetics (*32*, *33*) but also cell death, as well as cancer cell metabolism and proliferation (*34*–*36*). It has recently been proposed that MTFR2 regulates mitochondrial fission during mitosis (*37*) as well as cancer cell proliferation (*38*, *39*). Furthermore, while immunoprecipitation experiments have identified MTFR1L as a potential interactor with cristae regulator protein Mic60 and the fusion protein OPA1 (*40*), its subcellular localization and functions in the regulation of mitochondrial morphology and downstream action following AMPK activation remain unknown.

To shed light on the intricate interplay between mitochondrial morphology, AMPK, and cellular homeostasis, we have investigated not only MTFR1L localization and function but also its relevance as an AMPK substrate in mammalian cells *in vitro* and in cortical murine neurons in vivo. We show that MTFR1L is an OMM-localized protein whose loss induces a substantial elongation and interconnection of the mitochondrial network, associated with elevated levels of the IMM fusion protein, OPA1, and accompanied by an increased number of fusion events. Last, we demonstrate that MTFR1L is a physiological substrate for AMPK in intact cells, and that phosphorylation of Ser^{103} and Ser^{238} is required to control its function in the regulation of mitochondrial morphology at steady state, and to ensure AMPK-dependent stress-induced mitochondrial fragmentation. Our findings highlight MTFR1L as a central player in the adaptation of mitochondrial dynamics to metabolic change.

Results

MTFR1L is an OMM Protein

While MTFR1L has been shown to belong to the mitochondrial- localized MTFR1 family of proteins (*32*) and to be a putative substrate for AMPK (*30*, *31*), its expression and subcellular localization have not been

investigated. Analysis of protein sequence alignments revealed that MTFR1L (NM_19557.5), as well as the two putative AMPK phosphorylation sites Ser^{103} and Ser^{238} are conserved among vertebrates. Also conserved are hydrophobic residues at positions −5 and +4, and basic residues at position −3, relative to the phosphorylated serine residues (fig. S1), making both sites excellent fits to the well-established AMPK recognition motif (*41*). Predictive software (NPSA Prabi) suggested six putative alpha helices. In addition, according to National Center for Biotechnology Information (NCBI), human MTFR1L can be alternatively spliced to generate a shorter isoform that contains Ser^{103} but lacks Ser^{238} (NM001099627.1), which is, however, less well conserved among vertebrates and is absent in mice. Therefore, in this study, we exclusively focused on the characterization of the main longer MTFR1L isoform, which was identified in several phosphoproteomic studies as a potential AMPK substrate (*25*).

We first investigated the subcellular localization of MTFR1L by both subcellular fractionation and microscopy in HeLa and U2OS cells. Immunoblot analysis of cell fractions using a commercial rabbit antibody against the long isoform of MTFR1L revealed a specific band around 38 kDa (expected mass = 32 kDa) and a second band at 25 kDa that exclusively localized to the heavy membrane fraction, which contains crude mitochondria. The specificity of the antibody binding was validated by *MTFR1L*-targeted small interfering RNA (siRNA) treatment (Fig. 1A). These results were confirmed by immunofluorescence analysis, which showed that MTFR1L exhibited a mitochondrial localization, as shown by its endogenous colocalization with the OMM marker, TOM20 (Fig. 1B). Down-regulating MTFR1L expression led to a significant reduction of the signal observed at mitochondria, showing the specificity of both the antibody and the siRNAs used (Fig. 1, A and B). We next determined the submitochondrial localization of MTFR1L by treatment of isolated mitochondria with increasing concentrations of proteinase K to sequentially degrade exposed proteins from different mitochondrial compartments (Fig. 1C). Subsequent immunoblot analysis showed that the degradation of the MTFR1L band in response to proteinase K was similar to that of the OMM resident protein Mfn2. Initial degradation of MTFR1L and Mfn2 occurred with just 1 and 5 ug/ml of proteinase K, respectively, in contrast to the intermembrane space protein, AIF, and IMM protein, Mic60, which were degraded with 10 and 20 µg/ml of proteinase K, respectively (Fig. 1C). These findings demonstrate that MTFR1L is localized to the OMM. To investigate whether MTFR1L was inserted into the OMM, we treated isolated mitochondria with sodium carbonate (pH 11) followed by centrifugation.

Immunoblot analysis of the supernatant and pellet fractions revealed that MTFR1L assorted with other non-inserted proteins, such as cytochrome c, into the supernatant, indicating that MTFR1L is a labile protein associated with the cytosolic face of the OMM (Fig. 1D). However, the second band detected by the antibody at 25 kDa was not localized to either compartment, suggesting that it could represent an MTFR1L degradation product. Therefore, we decided to focus only on the long MTFR1L isoform detected at around 38 kDa through the rest of the study. Last, using mouse tissues, we showed that MTFR1L was ubiquitously expressed in all tissues examined, particularly enriched in the brain, uterus, and heart (Fig. 1E). Together, these results reveal that MTFR1L is a non-inserted mitochondrial protein that exclusively localizes to the cytosolic surface of the OMM.

Loss of MTFR1L leads to Mitochondrial elongation

Having established the OMM localization of MTFR1L, and because the other two members of the MTFR1 family (MTFR1 and MTFR2) have been proposed to regulate mitochondrial morphology via unknown mechanisms (*32*, *33*), we next investigated the contribution of MTFR1L to the regulation of mitochondrial dynamics. First, we analyzed mitochondrial morphology by confocal microscopy in U2OS and Cos-7 cells silenced for MTFR1L with two different siRNAs (fig. S2, A to K). Loss of MTFR1L led to a mitochondrial elongation phenotype in both cell lines with both siRNAs, characterized by an increase in cells harboring elongated mitochondria (fig. S2, A, C, G, and I), a decrease of mitochondrial number (fig. S2, D and J), and an increase in mitochondrial area (fig. S2, E and K). Compared to Drp1 silencing, which only led to highly elongated mitochondria (*14*), depletion of MTFR1L also induced an interconnected mitochondrial network characterized by increased mitochondrial branching and junctions in the region of interest (ROI; fig. S2F).

To confirm these results and to examine the effects of the permanent loss of MTFR1L, CRISPR-Cas9–mediated knockout (KO) of MTFR1L was generated in U2OS cells with guide RNAs (gRNAs) targeting either exon 3 or 4. Confocal microscopy analysis revealed that both MTFR1L KO U2OS clones

Figure 1

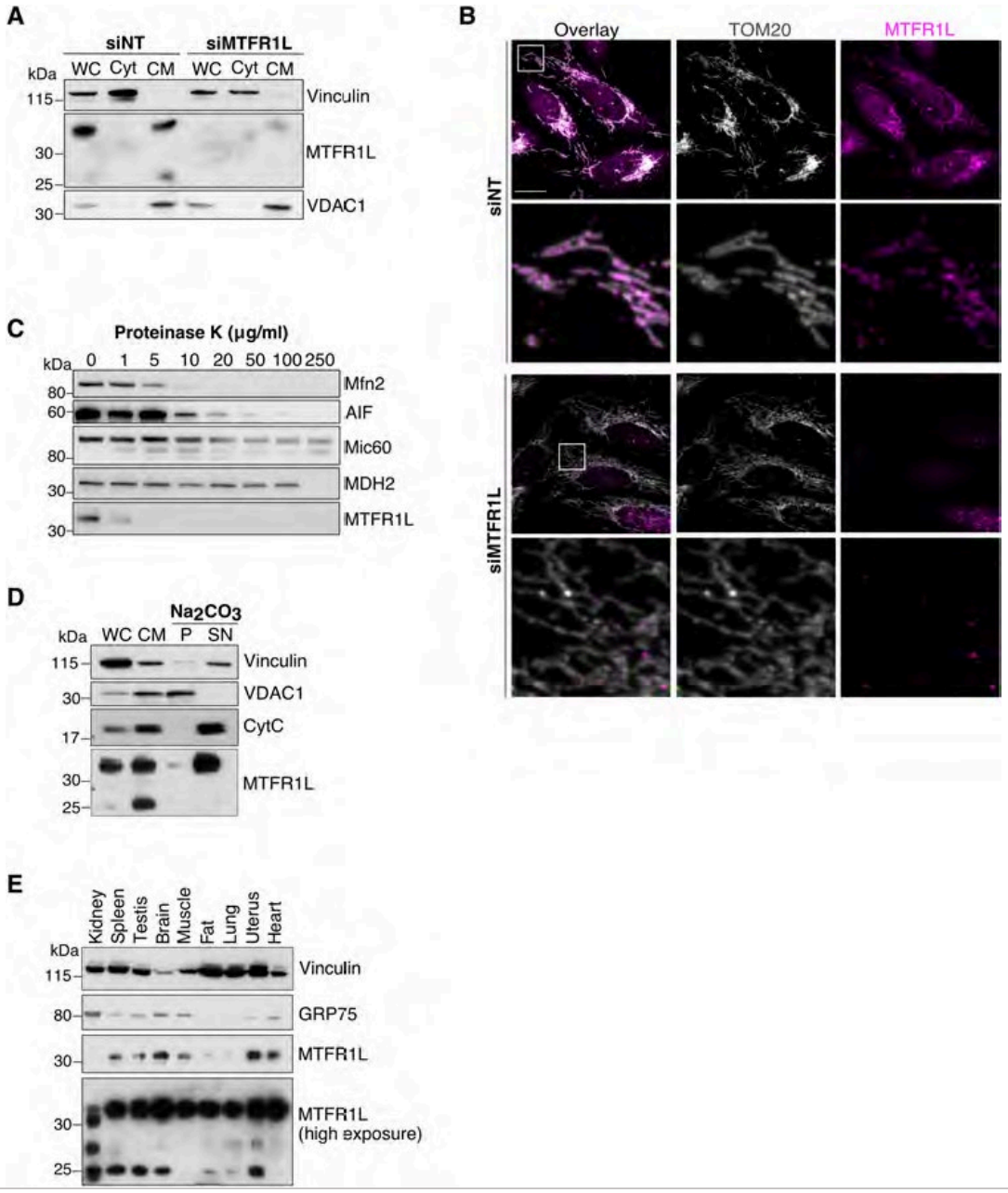

Fig. 1. MTFR1L is a mitochondrial protein. (A) Immunoblot analysis of subcellular fractionation showing MTFR1L localization in HeLa cells treated with nontargeted (NT) or MTFR1L siRNA. Total whole-cell (WC) lysates were fractionated into heavy membranes containing crude mitochondria (CM) and cytosolic (Cyt) fractions. Vinculin and VDAC1 were used as cytosolic and mitochondrial markers, respectively. (B) Representative confocal images of MTFR1L localization from U2OS cells silenced with NT or MTFR1L siRNAs. Mitochondria and MTFR1L were labeled using anti-TOM20 and anti-MTFR1L antibodies, respectively. Scale bar, 20 µm. (C) Proteinase K digestion assay on crude mitochondria isolated from HeLa cells. Crude mitochondrial fractions (CMFs) were treated with increasing concentrations of proteinase K and analyzed by immunoblot. Mfn2, AIF, Mic60, and MDH2 were used as OMM, intermembrane space, IMM, and matrix markers, respectively. (D) Sodium carbonate treatment of CMFs isolated from HeLa cells. Whole-cell (WC), crude mitochondria (CM), pellet (P), containing membrane inserted proteins, and supernatant (SN), containing soluble proteins, fractions were analyzed by immunoblot. Vinculin was used as a whole-cell marker, Mic60 and VDAC1 were used as controls for integral membrane proteins, whereas CytC was used as control for soluble proteins. (E) Immunoblot analysis of MTFR1L expression in different wild-type (WT) mouse tissues. Vinculin and GRP75 were used as loading controls. Two different time exposures are represented for MTFR1L, low and high. MTFR1L was detected using the Atlas antibody (HPA027124). See also fig. S1.

(KO1 and KO2) displayed around 80 and 60% of cells with elongated mitochondria, respectively (Fig. 2, A to C). In addition, similar to silenced cells, both MTFR1L KO clones exhibited an increase in mean mitochondrial area, as well as branching and junctions associated with a decrease in mitochondrial number (Fig. 2, D to F). Both MTFR1L KO clones displayed similar results, although MTFR1L KO1 cells exhibited the strongest phenotype and were used in the remainder of the study (referred to hereafter as MTFR1L KO). We further validated mitochondrial elongation in MTFR1L KO U2OS cells by overexpressing a photoactivatable green fluorescent protein (GFP) probe targeted to the mitochondrial matrix (OCT-PAGFP) (*42*) in conjunction with confocal live cell imaging analysis. As shown in Fig. 2 (G and H), MTFR1L KO cells exhibited a significant increase in the diffusion of the PA-GFP probe throughout the mitochondrial network compared to control cells, reinforcing the increased interconnectivity of the mitochondrial network previously observed. To extend further these results obtained by light microscopy, we investigated mitochondrial morphology by transmission electron microscopy (TEM). Analysis of TEM micrographs confirmed the mitochondrial elongation and interconnectivity phenotypes, as shown by an increase in organelle length and length/ width aspect ratio in MTFR1L KO U2OS cells compared to control U2OS cells (Fig. 2, I and J, and fig. S2, L and M).

Last, to confirm the specificity of the mitochondrial phenotype induced by loss of MTFR1L, we performed rescue experiments using an MTFR1L-P2A-mCherry plasmid, which enabled the visualization of MTFR1L-expressing cells. Re-expression of MTFR1L in MTFR1L KO U2OS cells rescued mitochondrial elongation, with an increase in mitochondrial number and a decrease in mitochondrial area, to levels similar to control cells (Fig. 2, K and L, and fig. S2, N to P). Overexpression of MTFR1L in wild-type (WT) cells also led to mitochondrial fragmentation and perinuclear clustering in 44% of the cells (Fig. 2L). We also generated an MTFR1L mutant lacking the first helix comprising the first 28 amino acids of the N-terminal domain. In contrast to WT MTFR1L, MTFR1L$^{1–28}$ was mainly expressed in the cytosol and, therefore, unable to rescue mitochondrial elongation observed in MTFR1L KO U2OS cells (fig. S3).

These results indicate that the N-terminal domain of MTFR1L is important not only for its localization but also for its capacity to regulate mitochondrial morphology. Together, these results demonstrate that loss of MTFR1L leads to a specific mitochondrial elongation phenotype, which indicates its contribution to the regulation of mitochondrial morphology.

Figure 2

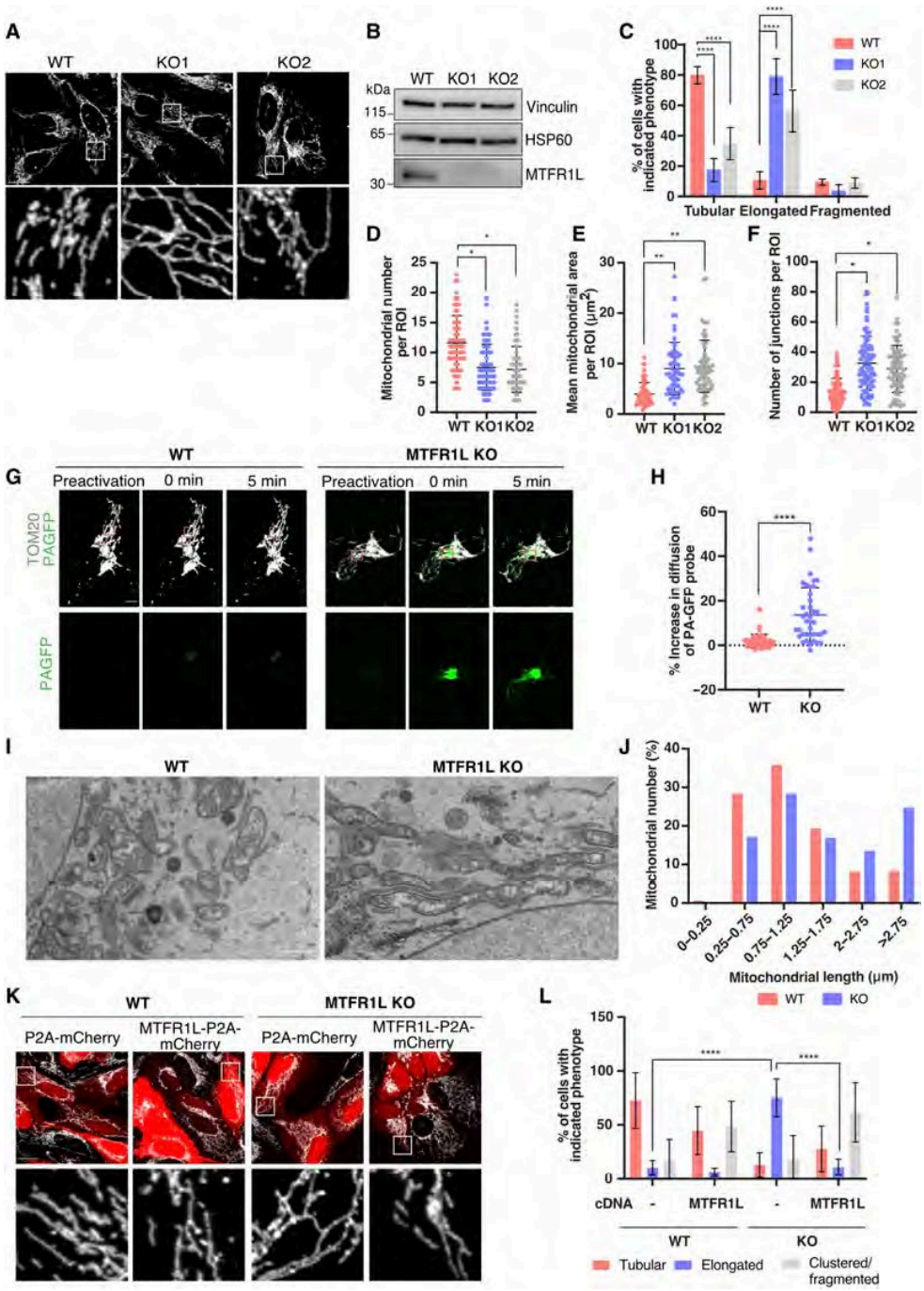

Fig. 2. Loss of MTFR1L leads to mitochondrial elongation. (A) Representative confocal images of mitochondrial morphology from WT and MTFR1L KO U2OS cells. Mitochondria were labeled with an anti-TOM20 antibody. Scale bar, 20 µm. (B) Immunoblot analysis of MTFR1L levels in MTFR1L KO U2OS clones. Vinculin and HSP60 were used as loading controls. (C) Quantification of mitochondrial morphology from (A). (D to F) Mitochondrial morphology was quantified as (D) mitochondrial number, (E) mean mitochondrial area, and (F) number of junctions, per ROI. (G) Live-cell imaging of WT and MTFR1L KO U2OS cells overexpressing the ornithine carbamoyl transferase (OCT)–photoactivable GFP (mt-PAGFP) probe and the mitochondrial marker TOM20-mCherry. Scale bar, 10 µm. (H) Quantification of the OCT-PAGFP probe diffusion from (G), calculated as a ratio between OCT-PAGFP–occupied area on total mitochondria network (TOM20-mCherry) at 0 and 5 min. (I) Representative TEM images from WT and MTFR1L KO U2OS cells. Scale bar, 1 µm. (J) Quantification of TEM images showing the distribution of mitochondrial length from (I). (K) Representative confocal images of mitochondrial morphology of WT and MTFR1L KO U2OS cells transiently overexpressing P2A-mCherry alone or MTFR1L-P2A-mCherry. Mitochondria were labeled with an anti-TOM20 antibody. Scale bar, 20 µm. (L) Quantification of mitochondrial morphology from (K). All values: mean Å} SD; at least three independent experiments. See also figs. S2 and S3.

Depletion of MTFR1L increases OPA1 levels and mitochondrial fusion events

Mitochondrial elongation can arise from either a defect in mitochondrial division or an increase in organelle fusion (*1*). To gain a deeper understanding of the underlying mechanism and to determine which process led to mitochondrial elongation in MTFR1L KO cells, we first investigated potential defects in mitochondrial division, by assessing the levels of various effectors of mitochondrial fission by immunoblot analyses. We observed no changes in fission-associated proteins in MTFR1L KO U2OS cells, or in MTFR1L U2OS– and Cos-7–silenced cells, including the main driver of mitochondrial division, Drp1, or its receptors MFF and MiD49/51 (Fig. 3A and fig. S4, A to E). We next examined the capacity of Drp1 to be recruited to mitochondrial membranes, a key step in mitochondrial division. Subcellular fractionation and confocal imaging of Drp1 subcellular distribution in MTFR1L KO U2OS cells revealed no defect in Drp1 recruitment to mitochondria (fig. S5, A and B). Last, to investigate the capacity of mitochondria to divide in cells lacking MTFR1L, we promoted Drp1-dependent mitochondrial division either by treatment with the mitochondrial uncoupler carbonyl cyanide 3-chlorophenylhydrazone (CCCP; fig. S5, C and D) or by overexpressing the pro-fission factor mitochondrial anchored protein ligase (MAPL; fig. S5, E and F) (*43*). Both conditions rescued the mitochondrial elongation phenotype and led to similar mitochondrial fragmentation as seen in control cells. We conclude that cells lacking MTFR1L retain their ability and machinery to trigger mitochondrial division. Thus, these results indicate that while MTFR1L loss leads to mitochondrial elongation, this phenotype is not due to either a defect in Drp1 recruitment to mitochondria or a lack of mitochondrial division.

We next investigated whether the loss of MTFR1L was instead associated with an increase in mitochondrial fusion. Immunoblot analysis revealed that loss of MTFR1L led to increased levels of all different OPA1 isoforms, the main actor of IMM fusion, but not of the outer membrane fusion regulators Mfn1 and Mfn2 (Fig. 3B and fig. S6, A to E). In addition, cross-linking experiments also showed an increase in OPA1 oligomer levels (Fig. 3C), suggesting that increased fusion because of OPA1 levels underlies the mitochondrial elongation phenotype observed in cells lacking MTFR1L. There was no increase in *Opa1* mRNA content in MTFR1L KO U2OS cells, as opposed to MTFR1L-silenced U2OS cells (fig. S6, F and G), suggesting a posttranscriptional mechanism accounting for elevated OPA1 levels, at least in MTFR1L KO cells. We demonstrated the specificity of this phenotype by reexpressing MTFR1L, which led to a significant

rescue of the increased OPA1 protein levels observed (Fig. 3D and fig. S6H). However, transient expression of non–mitochondrial-localized MTFR1L mutant in MTFR1L KO U2OS cells did not rescue OPA1 levels (fig. S3A), indicating the critical role of the mitochondrial localization of MTFR1L to control OPA1 levels.

We next performed live cell confocal microscopy analysis to quantify fusion and fission events in U2OS cells expressing the GFPOMP25 marker to label mitochondria. In contrast to mitochondrial division events, quantitative analysis revealed an increased number of fusion events and of the ratio of fusion to fission events in MTFR1L KO cells (Fig. 3E and fig. S7, A and B), confirming the excessive fusion and suggesting a role for MTFR1L in suppressing mitochondrial fusion. To extend these findings, we silenced the main proteins involved in mitochondrial fusion (OPA1, Mfn1, and Mfn2) and examined how this affected mitochondrial elongation induced by MTFR1L loss. Loss of either OPA1, Mfn1, or Mfn2 rescued the mitochondrial elongation observed in MTFR1L KO U2OS cells. This was associated with a reduction of cells harboring a hyperfused phenotype, an increase in mitochondrial number, and a reduction in mitochondrial area (Fig. 3, F to M, and fig. S7, C and D). Last, we hypothesized that if MTFR1L was negatively regulating fusion, as already proposed for Fis1 (*44*), its silencing in Drp1 KO cells, unable to divide their mitochondria, should lead to increased fusion events and induce interconnected mitochondria. As shown in fig. S7E, loss of MTFR1L in Drp1 KO cells further shifted the specific elongated mitochondria phenotype toward a branched and interconnected mitochondrial phenotype, similar to that found in MTFR1L KO cells (fig. S7, E to G). Thus, these results indicate that the loss of MTFR1L in Drp1 KO cells induced further mitochondrial fusion.

Mitochondrial morphology and increased levels of OPA1 are critical to enhance cell survival by acting on different mitochondrial features including mitochondrial cristae architecture (*45*, *46*) and resistance to apoptosis (*47*). TEM analysis revealed that MTFR1L KO U2OS cells exhibited an increase in mitochondrial cristae tightness characterized by a decrease in cristae width, similar to the phenotype observed upon overexpression of OPA1 (fig. S8, A and B) (*48*). In addition, immunoblot and immunofluorescence analyses showed that MTFR1L KO U2OS were also resistant to cell death induced by ABT 737 and actinomycin D treatment characterized by decreased levels of cleaved caspase 3 (fig. S8C) and a decrease of cells with cytosolic cytochrome c (fig. S8, D and E) compared to control-treated

Figure 3

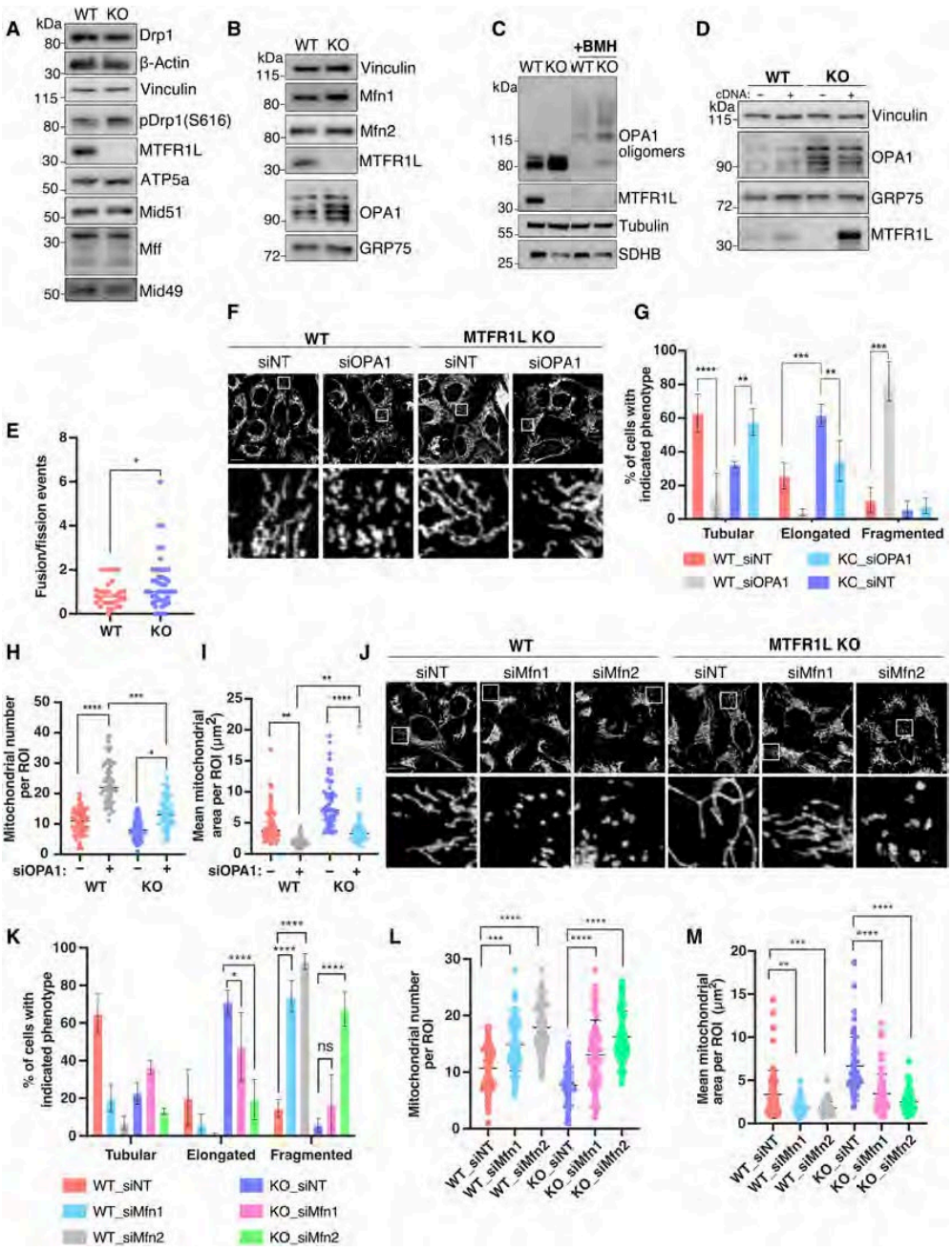

Fig. 3. Mitochondrial elongation induced by MTFR1L loss is due to increased mitochondrial fusion. (A and B) Immunoblots of proteins related to mitochondrial (A) division and (B) fusion, from WT and MTFR1L KO U2OS cells. Vinculin, β-actin, ATP5a, and GRP75 were used as loading controls. (C) Immunoblots of OPA1 oligomers from WT and MTFR1L KO U2OS cells treated with dimethyl sulfoxide (DMSO) or cross-linker 1,6-bismaleimidohexane (BMH). Tubulin and SDHB were used as loading controls. (D) Immunoblots of OPA1 levels from WT and MTFR1L KO U2OS cells transiently overexpressing empty vector pcDNA 3+ (−) and pcDNA 3-MTFR1L (+). Vinculin and GRP75 were used as loading controls. (E) Quantification of mitochondrial fusion and division events from WT and MTFR1L KO U2OS cells transiently overexpressing the mitochondrial marker GFP-OMP25. Representative quantification of the ratio between fusion and fission events per 625-μm2 ROI over a 5-min period is shown as a scatterplot. (F) Representative confocal images of WT and MTFR1L KO U2OS cells silenced with indicated siRNAs. Mitochondria were labeled using an anti-TOM20 antibody. (G) Quantification of mitochondrial morphology from (F). (H and I) Mitochondrial morphology was quantified as (H) mitochondrial number and (I) mean mitochondrial area, per ROI. (J) Representative confocal images of WT and MTFR1L KO U2OS cells silenced with indicated siRNAs. Mitochondria were labeled using an anti-TOM20 antibody. (K) Quantification of mitochondrial morphology from (J). (L and M) Mitochondrial morphology was quantified as (L) mitochondrial number and (M) mean mitochondrial area, per ROI. All scale bars, 20 um. All values: mean +- SD; at least three independent experiments. See also figs. S4 to S8.

U2OS cells, two hallmarks of apoptosis induction. Last, silencing OPA1 induced the presence of cytochrome c in the cytosol in MTFR1L KO–treated cells (fig. S8, D and E), corroborating the OPA1-dependent mitochondrial hyperfusion observed in cells lacking MTFR1L. Overall, these findings show that loss of MTFR1L increases levels of OPA1 and mitochondrial fusion and suggest that MTFR1L behaves as an anti-fusion protein, negatively regulating mitochondrial fusion events by controlling OPA1 levels.

AMPK-dependent MTFR1L phosphorylation controls mitochondrial morphology

Recent phosphoproteomic studies identified MTFR1L as a potential substrate of the master energy regulator AMPK and revealed two putative phosphorylated residues: Ser^{103} and Ser^{238} (*30*, *31*). To experimentally validate MTFR1L and the two phosphorylation sites as physiological AMPK targets, we generated two phospho-specific antibodies against MTFR1L $pSer^{103}$ and $pSer^{238}$. We also generated MTFR1L nonphosphorylatable mutant constructs by mutating these serine residues to alanine (S103A and S238A), and transiently expressed them in parallel with WT MTFR1L complementary DNA (cDNA), in both WT and AMPK-α1α2 double KO (DKO) U2OS cells generated using the Cas9 (D10A) double nickase system (*49*). Next, we analyzed MTFR1L phosphorylation under steady-state conditions and following AMPK activation with A-769662, a well-characterized AMPK activator (*50*, *51*). As expected in WT cells, A-769662 treatment led to AMPK activation, confirmed by the phosphorylation of acetyl coenzyme A carboxylase (ACC; Fig. 4A). Immunoblot analysis revealed MTFR1L phospho-specific bands, detected with antibodies raised against both $MTFR1L^{pS103}$ and $MTFR1L^{pS238}$, in cells expressing $MTFR1L^{WT}$ under basal conditions, which markedly increased in intensity upon A-769662 treatment (Fig. 4A). Furthermore, phosphorylation of MTFR1L at Ser^{103} or Ser^{238} was abolished in cells expressing $MTFR1L^{S103A}$ and $MTFR1L^{S238A}$, respectively, confirming the specificity of the antibodies and the phosphorylation of MTFR1L on these respective residues. Last, in contrast to WT cells, bands corresponding to phosphorylation of either MTFR1L Ser^{103} or Ser^{238} were not detected in AMPK- α1/α2 DKO U2OS cells, whether or not treated with A-769662, showing that MTFR1L phosphorylation at these sites was AMPK dependent. Together, these data revealed that MTFR1L is an AMPK target phosphorylated at both Ser^{103} and Ser^{238}.

Because our results indicated a contribution of MTFR1L in the regulation of mitochondrial fusion, and recent studies have highlighted the roles for AMPK-dependent phosphorylation of MFF (*29*) and ARMC10 (*30*) in mitochondrial dynamics, we hypothesized that MTFR1L phosphorylation would trigger

mitochondrial morphological changes in an AMPK-dependent manner. To investigate this hypothesis, we stably expressed MTFR1L^{WT}, the potentially active double phosphomimetic mutant MTFR1L$^{S103D/S238D}$ or the double nonphosphorylatable mutant MTFR1L$^{S103A/S238A}$ in WT, MTFR1L KO, and AMPK-α1α2 DKO U2OS cells, and analyzed mitochondrial morphology (Fig. 4, B to J, and fig. S9, A to F). Confocal microscopy showed that expression of both MTFR1L^{WT} and phosphomimetic MTFR1L$^{S103D/S238D}$ in WT U2OS cells led to fragmentation of the mitochondrial network, characterized by decreased mean mitochondrial area and length, along with mitochondrial perinuclear clustering (Fig. 4, B to D, and fig. S9, A and B). In contrast, expression of the double nonphosphorylatable mutant MTFR1L$^{S103A/238A}$ had no effect on mitochondrial morphology (Fig. 4, B to D, and fig. S9B).

In MTFR1L KO U2OS cells, expression of both WT and phosphomimetic MTFR1L$^{S103D/238D}$ rescued the mitochondrial hyperfusion phenotype and induced a fragmented and perinuclear clustered mitochondrial phenotype (Fig. 4, E to G, and fig. S9, C and D). However, expression of double nonphosphorylatable mutant MTFR1L$^{S103A/S238A}$ had no impact on mitochondrial morphology (Fig. 4, E to G, and fig. S9, C and D), indicating that MTFR1L phosphorylation is required to regulate mitochondrial dynamics. To elucidate the role of AMPK in this process, similar experiments were performed in AMPK-α1/α2 DKO U2OS cells, which exhibited elongated mitochondria compared to control U2OS cells (*29*) (compare elongated mitochondria in Fig. 4, H versus B). Compared to WT and MTFR1L KO U2OS cells, expression of MTFR1L^{WT} in AMPK-α1/α2 DKO U2OS cells did not induce marked mitochondrial fragmentation, nor a change in mean mitochondrial length and area (Fig. 4, H to J, and fig. S9, E and F). However, expression of phosphomimetic MTFR1L$^{S103D/S238D}$ still led to mitochondrial morphology remodeling and a shift in the mitochondrial network toward mitochondrial fragmentation and perinuclear clustering compared to all other conditions (Fig. 4, H to J, and fig. S9, E and F).

To further elucidate the role of MTFR1L phosphorylation in regulating mitochondrial morphology and fusion, we analyzed all OPA1 isoform levels in MTFR1L KO and AMPK-α1/α2 DKO U2OS cells expressing our different MTFR1L constructs. In contrast to the expression of double nonphosphorylatable mutant MTFR1L$^{S103A/S238A}$, stable expression of MTFR1L^{WT} decreased OPA1 levels in MTFR1L KO U2OS cells (Fig. 4K and fig. S9G). In addition, we observed an increase in OPA1 protein levels in AMPK-α1/α2

Figure 4

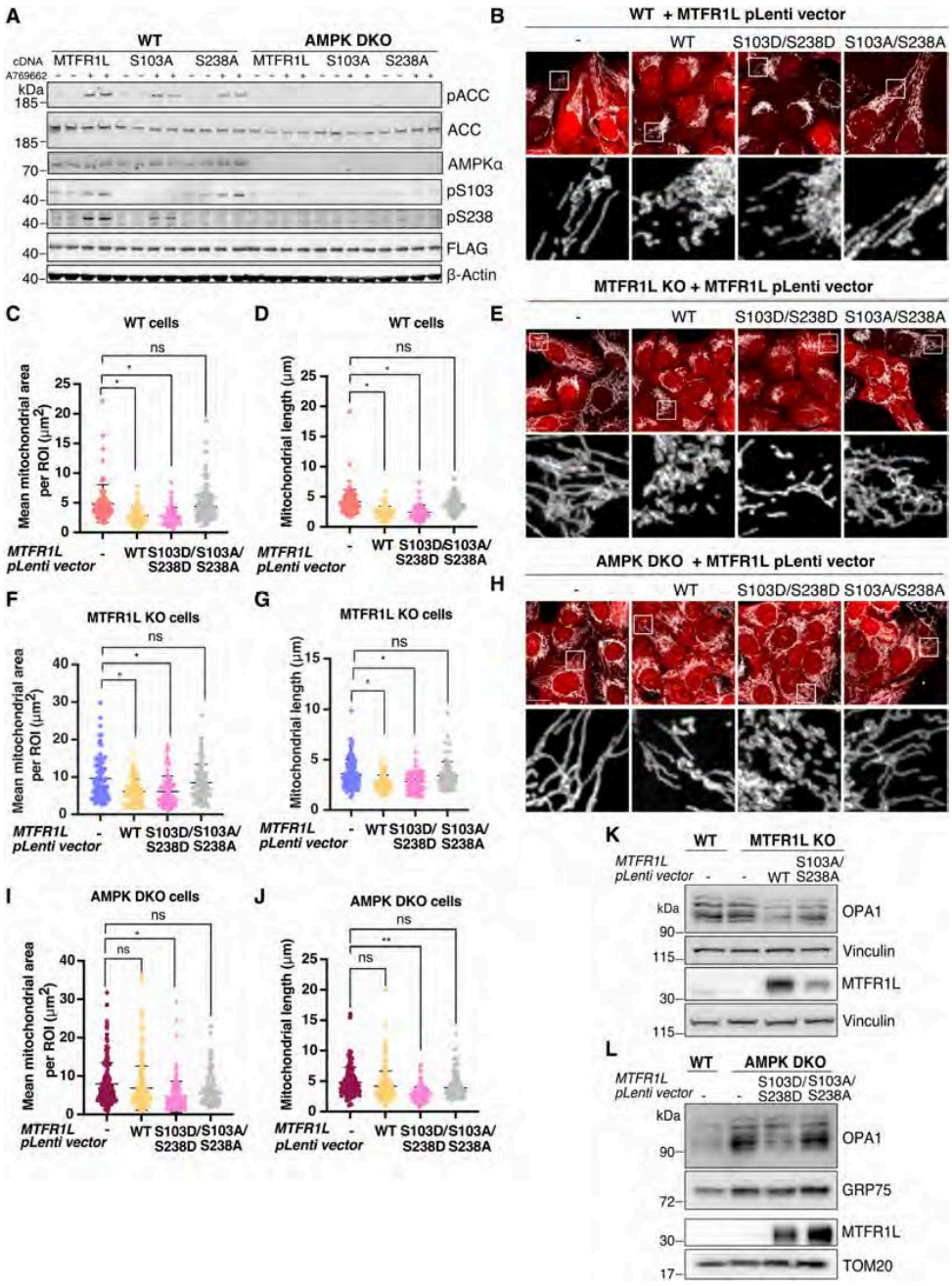

Fig. 4. AMPK-dependent phosphorylation of MTFR1L controls mitochondrial morphology. (**A**) Immunoblot analysis of indicated proteins and of MTFR1L phosphorylation in WT and AMPK-α1$^{-/-}$α2$^{-/-}$ DKO U2OS cells, transiently overexpressing FLAG-WT MTFR1L^{WT}, FLAG-MTFR1L^{S103A}, or FLAG-MTFR1L^{S238A} phosphomutants, and treated with DMSO (−) or AMPK activator, A769662 (+), for 1 hour at 200 μM. Specific rabbit anti-MTFR1L phosphospecific antibodies were used to detect the two distinct phosphorylations at Ser^{103} and Ser^{238}. Anti-FLAG was used to confirm overexpression of the different constructs, and β-actin was used as a loading control. Samples from two different experiments were loaded side by side. (**B**, **E**, and **H**) Representative confocal images of (B) WT, (E) MTFR1L KO, and (H) AMPK-α1α2 DKO U2OS cells stably expressing P2A-mCherry alone (−), MTFR1L^{WT}-P2A-mCherry, double phosphomimetic MTFR1L$^{S103D/S238D}$-P2A-mCherry, or double phosphomutant MTFR1L$^{S103A/S238A}$- P2A-mCherry. Mitochondria were labeled with an anti-TOM20 antibody. (**C**, **D**, **F**, **G**, **I**, and **J**) Mitochondrial morphology was quantified as (C, F, and I) mean mitochondrial area and (D, G, and J) mitochondrial length, per ROI from (B), (E), and (H). (**K**) Immunoblots of OPA1 levels from WT and MTFR1L KO U2OS cells stably expressing P2A-mCherry vector alone (−), MTFR1L^{WT}-P2A-mCherry, or MTFR1L$^{S103A/S238A}$-P2A-mCherry. Vinculin was used as loading control. (**L**) Immunoblots of OPA1 levels from WT and AMPK-α1α2 DKO U2OS cells transiently expressing P2A-mCherry vector alone (−), MTFR1L$^{S103D/S238D}$-P2A-mCherry, or MTFR1L$^{S103A/S238A}$-P2A-mCherry. GRP75 and TOM20 were used as loading controls. All scale bars, 20 μm. All values: mean ± SD; at least three independent experiments. See also fig. S9.

DKO U2OS, which was rescued by stably expressing MTFR1L$^{S103D/238D}$ but not the MTFR1L$^{S103A/S238A}$ mutant, similar to mitochondrial morphology analysis (Fig. 4L and fig. S9H). Thus, these results highlight that phosphorylation of MTFR1L is sufficient to induce mitochondrial fragmentation and indicate that the AMPK-MTFR1L axis is critical to drive mitochondrial network remodeling via the control of OPA1 levels.

MTFR1L is required for AMPK-dependent mitochondrial fragmentation

AMPK has evolved not only as an energy sensor and master regulator of cellular metabolism but also as a critical regulator of mitochondrial function including biogenesis, bioenergetics, and dynamics (*28*). During ETC-induced mitochondrial dysfunction, the decreased ATP/ adenosine diphosphate (ADP) ratio activates AMPK, which phosphorylates MFF, thereby increasing Drp1 recruitment and leading to mitochondrial division, which may facilitate clearance of dysfunctional mitochondria (*29*). To investigate whether MTFR1L was also required for AMPK-dependent morphological changes during stress, MTFR1L KO and silenced U2OS cells were treated with inhibitors of respiratory complex I (rotenone) and complex III (antimycin A), and mitochondrial morphology was monitored (Fig. 5, A to D). Antimycin A treatment of WT U2OS cells activated AMPK, as monitored by its phosphorylation and that of its substrate ACC (Fig. 5, E and F), which was accompanied by mitochondrial fragmentation compared to control untreated cells (Fig. 5, A to D). However, antimycin A treatment of MTFR1L KO U2OS cells failed to rescue mitochondrial hyperfusion or to induce mitochondrial fragmentation (Fig. 5, A to D). These results were also confirmed in MTFR1L-silenced U2OS where neither ETC inhibitors (antimycin A and rotenone) induced mitochondrial fragmentation compared to siNT-treated cells (figs. S10, A and B, and S11, A and B). Unexpectedly, immunoblot analysis revealed that treatment with these ETC inhibitors of both MTFR1L KO and silenced U2OS cells decreased AMPK activation, as indicated by decreased levels of phospho-ACC and phospho-AMPK compared to similarly treated control cells (Fig. 5, E and F, and figs. S10, C and D, and S11, C and D). These results suggest that mitochondrial hyperfusion observed in cells lacking MTFR1L could protect from ETC-induced dysfunction by maintaining a sufficient level of ATP production to maintain AMPK inactivated. To test this hypothesis, we analyzed mitochondrial bioenergetics in MTFR1L KO U2OS cells at steady states or during glucose starvation. Unexpectedly, neither oxygen consumption nor ATP/ADP ratio measured via luciferin bioluminescence was impaired in MTFR1L KO

Figure 5

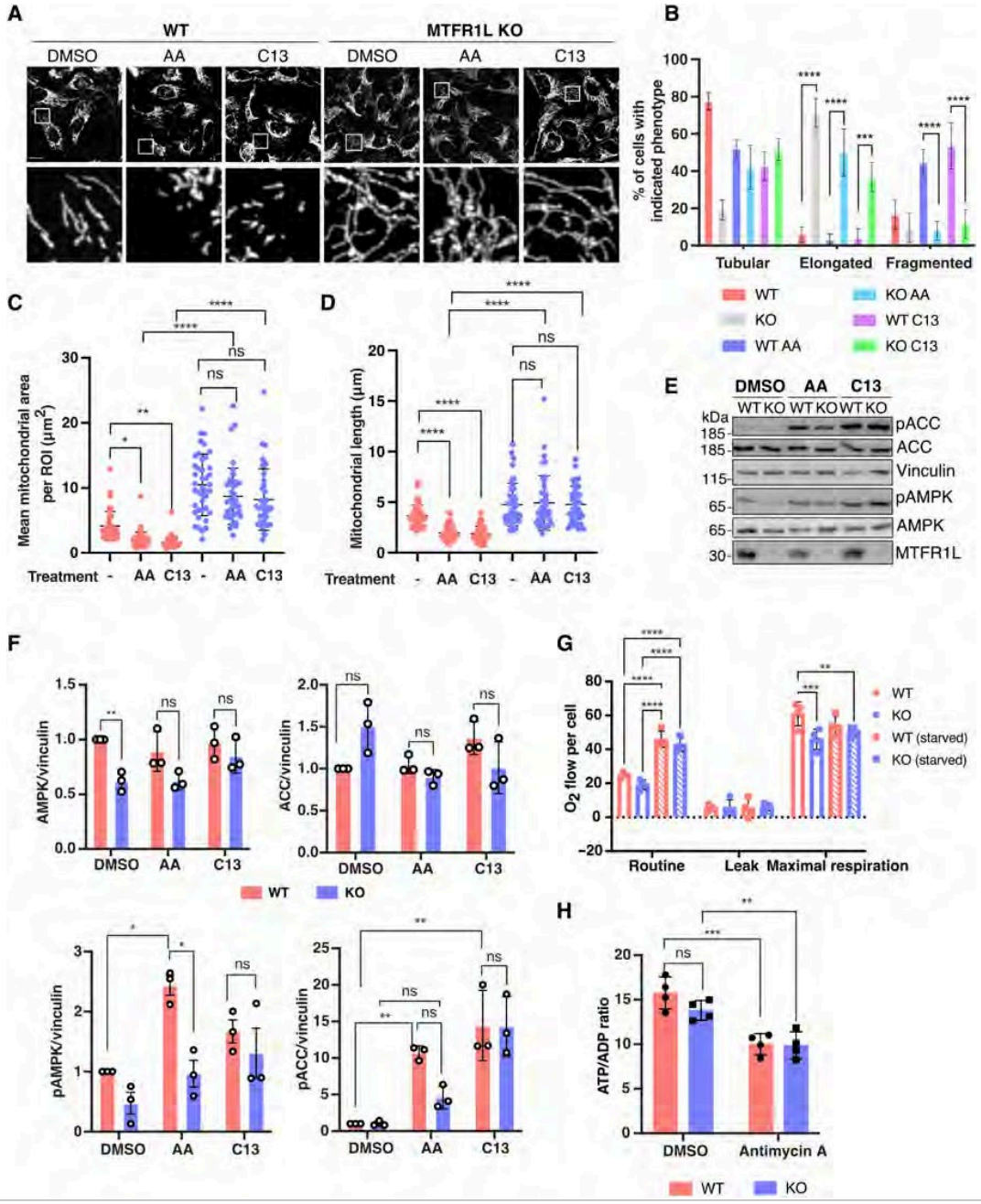

Fig. 5. MTFR1L is required for AMPK-driven mitochondrial fragmentation. (**A**) Representative confocal images of WT and MTFR1L KO U2OS cells treated with DMSO, 10 µM antimycin A (AA), or the allosteric AMPK activator C13 for 1 hour. Mitochondria were labeled with an anti-TOM20 antibody. Scale bar, 20 µm. (**B**) Quantification of mitochondrial morphology from (A). (**C** and **D**) Mitochondrial morphology was quantified as (C) mean mitochondrial area and (D) mitochondrial length, per ROI. (**E**) Immunoblot analysis of indicated proteins corresponding to (A) showing AMPK activation in WT and MTFR1L KO U2OS cells, treated with DMSO, 10 µM antimycin A (AA), or the allosteric AMPK activator C13 for 1 hour. Vinculin was used as a loading control. (**F**) Quantification of levels of the indicated proteins from (E). Signal intensities were quantified by densitometry and normalized to loading controls. *N* = 3 independent experiments. (**G**) High-resolution respirometry analyses performed in intact WT and MTFR1L KO U2OS cells using Oroboros instrument. ROUTINE: cellular basal oxygen consumption rate (pmol O_2/s) per million cells in supplemented medium or lacking glucose (starved for 4 hours). Leak is the nonphosphorylating respiration in the presence of ATP synthase inhibitor oligomycin. ETS: maximal respiration rate in the presence of the uncoupler CCCP. *N* = 3 independent experiments. (**H**) Quantification of the ATP/ADP ratio determined by bioluminescence assay from WT and MTFR1L KO ells treated with DMSO or antimycin A. *N* = 3 independent experiments. All values: mean ± SD or SEM; at least three independent experiments. See also figs. S10 and S11.

U2OS cells compared to control (Fig. 5, G and H). These results suggest that the cause of AMPK activation dampening observed in MTFR1L KO cells is not due to fluctuations in the ATP/ADP ratio level.

Last, to confirm that the lack of mitochondrial network remodeling in cells lacking MTFR1L was not due to decreased AMPK activation, MTFR1L KO U2OS cells were treated with compound 13 (C13), which is a cell-permeable prodrug that is converted inside cells into the AMP mimetic C2, a potent allosteric activator of AMPK (*52*, *53*). While C13 led to a similar level of AMPK activation in both WT and MTFR1L KO cells (Fig. 5, E and F), it failed to reduce mitochondrial hyperfusion or to induce mitochondrial fragmentation in MTFR1L KO U2OS cells as compared to WT U2OS-treated cells (Fig. 5, A to D).

Together, these results demonstrate that MTFR1L is critical to remodel the mitochondrial network upon stress-induced AMPK activation, to sustain cellular homeostasis, and to drive cell fate decisions.

MTFR1L phosphorylation regulates mitochondrial morphology *in vivo*

Given the prevalence of MTFR1L expression in the brain (Fig. 1E), which is supported by publicly available RNA sequencing and in situ hybridization datasets (fig. S12), we evaluated its function in neurons by investigating the role of MTFR1L and its phosphorylation in the regulation of mitochondrial morphology in the axons of layer 2/3 cortical pyramidal neurons (PNs) of mice *in vitro* and *in vivo*. Axonal mitochondria are ideal to test the function of pro-fission or anti-fusion protein candidates because (i) these mitochondria are very small (~1um length) and uniform in size (*54*) and (ii) we have shown recently that this size is maintained through high levels of MFF-Drp1–mediated fission (*54*).

Initial knockdowns were performed *in vitro* using ex utero electroporation to sparsely incorporate short hairpin RNA (shRNA; shMTFR1L or control shRNA) and overexpress genetically encoded OMM, mitochondrial matrix, and cytoplasmic targeting fluorophores into layer 2/3 cortical PNs (Fig. 6). Control experimental conditions were achieved by coculturing neurons electroporated with control shRNA with neurons electroporated with MTFR1L shRNA (co-electroporation with different combinations of cell filler and mitochondrial markers; fig. S13) to minimize confounding variables linked to culture conditions or other batch effects. Similar to our results obtained in U2OS and Cos-7 cells, confocal microscopy analysis revealed that knockdown of MTFR1L led to mitochondrial elongation in the axons of layer 2/3 cortical PNs *in vitro* (Fig. 6, A to D). In shMTFR1L-treated axons, the mitochondrial network, labeled with OMM and

Figure 6

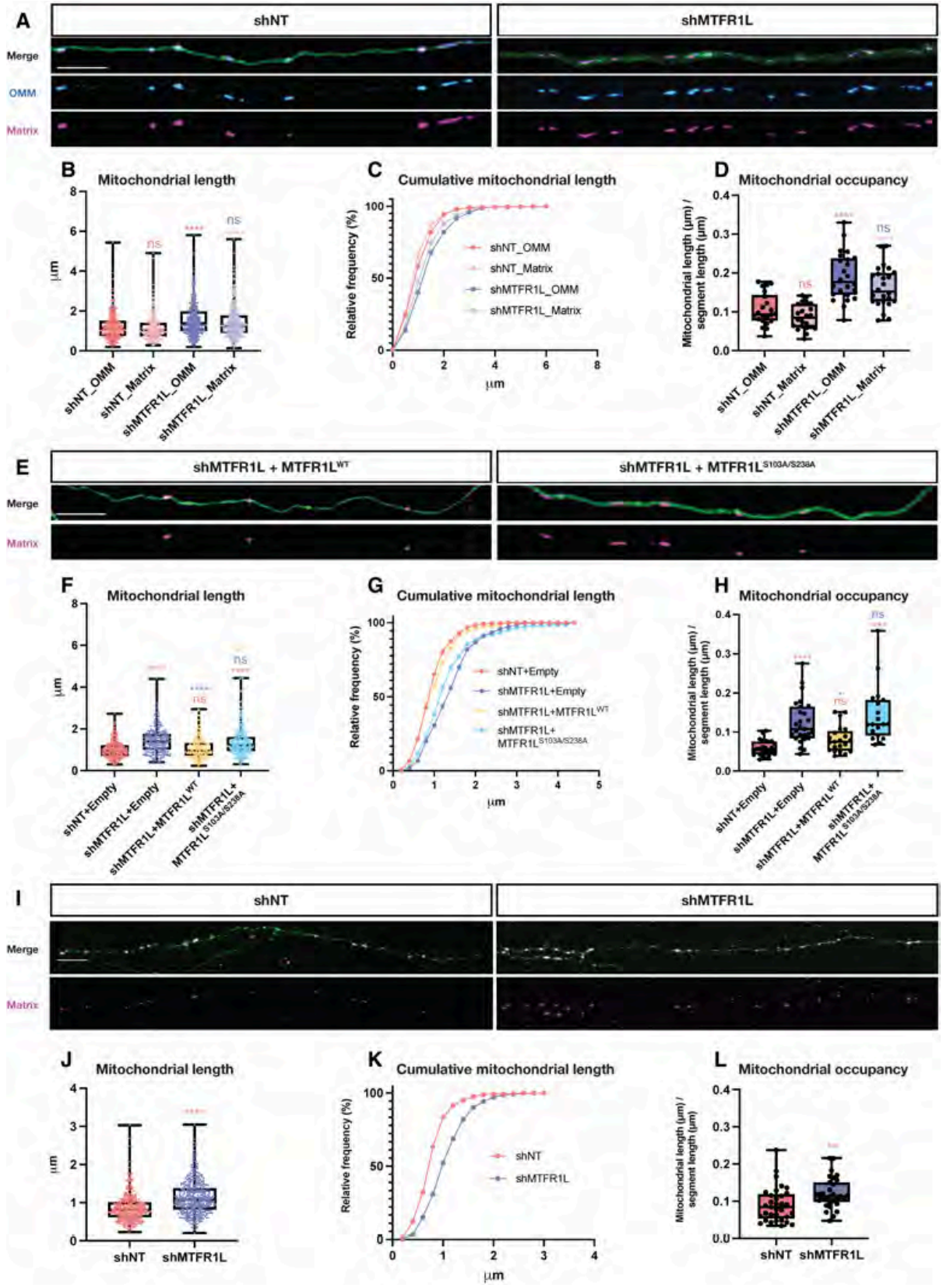
A
shNT
shMTFR1L
Merge
OMM
Matrix
B
Mitochondrial length
µm
ns
shNT_OMM
shNT_Matrix
shMTFR1L_OMM
shMTFR1L_Matrix
C
Cumulative mitochondrial length
Relative frequency (%)
shNT_OMM
shNT_Matrix
shMTFR1L_OMM
shMTFR1L_Matrix
µm
D
Mitochondrial occupancy
Mitochondrial length (µm) / segment length (µm)
E
shMTFR1L + MTFR1L^WT
shMTFR1L + MTFR1L^S103A/S238A
F
Mitochondrial length
shNT+Empty
shMTFR1L+Empty
shMTFR1L+MTFR1L^WT
shMTFR1L+ MTFR1L^S103A/S238A
G
Cumulative mitochondrial length
H
Mitochondrial occupancy
I
shNT
shMTFR1L
J
Mitochondrial length
K
Cumulative mitochondrial length
L
Mitochondrial occupancy

Figure 6 Cont…

Fig. 6. Knockdown of MTFR1L in mouse cortical PNs leads to elongated mitochondria and increased mitochondrial density in the axon. (**A**) Representative confocal images of axons from small hairpin (sh) nontargeted (shNT) or MTFR1L (shMTFR1L) expressing layer 2/3 PNs at 14 days *in vitro* (DIV). Axonal mitochondrial morphology was visualized by cortical ex utero electroporation of a combination of (i) genetically encoded mitochondrial markers: OMM-targeted mCherry (ActA-mCherry), matrix-targeted mtagBFP2 (mito-mTagBFP2), or matrix-targeted YFP (mito-YFP), (ii) cytoplasmic filler tdTomato or mtagBFP2, and (iii) either control shNT or shMTFR1L. Individual E15.5 brains electroporated were dissociated and cocultured. (**B** to **D**) Mitochondrial morphology was quantified from (A) as (B) mean mitochondrial length, (C) cumulative mitochondrial length, and (D) mitochondrial occupancy in the axons measured by the cumulative mitochondrial length in an axonal segment divided by the total segment length. (**E**) Representative confocal images of shMTFR1L-expressing DIV14 axons electroporated with mito-mTagBFP2 and tdTomato, and overexpressing either WT-MTFR1L^{WT} or double phosphomutant MTFR1L$^{S103D/S238D}$. (**F** to **H**) Mitochondrial morphology was quantified from (E) as (F) mean mitochondrial length, (G) cumulative mitochondrial length, and (H) mitochondrial occupancy in the axons. (**I**) Representative confocal images of contralateral axonal projections from shNT- or shMTFR1L-treated layer 2/3 PNs at postnatal day 21 (P21). Axonal mitochondrial morphology was visualized by cortical in utero electroporation of mito-YFP and tdTomato together with shNT or mitochondrial matrix (matrix-DsRed) probe and cytoplasmic filler Venus together with shMTFR1L. (**J** to **L**) Mitochondrial morphology was quantified from (I) as (J) mean mitochondrial length, (K) cumulative mitochondrial length, and (L) mitochondrial occupancy in the axons. All scale bars, 10 um. All values: mean ± SD; at least three independent experiments. See also figs. S12 and S13.

mitochondrial matrix markers, was characterized by an increase in mitochondria length and occupancy in axons, compared to shNT control (Fig. 6, B to D), indicating that loss of MTFR1L led to elongation of both mitochondrial compartments. Rescue experiments were then performed and expressing $MTFR1L^{WT}$ together with shMTFR1L rescued mitochondrial morphology to lengths similar to controls (Fig. 6, E to H). However, co-electroporation of the MTFR1L shRNA with double phosphomutant $MTFR1L^{S103A/S238A}$ construct was unable to rescue mitochondrial elongation as measured by mitochondrial length or axonal occupancy (Fig. 6, E to H), indicating that these AMPK-dependent phosphorylation sites are critical for the function of MTFR1L in the maintenance of mitochondrial size in axons of layer 2/3 PNs.

To assess MTFR1L knockdown *in vivo*, we electroporated shNT or shMTFR1L along with a cell fill marker and matrix-targeted fluorophore in E15.5 pups that were then perfused at P21, and axonal mitochondrial morphology was analyzed by confocal imaging of contralateral axonal projections. Knockdown of MTFR1L led to mitochondrial elongation in axonal segments projecting to contralateral layer 2/3 (Fig. 6, I to K), to a very similar degree than *in vitro*, and was associated with an increase of mitochondria occupancy in the axon (Fig. 6L). Together, these findings support a role for MTFR1L via its phosphorylation in maintaining axonal mitochondrial morphology *in vitro* and *in vivo* in cortical PNs.

Discussion

Mitochondrial dynamics entail a series of complex events that are fulfilled by major GTPase proteins. Over the years, numerous groups have unraveled and investigated previously unidentified proteins potentially involved in regulating these processes (*4*). In this study, we present the first characterization of MTFR1L, a newly recognized OMM protein regulating mitochondrial morphology. We demonstrate that MTFR1L is a genuine AMPK substrate and show that two residues phosphoryl ated by AMPK are critical for the function of MTFR1L in controlling mitochondrial dynamics, in both mammalian cells *in vitro* and murine neurons *in vivo*. Together, these results reveal MTFR1L as a central player in adapting mitochondrial dynamics to metabolic alterations.

Through gene editing techniques, we show that acute or chronic loss of MTFR1L through siRNA or CRISPR-Cas9–mediated technologies, respectively, leads to a robust mitochondrial hyperfusion phenotype that is conserved among different mammalian cell lines as well as in axons of layer 2/3 cortical PNs of mice. Mechanistic studies reveal that the loss of MTFR1L does not affect Drp1 mitochondrial

recruitment, nor the capacity of mitochondria to fragment upon enforced Drp1-dependent fragmentation, excluding a role of this protein in the division machinery per se. On the other hand, live-cell imaging and immunoblot analyses reveal a shift toward increased fusion events and increased levels of the IMM fusion regulator OPA1, respectively. In contrast to MFF- or Drp1-silenced cells (*55*), OPA1 silencing rescued the mitochondrial phenotypes in MTFR1L KO cells, including mitochondrial elongation and resistance to cell death. Last, rescue experiments revealed that the N-terminal domain of MTFR1L is required not only for MTFR1L mitochondrial localization but also for its capacity to regulate mitochondrial morphology. Collectively, these results indicate a role for MTFR1L in the negative regulation of mitochondrial fusion, rather than promoting division. Therefore, this study opens up avenues for understanding how the MTFR1 family regulates mitochondrial dynamics. Future investigations will be required to elucidate whether (i) the other MTFR1 members (MTFR1/MTFR2) regulate mitochondrial morphology through similar mechanisms or by directly controlling the mitochondrial fission process and (ii) MTFR1, MTFR2, and MTFR1L have diverged during evolution and acquired specialized roles to control mitochondrial dynamics in response to different stimuli.

Dynamic mitochondrial shape transitions are required not only to ensure proper mitochondrial function but also to respond to cellular needs, to adapt to different cellular stress and metabolic state, and to subsequently control cell fate decisions (*2*). For example, during mild stress, nutrient starvation, or mTORC1 inhibition, functional mitochondria elongate their network to sustain mitochondrial functions, increase bioenergetics, and protect themselves from autophagic degradation, ultimately enhancing cell survival (*56*–*58*). In contrast, upon severe mitochondrial stress, mitochondrial fragmentation is increased to allow autophagic degradation of damaged mitochondria (*59*), or ultimately to enhance apoptosis (*60*). Here, we propose that loss of MTFR1L leads to enhanced mitochondrial fusion via the increased protein levels of all different OPA1 isoforms. Up until now, few studies have documented a relative posttranscriptional up-regulation of OPA1 levels associated with a cellular adaptation to maintain homeostasis and survival. For example, during metabolic stress induced by cell starvation, OPA1 oligomerizes, leading to tightness of the cristae and mitochondrial elongation, to increase mitochondrial respiration to prevent cell death (*61*). In addition, OPA1 levels (and in particular increased OPA1 oligomers) have recently been proposed to be critical to maintain mitochondrial ultrastructure and cellular homeostasis upon antimycin A treatment (*48*).

Loss of MTFR1L leads to a decrease in AMPK activation not only at steady state but also upon ETC-induced AMPK activation. While these defects are not due to decreased ATP production measured by bioluminescence assay, it can be hypothesized that loss of MTFR1L induces a cellular metabolic rewiring mimicking mild cellular stress, which could lead to mitochondrial elongation to ensure cell survival. In addition, during selective conditions of stress, including ER stress or proapoptotic signals, mitochondria elongate via a process called stress-induced mitochondrial hyperfusion (SIMH), regulated by the SLP-2/OPA1/Mfn1 axis (*62*, *63*). Thus, loss of MTFR1L could trigger metabolic cellular stress, leading to the activation of SIMH to enhance cell survival. Further experiments should be performed to elucidate the mechanism of how MTFR1L loss leads to increased OPA1 levels and to determine whether loss of MTFR1L could lead to mitochondrial hyperfusion via SIMH. In addition, it will also be important to investigate how expression of the gain of function of MTFR1L or the phosphomimetic mutant MTFR1L$^{S103D/S238D}$ expression induces mitochondrial fragmentation and their perinuclear clustering.

Using biochemical approaches, we confirm MTFR1L as a physiological substrate of AMPK, which is phosphorylated at Ser^{103} and Ser^{238} both under basal conditions and upon AMPK activation. These results confirm previous independent studies that identified MTFR1L as a potential AMPK substrate through different phosphoproteomic screening approaches (*25*, *30*, *31*). We show that MTFR1L is required for AMPK-induced mitochondrial fragmentation, and that these phosphorylation events are critical for the regulation of mitochondrial morphology. MTFR1L^{WT} and MTFR1L$^{S103D/S238D}$ stable overexpression rescued mitochondrial hyperfusion and increased OPA1 protein levels observed in both MTFR1L KO and AMPK-α1α2 DKO cells, respectively, compared to MTFR1L$^{S103A/S238A}$. To date, phosphorylation of ARMC10 and MFF has been associated with regulating mitochondrial fission upon metabolic alterations (*29*, *30*). While ARMC10 interacts with the fission/fusion machinery, its mechanistic role has not yet been elucidated, unlike MFF phosphorylation that has been shown to increase Drp1 recruitment to mitochondria. In contrast, MTFR1L exerts a negative effect on fusion via the modulation of OPA1 levels. Recent studies have highlighted an AMPKOPA1 connection required to control mitochondrial morphology and cellular homeostasis in different contexts including T cell memory development and the regulation of the cardiovascular system (*64*–*66*). This further emphasizes the plethora of mechanisms by which AMPK regulates mitochondrial dynamics. In this regard, we hypothesize that, depending on the stimulus

modulating AMPK activity, different mitochondrial targets could be activated to control mitochondrial morphology, by specifically regulating either mitochondrial fission or fusion. These different levels of regulation will ensure an adequate mitochondrial network, allowing cells to efficiently adapt to different stresses. Collectively, this highlights the complex mechanisms required to control mitochondrial shape under stress conditions, and future studies may unravel the specificity of the AMPK-substrate axis.

Last, it will be essential to decipher which physiological stimuli activate the AMPK-MTFR1L-OPA1 axis to modulate MTFR1L levels for translational approaches. In this connection, modulation of OPA1 levels (and in particular its overexpression) has been previously shown to be beneficial in models of mitochondrial disease, including resistance to apoptosis and enhancement of ETC functionality (*67*, *68*). Thus, increasing OPA1 levels by targeting or inhibiting MTFR1L may represent a potential unexplored therapeutic target for mitochondrial diseases.

Supplemental Figures

Supplemental Figure S1

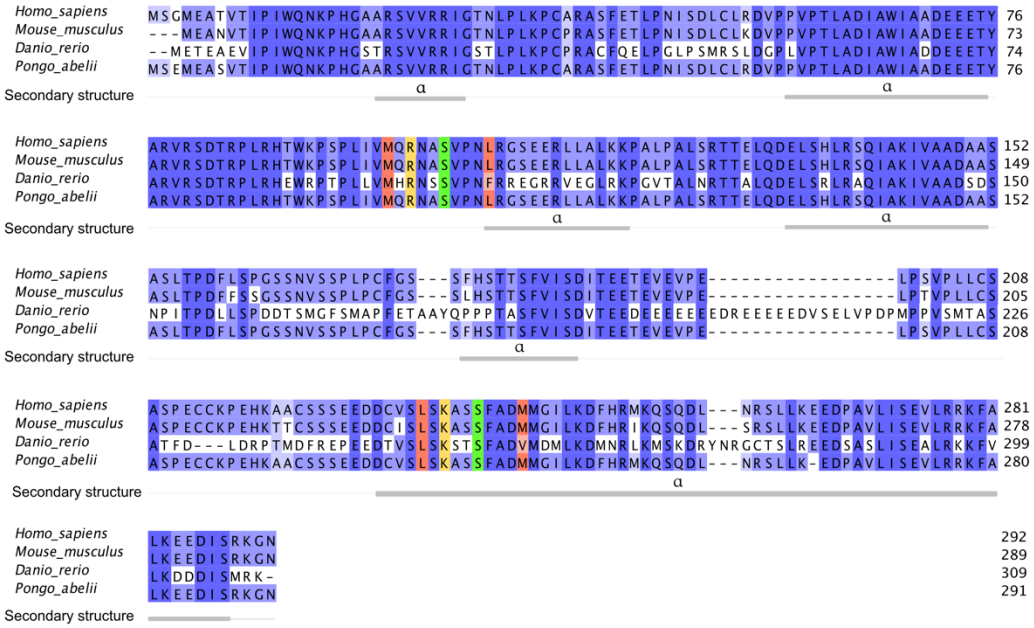

Figure S1, related to Figure 1. MTFR1L protein sequences analysis in vertebrates.
Clustal W multiple sequence alignment carried out in Jalview of MTFR1L from human (NM_19557.5), mouse (Q9CWE0.1), zebrafish (Q0VFP3.1), and monkey (Q5R3Z9.1), together with secondary structure prediction (NPSA Prabi). Conserved phosphorylation sites at Ser103 and Ser238 are highlighted in green. Conserved hydrophobic residues at positions -5 and +4, and basic residues at position -3, relative to the serine phosphorylation sites are highlighted in orange and
yellow, respectively.

Supplemental Figure S2

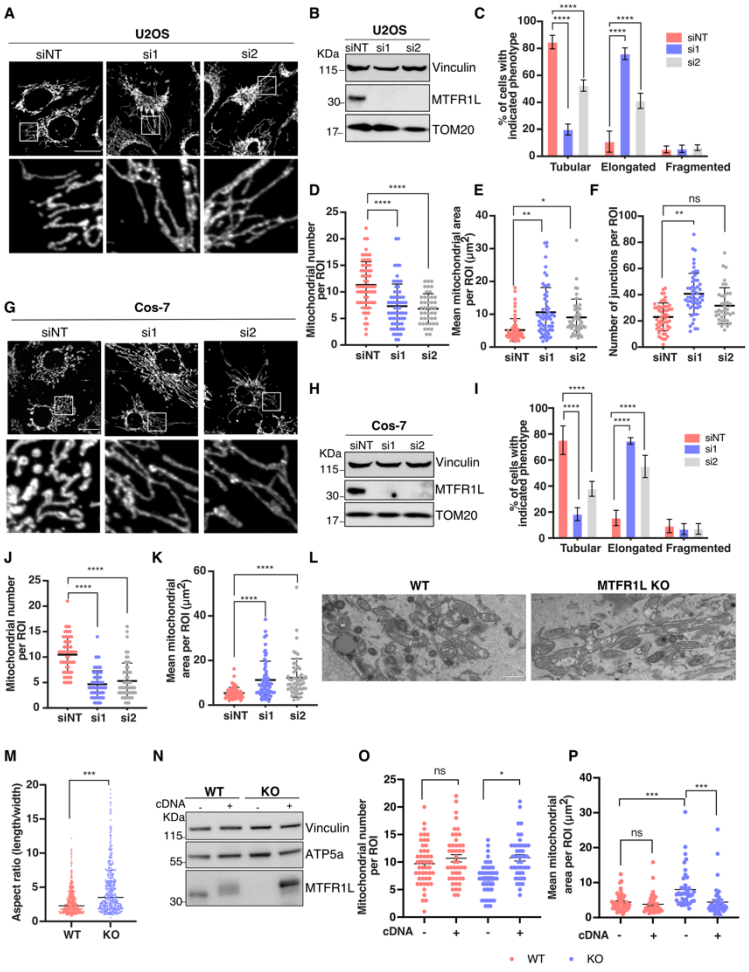

Figure S2, related to Figure 2. Mitochondrial elongation induced by MTFR1L loss is conserved across different cell lines. (**A**) Representative confocal images of mitochondrial morphology from U2OS cells treated with non-targeted (NT) or two different MTFR1L small-interference (si) RNAs (si1 and si2). Mitochondria were labelled with an anti-TOM20 antibody. Scale bar, 20 µm. (**B**) Immunoblot analysis showing the efficiency of MTFR1L siRNAs in U2OS cells. Vinculin and TOM20 were used as loading controls. (**C**) Quantification of mitochondrial morphology from NT and MTFR1L siRNAs-treated U2OS cells from (A). At least 30 cells were counted per experiment; n = 3 independent experiments. (**D-F**) Mitochondrial morphology was quantified as: (D) mitochondrial number, (E) mean mitochondrial area, and (F) number of junctions, per region of interest (ROI). At least 15 cells were counted per experiment; n = 3 independent experiments. (**G**) Representative confocal images of mitochondrial morphology from Cos-7 cells treated with NT or two different MTFR1L siRNAs (si1 and si2). Mitochondria were labelled with an anti- TOM20 antibody. Scale bar, 20 µm. (**H**) Immunoblot analysis showing the efficiency of MTFR1L siRNAs in Cos-7 cells. Vinculin and TOM20 were used as loading controls. (**I**) Quantification of mitochondrial morphology from NT and MTFR1L siRNAs-treated Cos-7 cells from (G). At least 30 cells were counted per experiment; n = 3 independent experiments. (**J-K**) Mitochondrial morphology was quantified as: (J) mitochondrial number, and (K) mean mitochondrial area, per ROI. At least 15 cells were counted per experiment; n = 3 independent experiments. (**L**) Additional examples of transmission electron microscopy (TEM) images from wild-type (WT) and MTFR1L knock-out (KO) U2OS cells. Scale bar, 1 µm. (**M**) Quantification of TEM images showing the width / length aspect ratio of mitochondria in WT and MTFR1L KO U2OS cells from Figure 2I. At least 400 mitochondria were counted; n = 2 independent experiments. (**N**) Immunoblot analysis showing the efficiency of MTFR1L-P2A-mCherry transient expression (+) in WT and MTFR1L KO U2OS cells. P2A-mCherry alone vector (-) was used as a control. Vinculin and ATP5a were used as loading controls. (**O-P**) Mitochondrial morphology was quantified from Figure 2K as (O) mitochondrial number, and (P) mean mitochondrial area, per ROI. At least 15 cells were counted per experiment; n = 3 independent experiments. All values: mean ± SD; at least three independent experiments. (C, I) Two-way ANOVA, Tukey's multiple comparison test; (D-F; J, K): Nested ordinary one-way ANOVA, Dunnet's multiple comparisons test; (M): non-parametric Mann-Whitney test; (O, P): Nested one-way ANOVA, Tukey's multiple comparisons test. * p<0.05; ** p<0.01; ***p<0.001; **** P<0.0001; ns p>0.05.

Supplemental Figure S3

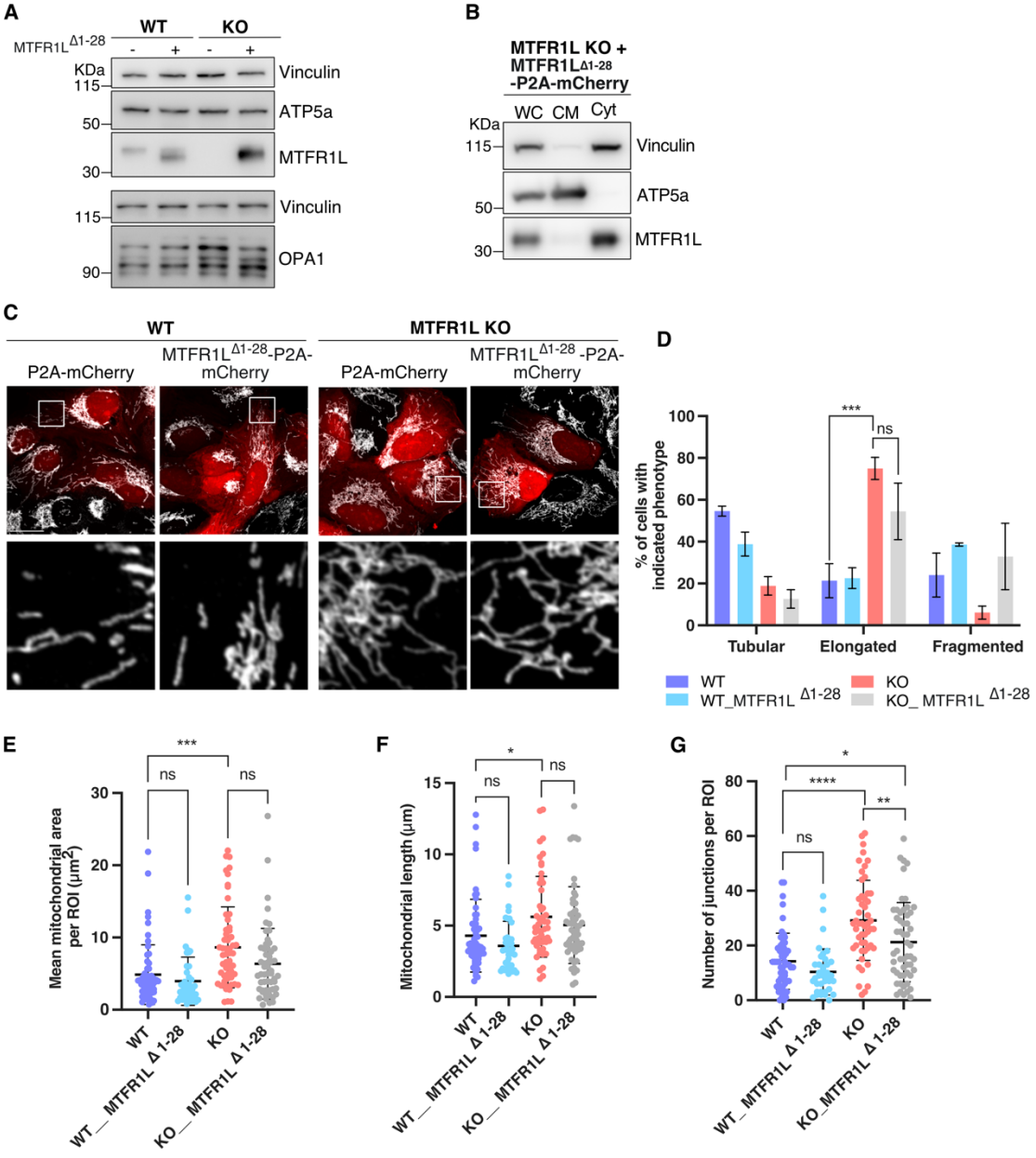

Figure S3, related to Figure 2. The N-terminal domain of MTFR1L is required for regulating mitochondrial morphology.
(**A**) Immunoblot analysis showing the efficiency of MTFR1L$^{\Delta 1\text{-}28}$-P2A-mCherry transient overexpression (+) in wild-type (WT) and MTFR1L knock-out (KO) U2OS cells. P2A-mCherry alone vector (-) was used as a control. Vinculin and ATP5a were used as loading controls. The same lysates were used to analyse OPA1 isoforms levels. Vinculin was used as a loading control. (**B**) Subcellular fractionation analysis of MTFR1L$^{\Delta 1\text{-}28}$ distribution in MTFR1L KO U2OS cells transiently overexpressing MTFR1L$^{\Delta 1\text{-}28}$-P2A-mCherry. Total whole cell (WC) lysates were fractionated into heavy membranes, containing crude mitochondria (CM), and cytosolic (Cyt) fractions. Vinculin and ATP5a were used as cytosolic and mitochondrial markers, respectively. (**C**) Representative confocal images of mitochondrial morphology of WT and MTFR1L KO U2OS cells transiently overexpressing P2A-mCherry alone or MTFR1L$^{\Delta 1\text{-}28}$-P2A-mCherry. Mitochondria were labelled with an anti-TOM20 antibody. Scale bar, 20 μm. (**D**) Quantification of mitochondrial morphology from (C). At least 30 cells were counted per experiment; n = 3 independent experiments. (**E-G**) Mitochondrial morphology was quantified as: (D) mean mitochondrial area, (E) mitochondrial length, and (F) number of junctions, per region of interest (ROI). At least 15 cells were counted per experiment; n = 3 independent experiments. All values: mean ± SD; at least three independent experiments. (D) Two-way ANOVA, Tukey's multiple comparison test; (E-G): ordinary one-way ANOVA, Tukey's multiple comparisons test; * p<0.05; ** p<0.01; ***p<0.001; **** P<0.0001; ns p>0.05.

Supplemental Figure S4

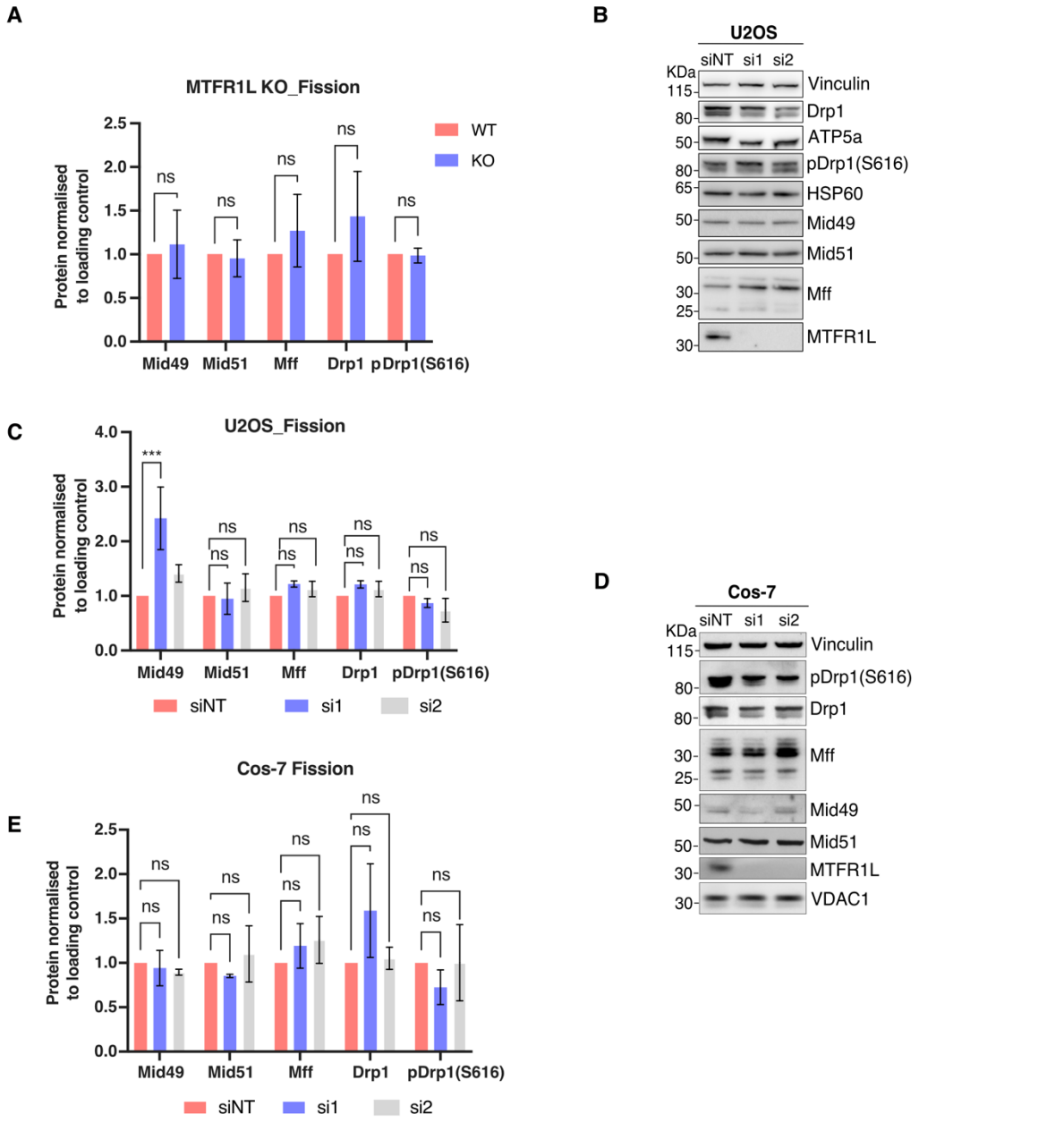

Figure S4, related to Figure 3. Loss of MTFR1L does not affect mitochondrial division and its respective machinery.
(A) Quantification of levels of the indicated proteins from Figure 3A. Signal intensities were quantified by densitometry and normalized to loading controls. N = 3 independent experiments. **(B, D)** Immunoblots of proteins related to mitochondrial division from (B) U2OS cells, and (D) Cos-7 cells, treated with non-targeted (NT) or two different MTFR1L small-interference (si) RNAs (si1 and si2). Vinculin, VDAC1, ATP5a, MTCO2 and HSP60 were used as loading controls. **(C, E)** Quantification of levels of the indicated proteins from (C) U2OS cells in (B), and (E) Cos- 7 cells in (D). Signal intensities were quantified by densitometry and normalized to loading controls. N = 3 independent experiments. All values: mean ± SEM; at least three independent experiments. (A, C, E): Two-way ANOVA, Tukey's multiple comparisons test, * p<0.05; ** p<0.01; ***p<0.001; **** P<0.0001; ns p>0.05.

Supplemental Figure S5

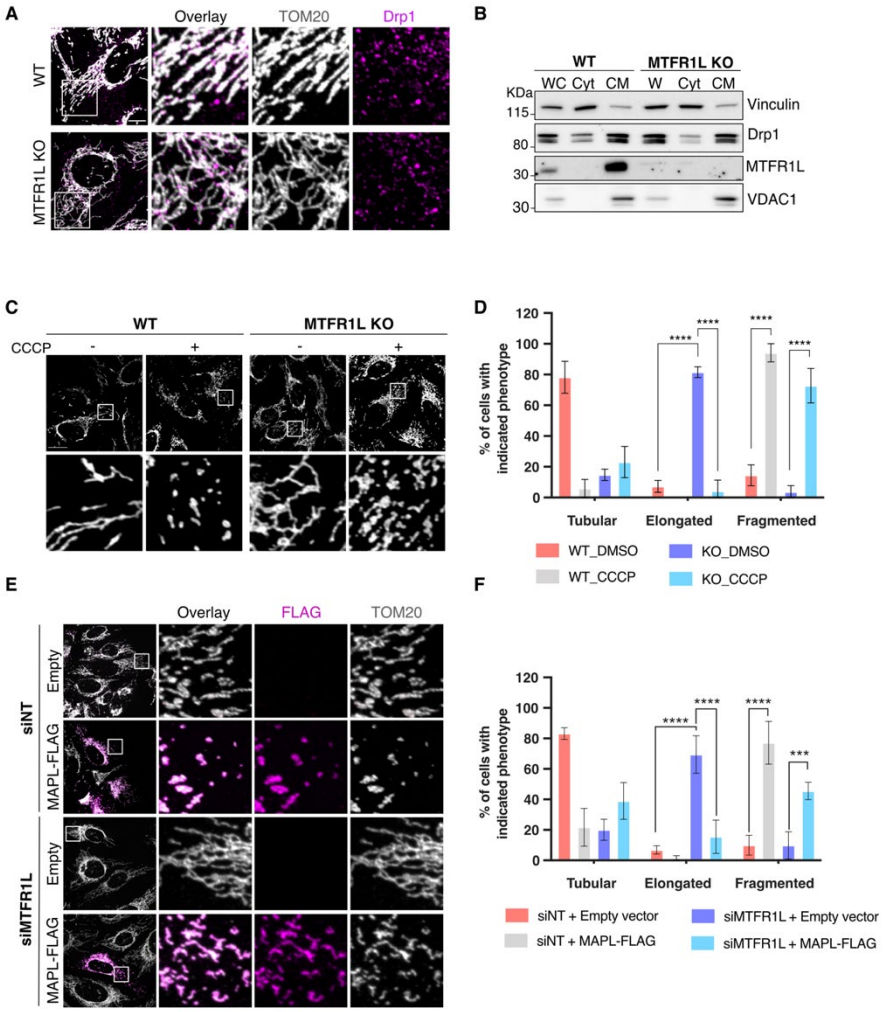

Figure S5, related to Figure 3. MTFR1L KO cells are sensitive to stimuli that trigger Drp1-dependent division.
(A) Representative confocal images of mitochondrial morphology and Drp1 localization in wild- type (WT) and MTFR1L knock-out (KO) U2OS cells. Drp1 and TOM20 were labelled with anti- Drp1 and anti-TOM20 antibodies, respectively. Scale bar, 20 μm. (B) Subcellular fractionation analysis of Drp1 distribution in WT and MTFR1L KO U2OS cells. Total whole cell (WC) lysates were fractionated into heavy membranes, containing crude mitochondria (CM), and cytosolic (Cyt) fractions. Vinculin and VDAC1 were used as cytosolic and mitochondrial markers, respectively. (C) Representative confocal images of mitochondrial morphology in WT and MTFR1L KO U2OS cells, treated with DMSO (-) or 20 μM CCCP (+) for 1 hour. Mitochondria were labelled with an anti-TOM20 antibody. Scale bar, 20 μm. (D) Quantification of mitochondrial morphology from (C). At least 30 cells were counted per experiment; n = 3 independent experiments. (E) Representative confocal images of mitochondrial morphology in non-targeted (NT) or MTFR1L small-interference (si) RNA treated U2OS cells transiently overexpressing empty vector (pcDNA 3.0) or MAPL-FLAG. Mitochondria and FLAG were labelled with anti-TOM20 and anti- FLAG antibodies, respectively. Scale bar, 20 μm. (F) Quantification of mitochondrial morphology from (E). At least 30 cells were counted per experiment; n = 3 independent experiments. All values: mean ± SD; at least three independent experiments; (D, F): Two-way ANOVA, Tukey's multiple comparisons test. * p<0.05; ** p<0.01; ***p<0.001; **** P<0.0001; ns p>0.05.

Supplemental Figure S6

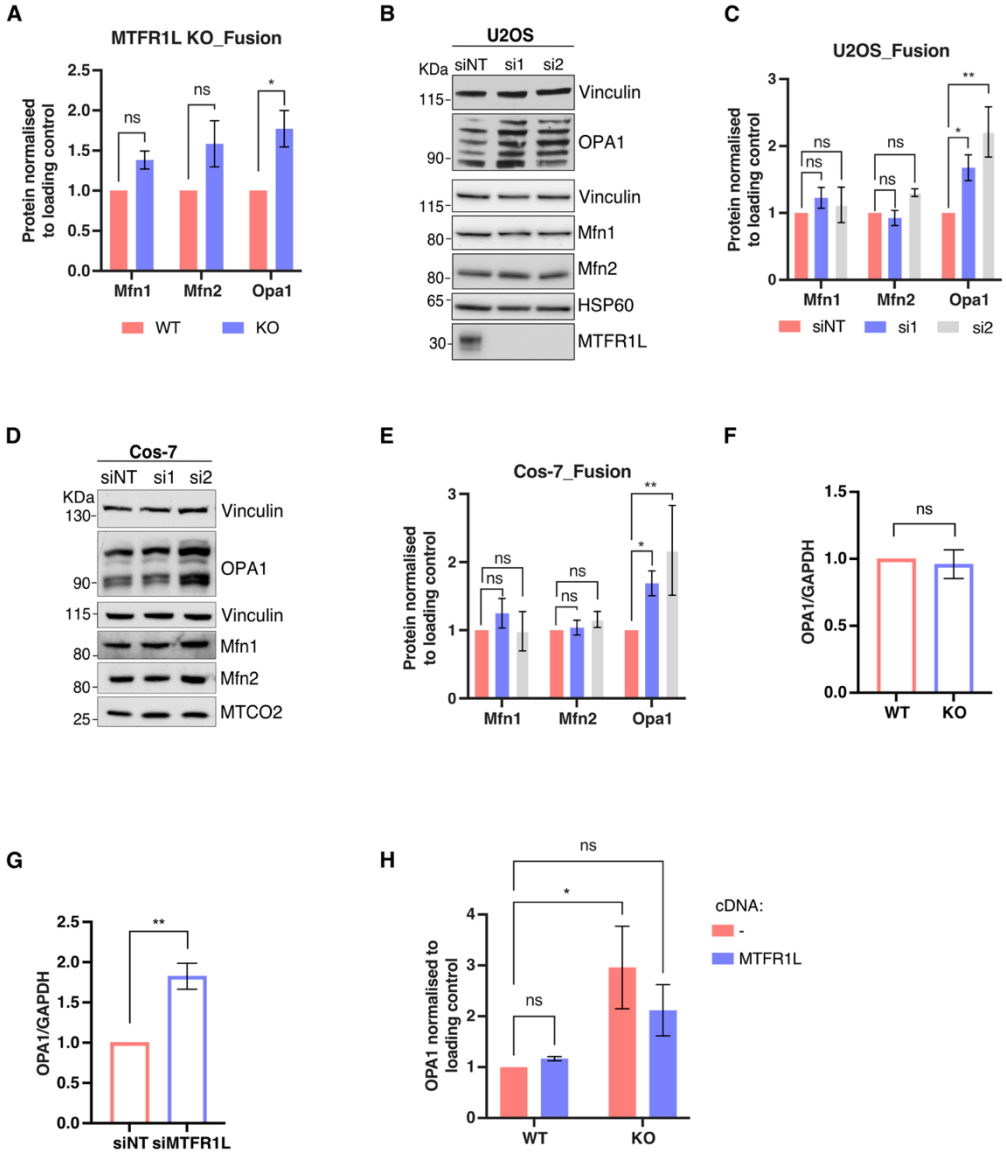

Figure S6, related to Figure 3. Loss of MTFR1L induces increased mitochondrial fusion and OPA1 protein levels.
(A) Quantification of levels of the indicated proteins from Figure 3B. Signal intensities were quantified by densitometry and normalized to loading controls. N = 3 independent experiments. **(B, D)** Immunoblots of proteins related to mitochondrial fusion from (B) U2OS cells, and (D) Cos- 7 cells, treated with non-targeted (NT) or two different MTFR1L small-interference (si) RNAs (si1 and si2). Vinculin, HSP60 and MTCO2 were used as loading controls. **(C, E)** Quantification of levels of the indicated proteins from (C) U2OS cells in (B), and (E) Cos- 7 cells in (D). Signal intensities were quantified by densitometry and normalized to loading controls. N = 3 independent experiments. (**F**) Quantification of OPA1 mRNA in wild-type (WT) and MTFR1L knock-out (KO) U2OS cells normalised to GAPDH mRNA, and expressed relative to WT control cells. N = 5 independent experiments. (**G**) Quantification of OPA1 mRNA in NT- and MTFR1L-silenced U2OS cells normalised to GAPDH mRNA, and expressed relative to siNT-treated U2OS cells. N = 3 independent experiments. (**H**) Quantification of total OPA1 levels from Figure 3D. Signal intensities were quantified by densitometry and normalized to loading controls. N = 3 independent experiments. All values: mean ± SEM; at least three independent experiments. (A, C, E, H): Two-way ANOVA, Tukey's multiple comparisons test. (F, G): two-tailed unpaired student's t-test. * p<0.05; ** p<0.01; ***p<0.001; **** P<0.0001; ns p>0.05.

Supplemental Figure S7

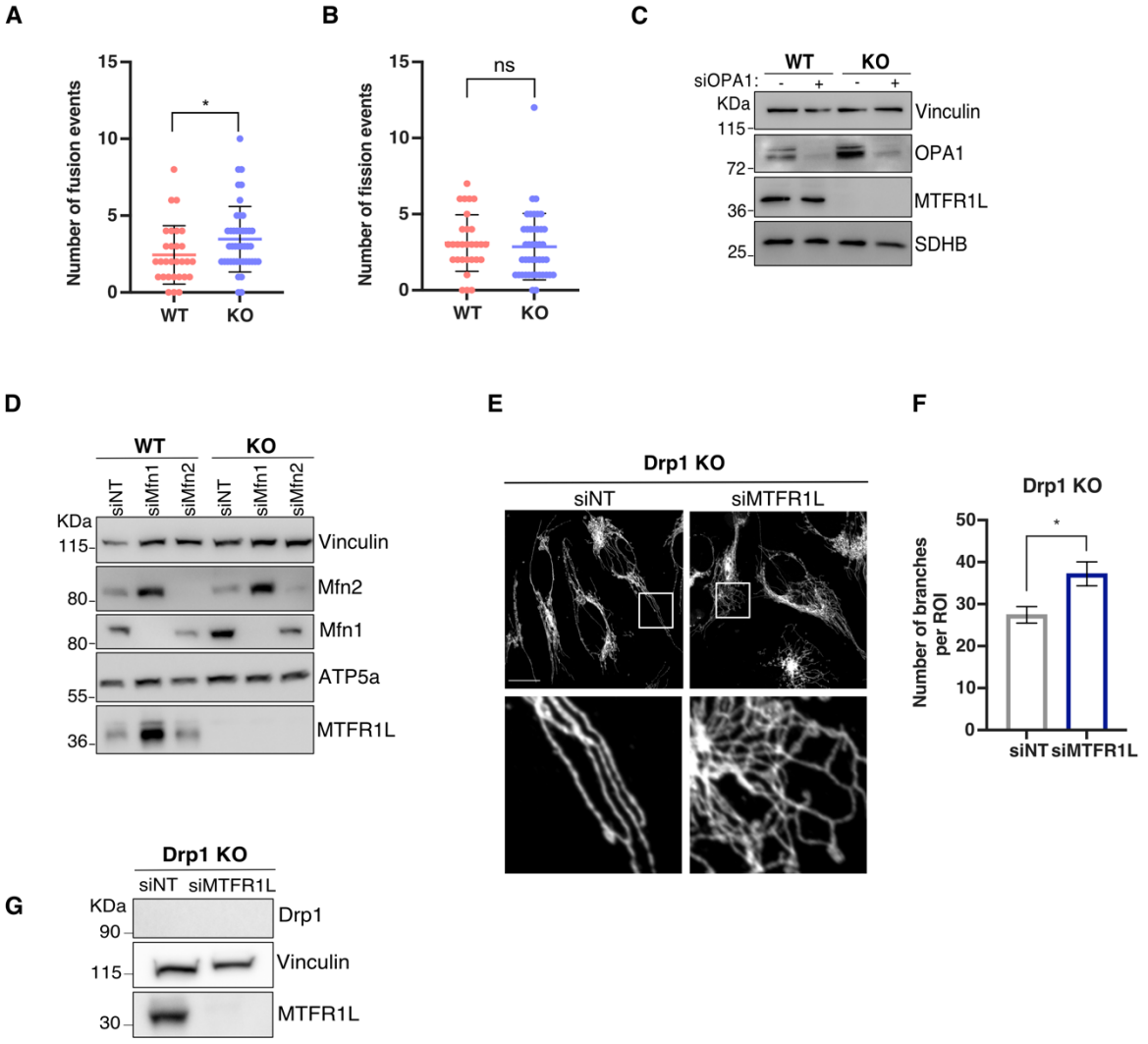

Figure S7, related to Figure 3. Loss of MTFR1L induces increased mitochondrial fusion events.
(A, B) Quantification of (A) mitochondrial fusion events, and (B) fission events, from wild-type (WT) and MTFR1L knock-out (KO) U2OS cells transiently overexpressing the mitochondrial marker, GFP-OMP25. Representative quantification of events per 625 μm^2 region of interest (ROI) over a 5-minutes period. At least 6 cells were counted per experiment; n = 3 independent experiments. (**C**) Immunoblot analysis showing the efficiency of OPA1 small-interference (si)RNA in WT and MTFR1L KO U2OS cells. Vinculin and SDHB were used as loading controls. (**D**) Immunoblot analysis showing the efficiency of Mfn1 and Mfn2 siRNAs in WT and MTFR1L KO U2OS cells. Vinculin and ATP5a were used as loading controls. (**E**) Representative confocal images of mitochondrial morphology from Drp1 KO HeLa cells silenced with NT or MTFR1L siRNAs. Mitochondria were labelled with an anti-TOM20 antibody. Scale bar, 20 µm. (**F**) Mitochondrial morphology was quantified from (E) as mitochondrial number of junctions, per region of interest (ROI). At least 15 cells were counted per experiment; n = 3 independent experiments. (**G**) Immunoblot analysis showing the efficiency of MTFR1L knockdown at three days in Drp1 KO cells. Vinculin was used as a loading control. All values: mean Å} SD; at least three independent experiments. (A, B): Mann-Whitney test. (F): two-tailed unpaired student's t-test; * p<0.05; ** p<0.01; ***p<0.001; **** P<0.0001; ns p>0.05.

Supplemental Figure S8

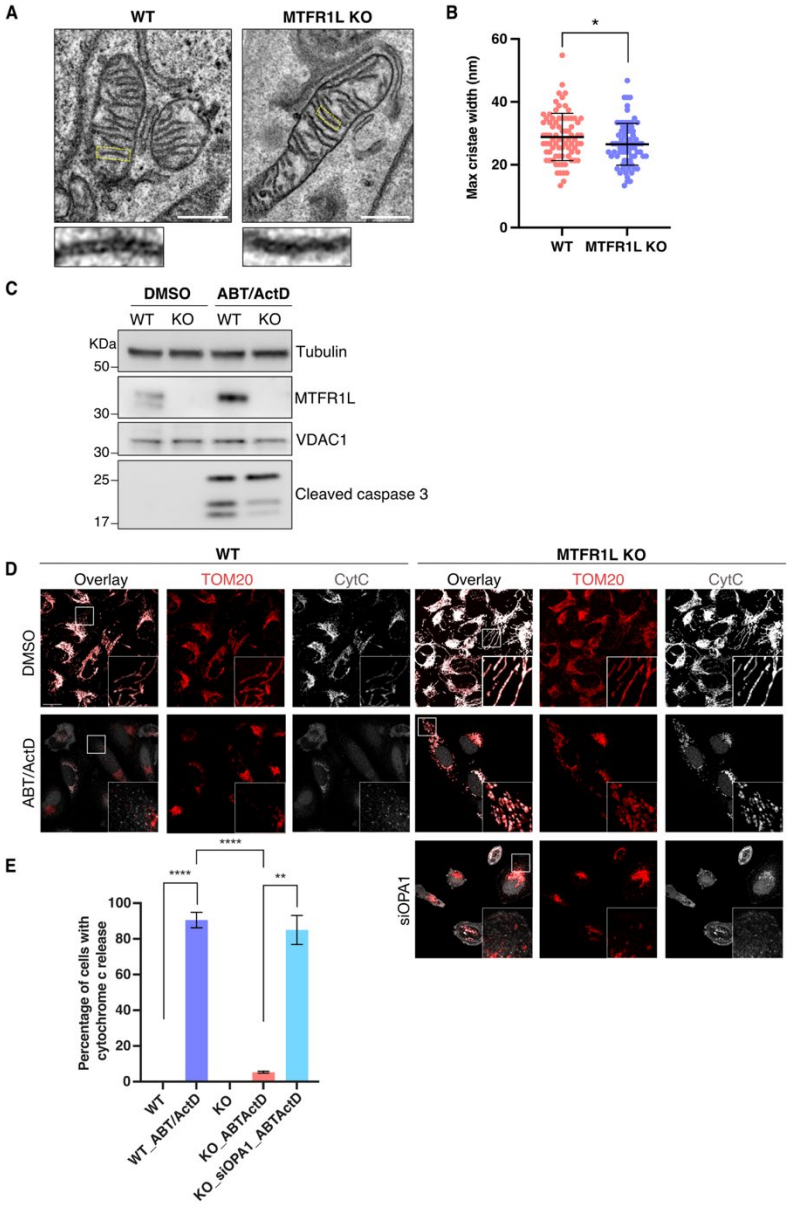

Figure S8. MTFR1L KO cells are resistant to apoptotic insults.

(**A**) Representative transmission electron micrographs from wild-type (WT) and MTFR1L knock- out (KO) U2OS cells. Scale bar, 500 nm. (**B**) Quantification of mitochondrial cristae width from WT and MTFR1L U2OS KO cells. At least 40 mitochondria were counted per experiment; n = 2 independent experiments. (**C**) Immunoblot analysis of indicated proteins from WT and MTFR1L KO U2OS cells treated with DMSO (-), or with 10 µM ABT 737 and 5 µM Actinomycin D (+) for 5 hours. Tubulin and VDAC1 were used as loading controls. (**D**) Representative confocal images from WT and MTFR1L KO U2OS cells silenced with OPA1 small-interference (si)RNA, treated with DMSO, or with 10 µM ABT 737, 5 µM Actinomycin D and 10 µM ZVAD for 5 hours. Mitochondria and cytochrome c were labelled with anti-TOM20 and anti-cytochrome c antibodies, respectively. Scale bar, 20 µm. (**E**) Quantification of cells from (D) with cytosolic cytochrome c. At least 15 cells were counted per experiment; n = 3 independent experiments. All values: mean ± SD; at least three independent experiments. (B): two-tailed unpaired student's t-test; (E): One-way ANOVA, Tukey's multiple comparisons test. * p<0.05; ** p<0.01; ***p<0.001; **** P<0.0001; ns p>0.05.

Supplemental Figure S9

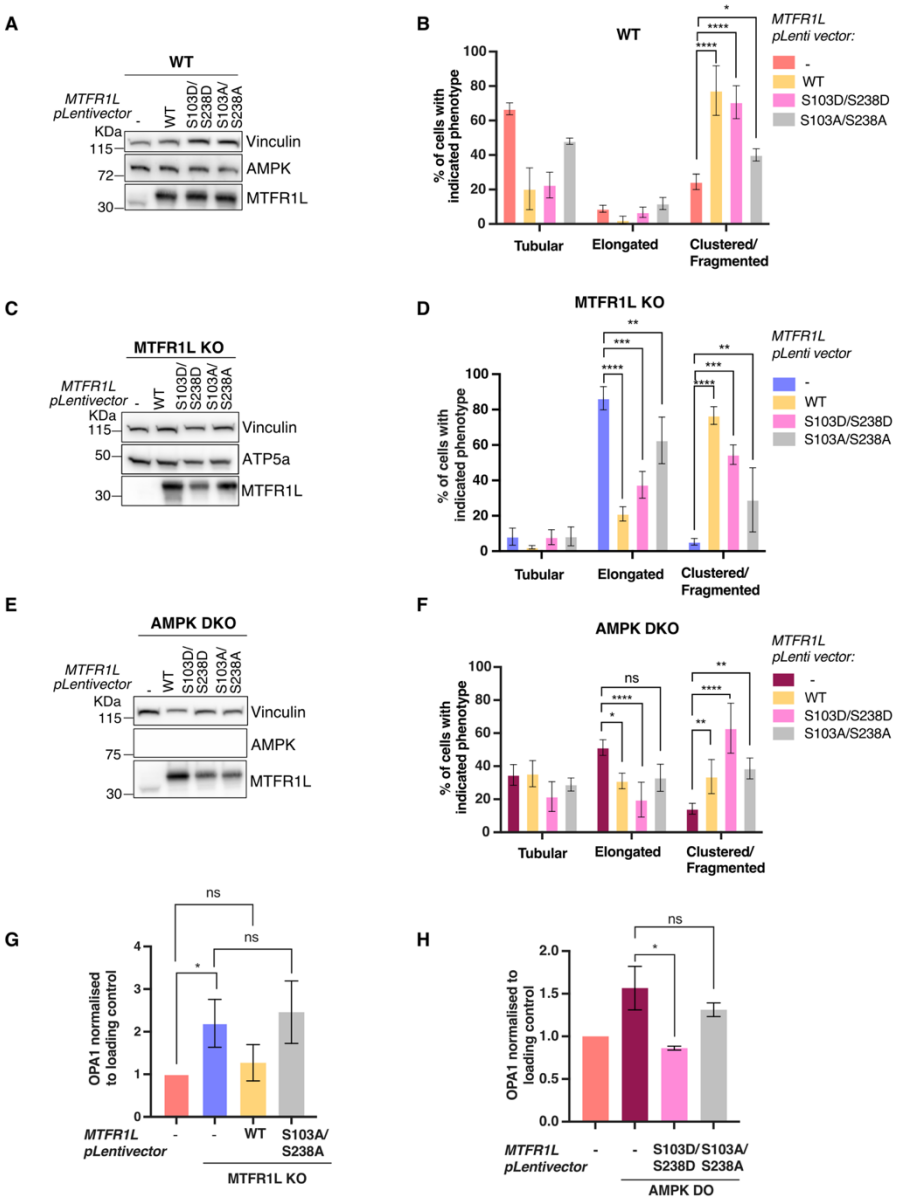

Figure S9, related to Figure 4. AMPK-dependent phosphorylation of MTFR1L controls mitochondrial morphology.
(A, C, E) Immunoblot analysis of indicated proteins showing the efficiency of MTFR1L-P2A-mCherry, MTFR1L$^{S103D/S238D}$-P2A-mCherry, and MTFR1L$^{S103A/S238A}$-P2A-mCherry stable expression in (A) wild-type (WT), (C) MTFR1L knock-out (KO), and (E) AMPK-α1α2 double KO (DKO) U2OS cells. P2A-mCherry alone vector was used as a control. Vinculin and ATP5a were used as loading controls. **(B, D, F)** Quantification of mitochondrial morphology from (B) WT (Figure 4B), (D) MTFR1L KO (Figure 4E), and (F) AMPK-α1α2 DKO (Figure 4H) U20S cells stably expressing P2A- mCherry, MTFR1L-P2A-mCherry, MTFR1L-$^{S103D/S238D}$-P2A-mCherry, and MTFR1L-$^{S103A/S238A}$-P2A-mCherry. At least 30 cells were counted per experiment; n = 3 independent experiments. **(G, H)** Quantification of OPA1 levels from Figure 4K, L. Signal intensities were quantified by densitometry and normalized to loading controls. N = 3 independent experiments. Values (B, D, F): mean ± SD; Values (G, H): mean ± SEM; of at least three independent experiments. (B, D, F): Two-way ANOVA, Tukey's multiple comparisons test; (G) Mann- Whitney t-test; (H) Kruskal-Wallis test with Dunn's multiple comparison test * p<0.05; ** p<0.01; ***p<0.001; **** P<0.0001; ns p>0.05.

Supplemental Figure S10

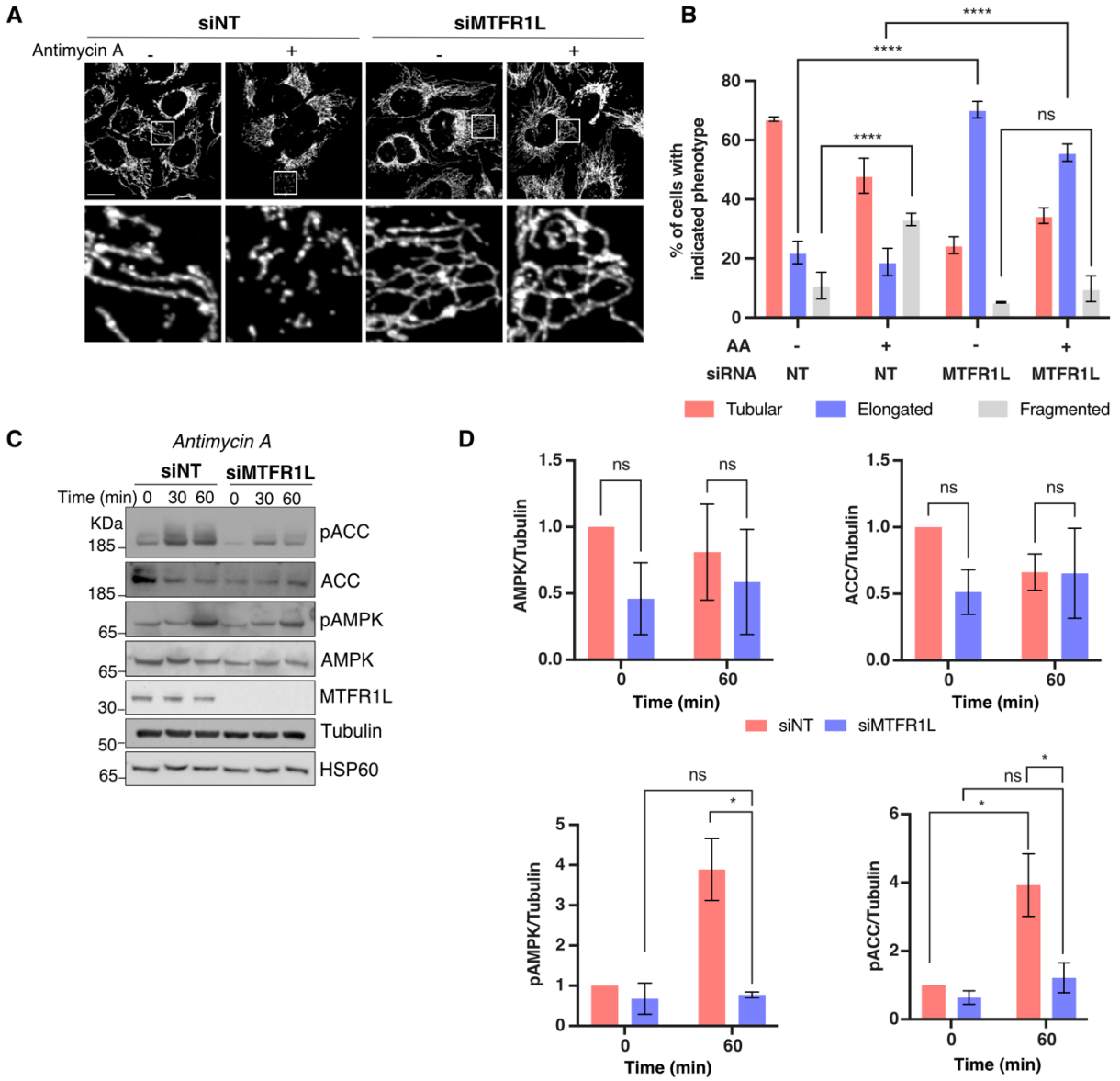

Figure S10, related to Figure 5. MTFR1L silenced cells are resistant to AMPK-induced mitochondrial fragmentation during Antimycin A treatment.

(A) Representative confocal images of mitochondrial morphology from U2OS cells silenced with non-targeted (NT) or MTFR1L small-interference (si) RNAs, and treated with DMSO (-), or 10 μM antimycin (+) A for 1 hour. Mitochondria were labelled with an anti-TOM20 antibody. Scale bar, 20 μm. **(B)** Quantification of mitochondrial morphology from (A). At least 30 cells were counted per experiment; n = 3 independent experiments; AA: antimycin A. (**C**) Immunoblot analysis of indicated proteins corresponding to (A) showing AMPK activation in U2OS cells silenced with NT or MTFR1L siRNAs, and treated with DMSO, or 10 μM antimycin A for indicated times. Tubulin and HSP60 were used as loading controls. (**D**) Quantification of levels of the indicated proteins at 1 hour of treatment from (C). Signal intensities were quantified by densitometry and normalized to loading controls. N = 3 independent experiments. All values: mean ± SD; at least three independent experiments. (B, D): Two-way ANOVA, Tukey's or Sidak's multiple comparisons test. * p<0.05; ** p<0.01; ***p<0.001; **** p<0.0001; ns p>0.05.

Supplemental Figure S11

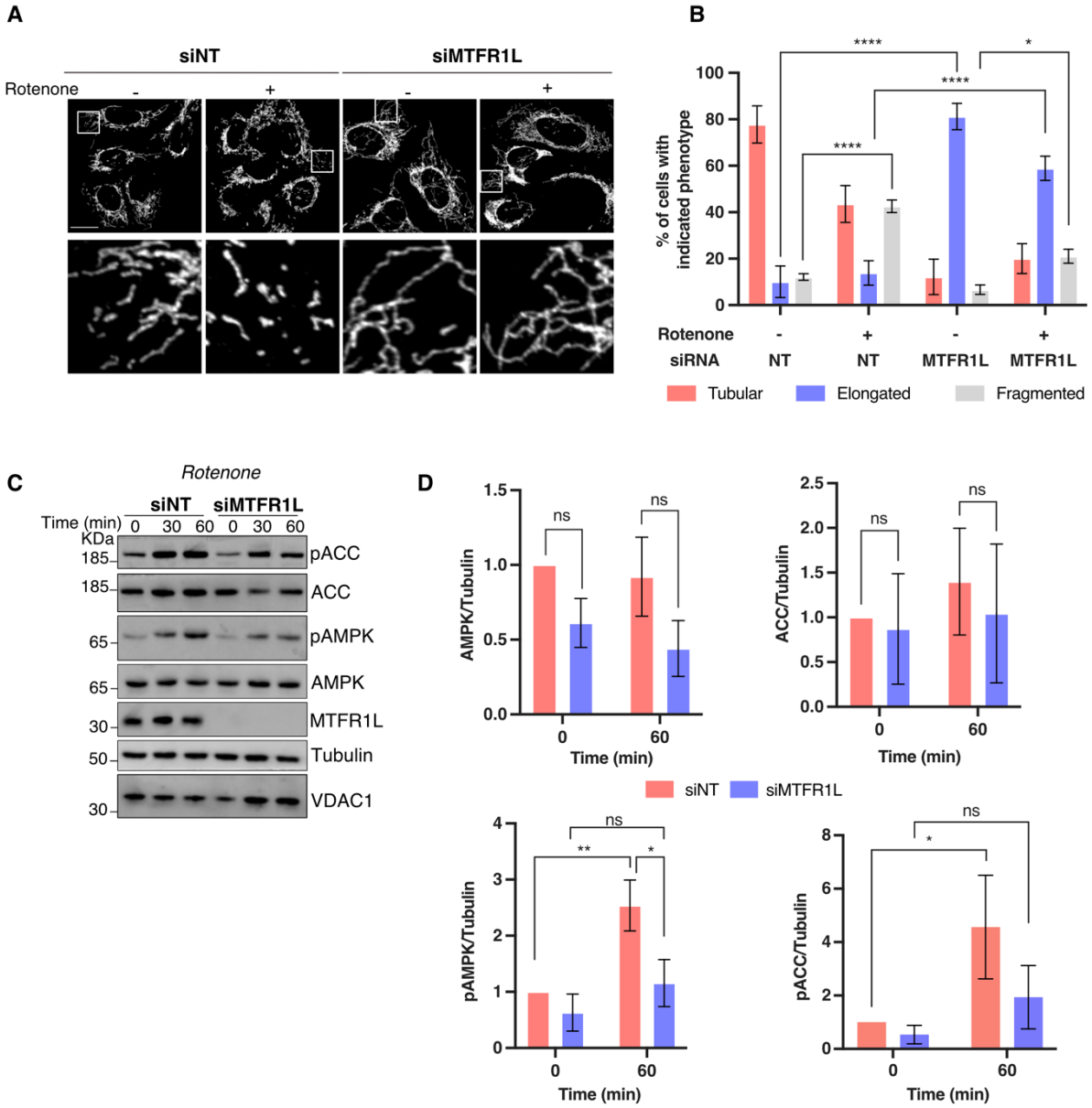

Figure S11, related to Figure 5. MTFR1L silenced cells are resistant to AMPK-induced mitochondrial fragmentation during Rotenone treatment.

(A) Representative confocal images of mitochondrial morphology from U2OS cells silenced with non-targeted (NT) or MTFR1L small-interference (si) RNAs, and treated with DMSO (-), or 250 ng/mL rotenone (+) for 1 hour. Mitochondria were labelled with an anti-TOM20 antibody. Scale bar, 20 µm. **(B)** Quantification of mitochondrial morphology from (A). At least 30 cells were counted per experiment; n = 3 independent experiments. (C) Immunoblot analysis of indicated proteins corresponding to (A) showing AMPK activation in U2OS cells silenced with NT or MTFR1L siRNAs, and treated with DMSO, or 250 ng/mL rotenone for indicated times. Tubulin and VDAC1 were used as loading controls. (D) Quantification of levels of the indicated proteins from (C). Signal intensities were quantified by densitometry and normalized to loading controls. N = 3 independent experiments. All values: mean ± SD; at least three independent experiments. (B, D): Two-way ANOVA, Tukey's or Sidak's multiple comparisons test. * p<0.05; ** p<0.01; ***p<0.001; **** p<0.0001; ns p>0.05.

Supplemental Figure S12

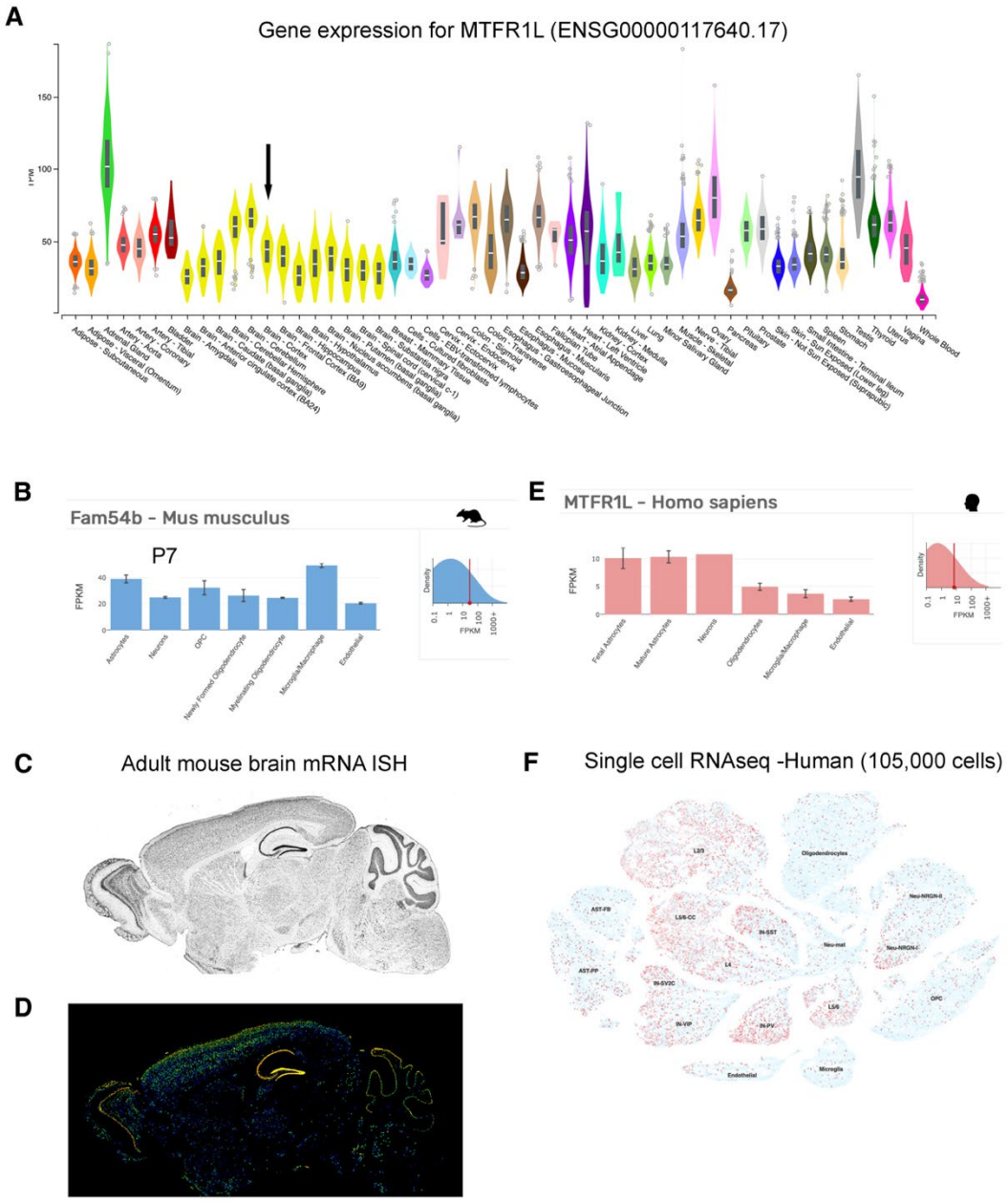

Figure S12, related to Figure 6. Analysis of MTFR1L expression in the brain.
(A) Publicly available RNAseq analysis showing gene expression of *MTFR1L* across human tissues. Arrow indicates expression in the cortex. **(B, C)** Publicly available RNA-Seq data analysis of (B) *MTFR1L* homolog, *Fam54b*, expression in P7 mice from different cell types in the brain, and (C) *MTFR1L* expression in different cell types in the human brain. **(D, E)** Publicly available (D) *in situ* hybridization of MTFR1L mRNA, and (E) MTFR1L protein expression, in adult mouse brain. **(F)** Publicly available single cell RNAseq from human cortex showing expression of MTFR1L in various types of neurons including layer 2/3 pyramidal neurons.

Supplemental Figure S13

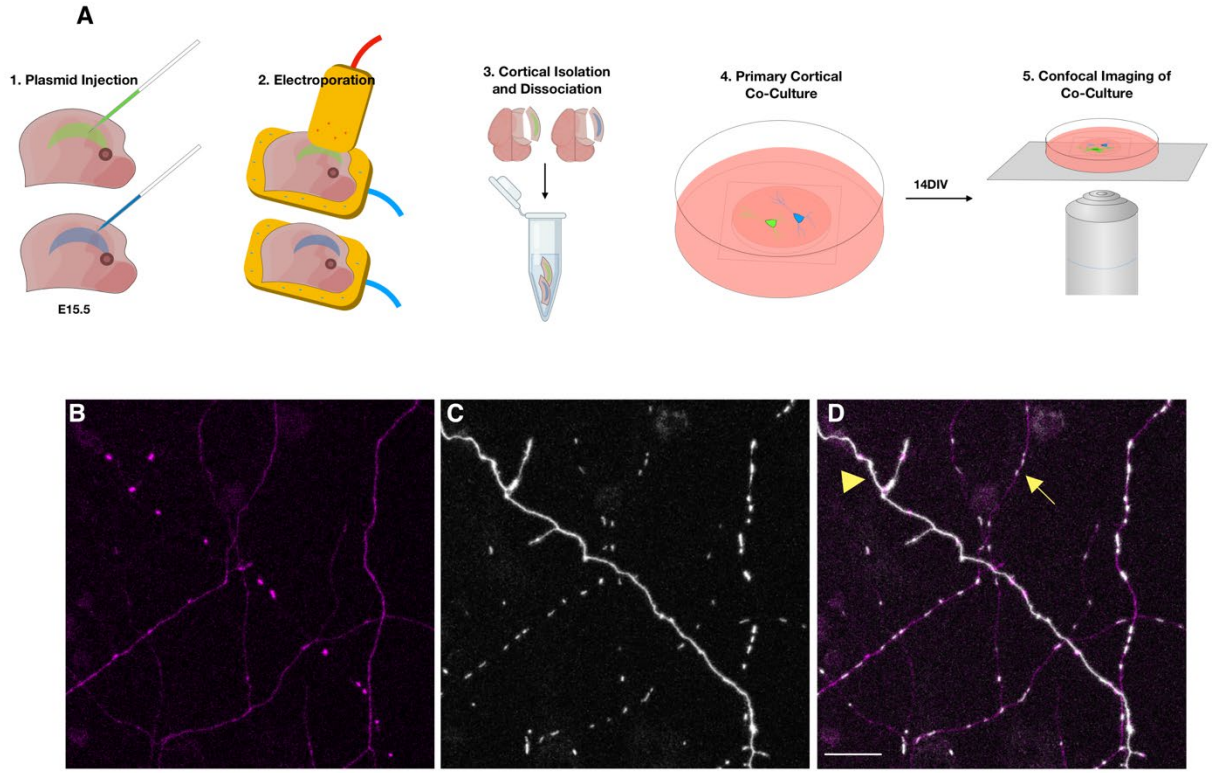

Figure S13, related to Figure 6. Technical description of the neuronal co-culture paradigm.
Neuronal co-cultures were used to minimize introduction of confounding variables caused by plate-to-plate variability. **(A)** Schematic depicting the co-culture technique used in the study (Figure 6A-H). Individual embryos were electroporated at E15.5 with an electroporation mixture for a single condition. A single cortical hemisphere from each condition was then dissected out, dissociated together, and plated. At DIV14, cells were fixed and imaged. **(B-D)** Representative high magnification confocal image of axons from two conditions plated together with (B) showing axon from short-hairpin (sh)MTFR1L condition visualized with cytosolic Venus and mitochondria from sh non targeted (NT) condition visualized with mtYFP, (C) showing mitochondria from shMTFR1L condition visualized with mtDsRed and axon from shNT condition visualized with cytosolic tdTomato, and (D) showing the merge composite of (B) and (C). Small arrow in (D) indicates shNT condition and plain bigger arrow represents shMTFR1L condition. Scale bar, 20 μm.

Methods

Cell lines

Cos-7, HeLa, human embryonic kidney (HEK)–293, and U2OS cells were obtained from the American Type Culture Collection. HeLa, HEK-293, and Cos-7 cells were cultured in high-glucose Dulbecco's modified Eagle's medium (DMEM) containing d-glucose (4.5 g/liter), sodium pyruvate (0.1 g/liter), and GlutaMAX supplemented with 2 mM l-glutamine, 1% nonessential amino acids, and final 10% of fetal bovine serum (FBS; Life Technologies, Gibco). U2OS cells were cultured in McCoy's 5A medium (Life Technologies, Gibco) containing the same composition of supplements. AMPK-a1a2 DKO U2OS cells were generated as described in (*49*). Cells were incubated at 37°C with 5% CO_2. Cells were tested for mycoplasma contamination using the Lookout Mycoplasma PCR Detection Kit (Sigma-Aldrich).

For neuronal culture, mouse brains were dissected out and the cortex was harvested in Hanks' balanced salt solution (HBSS) supplemented with Hepes (10 mM, pH 7.4). For cocultures, a single electroporated cortex from each condition was dissociated together in papain (Worthington; 14 U/ml) for 15 min at 37°C. After three washes in HBSS, brain cortices were dissociated in 1 ml of neurobasal medium (Invitrogen) with FBS (2.5%), N2 (1×), and B27 (1×) supplements. Dissociated cultures were plated on 35-mm poly-d-lysine (1 mg/ml; Thermo Fisher Scientific)–coated glass-bottom dishes (MatTek) and incubated at 37°C with 5% CO_2. After day *in vitro* (DIV) 5, 0.75 ml of culture medium was removed and replaced with 1 ml of fresh neurobasal medium without FBS every other day until imaged.

Treatments

ETC inhibitors, antimycin A (Sigma-Aldrich) and rotenone (Sigma- Aldrich), were used to treat cells at 10 μM and 250 ng/ml, respectively, for indicated times, using dimethyl sulfoxide (DMSO) as a control. CCCP (Sigma-Aldrich) was used at 20 □M for 60 min. For cross-linking experiments, cells were treated with 50 μM bismaleimidohexane in medium and incubated for 30 min at 37°C. Cells were then rapidly washed in cold phosphate-buffered saline (PBS) containing dithiothreitol (DTT; 20 mg/ml) and subsequently lysed for immunoblot analysis. For starvation experiments, cells were treated with DMEM lacking glucose (Life Technologies, Gibco) for 2 hours. For cell death experiments analyzed by immunoblot, cells were treated with 10 μM ABT 737 (Stratech Scientific) and 5 μM actinomycin D (Sigma-Aldrich) for 5 hours. For

cytochrome c release analysis by immunofluorescence, cells were treated with 10 μM ABT 737, 5 μM actinomycin D, and 10 μM of the pan-caspase inhibitor ZVAD-FMK (R&D Systems) for 5 hours. ***Mice***

All mice were handled in line with Columbia University's Institutional Animal Care and Use Committee. Timed-pregnant mice were purchased from Charles River Laboratories and electroporated at E15.5 with random assignment to control or experimental condition. Mouse organs were a gift from P. Chinnery (Department of Clinical Neurosciences, School of Clinical Medicine, University of Cambridge, Cambridge, UK).

Mutagenesis, siRNA, and plasmid transfections

For siRNA experiments, cells were transfected using Lipofectamine RNAiMAX (Invitrogen) with 20 nM siRNA for 3 days, following the manufacturer's instructions. Nontargeting (ON-TARGETplus SMARTpool D-0001810-10-20), Mfn1 (ON-TARGETplus SMARTpool, L-010670-01-0005), and Mfn2 (ON-TARGETplus SMARTpool L-012961-00-0005) siRNAs were purchased from Dharmacon. OPA1 siRNA was purchased from Sigma-Aldrich (5′-AAGUUAUCAGUCUGAGCCAGGUU-3′), which was previously described in (*55*). MTFR1L siRNAs were purchased from Integrated DNA Technologies (IDT): hs.Ri.MTFR1L.13.1 (si1) and hs.Ri.MTFR1L.13.2 (si2). For transient overexpression, plasmids were transfected using FuGene HD (Roche) according to the manufacturer's instructions. To generate plasmids containing MTFR1L, MTFR1L gBLOCK (IDT) (5′-

ATATATATGAATTCATGGACTACAAGGACGACGATGACAAGATGTCAGGAATGGAAGCCACTGTGAC
CATCCCAATCTGGCAAAACAAGCCACATGGGGCTGCTCGAAGTGTAGTAAGAAGAATTGGGACCAA
CCTACCCTTGAAGCCGTGTGCCCGGGCGTCCTTTGAGACCCTGCCCAACATCTCTGACCTGTGTTTG
AGAGATGTGCCCCCAGTCCCTACCCTGGCTGACATCGCCTGGATTGCTGCGGATGAAGAGGAGACA
TATGCCCGGGTCAGGAGTGATACGCGCCCCCTGAGGCACACCTGGAAACCCAGCCCTCTGATTGTC
ATGCAGCGCAATGCCTCTGTTCCCAACCTGCGTGGGTCCGAGGAGAGGCTTCTGGCCCTGAAGAAG
CCAGCTCTGCCAGCCCTAAGCCGCACTACTGAGCTGCAGGACGAGCTGAGCCACTTGCGCAGCCA
GATTGCAAAGATAGTGGCAGCTGATGCAGCTTCGGCTTCATTAACGCCAGATTTCTTATCTCCAGGA
AGTTCAAATGTCTCTTCTCCCTTACCTTGTTTTGGATCCTCATTCCACTCTACAACTTCCTTTGTCATT
AGTGACATCACCGAGGAGACAGAGGTGGAGGTCCCTGAGCTTCCATCAGTCCCCCTGCTTTGTTCT
GCCAGCCCTGAATGTTGCAAACCAGAACACAAAGCTGCCTGCAGTTCGTCTGAAGAGGATGACTGC

GTCTCTTTGTCCAAGGCCAGC A G C T T T G C A G A C A T G A T G G G T A T C C T G A A G GACTTTCACCGAATGAAACAGAGTCAAGATCTGAACCGGAGTTTATTGAAGGAGGAAGACCCTGCTG TGCTTATCTCTGAGGTCCTAAGGAGGAAGTTTGCTCTAAAGGAAGAAGATATCAGTAGAAAAGGAAA TTGACTCGAGA-TATATAT-3′) was digested and ligated into pcDNA 3.1 (Invitrogen) using Eco RI and Xho I restriction enzymes and was subsequently cloned into PCS2+ without a FLAG tag, and into P2A-mCherry-N1 (Addgene, #84329) using Xho I and Age I restriction enzymes. □MTFR1L $^{1–28}$ mutant was cloned into P2A-mCherry-N1 using an InFusion HD Cloning kit. MTFR1L phosphorylation site mutants (S103D/S238D; S103A/S238A) were generated using a QuikChange II site-directed mutagenesis kit (Agilent) and cloned into P2A- mCherry-N1.

To express MTFR1L in mouse neurons, sequences were changed from cytomegalovirus (CMV) promoter to pCAG. MTFR1L^{WT} was digested with Eco RI and Xho I and ligated into pcDNA3.1/Puro-CAG backbone from which VSFP-CR was extracted at the same restriction sites (Addgene, #40257) using an InFusion HD Cloning kit. The same backbone was used for the MTFR1L$^{S103A/S238A}$ construct; however, the Nhe I and Not I restriction sites were used.

Antibodies

Mouse monoclonal anti-VDAC (ab14734), anti-SDHA (ab14715), anti-ATP5a (ab14748), anti-MTCO2 (ab110258), anti-Mic60 (ab110329), and anti-GRP75 (ab2799) antibodies were obtained from Abcam. Rabbit polyclonal anti-Mid49 (16413-A-AP), anti-Mid51 (20164A-AP), anti-GRP75 (14887-1-AP), anti-MDH2 (15462-1AP), and anti-MFF (17090-A-AP) were obtained from Proteintech. Rabbit polyclonal anti-ACC (3662), anti-AMPK (2532S), anti-pACC (3661), anti-pAMPK (2535), anti-Mfn1 (14739), anti–cleaved caspase 3 (9661), and anti-Mfn2 (11925) were purchased from Cell Signaling Technologies. Mouse monoclonal anti-TOM20 (sc-17764), anti-HSP60 (sc-136291), anti-vinculin (V4505), and anti–β-tubulin (sc-23948) were from Santa Cruz Biotechnology. Mouse monoclonal anti-FLAG (F1804), anti–β-actin (A5541), and rabbit polyclonal MTFR1L (HPA027124) were purchased from Sigma-Aldrich. Mouse monoclonal anti–cytochrome c (556433) was purchased from BD Pharmingen. Mouse monoclonal anti-OPA1 (612607) and anti-Drp1 (611113) were purchased from BD Biosciences. Phospho-MTFR1L antibodies raised against residues Ser^{103} and Ser^{238} were generated from Orygen Antibodies Ltd. For immunoblot analysis, Amersham mouse (NA931)/ rabbit (NA934) immunoglobulin G (IgG) horseradish peroxidase– linked from

sheep/donkey (GE Healthcare), LICOR IRDye 680RD Goat anti-Rabbit IgG (926-68071) and RDye 800CW Goat anti-Mouse (926-32210) secondary antibodies (LI-COR), and DyLight 800 (Thermo Fisher Scientific) were used. For immunofluorescence, donkey anti-mouse Alexa Fluor 488 (A-21202), goat anti-rabbit Alexa Fluor 594 conjugate (A-11012), and goat anti-mouse highly cross-adsorbed Alexa Fluor Plus 488 (A-32723) secondary antibodies were obtained from Invitrogen.

Plasmid constructs and oligonucleotides

POCT-PA-GFP and MAPL-FLAG were obtained from H. McBride (McGill University, Canada). P2A-mCherry (84329), TOM20-mCherry (55146), and GFP-OMP25 (141150) were obtained from Addgene. Lentiviral cloning vectors, pWXLd-Ires-Hygro, psPAX2, and pMD2.G were obtained from M. Zeviani (MRC Mitochondrial Biology Unit, Cambridge). Myc-DDK–tagged MTFR1L (RC200212) was obtained from OriGene. The following constructs were already described: pCAG-TdTomato (*69*), pSCV2 (pCAG-mVenus) (*70*), pCAG-mtDsRed (*71*), pCAG-mTAGBFP2 (*54*), pCAG-mtYFP (*69*), pCAG-mtmTAGBFP2 (*69*), pCAG-ActA-mCherry (*72*), and pcDNA3.1/Puro-CAG-VSFP-CR (*73*).

Subcellular fractionation

Cells were washed once with cold PBS and scraped in mitochondrial isolation buffer (MIB) buffer [220 mM mannitol, 70 mM sucrose, 10 mM Hepes (pH 7.5), 1 mM EGTA, 1× protease cocktail inhibitor, 0.22 μm filtered at pH 7.4]. Cells were broken using a manual 7-ml dounce homogenizer (Kimble chase), at least 80 strokes, on ice, and cell breakage efficiency was checked under the microscope. Whole-cell fractions were saved, followed by centrifugations for 10 min at 800*g*, until no more nuclei and debris were observed. The supernatant was then centrifuged at 9000*g* for 10 min to obtain heavy membrane pellet, containing crude mitochondria [crude mitochondrial fraction (CMF)]. CMF was then washed twice with MIB and recentrifuged at 9000*g* for 15 min. The remaining supernatant of the CMF, containing cytosol and microsomes, was ultracentrifuged at 100,000*g* for 60 min (Beckman Coulter) to separate microsomes (pellet) and cytosolic (supernatant) fractions. All fractions were resuspended in MIB containing 1% Triton X-100 (Sigma-Aldrich). All centrifugation steps were carried out at 4°C.

Mitochondrial localization assays

Proteinase K protection assay was used to investigate MTFR1L mitochondrial subcompartment localization. Crude mitochondrial pellets obtained, as previously described, were resuspended in MIB and

quantified using Bradford assay (Bio-Rad). Proteinase K in modified MIB containing no protease inhibitor [10 mM Hepes (pH 7.4), 68 mM sucrose, 80 mM KCl, 0.5 mM EDTA, 2 mM $Mg(CH_3COO)_2$, 0.22 □m filtered] was used to resuspend 20 μg of mitochondria. Samples were incubated on ice for 30 min, followed by addition of final 2 mM phenylmethylsulfonyl fluoride resuspended in isopropanol on ice to inhibit protease activity. Samples were centrifuged at 10,600*g* for 15 min and washed twice with MIB containing protease inhibitors. Mitochondrial pellets were resuspended in MIB containing protease inhibitors to obtain a final concentration of 1 μg/μl, and the supernatant was discarded. All centrifugations were carried out at 4°C.

To establish whether proteins were inserted into membranes, 30 μg of CMF was treated with 0.1 M sodium carbonate (pH 11) and incubated on ice for 30 min. Samples were ultracentrifuged at 100,000*g* at 4°C for 60 min. The supernatant was saved as fraction containing solubilized proteins, whereas pellet contained inserted proteins. The samples were lysed in final 1% Triton X-100/MIB for 15 min on ice.

Respirometry

Oxygen consumption measurements were performed in intact cells resuspended in culture DMEM using the Oroboros Instruments High-Resolution Respirometer (*74*). Approximately 3×10^6 cells were used in each experiment. Basal (ROUTINE) respiration was recorded until the steady state was reached. The nonphosphorylating respiration (LEAK) was measured by adding 2.5 μM oligomycin to the chambers to inhibit the ATP synthase, and the respiration rates were left to reach the steady state. The uncoupled state or maximal capacity of the electron transfer system (ETS capacity) was achieved by titrating CCCP in 0.5 μM steps until the respiratory rates did not increase any further. Last, 2.5 μM antimycin A and 1 μM rotenone were added to inhibit complex III and complex I, respectively.

Immunofluorescence and confocal imaging

Cells were fixed in 5% paraformaldehyde (PFA) in PBS (pH 7.4) for 15 min at 37°C, with three subsequent washes in PBS. Autofluorescence was quenched with 50 mM ammonium chloride for 10 min at room temperature (RT) and three additional washes in PBS. Cells were then permeabilized with Triton X-100/0.1% PBS for 10 min, followed by three washes in PBS. Blocking was carried out in 10% FBS/PBS for 20 min. Primary antibodies were prepared in 5% FBS/ PBS and incubated on a shaker for 2 hours at RT or overnight at 4°C. Cells were washed three times in 5% FBS/PBS and incubated with the corresponding secondary antibody (dilution 1: 1000) prepared in 5% FBS/PBS. Coverslips were washed three times in

PBS and then in deionized water (DIW), dried, and mounted onto slides using fluorescence mounting medium (Dako).

Images were acquired on a Nikon Eclipse TiE inverted microscope coupled with an Andor Dragonfly 500 confocal spinning disk system using the 60× or 100× objective. Images were captured with seven stacks each of 0.2 □m using the Zyla 4.2 PLUS sCMOS camera (Andor), which was coupled to the Fusion software (Andor). Images were acquired in the same conditions with the same laser intensity (laser lines 488, 568, and 647 nm) and exposure time. Photoactivation of the ROI (25 □m^2) was performed using the Andor FRAPPA module. Raw seven-stack images were compiled into "max projection," converted into composites, and proceeded using the Fiji software (*14*).

All neuronal imaging was acquired with a Nikon Ti-E microscope equipped with an A1 confocal. Nikon Elements software was used to control the equipment and lasers. The Nikon 40× oil (1.30 numerical aperture) objective was used for both *in vivo* and *in vitro* imaging.

Transmission electron microscopy

WT and MTFR1L KO cells were seeded at 80 to 90% confluency on Thistle Scientific □-Dish 35 mm, high, containing Ibidi polymer coverslips (Ibidi, 81151). Cells were washed once with 0.9% saline solution, followed by a 4°C overnight fixation, and were processed for TEM preparation. Samples were fixed in fixative buffer [2% glutaraldehyde/2% formaldehyde in 0.05 M sodium cacodylate buffer (pH 7.4) containing 2 mM calcium chloride] overnight at 4°C. After five washes in 0.05 M sodium cacodylate buffer (pH 7.4), samples were osmicated (1% osmium tetroxide, 1.5% potassium ferricyanide, 0.05 M sodium cacodylate buffer, pH 7.4) for 3 days at 4°C. After five washes in DIW, samples were treated with 0.1% (w/v) thiocarbohydrazide/DIW for 20 min at RT in the dark. After five washes in DIW, samples were osmicated a second time for 60 min at RT (2% osmium tetroxide/DIW). Following five washes in DIW, samples were block-stained with uranyl acetate (2% uranyl acetate in 0.05 M maleate buffer, pH 5.5) for 3 days at 4°C. Samples were washed five times in DIW and then dehydrated in a graded series of ethanol (50%/70%/95%/100%/100% dry) and 100% dry acetonitrile, three times each for at least 5 min. Samples were infiltrated with a 50:50 mixture of 100% dry acetonitrile/Quetol resin [without benzyl dimethylamine (BDMA)] overnight, followed by 3 days in 100% Quetol (without BDMA). Then, the sample was infiltrated for 5 days in 100% Quetol resin with BDMA, exchanging the resin each day. The Quetol resin mixture is 12

g of Quetol 651, 15.7 g of nonenyl succinic anhydride, 5.7 g of methyl nadic anhydride, and 0.5 g of BDMA (all from TAAB). The Ibidi dishes were filled with resin to the rim, covered with a sheet of Aclar, and cured at 60°C for 3 days.

After curing, the Aclar sheets were removed and small sample blocks were cut from the Ibidi dish using a hacksaw. Thin sections (~70 nm) were prepared using an ultramicrotome (Leica Ultracut E). Resin blocks were orientated with the cell side toward the knife, and sections were collected on bare 300-mesh copper grids immediately when reaching the cell monolayer. Samples were imaged in a Tecnai G2 TEM (FEI/Thermo Fisher Scientific) run at 200 keV using a 20-□m objective aperture to improve contrast. Images were acquired using an ORCA HR high-resolution charge-coupled device camera (Advanced Microscopy Techniques Corp., Danvers, USA).

For mitochondrial cristae width analysis, the “measure” function in Fiji ImageJ was used. For cristae analysis, only mitochondria harboring at least five cristae structures clearly visible were analyzed.

ATP/ADP nucleotide quantification

ATP and ADP concentrations were measured using a luciferase-based assay as described previously (*75*). In brief, treated cells were scraped down into Eppendorf tubes, kept on ice, and lysed in ice-cold perchloric acid extractant [3% (v/v) $HClO_4$, 2 mM Na_2-EDTA, 0.5% Triton X-100] at a concentration of 300 µl/10^5 cells by vigorously vortexing before transferring samples back onto wet ice. Samples, along with ATP and ADP standards, were neutralized to pH 7 using potassium hydroxide solution (2 M KOH, 2 mM Na_2-EDTA, and 50 mM MOPS). To measure ADP concentration, 250 µl of neutralized sample was added to 250 µl of ATP sulfurylase assay buffer [20 mM Na_2MoO_4, 5 mM guanosine monophosphate (GMP), and 0.2 U of ATP sulfurylase (New England Biolabs, USA)], in tris-HCl buffer [100 mM tris-HCl and 10 mM $MgCl_2$ (pH 8.0)], incubated for 30 min at 30°C to convert the sample’s ATP to adenosine phosphosulfate (APS). ADP samples were then heated at 100°C for 5 min and cooled on ice. Standards (100 µl), samples for ATP measurement (100 µl), or samples for ADP measurement (200 µl) (in duplicate) were then added to 400 µl of tris- acetate (TA) buffer (100 mM tris, 2 mM Na_2-EDTA, and 50 mM $MgCl_2$, pH 7.75, with glacial acetic acid) in luminometer tubes. To measure ADP concentration, 10 □ of pyruvate kinase solution [100 mM phosphoenolpyruvate and 6 U of pyruvate kinase suspension (Sigma-Aldrich, #P1506)] was added to one set of ADP standards and one set of ADP samples and then incubated for 30 min at 25°C in the dark to

convert ADP to ATP. The duplicate tube (without addition of pyruvate kinase solution) served as an ADP "blank" value. The samples were then all assayed for ATP content in a Berthold AutoLumat Plus LB953 luminometer by addition of 100 µl of luciferase/luciferin solution {7.5 mM DTT, bovine serum albumin (BSA; 0.4 mg/ml), luciferase (1.92 µg/ml) (Sigma- Aldrich, #L9506), 120 µM d-luciferin (Sigma-Aldrich, #L9504), made in TA buffer [25% (v/v) glycerol]}, delivered via auto-injection, protected from light. Bioluminescence of the ATP- dependent luciferase activity was measured for 45 s after injection, and the data were quantified against standard curves.

SDS–polyacrylamide gel electrophoresis and immunoblot analysis

Cells were lysed in radioimmunoprecipitation assay buffer [20 mM tris (pH 8.0), 150 mM NaCl, 0.1% SDS, 1% deoxycholic acid, 1% NP-40, and complete protease inhibitor cocktail]. For pAMPK analysis, cells were lysed in 50 mM Hepes, 10% glycerol, 0.1% Triton X-100, 1 mM EDTA (pH 7.4), containing 1× protease cocktail inhibitor. Samples were normalized for protein concentration using a Bio-Rad protein assay (Bio-Rad), resolved by SDS–polyacrylamide gel electrophoresis, and transferred to nitrocellulose membrane (0.2 µm pore size; Bio-Rad) or polyvinylidene difluoride membrane (0.2 µm pore size, GE Healthcare) for the detection of phosphoproteins. Next, membranes were blocked with 5% nonfat milk or 5% BSA in PBS for 60 min at RT. Membranes were incubated with primary antibody at the appropriate dilution (in 2% milk or 2% BSA, in 0.05% Tween 20 in PBS) at 4°C overnight. Membranes were washed in 0.05% Tween 20 in PBS three times for 15 min and incubated with appropriate secondary antibodies (1.3,000 in 2% milk or 2% BSA, in 0.05% Tween 20 in PBS). Membranes were treated with Western Lightning Plus ECL (PerkinElmer) and exposed to chemiluminescence either on films (PROTEC) or on a digital ECL machine (Amersham) for image quantification. Immunoblots are representative of at least three biological replicates.

For Fig. 4A, the lysis buffer was 50 mM tris-HCl (pH 7.2), 150 mM NaCl, 1% Triton X-100, 50 mM NaF, 5 mM NaPPi, 1 mM EDTA, 1 mM EGTA, 1 mM DTT, and 1× protease inhibitor cocktail (EDTA-free) (Roche). Proteins were transferred to nitrocellulose membrane using the iBlot 2 system (Thermo Fisher Scientific). Membranes were treated with SuperSignal Western Blotting enhancer kit (Pierce), according to the manufacturer's instructions, and blocked for 1 hour in LI-COR Odyssey Intercept blocking buffer (PBS). Membranes were incubated at least overnight with primary antibody in primary antibody diluent (Pierce kit). Detection was performed using secondary antibody coupled to IR 680 or IR

800 dye, and the membranes were scanned using the LICOR Odyssey IR imager. Protein concentrations were determined by Coomassie blue binding with BSA as standard.

Quantitative reverse transcription polymerase chain reaction

Total RNAs from WT and MTFR1L KO U2OS cells and NT- and MTFR1L-silenced U2OS cells were isolated using an RNeasy kit (Qiagen), and cDNA was synthesized using a High-Capacity cDNA RT kit (Applied Biosystems), following the manufacturer's instructions. mRNA levels were then quantified using the QuantStudio 3 Real-Time PCR System. The following pairs of primers were used: hOPA1, 5′-GGCTCCTGACACAAAGGAAA-3′ (forward) and 5′-TCCTTCCATGAGGGTCCATT-3′ (reverse), as described by (*76*). Glyceraldehyde-3-phosphate dehydrogenase (GAPDH), 5′-GGTGAAGGTCGGAGTCAACG-3′ (forward) and 5′-GAGGGATCTCGCTCCTGGAAG-3′ (reverse).

KO cell line generation using CRISPR-Cas9

To generate an MTFR1L CRISPR-Cas9–mediated gene KO, U2OS cells were transfected with ps-CAS9-2A-EGFP plasmid containing the gRNA of interest (targeting either exon 3 or 4). gRNA sequences were designed using the online CRISPR software (https://chopchop. cbu.uib.no) and were selected on the basis of having low off-target effects. The following oligonucleotides were used: for targeting exon 3, 5′-CACCgGTGTGCCCGGGCGTCCTTTG-3′ (forward) and 5′-AAACCAAAGGACGCCCGGGCACACc-3′ (reverse); for targeting exon 4, 5′-CACCgTGACATCGCCTGGATTGCTG-3′ (forward) and 5′-AAACCAGCAATCCAGGCGATGTCAc-3′ (reverse). To generate Drp1 KO in HeLa cells, the following gRNA was used: 5′-CACCgAAATAGCTACGGTGAACCCG-3′ (forward) and 5′-AAACCGGGTTCACCGTAGCTATTTc-3′ (reverse). Forty- eight hours after transfection, cells were washed in PBS, trypsinized, and centrifuged. Cell pellet was resuspended in 300 □l of medium and filtered through 70-□m filter into fresh tubes. Cells were sorted into single cell into 96-well plates via fluorescence-activated cell sorting (FACS) and were incubated at 37°C in complete medium containing 20% FBS. After 2 to 3 weeks, single-cell colonies were observed and transferred into 24-well plates. Upon 80% of confluency, clones were tested for efficient KO by immunoblot and polymerase chain reaction (PCR).

Lentiviral production and transduction

WT, MTFR1L KO, and AMPK-α1α2 DKO U2OS cells were stably transduced with modified pWPXLd-ires-Hygro lentiviral expression vectors (obtained from M. Zeviani, Mitochondrial Biology Unit, University of Cambridge, UK) with P2A-mCherry alone, MTFR1L^{WT}-P2A-mCherry, MTFR1L S103D/S238D-P2A-mCherry, and MTFR1LS103A/S238A-P2AmCherry with an HD Infusion Cloning kit. Lentiviral particles were generated in HEK-293T cells via cotransfection of the target vector together with packaging psPAX2 (Addgene, #12260) and envelope pMD2.G (Addgene, #12259) vectors. Twenty-four hours after transduction, cells were selected for hygromycin resistance.

In utero electroporation/ex utero electroporation

Cortical layer 2/3 PNs were targeted by injecting endotoxin-free plasmid (2 to 5 mg/ml) and 1% Fast Green (Sigma-Aldrich) mixture into the lateral ventricles of E15.5 embryos using Picospritzer III (Parker). Electroporation was performed with five pulses of 45 V for 50 ms (ECM 830, BTX). Mice were then perfused with 4% PFA and 0.75% glutaraldehyde (both from Electron Microscopy Sciences) on postnatal day (P21). Following overnight incubation in fixation mixture, brains were washed three times in PBS before vibratome sectioning (Leica VT1200) at 125 □m and mounted on slides.

For ex utero electroporation, cortical layer 2/3 PNs were targeted by injecting endotoxin-free plasmid (2 to 5 mg/ml) and 1% Fast Green (Sigma-Aldrich) mixture into the lateral ventricles of E15.5 embryos using Picospritzer III (Parker). Electroporation was conducted with four pulses of 20 V for 100 ms (ECM 830, BTX). Plates were then fixed with 4% PFA and 0.75% on DIV14.

Quantification and statistical analysis

Image analysis

For mitochondrial morphology analysis, the mitochondrial network was primarily defined in control cells and categorized as elongated (highly connected, with a minimum of 10 free ends), fragmented (shorter, disassociated), and tubular (neither connected nor disassociated) mitochondria. Mitochondrial networks from treatments/ siRNA/KO conditions were assessed and compared to their corresponding controls. At least 30 cells per condition were counted. To further analyze mitochondrial morphology, 225-□m^2 mitochondrial ROIs from max projection images were selected in the cell periphery, thresholded manually, and were processed with the “smooth” function twice. The mitochondrial area and number analysis quantification was obtained using the “Analyze Particles” function in Fiji, using 0.1 μm as the maximum

length measured. For junction analysis, a 225-□m^2 peripheral mitochondrial ROI was analyzed using the analyze skeleton function, in Fiji. Mitochondrial length was measured using Mitomapr (*77*).

Quantification of mitochondrial fusion was based on previously described methods (*78*, *79*) with minor modifications. The total area of mitochondria was obtained by thresholding images of TOMM20-mCherry, and the photoactivated area was obtained by thresholding images of PA-GFP. The percentage of mitochondria containing PA-GFP was calculated for each time point. Subsequently, the difference in percentage of PA-GFP–containing mitochondria was calculated by subtracting the percentage of photoactivated mitochondria directly after activation from the percentage of photoactivated mitochondria 5 min later.

For live-cell imaging analysis, time-lapse videos were acquired over the course of 5 min with an image captured every 10 s. OMP25-GFP was used to label the mitochondria. A region of 625 μm^2 per cell was cropped using Fiji software, and the number of fission and fusion events was manually counted. For neurons, quantification was performed in Fiji ImageJ, using the segmented line tool to measure the length of both axonal segments and mitochondria.

Statistical analysis

For the bar graphs of mitochondrial morphology, quantitative reverse transcription PCR analysis, immunoblot quantification, and fission/fusion ratio, errors bars displayed on graphs represent the mean ± SEM or SD from at least three independent experiments. For Fig. 6, box plots represent minimum and maximum values, with the box denoting the 25th, 50th, and 75th percentiles from three independent experiments. For all other graphs, data are represented as scatterplots and errors bars displayed on graphs represent the mean ± SEM or SD from at least three independent experiments. The number of cells analyzed is shown in methods. Statistical significance was analyzed using nested one-way analysis of variance (ANOVA), one-way ANOVA, two-way ANOVA, Mann-Whitney, or unpaired *t* test. All statistical analyses were performed using GraphPad Prism software. *P < 0.05, **P < 0.01, ***P < 0.001, and ****P < 0.0001 were considered significant, and P > 0.05 was considered nonsignificant (ns).

Figure 2: (C and L): two-way ANOVA, Tukey's multiple comparison test; (D to F): nested ordinary one-way ANOVA, Dunnett's multiple comparisons test; (H): Mann-Whitney test. Figure 3: (G and K): two-way ANOVA, Tukey's multiple comparisons test. (E): two-tailed unpaired Student's *t* test. (H, I, L, and M): one-

way ANOVA, Tukey's multiple comparisons test. Figure 4: (C, D, F, G, I, and J): nested one-way ANOVA, Dunnett's multiple comparisons test. Figure 5: (C and D): one-way ANOVA with Tukey's multiple comparisons test. (B and F to H): two-way ANOVA with Tukey's multiple comparisons test. Figure 6: (B to D, F to H, and J to L): nonparametric Kruskal-Wallis test with Dunn's multiple comparison test.

Number of cells analyzed by microscopy

For quantification, the number of cells is presented from three independent experiments, otherwise specified.

Figure 2: 2C: *n* = 130, 127, and 138 cells for WT, KO1, and KO2, respectively. 2D: *n* = 63, 63, and 63 for WT, KO1, and KO2, respectively. 2E: *n* = 58, 57, and 58 cells for WT, KO1, and KO2, respectively. 2F: *n* = 99, 86, and 68 cells for WT, KO1, and KO2, respectively. 2H: *n* = 41 and 40 cells for WT and KO, respectively, from four independent experiments. 2J: *n* = 563 and 619 mitochondria counted for WT and KO, respectively. 2L: *n* = 93, 88, 109, and 102 cells for WT, WT + MTFR1L, MTFR1L KO, and MTFR1L KO + MTFR1L, respectively, from two independent experiments.

Figure S2: S2C: *n* = 160, 147, and 155 cells for siNT, si1, and si2, respectively. S2D: *n* = 64, 64, and 44 cells for siNT, si1, and si2, respectively. S2E: *n* = 64, 64, and 50 cells for siNT, si1, and si2, respectively. S2F: *n* = 53, 55, and 43 cells for siNT, si1, and si2, respectively. S2I: *n* = 194, 177, and 175 cells for siNT, si1, and si2, respectively. S2J: *n* = 63, 63, and 55 cells for siNT, si1, and si2, respectively. S2K: *n* = 63, 63, and 55 cells for siNT, si1, and si2, respectively. S2M: *n* = 563 and 619 total mitochondria counted for WT and KO, respectively. S2O: *n* = 46, 45, 45, and 44 cells for WT, WT + MTFR1L, MTFR1L KO, and MTFR1L KO + MTFR1L, respectively. S2P: *n* = 48, 43, 46, and 44 cells for WT, WT + MTFR1L, MTFR1L KO, and MTFR1L KO + MTFR1L.

Figure S3: S3D: □*n* = 82, 69, 78, and 117 cells for WT, WT + □MTFR1L $^{1–28}$, MTFR1L KO, and MTFR1L KO + MTFR1L $^{1–28}$, respectively. S3E: 58, 41, 55, and 54 cells for WT, WT + MTFR1L□$^{□1–28}$, MTFR1L KO, and MTFR1L KO + MTFR1L $^{1–28}$□, respectively. S3F: 54, 37, 51, and 54 cells for WT, WT + MTFR1L□$^{1–28}$, MTFR1L KO, and MTFR1L KO + MTFR1L $^{1–28}$□, respectively. S3G: 54, 37, 51, and 54 cells for WT, WT + MTFR1L□$^{1–28}$, MTFR1L KO, and MTFR1L KO + MTFR1L $^{1–28}$, respectively.

Figure S5: S5D: *n* = 105, 120, 108, and 94 cells for WT, WT + CCCP, KO, and KO + CCCP, respectively. S5F: *n* = 80, 79, 95, and 79 cells for siNT, siNT + MAPL-FLAG, siMTFR1L, and siMTFR1L + MAPL-FLAG, respectively.

Figure 3: 3E: *n* = 108 and 127 fission events and 92 and 149 fusion events for WT and MTFR1L KO, respectively, from at least 18 cells. 3G: *n* = 102, 99, 130, and 132 cells for WT, WT + siOPA1, KO, and KO + siOPA1, respectively. 3H, I: *n* = 63, 60, 61, and 63 cells for WT, WT + siOPA1, MTFR1L KO, and MTFR1L KO + siOPA1, respectively. 3K: *n* = 101, 112, 152, 148, and 132 cells for WT + siNT, WT + siMfn1, WT + siMfn2, KO + siNT, KO + siMfn1, and

KO + siMfn2, respectively. 3L: *n* = 61, 63, 62, 57, 63, and 62 cells for W + siNT, WT + siMfn1, WT + siMfn2, KO + siNT, KO + siMfn1, and KO + siMfn2, respectively. Figure 3M: n = 61, 63, 62, 54, 63, and 62 cells for WT + siNT, WT + siMfn1, WT + siMfn2, KO + siNT, KO + siMfn1, and KO + siMfn2, respectively.

Figure S7: S7E: *n* = 84 and 79 cells for siNT and siMTFR1L in Drp1 KO cells, respectively.

Figure 4: 4C: *n* = 97, 63, 55, and 82 cells for WT U2OS cells stably expressing empty P2A-mCherry, MTFR1L-P2A-mCherry, MTFR1L$^{S103D/S238D}$- P2A-mCherry, and MTFR1L$^{S103A/S238A}$-P2A-mCherry constructs, respectively. 4D: 97, 63, 55, and 82 cells for WT U2OS cells stably expressing empty P2A-mCherry, MTFR1L-P2A-mCherry, MTFR1LS103D/S238D-P2A-mCherry, and MTFR1LS103A/S238A-P2AmCherry constructs, respectively. 4F: *n* = 81, 73, 75, and 76 cells for MTFR1L KO cells stably expressing empty P2A-mCherry, MTFR1L-P2A-mCherry, MTFR1L$^{S103D/S238D}$-P2A-mCherry, and MTFR1L$^{S103A/S238A}$-P2A-mCherry constructs, respectively. 4G: 87, 71, 59, and 77 cells for MTFR1L KO cells stably expressing empty P2A-mCherry, MTFR1L-P2A-mCherry, MTFR1L$^{S103D/S238D}$-P2AmCherry, and MTFR1L$^{S103A/S238A}$-P2A-mCherry constructs, respectively. 4I: 156, 173, 122, and 88 cells for AMPKDKO cells were counted stably expressing empty P2A-mCherry, MTFR1L-P2A-mCherry, MTFR1LS103D/S238D-P2A-mCherry, and MTFR1LS103A/S238A-P2AmCherry constructs, respectively. 4J: 151, 167, 120, and 88 cells for AMPKDKO cells stably expressing empty P2A-mCherry, MTFR1L-P 2A-mCherry, MTFR1LS103D/S238D-P2A-mCherry, and MTFR1LS103A/S238A- P2A-mCherry constructs, respectively.

Figure S8: S8B: *n* = 80 mitochondria for WT and MTFR1L KO cells. S8E: *n* = 64, 130, 110, 98, and 112 cells for WT_DMSO, WT_ ABT/ActD, MTFR1L KO_DMSO, MTFR1L KO_ABT/ActD, and MTFR1L KO_ siOPA1_ABT/ActD, respectively.

Figure S9: S9B: *n* = 207, 192, 147, and 165 cells for WT U2OS cells stably expressing empty P2A-mCherry, MTFR1L-P2A-mCherry, MTFR1LS103D/S238D-P2A-mCherry, and MTFR1LS103A/S238A-P2AmCherry constructs, respectively. S9D: 238, 272, 186, and 209 cells for MTFR1L KO cells stably expressing empty P2A-mCherry, MTFR1L-P2A-mCherry, MTFR1L$^{S103D/S238D}$-P2A-mCherry, and MTFR1L$^{S103A/S238A}$-P2A-mCherry constructs, respectively. S9F: *n* = 331, 296, 270, and 180 cells for AMPKDKO cells stably expressing empty P2A-mCherry, MTFR1L-P2A-mCherry, MTFR1L$^{S103D/S238D}$- P2A-mCherry, and MTFR1L$^{S103A/S238A}$-P2A-mCherry constructs, respectively.

Figure 5: 5B: *n* = 161, 148, 147, 210, 183, and 142 cells for WT_

DMSO, WT_AA, WT_C13, KO_DMSO, KO_AA, and KO_C13, respectively. 5C: *n* = 43, 48, 43, 41, 41, and 38 cells for WT_DMSO, WT_AA, WT_C13, KO_DMSO, KO_AA, and KO_13, respectively. 5D: *n* = 43, 48, 43, 41, 41, and 38 cells for WT_DMSO, WT_AA, WT_C13, KO_DMSO, KO_AA, and KO_C13, respectively.

Figure S10: S10B: *n* = 179, 172, 249, and 167 cells for siNT_DMSO, siNT_AA, siMTFR1L_DMSO, and siMTFR1L_AA, respectively.

Figure S11: S11B: *n* = 186, 182, 171, and 194 cells for siNT_DMSO, siNT_rotenone, siMTFR1L_DMSO, and siMTFR1L_rotenone, respectively.

Figure 6: For cocultures, only one axonal segment was quantified per cell: (B to D) $n_{shNT\_}$ = 22 and $n_{shMTFR1L}$ = 24; (F to H) n_{shNT} = 26, *n*shMTFR1L = 27, *n*shMTFR1L_WT = 21, and *n*shMTFR1L_S103A/238A = 19. The total number of mitochondria per condition was as follows: (B to D) n_{shNT} = 310 and $n_{shMTFR1L}$ = 506; (F to H) n_{shNT} = 248, *n*shMTFR1L = 254, *n*shMTFR1L_WT = 222, and *n*shMTFR1L_S103A/238A = 282. For slices, 33 axonal segments for shNT were quantified across three animals and 31 axonal segments for shMTFR1L. The total number of mitochondria was as follows: (J to L) n_{shNT} = 409 and $n_{shMTFR1L}$ = 441.

Acknowledgements

We acknowledge the facilities and the scientific and administrative assistance from the MRC Mitochondrial Biology Unit, University of Cambridge, UK. We are particularly grateful for the assistance provided by F. Gallo and K. Muller from Cambridge Advanced Imaging Centre, University of Cambridge, UK, for sample

preparation and TEM. We thank A. Gomez Duran and S. Nagashima for insightful scientific advices and P. Chinnery and Z. Golder (Department of Clinical Neurosciences, University of Cambridge, Cambridge, UK) for providing tissues from mice.

Author Contributions

L.T. designed and carried out the experiments, performed statistical analysis, and generated the figures; F.M.R. generated phospho-antibodies against MTFR1L, provided reagents, and performed immunoblots, under the supervision of D.G.H.; S.H. and D.M.V. carried out all experiments in murine neurons, analyzed the data, performed statistical analysis, and generated the figures, under the supervision of F.P.; M.S. contributed to confocal imaging acquisition and fluorescence recovery after photobleaching (FRAP) experiments and wrote the macro for analysis; V.P. contributed to the initial stage of the project; M.P. performed respirometry experiments and analysis; A.V.G. measured ATP/ADP levels, under the supervision of M.P.M.; L.-C.T. analyzed cristae architecture and, with M.J. and H.A., contributed to immunoblot analysis and generated Drp1 KO CRISPR-Cas9 cell line; L.T. and J.P. wrote the manuscript with inputs from all authors; J.P. conceived and oversaw the study.

References

1. L. Tilokani, S. Nagashima, V. Paupe, J. Prudent, Mitochondrial dynamics: Overview of molecular mechanisms. *Essays Biochem.* **62**, 341–360 (2018).
2. T. Wai, T. Langer, Mitochondrial dynamics and metabolic regulation. *Trends Endocrinol. Metab.* **27**, 105–117 (2016).
3. L. C. Tabara, J. L. Morris, J. Prudent, The complex dance of organelles during mitochondrial division. *Trends Cell Biol.* **31**, 241–253 (2021).
4. F. Kraus, K. Roy, T. J. Pucadyil, M. T. Ryan, Function and regulation of the divisome for mitochondrial fission. *Nature* **590**, 57–66 (2021).
5. M. Giacomello, A. Pyakurel, C. Glytsou, L. Scorrano, The cell biology of mitochondrial membrane dynamics. *Nat. Rev. Mol. Cell Biol.* **21**, 204–224 (2020).
6. J. R. Friedman, L. L. Lackner, M. West, J. R. DiBenedetto, J. Nunnari, G. K. Voeltz, ER tubules mark sites of mitochondrial division. *Science* **334**, 358–362 (2011).

7. S. Gandre-Babbe, A. M. van der Bliek, The novel tail-anchored membrane protein MFF controls mitochondrial and peroxisomal fission in mammalian cells. *Mol. Biol. Cell* **19**, 2402–2412 (2008).

8. C. S. Palmer, L. D. Osellame, D. Laine, O. S. Koutsopoulos, A. E. Frazier, M. T. Ryan, MiD49 and MiD51, new components of the mitochondrial fission machinery. *EMBO Rep.* **12**, 565–573 (2011).

9. O. C. Loson, Z. Song, H. Chen, D. C. Chan, Fis1, MFF, MiD49, and MiD51 mediate Drp1 recruitment in mitochondrial fission. *Mol. Biol. Cell* **24**, 659–667 (2013).

10. E. Smirnova, L. Griparic, D. L. Shurland, A. M. van der Bliek, Dynamin-related protein Drp1 is required for mitochondrial division in mammalian cells. *Mol. Biol. Cell* **12**, 2245–2256 (2001).

11. E. Ingerman, E. M. Perkins, M. Marino, J. A. Mears, J. M. McCaffery, J. E. Hinshaw, J. Nunnari, Dnm1 forms spirals that are structurally tailored to fit mitochondria. *J. Cell Biol.* **170**, 1021–1027 (2005).

12. J. A. Mears, L. L. Lackner, S. Fang, E. Ingerman, J. Nunnari, J. E. Hinshaw, Conformational changes in Dnm1 support a contractile mechanism for mitochondrial fission. *Nat. Struct. Mol. Biol.* **18**, 20–26 (2011).

13. Y. C. Wong, D. Ysselstein, D. Krainc, Mitochondria-lysosome contacts regulate mitochondrial fission via RAB7 GTP hydrolysis. *Nature* **554**, 382–386 (2018).

14. S. Nagashima, L.-C. Tábara, L. Tilokani, V. Paupe, H. Anand, J. H. Pogson, R. Zunino, H. M. McBride, J. Prudent, Golgi-derived PI(4)P-containing vesicles drive late steps of mitochondrial division. *Science* **367**, 1366–1371 (2020).

15. S. Cipolat, T. Rudka, D. Hartmann, V. Costa, L. Serneels, K. Craessaerts, K. Metzger, C. Frezza, W. Annaert, L. D'Adamio, C. Derks, T. Dejaegere, L. Pellegrini, R. D'Hooge, L. Scorrano, B. de Strooper, Mitochondrial rhomboid PARL regulates cytochrome c release during apoptosis via OPA1-dependent cristae remodeling. *Cell* **126**, 163–175 (2006).

16. Z. Song, M. Ghochani, J. M. McCaffery, T. G. Frey, D. C. Chan, Mitofusins and OPA1 mediate sequential steps in mitochondrial membrane fusion. *Mol. Biol. Cell* **20**, 3525–3532 (2009).

17. S. Mattie, M. Krols, H. M. McBride, The enigma of an interconnected mitochondrial reticulum: New insights into mitochondrial fusion. *Curr. Opin. Cell Biol.* **59**, 159–166 (2019).

18. T. Koshiba, S. A. Detmer, J. T. Kaiser, H. Chen, J. M. McCaffery, D. C. Chan, Structural basis of mitochondrial tethering by mitofusin complexes. *Science* **305**, 858–862 (2004). 19. T. Ban, T. Ishihara, H. Kohno, S. Saita, A. Ichimura, K. Maenaka, T. Oka, K. Mihara, N. Ishihara, Molecular basis of selective mitochondrial fusion by heterotypic action between OPA1 and cardiolipin. *Nat. Cell Biol.* **19**, 856–863 (2017).

20. J. Nunnari, A. Suomalainen, Mitochondria: In sickness and in health. *Cell* **148**, 1145–1159 (2012).

21. X. Liu, D. Weaver, O. Shirihai, G. Hajnoczky, Mitochondrial 'kiss-and-run': Interplay between mitochondrial motility and fusion-fission dynamics. *EMBO J.* **28**, 3074–3089 (2009).

22. G. Twig, A. Elorza, A. J. A. Molina, H. Mohamed, J. D. Wikstrom, G. Walzer, L. Stiles, S. E. Haigh, S. Katz, G. Las, J. Alroy, M. Wu, B. F. Py, J. Yuan, J. T. Deeney, B. E. Corkey, O. S. Shirihai, Fission and selective fusion govern mitochondrial segregation and elimination by autophagy. *EMBO J.* **27**, 433–446 (2008).

23. R. G. Abrisch, S. C. Gumbin, B. T. Wisniewski, L. L. Lackner, G. K. Voeltz, Fission and fusion machineries converge at ER contact sites to regulate mitochondrial morphology. *J. Cell Biol.* **219**, e201911122 (2020).

24. A. Gonzalez, M. N. Hall, S. C. Lin, D. G. Hardie, AMPK and TOR: The yin and yang of cellular nutrient sensing and growth control. *Cell Metab.* **31**, 472–492 (2020).

25. N. J. Hoffman, B. L. Parker, R. Chaudhuri, K. H. Fisher-Wellman, M. Kleinert, S. J. Humphrey, P. Yang, M. Holliday, S. Trefely, D. J. Fazakerley, J. Stöckli, J. G. Burchfield, T. E. Jensen, R. Jothi, B. Kiens, J. F. P. Wojtaszewski, E. A. Richter, D. E. James, Global phosphoproteomic analysis of human skeletal muscle reveals a network of exercise-regulated kinases and AMPK substrates. *Cell Metab.* **22**, 922–935 (2015).

26. J. C. Drake, R. J. Wilson, R. C. Laker, Y. Guan, H. R. Spaulding, A. S. Nichenko, W. Shen, H. Shang, M. V. Dorn, K. Huang, M. Zhang, A. B. Bandara, M. H. Brisendine, J. A. Kashatus, R. Sharma, A. Young, J. Gautam, R. Cao, H. Wallrabe, P. A. Chang, M. Wong, E. M. Desjardins, S. A. Hawley, G. J. Christ, D. F. Kashatus, C. L. Miller, M. J. Wolf, A. Periasamy, G. R. Steinberg, D. G. Hardie, Z. Yan, Mitochondria-localized AMPK responds to local energetics and contributes to

exercise and energetic stress-induced mitophagy. *Proc. Natl. Acad. Sci. U.S.A.* **118**, e2025932118 (2021).

27. Y. Zong, C.-S. Zhang, M. Li, W. Wang, Z. Wang, S. A. Hawley, T. Ma, J.-W. Feng, X. Tian, Q. Qi, Y.-Q. Wu, C. Zhang, Z. Ye, S.-Y. Lin, H.-L. Piao, D. G. Hardie, S.-C. Lin, Hierarchical activation of compartmentalized pools of AMPK depends on severity of nutrient or energy stress. *Cell Res.* **29**, 460–473 (2019).

28. S. Herzig, R. J. Shaw, AMPK: Guardian of metabolism and mitochondrial homeostasis. *Nat. Rev. Mol. Cell Biol.* **19**, 121–135 (2018).

29. E. Q. Toyama, S. Herzig, J. Courchet, T. L. Lewis Jr., O. C. Losón, K. Hellberg, N. P. Young, H. Chen, F. Polleux, D. C. Chan, R. J. Shaw, AMP-activated protein kinase mediates mitochondrial fission in response to energy stress. *Science* **351**, 275–281 (2016).

30. Z. Chen, C. Lei, C. Wang, N. Li, M. Srivastava, M. Tang, H. Zhang, J. M. Choi, S. Y. Jung, J. Qin, J. Chen, Global phosphoproteomic analysis reveals ARMC10 as an AMPK substrate that regulates mitochondrial dynamics. *Nat. Commun.* **10**, 104 (2019).

31. B. E. Schaffer, R. S. Levin, N. T. Hertz, T. J. Maures, M. L. Schoof, P. E. Hollstein, B. A. Benayoun, M. R. Banko, R. J. Shaw, K. M. Shokat, A. Brunet, Identification of AMPK phosphorylation sites reveals a network of proteins involved in cell invasion and facilitates large-scale substrate prediction. *Cell Metab.* **22**, 907–921 (2015).

32. M. Monticone, I. Panfoli, S. Ravera, R. Puglisi, M.-M. Jiang, R. Morello, S. Candiani, L. Tonachini, R. Biticchi, A. Fabiano, R. Cancedda, C. Boitani, P. Castagnola, The nuclear genes Mtfr1 and Dufd1 regulate mitochondrial dynamic and cellular respiration. *J. Cell. Physiol.* **225**, 767–776 (2010).

33. L. Tonachini, M. Monticone, C. Puri, C. Tacchetti, P. Pinton, R. Rizzuto, R. Cancedda, S. Tavella, P. Castagnola, Chondrocyte protein with a poly-proline region (CHPPR) is a novel mitochondrial protein and promotes mitochondrial fission. *J. Cell. Physiol.* **201**, 470–482 (2004).

34. K. Wang, D.-L. Zhang, B. Long, T. An, J. Zhang, L.-Y. Zhou, C.-Y. Liu, P.-F. Li, NFAT4dependent miR-324-5p regulates mitochondrial morphology and cardiomyocyte cell death by targeting Mtfr1. *Cell Death Dis.* **6**, e2007 (2015).

35. Y. Li, Y. Liu, K. Jin, R. Dong, C. Gao, L. Si, Z. Feng, H. Zhang, H. Tian, Negatively regulated by miR-29c-3p, MTFR1 promotes the progression and glycolysis in lung adenocarcinoma via the AMPK/mTOR signalling pathway. *Front. Cell Dev. Biol.* **9**, 771824 (2021).

36. P. Chen, J. Zhong, J. Ye, Y. He, Z. Liang, Y. Cheng, J. Zheng, H. Chen, C. Chen, miR-324-5p protects against oxidative stress-induced endothelial progenitor cell injury by targeting Mtfr1. *J. Cell. Physiol.* **234**, 22082–22092 (2019).

37. Y. Luo, S.-T. Liu, MTFR2 regulates mitochondrial fission and impacts spindle integrity during mitosis. bioRxiv 2020.09.13.293621 [Preprint]. 13 September 2020. https://doi.org/10.1101/2020.09.13.293621.

38. G. Lu, Y. Lai, T. Wang, W. Lin, J. Lu, Y. Ma, Y. Chen, H. Ma, R. Liu, J. Li, Mitochondrial fission regulator 2 (MTFR2) promotes growth, migration, invasion and tumour progression in breast cancer cells. *Aging (Albany NY)* **11**, 10203–10219 (2019).

39. W. Wang, M. Xiong, L. Jiang, Z. Chen, Y. Shao, MTFR2 promotes the proliferation, migration, and invasion of oral squamous carcinoma by switching OXPHOS to glycolysis. *Front. Oncol.* **10**, 858 (2020).

40. A. Janer, J. Prudent, V. Paupe, S. Fahiminiya, J. Majewski, N. Sgarioto, C. Des Rosiers, A. Forest, Z.-Y. Lin, A.-C. Gingras, G. Mitchell, H. M. McBride, E. A. Shoubridge, SLC25A46 is required for mitochondrial lipid homeostasis and cristae maintenance and is responsible for Leigh syndrome. *EMBO Mol. Med.* **8**, 1019–1038 (2016).

41. D. G. Hardie, B. E. Schaffer, A. Brunet, AMPK: An energy-sensing pathway with multiple inputs and outputs. *Trends Cell Biol.* **26**, 190–201 (2016).

42. G. H. Patterson, J. Lippincott-Schwartz, A photoactivatable GFP for selective photolabeling of proteins and cells. *Science* **297**, 1873–1877 (2002).

43. E. Braschi, R. Zunino, H. M. McBride, MAPL is a new mitochondrial SUMO E3 ligase that regulates mitochondrial fission. *EMBO Rep.* **10**, 748–754 (2009).

44. R. Yu, S. B. Jin, U. Lendahl, M. Nister, J. Zhao, Human Fis1 regulates mitochondrial dynamics through inhibition of the fusion machinery. *EMBO J.* **38**, e99748 (2019).

45. C. Glytsou, E. Calvo, S. Cogliati, A. Mehrotra, I. Anastasia, G. Rigoni, A. Raimondi, N. Shintani, M. Loureiro, J. Vazquez, L. Pellegrini, J. A. Enriquez, L. Scorrano, M. E. Soriano, Optic atrophy 1 is epistatic to the core MICOS component MIC60 in mitochondrial cristae shape control. *Cell Rep.* **17**, 3024–3034 (2016).

46. B. Gottschalk, C. Klec, G. Leitinger, E. Bernhart, R. Rost, H. Bischof, C. T. Madreiter-Sokolowski, S. Radulović, E. Eroglu, W. Sattler, M. Waldeck-Weiermair, R. Malli, W. F. Graier, MICU1 controls cristae junction and spatially anchors mitochondrial Ca^{2+} uniporter complex. *Nat. Commun.* **10**, 3732 (2019).

47. S. Frank, B. Gaume, E. S. Bergmann-Leitner, W. W. Leitner, E. G. Robert, F. Catez, C. L. Smith, R. J. Youle, The role of dynamin-related protein 1, a mediator of mitochondrial fission, in apoptosis. *Dev. Cell* **1**, 515–525 (2001).

48. R. Quintana-Cabrera, C. Quirin, C. Glytsou, M. Corrado, A. Urbani, A. Pellattiero, E. Calvo, J. Vázquez, J. A. Enríquez, C. Gerle, M. E. Soriano, P. Bernardi, L. Scorrano, The cristae modulator Optic atrophy 1 requires mitochondrial ATP synthase oligomers to safeguard mitochondrial function. *Nat. Commun.* **9**, 3399 (2018).

49. S. A. Hawley, F. A. Ross, F. M. Russell, A. Atrih, D. J. Lamont, D. G. Hardie, Mechanism of activation of AMPK by cordycepin. *Cell Chem. Biol.* **27**, 214–222.e4 (2020).

50. B. Xiao, M. J. Sanders, D. Carmena, N. J. Bright, L. F. Haire, E. Underwood, B. R. Patel, R. B. Heath, P. A. Walker, S. Hallen, F. Giordanetto, S. R. Martin, D. Carling, S. J. Gamblin, Structural basis of AMPK regulation by small molecule activators. *Nat. Commun.* **4**, 3017 (2013).

51. B. Cool, B. Zinker, W. Chiou, L. Kifle, N. Cao, M. Perham, R. Dickinson, A. Adler, G. Gagne, R. Iyengar, G. Zhao, K. Marsh, P. Kym, P. Jung, H. S. Camp, E. Frevert, Identification and characterization of a small molecule AMPK activator that treats key components of type 2 diabetes and the metabolic syndrome. *Cell Metab.* **3**, 403–416 (2006).

52. R. W. Hunter, M. Foretz, L. Bultot, M. D. Fullerton, M. Deak, F. A. Ross, S. A. Hawley, N. Shpiro, B. Viollet, D. Barron, B. E. Kemp, G. R. Steinberg, D. G. Hardie, K. Sakamoto, Mechanism of action of compound-13: An α1-selective small molecule activator of AMPK. *Chem. Biol.* **21**, 866–879 (2014).

53. J. E. Gomez-Galeno, Q. Dang, T. H. Nguyen, S. H. Boyer, M. P. Grote, Z. Sun, M. Chen, W. A. Craigo, P. D. van Poelje, D. A. MacKenna, E. E. Cable, P. A. Rolzin, P. D. Finn, B. Chi, D. L. Linemeyer, S. J. Hecker, M. D. Erion, A potent and selective AMPK activator that inhibits de novo lipogenesis. *ACS Med. Chem. Lett.* **1**, 478–482 (2010).

54. T. L. Lewis Jr., S. K. Kwon, A. Lee, R. Shaw, F. Polleux, MFF-dependent mitochondrial fission regulates presynaptic release and axon branching by limiting axonal mitochondria size. *Nat. Commun.* **9**, 5008 (2018).

55. H. Otera, N. Miyata, O. Kuge, K. Mihara, Drp1-dependent mitochondrial fission via MiD49/51 is essential for apoptotic cristae remodeling. *J. Cell Biol.* **212**, 531–544 (2016).

56. A. S. Rambold, B. Kostelecky, N. Elia, J. Lippincott-Schwartz, Tubular network formation protects mitochondria from autophagosomal degradation during nutrient starvation. *Proc. Natl. Acad. Sci. U.S.A.* **108**, 10190–10195 (2011).

57. L. C. Gomes, G. Di Benedetto, L. Scorrano, During autophagy mitochondria elongate, are spared from degradation and sustain cell viability. *Nat. Cell Biol.* **13**, 589–598 (2011).

58. M. Morita, J. Prudent, K. Basu, V. Goyon, S. Katsumura, L. Hulea, D. Pearl, N. Siddiqui, S. Strack, S. M. Guirk, J. St-Pierre, O. Larsson, I. Topisirovic, H. Vali, H. M. McBride, J. J. Bergeron, N. Sonenberg, mTOR controls mitochondrial dynamics and cell survival via MTFP1. *Mol. Cell* **67**, 922–935.e5 (2017).

59. K. Ma, G. Chen, W. Li, O. Kepp, Y. Zhu, Q. Chen, Mitophagy, mitochondrial homeostasis, and cell fate. *Front. Cell Dev. Biol.* **8**, 467 (2020).

60. M. Karbowski, Y.-J. Lee, B. Gaume, S.-Y. Jeong, S. Frank, A. Nechushtan, A. Santel, M. Fuller, C. L. Smith, R. J. Youle, Spatial and temporal association of Bax with mitochondrial fission sites, Drp1, and Mfn2 during apoptosis. *J. Cell Biol.* **159**, 931–938 (2002).

61. D. A. Patten, J. Wong, M. Khacho, V. Soubannier, R. J. Mailloux, K. Pilon-Larose, J. G. MacLaurin, D. S. Park, H. M. McBride, L. Trinkle-Mulcahy, M.-E. Harper, M. Germain, R. S. Slack, OPA1-dependent cristae modulation is essential for cellular adaptation to metabolic demand. *EMBO J.* **33**, 2676–2691 (2014).

62. D. Tondera, S. Grandemange, A. Jourdain, M. Karbowski, Y. Mattenberger, S. Herzig, S. da Cruz, P. Clerc, I. Raschke, C. Merkwirth, S. Ehses, F. Krause, D. C. Chan, C. Alexander, C. Bauer, R. Youle, T. Langer, J.-C. Martinou, SLP-2 is required for stress-induced mitochondrial hyperfusion. *EMBO J.* **28**, 1589–1600 (2009).

63. J. Lebeau, J. M. Saunders, V. W. R. Moraes, A. Madhavan, N. Madrazo, M. C. Anthony, R. L. Wiseman, The PERK arm of the unfolded protein response regulates mitochondrial morphology during acute endoplasmic reticulum stress. *Cell Rep.* **22**, 2827–2836 (2018). 64. J. He, X. Shangguan, W. Zhou, Y. Cao, Q. Zheng, J. Tu, G. Hu, Z. Liang, C. Jiang, L. Deng, S. Wang, W. Yang, Y. Zuo, J. Ma, R. Cai, Y. Chen, Q. Fan, B. Dong, W. Xue, H. Tan, Y. Qi, J. Gu, B. Su, Y. Eugene Chin, G. Chen, Q. Wang, T. Wang, J. Cheng, Glucose limitation activates AMPK coupled SENP1-Sirt3 signalling in mitochondria for T cell memory development. *Nat. Commun.* **12**, 4371 (2021).

65. L. Z. Qiu, W. Zhou, L.-X. Yue, Y.-H. Wang, F.-R. Hao, P.-Y. Li, Y. Gao, Repeated aconitine treatment induced the remodeling of mitochondrial function via AMPK-OPA1-ATP5A1 pathway. *Front. Pharmacol.* **12**, 646121 (2021).

66. M. Wang, R.-Y. Wang, J.-H. Zhou, X.-H. Xie, G.-B. Sun, X.-B. Sun, Calenduloside E ameliorates myocardial ischemia-reperfusion injury through regulation of AMPK and mitochondrial OPA1. *Oxid. Med. Cell. Longev.* **2020**, 2415269 (2020).

67. T. Varanita, M. E. Soriano, V. Romanello, T. Zaglia, R. Quintana-Cabrera, M. Semenzato, R. Menabò, V. Costa, G. Civiletto, P. Pesce, C. Viscomi, M. Zeviani, F. di Lisa, M. Mongillo, M. Sandri, L. Scorrano, The OPA1-dependent mitochondrial cristae remodeling pathway controls atrophic, apoptotic, and ischemic tissue damage. *Cell Metab.* **21**, 834–844 (2015). 68. G. Civiletto, T. Varanita, R. Cerutti, T. Gorletta, S. Barbaro, S. Marchet, C. Lamperti, C. Viscomi, L. Scorrano, M. Zeviani, Opa1 overexpression ameliorates the phenotype of two mitochondrial disease mouse models. *Cell Metab.* **21**, 845–854 (2015).

69. T. L. Lewis Jr., G. F. Turi, S. K. Kwon, A. Losonczy, F. Polleux, Progressive decrease of mitochondrial motility during maturation of cortical axons in vitro and in vivo. *Curr. Biol.* **26**, 2602–2608 (2016).

70. R. Hand, F. Polleux, Neurogenin2 regulates the initial axon guidance of cortical pyramidal neurons projecting medially to the corpus callosum. *Neural Dev.* **6**, 30 (2011).

71. J. Courchet, T. L. Lewis Jr., S. Lee, V. Courchet, D.-Y. Liou, S. Aizawa, F. Polleux, Terminal axon branching is regulated by the LKB1-NUAK1 kinase pathway via presynaptic mitochondrial capture. *Cell* **153**, 1510–1525 (2013).

72. M. C. Lee, M. S. Nahorski, J. R. F. Hockley, V. B. Lu, G. Ison, L. A. Pattison, G. Callejo, K. Stouffer, E. Fletcher, C. Brown, I. Drissi, D. Wheeler, P. Ernfors, D. Menon, F. Reimann, E. St. John Smith, C. Geoffrey Woods, Human labor pain is influenced by the voltagegated potassium channel K_V6.4 subunit. *Cell Rep.* **32**, 107941 (2020).

73. A. J. Lam, F. St-Pierre, Y. Gong, J. D. Marshall, P. J. Cranfill, M. A. Baird, M. R. McKeown, J. Wiedenmann, M. W. Davidson, M. J. Schnitzer, R. Y. Tsien, M. Z. Lin, Improving FRET dynamic range with bright green and red fluorescent proteins. *Nat. Methods* **9**, 1005–1012 (2012).

74. D. Pesta, E. Gnaiger, High-resolution respirometry: OXPHOS protocols for human cells and permeabilized fibers from small biopsies of human muscle. *Methods Mol. Biol.* **810**, 25–58 (2012).

75. B. L. Strehler, Basic mechanisms of aging: Aging and the utilization of informational patterns. *Scand. J. Clin. Lab. Invest. Suppl.* **65**, 25–32 (1974).

76. C. Tezze, V. Romanello, M. A. Desbats, G. P. Fadini, M. Albiero, G. Favaro, S. Ciciliot, M. E. Soriano, V. Morbidoni, C. Cerqua, S. Loefler, H. Kern, C. Franceschi, S. Salvioli, M. Conte, B. Blaauw, S. Zampieri, L. Salviati, L. Scorrano, M. Sandri, Age-associated loss of OPA1 in muscle impacts muscle mass, metabolic homeostasis, systemic inflammation, and epithelial senescence. *Cell Metab.* **25**, 1374–1389.e6 (2017).

77. Y. Zhang, A. Lanjuin, S. R. Chowdhury, M. Mistry, C. G. Silva-García, H. J. Weir, C.-L. Lee, C. C. Escoubas, E. Tabakovic, W. B. Mair, Neuronal TORC1 modulates longevity via AMPK and cell nonautonomous regulation of mitochondrial dynamics in *C. elegans*. *eLife* **8**, e49158 (2019).

78. R. Zunino, A. Schauss, P. Rippstein, M. Andrade-Navarro, H. M. McBride, The SUMO protease SENP5 is required to maintain mitochondrial morphology and function. *J. Cell Sci.* **120**, 1178–1188 (2007).

79. R. Anand, T. Wai, M. J. Baker, N. Kladt, A. C. Schauss, E. Rugarli, T. Langer, The i-AAA protease YME1L and OMA1 cleave OPA1 to balance mitochondrial fusion and fission. *J. Cell Biol.* **204**, 919–929 (2014).

Appendix B: Axon morphogenesis and maintenance require an evolutionary conserved safeguard of Wnk kinases antagonizing Sarm and Axed

Azadeh Izadifar, Julien Courchet, **Daniel M. Virga**, Tine Verreet, Stevie Hamilton, Derya Ayaz, Anke Misbaer, Sofie Vandenbogaerde, Laloe Monteiro, Milan Petrovic, Sonja Sachse, Bing Yan, Maria-Luise Erfurth, Dan Dascenco, Yoshiaki Kise, Jiekun Yan, Gabriela Edwards-Faret, Tommy Lewis, Franck Polleux, and Dietmar Schmucker (2021) Neuron 109, 2864-2883.
https://doi.org/10.1016/j.neuron.2021.07.006

There has been extensive research into the molecular mechanisms of both axonal development and injury-induced or disease pathology-induced axonal degeneration. However, few studies have identified effectors that are necessary for axonal maintenance. Using a genetic screen, we identified a novel axon development and maintenance protein, WNK, in Drosophila and confirmed it's conserved function mammalian neurons such that loss of this protein is sufficient to prevent axonal branching and induce spontaneous axonal degeneration.

For this study, I conceived of, performed, and configured all of the murine experiments featured in the main text (Figure 4, Figure 5, Figure 6, Supplemental Figure S8), quantified in full Figure 5 and Figure 6, quantified in part Figure 4. This required development of a novel longitudinal imaging assay (Figure 5) and development of a novel, inducible shRNA reporter construct (Figure 6). I also drafted all of the corresponding figures, legends, results, and materials and methods for these experiments, and edited the rest of the manuscript. This work was published in its entirety in Neuron in 2021.

Abstract

The molecular and cellular mechanisms underlying complex axon morphogenesis are still poorly understood. We report a novel, evolutionary conserved function for the Drosophila Wnk kinase (dWnk) and its mammalian orthologs, WNK1 and 2, in axon branching. We uncover that dWnk, together with the neuroprotective factor Nmnat, antagonizes the axon-destabilizing factors D-Sarm and Axundead (Axed) during axon branch growth, revealing a developmental function for these proteins. Overexpression of D-Sarm or Axed results in axon branching defects, which can be blocked by overexpression of dWnk or Nmnat. Surprisingly, Wnk kinases are also required for axon maintenance of adult Drosophila and mouse cortical pyramidal neurons. Requirement of Wnk for axon maintenance is independent of its developmental function. Inactivation of dWnk or mouse Wnk1/2 in mature neurons leads to axon degeneration in the adult brain. Therefore, Wnk kinases are novel signaling components that provide a safeguard function in both developing and adult axons.

Introduction

A hallmark in the generation of neuronal cell type diversity is the acquisition of diverse morphologies, which requires the formation of axonal and dendritic compartments ranging from simple to highly complex, depending on the degree of neurite branching. Specifying the degree and pattern of neurite branching is crucial in brain development, as it directly impacts the total number and spatial distribution of synaptic contacts of each circuit element (Courchet et al., 2013; Iascone et al., 2020; Chia et al., 2014; Urwyler et al., 2019). However, the identity of the molecular effectors determining how diverse, cell-type-specific patterns of axon arborization are established and how they are stabilized as well as maintained throughout the life of an organism remains a major challenge (Südhof, 2017).

We performed a reverse genetic screen to identify novel regulators of axon branching by utilizing an experimental system in Drosophila that combines efficient single-neuron labeling and simultaneous knockdown of candidate genes (Urwyler et al., 2019). Clear orthologs of selective candidates were then further examined in vertebrates. Using this approach, we found that loss of the Drosophila dWnk kinase specifically disrupts axon growth and branch patterning of mechanosensory neurons. Surprisingly, unlike other essential regulators of axon branching (Sudarsanam et al., 2020; He et al., 2014; Dascenco et al., 2015; Lewis et al., 2013), we discovered that dWnk is also continuously required in mature neurons for

axon maintenance. Moreover, comparative studies in mouse cortical pyramidal neurons (PNs) provide strong evidence that both of these functions of Wnk kinases are conserved and required in PNs, i.e., long-range projecting mammalian neurons of the central nervous system (CNS).

Wnk kinases are present in most multicellular organisms, including plants and some unicellular organisms, but not in yeast (Hoorn et al., 2011; McCormick and Ellison, 2011). Mammals have four Wnk kinases (WNK1–4) and Drosophila one (dWnk). The WNK (‘‘with no K(lysine)’’) kinases are catalytically active but are referred to as ‘‘atypical kinases’’ because a catalytically important lysine residue is swapped from subdomain II to subdomain I (Xu et al., 2000; Verissimo and Jordan, 2001). WNK proteins are involved in a broad spectrum of diseases (e.g., hypertension, sensory and autonomic neuropathy, osteoporosis, and many different cancers; McCormick and Ellison, 2011; Alessi et al., 2014; Siew and O’Shaughnessy, 2013; Sato and Shibuya, 2018).

The majority of studies on human WNK kinases have been conducted in the context of blood pressure regulation, due to the identification of mutations in human patients with hereditary hypertension (familial hyperkalemia and hypertension [FHHt] or Gordon’s syndrome; Wilson et al., 2001). For this reason, a major focus in dissecting WNK function has been on studying renal regulation of ion transport (Alessi et al., 2014; Yang et al., 2003; Pela, 2012; Vidal-Petiot et al., 2013; Jun et al., 2009; Costa et al., 2015). However, regulation of ion homeostasis is only one of multiple functions of WNK kinases (Siew and O’Shaughnessy, 2013; Gallolu et al., 2018), and they are broadly expressed, including in the developing as well as mature brain. In rare cases, WNK function has been linked to a severe form of peripheral sensory neuropathy (hereditary sensory and autonomic neuropathy type 2, HSNA2; Lafreniere et al., 2004; Rivière et al., 2004; Roddier et al., 2005; Coen et al., 2006); however, their developmental, cellular, and molecular mechanisms are poorly understood in neurons. The fact, however, that most identified mutations cluster in a neuron-specific alternatively spliced exon (HSN2) of human Wnk1 supports the notion that Wnk1 kinase plays an important role in sensory neurons (Shekarabi et al., 2008; Yuan et al., 2017; Rahmani et al., 2018).

In the process of studying the role of dWnk kinase in fly sensory neurons, we identified novel interactors of Wnk kinases. Specifically, we found that nicotinamide mononucleotide adenylyltransferase (Nmnat), Sarm, and Axundead (Axed) are molecular interactors of dWnk. While Nmnat is broadly required for axon maintenance, Sarm and Axed are primarily studied for their roles as effectors in active axon

degeneration (e.g., in Wallerian degeneration) in response to axon injury (Coleman and Freeman, 2010; Gilley and Coleman, 2010; Neukomm et al., 2017; Osterloh et al., 2012). We provide evidence that dWnk and Nmnat have synergistic functions in axon growth and branching but are also required in postdevelopmental processes to continuously support axon maintenance. The function of dWnk is evolutionarily conserved, as their mouse orthologs WNK1 and WNK2 are both required in cortical PNs during axon morphogenesis as well as maintenance. Genetic epistasis analysis demonstrates that both dWnk and Nmnat functions during axon development and axon maintenance are mediated by antagonizing the axon destruction function of Sarm and Axed. Depletion of axonprotective factors (e.g., dWnk/WNK1/2 and Nmnat) during development leads to axon branching defects, whereas their depletion in mature neurons eliminates their safeguard function and initiates spontaneous axon degeneration in the absence of axon injury.

Results

Wnk is required for axonal branch patterning in fly mechanosensory neurons

To identify signaling factors regulating axon branching during CNS development, we focused on the central projections of Drosophila mechanosensory neurons that innervate sensory bristles of the adult fly thorax (Figures 1A and 1B). Mechanosensory neurons from the central domain of the thorax all extend axonal projections to the ventral nerve cord (VNC), where they establish a cell-type-specific and stereotyped axonal branching pattern (Chen et al., 2006). Single-cell labeling using either lipophilic dye fills (Chen et al., 2006) or genetic mosaic labeling (He et al., 2014; Urwyler et al., 2015) allows the visualization of the precise axonal branching pattern within the VNC (Figures 1B and 1D). In a reverse genetic screen, we examined the potential role of the majority of Drosophila kinases as well as phosphatases (Dascenco et al., 2015) and found that RNAi-mediated knockdown of Drosophila Wnk kinase (dWnk) leads to a rather unique phenotype characterized by strong impairment of axonal

Figure 1

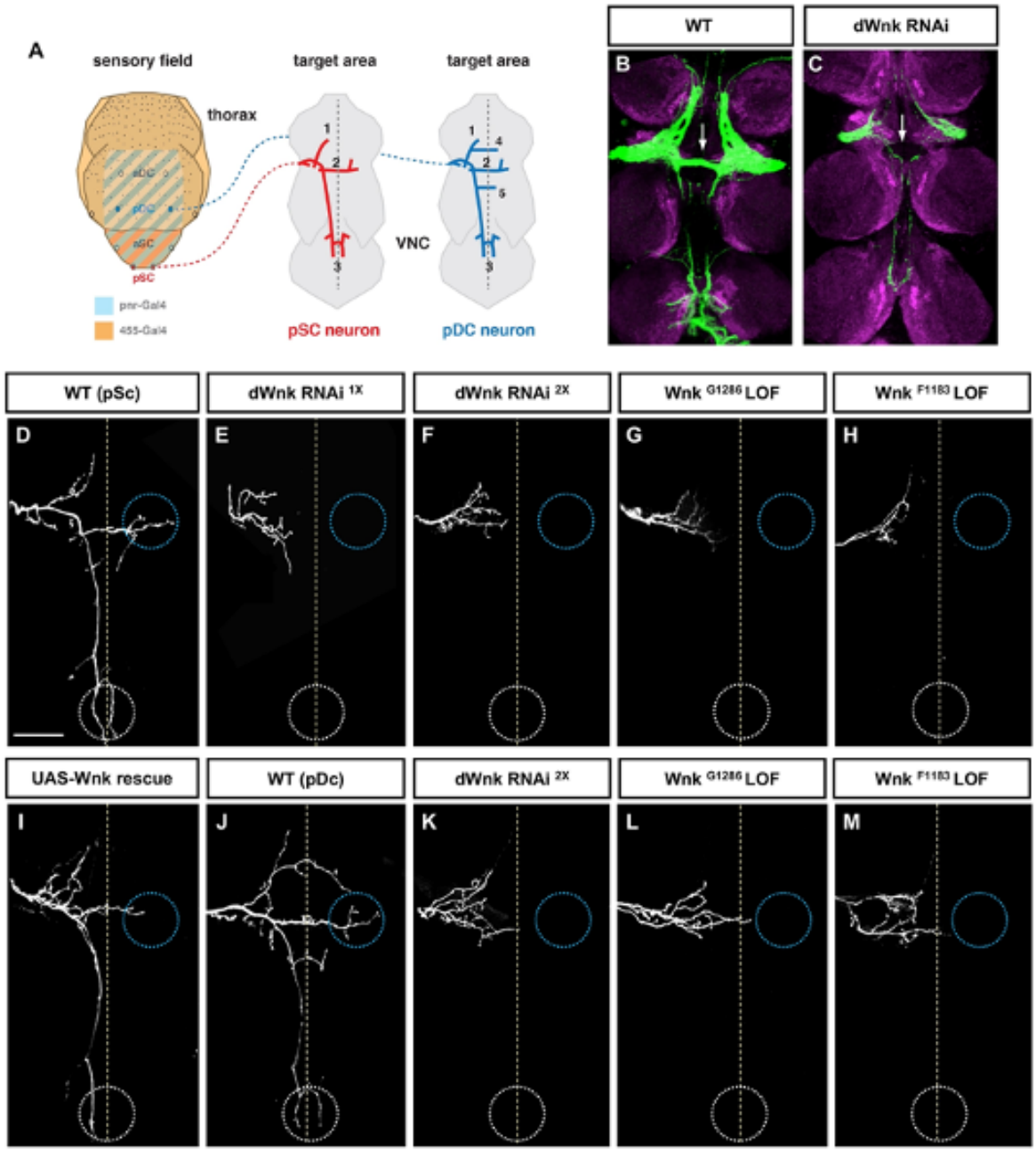

Figure 1. Loss of *Drosophila* dWnk results in axon branching defects in mechanosensory neurons.
(A) Stereotyped branching pattern of *Drosophila* mechanosensory neurons. **(B and C)** GFP- labeled population of ms-axons within the anterior part of the VNC. Note the complete lack of commissure (white arrows) in dWnk RNAi knock down. **(D to M)** Representative confocal images of mechanosensory neurons dye-filled with carbocyanine dyes. **(D and J)** WT pSc and pDc mechanosensory neurons displaying the stereotyped branching pattern. **(E, F and K)** dWnk RNAi and double RNAi (RNAi ^{2X}) mediated knock-down defects results in branching defects. **(I)** Overexpression of dWnk can rescue branching defects in dWnk LOF. **(G, H, L, M)** dWnk LOF phenotypes using MARCM clones of two dWnk alleles, Wnk ^{G1286} and Wnk ^{F1183} also lead to defects in axon branch growth and patterning.

branching of many mechanosensory axon projections (Figures 1B and 1C). Specifically, knockdown of dWnk in posterior scutellar (pSC) mechanosensory neurons strongly impaired axon collateral formation and patterning within the Drosophila CNS (Figures 1D–1F). In mutant axons, extensions of collaterals alon g the long posterior and contralateral projections were almost absent. Instead, a plexus of unpatterned and seemingly randomly projecting short axon branches were formed (Figures 1E and 1F).

We next examined two dWnk loss-of-function (LOF) alleles (Wnk^{G1286} and Wnk^{F1183}) using mosaic analysis with a repressible cell marker (MARCM). These LOF alleles harbor ethyl methanesulfonate-induced point mutations, resulting in strong (Wnk^{G1286}) or complete (Wnk^{F1183}) LOF (Figure S1), and have previously been characterized (Berger et al., 2008). Anti-Wnk antibodies show that dWnk is broadly expressed throughout the nervous system (Figures S1D–S1F and S2A–S2D) and absent in homozygous WnkF1183 animals (Figures S1B–S1G). Immunostaining reveals that endogenous dWnk protein localizes to the cytoplasm and also throughout axonal processes, including growth cones (Figures S2E–S2H). Single-cell labeling in both homozygous mutant pSc neurons (Figures 1G and 1H) revealed qualitatively similar axon branching defects as found by RNAi-mediated knockdown of dWnk (Figures 1E and 1F). These defects were substantially rescued cell autonomously by overexpression of dWnk cDNA in mechanosensory neurons (Figure 1I). Moreover, an analogous analysis of a functionally similar yet different mechanosensory neuron, the posterior dorsocentral neuron (pDc) (Figure 1A), revealed similar defects of axon branching as found in pSc neurons (Figures 1J–1M). Moreover, analysis of other neuron types using knockdown or LOF alleles revealed a strong requirement of dWnk in olfactory sensory neurons with defects in axon growth, branching, and targeting (Figures S3A–S3F). In addition to these requirements in sensory neurons, dWnk is also required in interneurons of the visual system (DCN; Figures S3G and S3H). Analysis of dorsal cluster neurons (DCN) neurons suggests the possibility that dWnk is primarily important for axon branch extension within the target area, but not in growth or branching of the dendritic compartment. Analysis of MARCM clones of DCN neurons in adult flies (Figures S3I and S3J) as well as clones of dorsal arborization neurons (ddaE-class I sensory neurons) in larvae did not reveal any defects in dendrite patterning of these neurons (Figures S3K and S3L). Taken together, this suggests a cell-autonomous requirement of Drosophila Wnk in multiple sensory and interneuron types and that this function is specific to axon morphogenesis.

Loss of dWnk in mechanosensory neurons leads to early-onset axon degeneration in adult flies

The phenotypic effects on axon branching characterizing dWnk RNAi knockdown or MARCM clones for strong LOF alleles were similar (Figures 1C, 1E–1H, and 1K–1M). However, we noted that many samples of flies with Wnk^{G1286} or Wnk^{F1183} mutant mechanosensory neurons and in particular samples older than 2 days (post-eclosion) had no axonal projections within the VNC target area (Figure 2).

We therefore determined quantitatively the number of samples where mutant axons had reached the VNC in adult flies at different time points post-eclosion (Figures 2D–2H). Within the first 24 h (<day 1) after eclosion, ~40% of Wnk^{F1183} and ~80% of Wnk^{G1286} mutant neurons still had central axonal projections in the VNC. In all samples where an axon was present in the VNC target area, we observed strong axon branching defects similar to the RNAi knockdown samples (Figures 2D–2F). In older adult flies, however, no axon or only traces of remaining axon branches were detectable in Wnk^{F1183} mutant neurons and very few in Wnk^{G1286} mutant neurons (Figures 2G and 2H), suggesting a progressive loss of axons over time.

In contrast, either at day 1 or in older flies, we never observed a loss of axons in the VNC of flies expressing a single copy of upstream activating sequence (UAS)-dWnk RNAi (dWnk $RNAi^{1x}$), despite strong and highly penetrant axon branching defects (Figure 1E; left panel of Figure 2H). Therefore, we examined whether enhancing the RNAi-mediated knockdown of dWnk would initiate degeneration. Indeed, using two copies of UAS-dWnk RNAi (dWnk $RNAi^{2x}$) did lead to a 50% reduction of distal axons in the respective samples compared to controls or single-copy UAS-dWnk RNAi (Figure 2H). These results suggest a dose dependence of dWnk expression for proper axon maintenance in mechanosensory neurons. However, the axon branching defects displayed little phenotypic variability because they were observed in all RNAi or LOF alleles examined (see above; Figure 1 and left panel of Figure 2H). In contrast, the degeneration following the loss of dWnk function showed significant allelic differences; appeared to be progressive; and, only in mutants carrying the strongest loss of dWnk allele, all axons had degenerated in 3 days or older flies (Figure 2H).

Figure 2

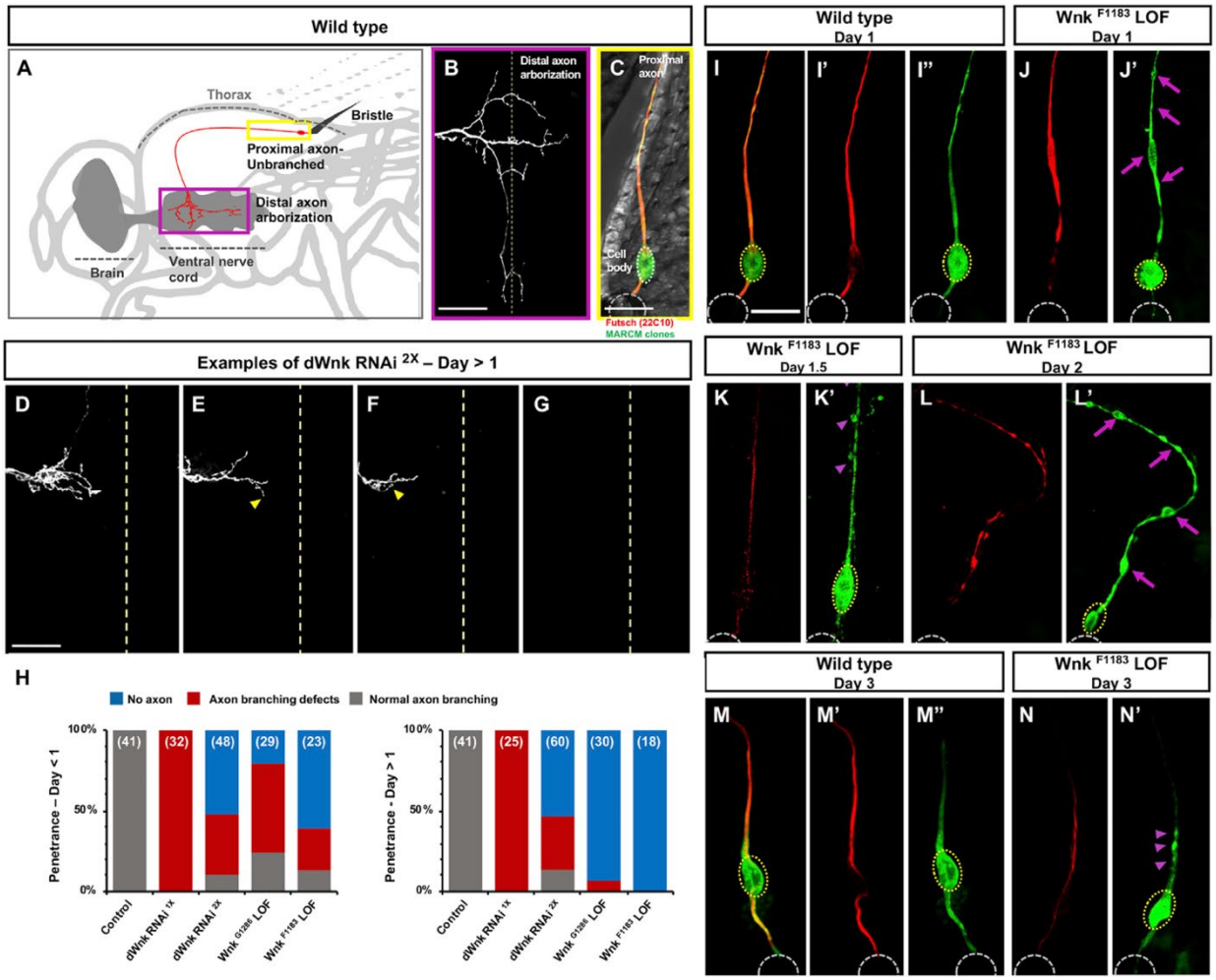

Figure 2. Loss of *Drosophila* dWnk function causes early onset neurodegeneration in mature sensory neurons and progressive loss of axons on thorax. (A) schematic of Drosophila thorax show the location of the scutellar mechaosensory neurons (green box) with a part of the proximal axon (dashed line in blue), cell body, dendrite (blue box) and distal axon in the ventral nerve cord (green box). **(B)** magnified image of distal axon showing barbarization of mechanosensory neurons. **(C)** a part of scutellum of adult *Drosophila* thorax (in gray) with anti22C10 (microtubule binding protein) staining labeling of mechanosensory neuron (here pSc neurons). 22C10 labels all axons in red and the CD8-GFP labeling axon membrane **(C, I to O)**. **(D to G)** Loss of axon terminals in *Drosophila* mechanosensory neurons between 1 and 3 days in dWnk LOF. The axon degeneration in loss of dWnk knock down neurons starts at day 1 **(D)** followed by degeneration of distal axons **(E and F)**, and resulted in loss of axons in three days old samples **(G)**. **(H)** Quantification of the total number of degeneration processes in RNAi-mediated knock-down of dWnk (one copy and two copies and two different Wnk alleles ($WnkG^{1286}$ and $WnkF^{1183}$) at two developmental stages, one day and three days **(I to O)** process of axon degeneration in wild type **(I and M)** and dWnk homozygous mutant neurons using MARCM **(J-L and N-O)** in different developmental stages. **(J and L)** Genetic mosaic analysis shows that loss of dWnk leads to axon swelling and blebbing (arrows in magenta). Then, the axon starts to undergo fragmentation (arrow heads in magenta) **(K)**, followed by complete fragmentation and clearance of axonal debris **(N and O)**.

To better characterize the progressive nature of the axon degeneration phenotype due to dWnk LOF, we took advantage of the fact that we could visualize and identify the proximal part of the main axon (unbranched axon) close to the cell body (Figures 2A and 2C) through the thin cuticle of the thorax by using singleneuron GFP expression and antibody-based detection of microtubule organization (using anti-22C10 antibody against Futsch, a microtubule-associated protein in Drosophila neurons; Figure 2C). We examined wild-type and dWnk mutant neurons (dendrite, soma, and axon) in the scutellar part of adult flies (Figures 2I–2N).

We detected a near continuous labeling of the axon and microtubule cytoskeleton using membrane-tethered CD8-GFP and anti-22C10 antibody staining in wild-type control samples (Figures 2I and 2M). In contrast, dWnk mutant neurons showed moderate signs of axonal degeneration already in 1-day-old flies (Figure 2J). In particular, in mutant neurons with strong dWnk LOF, the severity of axonal defects correlated with the age of the flies (Figures 2L and 2N). In 3-day-old mutant neurons, we often detected only segments of the most proximal axon and membrane blebbing or loss of cytoskeletal integrity were prominent (Figure 2N). These results provide evidence that loss of dWnk in mechanosensory neurons triggers progressive and spontaneous axon degeneration.

It seems plausible that the distal axon branching defects within the VNC lead directly to axon degeneration, possibly as a consequence of losing target-derived trophic support once these mechanosensory axons reached the CNS.

Nevertheless, to test more directly an adult-specific requirement for axon maintenance, we induced RNAi-dependent knockdown of dWnk following the completion of axon branching at the end of pupal stages (Figures S4A and S4B). We used temperature shifts to control the timing of RNAi expression such that dWnk expression is either absent during larval and early pupal stages, which reproduced the axon branching followed by axon degeneration as shown above (Figures S4B–S4E), or present during the developmental phase of axon growth and branching but absent starting at late pupal and adult stages (Figures S4B, S4C, S4F, and S4G). Indeed, the latter manipulation, i.e., a late knockdown of dWnk, did not disrupt the axon branch patterning at early stages (Figures S4B, S4C, and S4F) but clearly triggered axon degeneration of adult mechanosensory neurons 3–5 days after hatching (Figure S4G). This temporal

dissection of dWnk knockdown supports the model of a requirement of adult expression of dWnk for axon maintenance, independent of its role in axon development.

In summary, dWnk mutant mechanosensory axons can grow from the periphery to the VNC but require dWnk function during axonal branch growth and patterning of its arborization in the VNC target area.

Loss of dWnk impairs axonal branch extension and stabilization during early developmental stages

In order to better characterize the role of dWnk during axon morphogenesis, we analyzed axon growth at multiple time points (2-h time windows) during pupal development (Figure 3A). In wild-type animals, axon extension into the VNC is completed before 30 h of pupal development. At this time point, unpatterned axon sprouting is initiated. Subsequent branch extensions, consolidation, and selective primary collateral formation proceed within the next 10 h (Figures 3A–3G). In contrast, Wnk knockdown (Wnk RNAi^{2x}; Figures 3H–3M) or Wnk mutants axons (Wnk LOF; Figures 3N–3S) show an abnormal axon morphogenesis starting at the early sprouting stage, where a strong reduction in filopodial extensions is already visible at 30 h of pupal development. Throughout the entire axon branching period, we detected a reduction of the overall number of filopodia (Figure 3T). At subsequent stages, axon branches grow and continue to extend but follow erroneous paths and with strong deficits in spatial patterning of axon collaterals (Figures 3J–3M and 3P–3S). We observed these mutant phenotypes with abnormal axon growth and branch patterning using knockdown or MARCM analysis of null mutant neurons. These results exclude the possibility that mechanosensory axons might first develop normally but then regress by limited degeneration of terminal axon branches. In contrast, they support a requirement of dWnk in filopodial and axon branch extension and stabilization as well as axon branch guidance.

Wnk function in axonal morphogenesis is conserved in mouse cortical PNs

dWnk has four related orthologs in mammals named WNK1–4, and several studies have shown that, in particular, WNK1 and WNK4 have prominent roles in the regul ation of ion homeostasis in mammalian kidneys (Richardson et al., 2008; Shekarabi et al., 2008, 2017). Given the striking neurodevelopmental defects due to loss of dWnk in mutant Drosophila neurons, we investigated whether mammalian WNK

Figure 3

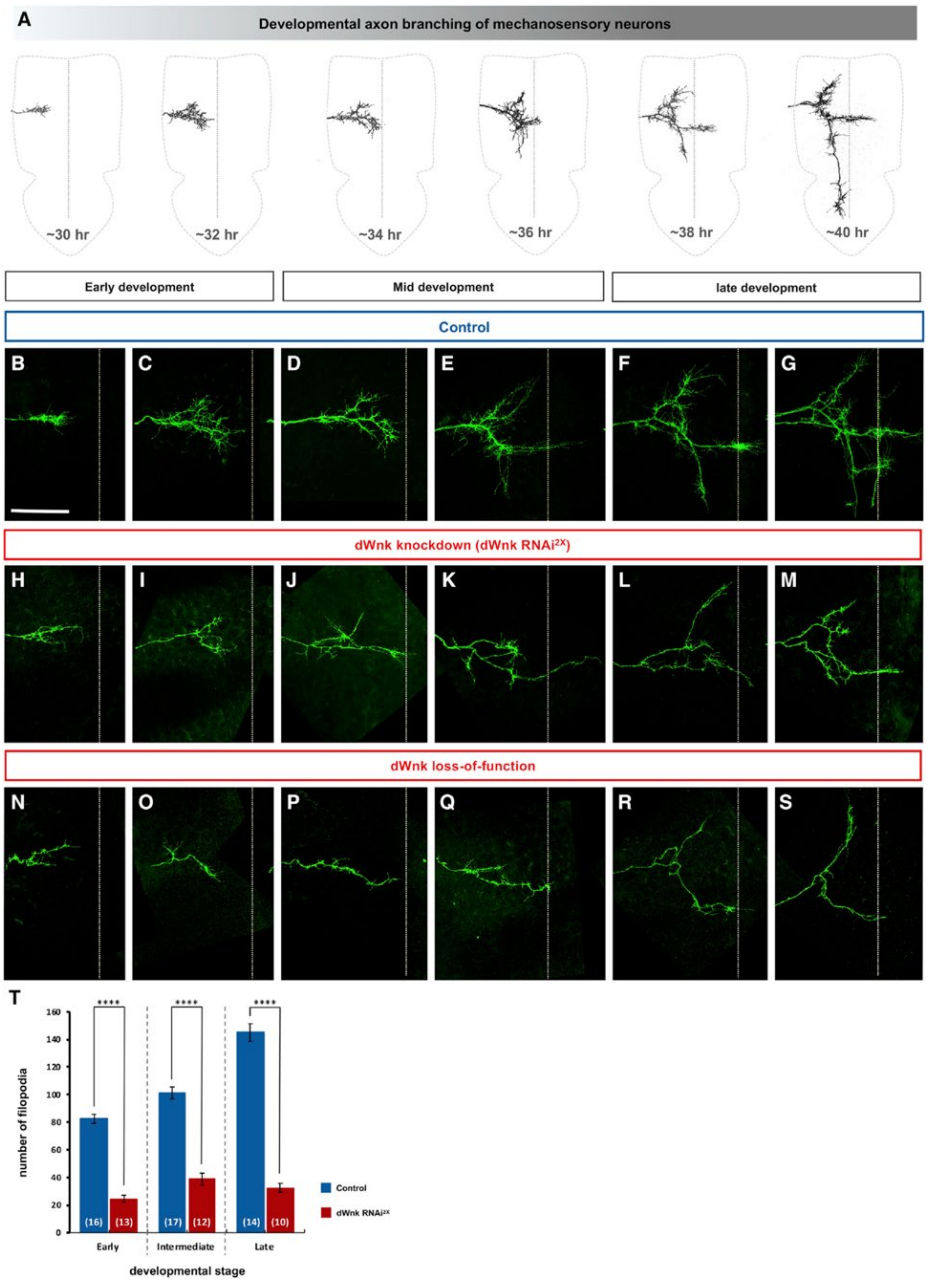

Figure 3. dWnk is required for developmental axon branching
(A) Schematic of a *Drosophila* mechanosensory neuron development. (A–C) During early development, WT pDC neurons growth cones enter the CNS at ~30 h APF (after puparium formation) and undergo extensive expansion at ~32 h APF. (A and D) During the intermediate phases, the growth cones composed of filopodia-like extension start to expand and sprout into all directions at ~34 h APF. (A and E) The number and length of filopodia are dramatically increased and segregated in opposite directions, along the anterior posterior axis as well as toward the midline at ~36 h APF. (A and F) In late development, the main axon shaft is growing in length and the midline projecting axon becomes more prominent and grows contralaterally ~38 h. (A and G) This process is sustained until the neurons reach their final length at ~40 h APF, after which the axon matures and stabilizes its branching pattern. (H–M) Growth cones of Dc neurons with dWnk double RNAi knockdown and Wnk LOF (N–S) are highly abnormal, exhibiting a reduced number of filopodia-like extensions. During the entire time course, Wnk mutant axons are not capable of executing a normal axonal branching program. (H–S) Even starting from the earliest time points of axonal sprouting (~30–32 h APF), the erroneous growth of axon collaterals, as well as strong deficits in spatial patterning of axon collaterals, persists into later stages (~30–32 h APF). (T) Quantification of the total number of filopodia at different developmental stages in control and Wnk mutant in animals of the genotypes indicated in (B)–(M). The tests were considered significant when $p < 0.05$, with the following criteria: *$p < 0.05$; **$p < 0.01$; ***$p < 0.001$; and ****$p < 0.0001$; ordinary one-way ANOVA with multiple comparisons. Scale bar: 20μm

kinases play evolutionary conserved roles in axon branching and axon maintenance using mouse cortical PNs, which are long-range projecting principal glutamatergic neurons in the mammalian cortex.

Using a public database (Genepaint) for mRNA expression by *in situ* hybridization (ISH) in mouse embryo at embryonic day (E) 14.5, Wnk1 mRNA displays a ubiquitous expression and is expressed strongly in the periventricular region of the developing brain, including the cortex (arrow in Figure S5A). Wnk2 mRNA expression is largely restricted to the CNS with high expression in the developing cortex (arrow in Figure S5B). Wnk3 and Wnk4 were not detected by ISH in the developing CNS at E14.5 (Figures S5C and S5D). Interestingly, the same general trend was found in adult mouse brain using a different database (Allen Brain Institute), where ISH revealed that Wnk1 and Wnk2 are expressed broadly in all regions of the CNS, but Wnk3-4 mRNA are not detectable (Figures S5E–S5H). Finally, to determine whether the same trend of adult expression found in mouse brain applied to various cell types in the adult human cortex, we used a publicly available single-cell RNA sequencing (scRNA-seq) database (UCSC Cell Browser). This revealed the same trend as in adult mouse brain, showing that, in the human cortex, WNK1 and WNK2 share a highly similar cell type expression pattern being most abundant in principal PNs from layer 2/3, 4, and 5/6 as well as in cortical interneuron sub-populations and some nonneuronal cell types (Figures S6A and S6B), whereas WNK3 and WNK4 are almost completely absent from any adult human cortical cell types (Figures S6C and S6D).

To investigate whether the mouse Wnk1 and/or Wnk2 are required for axon growth and branching of cortical PNs, we performed in utero cortical electroporation (IUCE) of short hairpin RNA (shRNA) encoding plasmids targeting Wnk1 or Wnk2 (Figure S7) at E15.5, in order to target cortico-cortical projecting layer 2/3 PNs in the primary somatosensory cortex. Brains of electroporated mice were harvested at various postnatal stages: (1) at postnatal day (P)10, an immature stage when axons have reached the contralateral hemisphere but just started to defasciculate and invade the cortex, where they are still undergoing terminal branching (Figure 4A); (2) at P15, an intermediate stage where axons are progressively increasing their branching in their target layers 2/3 and 5 (Figure 4B); (3) at P21, a juvenile stage with adult-like terminal branching of callosal axons (Figure 4C); and (4) at P35, an adult stage. In layer 2/3 PNs expressing either Wnk1 shRNA (Figures 4E–4H) or Wnk2 shRNA (Figures 4I–4L), a

Figure 4

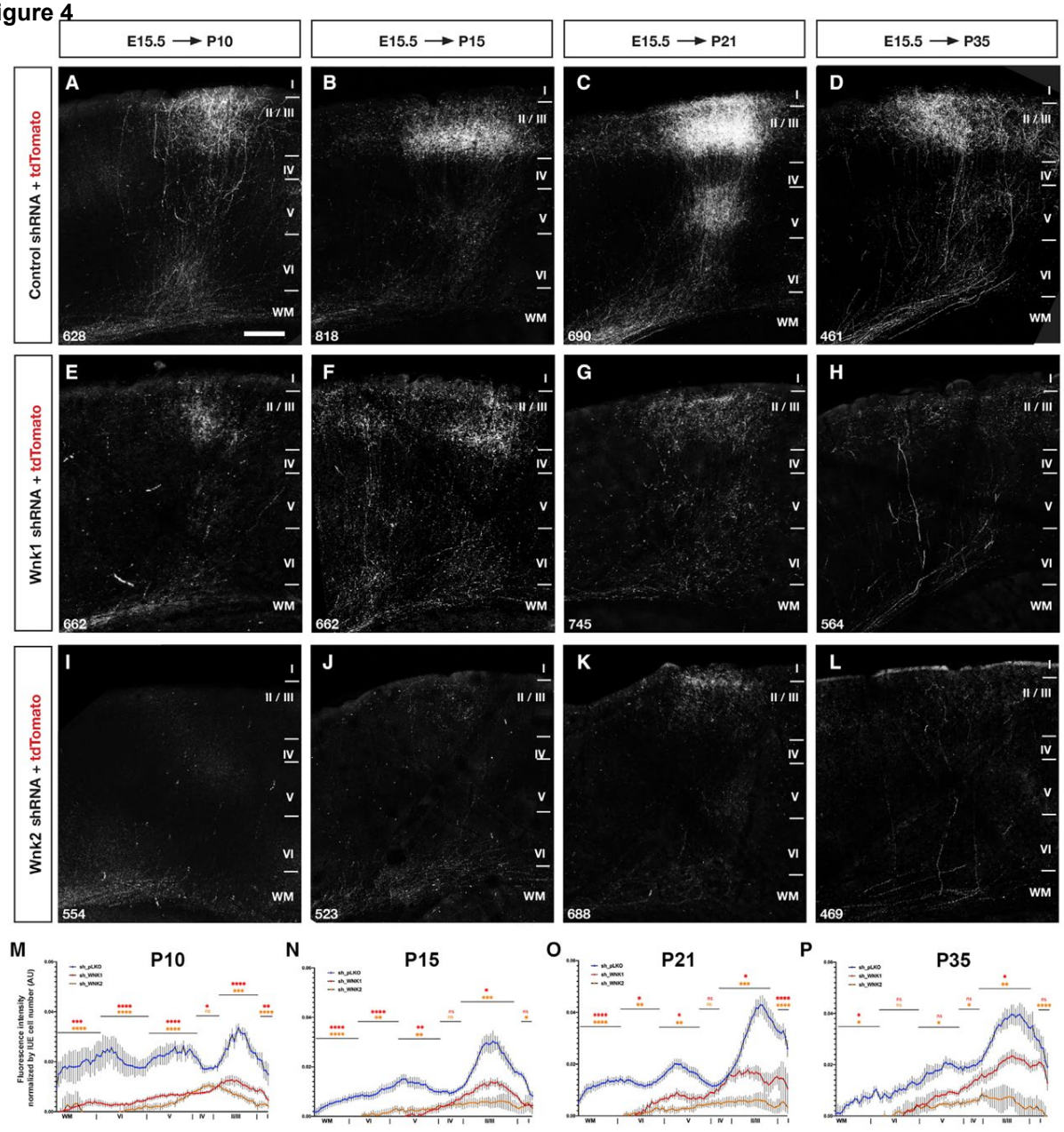

Figure 4. Wnk1 and Wnk2 are both required for terminal axon branching and maintenance *in vivo*

(A–L) Representative images of the axons on the contralateral side of the electroporation in layer 2/3 PNs co-electroporated with tdTomato and control shRNA (A–D) or *Wnk1* shRNA expressing (E–H) or *Wnk2* shRNA (I–L). *In utero* cortical electroporation (IUCE) was performed at E15 to electroporate neural progenitors generating layer 2/3 PNs and harvested at the following time points: P10 (immature); P15 (branching increasing); P21 (peak of branching); and P35 (adult pattern). Both *Wnk1* and *Wnk2* shRNA knockdowns significantly reduce terminal branching of the callosal axons that reached the contralateral side and also reduce the total number of axons present at P35 (see also Figure S9 for images of axons present at the midline at these time points). The numbers in the bottom left corner of each image correspond to the number of electroporated neurons on the ipsilateral side of each corresponding section. These neuron counts were performed using a machine-learning-based segmentation tool (Ilastik—see STAR Methods for details) and used to normalize the optical density measurements of tdTomato+ axons. (M–P) Optical density measurements of tdTomato+ axons on the contralateral side normalized by the number of electroporated neurons on the ipsilateral side of each section. Three sections from each brain were quantified. $n_{pLKO\ P10} = 3$; $n_{pLKO\ P15} = 3$; $n_{pLKO\ P21} = 5$; $n_{pLKO\ P35} = 5$; $n_{WNK1\ P10} = 4$; $n_{WNK1\ P15} = 3$; $n_{WNK1\ P21} = 3$; $n_{WNK1\ P35} = 5$; $n_{WNK2\ P10} = 3$; $n_{WNK2\ P15} = 3$; $n_{WNK2\ P21} = 4$; $n_{WNK2\ P35} = 3$. Statistical analysis: a two-way ANOVA followed by multiple Tukey's comparisons test: *$p < 0.05$; **$p < 0.01$; ***$p < 0.001$; ****$p < 0.0001$. Scale bar in (A)–(L): 100 μm.

population of axons reach the contralateral hemisphere at P10 (Figures 4E and 4I), but terminal axon branching is severely affected through the intermediate stages (Figures 4F, 4G, 4J, and 4K), never reaching wild-type control levels even at adult stages with only a few axons left at P35 (Figures 4H and 4L). Quantification of the optical density from tdTomato+ axons throughout all cortical layers normalized by the total number of electroporated cell body of layer 2/3 PNs on the ipsilateral side demonstrates that Wnk1 or Wnk2 shRNA-expressing axons are severely reduced on the contralateral side compared to control shRNA-expressing axons at all stages examined (Figures 4M–4P).

Analysis of axon density at the midline (corpus callosum) in Wnk1 or Wnk2 shRNA-expressing neurons confirm that axons successfully cross the midline and are present from P10 to P21 but show significant reduction in number by P35 compared to control (Figures S8A–S8L).

To quantify axon growth and branching at single-cell resolution, we turned to ex utero cortical electroporation (EUCE) followed by dissociated culture *in vitro* as previously described (Courchet et al., 2013). We compared axon morphology in control, WNK1 overexpression (OE), as well as Wnk1 or Wnk2 shRNA-mediated knockdown conditions. Compared to control neurons, overexpression of WNK1 led to longer axons, with more collateral branches (Figures S9A and S9B). Conversely, shRNA-mediated knockdown of either Wnk1 or Wnk2 resulted in cortical PNs with shorter and less-branched axons (Figures S9C and S9D). Quantifications confirmed a dose-dependent effect of WNK1 on axon length and collateral branching (Figures S9E–S9G). Wnk1 or Wnk2 knockdown led to a similar reduction of axon length and collateral branching without any additive effect of the double knockdown of Wnk1 and Wnk2 (Figures S9H–S9J), suggesting they belong to the same pathway. Interestingly, effect of Wnk1 knockdown or overexpression is restricted to axon morphogenesis because we did not observe any consequence of Wnk1 modulation (WNK1 overexpression or Wnk1 knockdown) on dendritic morphology at 21 days *in vitro* (DIV) (Figures S9K–S9M). This is consistent with results presented above (Figures S3I–S3L) showing that loss of dWnk in Drosophila DCN and sensory ddaE-class I neurons leads to strong axonal but no dendritic morphogenesis defects within the same neurons.

To further confirm that WNK1 and WNK2 affect axon growth and branching, we performed time-lapse imaging of axonal development over 16 h (10-min imaging interval) and quantified axon elongation and branch formation (Figures S10A and S10B). Axon elongation was disrupted by a failure to consolidate

growth at the tip of the axon. Indeed, short periods of growth cone progression (Figure S10C, green arrowhead) alternated with growth cone retraction (purple arrowhead) and initiation of an alternative growth cone from an above position on the axon shaft. Although the growth cone speed during the periods of growth was identical in control and knockdown condition, we measured a reduced time spent growing and increased pause duration in Wnk1 and Wnk2 knockdown neurons, resulting in a net decrease of axon elongation (Figures S10D–S10G). Finally, we measured that branch dynamics were altered with a decrease of the fraction of new, stable branches created and an increase in transient (<2 h) branches (Figure S10H). Altogether, these results demonstrate that mouse WNK1 and WNK2 are directly involved in axon development similarly to their Drosophila counterpart.

Wnk1 and Wnk2 are required in axon maintenance in developing neurons

Following expression of Wnk1 or Wnk2 shRNA, we observed a gradual, significant reduction in mVenus+ axonal labeling in the corpus callosum at the midline compared to control shRNA (Figures S8A–S8L) and a marked loss of axon branching both *in vivo* (Figure 4) and *in vitro* at least at early stages of neuronal differentiation (Figure S9). These data suggest that Wnk1 or Wnk2 are not only required for axon branching but might also be required for axon maintenance.

We used very sparse EUCE in order to obtain individual cortical PNs that can be optically isolated and performed timelapse analysis by repetitively imaging individual neurons once every 24 h from 5 to 10 DIV (Figure 5A). In cortical PNs expressing control shRNA, we observed progressive but extensive axon growth and branching (Figures 5A, 5F, and 5G; see Videos S1 and S2) but never spontaneous axon fragmentation and degeneration in these culture conditions.

Cortical PNs expressing Wnk1 or Wnk2 shRNA display two classes of phenotypes: in ~55% cortical PNs expressing Wnk1 shRNA (Figure 5B) and ~65% of cortical PNs expressing Wnk2 shRNA (Figure 5C), we observed reduced axon growth and branching but no sign of axon fragmentation or degeneration at least by 10 DIV (Figure 5F; see also Videos S3 and S5). Furthermore, in the remaining ~45% of cortical PNs expressing Wnk1 shRNA and ~35% of cortical PNs expressing Wnk2 shRNA, we observed initially reduced axon growth and branching followed by striking patterns of rapid axon

Figure 5

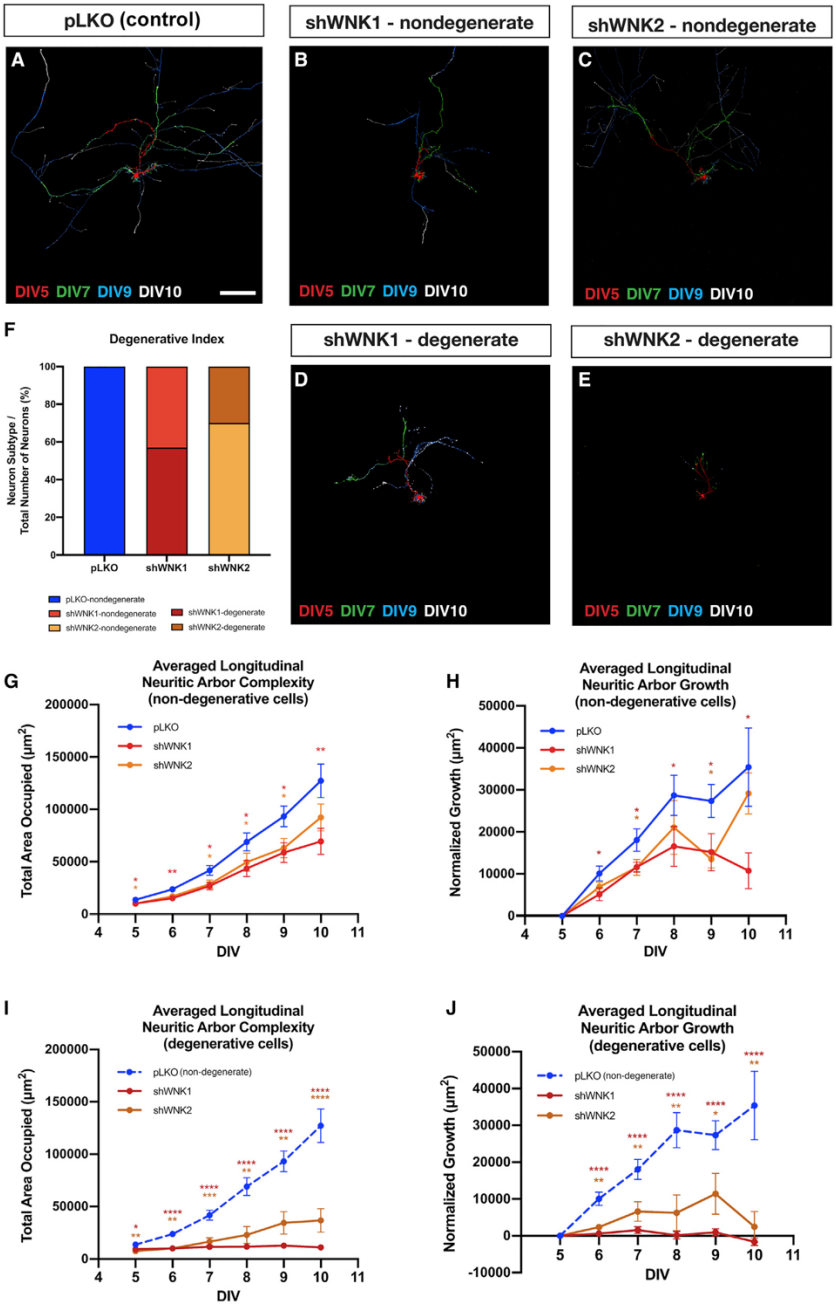

Figure 5. *Wnk1* and *Wnk2* control axon branching and degeneration in cortical pyramidal neurons *in vitro*
(A–E) Representative cortical layer 2/3 pyramidal neurons imaged longitudinally at 5, 6, 7, 8, 9, and 10 DIV with only 5, 7, 9, and 10 DIV *ex utero* electroporated with control shRNA (pLKO-scramble; A) or with shRNA targeting *Wnk1* (B and D) or *Wnk2* (C and E). We distinguished two classes of neurons based on their phenotypes: neurons that showed clear signs of degeneration (axon blebbing and ultimately cell fragmentation; B and C) and neurons that did not show any sign of degeneration at least during the 10 DIV (D and E). Neuronal morphology was visualized by tdTomato expression and pseudo-colored to represent consecutive days of imaging. (F) Quantification of ultimate neuronal fate at 10 DIV for the pLKO, shWNK1, and shWNK2 conditions as determined by the presence (degenerate) or absence (non-degenerate) of neuronal fragmentation. (G–J) Quantification of axonal arbor complexity and growth as measured by the total area occupied by the axon (G and I) of either non-degenerate (G) or degenerate (I) neurons and by the axon growth rate (H and J) as measured by the total area occupied by the axon cumulatively gained each day for both non- degenerate (H) and degenerate (J) neurons. Statistical analyses: non-parametric Mann-Whitney test comparing each condition at each time point, with the data presented in (G)–(J) as mean and SEM. Number of neurons for quantification: n_{pLKO} = 19; n_{shWNK1} = 28; n_{shWNK2} = 23 from at least three independent experiments. Significance: *p < 0.05 with the following criteria: *p < 0.05; **p < 0.01; ***p < 0.001; and ****p < 0.0001. Scale bar in (A)–(E): 100 µm.

fragmentation and degeneration occurring between 7 and 8 DIV (Figures 5D–5F; Videos S4 and S6). Quantification of the dynamics of axon growth and branching (cumulative axon length and area; Figures 5G and 5I) or normalized growth rate (increase in total axonal length per day; Figures 5H and 5J) demonstrated that axon growth and branching is significantly reduced in axons expressing Wnk1 or Wnk2 shRNA in both classes of axons.

Our *ex utero* electroporation protocol is performed in both cases at E15, targeting the progenitors lining the ventricular zone at that time, which generate exclusively layer 2/3 PNs in the dorsal telencephalon. However, the limitation of this approach is that, upon electroporation, the neural progenitors pick up various amount of the plasmid and subsequently can divide several times to generate layer 2/3 PNs, thereby creating a ‘‘mosaic’’ expression of cDNA- or shRNA-encoding plasmids. We favor this explanation to describe the range of phenotypes obtained, leading to two extreme phenotypes upon Wnk1 or Wnk2 shRNA-mediated knockdown: (1) one class of neurons where axon branching and growth is affected, but not axon maintenance (presumably the neurons where knockdown of Wnk1 or 2 is suboptimal) and (2) a second class of neurons where axon branching and maintenance is affected (presumably the neurons where knockdown of Wnk1 or 2 is above a certain threshold). This interpretation is reinforced by the analysis performed in Drosophila, where neurons expressing 13 RNAi (expressed genomically here) show severe axon branching defect, but not axon degeneration, and neurons expressing 23 RNAi show initially axon branching defects but ultimately axon degeneration (Figure 2).

Wnk1 and Wnk2 are required for axon maintenance in adult neurons

In order to directly test whether Wnk1 and Wnk2 are required for axon maintenance in adult mouse cortical PNs, we developed a new experimental approach that enables inducible expression of shRNA *in vivo*. Our strategy revolves around two parts (Figures 6A and 6B): (1) we used IUCE (E15) to co-express a plasmid expressing a tamoxifen-inducible form of Cre (ERT2-Cre-ERT2) and a novel plasmid expressing the red fluorophore mStrawberry in the absence of tamoxifen but upon tamoxifen-dependent Cre activation; the CAG promoter and enhancer cassette orientation is flipped, leading to expression of a bi-cistronic mRNA encoding EGFP and a Wnk1 or Wnk2 shRNA upon mRNA processing (Figure 6A). We performed tamoxifen induction of Cre-mediated recombination (and induced shRNA expression) using

Figure 6

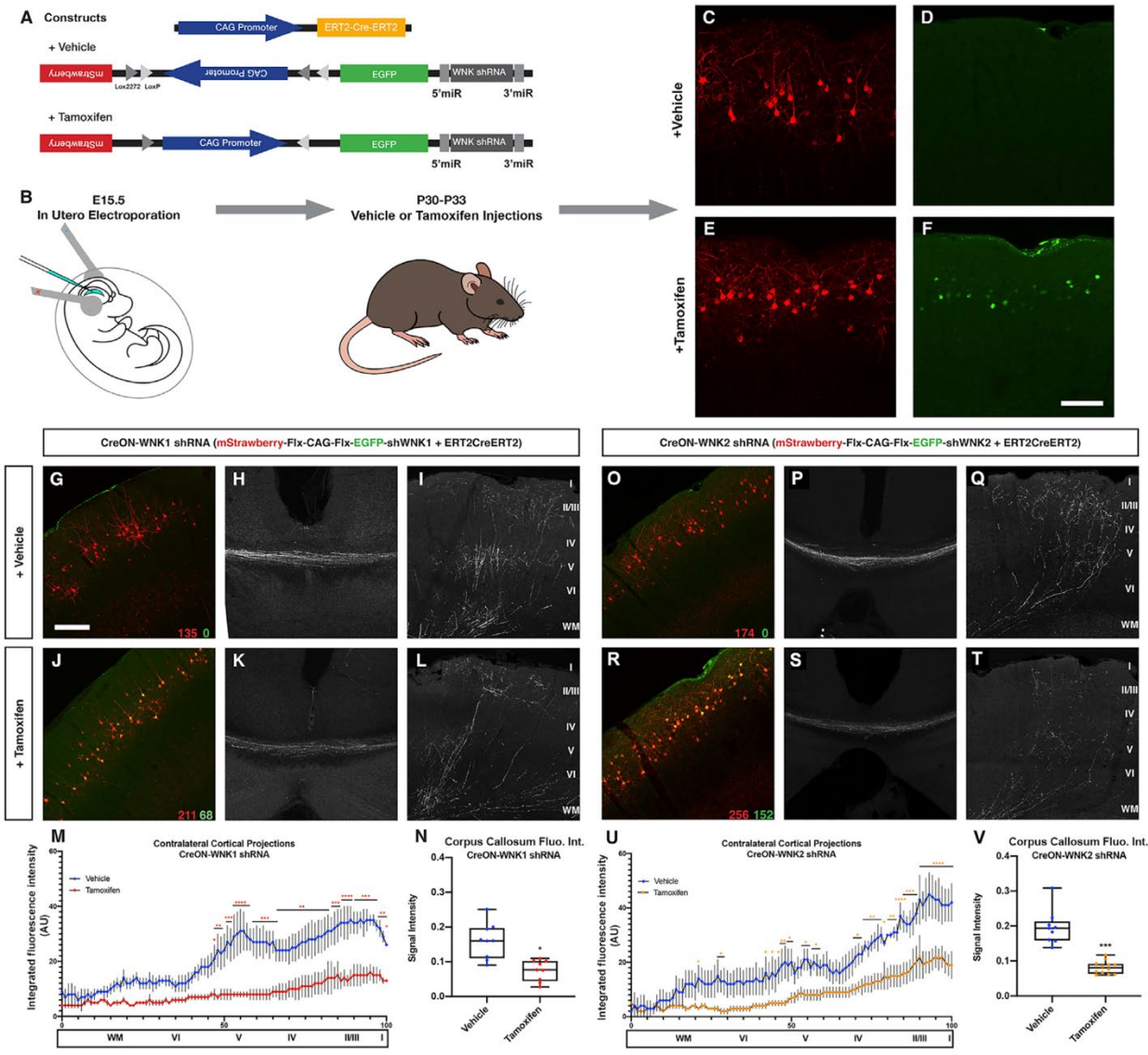

Figure 6. Adult knockdown of *Wnk1* or *Wnk2* causes axonal degeneration in mouse cortical layer 2/3 pyramidal neurons
(A and B) Design of the conditional shRNA expression plasmids (CreON-shWNK) used to achieve inducible, adult knockdown of *wnk1* and *wnk2* in layer 2/3 PNs of the mouse cortex. Our strategy uses co-electroporation of a tamoxifen-inducible form of Cre recombinase (ERT2-Cre-ERT2) in combination with a plasmid where a cytomegalovirus (CMV) enhancer/chicken-b-Actin promoter (CAG) cassette flanked by incompatible Lox sites (Lox2272 and LoxP; subsequently referred to as FLEX plasmid) drives the expression of a fluorescent mStrawberry protein in absence of tamoxifen. In the presence of tamoxifen, Cre recombines the CAG promoter and flips its orientation to drive the expression of a mRNA coding for EGFP and WNK shRNA (after 5^0 and 3^0 microRNA [miRNA] processing). Our experimental design (B) is as follows: at E15.5, mice undergo *in utero* electroporation with the CreON-shWNK plasmid and tamoxifen-dependent pCA- G::ERT2-Cre-ERT2; at P30–P33, adult mice undergo four (one per day) consecutive intraperitoneal injections with tamoxifen diluted in corn oil (0.1 mg/g of bodyweight) or control vehicle only (corn oil); and at P37 (8 days following first injection), mice were perfused and their brains sectioned, immuno-amplified, and imaged. (C–F) Representative images of adult layer 2/3 PNs on ipsilateral side relative to *in utero* electroporated cortex of mice injected with vehicle (C and D) or with tamoxifen (E and F). (G–L) Detail of a coronal brain section of a P37 mouse *in utero* co-electroporated with CreON-shWNK1 and ERT2CreERT2 showing (H and K) a reduction of callosal axonal projections and (I and L) a reduction in contralateral axonal branching upon adult knockdown of WNK1. Red inset numbers indicated the number of electroporated PNs; green inset numbers represent the number of EGFP+ PNs.

four daily tamoxifen intraperitoneal (i.p.) injections at P30–P33. This approach is robust because, in the absence of tamoxifen, we observed many mStrawberry-expressing layer 2/3 PNs (Figure 6C), but we never EGFP co-expressing neurons (Figure 6D; see also Figures 6G and 6P). However, in mice injected with tamoxifen, we observed a large fraction of layer 2/3 PNs co-expressing EGFP at various levels (~30%–50% co-expression; Figures 6E and 6F).

This approach therefore allowed us to test whether inducible shRNA knockdown of Wnk1 or Wnk2 in adult layer 2/3 PNs is required for axon maintenance. 7 days following the first tamoxifen injection (i.e., at P37) or injection of vehicle (corn oil) for the control group, we imaged axons of layer 2/3 PNs at the midline (corpus callosum) or on the contralateral side, where they undergo terminal axon branching. Both Wnk1 and Wnk2 shRNA expression leads to significant reduction of the fraction of axons relative to the number of electroporated neurons at the corpus callosum (Figures 6K and 6T) and on the contralateral side (Figures 6L and 6U) compared to control (Figures 6H, 6I, 6Q, and 6R). Quantification of optical density of mStrawberry+ axons on the contralateral side (normalized to number of electroporated neurons) demonstrates a significant reduction in axon density in Wnk1 shRNA-expressing neurons (Figure 6M) or Wnk2 shRNA-expressing neurons (Figure 6V) compared to control. The same significant reduction in optical density of mStrawberry+ axons at the midline is observed in Wnk1 or Wnk2 shRNA-expressing axons compared to control (Figures 6N and 6W). These results demonstrate that Wnk1 and Wnk2 are required for axon maintenance in adult mouse PNs.

Loss of Nmnat and gain of dSarm or Axed disrupts axon branching during development

Mammalian WNK1 and WNK4 are known to regulate two downstream kinases (i.e., serine-threoninie kinase OSR1 and STE20/SPS1-related proline/alanine-rich kinase) (OSR1/SPAK) and target the sodium Na+:Cl- cotransporter (NCC)/potassium KCL (KCC) cotransporters in kidney cells (Vitari et al., 2005; Moriguchi et al., 2005; Anselmo et al., 2006; Gagnon et al., 2006). This regulation is essential for blood pressure regulation (Richardson and Alessi, 2008; Wu et al., 2019; Hadchouel et al., 2016). Disruption of these WNK-dependent functions constitutes the basis of hypertension in several hereditary human diseases (Rafiqi et al., 2010). In order to explore the molecular mechanisms underlying WNK function in axon branching and degeneration, we initially tested whether downregulation of Frayed, the Drosophila ortholog of OSR1 and

SPAK kinases, or NCC and KCC phenocopied dWnk LOF axon branching defects. However, we could not detect dWnk-like axonal branching defects upon RNAi knockdown of Frayed or KCC (Figure S11).

In our efforts to identify other potential factors mediating the function of dWnk, we tested previously identified effectors of axon maintenance (Gilley and Coleman, 2010; Neukomm et al., 2017; Babetto et al., 2013; Conforti et al., 2014; Essuman et al., 2017). In a candidate screen, we discovered that LOF and RNAi knockdown of Nmnat in mechanosensory neurons leads to axon branching defects remarkably similar to dWnk LOF defects (Figures 7A and 7C–7E). A previous study provided evidence that reduction of Nmnat in Drosophila sensory neurons leads to activation of dSarm as well as a newly identified protein Axundead (Axed) to execute axon degeneration (Neukomm et al., 2017). Consistent with these findings, we found that overexpression of Axed or dSarm caused axon branching defects similar to loss of dWnk or loss of Nmnat (Figures 7F and 7G). These results provide evidence that Nmnat is required developmentally for axon branching of mechanosensory neurons. Moreover, overexpression of Axed or dSarm during axon development resulted in axon branching defects remarkably similar to loss of dWnk or Nmnat.

dWnk regulates axon branching and maintenance by regulating Nmnat, dSarm, and Axed

In order to address the functional relationship of dWnk and these components, we used genetic epistasis analysis (Figures 7 and S12). We found that both loss of Axed and dSarm can suppress the axon branching defects in dWnk mutant neurons (Figures 7C, 7I, 7J, 7O, S12A–S12E, and S12Q) and prevents loss of axons (Figures 7S, 7T, 7W, 7X, S12K–S12M, and S12R). Conversely, the gain of function branching defects and loss of axons upon Axed and dSarm overexpression can be suppressed by co-overexpression of dWnk (Figures 7F, 7G, 7M–7O, S12FS12J, S12N–S12P, and S12R). This argues for an antagonistic functional relation between dWnk and the axon destruction factors Axed and dSarm during axon branching as well as maintenance.

Overexpression of dWnk or Nmnat alone did not result in any dominant phenotypic defects (Figures 7B and 7H). However, we found that the axon branching defects characteristic for dWnk mutant neurons can be suppressed by Nmnat overexpression (Figures 7C, 7H, 7K, and 7O). Conversely, axon branching defects characterizing Nmnat RNAi knockdown neurons can be rescued by overexpression of dWnk (Figures 7E, 7L, and 7O). We further observed that overexpression of Nmnat in pSc neurons can

Figure 7

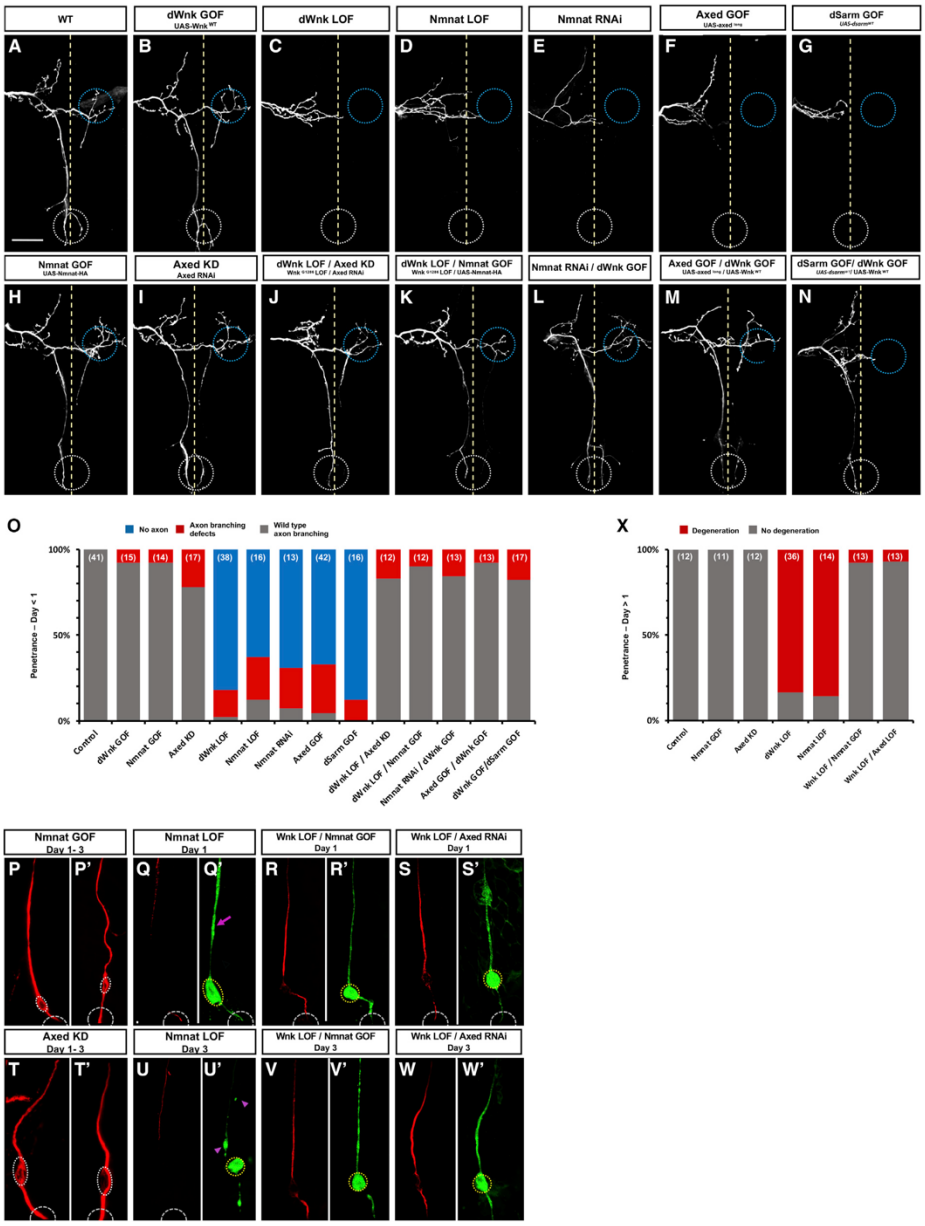

Figure 7. Genetic epistatic analysis reveals that dWnk positively enhances Nmnat function and negatively regulates Axed and dSarm in the control of both axon branching and axon maintenance

(A–N) Representative confocal images of mechanosensory neurons dye filled with carbocyanine dyes. (A) WT mechanosensory neurons displaying the stereotyped branching pattern. (C–G) dWnk loss of function (LOF), Nmnat LOF, Nmnat RNAi, Axed overexpression (gain of function, GOF), and overexpression of dSarm are showing very similar phenotype, i.e., axon branching defects with loss of distal axon terminals. (B, H, and I) overexpression of dWnk and Nmnat as well as Axed knockdown are showing normal branching pattern. (J and K) dWnk LOF-induced axon branching defects can be rescued by Axed RNAi knockdown and overexpression of Nmnat, which is showing normal branching pattern. (L–N) Overexpression of dWnk can maintain the axonal branches otherwise disrupted by Nmnat RNAi, Axed GOF, and dSarm GOF. (O) Quantification of axonal branching defects observed in the various conditions described above. (P–W) Visualizing distal to proximal axon degeneration of mechanosensory neurons in thorax at day 1 and 3. (P and T) Nmnat OE and Axed knockdown are showing a near continuous labeling of the microtubule cytoskeleton using anti-22C10 antibody staining same as WT control samples. (Q and U) Genetic mosaic analysis of Nmnat homozygous mutant mechanosensory neurons shows that lacking Nmnat leads to axon swelling and blebbing (arrows in magenta) in 1-day-old samples followed by axon fragmentation and clearance of axonal debris (arrowheads in magenta) in 3-day-old samples. (R and V) Overexpression of Nmnat can rescue the axon degeneration caused by loss of dWnk. (S and W) Knockdown of Axed prevents axon degeneration caused by dWnk LOF. (X) Quantification of axon degeneration in mechanosensory neuron proximal to the cell body located in thorax in the various conditions described for (P)–(W'). Scale bar: 20 μm.

also suppress or slow down the degeneration of axons in dWnk mutant neurons (Figures 7P–7R, 7U, 7V, and 7X). In summary, the genetic analysis of fly mechanosensory neurons suggest that dWnk functions synergistically with Nmnat in order to prevent gain of activity of dSarm and Axed, which can disrupt both (1) axon branching during development and (2) axon maintenance in mature neurons.

Wnk and Nmnat proteins can form complexes and are depleted by Sarm1 activity

We conducted a series of biochemical immunoprecipitations to test potential protein interactions of dWnk as well as mammalian WNK1/2 with the axon maintenance or destruction factors examined in the genetic analysis (Figure 8). We found that immunoprecipitation of endogenous dWnk from S2 cell extracts can pull down tagged dNmnat (Figure 8A). This is consistent with published findings, where dWnk was identified by mass spectrometry from a complex co-purified with Nmnat overexpressed in fly brains (Ali et al., 2016). For the mammalian homologs Wnk1/ 2, we found that Nmnat2 can be co-immunoprecipitated with Wnk1, suggesting conserved Wnk-Nmnat interactions. We found that these interactions are likely occurring via the N-terminal part of Wnk1 and to a lesser degree with the kinase domain of Wnk1 itself (Figure 8B). We further found that Wnk1 can be immunoprecipitated with Wnk2 and vice versa (Figure 8C), consistent with the finding that both kinases are functionally required in mouse PNs.

We further tested potential dWnk interactions with the axon destructive factors Axed and dSarm. We found that coexpressed Axed (V5-tagged) and dWnk could form complexes in Drosophila S2 cells (Figure S13A). Drosophila Axed is a member of the large Broad-Complex, Tramtrack and Bric a brac (BTB-domain)-containing family of proteins. Although currently no functional mammalian ortholog of Axed is known, we found that mammalian Wnk2 has the potential to interact with Drosophila Axed and a subset of related BTB-domain-containing proteins (Figures S13B–S13F). In contrast, the functional conservation of Drosophila dSarm and mammalian Sarm1 is well documented by molecular and genetic studies. We therefore tested the potential molecular interactions of the axon-protective WNK1 and WNK2 kinases and degeneration effector SARM1. Surprisingly, however, co-overexpression of SARM1 with either WNK1 or WNK2 caused a strong decrease in both WNK1 or WNK2 protein abundance (Figures 8D and 8G). Yet by testing different expression levels of SARM1 and WNK1 or WNK2, we nevertheless were able to co-immunoprecipitate SARM1 and WNK1 or WNK2 (Figures S14A and S14B). Importantly, the coexpression experiments revealed not only that SARM1 protein overexpression either directly or indirectly triggers

Figure 8

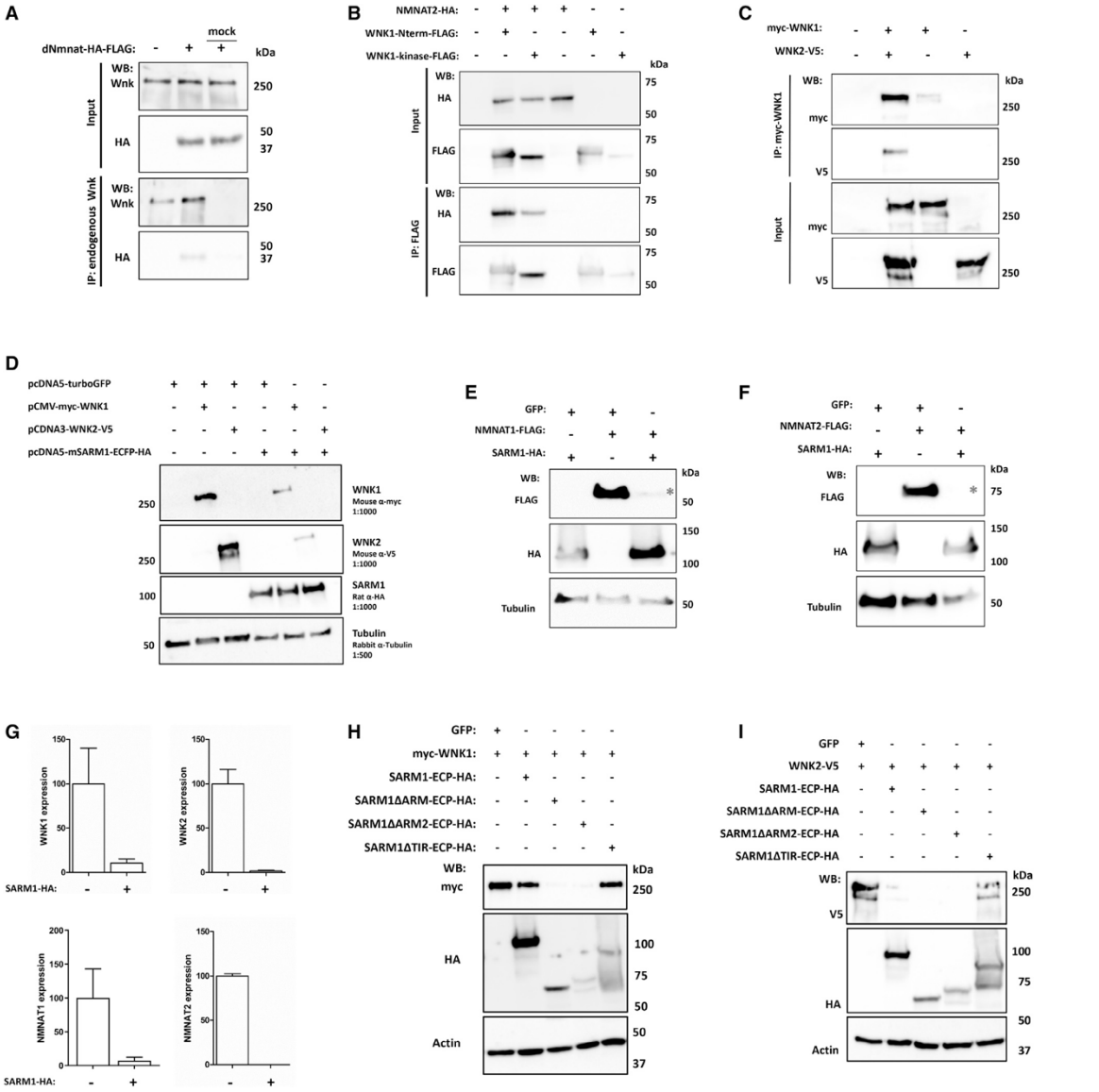

Figure 8. SARM1-dependent downregulation of Wnk and Nmnat
(A) dWnk interacts with dNmnat. dNmnat expression was induced using $CuSO_4$ in stable *Drosophila* S2 cells. Endogenous dWnk was precipitated using magnetic beads, and co-precipitated protein complexes were analyzed using an hemagglutinin (HA)-tag-specific antibody. Non-coated beads were used as mock control. (B) The mammalian N-terminal domain of WNK1 interacts more stringently with mammalian NMNAT2 than its kinase domain. Validation of interactions by co- immunoprecipitation is shown. HEK293T cells were co-transfected with rat WNK1 domains together with human HA-tagged NMNAT2. WNK1 domains were precipitated using anti-FLAG magnetic agarose. Co-precipitated protein complexes were analyzed by western blot (WB) using an HA-tag-specific antibody. (C) Mammalian WNK1 and WNK2 are interacting. Validation of interaction by co-immunoprecipitation is shown. SH-SY5Y cells were co-transfected with mammalian myc-tagged WNK1 and V5-tagged WNK2. WNK1 was precipitated using anti-myc magnetic beads, and co-precipitated protein complexes were visualized by WB using a V5-tag specific antibody. (D–G) SARM1 NAD+ catalytic activity is required for regulation of WNK1, WNK2, and NMNAT2 expression. WB images and quantification of expression of myc- tagged WNK1 and WNK2-V5 (D), NMNAT1-FLAG (E), and NMNAT2-FLAG (F) when co-transfected with either a GFP-containing plasmid or SARM1-HA are shown. Graphs represent optical density measurements for indicated bands showing mean ± SEM of 2–4 independent experiments (G). a-tubulin was used as loading control. (H and I) $SARM1^{DTIR}$-HA does not reduce expression levels of myc-tagged WNK1 (H) and V5-tagged WNK2 (I) to the same extent as full-length SARM1-HA and $SARM^{DARM}$ mutants. For both WBs, actin was used as a loading control.

rapid depletion of WNK1 and WNK2 in HEK293T (Figure 8D; quantification in Figure 8G) or SH-SY5Y cells (Figure S14B) but also that NMNAT1 as well as NMNAT2 levels were nearly completely depleted when co-expressed with SARM1 (Figures 8E and 8F; quantification in Figure 8G). Application of commonly used inhibitors of proteasomal degradation to cells co-expressing Sarm1 and Wnk2 or Nmnat2 did not block this depletion of Wnk2 and Nmnat2 protein (Figure S14B). We further detected no decrease in mRNA expression of Wnk1/2 or Nmnat1/2 upon overexpression of Sarm1 (Figure S14C). It has been reported that Nmnat2 protein is labile and has a rapid turnover time, whereas the mutant (and axon-protective) Nmnat-fusion protein Wallerian degeneration slow (WldS) is significantly more stable (Coleman and Freeman, 2010). Consistent with previous reports and this hypothesis, we found that blocking de novo protein synthesis in cells expressing Nmnat2 by addition of cycloheximide, Nmnat2 protein, but not WldS, is rapidly lost (Figure S14E). Importantly, Nmnat2 depletion is also more sensitive to Sarm1 overexpression than WldS. We therefore hypothesize that one potential mechanism by which Sarm1 could trigger depletion of Wnk or Nmnat proteins is through inhibition of de novo protein synthesis. The direct target of Sarm1 underlying this translational control is currently not known. However, testing different mutant forms of Sarm1 provided evidence that this potential translational control function of Sarm1 requires its catalytic nicotinamide adenine dinucleotide (NAD+) consuming function (Figures 8H and 8I). Specifically, we co-expressed Wnk1 (Figure 8H) and Wnk2 (Figure 8I) with Sarm1 protein forms that enhance or lack catalytic activity. We found that dominant active Sarm1 mutants are even more potent than wild-type Sarm1 in depleting Wnk1 and Wnk2 protein. In contrast, a Sarm1 mutant that lacks the catalytic domain is not able to deplete Wnk1 or Wnk2 protein (Figures 8H and 8I). Although it is known that Nmnat can enzymatically increase NAD+ levels, it is unclear how Wnk proteins exert their role in axon protection. We found, however, that dWnk wild-type function as well as its ability to suppress dSarm gain of function depend on its kinase activity (Figure S15).

Together, these results suggest that the degeneration effector SARM1 is capable of downregulating WNK and NMNAT expression when co-expressed in cell culture. This *in vitro* result is consistent with our genetic epistasis experiments showing antagonistic relations between dWnk/Nmnat and dSarm.

Discussion

In this study, we report that the function of the Wnk-family kinases (Drosophila dWnk and mammalian WNK1/2) are required in developmental axonal branch patterning as well as axon maintenance. We show that phenotypic defects observed in mechanosensory axons of dWnk mutant neurons are indistinguishable from defects observed in Nmnat mutant neurons. Both dWnk and Nmnat mutant mechanosensory axons can grow from the periphery to the VNC but require dWnk as well as Nmnat function during axonal branch growth and patterning. Moreover, a post-developmental knockdown of dWnk triggered progressive degeneration in mature and fully developed mechanosensory axons. Such an adult-specific function is also analogous to the well-documented role of Nmnat in axon maintenance (Gilley and Coleman, 2010; Wen et al., 2011; Ali et al., 2013; Sasaki et al., 2016). Although Nmnat has been studied most extensively for its role in axon maintenance in injury models or neurodegenerative disease models, it has been reported previously that LOF mutants are lethal and show axonal defects (Huppke et al., 2019; Lukacs et al., 2019). Furthermore, we show here that the dual developmental and maintenance functions of dWnk are evolutionary conserved, as knockdown of WNK1 and WNK2 results in remarkably similar axon morphogenesis defects and trigger axon degeneration in mouse cortical neurons. We conclude that, in neurons, Wnk kinases exert novel functions that are analogous and synergistic to conserved Nmnat functions. The discovery of Wnk kinases having important neuroprotective roles analogous to Nmnat offers new tools and insights to further dissect the complex regulatory network underlying active axon degeneration.

Formally, the adult maintenance defects that we observed upon Wnk depletion could be a consequence of developmental defects. However, several reasons argue strongly against this possibility: first, the in vivo knockdown of WNK1 and WNK2 after P30 in mouse cortical layer 2/3 PNs triggered degeneration of axons of mature neurons. Second, knockdown of dWnk at post-developmental (late pupal) stages does not alter the axonal branching or targeting of mechanosensory neurons but triggered spontaneous degeneration of adult mechanosensory axons after 3 days post-eclosion. Third, a single-copy RNAi knockdown of dWnk resulted in strong axon branching defects. Fourth, in previous studies, we identified and characterized several mutants that lead to severe axon branching defects of mechanosensory axons. For example, in Dscam1-null mutant clones, the axon branching defects are even more severe than

in dWnk mutant clones, yet we found no sign of axon degeneration even in 1 week or older flies (see examples in He et al., 2014 and Dascenco et al., 2015). Fifth, even in cases of very short axon branches in dWnk or other mutants with a complete absence of contralateral projecting axon collaterals, the distal part of the mutant axons still reaches the corresponding ipsilateral target area. Given that putative trophic signals would have to support axons on both sides of the VNC, it seems highly unlikely that target-derived trophic signals would only support contralateral projecting axon arbors. In summary, our data provide strong evidence that Wnk kinases have dual roles: first, during developmental axon morphogenesis and, second and independently, during continuous axon maintenance in mature neurons.

A key question raised by these results is: how similar are the molecular processes in developmental axon growth and branching and adult maintenance? A related question has been discussed in a hallmark review (Raff et al., 2002). This perspective article discussed the discovery that neurons can activate a self-destructive program independent of general apoptosis. The authors noted that neurons ‘‘apparently have a second, molecularly distinct self-destruct program in their axon.’’ And the authors raise the incisive question: ‘‘Do neurons also use this second program to prune their axonal tree during development and to conserve resources in response to chronic insults?’’

We assume that ‘‘pruning of axonal branches during development’’ could—as a cellular mechanism—also be involved in axonal branch patterning as analyzed here. Specifically, we view the developmental axon branching of mechanosensory axons as a process where continuous competitive interactions among nascent branches select for stabilization or retraction (timescale minutes or few hours). In contrast, the well-characterized pruning of axons during metamorphosis (e.g., mushroom body remodeling) is initiated when axon branches and connectivity have been already established. This type of pruning (remodeling) requires primarily a destabilization of a fully established axon projection and is likely different from axonal branch selection as investigated here. Consistent with this idea is the finding that Nmnat is not required in axon pruning of mushroom body neurons (Hoopfer et al., 2006).

Our results now provide genetic and molecular data that support the notion that components of a ‘‘distinct self-destruct program’’ are involved in axon branch stabilization and destabilization. We further suggest that molecular control mechanisms of axon branching and axon destruction (or preventing axon destruction, i.e., axon maintenance) are mechanistically related. Specifically, the dynamics of axon

branching requires the selection of an exuberant number of nascent axon branches by either stabilizing or destabilizing nascent branches (Lewis et al., 2013). During axon morphogenesis, the majority of filopodia and nascent branches are retracted to maintain just a few that are consolidated into axon collaterals. It seems plausible, therefore, that axon branch retraction in developing neurons might involve molecular effectors that are also required for a distinct type of axon branch pruning. Based on our *in vitro* studies, we speculate that regulation of de novo protein synthesis could be the molecular process that is targeted in both axon branching and axon maintenance.

Based on our new findings, we suggest that Wnk as well as Nmnat are necessary components of axon branching as well as axon maintenance. Support for this model comes from the results of our genetic epistasis analysis. The loss of dWnk during axon branching is only a problem if Sarm or Axed are present: in the absence of Axed (the most downstream effector of the destruction program in Drosophila known so far; Neukomm et al., 2017), loss of dWnk does not cause defects in axonal branching or maintenance. Implicit to this model is that dWnk is unlikely instructing axon branching but rather provides a safeguard function curbing destructive effectors such that retraction, pruning, or branch destruction can be restricted and constrained in a spatially restricted manner. A further implication of this model is the notion that loss of dWnk effectively represents a gain of function (on switch) of an axonal destruction program in developing axons.

In this context, it is also interesting to note that expression of Nmnat can compensate (i.e., rescue) for loss of dWnk in both axon branching and maintenance. It is well established that local depletion of Nmnat in adult neurons does directly lead to axon degeneration, i.e., has a role in axon maintenance independent of its developmental role (Milde et al., 2013). This is consistent with our new finding that post-developmental inactivation of dWnk or mammalian Wnk1/2 triggers axon degeneration.

Nmnat has been previously shown to protect from axon degeneration following axotomy by counter-acting Sarm-induced NAD+ depletion (Essuman et al., 2017; Sasaki et al., 2016; Yang et al., 2015; Gerdts et al., 2015) and Axed activity (Neukomm et al., 2017). We show in the present study that, even in the absence of axon injury, loss of Nmnat as well as loss of dWnk or overexpression of dSarm and Axed leads to progressive degeneration of adult mechanosensory axons without injury. This is consistent with previous reports showing that Nmnat loss in sensory neurons of the wing leads to spontaneous axon degeneration

in adult flies (Fang et al., 2012) or that loss of NMNAT2 leads to truncation of peripheral nerve and CNS axon tracts in mice (Gilley et al., 2013). A role of Wnk1 in axon maintenance is also consistent with the finding that WNK function has been linked to a severe form of peripheral neuropathy (Lafreniere et al., 2004; Rivie` re et al., 2004; Roddier et al., 2005; Coen et al., 2006).

Our results, therefore, support the notion that both axon morphogenesis and maintenance require a constitutive involvement of Wnk and Nmnat.

A link between dWnk, Nmnat, and axon destructive factors is further corroborated by our biochemical experiments co-expressing these factors and using co-immunoprecipitations to analyze protein-protein interactions of dWnk or mammalian WNK1/2. First, our results suggest the possibility that dWnk, Nmnat, Sarm1, and Axed are able to form mixed complexes. Moreover, mammalian WNK1 can interact with WNK2 and Nmnat2 as well as SARM1. Although previous work has not identified Nmnat proteins as potential Wnk kinase substrates, our results suggest that this possibility is worthwhile to examine in future experiments. Second, whereas a vertebrate ortholog of Axed has not been described, we found that mammalian SARM1 overexpression strongly downregulates levels of WNK1, WNK2, NMNAT2, and NMNAT1. However, future experiments will have to confirm that this downregulation of proteins by Sarm1 is also occurring in neurons *in vivo*.

It has been reported that inhibition of axon degeneration can be accomplished by increasing or stabilizing levels of Nmnat protein (Babetto et al., 2013). Moreover, Highwire/Phr1, which is an additional conserved factor functioning in Wallerian degeneration, directly promotes the downregulation of Nmnat, and axon degeneration is strongly inhibited in Highwire/Phr1 mutants (Xiong et al., 2012). This previously described regulation of Nmnat levels is mediated via mitogen-activated protein kinase (MAPK) signaling and ubiquitin-dependent proteolysis. Our findings reported here suggest that Sarm1 may rather inhibit de novo protein synthesis in order to deplete Nmnat and other axon protective factors. Future studies will have to investigate in detail how the SARM1-dependent depletion of NAD+ also leads to a Wnk/Nmnat protein depletion as described here. Particularly interesting will be to determine how the destructive activity of Sarm protein can be limited during development to selective axon branch compartments in order to enable local axon branch pruning but prevent progressive axon degeneration.

Finally, Nmnat function has not only been involved in neuroprotection as a response to injury, such as axotomy, but also in a diverse range of neurodegenerative diseases, such as spinocerebellar ataxia (Zhai et al., 2008; Ruan et al., 2015), fronto-temporal dementia (FTD) and Parkinsonism (Ali et al., 2013), or glaucomatous optic neuropathy (Munemasa and Kitaoka, 2015), or following growth factor deprivation (Vohra et al., 2010). Future studies will need to consider the possibility that the newly identified dWnk and WNK1 and WNK2 kinases may also play similar neuroprotective roles in diverse types of neurodegenerative conditions.

Supplemental Figures

Supplemental Figure S1

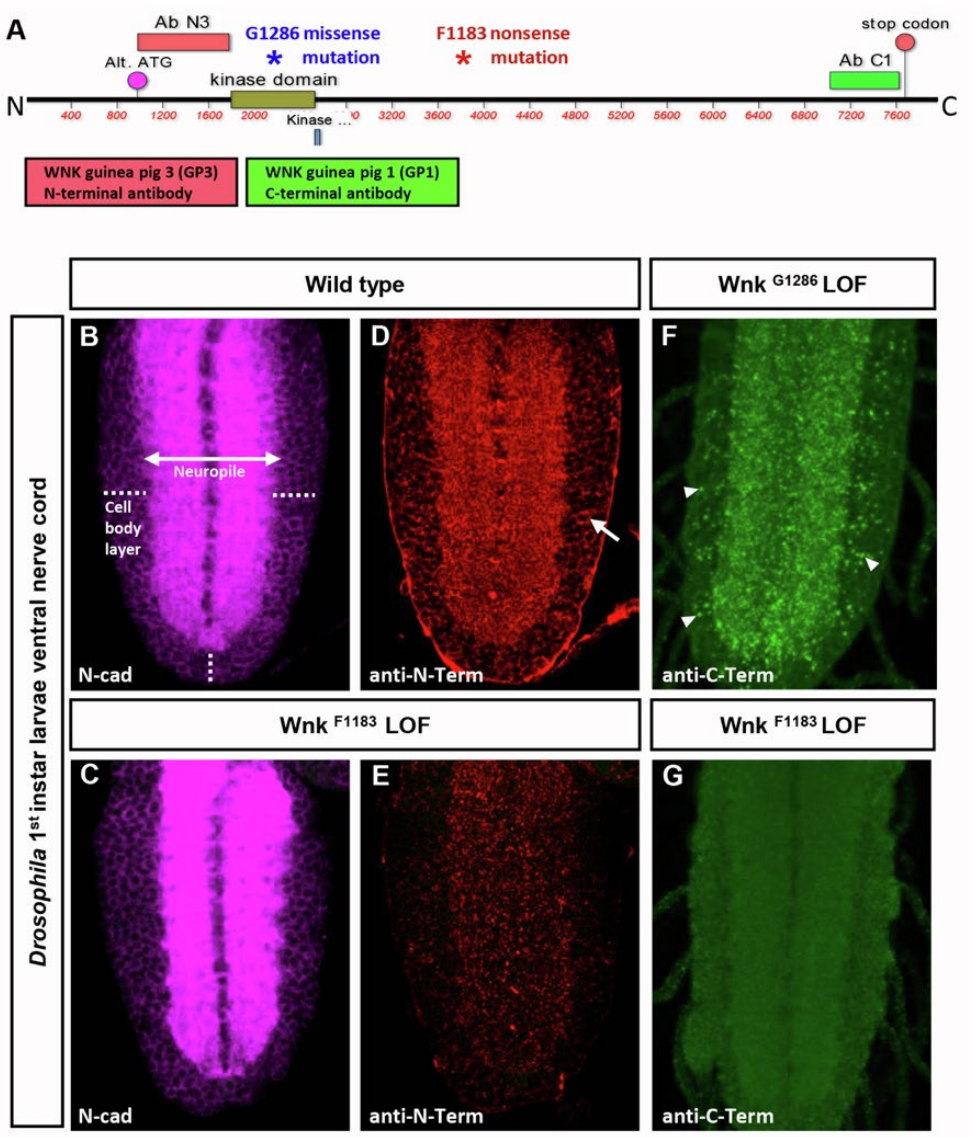

Figure S1. Characterization of dWnk alleles and anti-Wnk antibodies (A) Schematic of *Drosophila* Wnk protein indicating the location of two loss of function alleles (stars). The Wnk^{G1286} allele carries a missense mutation in the kinase domain and the Wnk^{F1183} allele has a non-sense mutation in the middle of the open reading frame (ORF). Two protein fragments (Ab N3 and AbC1) were used to raise N-terminal and C-terminally directed anti-Wnk antibodies. **(B-G)** First instar VNC samples of wildtype or homozygous mutant animals were stained with anti-Wnk antibodies. Anti-Ncad staining was used as a control protein expressed throughout the neuropil. **(B** and **D)** dWnk is present in the neuropil and cell body layer with apparent cytoplasmic localization (arrow) (F) Abnormal punctate (possibly vesicular) staining of Wnk protein in homozygous Wnk^{G1286} indicates that subcellular distribution of protein is strongly affected. **(E** and **G)** dWnk protein is absent in homozygous Wnk^{F1183} samples.

Supplemental Figure S2

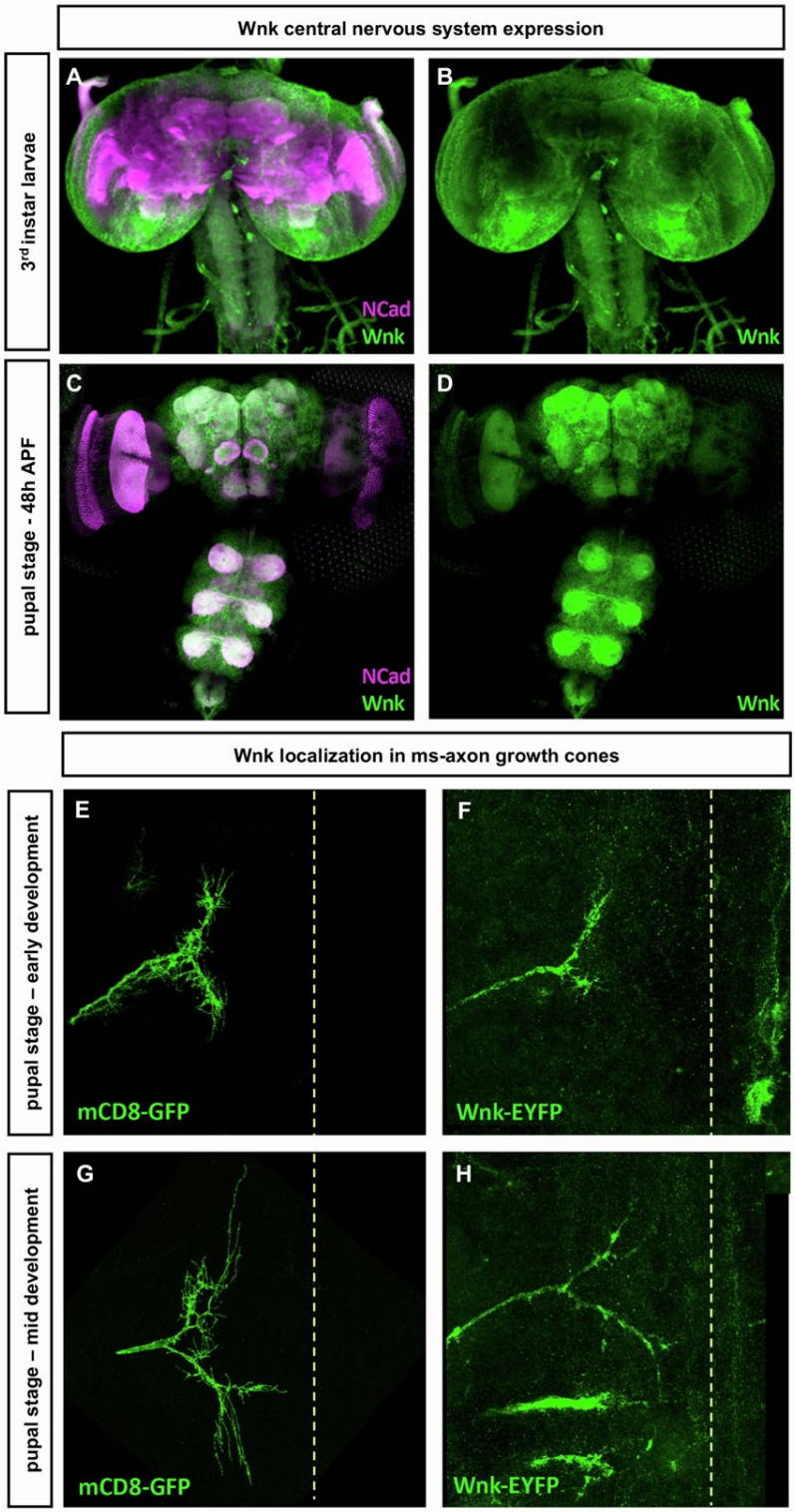

Figure S2. dWnk is broadly expressed in the developing CNS. (A-D) Central nervous system (brain and ventral nerve cord) of wild type animals stained with anti-NCad and anti- Wnk antibodies at end of larval 3rd instar **(A-B)** and pupal stage (48h APF) **(C-D)**. **(E-H)** Wnk localization in mechanosensory axon growth cones. Wild-type DC neurons growth cone during early development and the intermediate phases tagged with mCD8-GFP **(E** and **G)** and Wnk-EYFP **(F** and **H).**

Supplemental Figure S3

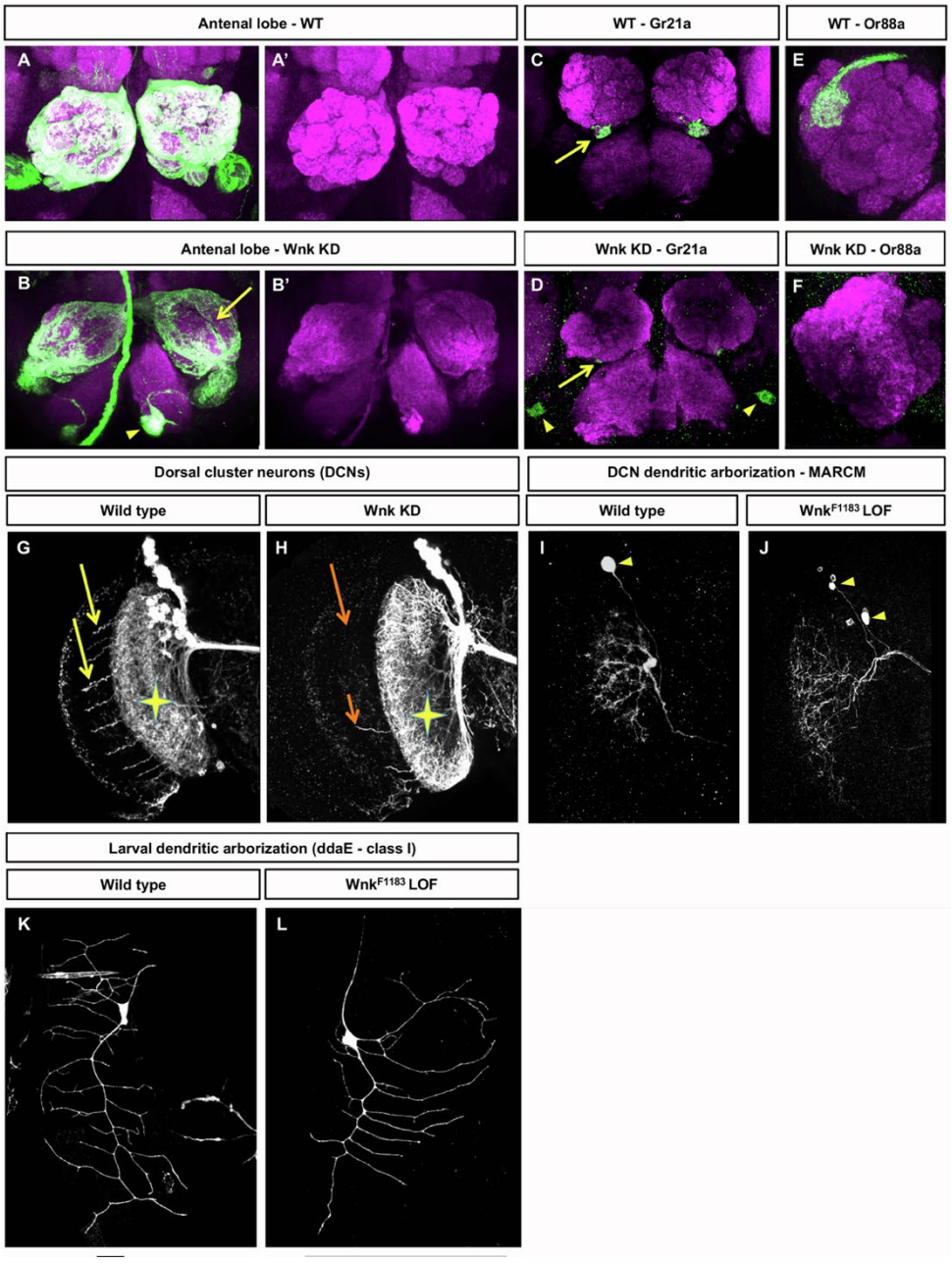

Figure S3. WNK affects wiring of multiple neuron types but function is specific for axonal versus dendritic compartment. **(A-F)** Glomeruli targeting of OR axons severely disrupted in the fly upon WNK1 inactivation. **(G-H)** dWnk is required for axon branch development of Dorsal Cluster Neurons (DCNs) but function is specific for axonal versus dendritic compartment. Confocal section through the adult brain of control samples showing the proximal dendritic compartment (star) and distal axon branch extensions (arrows) from the lobula to the medulla. **(H)** In a sample of dWnk RNAi knock down, a severe reduction in the number of axons branches (arrows) is observed. However, the dendritic compartment appears unaffected (star) which is confirmed at the single neuron resolution in the panels **I** and **J**. DCN neurons were visualized using Ato-Gal4 driving UAS-GFP. Knock- down of dWnk was achieved using Ato-Gal4 driving UAS-dWnk dsRNA. **(I-J)** Single GFP-positive mutant DCNs is generated using the MARCM technique. yellow arrowheads mark DCN soma and their respective dendritic compartments in both wild type and Wnk LOF. **(K-L)** dWnk kinase is also not required for dendritic patterning of class I da neurons. **(K-L)** Representative images of class I da neuron dendrites from wild type and dWnk LOF larvae. Single GFP-positive control and mutant da neurons are generated using the MARCM technique. (B) No significant differences in the number of dendrites were identified between wild type and dWnk LOF.

Supplemental Figure S4

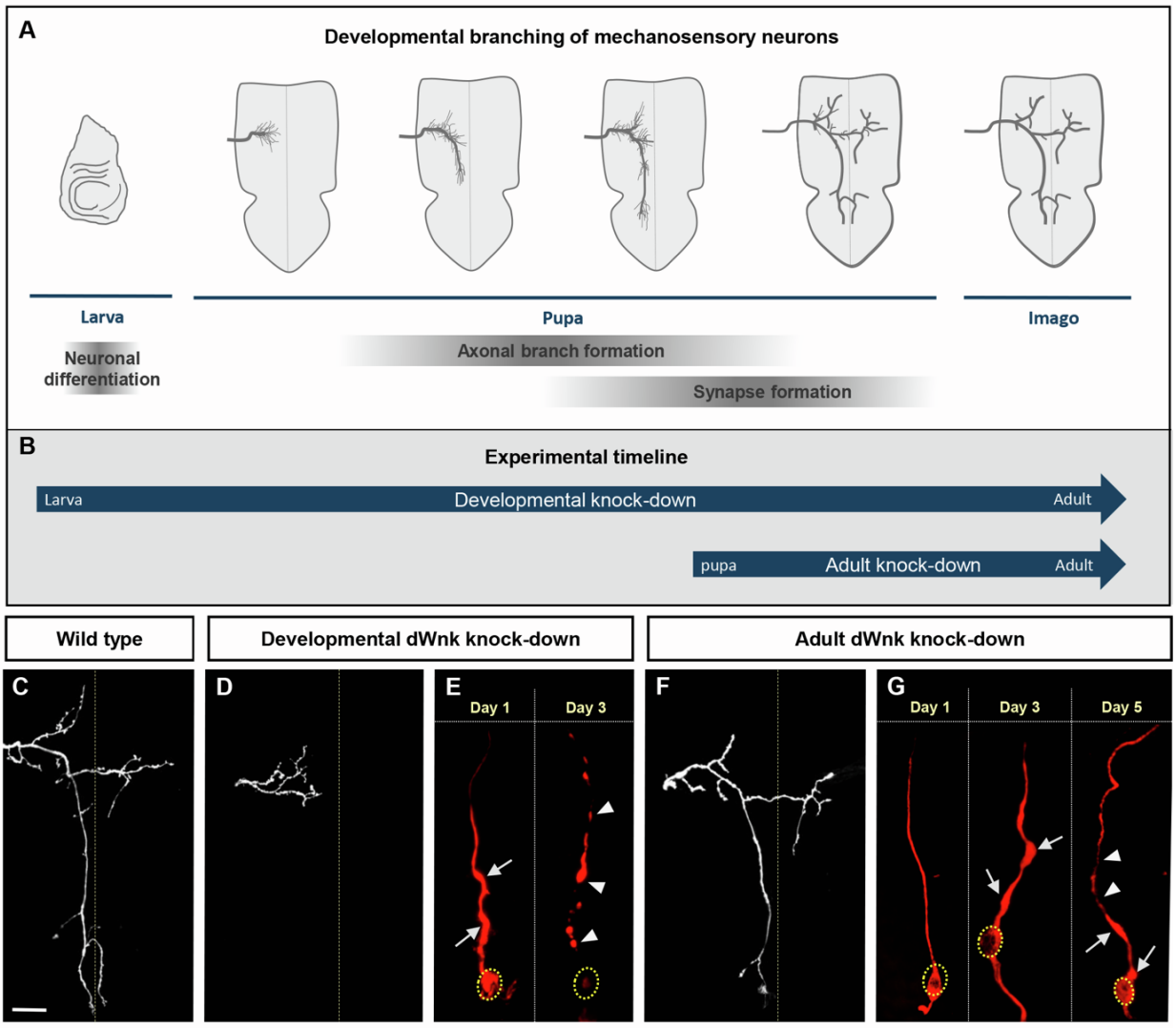

Figure S4. dWnk is required for axon maintenance independent of its role in developmental axon branching. (A) Schematic of a *Drosophila* mechanosensory neuron development. In wild-type, mechanosensory neuron differentiation starts in the imaginal disc of *Drosophila* larva. During early pupal development, the growth cones composed of filopodia- like extension starting to expand and sprout into all directions. During the intermediate phases, the number and length of filopodia is dramatically increased and segregated in opposite directions, along the anterior-posterior axis as well as toward the midline. In later stages, the main axon shaft is growing in length and the midline projecting axon becomes more prominent and grows contralaterally. In adult stages, the main primary branches give rise to an anterior ipsilateral branch, a posterior ipsilateral branch and an anterior midline crossing collateral and more variable, smaller secondary branches **(C)**. Complete and early developmental knock- down of dWnk **(B** and **D-E)** leads to severe mechanosensory neuron branching defects where branches do not extend **(D)**. The proximal part of the axon **(E)** undergoes axon swelling and blebbing (white arrows) in day one and the axon starts to undergo fragmentation (white arrow heads) in day three, followed by complete fragmentation and clearance of axonal debris in day five (data was not shown). RNAi-based knock-down of dWnk after axonal branching occurred **(B** and **F-G)** allows normal development of the main axon branches in the VNC. However, after depletion of dWnk adult axons start to degenerate. Note that three to five days post hatching the proximal part of the axon exhibits swellings (white arrows) and disintegration (white arrowheads) **(G)**.

Supplemental Figure S5

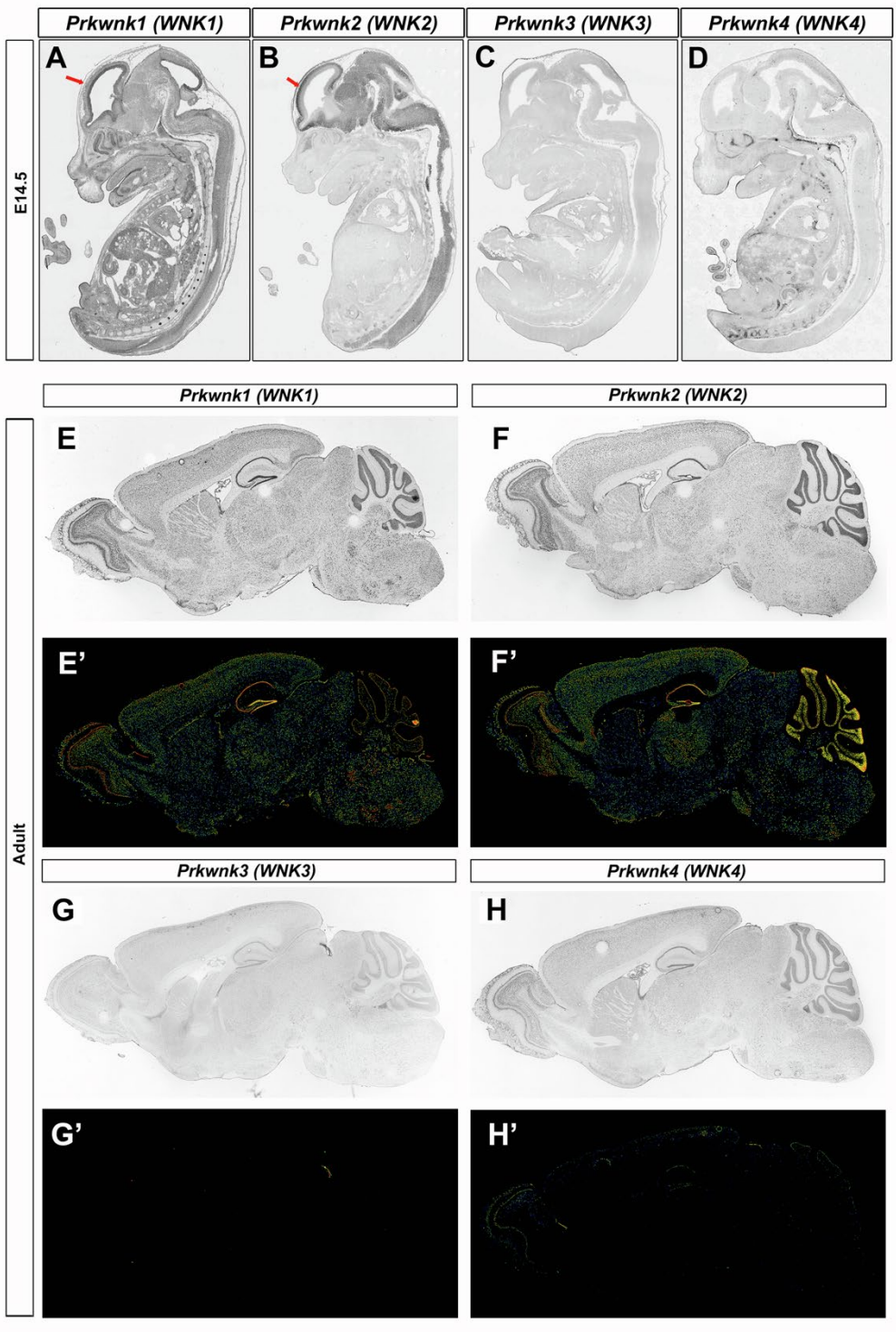

Figure S5. *Wnk1-2* are the main *Wnk* isoforms expressed in the mouse embryonic and adult brain. (A-D) In situ hybridization showing expression of all 4 *Wnk* genes in the mouse embryo. Sagittal section of mouse embryo at age E14.5. Pictures available from Genepain.org. **(E-H)** In situ hybridization showing expression of all 4 *Wnk* genes in the adult mouse brain. Sagittal section of mouse brain from the Allen Brain Atlas.

Supplemental Figure S6

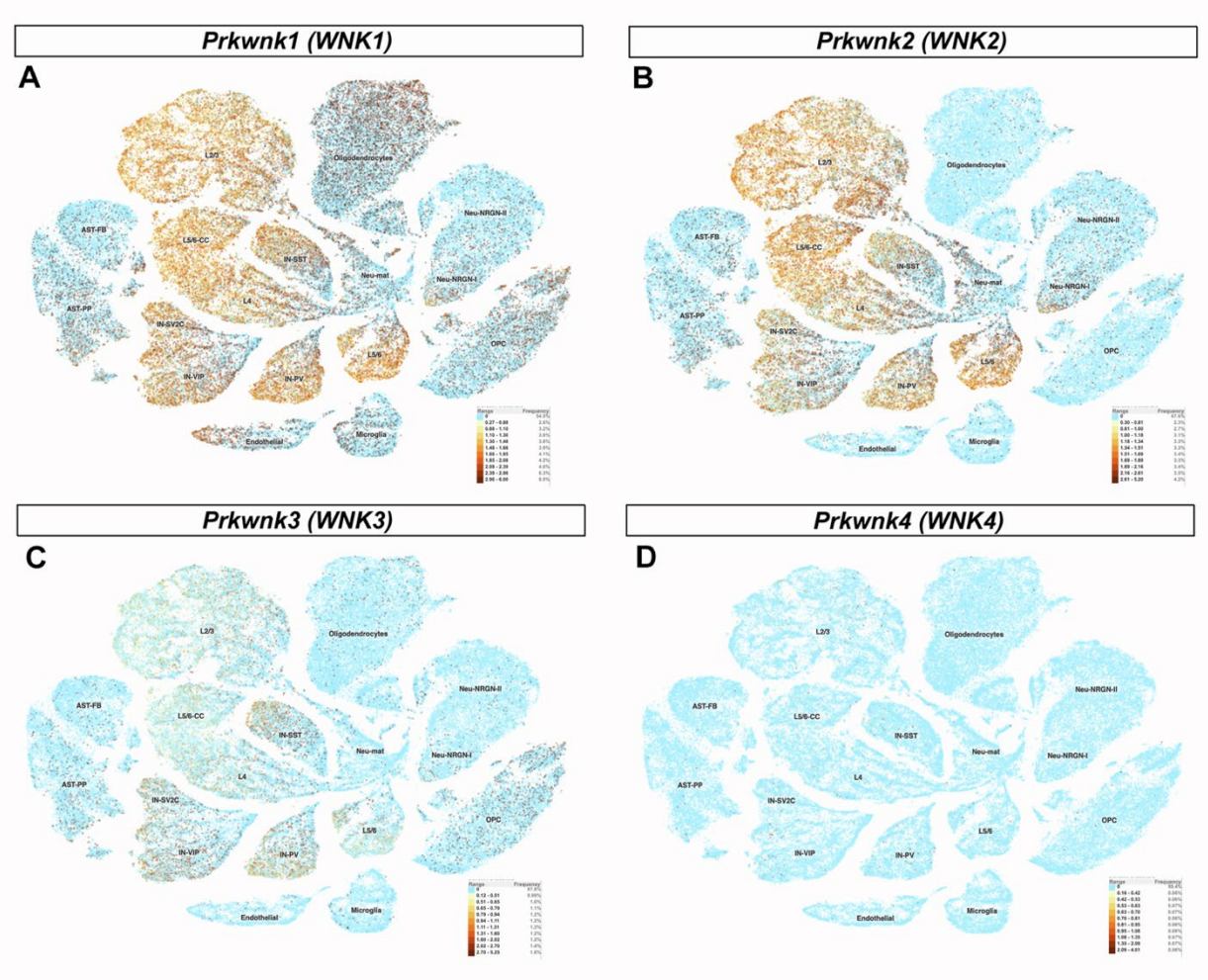

Figure S6. Comparative expression of *Wnk1-4* mRNA in the developing human cortex. (A-D) Quantitative expression of *Wnk1-4* through single cell RNA sequencing (scRNAseq) from human developing and adult cortex. Data were obtained from the publicly available repository of the UCSC cell browser (https://autism.cells.ucsc.edu). Wnk1 and Wnk2 is mostly expressed in cortical excitatory and inhibitory neurons but in very few non-neuronal cells (with exception of Wnk1 in oligodendrocytes). Wnk3 is expressed at very low levels in the same neuronal subtypes and Wnk4 is not detectable. Abbreviations: L2/3: layer 2/3 excitatory neurons; L5/6-CC: layer 5/6 cortico-cortical projecting excitatory neurons; L5/6: layer 5/6 corticofugal projecting excitatory neurons; IN-VIP: VIP interneurons; IN-SST: somatostatin interneurons; IN-SV2C: SV2C interneurons IN-PV: PV interneurons (large basket cells); OPC: Oligodendrocyte precursor cells; AST-FB: fibrous astrocytes; AST-PP: protoplasmic astrocytes; Neu-Mat: Maturing neurons; Neu-NRGN-I and -II; neuregulin expressing neurons.

Supplemental Figure S7

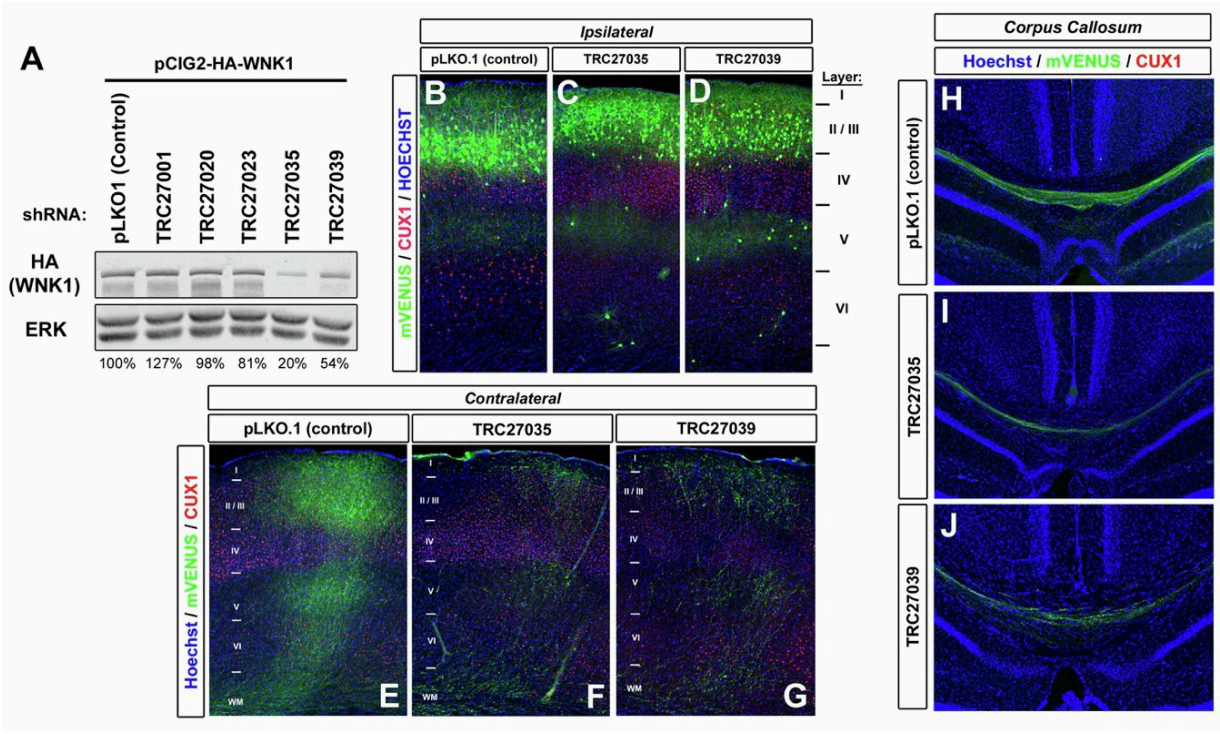

Figure S7. Similar phenotype resulting from the inhibition of *Wnk1* by using two distinct shRNA constructs. (A) Validation of *Wnk1* shRNA-mediated knockdown by Western-blot in HEK293T cells using the indicated plasmids. HA-tagged mouse WNK1 was used to control knockdown efficiency. Band was normalized to ERK immunoreactivity. Percentages indicate residual WNK1 expression. **(B-J)** Representative images following *in utero* electroporation with the indicated plasmids. Mice were sacrificed at P21. Electroporated neurons are visualized by mVenus expression. Staining with CUX1 and Hoechst as indicated. Magnification of the ipsilateral side **(B-D)**, contralateral side **(E-G)** and midline **(H-J)** shows that targeting *Wnk1* expression with two independent shRNA plasmids results in a similar phenotype on axon branching and/or maintenance.

Supplemental Figure S8

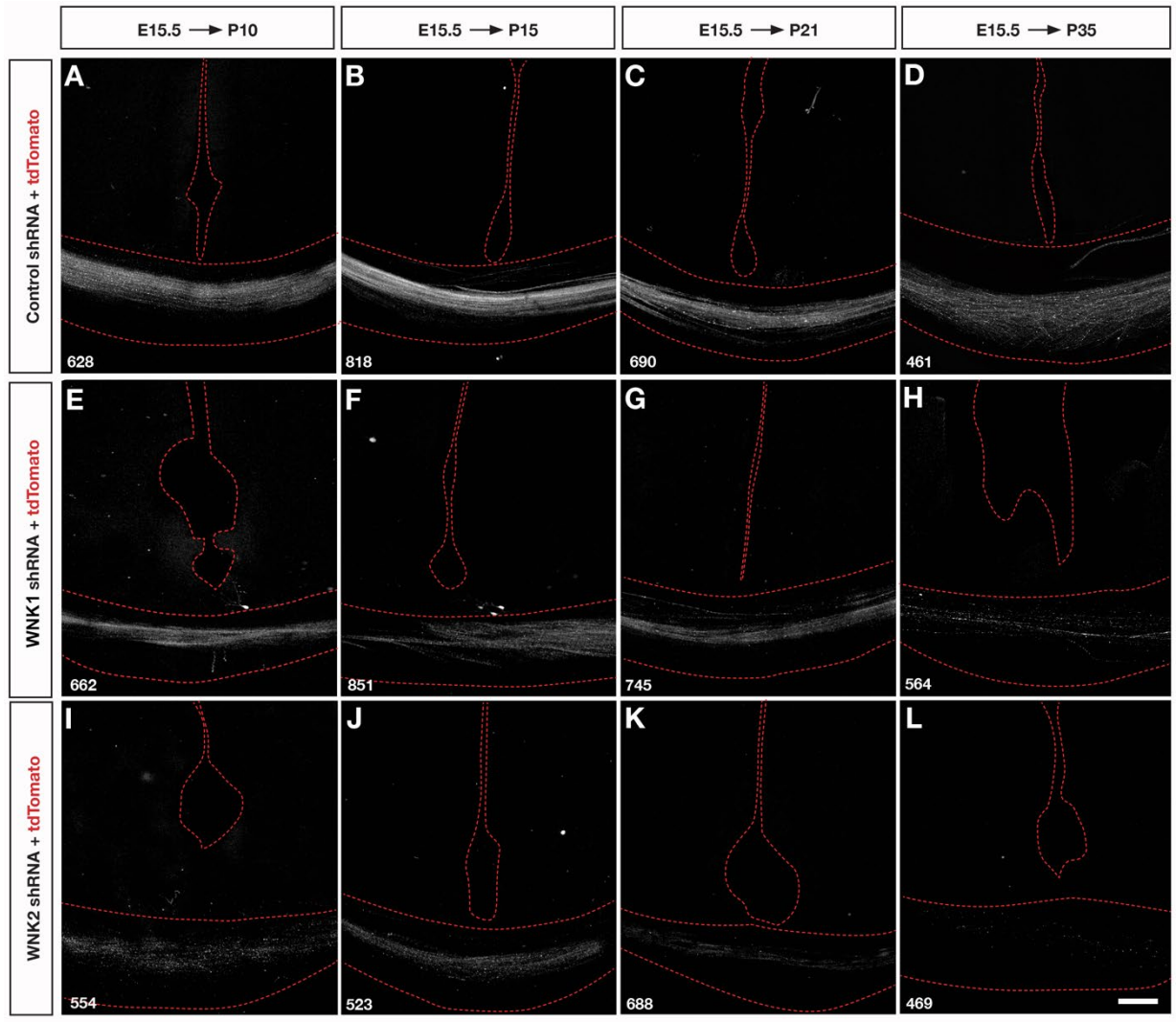

Figure S8. *Wnk1* and *Wnk2* are required for axon maintenance of mouse callosal axons *in vivo*. (A-L) High magnification of tdTomato+ axons located at the corpus callosum from layer 2/3 PNs electroporated as indicated (same brains as in **Figure 4**). Note that in both Wnk1 and Wnk2 shRNA mediated knockdown, the number of axons present at the CC decreases progressively at P21 and P35 compared to P10-15. The numbers in the lower left of each image corresponds to the total number of electroporated neurons on the ipsilateral side of section. Scale bar: 100 microns.

Supplemental Figure S9

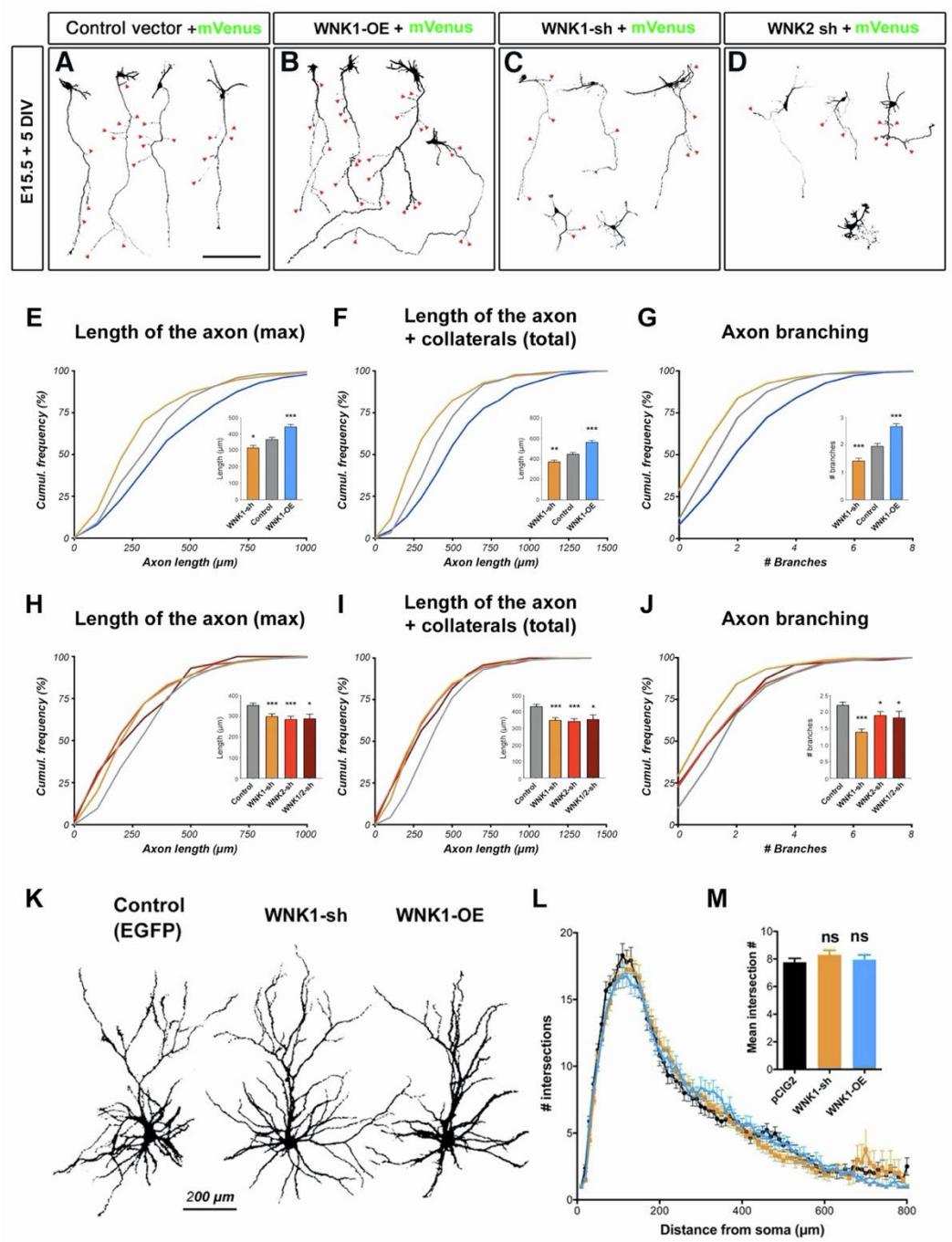

Figure S9. WNK1 and WNK2 control cortical axon development in the mouse but Wnk1 has no effect on dendritic arborization in layer 2/3 PNs. (A-D) Representative neurons imaged after 5 DIV in control condition (pSCV2) **(A)**, or following overexpression (OE) of WNK1 **(B)**, shRNA mediated knockdown of *Wnk1* **(C)** or *Wnk2* **(D)**. Neuron morphology was visualized by mVenus expression. Red arrowhead: collateral axon branches. Quantification of axon length **(E** and **H)**, total axon length (main axon + collaterals) **(F** and **I)** and number of collateral branches per axon **(G** and **J).** Graphs represent the cumulative frequency (in % of total number of neurons). Histograms represent average ± SEM. Data from 3 independent experiments. Statistical analyses: one way ANOVA followed by Dunnett's multiple comparisons test. **(E-G)** nWNK1-sh=228, nControl=226, nWNK1-OE=330. **(H-J)** nControl=300, nWNK1- sh=246, nWNK2-sh=210, nWNK1/2-sh=71. **(K-M)** Representative morphology (soma and dendrites) of mouse layer 2/3 PNs at 21DIV in control conditions or following shRNA mediated knockdown of *Wnk1* or overexpression of WNK1. Quantification of dendritic arborization through a Scholl analysis **(L-M)** shows no difference in dendritic branching. NpCIG2=38, nWNK1-OE=38, nWNK1sh=40 neurons.

Supplemental Figure S10

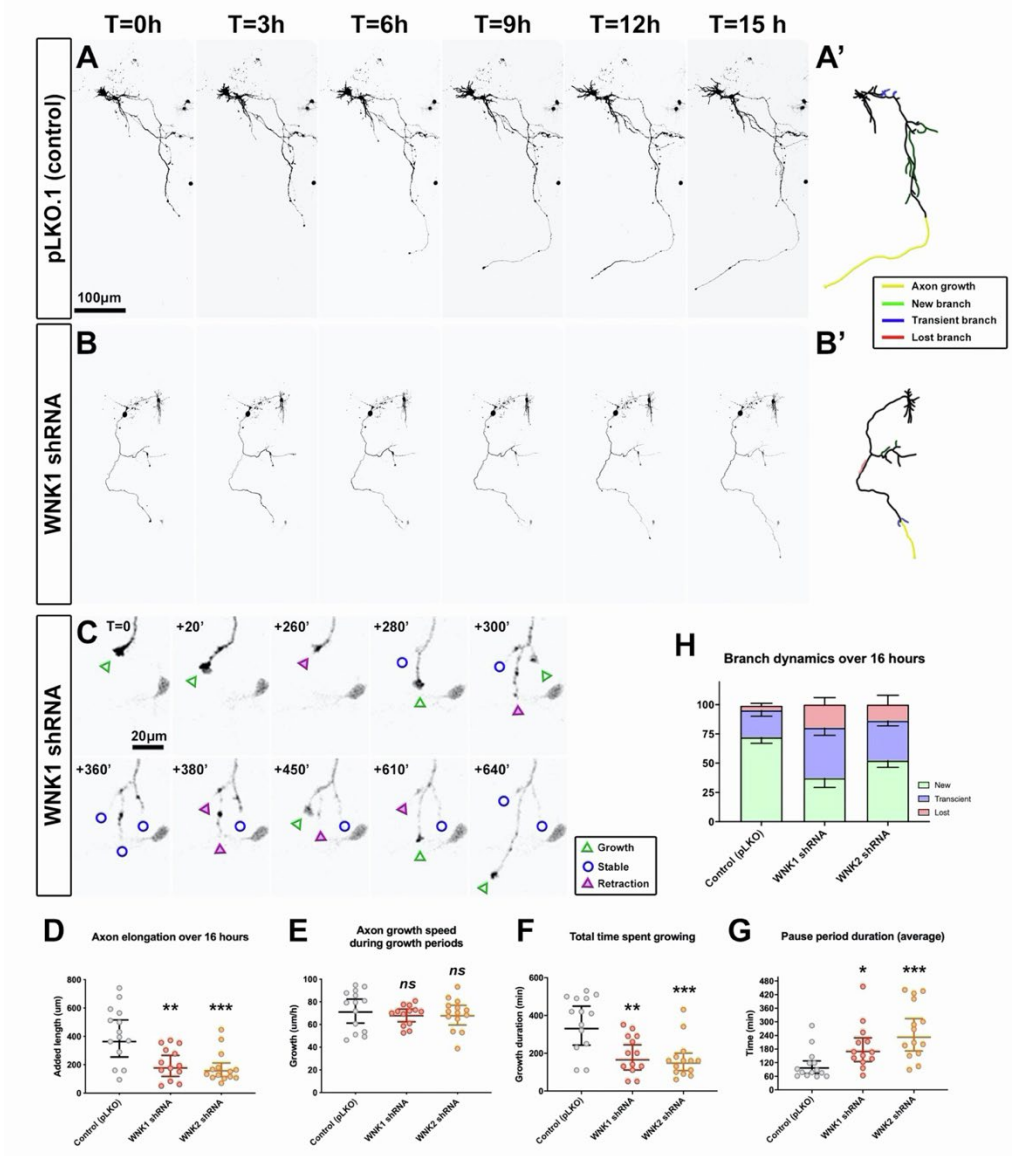

Figure S10. Dynamics of axon growth and branching *in vitro* upon knockdown of mouse WNK proteins. (A-B) Patterns of axon growth and branching over 15h of time-lapse videomicroscopy for layer 2/3 PNs ex utero electroporated at E15 and cultured for 6DIV expressing a control vector (pLKO.1) **(A)** of with shRNA targeting WNK1 **(B)**. Neurons were imaged for the indicated times. Axon morphology was determined by co-electroporation of a Venus encoding plasmid. **(A'-B')** Tracing of axonal branches of neurons shown in **(A-B)** over a 15 hours period. Colors indicate main axon growth over 15 hours (yellow), extension of new branches that persist up to the end of the movie (new branches, green), the formation of new branches that retract before the end of the movie (transient branches, blue) and the elimination of axon branches present at the origin of the movie (lost branches, red. **(C)** Magnification of the growth cone at the tip of the main axon in a neuron electroporated with shRNA targeting WNK1 shows dynamics of growth cone formation and elongation (green arrowhead), stalling (blue circle) or retraction (magenta arrowhead). The formation of multiple growth cones that extend the axon in one direction then retract was only observed upon WNK1 or WNK2 knockdown. **(D-G)** Quantification of axon elongation rate **(D)**, of the speed of growth of the axon during the periods of elongation **(E)**, of the total duration of growth **(F)** and of the average pausing time **(G)** of neurons electroporated with shRNAs against WNK1 and WNK2. Data represent the median value ±95%CI. Each dot represents one neuron. Data are a minimum of three independent experiments. ncontrol=14, nWNK1sh=13, nWNK2sh=14. Statistical analyses: Kruskal-Wallis test followed by Dunn's multiple comparisons test. **(H)** Quantification of the average number (±SEM) of new, lost and transient branches shows an increase in transient or lost branches in neurons electroporated with a control plasmid of with shRNAs targeting WNK1 or WNK2.

Supplemental Figure S11

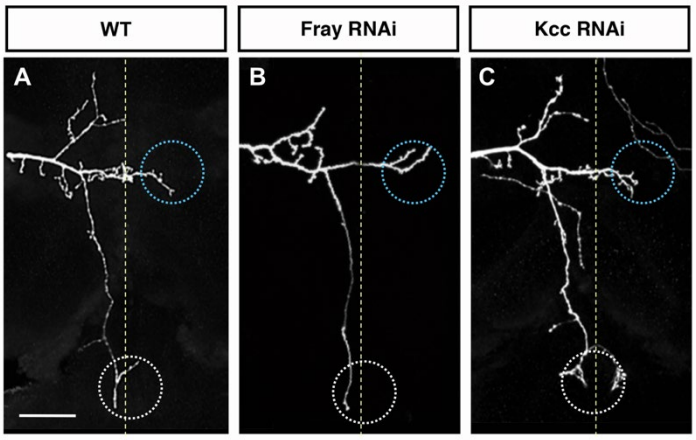

Figure S11. CNS axon projections of mechanosensory neurons are normal in RNAi knock- down of Frayed or KCC (A-C). All stereotyped axonal collateral projections are present in samples with RNAi knock-down of either Fray or KCC.

Supplemental Figure S12

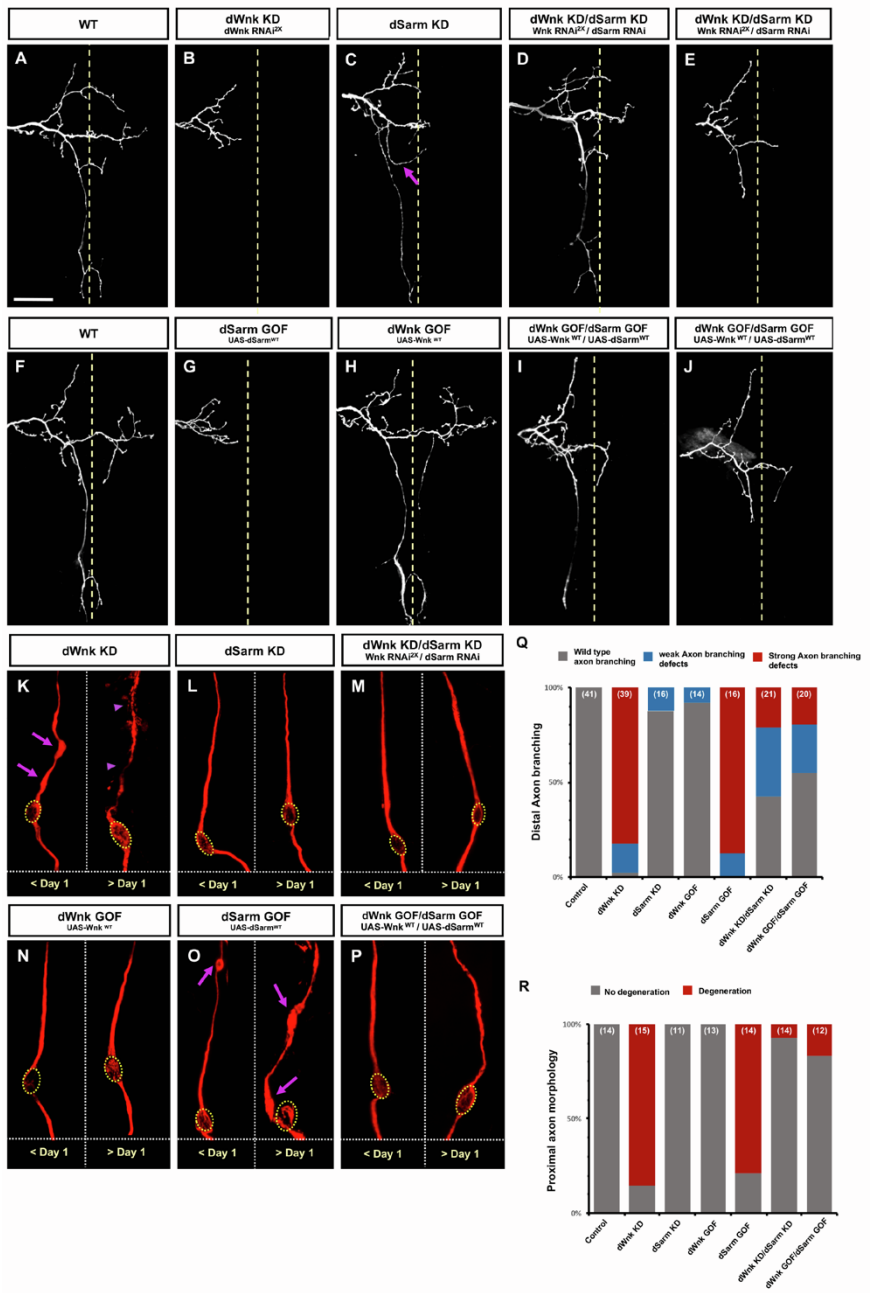

Figure S12. dWnk antagonizes dSarm function in axon branching. (A and **F)** WT mechanosensory neurons displaying the stereotyped branching pattern. **(B** and **G)** dWnk knock down (KD) and overexpression of dSarm are showing very similar phenotype i.e., axon branching defects with loss of distal axon terminals. **(C** and **H)** dSarm knock down as well as overexpression of dWnk are showing normal branching pattern. **(D** and **E)** dWnk knock down induced axon branching defects can be rescued by dSarm RNAi-knockdown. **(E** and **J)** Overexpression of dWnk can maintain the axonal branches otherwise disrupted by dSarm GOF. **(Q)** Quantification of axonal branching defects observed in the various conditions described above. **(K-P)** Visualizing distal to proximal axon degeneration of mechanosensory neurons in thorax using anti-22C10 antibody staining for samples before and after Day 1 post eclosion**. (K** and **O)** Double RNAi mediated knock down of dWnk and overexpression of dSarm lead to axon swelling and blebbing (arrows in magenta) followed by axon fragmentation (arrowheads in magenta) in samples older than one day. **(L** and **N)** dSarm KD and dWnk OE are showing a near continuous labeling of the microtubule cytoskeleton using anti-22C10 antibody staining. **(M)** Knock-down of dSarm prevent axon degeneration caused by dWnk KD. **(P)** Overexpression of dWnk can rescue the axon degeneration caused by overexpression of dSarm. **(R)** Quantification of mechanosensory neuron proximal axon degeneration in thorax observed in the various conditions described above.

Supplemental Figure S13

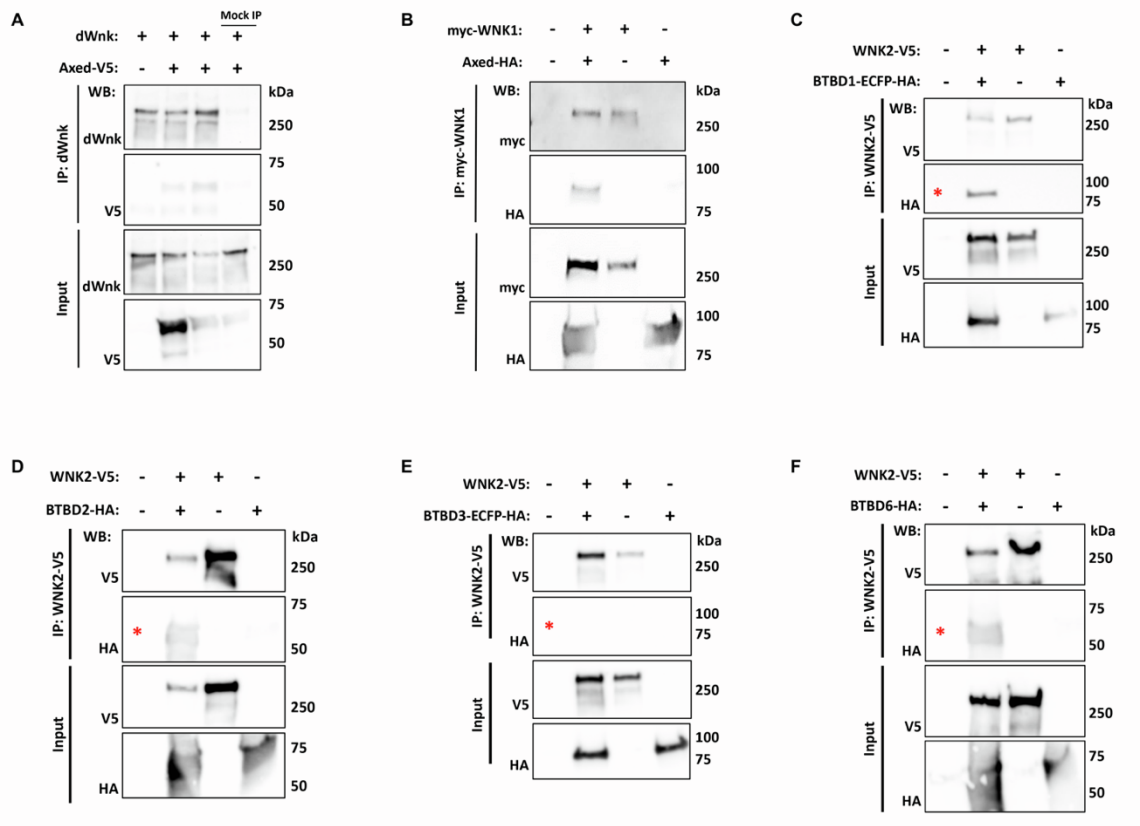

Figure S13. Wnk interacts with Axed. **(A)** Stable *Drosophila* S2 cells were transfected with dWnk and Axed expression was induced using CuSO4 at 6 and 24 hours after transfection. dWnk was precipitated using magnetic beads and co-precipitated protein complexes were analyzed using a V5-tag specific antibody. Non-coated beads were used as mock control. **(B)** Axed expression does not influence WNK1. Lysates were collected from HEK293T cells transfected with a GFP-containing plasmid in combination with either myc-tagged WNK1 and/or V5-tagged Axed. Proteins were visualized using indicated specific antibodies. An anti β-tubulin antibody was used as loading control. **(C-F)** Mammalian WNK2 interacts with BTBD1, BTBD2 and BTBD6 but not BTBD3. Validation of interactions by co-immunoprecipitation. HEK293T cells were co- transfected with BTBD1-HA **(C)**, BTBD2-HA **(D)**, BTBD3-HA **(E)** and BTBD6-HA **(F)** together with V5-tagged WNK2. WNK2 was precipitated using anti-V5 magnetic beads and co-precipitated protein complexes were analyzed by WB using an HA-tag specific antibody.

Supplemental Figure S14

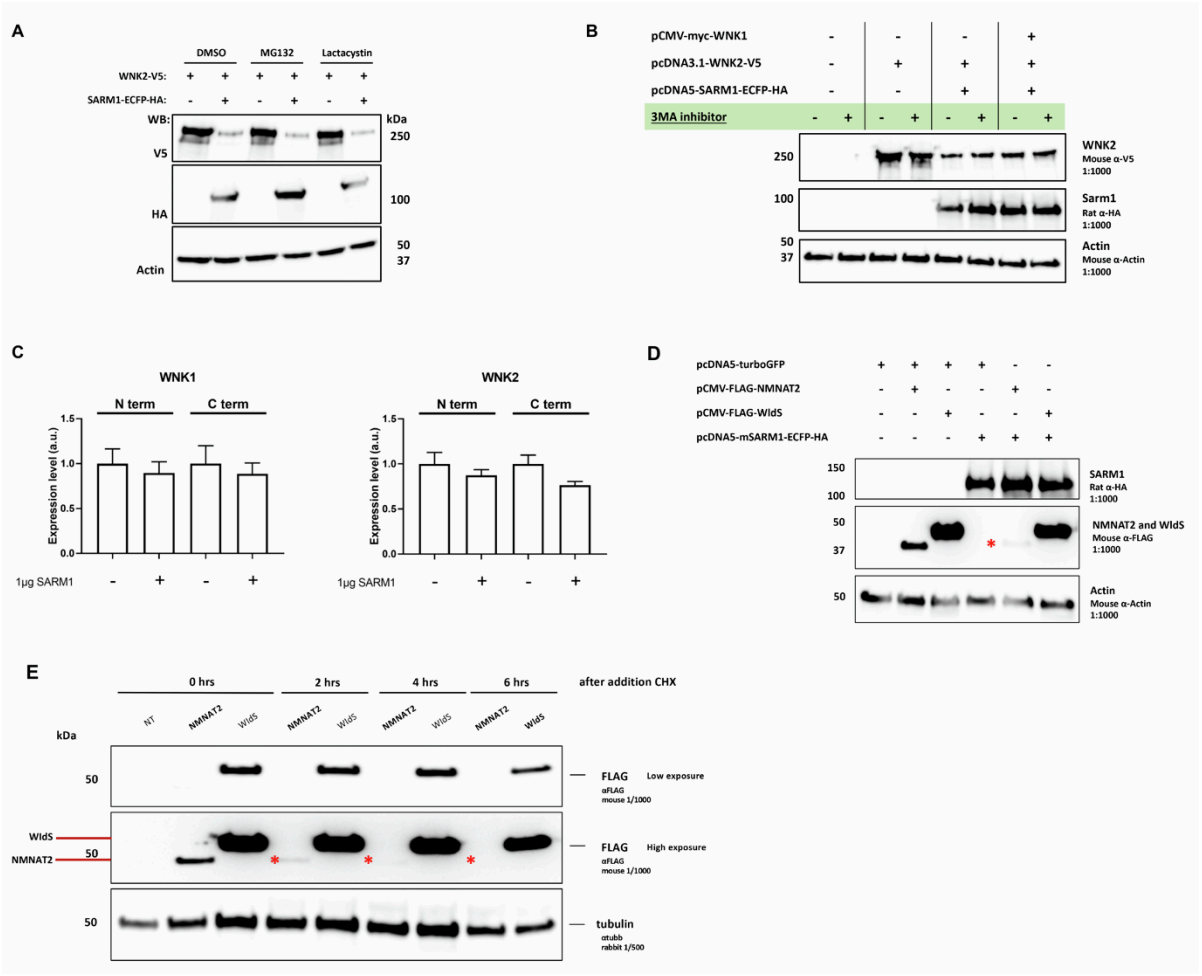

Figure S14. WldS, a long-lived protein, is not depleted by SARM1 expression.
(A) SARM1-dependent depletion of WNK2 expression is not affected by proteasome blockage. SH-SY5Y cells were co-transfected with V5-tagged WNK2, either with a GFP- containing plasmid or SARM1-HA. After treating cells with the proteasome inhibitors MG132 and lactacystin (6 hours), cells were lysed and lysates were analyzed by western blot (WB) using anti-V5 and anti-HA antibodies. **(B)** SARM1-dependent depletion of WNK2 expression is not affected by autophagy inhibition. SH-SY5Y cells were co-transfected with mammalian WNK2-V5 in combination with either SARM1-HA and/or myc-WNK1. Cells were lysed after treatment with 3-MA (6 hours), an inhibitor of autophagy/PI3K. Using HA-tag and V5-tag specific antibodies, proteins were visualized by WB. An anti-actin antibody was used as loading control. **(C)** mRNA levels of both mammalian WNK1 and WNK2 are not affected by SARM1. HEK293T cells were co-transfected with WNK1 or WNK2 and SARM1. Isolated RNA was reverse transcribed and analyzed for gene expression of WNK1 and WNK2 by RT-PCR. Values represent means ± SEM. Expression is indicated relative to GAPDH expression. Three independent experiments were performed. **(D)** SARM1 lowers expression of mammalian NMNAT2, but not of WldS. SH-SY5Y cells were co-transfected with either FLAG-NMNAT2 or FLAG-WldS with or without SARM1-HA. Proteins were detected by WB using FLAG-tag, HA-tag, and anti-α-actin (loading control) specific antibodies. **(E)** NMNAT2 is labile, while WldS is a very stable protein. HEK293T cells were transfected with mammalian NMNAT2-FLAG or FLAG-WldS. Cells were lysed at indicated time points after addition of the protein translation inhibitor CHX. WB was performed using an anti-FLAG antibody and anti β-tubulin was used as loading control.

Supplemental Figure S15

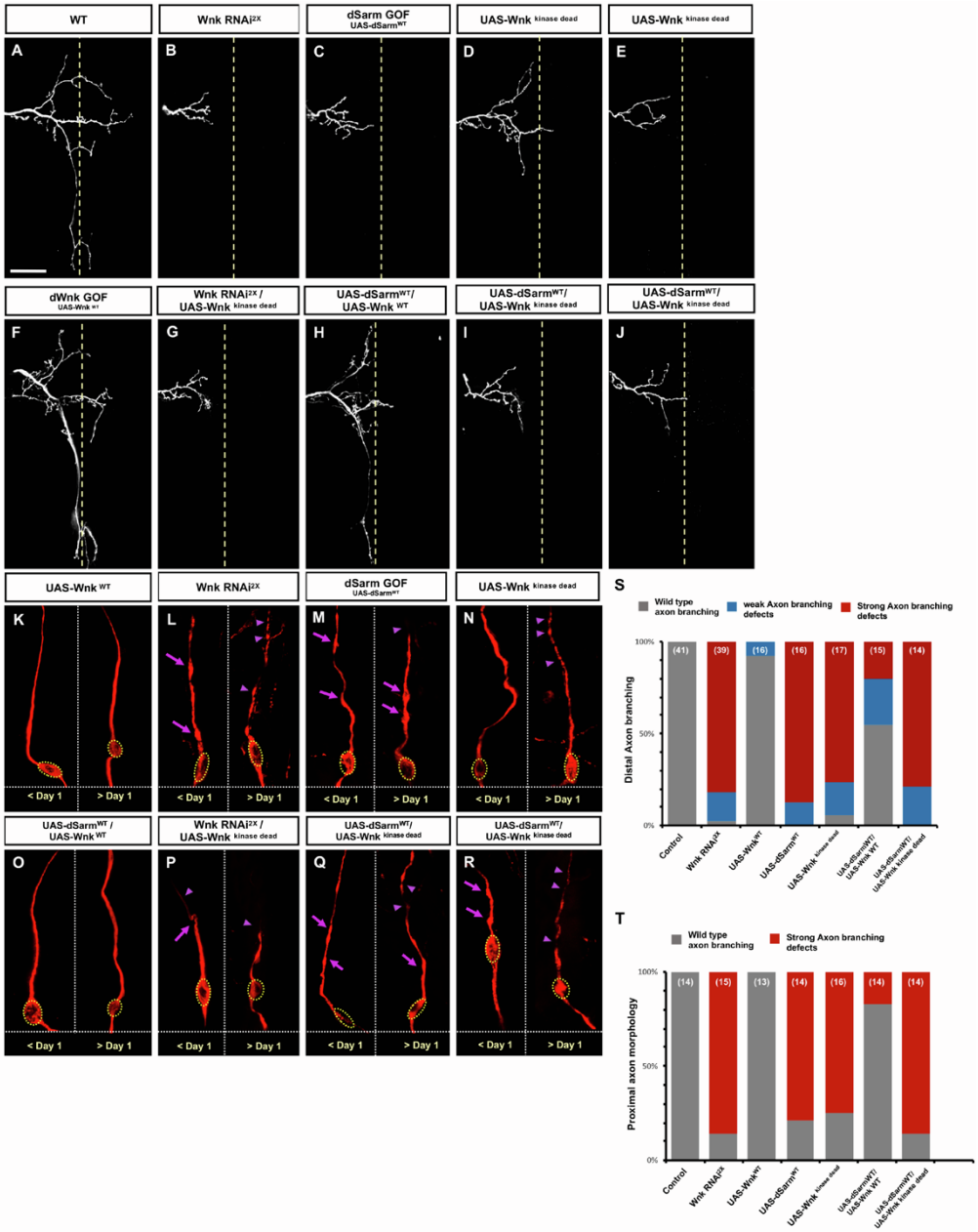

Figure S15. Kinase activity of Wnk is essential for axon branching and axon maintenance. (A) WT mechanosensory neurons displaying the stereotyped branching pattern. **(B-E)** dWnk knock down (KD), overexpression of dSarm as well as kinase dead version of dWnk are showing very similar phenotype i.e., axon branching defects with loss of distal axon terminals. **(F)** overexpression of dWnk are showing normal branching pattern. **(H)** Overexpression of dWnk can maintain the axonal branches otherwise disrupted by dSarm GOF. **(G and I-J)** dWnk knock down and overexpression of dSarm induced axon branching defects cannot be rescued by kinase dead version of dWnk. **(S)** Quantification of axonal branching defects observed in the various conditions described above. **(K-R)** Visualizing distal to proximal axon degeneration of mechanosensory neurons in thorax using anti-22C10 antibody staining for samples before and after Day 1 post eclosion**. (K)** dWnk OE are showing a near continuous labeling of the microtubule cytoskeleton using anti-22C10 antibody staining. **(L-N)** Double RNAi mediated knock down of dWnk, overexpression of dSarm and dWnk kinase dead lead to axon swelling and blebbing (arrows in magenta) followed by axon fragmentation (arrowheads in magenta) in samples less and older than one day. **(O)** Overexpression of dWnk can rescue the axon degeneration caused by overexpression of dSarm. **(P-R)** Kinase dead version of dWnk cannot prevent axon degeneration caused by dWnk KD and dSarm overexpression. **(T)** Quantification of mechanosensory neuron proximal axon degeneration in thorax observed in the various conditions described above.

Methods

Experimental Models and Subject Details

Flies (D. melanogaster) genotypes for all experiments and all figure panels are listed in Table S1. For all genetic crosses males and female flies were used. UAS-RNAi lines were obtained from the Vienna Drosophila Resource Center (Vienna, Austria) or from the Bloomington Drosophila stock center (Indiana University, USA). All crosses were performed at 25ºC, except for late knock-down of dWnk, for which a shift from 18ºC to 29ºC at late-pupal stage (after axon branching had already occurred) was used to prevent RNAi activation during development, and the presence of normal axon morphologies was confirmed in young adult control flies. Single-cell labeling and transgene expression were performed as described (Urwyler et al., 2019). For analysis of axon branch patterns of dye-labeled mechanosensory neurons at adult stages only VNCs of female animals were used in order to avoid variability due to size differences of male and female flies. In all other experiments male and female animals were used.

Mice were used according to protocols approved by the Institutional Animal Care and Use Committee at Columbia University Medical School and the Ethics committee of the University of Lyon, and in accordance with National Institutes of Health guidelines and the French and European Union legislation. All animals were maintained in a 12-hour light/dark cycle. We crossed C57BL/6J males with 129/SvJ females to generate F1 hybrids (C57BL/6J x 129/SvJ). Time-pregnant F1 hybrid females were obtained by overnight breeding with C57BL/6J males. Noon following breeding was considered E0.5. Embryos of both sexes were used in electroporation procedures. Electroporations were performed at developmental stage E15.5. Mice were sacrificed at the age indicated in the figures.

Plasmids and molecular cloning

Empty vector pLKO.1 and shRNA targeting plasmids toward mouse WNK1 (TRC0000027035 and TRC0000027039) or mouse WNK2 (TRC0000027606, TRC0000027661 and TRC0000027668) were selected from The RNAi Consortium shRNA Library (TRC) from the Broad Institute and purchased from OpenBioSystems. Unless stated otherwise shRNA plasmids targeting a same gene were pooled at a 1:1 (WNK1) or 1:1:1 (WNK2) ratio and used at the final concentration of 1 mg/mL for in utero cortical electroporation or ex vivo electroporation. The CreON-shWNK plasmids were synthesized (Vigene) using these same shRNA targeting sequences under a CMV promoter. The CMV promoter was then replaced

with a CMV enhancer/chicken b-Actin promoter (CAG) sing PCR amplification and InFusion cloning (Clonetech). pCAG-ERT2CreERT2 has been described previously (Matsuda and Cepko, 2007) and was purchased via Addgene (Addgene #13777).

Plasmids containing rat myc-WNK1, human WNK2-V5, and mouse SARM1 were a gift from Melanie Cobb, Joseph Costello, and Yi-Ping Hsueh, respectively (Addgene plasmid #38779, #24569, and #50707) (Xu et al., 2000; Chen et al., 2011; Hong et al., 2007). The mVenus expressing vector pSCV2 was described previously (Hand and Polleux, 2011). Human NMNAT1 and NMNAT2 were PCR amplified from clone HsCD00353283 and HsCD00399665 from the DNASU plasmid repository. dWnk and Axed were amplified from Drosophila cDNA and cloned into pUASTattB using Gibson Assembly (NEB E2611S). In order to create a stable Drosophila cell line, Axed was additionally subcloned into pMT-V5-His A (Thermo Scientific) using Gibson Assembly, and pCoBlast (Thermo Scientific) was used as a selection vector. All expression vectors used for cell line transfections were further constructed using the Gateway cloning system (Life Technologies). In brief, NMNAT1, NMNAT2, and SARM1 open reading frames were amplified by PCR adding a 50 attB1 site and a mammalian Kozak sequence in the forward primer, as well as a 30 attB2 sequence in the reverse primer. SARM1DTIR was generated by amplifying solely the N-terminal SARM1, excluding the 165 amino acids at the C-terminal comprising the TIR (Toll/ Interleukin-1 Receptor) domain. The stop codon was removed to allow in-frame C-terminal tagging. In a similar manner, turboGFP (GFP) was amplified with the retention of the stop codon to use as a transfection control. The amplicons were subcloned into a modified version of pDONR223 (Rual et al., 2004) by a BP transferase reaction. Subsequently, an LR reaction was performed according to the manufacturer's instructions with pcDNA5FRT-TO-GW-EYFP-FLAG and pcDNA5FRT-TO-GW-ECFP-HA destination vectors to generate NMNAT1-EYFP-FLAG, NMNAT2-EYFP-FLAG, SARM1-ECFP-HA, and SARM1DTIR -ECFP-HA. Finally, pCMV-FLAGNMNAT2 and pCMV-FLAG-WldS were a gift of the Coleman lab.

Cell cultures and transfections

Primary neuronal cultures were performed as described previously (Polleux and Ghosh, 2002). Mouse cortices were dissected in Hank's Buffered Salt Solution (HBSS) supplemented with 2.5 mM HEPES, 1 mM CaCl2 (Sigma), 1 mM MgSO4 (Sigma), 4 mM NaHCO3 (Sigma) and 30 mM D-glucose (Sigma), hereafter referred to as cHBSS. Cortices were dissociated in cHBSS containing papain (Worthington) and DNase I

(100 mg/mL, Sigma) for 20 min at 37ºC, washed three times and manually triturated in cHBSS supplemented with DNase. Cells were then plated at 7.5 x 10^4 cells per 35 mm glass bottom dish (Matek) coated with 1 mg/mL poly-D-lysine (Sigma) and cultured for 5, 10, 15 or 20 days in Neurobasal medium supplemented with 1x B27, 1x N2, 2 mM L-glutamine and 5 units/mL penicillin- 50 mg/mL streptomycin.

SH-SY5Y cells (ATCC, CRL-2266) and HEK293T cells (ATCC, CRL-3216) were cultured in DMEM/F12 and DMEM, respectively, supplemented with 10% FBS, 2 mM L-Glutamine and 100 units/mL penicillin- 100 mg/mL streptomycin. Cell transfection were performed in 6-well plates using GENIUS DNA transfection reagent with 2 mg of each plasmid. Unless otherwise indicated, all products for cell cultures were obtained from Invitrogen/Life Technologies. For cycloheximide (CHX) experiments, HEK293T cells were treated with the inhibitor at 100 mg/mL starting 24 hours after transfection. Protein lysates were prepared at t = 0 (no CHX treatment) and at 2, 4 and 6 hours of CHX treatment.

Drosophila S2 cells were obtained from DGRC and grown in Schneiders medium supplemented with 10% HI FBS and 100 units/mL penicillin- 100 mg/mL streptomycin (Invitrogen/Life Technologies). The stable cell line expressing Axed-V5 was grown in the presence of blasticidin (Life Technologies). Expression was induced using 500 mM CuSO4. Cells were transfected using the Amaxa Nucleofector II device (Lonza) with 1 to 2 mg of DNA (solution V, program D023).

Ex utero and in utero cortical electroporations

Ex utero electroporation of mouse dorsal telencephalic progenitors was performed as previously described (Courchet et al., 2013) by injecting plasmid DNA (1-2 mg/mL endotoxin-free plasmid DNA, Midi prep kit from Macherey-Nagel) plus 0.5% Fast Green (1:20 ratio, Sigma) using the picospritzer III (Parker) microinjector into the lateral ventricles of isolated E15.5 embryonic heads that were decapitated and placed in complete HBSS (Polleux and Ghosh, 2002). Electroporations were performed on the whole head (skin and skull intact) with gold-coated electrodes (GenePads 5 3 7 mm BTX) using an ECM 830 electroporator (BTX) and the following parameters: five 100 ms long pulses separated by 100 ms long intervals at 20 V. Immediately after electroporation, cortices were prepared for primary neuronal culture.

Protocol for in utero electroporation is fully described in Meyer-Dilhet and Courchet (2020). We used timed-pregnant F1 females from C57BL/6J X 129/SvJ crosses (The Jackson Laboratory). Electroporation was performed at E15.5 to target progenitors generating cortical layer 2/3 PNs. The

electroporation settings were: 4 pulses of 45 V for 50 ms with 500 ms interval. Electroporated mice were sacrificed at the indicated ages.

Immunoprecipitations

Immunoprecipitations were performed as described before (Sachse et al., 2019). Briefly, SH-SY5Y or HEK293T cells were harvested 24 to 48 hours after transfections in ice-cold 1x PBS and lysed in RIPA buffer (25 mM Tris pH 7.6, 150 mM NaCl, 1% sodiumdeoxycholate, 0.5% NP-40, 1% SDS, 0.5% Triton X-100, 5% glycerol) containing Halt protease and phosphatase inhibitor cocktail (Pierce). Input extracts were cleared by centrifugation and tagged proteins were precipitated for one hour at RT followed by extensive washing in RIPA buffer or TBS-Tween. For immunoprecipitation, we used the following magnetic beads: mouse anti-c-myc, mouse anti-HA (both Pierce), and mouse anti-HA (MBL). Following precipitations, protein complexes were heat-eluted in SDS sample buffer or 0.1M glycine.

Immunoprecipitation in S2 cells was performed 48 hours after the induction of the stable S2 cell line expressing Axed-V5. Induction was carried out 6 or 24 hours after transfection with the plasmid containing dWnk. Cells were harvested in RIPA buffer supplemented with protease and phosphatase inhibitors and proteins were precipitated for two hours at RT. The The Dynabeads Antibody Coupling kit (Invitrogen) was used to coat 3 mg beads with the custom-made dWnk antibody. 1 mg beads were used for the mock IP. Coupling of the antibody to the beads was carried out at 37ºC overnight.

Western blotting

Denaturated protein samples were submitted to SDS-PAGE and transferred to polyvinylidene difluoride (PVDF) or nitrocellulose membranes (Biorad). Primary antibody incubation was performed overnight at 4ºC using the appropriate antibody diluted in TBS-Tween (0.1%) containing 5% milk or BSA. HRP-conjugated secondary antibodies were incubated at room temperature for 1 to 2 hours in in TBS-Tween with milk or BSA. Protein bands were visualized with a ProteinSimple FluorChemQ imaging system or Chemi-Doc_IT imager (UVP) using ECL reagent (Pierce). Three or more independent experiments were performed for all immunoblotting data.

Dye labeling of Drosophila mechanosensory neuron axons

Dye fills were performed as described previously (Chen et al., 2006). Adult flies were glued to an insect pin (Fine Science Tools, #26000-25) and large mechanosensory bristles on the dorsal thorax were plucked

manually with forceps. Flies were subsequently beheaded, their abdomen opened and fixed overnight at 4ºC in 3.7% (w/v) paraformaldehyde (Electron Microscopy Sciences) in 0.2 M sodium carbonate-bicarbonate (‘‘carb-bicarb’’) buffer. After washes in 0.2 M carb-bicarb, flies were briefly dried and the lipophilic fluorescent dyes DiD (20 mg/mL in 100% ethanol, ThermoFisher, #D7757) and DiI (20 mg/mL in 1:1 dimethyl formamide:ethanol, ThermoFisher, #D3911) were applied to the exposed bristle sockets with glass micropipettes (Sutter Instruments, #BF100-5010). Flies were incubated 48 hours in a humid chamber at room temperature, the ventral nerve cords (VNCs) were dissected in 0.2 M carb-bicarb buffer and filled mechanosensory axons were imaged on an LSM710 and LSM780 (Zeiss) confocal microscopes.

Labeling and analysis of growth cones of mechanosensory neurons during development

Genetic labeling of single pDc neurons was adapted from a genetic labeling strategy to investigate the developmental mechanism by which Wnk regulate axonal branch formation. Briefly, Flp-recombinase was expressed in precursors of pDc neurons using DC1.4 enhancer, which gives rise to stochastic expression. In this flp-out setups, pnr-gal4 activity was restricted by using DC1.4-Flp to excise an FRT-flanked transcriptional STOP cassette from a UAS-mCD8::GFP reporter construct, whose expression is then trans-activated by pnr-Gal4. The defective branching pattern of adult pDc neurons with dWnk double RNAi knock-down is fully penetrant (n = 47). The phenotypic defect(s) of the adult mutant pDc axon projection is identical to single pDc axons of dWnk null mutant clones (generated by MARCM). White pupae were allowed to develop for various time intervals at 25ºC until ~30 to 40 hr for wild-type and dWnk-knockdown. Dissected VNCs were stained with anti-GFP. Images were taken on a Zeiss LSM710 confocal microscope with a 60X lens. Filopodia were counted manually in Fiji / ImageJ in confocal microscopy image stacks of developing dWnk-knockdown and control animals with single mechanosensory neurons labeled with CD8::GFP.

Conditional knockdown of WNK

E15.5 embryos of time-pregnant F1 females from C57BL/6J x 120/SvJ were in utero electroporated with pCAG-ERT2CreERT2 (1 mg/mL) and a 1:1 ratio of either CreONWNK1-TRCN0000027035 and CreONWNK1-TRCN0000027039 or CreONWNK2TRCN0000027661 and CreONWNK1-TRCN0000027668 (4 mg/mL). Activation of the ERT2CreERT2 fusion protein was achieved by intraperitoneal administration of tamoxifen for three consecutive days, starting at P30, (0.10 mg/g of bodyweight) dissolved in corn oil (20 mg/mL) as previously described (Matsuda and Cepko, 2007). Corn oil

alone was used as a vehicle control for littermates. Four days after the last injection i.e., 7 days following first injection (P37), mice were sacrificed via perfusion of 4% paraformaldehyde (PFA, Electron Microscopy Sciences) and 0.075% Glutaraldehyde (Electron Microscopy Sciences) followed by overnight post-fixation in 4% PFA/0.075% Glutaraldehyde.

Immunohistochemistry of Brain Slices

Post-fixed brains were sectioned via vibratome (Leica VT1200) at 110 mm. Floating sections were then incubated for 1 hour in 4% Normal Goat Serum, 2% BSA, 0.3% Triton X-100 in PBS to block non-specific binding. Primary and secondary antibodies were diluted as follows: chicken anti-GFP (5 mg/mL, Aves Lab-recognizes GFP and YFP; rabbit anti-RFP (1:1,000, Abcam–recognizes mTagBFP2, DsRED, and tdTomato); AlexaFluor goat anti-Chicken 488 (1:1000, Invitrogen); AlexaFluor goat anti-Rabbit 546 (1:1,000, Invitrogen). Floating sections were incubated overnight at 4ºC in the primary antibodies, washed three times in PBS for 5 minutes each, then incubated in secondary antibodies for 5 hours at room temperature. Sections were mounted on slides and coverslipped with Fluoromount-G mounting medium (SouthernBiotech).

Immunolabelling

Cells were fixed for 5 min at room temperature in 4% (w/v) paraformaldehyde (Electron Microscopy Sciences) in PBS. Fixed cells were subsequently incubated in Permeabilisation Buffer (PB) (1x PBS supplemented with 0.1% Triton X-100 and 1% BSA (Sigma)) for 60 minutes to permeabilize and block non-specific staining. Primary antibodies were incubated for 1 hour at room temperature in PB, followed by an incubation with secondary antibodies for 30 min at room temperature in PB. Coverslips were mounted on slides with Vectashield mounting medium.

Drosophila single mechanosensory neuron labeling with axon and synaptic markers was done as described previously (Chen et al., 2006).

Mice were anaesthetized with isofluorane before intracardiac perfusion with 4% (w/v) paraformaldehyde in PBS followed by postfixation in 4% PFA for 2 hours. 125 mm coronal brain sections were obtained using a vibrating microtome (Leica VT1200S). Sections were permeabilized 30 minutes in PB then incubated overnight with the indicated primary antibodies diluted in PB. Secondary antibodies were

incubated for 1 hour at room temperature in PB. Slices were mounted on microscopy slides using Vectashield mounting medium.

Antibodies

The dWnk antibody was custom developed. For dWnk protein production in bacteria, PCR products of N-terminal and C-terminal fragments (as indicated in Figure S2) were amplified and cloned into pET vectors. Protein fragments expressed from these plasmids were tagged with 6xHis. Constructs were transformed into BL21DE3 competent cells (Agilent, #200131). Expression was induced in liquid LB medium cultures by adding IPTG (Sigma, #I6758-1G). Cells were grown for another 3 to 4 hours at 25ºC and subsequently lysed in lysis buffer containing 50 mM Tris-HCl (pH 7.5), 150 mM NaCl and 2 mM DTT with sonication. His-tagged proteins in the lysate were purified by use of Ni-NTA agarose beads (QIAGEN, #30210) and washed in 30 mM imidazole in lysis buffer. Protein was eluted with 300 mM imidazole in lysis buffer. The eluate was further purified on an Amicon Ultra 0.5 mL 3K UFC column (#500396). Purified proteins were used for immunization of guinea pigs. Polyclonal antibody production was done by Covance (Denver, PA, USA). The dWnk antibody was used at a 1:300 dilution.

Other primary antibodies used in this study were: chicken anti-GFP (5 mg/mL, Aves Lab), mouse anti-SMI312R (1:1000, Covance), rabbit anti-MAP2 (1:1000, Millipore), rabbit anti-Cux1 (1:500, Santa Cruz), rat anti-HA high affinity (1:1000, Roche), rabbit anti-FLAG (1:2500, Sigma), mouse anti-V5 (1:1000, Sigma), rabbit anti-myc (1:1000, Abcam), rabbit anti-tubulin (1:1000, Novus Biologicals), rabbit anti-GFP (Invitrogen, 1:500), mouse anti-GFP (Abcam, 1:500), rabbit anti-DsRed (Takara Bio, 1:500), mouse anti-Fasciclin II (DSHB Hybridoma Product 1D4 anti-Fasciclin II, 1:20), and rat anti-N-Cadherin (DSHB Hybridoma Product DN-Ex #8, 1:20). Alexa-conjugated secondary antibodies (Invitrogen) were used at a 1:2000 dilution. HRP-conjugated secondary antibodies (Invitrogen or Jackson Laboratories) were used at a 1:10000 dilution. Nuclear DNA was stained using Hoechst 33258 (1:10000, Pierce).

Confocal image acquisition and analysis

Confocal images were acquired with a Nikon Ti-E microscope equipped with the A1 laser scanning confocal microscope using the Nikon software NIS-Elements (Nikon Corporation, Melville, NY). Dye-filled Drosophila axons were imaged using an LSM710 (Zeiss) confocal microscope. Analysis of confocal images was performed with NIS-Elements software or ImageJ.

Ilastik Cell Density Counter

The interactive density counter workflow from open-source software, Ilastik (Berg et al., 2019), was used to quantify the number of layer 2/3 PNs electroporated in each brain section quantified for axon optical density in Figures 4 and 6. This workflow is useful for identifying overlapping objects that classic segmentation and detection approaches cannot separate. The counter employs a supervised learning strategy guided by user annotations of background and object, which then serve as inputs into a Random Forrest regression that estimates every pixel's density. 10x confocal images from four different brain slices that spanned all time points were used for training the algorithm. Post processing of our Ilastik density outputs were performed in FIJI ImageJ. This included binarizing and watershedding images. To count cells, we employed FIJI's analyze particles function, excluding small objects and objects with low sphericity to remove objects corresponding to dendrite branches. To validate our Ilastik workflow we compared the cell count to manual counts performed by multiple observers (three). The number of cells per image estimated by Ilastik and Fiji pipeline lied within 10% of values obtained by human observers in a manner that was independent of density of electroporated neurons.

Quantification and Statistical Analysis

Data acquisition and quantification were performed non-blinded. Acquisition was performed in Microsoft Excel, statistical analyses were performed using Prism (GraphPad Software). Statistical details (definition of test, exact value of n (e.g., number of Drosophila VNCs, number of mouse brains, etc.), mean ± deviations, p values) are listed in Figure Legends and below. Figure 3T: Ordinary one-way ANOVA with multiple Tukey's comparisons test, nWT-early = 16; nWnkKD-early = 13; nWT-intermediate = 17; nWnkKD-intermediate = 12; nWT-late = 14; nWnkKD-late = 10. The tests were considered significant when $p < 0.05$, with the following criteria: * $p < 0.05$, ** $p < 0.01$, *** $p < 0.001$, **** $p < 0.0001$. Figures 4M–4P: Two-way ANOVA followed by multiple Tukey's comparisons test. Three sections from each brain were quantified, npLKO P10 =3; npLKO P15 =3; npLKO P21 =5; npLKO P35 =5; nWNK1 P10 =4; nWNK1 P15 =3; nWNK1 P21 =3; nWNK1 P35 =5; nWNK2 P10 =3; nWNK2 P15 = 3; nWNK2 P21 = 4; nWNK2 P35 = 3. Statistical analysis: * $p < 0.05$, ** $p < 0.01$, *** $p < 0.001$, **** $p < 0.0001$. Figures 5G–5J: Two-way ANOVA followed by multiple Tukey's comparisons test. Number of neurons for quantification: npLKO = 19, nshWNK1 = 28, nshWNK2 = 23 from at least three independent experiments. Significance: * $p < 0.05$ with the following

criteria: * p < 0.05; ** p < 0.01; ***p < 0.001; ****p < 0.0001. Figure 6: Mann-Whitney test (N and W) or a two-way ANOVA followed by Tukey's multiple comparisons test (M and V): * p < 0.05, ** p < 0.01, *** p < 0.001, **** p < 0.0001. Number of mice for each experimental condition: nCreON-shWNK1 + Vehicle =3; nCreON-shWNK1 + Tamoxifen =3; nCreON-shWNK2 + Vehicle =3; nCreON-shWNK2 + Tamoxifen = 4. At least 3 sections analyzed per brain as described for Figure 4.

Acknowledgements

This work was supported by FWO (G077013N and G0B8919N to D.S.; G1214420N to G.E.-F.), VIB Belgium (D.S.), the Humboldt Foundation (D.S.), the Fondation pour la Recherche Medicale (AJE20141031276) and ERC Starting Grant (678302-NEUROMET) (J.C.), NINDS NS107483 (F.P.), an award from the Roger De Spoelberch Fondation (F.P.), and an award from the Thompson Family Foundation Initiative (F.P.). This work was performed within the framework of the LABEX CORTEX (ANR-11-LABX-0042/ANR-11-IDEX-0007). We thank our lab members for critical reading of the manuscript. Stocks obtained from the Bloomington Drosophila Stock Center (NIH P40OD018537) were used in this study. We thank M. Freeman, L. Neukomm, and T. Suzuki for sharing mutant fly stocks. We thank the personnel from the SCAR and ALECS-SPF mouse facility for animal care.

Author Contributions

A.I., J.C., F.P., and D.S. designed the experiments and wrote the manuscript. A.I., D.A., S.V., M.P., D.D., Y.K., J.Y., and G.E.-F. conducted the developmental and Drosophila genetics experiments. J.C., D.M.V., S.H., L.M., and T.L. conducted the *in vivo* and *in vitro* mouse experiments. T.V., A.M., S.V., S.S., B.Y., M.-L.E., J.Y., and J.C. conducted molecular and cell culture work.

References

Ali YO, Li-Kroeger D, Bellen HJ, Zhai, RG, Lu HC. NMNATs, evolutionarily conserved neuronal maintenance factors. Trends Neurosci. 2013; 36:632-640. [PubMed: 23968695]

Babetto E, Beirowski B, Russler EV, Milbrandt J, DiAntonio A. The Phr1 ubiquitin ligase promotes injury-induced axon self-destruc- tion. Cell Rep. 2013; 30:1422-1429. [PubMed: 23665224]

Berger J, Senti KA, Senti G, Newsome TP, Asling B, Dickson BJ, Suzuki T. Systematic identification of genes that regulate neuronal wiring in the Drosophila visual system. PLoS Genet. 2008; 4:e1000085. [PubMed: 18516287]

Coen K, Pareyson D, Auer-Grumbach M, Buyse G, Goemans N, Claeys KG, Verpoorten N, Laurà M, Scaioli V, Salmhofer W, Pieber TR, Nelis E, De Jonghe P, Timmerman V. Novel mutations in the HSN2 gene causing hereditary sensory and autonomic neuropathy type II. Neurology. 2006; 66:748-751. [PubMed: 16534117]

Coleman MP, Freeman MR. Wallerian degeneration, wld(s), and nmnat. Annu Rev Neurosci. 2010; 33:245-67. [PubMed: 20345246]

Conforti L, Gilley J, ColemanMP. Wallerian degeneration: an emerging axon death pathway linking injury and disease. Nat. Rev. Neurosci. 2014; 15:394-409 (2014). [PubMed: 24840802]

Costa AM, Pinto F, Martinho O, Oliveira MJ, Jordan P, Reis RM. Silencing of the tumor suppressor gene WNK2 is associated with upregulation of MMP2 and JNK in gliomas. Oncotarget. 2015; 6:1422-34. [PubMed: 25596741]

Courchet J, Lewis TL Jr, Lee S, Courchet V, Liou DY, Aizawa S, Polleux F. Terminal axon branching is regulated by the LKB1-NUAK1 kinase pathway via presynaptic mitochondrial capture. Cell. 2013; 153:1510-1525. [PubMed: 23791179]

Dascenco D, Erfurth ML, Izadifar A, Song M, Sachse S, Bortnick R, Urwyler O, Petrovic M, Ayaz D, He H, Kise Y, Thomas F, Kidd T, Schmucker D. Slit and Receptor Tyrosine Phosphatase 69D Confer Spatial Specificity to Axon Branching via Dscam1. Cell. 2015; 162:1140-1154.

[PubMed: 26317474]

Essuman K, Summers DW, Sasaki Y, Mao X, DiAntonio A, Milbrandt J. The SARM1 Toll/Interleukin-1 Receptor Domain possesses intrinsic NAD+ cleavage activity that promotes pathological axonal degeneration. Neuron. 2017; 93:1334-1343. [PubMed: 28334607]

Fang Y, Soares L, Teng X, Geary M, Bonini NM. A novel Drosophila model of nerve injury reveals an essential role of Nmnat in maintaining axonal integrity. Curr Biol. 2012; 22:590-5. [PubMed: 22425156]

Gilley J, Coleman MP. Endogenous Nmnat2 is an essential survival factor for maintenance of healthy axons. PLoS Biol. 2010; 8(1):e1000300. [PubMed: 20126265]

Gilley J, Adalbert R, Yu G, Coleman MP. Rescue of peripheral and CNS axon defects in mice lacking NMNAT2. J Neurosci. 2013; 33:13410-24. [PubMed: 23946398]

Gilley J, Orsomando G, Nascimento-Ferreira I, Coleman MP. Absence of SARM1 rescues development and survival of NMNAT2-deficient axons. Cell Rep. 2015; 10:1974-81. [PubMed: 25818290]

Hadchouel J, Ellison DH, Gamba G. Regulation of renal electrolyte transport by WNK and SPAK-OSR1 Kinases. Annu. Rev. Physiol. 2016; 78:367-389. [PubMed: 26863326]

Hadchouel K, O'Shaughnessy KM. Extrarenal roles of the with-no-lysine[K] kinases (WNKs). Clin. Exp. Pharmacol. Physiol. 2013; 40:885-894. [PubMed: 23662678]

Hand RA, Khalid S, Tam E, Kolodkin AL. Axon dynamics during neocortical laminar innervation. Cell Rep. 2015; 12:172-182. [PubMed: 26146079]

He H, Kise K, Izadifar A, Urwyler O, Ayaz D, Parthasarthy A, Yan B, Erfurth ML, Dascenco D, Schmucker D. Cell-intrinsic requirement of Dscam1 isoform diversity for axon collateral formation. Science. 2014; 344:1182-1186. [PubMed: 24831526]

Hong C, Moorefield KS, Jun P, Aldape KD, Kharbanda S, Phillips HS, Costello JF. Epigenome scans and cancer genome sequencing converge on WNK2, a kinase-independent suppressor of cell growth. Proc. Natl. Acad. Sci. 2007; 104:10974-10979. [PubMed: 17578925]

Hoorn EJ, Nelson JH, McCormick JA, Ellison DH. The WNK kinase network regulating sodium, potassium, and blood pressure. J. Am. Soc. Nephrol. 2011; 22:605-614. [PubMed: 21436285]

Huppke, P., Wegener, E., Gilley, J., Angeletti, C., Kurth, I., Drenth, J.P.H., Stadelmann, C., BarrantesFreer, A., Bruck, W., Thiele, H.*, et al.*. Homozygous NMNAT2 mutation in sisters with polyneuropathy and erythromelalgia. Exp Neurol 2019; *320*, 112958.

Lukacs, M., Gilley, J., Zhu, Y., Orsomando, G., Angeletti, C., Liu, J., Yang, X., Park, J., Hopkin, R.J., Coleman, M.P.*, et al.*. Severe biallelic loss-of-function mutations in nicotinamide mononucleotide adenylyltransferase 2 (NMNAT2) in two fetuses with fetal akinesia deformation sequence. Exp Neurol 2019; *320*, 112961.

Jun P, Hong C, Lal A, Wong JM, McDermott MW, Bollen AW, Plass C, Held WA, Smiraglia DJ, Costello JF. Epigenetic silencing of the kinase tumor suppressor WNK2 is tumor-type and tumor-grade specific. Neuro. Oncol. 2009; 11:414-422. [PubMed: 19001526]

Lewis TL Jr, Courchet J, Polleux F. Cell biology in neuroscience: Cellular and molecular mechanisms underlying axon formation, growth, and branching. J Cell Biol. 2013; 202:837-48. [PubMed: 24043699]

Munemasa Y, Kitaoka Y. Autophagy in axonal degeneration in glaucomatous optic neuropathy. Prog. Retin. Eye Res. 2015; 47:1-18. [PubMed: 25816798]

Neukomm LJ, Burdett TC, Seeds AM, Hampel S, Coutinho-Budd JC, Farley JE, Wong J, Karadeniz YB, Osterloh JM, Sheehan AE, Freeman MR. Axon death pathways converge on Axundead to promote functional and structural axon disassembly. Neuron. 2017; 95:78-91. [PubMed: 28683272]

Pela I. Familial Hyperkalemic Hypertension: A New Early-onset Pediatric Case. Clin Pediatr Endocrinol. 2012; 21:5-9. [PubMed: 23926404]

Polleux F, Ghosh A. The slice overlay assay: a versatile tool to study the influence of extracellular signals on neuronal development. Sci. STKE. 2002; 136:pl9. [PubMed: 12060788]

Raff MC, Whitmore AV, Finn JT. Axonal self-destruction and neurodegeneration. Science. 2002; 296:868-71. [PubMed: 11988563]

Richardson C, Alessi DR. The regulation of salt transport and blood pressure by the WNK-SPAK/OSR1 signalling pathway. J Cell Sci. 2008; 121:3293-304. [PubMed: 18843116]

Rotthier A, Baets J, De Vriendt E, Jacobs A, Auer-Grumbach M, Lévy N, Bonello-Palot N, Kilic SS, Weis J, Nascimento A, Swinkels M, Kruyt MC, Jordanova A, De Jonghe P, Timmerman

V. Genes for hereditary sensory and autonomic neuropathies: a genotype-phenotype correlation. Brain. 2009; 132:699-2711. [PubMed: 19651702]

Ruan K, Zhu Y, Li C, Brazill JM, Zhai RG. Alternative splicing of Drosophila Nmnat functions as a switch to enhance neuroprotection under stress. Nat. Commun. 2015; 6:10057. [PubMed: 26616331]

Sachse SM, Lievens S, Ribeiro LF, Dascenco D, Masschaele D, Horré K, Misbaer A, Vanderroost N, De Smet AS, Salta E, Erfurth ML, Kise Y, Nebel S, Van Delm W, Plaisance S, Tavernier J, De Strooper B, De Wit J, Schmucker D. Nuclear import of the DSCAMcytoplasmic domain drives signaling capable of inhibiting synapse formation. EMBO J. 2019; 38:e99669. [PubMed: 30745319]

Shekarabi M, Zhang J, Khanna AR, Ellison DH, Delpire E, Kahle KT. WNK Kinase Signaling in Ion Homeostasis and Human Disease. Cell Metab. 2017; 25:285-299. [PubMed: 28178566]

Südhof TC. Molecular Neuroscience in the 21st Century: A Personal Perspective. Neuron. 2017; 96:536-541. [PubMed: 29096071]

Urwyler O, Izadifar A, Dascenco D, Petrovic M, He H, Ayaz D, Kremer A, Lippens S, Baatsen P, Guérin CJ, Schmucker D. Investigating CNS synaptogenesis at single-synapse resolution by combining reverse genetics with correlative light and electron microscopy. Development. 2015; 142:394-405. [PubMed: 25503410]

Urwyler O, Izadifar A, Vandenbogaerde S, Sachse S, Misbaer A, Schmucker D. Branchrestricted localization of phosphatase Prl-1 specifies axonal synaptogenesis domains. Science. 2019; 364:eaau9952. [PubMed: 31048465]

Vidal-Petiot E, Elvira-Matelot E, Mutig K, Soukaseum C, Baudrie V, Wu S, Cheval L, Huc E, Cambillau M, Bachmann S, Doucet A, Jeunemaitre X, Hadchouel J. WNK1-related Familial Hyperkalemic Hypertension results from an increased expression of L-WNK1 specifically in the distal nephron. Proc Natl Acad Sci U S A. 2013; 110:14366-71. [PubMed: 23940364]

Vohra BP, Sasaki Y, Miller BR, Chang J, DiAntonio A, Milbrandt J. Amyloid precursor protein cleavage-dependent and -independent axonal degeneration programs share a common nicotinamide mononucleotide adenylyltransferase 1-sensitive pathway. J. Neurosci. 2010; 30:13729-13738. [PubMed: 20943913]

Wilson FH, Disse-Nicodème S, Choate KA, Ishikawa K, Nelson-Williams C, Desitter I, Gunel M,Milford DV, Lipkin GW, Achard JM, Feely MP, Dussol B, Berland Y, Unwin RJ, Mayan H,

Simon DB, Farfel Z, Jeunemaitre X, Lifton RP. Human hypertension caused by mutations in WNK kinases. Science. 2001; 293:1107-1112. [PubMed: 11498583]

Wu A, Wolley M, Stowasser M. The interplay of renal potassium and sodium handling in blood pressure regulation: critical role of the WNK-SPAK-NCC pathway. J. Hum. Hypertens. 2019; 33:508-523. [PubMed: 30723251]

Xu B, English JM, Wilsbacher JL, Stippec S, Goldsmith EJ, Cobb MH. WNK1, a novel mammalian serine/threonine protein kinase lacking the catalytic lysine in subdomain II. J. Biol. Chem. 2000; 275:16795-16801. [PubMed: 10828064]

Yang CL, Angell J, Mitchell R, Ellison DH. WNK kinases regulate thiazide-sensitive Na-Cl cotransport. J. Clin. Invest. 2003; 111:1039-1045. [PubMed: 12671053]

Zhai RG, Zhang F, Hiesinger PR, Cao Y, Haueter CM, Bellen HJ. NAD synthase NMNAT acts as a chaperone to protect against neurodegeneration. Nature. 2008; 452:887-91. [PubMed: 18344983]

Appendix C: CD45 is a Sialic Acid Dependent Binding Partner of the Alzheimer's Disease Protein CD33

Vo N*, Rillahan C*, **Virga DM**, Taga M, Connor S, Rashid M, Chintamen S, Guzman G, Kholer JJ, Schenone M, De Jager PL, Elyaman W, Carr SA, Bradshaw E (2023) Nat. Neuroscience, *In Revision*

Many genetic mutations have been implicated as risk factors in Alzheimer's disease. Though significant research has explored the role of these risk-associated alleles in microglial function, few have explored the role of CD33 and/or CD45. Here, we characterized the role of CD45 in microglial function, and specifically the role that alleles associated with either increased or decreased risk for Alzheimer's in CD33/CD45 play in microglial consumption and synaptic loss.

In this study, I conceived of, performed, analyzed, configured, and drafted all of the co-culture experiments with murine neurons (Figure 6). This required development of a novel human microglial-murine primary cortical neuronal culture, as well as a novel microglial consumption analysis. I also worked extensively on the manuscript, drafting all of the materials related to my experiments and heavily editing the rest of the paper. This paper is in revisions at *Nature Neuroscience* at the time of this thesis. Please note: This work was done completely independently, in full.

Abstract

Genome-wide association studies have identified and validated the innate immune gene *CD33* as associated with Alzheimer's disease (AD) susceptibility. CD33 is a sialic acid-binding protein expressed on the surface of myeloid cells, and higher CD33 expression levels in the brain have been associated with more advanced cognitive decline and AD. Individuals with the AD-associated rs3865444^{CC} risk genotype have increased expression of full-length CD33, the isoform containing the sialic acid-binding domain, compared to those with the rs3865444^{AA} protective genotype which lacks this domain. Using a novel glycan-photo-crosslinking strategy and mass spectrometry we identified immune cell-specific sialic acid-dependent and independent CD33 binding partners, including CD45. We have validated CD45 as a sialic acid-specific binding partner for CD33 *in vitro* as well as *in situ* and demonstrate that CD33 modulates CD45's phosphatase activity via its sialic acid-binding domain. We also explored the microglial functional implications of these molecules. In conclusion, we have identified and validated the functional relevance of CD33 binding partners that are specific to the sialic acid-binding domain of CD33, the domain that is modulated by the AD association.

Introduction

Outside of the nervous system, CD33 is predominately expressed on cells of the myeloid lineage[1], although it can be upregulated on a subset of adaptive immune cells as well[2]. In the central nervous system (CNS), it is highly expressed on microglia[3]. Microglia, as the innate immune cells of the CNS, not only protect the CNS from foreign infections, but also help maintain the health of neurons[4 5] using processes that require a fine balance of inhibitory and activating signaling to carry out the requisite function. Towards this end, microglia express many cell surface recognition molecules that tie extracellular events to intracellular signaling. Among these are a variety of lectins including Siglecs (sialic acid-binding immunoglobulin-like lectins)[6]. CD33, also known as Siglec-3, is thought to be a negative regulator of microglia function as it contains an immunoreceptor tyrosine-based inhibitory motif (ITIM) domain.

Genome-wide association studies (GWAS) identified the CD33 locus as a risk factor for AD[7,8]. We demonstrated previously that individuals with the AD-associated rs3865444^{CC} risk allele have increased expression of the full-length isoform of CD33 (CD33^{M}) on the surface of their innate immune cells compared to those with the rs3865444^{AA} protective genotype[9-11]. The risk allele is also associated with

diminished internalization of amyloid-β1-42 peptide ($A\beta_{1-42}$), accumulation of neuritic amyloid pathology in the brain, higher fibrillar amyloid level on *in vivo* positron emission tomography imaging, and increased numbers of human microglia with small, thick processes, and a rounded morphology[9]. The causative SNP is most likely rs12459419, which is in high linkage disequilibrium with the SNP, rs3865444 that was discovered in genome-wide association studies[10,12]. The SNP rs12459419 is thought to modulate splicing of exon 2 of CD33 which encodes the sialic acid-binding domain, resulting in an increase of the exon 2 containing isoform of CD33 ($CD33^M$) in individuals with the risk allele, suggesting that the sialic acid-binding domain is critical for the genetic association of the CD33 locus with susceptibility to AD. While CD33 is known to have high binding activity for α2,6-linked and α2,3-linked sialic acid bearing glycans[13,14], the protein binding partners carrying these molecules, and thereby regulated by CD33 in myeloid cells are currently unknown. Here we identify myeloid sialic-acid-specific binding partners of CD33.

Results

Since the Alzheimer's disease risk allele at the CD33 locus leads to a higher expression of the CD33 isoform containing the sialic-acid binding domain, we hypothesized that in order to understand the role of CD33 in AD we needed to determine the CD33 sialic acid specific binding partners in human myeloid cells. In order to identify these binding partners, we incubated the human myeloid cell line THP-1 with a mannosamine analog, Ac_4ManNDAz[15,16]. This molecule is taken up by cells through passive diffusion, deacetylated, and converted into the corresponding sialic acid containing a photo-crosslinker at a position not known to interfere with CD33 binding. When treated with UV light a covalent connection is made between the modified sialic acid and neighboring molecules, allowing for the *in situ* identification of the glycoproteins interacting with CD33 by subsequent immunoprecipitation (IP) and nanoscale liquid chromatography coupled to mass spectometry (nanoLC-MS). In comparison to control THP-1 cells either not given the photo-crosslinking sugar or not treated with UV light, we identified SPN/CD43, PTPRC/CD45, SLC2A1/GLUT1 and CLEC11A as sialic acid specific binding partners for CD33 with adjusted p-values of less than 0.05 (**Supplemental Tables 1 and 2, and Figure 1a,b**).

As CD45, an immune cell specific phosphatase, has been implicated in AD[17 18 19], we decided to pursue this interaction with CD33 further. We validated that CD45 was a CD33 binding partner in THP-1 cells by utilizing an orthogonal approach, the proximity ligation assay (PLA), which can sensitively identify

proteins in close proximity (40 nm or less), without a need for a crosslinking strategy (**Figure 2a**). When CD33 protein expression was eliminated with CRISPR/Cas9, the PLA signal between CD33 and CD45 was no longer present (**Figure 2b and Supplemental Figure 1**). Finally, we confirmed that the interaction between CD33 and CD45 is occurring in *cis*. We combined THP-1 cells with either CD33 or CD45 removed by CRISPER/Cas9, so that no cell had both molecules expressed, and found that the interaction between the two molecules was disrupted when the two molecules were not expressed on the same cell, suggesting that the interaction occurs in *cis* and is not observed in *trans*. (**Figure 2c and Supplemental Figure 2**). This is consistent with CD33 being a short siglec and not extending far beyond the cell surface glycocalyx[20].

Previously, we had shown that the AD-associated SNP rs3865444 leads to variation of the sialic acid-binding domain containing isoform of CD33 ($CD33^{M}$) on the surface of monocytes and monocyte-derived microglia-like cells (MDMi)[9,21]. In order to confirm the interaction observed in THP-1 cells, we examined the interaction of CD33 and CD45 by PLA in *ex vivo* monocytes from genotyped individuals. We found that in the primary monocytes, as in the THP-1 cells, CD33 and CD45 are in close enough proximity to be interacting with one another, leading to a signal by PLA (**Figure 3a,b,c**). Upon quantification, we found that monocytes from individuals with the AD-associated risk $rs3865444^{CC}$ genotype had significantly more interactions between CD33 and CD45 than monocytes from individuals with the protective SNP, $rs3865444^{AA}$ (**Figure 3d**). This is consistent with there being less $CD33^{M}$ on the surface of monocytes from individuals with the protective genotype[9].

In order to demonstrate that the CD33 and CD45 interaction is dependent on the sialic acid-binding domain of CD33, we expressed CD33 containing a mutation at the critical sialic-acid binding amino acid, Arginine 119 (R119)[22] in CD33 deleted THP-1 cells and performed PLA. No signal was detected, indicating that mutating CD33 at R119 eliminated the interaction between CD33 and CD45 when compared to the re-expression of wild-type $CD33^{M}$ (**Figure 3e, f, j**). This confirmed not only that CD33 and CD45 are interacting, but that the interaction is sialic acid-dependent.

To examine if, in addition to the sialic-acid dependent extracellular interaction, there is an intracellular interaction between $CD33^{M}$ and CD45, we mutated the key tyrosines in the ITIM and ITIM-like domains of $CD33^{M}$ and again measured CD33 and CD45 interaction using PLA. Tyrosine 340 (Y340) in the ITIM domain is known to be required for the binding of SHP-1, a phosphatase often utilized by CD33[22].

Mutating Y340 led to a complete disruption of the interaction between $CD33^{M}$ and CD45 similar to what was seen with the R119K sialic-acid domain mutation (**Figure 3g, j**). Mutating tyrosine 358 (Y358) in the ITIM-like domain reduced the interaction, but not to the same extent as R119K (**Figure 3h, j**). As expected, the double mutant Y340/Y358 also significantly reduced the interaction (**Figure 3i, j**). This indicates that the interaction between $CD33^{M}$ and CD45 requires both the sialic acid binding domain and the key signaling ITIM domain.

Siglecs are known to act as negative regulators of their binding partners and thereby fine-tune cell signaling events[23]. This led us to wonder if CD33 similarly negatively regulates CD45 function, specifically its phosphatase activity. Using THP-1 and THP-1 CD33KO cells we found that a lack of CD33 led to an increase in phosphatase activity with and without LPS stimulation (**Figure 4a**). To determine if this increase in phosphatase activity was due to CD33's ability to bind to sialic acid, we compared THP1 CD33KO cells with re-expressed wild-type $CD33^{M}$ or the R119K mutant. We found that both at baseline and in the presence of LPS stimulation, cells expressing the R119K mutant version of CD33, which cannot bind to sialic acid, have greater phosphatase activity (**Figure 4b**).

Having established a functional interaction between $CD33^{M}$ and CD45, we wanted to examine the interaction between $CD33^{M}$ and CD45 in an AD-relevant context. First, we stressed MDMi, a model of human microglia, with aggregated $A\beta_{1\text{-}42}$ and found that this increased the number of interactions between $CD33^{M}$ and CD45 per cell (**Figure 5a-g**). This could be due to the upregulation of CD33 protein expression on the surface of the cells, as a previous report demonstrated that CD33 protein expression is increased on microglia in the AD brain[24]. Next, we examined the interaction *in situ*, and found that CD45 positive cells within the cortex of the CNS, predominately microglia, were positive by PLA for interactions between CD33 and CD45 in the CNS (**Figure 5h**). Upon quantifying the interaction, we found that CD45 positive cells from individuals with the AD-associated risk $rs3865444^{CC}$ genotype had more interactions between CD33 and CD45 than microglia from individuals with the protective SNP, $rs3865444^{AA}$, this suggests that there is an increased interaction between CD33 and CD45 in both the peripheral and central immune system of individuals with the risk allele. (**Supplemental Figure 3**).

We previously linked the CD33 genotype to modulation of amyloid-beta uptake[9] in that the risk allele leads to a reduction of uptake, and this is driven by the expression of $CD33^{M}$[24]. However, it is unclear

what other microglial phenotypes may be altered by genetic variation at the *CD33* locus. Loss of synaptic density has been found to be an early event in AD[25,26], and microglia have been both positively and negatively implicated in this process[27-29]. Therefore, using the human microglial clone 3 cell line (HMC3) cocultured with long-term murine cortical pyramidal neurons (PNs) *ex utero* electroporated with tdTomato[30,31] (**Figure 6a**), we evaluated the relationship between microglial $CD33^M$ and CD45 expression and $A\beta_{1-42}$-mediated spine loss in neurons. Co-culturing HMC3 cells expressing GFP alone (plasmid control) in the presence of PNs was not sufficient to induce significant changes in spine density or neuronal morphology (**Figure 6b,e**). Upon the addition of oligomerized $A\beta_{1-42}$, the neurons exhibited a significant reduction in dendritic spine density, as shown previously[32]. In addition to spine density, we were able to measure $A\beta_{1-42}$ uptake by the HMC3 cells. By imaging at high resolution, we were able to volumetrically capture individual microglia as well as the fluorescent $A\beta_{1-42}$ they had consumed (**Figure 6c**). By quantifying the total volume of the microglia and subsequently the volume of each microglia occupied by $A\beta_{1-42}$, we were able to measure microglial consumption (**Figure 6d**). We found that not only does the removal of CD33 in HMC3 cells lead to an increase of $A\beta_{1-42}$ uptake but also a protection from amyloid induced spine density reductions, while overexpression of $CD33^M$ leads to a reduction in amyloid internalization but had no effect on amyloid induced spine density reduction of synaptically connected, fully developed primary neurons compared to the plasmid control HMC3. Removing CD45 had the same phenotype as overexpression of $CD33^M$ (**Figure 6b, c, d, and Supplemental Figure 4**). Altogether, these results suggest the inhibition of CD45 by $CD33^M$ promotes decreased $A\beta_{1-42}$ consumption and results in a more significant reduction in dendritic spines upon treatment with $A\beta_{1-42}$.

Discussion

Once the *CD33* locus was identified as being an AD genetically associated locus[8,37], we and others interrogated the functional consequences of the AD-associated genetic variation in the CD33 locus. The risk allele was found to reduce uptake ability of amyloid-β[9,24], and here we validate the finding with the removal of CD33 in the HMC3 cell line leading to an increase in internalization of amyloid-β. Additionally, we found that the removal of CD33 from this microglia cell line leads to protection of neurons from amyloidβ induced spine loss. Since synapse loss is correlated with cognitive impairment[38], this is supportive of future CD33-targeted therapies being able to slow decline in amyloidβ positive individuals.

Our group along with the Estus group determined that the CD33 risk allele leads to decreased splicing of exon 2, the exon that codes for the sialic-acid binding domain, and increased expression of the exon 2-containing $CD33^{M}$ isoform[10,12]. Therefore, individuals with the risk allele have greater protein expression of the inhibitory, sialic-acid binding $CD33^{M}$ isoform on the surface of their myeloid cells. However, what proteins CD33 interacts with through its sialic-acid binding-domain, and thereby regulates, are completely unknown. Here we identify novel sialic-acid dependent binding partners of CD33 in innate immune cells, including microglia. We demonstrate that CD45 is one of these binding partners. We see an increased interaction of these two molecules in individuals homozygous for the AD risk allele, which is presumably due to the genetically dictated increase of the sialic-acid binding isoform. We also determined that they are interacting in the CNS of patients with AD and found that when we add aggregated Aβ1-42 to mimic a plaque environment we see an increase in interactions of CD33 with CD45 per cell.

CD45 is a protein tyrosine phosphatase expressed on all immune cells including the majority of human adult microglia[3,39], which dephosphorylates Src kinases[40]. What we report here is that CD45 is a sialic acid-dependent binding partner of CD33, and that this interaction leads to a suppression of phosphatase function, in keeping with the known function of Siglecs. Interestingly, when PSAPP mice were crossed with CD45-/- mice it was found that CD45 deficiency accelerated cerebral amyloidosis and these mice had increased neuronal loss. The CD45 deficient murine microglia were also found to be defective in amyloid-β uptake[19], which is consistent with our findings here, where we see a loss of amyloid-β internalization in HMC3 cells with CD45 expression reduced, and no protection from amyloid-β induced spine loss. In the human system, CD45 was found to be increased in the frontal cortex and hippocampus of AD patients, as well as being identified as a key driver by transcriptomic analyses[17,18]. In conclusion, our work identified previously unknown sialic acid-specific binding partners of CD33, and we demonstrated that CD33 does in fact work as an inhibitory molecule and suppresses CD45 function. We also validated the importance of both these molecules in the uptake of amyloid-β, and interestingly, the involvement of CD33 in neuronal spine loss.

Our focus here was on binding partners of CD33 produced by innate immune cells. In the companion paper to this one, Dodd *et al*., it was found that clusterin is also a sialic acid-dependent binding

partner for CD33. Clusterin, also a genetically associated protein, is predominately produced by astrocytes and therefore represents crosstalk between different cell types utilizing genetically implicated proteins. It will now be of interest to determine how trans-acting ligands (such as Clusterin) and cis-acting ligands (such as CD45) interact to coordinately determine CD33 activation status.

Figures

Figure 1

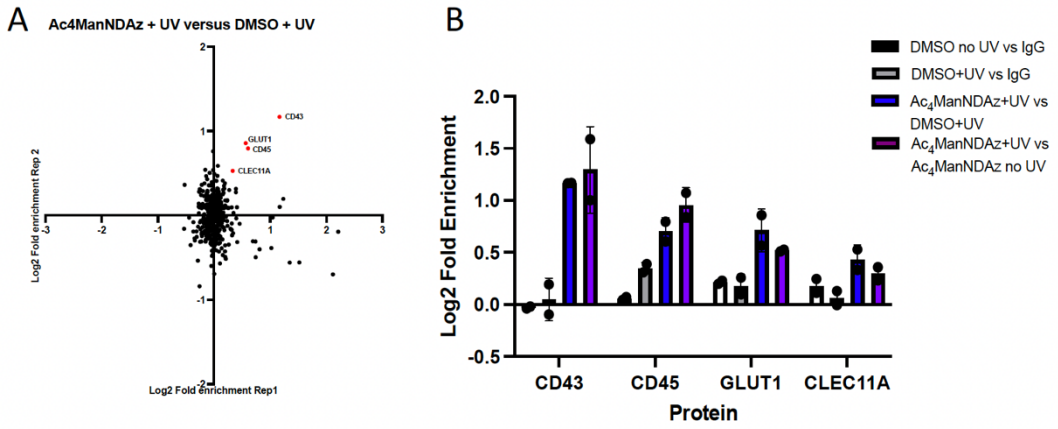

Figure 1: NanoLC-MS identifies CD43, CD45, GLUT1, and CLEC11A as sialic acid specific binding partners of CD33. (a) Proteins that were significantly enriched as CD33 binding proteins as defined as associating with CD33 after THP-1 cells were treated with Ac_4ManNDAz and treated with UV light compared to THP-1 cells treated with DMSO alone and UV light. (b) These proteins were not enriched in the CD33 immunoprecipitation without Ac_4ManNDAz compared to IgG control immunoprecipitation, demonstrating their specificity for the sialic acid binding domain. These proteins were enriched after the Ac_4ManNDAz plus UV light treatment compared to the Ac_4ManNDAz treatment without UV light crosslinking. Error bars denote the standard deviation between technical replicates.

Figure 2

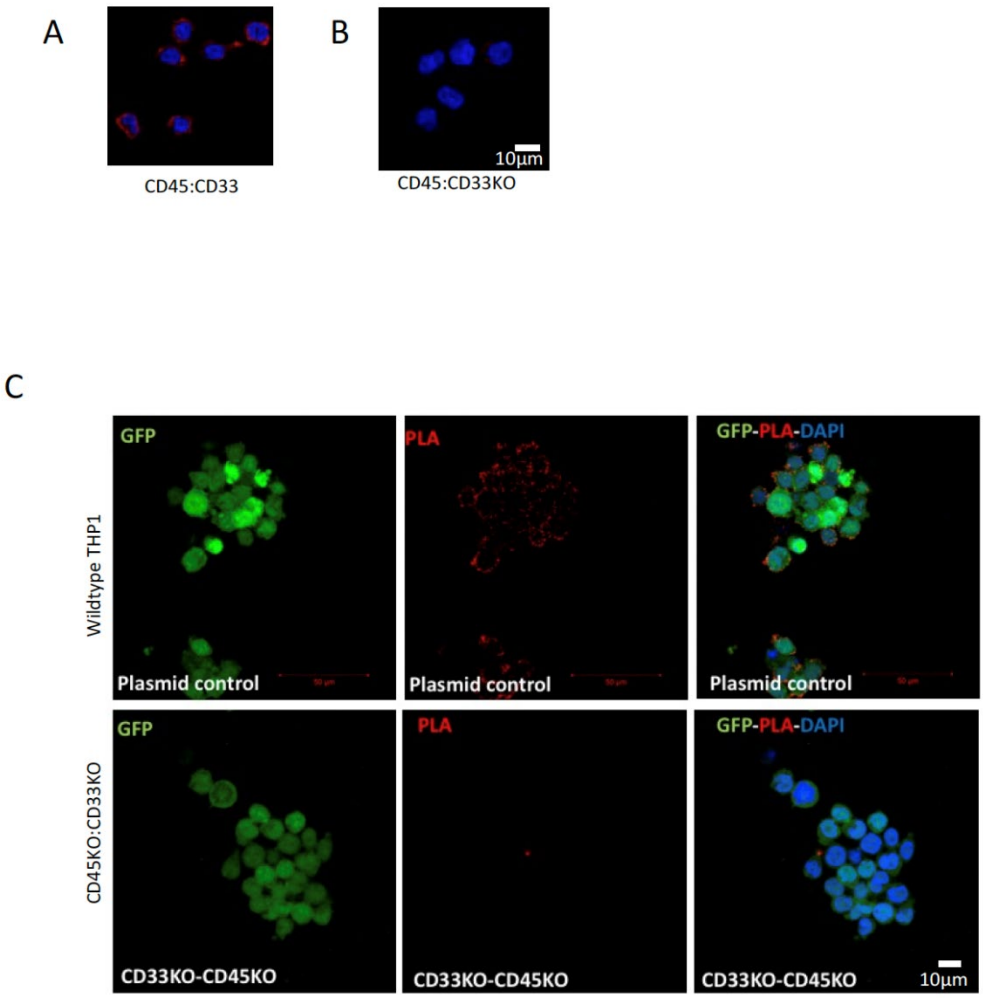

Figure 2: CD33 binds to CD45 in *cis*. (a) The mass spectrometry findings of CD33 and CD45 interacting were validated in THP-1 cells using the proximity ligation assay. (b) The removal of CD33 from the THP-1 cell line led to the elimination of the interaction between CD33 and CD45 as detected by PLA. (c) Combining THP-1 cells with either CD33 removed or CD45 removed via Crispr/Cas9 leads to a reduction in the interaction between CD33 and CD45 suggesting the interaction is occurring in *cis*.

Figure 3

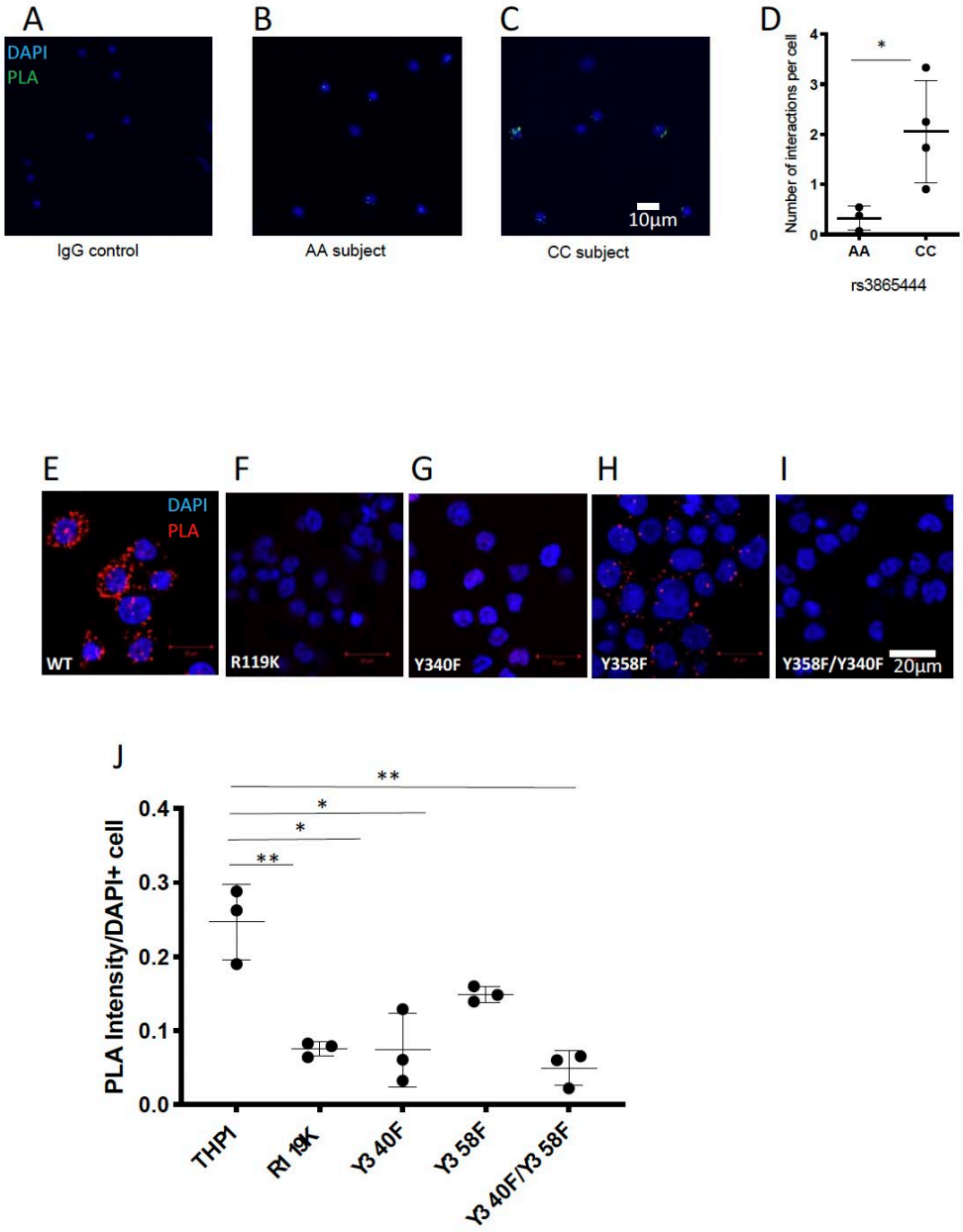

Figure 3: The interaction between CD33 and CD45 is modified by genotype, the sialic-acid binding domain and the ITIM domain. (a-d) CD33 and CD45 interact in primary human monocytes as determined by PLA, and individuals with the rs3865444^{CC} genotype have more interactions per cell than individuals with the rs3865444^{AA} genotype. Each dot represents an individual. (e-j) Mutations in the sialic acid binding domain (R119K) and the ITIM domain (Y340F) disrupt the interaction between CD33 and CD45. Mutation in the ITIM-like domain (Y358F) leads to a reduction in the interaction. Each dot represents a technical replicate. Unpaired t-test. *p<0.05, **p<0.01.

Figure 4

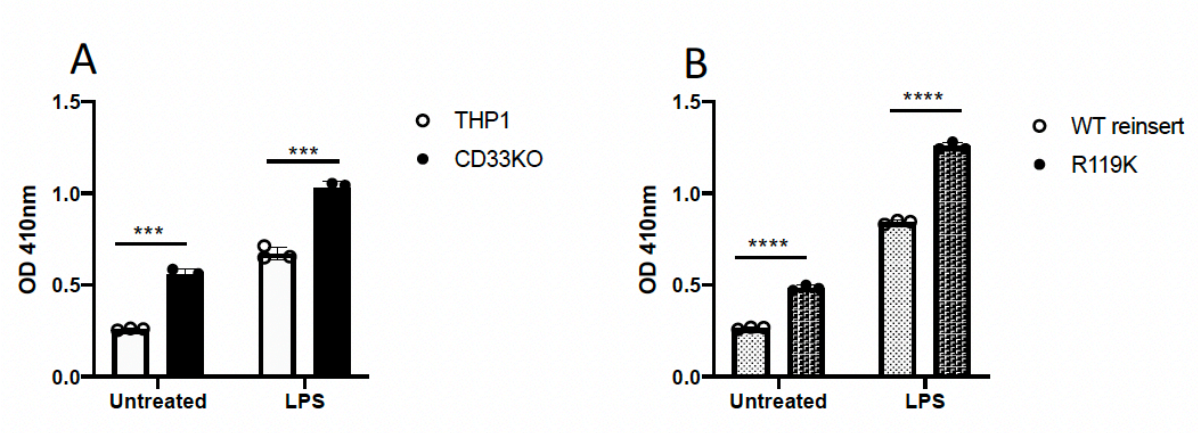

Figure 4: Phosphatase activity is increased when CD33 is removed, or the sialic-acid binding domain is mutated. (a) CD33KO THP-1 cells have higher phosphatase activity compared to WT THP-1 cells, both at baseline and after LPS activation. (b) CD33KO THP1 cells with CD33 R119K expressed have higher phosphatase activity compared to CD33KO THP-1 cells with WT CD33 expressed, both at baseline and after LPS activation. Each dot represents a technical replicate. Unpaired t-test. ***p<0.001; ****p<0.0001.

Figure 5

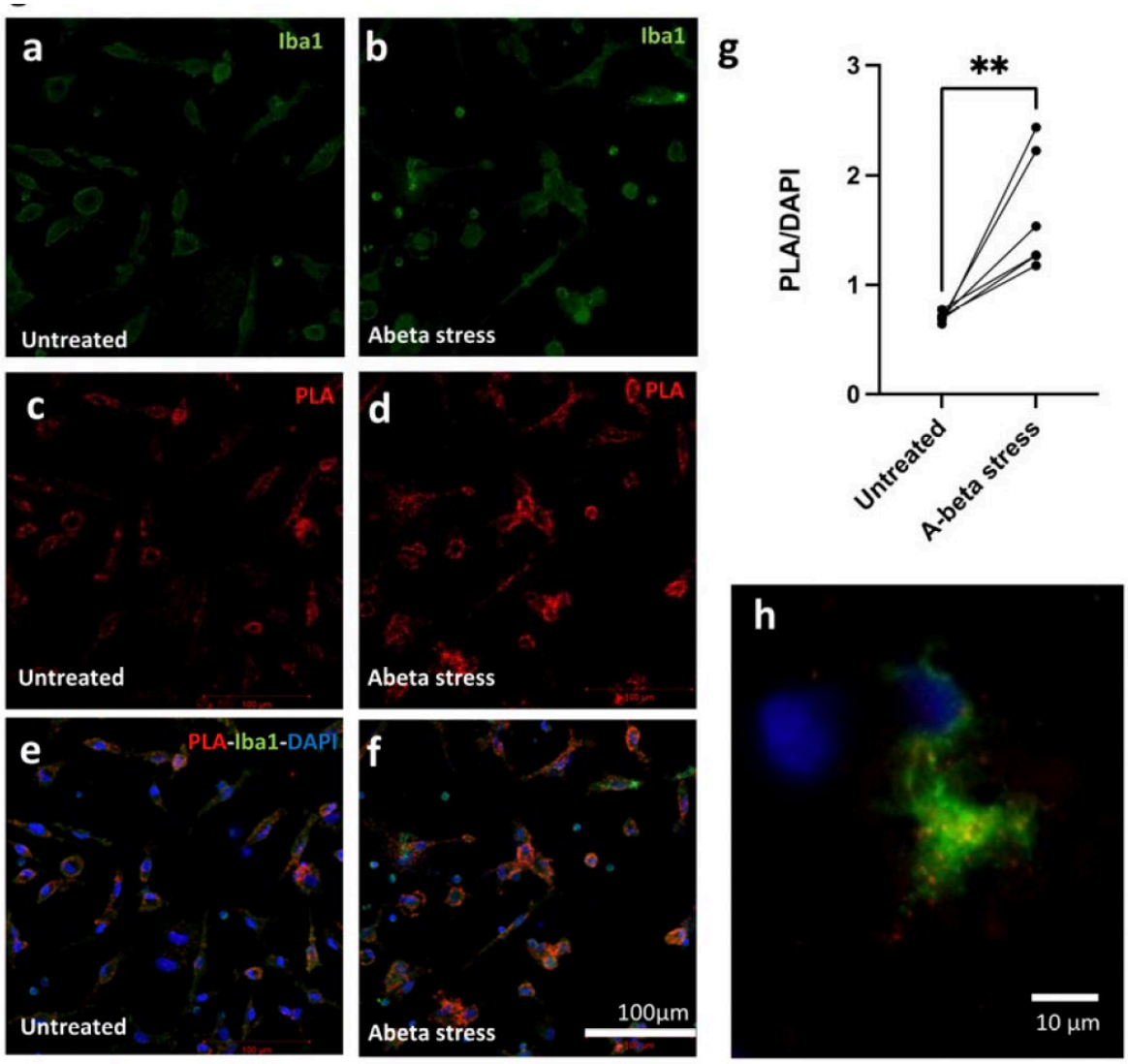

Figure 5: CD33 and CD45 interact in microglia and microglia-like cells, and A-beta stress increases the frequency of the interaction. (a-g) MDMi were treated with aggregated Aβ1-42 stress for 24 hours and then examined for an interaction between CD33 and CD45. (g) There was an increase in the number of interactions between CD33 and CD45 after aggregated Aβ1-42 stress compared to untreated MDMi, as measured by the intensity of each DAPI-positive cell using a paired t-test. Each dot represents an individual. (h) A representative image of a microglia cell demonstrating interaction between CD33 and CD45 *in situ*.

Figure 6

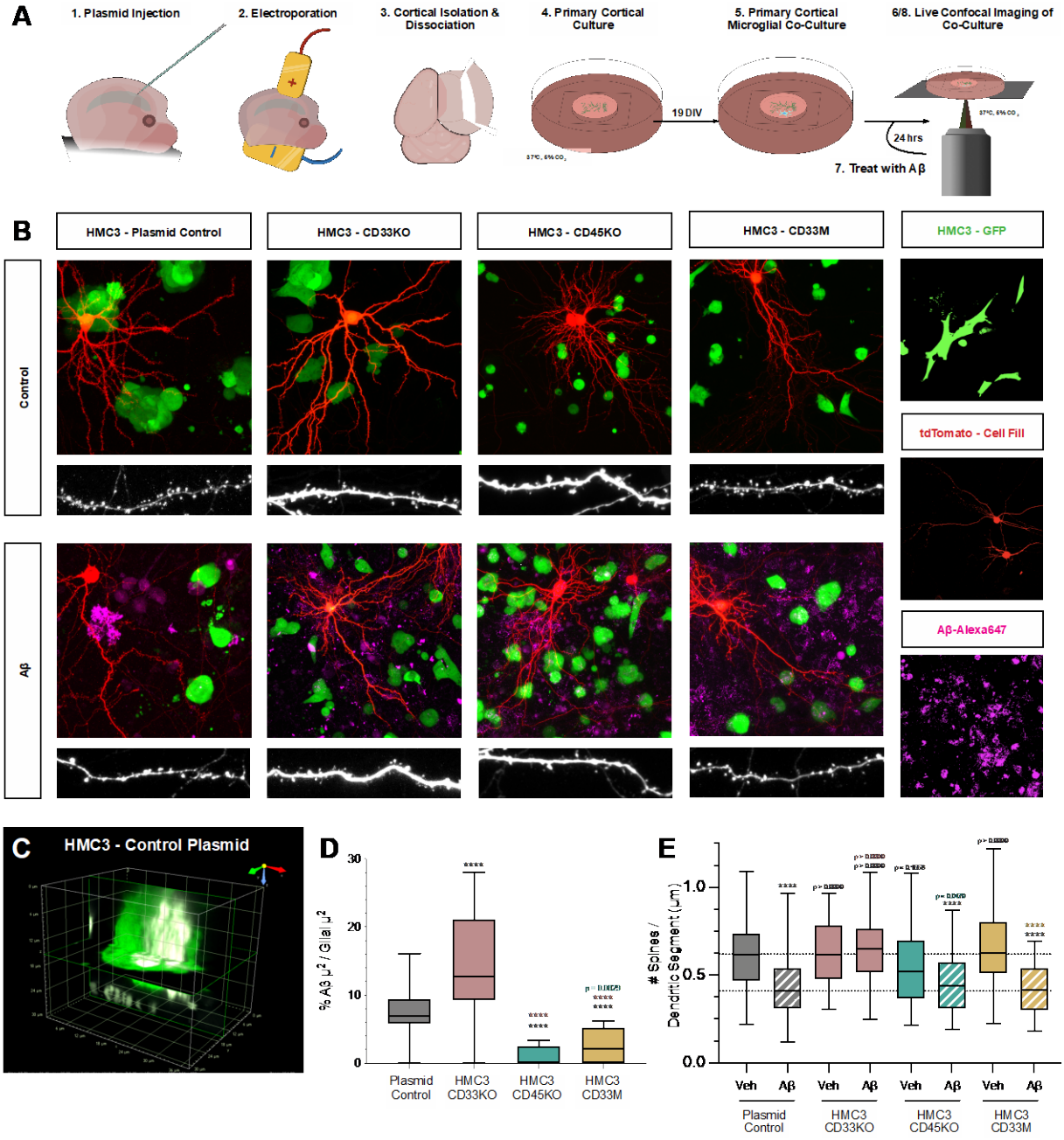
A
1. Plasmid Injection
2. Electroporation
3. Cortical Isolation & Dissociation
4. Primary Cortical Culture
5. Primary Cortical Microglial Co-Culture
6/8. Live Confocal Imaging of Co-Culture
19 DIV
24 hrs
7. Treat with Aβ
B
HMC3 - Plasmid Control
HMC3 - CD33KO
HMC3 - CD45KO
HMC3 - CD33M
HMC3 - GFP
tdTomato - Cell Fill
Aβ-Alexa647
Control
Aβ
C
HMC3 - Control Plasmid
D
% Aβ μ² / Glial μ²
Plasmid Control
HMC3 CD33KO
HMC3 CD45KO
HMC3 CD33M
E
Spines / Dendritic Segment (μm)
Veh
Aβ
Plasmid Control
HMC3 CD33KO
HMC3 CD45KO
HMC3 CD33M

Figure 6 Cont…

Figure 6. CD33KO prevents Aβ1-42-mediated spine loss and increases microglial Aβ1-42 consumption in primary neuronal and human microglial co-cultures. (**a**) Schematic representation of the experimental set-up. Briefly, E15.5 mouse embryos are electroporated with pCAG-tdTomato to target L2/3 cortical progenitors, the cortex is dissected, dissociated, and cultured for 18 days before human microglia carrying various alleles are added to the cultures. The cultures are then imaged live via confocal microscopy, treated with Aβ1-42 and imaged again. **(b)** Representative images of sparsely electroporated primary cortical neurons (red, tdTomato) and human microglia (green, GFP) co-cultures before and after treatment with Aβ1-42 (magenta, Alexa647; 0.5 µg/ml) at 20 and 21DIV respectively. Additional insets include secondary dendritic segments and isolated channels. **(c)** An x-y sliced, representative three-dimensional volumetric digital reconstruction of an individual HMC3-Control Plasmid microglia from neuronal-glial co-culture demonstrating Aβ1-42 consumption and co-localization. **(d)**, Quantification of Aβ1-42 consumption. All consumption analyses were done blind to experimental conditions as described in materials and methods using NIS-Elements. Briefly, the microglial population's total volume was quantified. The 3D area occupied by Aβ1-42 was then quantified and instances where the two signals co-localized, which is designated consumption, was divided by the total volume of the microglia as a function of percentage of microglia occupied by Aβ1-42. **(e)** Quantification of spine density. All the spine density analyses were done blind to the experimental conditions and were done by manual counting using FIJI. All of the statistical analyses were performed with Prism9 (GraphPad Software). Data is represented by box plots displaying Tukey error bars, with the box denoting 25th, 50th (median) and 75th percentile from 3-6 independent experiments. nControl Plasmid = 39 neurons, 117 dendritic segments ; nControl Plasmid + Aβ = 49 neurons, 123 dendritic segments—6 biological replicates; nCD33KO = 27 neurons, 78 dendritic segments ; nCD33KO + Aβ = 28 neurons, 83 dendritic segments— 3 biological replicates; nCD45KO = 27 neurons, 79 dendritic segments ; nCD45KO + Aβ = 26 neurons, 78 dendritic segments—3 biological replicates; nCD33M = 19 neurons, 71 dendritic segments ; nCD33M + Aβ = 22 neurons, 81 dendritic segments—3 biological replicates; Statistical analyses were performed using Kruskal-Wallis test followed by Dunn's multiple comparisons. The tests were considered significant when $p < 0.05$ with the following criteria: * $p < 0.05$; ** $p < 0.01$; *** $p < 0.001$; **** $p < 0.0001$; ns, not significant. Color of the p value indicates to what the condition is compared to.

Supplemental Figures

Supplemental Figure S1

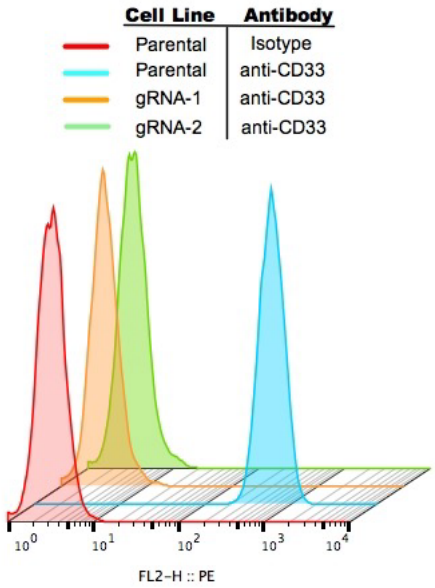

Supplemental Figure 1: CD33 expression was deleted from the THP- 1 cell line using Crispr/Cas9, and reduction in CD33 protein expression was validated by flow cytometry.

Supplemental Figure S2

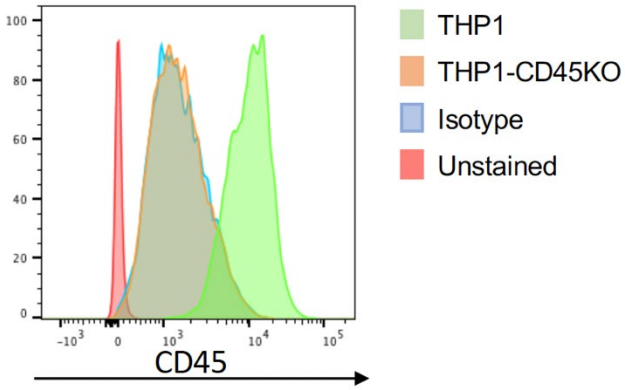

Supplemental Figure 2: CD45 expression was deleted from the THP- 1 cell line using Crispr/Cas9, and reduction in CD45 protein expression was validated by flow cytometry.

Supplemental Figure S3

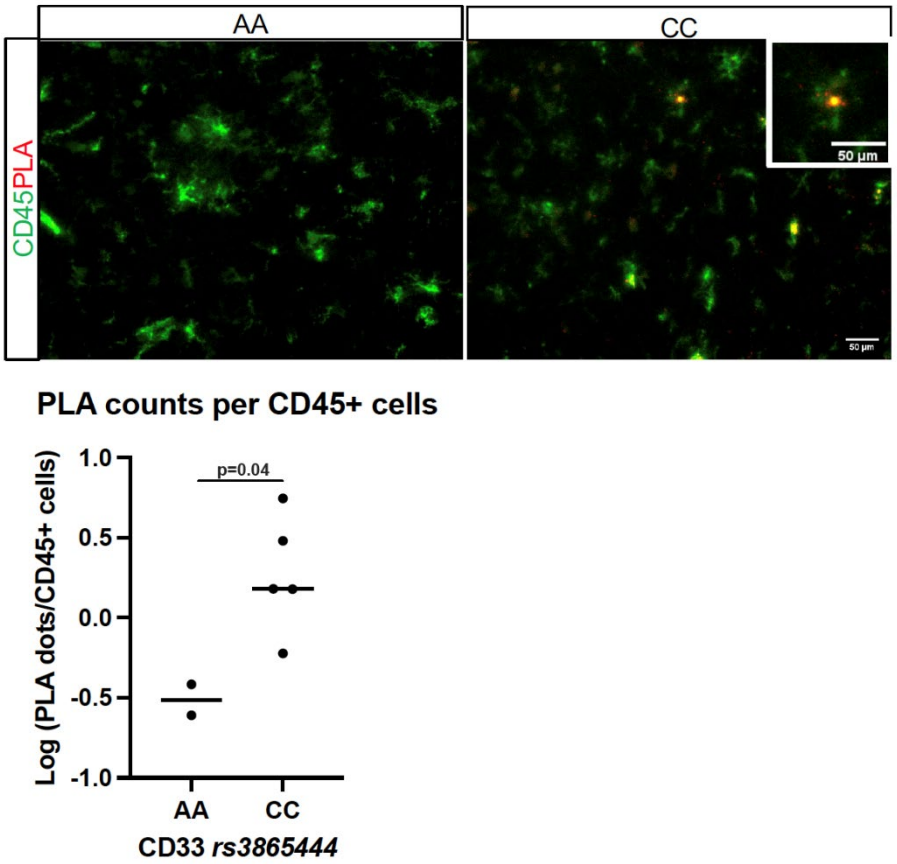

Supplemental Figure 3: CD45 and CD33 are in close enough proximity to be interacting *in situ* as detected by proximity ligation assay. Individuals with the CD33 homozygous protective genotype (N=2) have less CD33:CD45 interaction than individuals homozygous for the risk allele (N=5). Unpaired t-test of log transformation. One of the individuals with the protective genotype had diffuse Lewy body disease (DLBD) and the other had AD with Lewy body disease. The five individuals with the risk allele had the following diagnoses: 3 with AD and 2 with DLBD.

Supplemental Figure S4

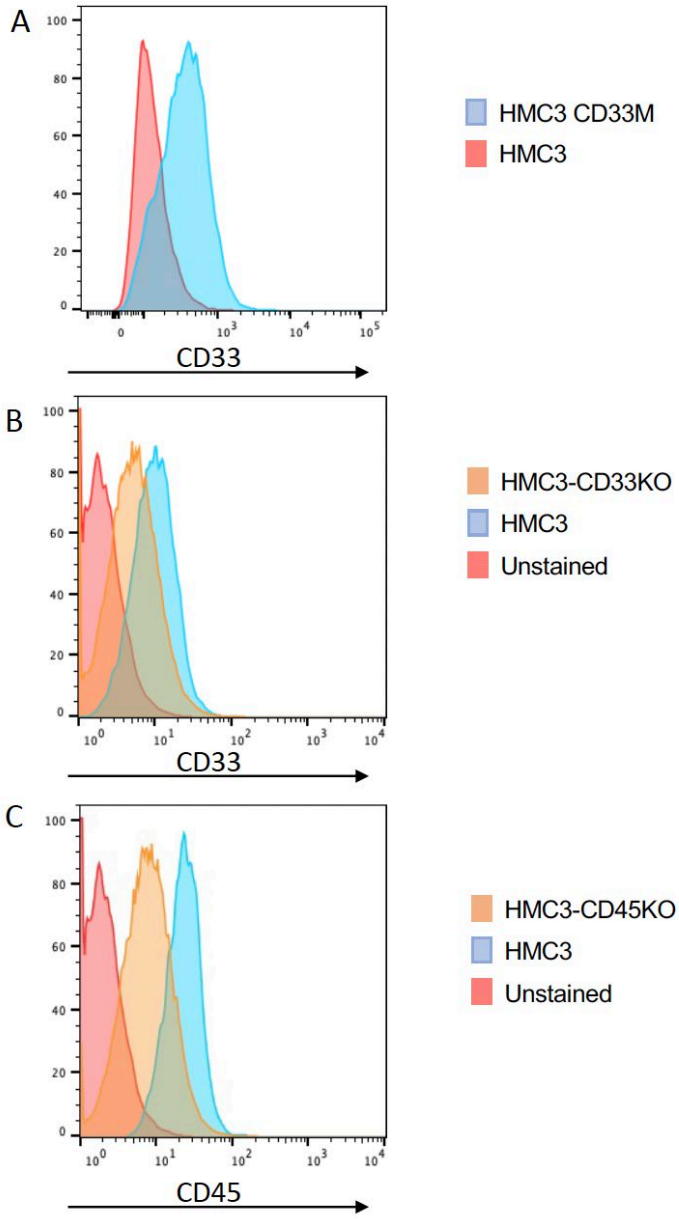

Supplemental Figure 4: (A) CD33M was overexpressed and **(B)** CD33 and **(C)** CD45 expression was deleted from the HMC3 cell line using Crispr/Cas9, and changes in CD33 or CD45 protein expression was validated by flow cytometry.

Materials and Methods

Cell culture (THP-1, monocytes, MDMi)

The THP-1 cell line was cultured in RPMI-1640 Glutamax (Life Technologies) medium containing 10% fetal bovine serum (FBS; Corning), 20 mM HEPES (Lonza), 1mM Sodium Pyruvate (Lonza), 1X MEM-NEAA (Life Technologies), and supplemented with 1% Penicillin-Streptomycin (Life Technologies).

PBMCs from healthy individuals from the PhenoGenetic Project or the New York Blood Center were selected based on their genotype for rs3865444. Informed consent was obtained from all human subjects. All blood draws and data analyses were done in compliance with protocols approved by the institutional review boards of each institution. PBMCs were separated by Lymphoprep gradient centrifugation (StemCell Technologies). PBMCs were frozen at a concentration of $1x10^7$ cells/ml in 10% dimethyl sulfoxide (DMSO; Sigma Aldrich) and 90% (v/v) fetal bovine serum (FBS; Corning). Before each study, aliquots of frozen PBMCs were thawed and washed in 10 ml of phosphate-buffered saline (PBS). Monocytes were positively collected from whole PBMCs using anti-CD14+ microbeads (Miltenyi Biotec) and plated at 1.5×10^5 cells per well in 96-well plates. To induce the differentiation of MDMi, we incubated monocytes under serum-free conditions using RPMI-1640 Glutamax (Life Technologies) with 1% Penicillin-Streptomycin (Life Technologies) and Fungizone (2.5 µg/ml; Life Technologies) and a mixture of the following human recombinant cytokines: M-CSF (10 ng/ml; Biolegend, 574806), GM-CSF (10 ng/ml, R&D Systems, 215-GM-010/CF), NGF-β (10 ng/ml, R&D Systems, 256-GF-100), CCL2 (100 ng/ml; Biolegend, 571404), and IL-34 (100 ng/ml; R&D Systems, 5265IL-010/CF) under standard humidified culture conditions (37°C, 5% CO_2) for 10 days[21].

Photo-crosslinking

Ac_4ManNDAz was prepared as described previously[15,16]. THP-1 cells were seeded at 0.4×10^6 cells/mL and cultured with DMSO or 0.1 mM Ac_4ManNDAz for 3 days (0.1% DMSO final concentration), harvested, and resuspended in ice cold PBS at 2.5 x 10^6 cells/mL. They were then irradiated for 10 mins at 365 nm on ice in clear 6-well plates (Corning) with a UV irradiator. Cells were then pelleted and lysed in RIPA buffer with protease and phosphatase inhibitors.

Immunoprecipitation (IP) and Mass Spectrometry (MS)

For MS experiments, 50 x 10^6 cells were harvested after Ac_4ManNDAz or DMSO treatment, irradiated or left untreated, and lysed as above. For immunoprecipitiation MS experiments, lysates (5 mg) were incubated with 25 ug of anti-CD33 antibody (WM-53, Biolegend) overnight with end-over-end rotation at 4°C. 250 µL of Protein G Dynabeads (Invitrogen) were resuspended, the supernatant was removed, and then the above lysate and antibody was added. After 8 hours with end-over-end rotation at 4°C, beads were washed three times with TBS, resuspended in 10µL of TBS, and immediately frozen at -80°C immediately until MS processing.

Protein digestion and labeling with TMT isobaric mass tags. The beads from immunopurification were washed once with IP lysis buffer, then three times with PBS. The lysates of each replicate were resuspended in 90µL digestion buffer (2M Urea, 50 mM Tris HCl) and 2µg of sequencing grade trypsin was added, with 1 hour shaking at 700rpm. The supernatant was removed and placed in a fresh tube. The beads were then washed twice with 50µL digestion buffer and combined with the supernatant. The combined supernatants were reduced (2µL 500 mM DTT, 30 minutes, RT), alkylated (4µL 500 mM IAA, 45 minutes, dark) and a longer overnight digestion performed: 2µg (4µL) trypsin, with shaking overnight. The samples were then quenched with 20µL 10% FA and desalted on 10mg Oasis cartridges. Desalted peptides were labeled with TMT10 reagents lot QL228730 (Thermo Fisher Scientific) according to the table below. Peptides were dissolved in 25µL of fresh 100mM HEPES buffer. The labeling reagent was resuspended in 42µL of acetonitrile and 10µL added to each sample as described below. After 1 h

incubation the reaction was stopped with 8µL of 5mM Hydroxylamine.

Protein identification with nanoLC–MS system. Reconstituted peptides were separated on an online nanoflow EASY-nLC 1000 UHPLC system (Thermo Fisher Scientific) and analyzed on a benchtop Orbitrap Q Exactive plus mass spectrometer (Thermo Fisher Scientific). The peptide samples were injected onto a capillary column (Picofrit with 10 µm tip opening / 75 µm diameter, New Objective, PF360-75-10-N-5) packed in-house with 20 cm C18 silica material (1.9 µm ReproSil-Pur C18-AQ medium, Dr. Maisch GmbH) and heated to 50 °C in column heater sleeves (Phoenix-ST) to reduce backpressure during UHPLC separation. Injected peptides were separated at a flow rate of 200 nL/min.

with a linear 230 min gradient from 100% solvent A (3% acetonitrile, 0.1% formic acid) to 30% solvent B (90% acetonitrile, 0.1% formic acid), followed by a linear 9 min gradient from 30% solvent B to 60% solvent

B and a 1 min ramp to 90%B. Each sample was run for 260 min, including sample loading and column equilibration times. The Q Exactive instrument was operated in the data-dependent mode acquiring HCD MS/MS scans (R=17,500) after each MS1 scan (R=70,000) on the 12 topmost abundant ions using an MS1 ion target of 3x 10^6 ions and an MS2 target of 5x10^4 ions. The maximum ion time utilized for the MS/MS scans was 120 ms; the HCD-normalized collision energy was set to 27; the dynamic exclusion time was set to 20s, and the peptide match and isotope exclusion functions were enabled.

Database search and data processing. All mass spectra were processed using the Spectrum Mill software package v6.0 pre-release (Agilent Technologies) which includes modules developed by the Carr laboratory for TMT10-based quantification. For peptide identification MS/MS spectra were searched against human Uniprot database to which a set of common laboratory contaminant proteins was appended. Search parameters included: ESI-QEXACTIVE-HCD scoring parameters, trypsin enzyme specificity with a maximum of two missed cleavages, 40% minimum matched peak intensity, +/- 20 ppm precursor mass tolerance, +/- 20 ppm product mass tolerance, and carbamidomethylation of cysteines and TMT6 labeling of lysines and peptide n-termini as fixed modifications.

Allowed variable modifications were oxidation of methionine, N-terminal acetylation, Pyroglutamic acid (N-termQ),Deamidated (N),Pyro Carbamidomethyl Cys (N-termC),with a precursor MH+ shift range of -18 to 64 Da. Identities interpreted for individual spectra were automatically designated as valid by optimizing score and delta rank1-rank2 score thresholds separately for each precursor charge state in each LC-MS/MS while allowing a maximum target-decoy-based false-discovery rate (FDR) of 1.0% at the spectrum level. TMT10 reporter ion intensities were corrected for isotopic impurities in the Spectrum Mill protein/peptide summary module using the afRICA correction method which implements determinant calculations according to Cramer's Rule[33] and correction factors obtained from the reagent manufacturer's certificate of analysis (https://www.thermofisher.com/order/catalog/product/90406) for lot number QL228730.

Proximity Ligation Assay (PLA)

The PLA assay was performed as per the manufacturer's instruction (Sigma Aldrich). Briefly, THP-1 cells, monocytes, or MDMi were fixed in 4% Paraformaldehyde (PFA) (Electron Microscopy Sciences) for 15 minutes at room temperature. They were then permeabilized in PBS containing 1% Triton X-100 (Sigma

Aldrich) for 15 minutes before being blocked by 10% normal goat serum in PBS with 1% Triton for 30 minutes.

In the first antibody incubation, rabbit anti-human CD33 (Sigma Aldrich, HPA035832, 1:400) and mouse anti-human CD45 (Novus, NB500-319, 1: 400), were performed overnight at 4°C. After two washes with buffer A (Sigma Aldrich), secondary antibodies conjugated with oligonucleotides (PLA probe MINUS and PLA probe PLUS, Sigma Aldrich) were added to the reaction and incubated for one hour. The samples were then washed with Buffer A two times. The Ligation solution, consisting of two oligonucleotides and Ligase, was added and the oligonucleotides hybridized to the two PLA probes. Then the samples were washed with Buffer A two more times. The Amplification solution, consisting of nucleotides and fluorescently labeled oligonucleotides, were added together with the polymerase. The oligonucleotide arm of one of the PLA probes acts as a primer for a rolling-circle amplification (RCA) reaction using the ligated circle as a template, generating a concatemeric (repeated sequence) product. The fluorescently labeled oligonucleotides will hybridize to the RCA product. The samples were washed with Buffer B and then mounted with Duolink In Situ Mounting Medium with DAPI (Sigma Aldrich).

The signal is visible as a distinct fluorescent spot and analyzed by confocal (Zeiss LSM 700) and fluorescence (Zeiss Axio) microscopies.

In Situ PLA

Autopsy tissue was obtained from the New York Brain Bank at Columbia University (**Supplemental Table 3**). Samples were collected in compliance with protocols approved by the Columbia Human Research Committee. The genotype for CD33 was determined using Custom Taqman SNP Genotyping Assay (ThermoFisher Scientific, Assay ID AHLJYS8) on the QuantStudio 7 Flex Real-Time PCR System. The frozen tissues were thawed at room temperature for 10 min after being taken from the -80°C freezer. The tissues were fixed with pre-cooled 100% ethanol at -20°C for 15 min. After being washed three times with PBS, the tissues were immersed in PBS for 10 min. and then blocked in 3% BSA with 0.1% Triton-X for 1 hr. Tissues were washed three times for 5 min each in PBS. Incubation with primary antibodies was performed overnight at 4°C in 1% BSA. The PLA secondary probes were diluted 1:5 in antibody diluent and incubated for 20 min at room temperature. The samples were washed three times with PBS. The slides

were incubated in the probe mixture at 37^{0}C for 1.5 hours in a humidified chamber, followed by washing with DuoLink buffer A two times and incubation with ligation solution at 37^{0}C for

1.5 hours in a humidified chamber and washed with Buffer A two times for 10 min at room temperature. The slides were then incubated with amplification-polymerase solution at 37^{0}C for 100 min. in a humidified chamber and washed with Buffer B two times for 10 min in room temperature. To identify microglia, slides were incubated with anti-CD45 (Novus, MEM-28) at a 1:100 dilution for 1.5 hours and washed three times in PBS followed by an incubation with the secondary antibody for 1 hour and washed three times with PBS. Slides were incubated with Sudan Black B (1% w/v in 100% ethanol, Sigma Aldrich) for 3 min to quench the autofluorescence and washed three times with PBS. Finally, the sections were mounted with Duolink In Situ Mounting Medium with DAPI and imaged with an immunofluorescence microscope.

Knockout Cell Generation

THP-1-Cas9 or HMC3-Cas9 expressing cells were generated via lentiviral integration and blasticidin selection of single cell clones using the Lenti-Cas9-Blast plasmid (Addgene 52962). gRNAs for CD33 and CD45 were designed using the Broad GPP webportal and cloned into the pLKO-sgRNA-EFS-GFP vector (52962) using established protocols[34]. Non-integrating lentiviruses where then generated using Lenti-X Packaging Single Shots (Clontech) and used to infect the above cells. Infection and deletion were assessed using GFP and cell-surface staining. Knockout cells thereby generated were then sorted by flow cytometry and single cell clones were generated by limiting dilution.

gRNA:

CD33 CRISPR F1 Sequence: GCCACTCACCTGCCCACAGC

CD33 CRISPR R1 Sequence: GGCTACTGCTGCCCCTGCTG

CD45 CRISPR F1: CACCGGAAACTTGCTGAACACCCG

CD45 CRISPR R1: AAACCGGGTGTTCAGCAAGTTTCC

CD33 Mutant Cell Lines

A CD33 encoding lentivirus was obtained from Origene (RC207023L1) and various CD33 mutants were made (R119K, Y340F, Y358F, and Y340F/Y358F) using the Q5 SiteDirected Mutagenesis Kit (New England Biolabs). Lentiviruses were then transfected into CD33 KO cells and cells with similar expression levels were then sorted using flow cytometry.

Primers:

R119K F Primer: ATACTTCTTTAAGATGGAGAGAGGAAG

R119K Reverse: GAACCATTATCCCTCCTC

Y340F F: GGAGCTGCATTTTGCTTCCCTCA

Y340F R: TCATCCATCTCCACAGTAGG

Y358F F: CTCCACCGAATTCTCAGAGGTCAG

Y358F R: GTGTCCTTGGAAGGATTCATC

Phosphatase Activity Assay

5 x 10^5 THP-1, THP-1 CD33KO, THP-1 CD33R119K, or THP-1 CD33WT cells were pre-incubated with or without LPS (10 ng/ml) (Invitrogen) at 37°C for 18h and CD45 phosphatase activity was determined essentially as described[35]. Briefly, cells were washed with ice-cold PBS and lysed in Ph lysis buffer (20nM HEPES (Fisher scientific), pH 7.2, 2 mM EDTA (Invitrogen), 2 mM dithiothreitol (Sigma Aldrich), 1% Nonidet P40 Substitute solution (Sigma Aldrich) and 10% (v/v) Glycerol (Sigma Aldrich) containing complete, Mini, EDTA-free Protease Inhibitor Cocktail (Roche). Cellular debris and nuclear material were removed by centrifugation at 20,000 x g for 15 min at 4°C. Phosphatase activity was determined by incubation of 20 g of lysed proteins for 4h at 37°C with 1 mg/ml 4-Nitrophenyl phosphate disodium salt hexahydrate (Sigma Aldrich) in CD45 Ph assay buffer (100 nM HEPES, pH 7.2, 2 mM EDTA and 2 mM dithiothreitol). The resulting color change was assessed at 410 nm.

Amyloid-beta Treatment

The $A\beta_{1-42}$was reconstituted in 1% of NH_4OH in MilliQ water for 10 min at RT. Then, the solution was incubated at 37°C for 1 week with rotation. Cells at a concentration of 1x10^6 were incubated with 250nM aggregated amyloid beta in RPMI medium for 24 h at 37°C. Then the cells were washed with PBS two times before analysis by PLA.

Primary Cortical Culture

Cortices from E15.5 mouse embryos, from timed pregnant CD1 mice (Crl:CD1(ICR)) obtained from Charles River, were dissected and electroporated, followed by dissociation in complete Hank's balanced salt solution (cHBSS) containing papain (Worthington) and DNase I (100µg/mL, Sigma) for 15 minutes at 37ºC, washed three times, and manually triturated in DNase I (100µg/mL) containing neurobasal medium (Life

Technology) supplemented with B27 (1x, Thermo Fischer Scientific), FBS (2.5% Gibson), N2 (1x, Thermo Fischer Scientific), and GlutaMax (2mM, Gibco). Cells were plated at 1.0 x 10^5 cells per 35mm glass bottom dish (MatTek) that had been coated with poly-D-lysine (1mg/mL, Sigma) over night. One-half of the medium was changed every 5-7 days thereafter with non-FBS containing medium, and maintained for 20-22 days at 37ºC in 5% CO_2.

***Ex utero* Electroporation**

Ex utero electroporation of mouse dorsal telencephalic progenitors was performed as previously described[30] by injecting plasmid DNA (1-2 µg/µL endotoxin-free plasmid DNA, Midi prep kit from Macherey-Nagel) plus 0.5% Fast Green (1:20 ratio, Sigma) using the picospritzer III (Parker) microinjector into the lateral ventricles of isolated E15.5 embryonic heads that were decapitated and placed in complete HBSS[36]. Electroporations were performed on the whole head (skin and skull intact) with gold-coated electrodes (GenePads 5 × 7 mm BTX) using an ECM 830 electroporator (BTX) and the following parameters: five 100 ms long pulses separated by 100 ms long intervals at 20 V. Immediately after electroporation, cortices were prepared for primary neuronal culture.

Primary Cortical and Human Microglia cell line Co-Culture

HMC3 grown at 37ºC in 5% CO_2 in complete MEM containing FBS (10%, Gibson) with Pen-Strep (2%, Gibco) (and for the $CD33^M$ line neomycin solution (2%, Santa Cruz)) were dissociated using Trypsin-EDTA (0.05%, Gibco), counted, and plated drop-wise onto 19DIV electroporated primary cortical mouse neurons, as described above, at 200,000 2.0 x 10^5 cells per 35mm glass bottom dish (MatTek).

Aβ1-42 Stock Preparation

HiLyte™ Fluor 647 - labeled Beta - Amyloid1-42 (AnaSpec) was reconstituted in 50µL Ammonia Hydroxide and 3950 ul RPMI-1640 Glutamax (Life Technologies) medium. The stock was stored in -80 ºC.

Imaging

Imaging of dissociated neurons was performed between 20-22 DIV in 1,024 x 1,024 resolution with a Nikon Ti-E microscope equipped with A1R laser-scanning confocal microscope using the Nikon software NIS-elements (Nikon, Melville, NY, USA). We used the following objectives (Nikon): 40x (for analysis of microglial consumption) and 60x Apo TIRF; NA 1.49 (for analysis of spine densities of cultured neurons).

Analysis of Spine Density

Dendritic spine densities were estimated on secondary or tertiary dendritic branches for cultured neurons using Fiji software (ImageJ, NIH). Spines were quantified over an average of 40μm in cultures, between 2-3 segments per cell. Spine density was defined as the number of quantified spines divided by the length over which the spines were quantified.

Analysis of Microglial Consumption

Using Nikon software NIS-elements (Nikon, Melville, NY, USA), a binary threshold for each individual channel (FITC = Glia, Cy5 = Aβ) was set for each z-slice imaged. Upon binarization, the area occupied by signal was quantified in μm^2 for each channel individually for each z-slice. Subsequently, the area of any co-localization between the FITC channel and Cy5 channel for each z-slice was quantified in μm^2. In doing so, a 3D volumetric representation of each microglia was captured as a series of 2D area slices, in addition to a 3D volumetric representation of the Aβ. The total volume of microglial space, represented by stacked 2D area, occupied by Aβ (Cy5) was then calculated by taking the 2D area of co-localization—i.e., the area of space occupied by all Aβ signal within a single z-slice—and dividing it by the total possible 2D area—i.e., the area of space occupied by all microglia within a single z-slice—of the microglial population, and repeating for each z-slice for the image. This produces a curve representative of the area of 3D microglial space occupied by Aβ.

Acknowledgements

The authors are grateful to the participants of the NYBC and NYBB for the time and specimens that they contributed. We would like to thank Franck Polleux for his support and advice. Research reported in this publication was performed in the Cytometry Core of the Columbia Center for Translational Immunology (CCTI) Flow Cytometry Core, supported in part by the Office of the Director, National Institutes of Health under awards S10RR027050. We thank the Columbia University Alzheimer's Disease Research Center, funded by NIH grant P30AG066462 to S.A. Small (P.I.), and A. Teich for providing biological samples and associated information. This work was supported by the US National Institutes of Health grants RF1AG058852, R01AG043617, R01GM090271, U01AG046152, R01AG048015, and T32AI148099. The content is solely the responsibility of the authors and does not necessarily represent the official views of the National Institutes of Health.

Author Contributions

N.V., C.R., D.M.V. and E.M.B. implemented the study and wrote the manuscript, and all authors read and edited the manuscript. Mass spectrometry experiments were designed and executed by C.R., P.L.D., G.G., J.J.K., M.S., S.A.C, and E.M.B. N.V., M.T., S.M.C., M.R., S.C., and E.M.B designed and conducted the PLA experiments. N.V., W.E., and E.M.B., designed and conducted the phosphatase experiments. D.M.V., N.V., W.E., and E.M.B. designed and conducted the co-culture experiments.

References

1. Andrews RG, Torok-Storb B, Bernstein ID. Myeloid-associated differentiation antigens on stem cells and their progeny identified by monoclonal antibodies. *Blood*. Jul 1983;62(1):124-32.
2. Nakamura Y, Noma M, Kidokoro M, et al. Expression of CD33 antigen on normal human activated T lymphocytes. *Blood*. Mar 1 1994;83(5):1442-3.
3. Olah M, Patrick E, Villani AC, et al. A transcriptomic atlas of aged human microglia. *Nature communications*. Feb 7 2018;9(1):539. doi:10.1038/s41467-018-02926-5
4. Crapser JD, Arreola MA, Tsourmas KI, Green KN. Microglia as hackers of the matrix: sculpting synapses and the extracellular space. *Cell Mol Immunol*. 11 2021;18(11):2472-2488. doi:10.1038/s41423-021-00751-3
5. Waltl I, Kalinke U. Beneficial and detrimental functions of microglia during viral encephalitis. *Trends Neurosci*. 02 2022;45(2):158-170. doi:10.1016/j.tins.2021.11.004
6. Estus S, Shaw BC, Devanney N, Katsumata Y, Press EE, Fardo DW. Evaluation of CD33 as a genetic risk factor for Alzheimer's disease. *Acta neuropathologica*. Aug 2019;138(2):187-199. doi:10.1007/s00401-019-02000-4
7. Hollingworth P, Harold D, Sims R, et al. Common variants at ABCA7, MS4A6A/MS4A4E, EPHA1, CD33 and CD2AP are associated with Alzheimer's disease. *Nat Genet*. May 2011;43(5):429-35. doi:10.1038/ng.803
8. Naj AC, Jun G, Beecham GW, et al. Common variants at MS4A4/MS4A6E, CD2AP, CD33 and EPHA1 are associated with late-onset Alzheimer's disease. *Nat Genet*. May 2011;43(5):436-41. doi:10.1038/ng.801

9. Bradshaw EM, Chibnik LB, Keenan BT, et al. CD33 Alzheimer's disease locus: altered monocyte function and amyloid biology. Research Support, N.I.H., Extramural Research Support, Non-U.S. Gov't. *Nature neuroscience*. Jul 2013;16(7):848-50. doi:10.1038/nn.3435

10. Raj T, Ryan KJ, Replogle JM, et al. CD33: increased inclusion of exon 2 implicates the Ig V-set domain in Alzheimer's disease susceptibility. *Hum Mol Genet*. Jan 12 2014;doi:10.1093/hmg/ddt666

11. Chan G, White CC, Winn PA, et al. CD33 modulates TREM2: convergence of Alzheimer loci. *Nat Neurosci*. Nov 2015;18(11):1556-8. doi:10.1038/nn.4126

12. Malik M, Simpson JF, Parikh I, et al. CD33 Alzheimer's risk-altering polymorphism, CD33 expression, and exon 2 splicing. *The Journal of neuroscience : the official journal of the Society for Neuroscience*. Aug 14 2013;33(33):13320-5. doi:10.1523/jneurosci.1224-13.2013

13. Freeman SD, Kelm S, Barber EK, Crocker PR. Characterization of CD33 as a new member of the sialoadhesin family of cellular interaction molecules. *Blood*. Apr 15 1995;85(8):2005-12.

14. Brinkman-Van der Linden EC, Varki A. New aspects of siglec binding specificities, including the significance of fucosylation and of the sialyl-Tn epitope. Sialic acid-binding immunoglobulin superfamily lectins. *The Journal of biological chemistry*. Mar 24 2000;275(12):8625-32.

15. Bond MR, Zhang H, Vu PD, Kohler JJ. Photocrosslinking of glycoconjugates using metabolically incorporated diazirine-containing sugars. *Nat Protoc*. 2009;4(7):1044-63. doi:10.1038/nprot.2009.85

16. Tanaka Y, Kohler JJ. Photoactivatable crosslinking sugars for capturing glycoprotein interactions. *J Am Chem Soc*. Mar 19 2008;130(11):3278-9. doi:10.1021/ja7109772

17. Hopperton KE, Mohammad D, Trepanier MO, Giuliano V, Bazinet RP. Markers of microglia in post-mortem brain samples from patients with Alzheimer's disease: a systematic review. *Molecular psychiatry*. Feb 2018;23(2):177-198. doi:10.1038/mp.2017.246

18. Mukherjee S, Perumal TM, Daily K, et al. Identifying and ranking potential driver genes of Alzheimer's disease using multiview evidence aggregation. *Bioinformatics*. Jul 15 2019;35(14):i568-i576. doi:10.1093/bioinformatics/btz365

19. Zhu Y, Hou H, Rezai-Zadeh K, et al. CD45 deficiency drives amyloid-beta peptide oligomers and neuronal loss in Alzheimer's disease mice. *The Journal of neuroscience: the official journal of the Society for Neuroscience*. Jan 26 2011;31(4):1355-65. doi:10.1523/jneurosci.3268-10.2011

20. Crocker PR, Paulson JC, Varki A. Siglecs and their roles in the immune system. *Nat Rev Immunol*. Apr 2007;7(4):255-66. doi:nri2056 [pii] 10.1038/nri2056

21. Ryan KJ, White CC, Patel K, et al. A human microglia-like cellular model for assessing the effects of neurodegenerative disease gene variants. *Science translational medicine*. Dec 20 2017;9(421)doi:10.1126/scitranslmed.aai7635

22. Taylor VC, Buckley CD, Douglas M, Cody AJ, Simmons DL, Freeman SD. The myeloid-specific sialic acid-binding receptor, CD33, associates with the protein-tyrosine phosphatases, SHP-1 and SHP-2. *The Journal of biological chemistry*. Apr 23 1999;274(17):11505-12.

23. Crocker PR, Redelinghuys P. Siglecs as positive and negative regulators of the immune system. *Biochem Soc Trans*. Dec 2008;36(Pt 6):1467-71. doi:10.1042/bst0361467

24. Griciuc A, Serrano-Pozo A, Parrado AR, et al. Alzheimer's disease risk gene CD33 inhibits microglial uptake of amyloid beta. Research Support, N.I.H., Extramural Research Support, Non-U.S. Gov't. *Neuron*. May 22 2013;78(4):631-43. doi:10.1016/j.neuron.2013.04.014

25. Scheff SW, Price DA, Schmitt FA, Mufson EJ. Hippocampal synaptic loss in early Alzheimer's disease and mild cognitive impairment. *Neurobiology of aging*. Oct 2006;27(10):1372-84. doi:10.1016/j.neurobiolaging.2005.09.012

26. Jackson J, Jambrina E, Li J, et al. Targeting the Synapse in Alzheimer's Disease. *Front Neurosci*. 2019;13:735. doi:10.3389/fnins.2019.00735

27. Hong S, Beja-Glasser VF, Nfonoyim BM, et al. Complement and microglia mediate early synapse loss in Alzheimer mouse models. *Science*. May 6 2016;352(6286):712-716. doi:10.1126/science.aad8373

28. Paolicelli RC, Jawaid A, Henstridge CM, et al. TDP-43 Depletion in Microglia Promotes Amyloid Clearance but Also Induces Synapse Loss. *Neuron*. Jul 19 2017;95(2):297-308 e6. doi:10.1016/j.neuron.2017.05.037

29. Shi Q, Chowdhury S, Ma R, et al. Complement C3 deficiency protects against neurodegeneration in aged plaque-rich APP/PS1 mice. *Science translational medicine*. May 31 2017;9(392) doi:10.1126/scitranslmed.aaf6295

30. Courchet J, Lewis TL, Lee S, et al. Terminal axon branching is regulated by the LKB1-NUAK1 kinase pathway via presynaptic mitochondrial capture. *Cell*. Jun 20 2013;153(7):1510-25. doi:10.1016/j.cell.2013.05.021

31. Meyer-Dilhet G, Courchet J. In Utero Cortical Electroporation of Plasmids in the Mouse Embryo. *STAR Protoc*. 06 19 2020;1(1):100027. doi:10.1016/j.xpro.2020.100027

32. Lee A, Kondapalli C, Virga DM, et al. Aβ42 oligomers trigger synaptic loss through CAMKK2-AMPK-dependent effectors coordinating mitochondrial fission and mitophagy. *Nat Commun*. 08 01 2022;13(1):4444. doi:10.1038/s41467-022-32130-5

33. Shadforth IP, Dunkley TP, Lilley KS, Bessant C. i-Tracker: for quantitative proteomics using iTRAQ. *BMC Genomics*. Oct 20 2005;6:145. doi:10.1186/1471-21646-145

34. Institute B. https://portals.broadinstitute.org/gpp/public/resources/protocols

35. van Vliet SJ, Gringhuis SI, Geijtenbeek TB, van Kooyk Y. Regulation of effector T cells by antigen-presenting cells via interaction of the C-type lectin MGL with CD45. *Nature immunology*. Nov 2006;7(11):1200-8. doi:10.1038/ni1390

36. Polleux F, Ghosh A. The slice overlay assay: a versatile tool to study the influence of extracellular signals on neuronal development. *Sci STKE*. Jun 11 2002;2002(136):pl9. doi:10.1126/stke.2002.136.pl9

37. Hollingworth P, Harold D, Sims R, et al. Common variants at ABCA7, MS4A6A/MS4A4E, EPHA1, CD33 and CD2AP are associated with Alzheimer's disease. Meta-Analysis Research Support, N.I.H., Extramural Research Support, Non-U.S. Gov't. *Nature genetics*. May 2011;43(5):429-35. doi:10.1038/ng.803

38. Terry RD, Masliah E, Salmon DP, et al. Physical basis of cognitive alterations in Alzheimer's disease: synapse loss is the major correlate of cognitive impairment. *Ann Neurol*. Oct 1991;30(4):572-80. doi:10.1002/ana.410300410

39. Masliah E, Mallory M, Hansen L, et al. Immunoreactivity of CD45, a protein phosphotyrosine phosphatase, in Alzheimer's disease. *Acta neuropathologica*. 1991;83(1):12-20.

40. Penninger JM, Irie-Sasaki J, Sasaki T, Oliveira-dos-Santos AJ. CD45: new jobs for an old acquaintance. *Nature immunology*. May 2001;2(5):389-96. doi:10.1038/87687